



UNIVERSITAT DE
BARCELONA

Engineered functional skeletal muscle tissues for *in vitro* studies

Xiomara Gislen Fernández Garibay

ADVERTIMENT. La consulta d'aquesta tesi queda condicionada a l'acceptació de les següents condicions d'ús: La difusió d'aquesta tesi per mitjà del servei TDX (www.tdx.cat) i a través del Dipòsit Digital de la UB (diposit.ub.edu) ha estat autoritzada pels titulars dels drets de propietat intel·lectual únicament per a usos privats emmarcats en activitats d'investigació i docència. No s'autoritza la seva reproducció amb finalitats de lucre ni la seva difusió i posada a disposició des d'un lloc aliè al servei TDX ni al Dipòsit Digital de la UB. No s'autoritza la presentació del seu contingut en una finestra o marc aliè a TDX o al Dipòsit Digital de la UB (framing). Aquesta reserva de drets afecta tant al resum de presentació de la tesi com als seus continguts. En la utilització o cita de parts de la tesi és obligat indicar el nom de la persona autora.

ADVERTENCIA. La consulta de esta tesis queda condicionada a la aceptación de las siguientes condiciones de uso: La difusión de esta tesis por medio del servicio TDR (www.tdx.cat) y a través del Repositorio Digital de la UB (diposit.ub.edu) ha sido autorizada por los titulares de los derechos de propiedad intelectual únicamente para usos privados enmarcados en actividades de investigación y docencia. No se autoriza su reproducción con finalidades de lucro ni su difusión y puesta a disposición desde un sitio ajeno al servicio TDR o al Repositorio Digital de la UB. No se autoriza la presentación de su contenido en una ventana o marco ajeno a TDR o al Repositorio Digital de la UB (framing). Esta reserva de derechos afecta tanto al resumen de presentación de la tesis como a sus contenidos. En la utilización o cita de partes de la tesis es obligado indicar el nombre de la persona autora.

WARNING. On having consulted this thesis you're accepting the following use conditions: Spreading this thesis by the TDX (www.tdx.cat) service and by the UB Digital Repository (diposit.ub.edu) has been authorized by the titular of the intellectual property rights only for private uses placed in investigation and teaching activities. Reproduction with lucrative aims is not authorized nor its spreading and availability from a site foreign to the TDX service or to the UB Digital Repository. Introducing its content in a window or frame foreign to the TDX service or to the UB Digital Repository is not authorized (framing). Those rights affect to the presentation summary of the thesis as well as to its contents. In the using or citation of parts of the thesis it's obliged to indicate the name of the author.



UNIVERSITAT DE
BARCELONA

Doctoral thesis

Engineered functional skeletal muscle tissues for *in vitro* studies

Xiomara Gislen Fernández Garibay

Engineered functional skeletal muscle tissues for *in vitro* studies

Memòria presentada per optar al grau de doctor per la
Universitat de Barcelona

Programa de Doctorat en **Nanociències**



Autora: **Xiomara Gislen Fernández Garibay**

Director:

Prof. Javier Ramón Azcón

Tutor:

Prof. Josep Samitier Martí



UNIVERSITAT DE
BARCELONA



Institute for Bioengineering of Catalonia

The research presented in this thesis was carried out in the Biosensors for Bioengineering group at the Institute for Bioengineering of Catalonia (IBEC), in Barcelona Spain, and received funding from the European Research Council program under the grant ERC-StG-DAMOC (714317) and a predoctoral fellowship (BES-2016-076681) from the Spanish Ministry of Economy and Competitiveness (MINECO).

ACKNOWLEDGEMENTS

Ahora que el resto está escrito, me queda agradecer a las personas que formaron parte de esta etapa, dentro y fuera de lo académico. Gracias a todos.

A mi director de tesis, Javi, gracias por haber confiado en mí desde el inicio de los “Ramones”. Gracias por la guía, el apoyo y por siempre tener las puertas abiertas para nosotros. Por recordarnos la importancia del equilibrio entre la ciencia y todo lo demás.

A Juanma, por haberme guiado desde tu llegada al laboratorio. He aprendido mucho de ti como científico y persona en estos años. Gracias por animarme a celebrar los pequeños éxitos y por la motivación en los momentos que más he necesitado.

Gracias a Ferran por ser el mejor compañero de PhD, de real and fake science. Gracias por escucharme, por compartir las penas y risas después de cada experimento fallido. Creo que fueron pocos los días en los que no hubieron risas. No terminaría de escribir cada anécdota. Gracias. También a Elsie (Laura) que llegó a completar nuestro grupo de predocs. Gracias por ser única, por tu amistad y por tantas conversaciones y momentos especiales.

A TODOS los “Ramones” de ayer y hoy. Gracias. No quiero imaginarme cómo habría sido el doctorado sin el ambiente tan cercano y agradable de nuestro grupo. A Mariale, Àlex, Jordina y Albert, por todo lo que han contribuido a este trabajo. Mariale, gracias por guiarme, por tus consejos, cariño y por hacerme sentir en familia. Àlex, por tu buen humor que dejó huella en nuestro grupo. Jur, gracias por las charlas y porque trabajar contigo siempre fue muy agradable. Albert, gracias por tu amistad y todos los momentos que compartimos. Muchísimas gracias a todos los integrantes actuales de Muscle, Islet, BLOC, Biosensors y Liver team por su apoyo y palabras de ánimo durante la escritura.

Agradezco a los coautores de los artículos presentados en esta tesis. Ha sido un placer colaborar con todos ustedes. Gracias a los investigadores de i3Bs por recibirme en Portugal, por su tiempo y dedicación. Muchas gracias a mi tutor Josep Samitier, Andrea García, Elena Martínez y a todos los miembros de Biomimetic Systems for Cell Engineering (IBEC) por haber ayudado a dar forma a este proyecto y por el apoyo durante estos años.

Gracias a los amigos que fueron gran apoyo moral durante el doctorado, en las buenas y en las malas, desde cerca o a la distancia. Clara, Léa, Michou, Valeria, Almita, Katerin, Chiara, César y Rafa. ¡Gracias!

Por último, quiero dedicar esta tesis a mi familia, Mamá, papá, tía Dora, Adrian, Diana y Valeria. Gracias por apoyarme siempre y por estar junto a mí. Los quiero mucho.

TABLE OF CONTENTS

ACKNOWLEDGEMENTS	5
TABLE OF CONTENTS	7
PROLOGUE	13
AUTHOR'S CONTRIBUTIONS	15
ABSTRACT	21
LIST OF ABBREVIATIONS.....	25
Chapter 1. INTRODUCTION	29
1.1. Tissue engineering for <i>in vitro</i> research.....	31
1.1.1. The basic paradigm of tissue engineering.....	31
The native extracellular matrix	32
1.1.2. Tissue-engineered 3D cell culture platforms	33
Conventional cell-based assays and animal models	33
Microenvironmental cues in 2D vs. 3D cell culture	35
Biomaterials for 3D cell culture	36
1.1.3. Hydrogels as scaffolds for tissue engineering	36
Hydrogel compositions: natural vs. synthetic	37
Critical features of hydrogels for 3D cell culture.....	38
Hydrogel formation: chemical or physical crosslinking	39
Hydrogel microfabrication strategies	41
1.2. The skeletal muscle tissue	44
1.2.1. Anatomy and physiology.....	44
Cellular structure of the skeletal muscle	44
Contraction and force generation.....	46
1.2.2. Skeletal muscle development	47
1.2.3. Composition of the skeletal muscle extracellular matrix	48
1.2.4. Skeletal muscle metabolism	49
Energy metabolism.....	49
Insulin resistance and type 2 diabetes	49
Skeletal muscle as an endocrine organ	51
1.2.5. Muscular dystrophies.....	55
Myotonic dystrophy type 1.....	56
1.3. Skeletal muscle tissue <i>in vitro</i> models	59
1.3.1. Cell sources.....	65
C2C12 murine myoblasts	65
Human primary muscle stem cells	65
Immortalized human muscle precursor cells.....	66
Transdifferentiated human fibroblasts.....	66
Human pluripotent stem cells (hPSCs)-derived myoblasts.....	66
1.3.2. Microfabricated topographical cues for 2D cell culture models of skeletal muscle	67
1.3.3. Tissue-engineered <i>in vitro</i> 3D models.....	69
Murine 3D skeletal muscle models	70
Human 3D skeletal muscle models.....	72
Engineered human skeletal muscles for drug screening platforms	74
1.3.4. Modeling muscular dystrophies <i>in vitro</i>	75

Chapter 2. OBJECTIVES	79
Chapter 3. MATERIALS AND METHODS	83
3.1. Cell culture	85
3.1.1. Murine myoblasts cell culture.....	85
3.1.2. Human immortalized fibroblasts cell culture	86
3.1.3. Human immortalized muscle satellite stem cells culture.....	86
3.2. Composite hydrogels as scaffolds for skeletal muscle tissue engineering	87
3.2.1. Synthesis and characterization of prepolymer precursors	87
Synthesis of gelatin methacryloyl.....	87
Synthesis of carboxymethyl cellulose methacrylate.....	87
Colorimetric TNBSA assay.....	88
Nuclear magnetic resonance (NMR)	89
3.2.2. Preparation of prepolymer solutions.....	89
3.2.3. Physical characterization of composite hydrogels	89
Swelling analysis	89
Degradation analysis.....	90
Mechanical analysis	90
Scanning electron microscopy imaging and pore size analysis.....	91
3.3. C2C12 cell culture in composite hydrogels for 3D bioprinting of skeletal muscle tissue	92
3.3.1. Preparation of cell-laden prepolymer solutions	92
3.3.2. Cell metabolic activity under different GelMA hydrogel fabrication conditions	92
3.3.3. Cell viability and proliferation in 3D composite hydrogels.....	93
Cell viability assay	93
Cell proliferation in 3D composite hydrogels.....	94
3.3.4. 3D Bioprinting of cell-laden composite hydrogels and differentiation into myotubes.....	94
3.3.5. Myotube alignment and fusion index analysis	95
3.3.6. Statistical analysis	95
3.4. Skeletal muscle tissue formation in photomold patterned hydrogels.....	95
3.4.1. Fabrication of microstructured PDMS stamps	96
Microfabrication of silicon molds	96
Replica molding of microstructured PDMS stamps.....	96
3.4.2. C2C12 encapsulation in micropatterned hydrogels	96
3.4.3. Cell viability and morphology in micropatterned hydrogels.....	97
3.4.4. Immunofluorescence staining	98
3.5. Fabrication of myotonic dystrophy type 1 (DM1) human skeletal muscle microtissues	98
3.5.1. Glass coverslip functionalization	98
3.5.2. Human fibroblasts encapsulation	99
3.5.3. Cell viability assay	99
3.5.4. Antisense oligonucleotide treatment	99
3.5.5. Fluorescence <i>in situ</i> hybridization	100
3.5.6. Immunofluorescence staining	100
3.5.7. Fusion index and myotube size analysis.....	101
3.5.8. RNA extraction, RT-PCR, and real-time PCR	101
3.5.9. Western blotting.....	103

3.5.10.	Statistical analysis	103
3.6.	Human platelet lysate-based nanocomposite hydrogels for skeletal muscle tissue engineering	104
3.6.1.	Fabrication of the hydrogel casting platforms.....	104
	Fabrication of the master mold.....	104
	Fabrication of the negative mold	104
	Replica molding of PDMS platforms	105
3.6.2.	Preparation of the nanocomposite hydrogel (HUgel).....	105
	Preparation of HUgel precursors.....	105
	Cell encapsulation by HUgel casting in PDMS platforms	106
3.6.3.	Immunofluorescence staining	106
3.6.4.	Electrical Pulse Stimulation.....	107
3.6.5.	Imaging.....	107
3.6.6.	Force measurements.....	107
3.6.7.	Statistical analysis	108
Chapter 4.	RESULTS.....	109
4.1.	Composite Biomaterials as Long-Lasting Scaffolds for 3D Bioprinting of Highly Aligned Muscle Tissue	111
4.1.1.	Introduction.....	112
4.1.2.	Experimental procedure.....	114
	Synthesis of polymer precursors.....	114
	Nuclear Magnetic Resonance	115
	Preparation of prepolymer solutions	115
	Multifactorial analysis to assess cell viability under 3D bioprinting conditions	115
	Swelling analysis of composite hydrogels.....	116
	Degradation of composite hydrogels.....	117
	Analysis of the mechanical properties of composite hydrogels	117
	Pore size quantification	117
	3D culture of C2C12 myoblasts embedded in the composite hydrogels	118
	C2C12 survival in the composite hydrogels	118
	C2C12-laden composite hydrogels bioprinting and C2C12 differentiation into myotubes.....	119
	Myotube alignment and fusion index analysis.....	119
	Statistical analysis	120
4.1.3.	Results and discussion	120
	Synthesis and characterization of methacrylated polymers.....	120
	Assessment of optimal C2C12 survival after encapsulation in composite hydrogels.....	121
	Hydrogel swelling and degradation	123
	Composite hydrogels with tunable mechanical properties.....	125
	Pore size and pore size distribution	127
	Long-term C2C12 viability and proliferation within composite hydrogels	128
	Composite hydrogels as a bioink for muscle tissue bioprinting	131
4.1.4.	Conclusions	134
4.2.	Muscle-on-a-chip with an on-site multiplexed biosensing system for <i>in situ</i> monitoring of secreted IL-6 and TNF- α	135
4.2.1.	Introduction.....	136
4.2.2.	Experimental procedure.....	138
	Cell culture	138
	Synthesis of prepolymer precursors.....	138

	Preparation of prepolymer solutions	139
	Hydrogel characterization.....	139
	Cell encapsulation in 3D micropatterns.....	140
	C2C12 morphology and viability in composite hydrogels	141
	Immunofluorescence staining	141
	Microdevice fabrication.....	142
	Fabrication of the biosensing platform	143
	Statistical analysis	145
4.2.3.	Results and discussion	146
	Description of the integrated platform	146
	Muscle-on-a-chip integrated with an on-site multiplexed sensing system for in situ monitoring of secreted myokines.....	147
	In situ monitoring of secreted myokines upon electrical and biological stimulation	155
4.2.4.	Conclusions	157
4.3.	Bioengineered <i>in vitro</i> 3D model of myotonic dystrophy type 1 human skeletal muscle	159
4.3.1.	Introduction.....	160
4.3.2.	Experimental procedure.....	162
	Cell culture	162
	Microstructured stamps fabrication	163
	Prepolymer preparation.....	164
	Cell encapsulation in 3D microstructured hydrogels.....	164
	Hydrogel characterization.....	166
	Cell viability assay	167
	Antisense oligonucleotide treatment	167
	Fluorescence in situ hybridization (FISH)	167
	Immunofluorescence staining	168
	Imaging.....	168
	Fusion index and myotube size analysis.....	168
	RNA extraction, RT-PCR and real-time PCR.....	169
	Western blotting	169
	Statistical analysis	170
4.3.3.	Results and discussion	170
	A fabrication protocol to obtain 3D skeletal muscle microtissues	170
	Physical properties of GeIMA-CMCMA hydrogels	174
	3D model of DM1 retains molecular features of the disease and provides a new structural phenotype for preclinical research	175
	AntagomiR treatments rescue bioengineered 3D DM1 muscle phenotypes ..	179
4.3.4.	Conclusions	182
4.4.	Human platelet lysate-based nanocomposite hydrogels for skeletal muscle tissue engineering	183
4.4.1.	Introduction.....	184
4.4.2.	Experimental procedure.....	186
	Cell culture	186
	Fabrication of the hydrogel casting platforms	186
	Preparation of the nanocomposite hydrogel (HUGel).....	188
	Immunofluorescence staining	189
	Electrical Pulse Stimulation.....	189
	Imaging.....	190
	Force measurements	190

	Statistical analysis	190
4.4.3.	Results and discussion	191
	Human skeletal muscle tissue formation in hydrogel casting platforms	191
	a-CNC content can be modulated to promote myotube formation	193
	Nanocomposite hydrogels support the formation of functional human skeletal muscle tissues in a xeno-free cell culture system.....	195
	Perspectives of this work.....	197
4.4.4.	Conclusions	199
Chapter 5.	GENERAL RESULTS AND DISCUSSION	201
Chapter 6.	CONCLUSIONS	223
	REFERENCES	229
Appendix A.	JOURNAL ARTICLES PRESENTED IN THIS THESIS	263
Appendix B.	OTHER PUBLICATIONS.....	329

PROLOGUE

This doctoral thesis was performed in the Biosensors for Bioengineering group at the Institute for Bioengineering of Catalonia (IBEC) from April 2017 to June 2021. The work presented in this thesis was mainly funded by the European Research Council program under the grant ERC-StG-DAMOC (714317) and a predoctoral fellowship (BES-2016-076681) from the Spanish Ministry of Economy and Competitiveness (MINECO). The thesis focused on engineering 3D models of skeletal muscle tissue for their applications in muscle metabolism studies and the preclinical research of muscular dystrophies.

The structure of the thesis is the following: **Chapter 1** provides a general introduction to the work, **Chapter 2** describes the hypothesis and objectives, **Chapter 3** includes the detailed general materials and methods, and **Chapter 4** contains the main results, which are presented as a compilation of three published articles and one manuscript in preparation. Then, **Chapter 5** covers the general results and discussion, and **Chapter 6** corresponds to the conclusions. A copy of the original published articles presented in this thesis can be found in **Appendix A**. Finally, other publications derived from this work can be found in **Appendix B** (original research and review article).

This doctoral thesis began with the synthesis and characterization of different gelatin-based composite hydrogels and their evaluation as biomaterials for the 3D bioprinting of murine skeletal muscle tissues (**Chapter 4.1**). Next, one of the previously studied biomaterials was used to develop skeletal muscle microtissues through a photomold patterning technique that allowed the integration into a biosensing platform for *in situ* muscle metabolism studies (**Chapter 4.2**). The next step was to improve the photomold patterning protocol and optimize it to generate human skeletal muscle microtissues (**Chapter 4.3**). This protocol was used to develop the first 3D skeletal muscle model of myotonic dystrophy type 1 from patient-derived cells. Finally, the preliminary results on the generation of functional human skeletal muscle in a *xeno*-free 3D culture system are presented in **Chapter 4.4**. This last project started during a short research stay at the Institute for Biomaterials, Biodegradables, and Biomimetics (i3Bs, University of Minho) and is currently being continued at IBEC.

AUTHOR'S CONTRIBUTIONS

The results of this doctoral thesis entitled “**Engineered functional skeletal muscle microtissues for *in vitro* studies**” are presented as a compilation of three original peer-reviewed articles and one manuscript in preparation. Xiomara Gislen Fernández Garibay, as a PhD student, participated in the conception, planning, experimental work, data analysis, and manuscript writing in all the articles. The impact factor and detailed contribution of each co-author are described below.

- García-Lizarribar A^{1,2,*}, **Fernández-Garibay X^{1,*}**, Velasco-Mallorquí F¹, Castaño A G¹, Samitier J^{1,2,3}, and Ramon-Azcon J¹ 2018 Composite Biomaterials as Long-Lasting Scaffolds for 3D Bioprinting of Highly Aligned Muscle Tissue. *Macromol. Biosci.* **18** 1800167. *Authors contributed equally to this work.

¹ Institute for Bioengineering of Catalonia (IBEC), The Barcelona Institute of Science and Technology (BIST), Baldiri Reixac 10-12, 08028 Barcelona, Spain

² Centro de Investigación Biomédica en Red (CIBER), Av. Monforte de Lemos 3-5, Pabellón 11, Planta 0, 28029 Madrid, Spain

³ Department of Electronic and Biomedical Engineering, University of Barcelona (UB), Martí i Franquès 1-11, 08028 Barcelona, Spain

Impact factor (2018): 2.895

Quartile according to the JCR impact factor (2018): Q1 in Polymer Science (21/87); Q2 in Biochemistry & Molecular Biology (146/299); Q3 in Materials Science, Biomaterials (18/32)

A G-L and X F-G contributed equally to this work. A G-L, X F-G, F V-M, J S, and J R-A conceived this work. J R-A coordinated and guided the experimental work. A G-L, X F-G, F V-M, and A G C performed the experiments. A G-L, X F-G, F V-M, A G C, and J R-A contributed to the interpretation of the results and data analysis. J S and J R-A acquired the funding. A G-L and X F-G wrote the manuscript with the supervision of A G C and J R-A and input from all the authors.

Part of this work regarding GelMA-AlgMA synthesis, characterization, and its use as bioink for 3D printing of skeletal muscle tissue may be used in the future Doctoral Thesis of Andrea García-Lizarribar (Doctoral Program in Biomedicine, Faculty of Medicine, University of Barcelona) under the direction of Prof. Josep Samitier.

- Ortega M A, **Fernández-Garibay X**, Castaño A G, De Chiara F, Hernández-Albors A, Balaguer-Trias J and Ramón-Azcón J 2019 Muscle-on-a-chip with an on-site multiplexed biosensing system for in situ monitoring of secreted IL-6 and TNF- α . *Lab Chip* **19** 2568–80.

-Institute for Bioengineering of Catalonia (IBEC), The Barcelona Institute of Science and Technology (BIST), Baldiri Reixac 10-12, 08028 Barcelona, Spain

Impact factor (2019): 6.774

Quartile according to the JCR impact factor (2019): Q1 in Instruments & Instrumentation (3/64); Q1 in Chemistry, Analytical (8/86); Q1 in Chemistry, Multidisciplinary (30/177)

M A O, X F-G, A G C, A H-A, and J R-A. conceived and planned the experiments. X F-G and A G C carried out biological experiments related to 3D SM tissue formation, characterization, and data analysis. M A O, A H-A, and J B developed the sensing platform. M A O and J B performed sensing experiments and acquisition of data. M A O, A G C, A H-A, and J R-A contributed to the interpretation of the sensing results. F D C and M A O drafted and edited the manuscript. J R-A supervised the project and acquired the funding. All authors provided critical feedback and helped shape the research, analysis, and manuscript.

- **Fernández-Garibay X¹**, Ortega M A¹, Cerro-Herreros E^{2,3,4}, Comelles J^{1,5}, Martínez E^{1,5,6}, Artero R^{2,3,4}, Fernández-Costa J M¹ and Ramón-Azcón J^{1,7} 2021 Bioengineered in vitro 3D model of myotonic dystrophy type 1 human skeletal muscle. *Biofabrication* **13** 035035.

¹ Institute for Bioengineering of Catalonia (IBEC), The Barcelona Institute of Science and Technology (BIST), Baldiri Reixac 10-12, 08028 Barcelona, Spain

² University Institute for Biotechnology and Biomedicine (BIOTECMED), University of Valencia, Dr. Moliner 50, 46100 Burjassot, Valencia, Spain

³ Translational Genomics Group, InCliva Health Research Institute, Dr. Moliner 50, 46100 Burjassot, Valencia, Spain

⁴ Joint Unit InCliva-CIPF, Dr. Moliner 50, 46100 Burjassot, Valencia, Spain

⁵ Department of Electronics and Biomedical Engineering, University of Barcelona (UB), Martí i Franquès 1-11, 08028 Barcelona, Spain

⁶ Centro de Investigación Biomédica en Red (CIBER), Av. Monforte de Lemos 3-5, Pabellón 11, Planta 0, 28029 Madrid, Spain

⁷ Institució Catalana de Reserca i Estudis Avançats (ICREA), Passeig de Lluís Companys, 23, 08010 Barcelona, Spain

Impact factor (2020): 9.954

Quartile according to the JCR impact factor (2020): Q1 in Materials Science, Biomaterials (3/40); Q1 in Engineering, Biomedical (7/90)

X F-G, J M F-C, R A, and J R-A conceived this work. X F-G and J M F-C performed and coordinated the experiments and data analysis. M A O designed and fabricated the micropatterned silicon molds, E C-H did the molecular validation of antagomiR treatments, J C and E M performed the AFM measurements and data analysis. J R-A, R A, and E M acquired the funding for this project. X F-G and J M F-C prepared the manuscript with the supervision of J R-A and input from all the authors.

- **Fernández-Garibay X¹**, Gomez-Florit M^{2,3,4}, Mangas-Florencio L¹, Domingues R M^{2,3,4}, Reis R L^{2,3,4}, Gomes M E^{2,3,4}, Fernández-Costa J M¹ and Ramón-Azcón J^{1,5} 2021 Human platelet lysate-based nanocomposite hydrogels for skeletal muscle tissue engineering. *Manuscript in preparation*.

¹ Institute for Bioengineering of Catalonia (IBEC), The Barcelona Institute of Science and Technology (BIST), Baldiri Reixac 10-12, 08028 Barcelona, Spain

² 3B's Research Group, I3Bs—Research Institute on Biomaterials, Biodegradables and Biomimetics, University of Minho, Headquarters of the European Institute of Excellence on Tissue Engineering and Regenerative Medicine, Avepark, Zona Industrial da Gandra, 4805-017 Barco—Guimarães, Portugal

³ ICVS/3B's—PT Government Associate Laboratory, Braga/Guimarães 4805-017, Portugal

⁴ The Discoveries Centre for Regenerative and Precision Medicine, Headquarters at University of Minho, Avepark, 4805-017 Barco, Guimarães, Portugal

⁵ Institució Catalana de Reserca i Estudis Avançats (ICREA), Passeig de Lluís Companys, 23, E08010 Barcelona, Spain

X F-G, M G-F, R M D, J M F-C, and J R-A conceived this work. X F-G performed the experiments and data analysis. M G-F synthesized the a-CNC. J M F-C and L M-F designed and fabricated the hydrogel casting platforms. J R-A, M E G, and R L R acquired the funding for this project. M G-F, R M D, J M F-C, and J R-A provided critical feedback and helped shape the research and analysis. X F-G prepared the manuscript with the supervision of J R-A and input from all the authors.

Prof. Dr. Javier Ramón Azcón

I certify the above-mentioned information is true.

ABSTRACT

The skeletal muscle is the largest tissue of the human body. Its main function is to generate contractile forces, essential for locomotion, thermogenesis, and metabolism. Fundamental research on skeletal muscle in health and disease, and preclinical research for new therapies, are currently based on 2D *in vitro* cell cultures and *in vivo* animal models. However, these strategies have important shortcomings. For instance, conventional cell culture models cannot emulate the complex 3D architecture of native skeletal muscle, and the species-specific differences in animal models limit their relevance to humans. In contrast, engineered skeletal muscle tissues are emerging as *in vitro* 3D cell culture models that complement existing 2D strategies. These engineered tissues can offer an improved microenvironment resembling native muscle tissue, comprised of bundles of aligned, multinucleated fibers. Therefore, the main objective of this thesis was to develop 3D skeletal muscle tissues for *in vitro* studies of muscle metabolism and disease modeling.

Skeletal muscle precursor cells were encapsulated in microfabricated hydrogel scaffolds, introducing the appropriate topographical and microenvironmental cues to guide muscle fiber formation. First, photocrosslinkable gelatin methacryloyl (GelMA)-based composite hydrogels were synthesized and evaluated as cell-laden bioinks for 3D bioprinting of murine skeletal muscle tissue. The fabrication conditions were optimized to ensure the biocompatibility of the process and promote *in vitro* myogenesis. Our results demonstrated that the composite hydrogels have a higher resistance to degradation than GelMA hydrogels. Thus, the bioprinted scaffolds maintained their 3D structure over a prolonged culture period. Furthermore, the shear stress during extrusion bioprinting combined with the appropriate scaffold geometry resulted in highly aligned myoblasts that correctly differentiated into multinucleated myotubes. Considering these results, GelMA-carboxymethylcellulose methacrylate (CMCMA) hydrogels were then used to generate skeletal muscle microtissues in long-lasting cell cultures. Photomold patterning of cell-laden GelMA-CMCMA filaments led to the formation of highly aligned 3D myotubes expressing sarcomeric proteins. Moreover, the presented protocols were highly biocompatible and reproducible.

Murine skeletal muscle microtissues were fabricated in a microfluidic platform integrated with an electrical stimulation system and biosensors for monitoring muscle

metabolism *in situ*. Here, we measured the contraction-induced release of muscle-secreted cytokines upon electrical or biological stimulation. The obtained results confirmed the endocrine function of the bioengineered tissues, obtaining *in vivo*-like responses upon exercise or endotoxin-induced inflammation. Then, the photomold patterning protocol was optimized for human cells to develop the first *in vitro* 3D model of myotonic dystrophy type 1 (DM1) human skeletal muscle. DM1 is the most prevalent hereditary myopathy in adults, and there is no effective treatment to date. We proved that 3D micropatterning enhances DM1 myotube formation compared to 2D cultures. Furthermore, we detected the reduced thickness of 3D DM1 myotubes compared to healthy controls, which was proposed as a new *in vitro* structural phenotype. Thus, as a proof-of-concept, we demonstrated that treatment with an antisense oligonucleotide, antagomiR-23b, could rescue both molecular and structural phenotypes in these bioengineered DM1 muscle tissues.

Finally, animal-derived components were eliminated to develop *in vitro* functional tissues in xeno-free cell culture as a next step towards improving bioengineered human skeletal muscle tissues. Cell-laden nanocomposite hydrogels consisting of human platelet lysate and functionalized cellulose nanocrystals (HUGel) were fabricated in hydrogel casting platforms that implemented uniaxial tension during matrix remodeling. We modulated the content of cellulose nanocrystals to tune the mechanical and biological properties of HUGel and favor the formation of long, highly aligned myotube bundles. Additionally, we performed *in situ* force measurements of electrical stimulation-induced contractions. Altogether, the results presented in this thesis provide promising approaches to advanced cell culture models of skeletal muscle tissue that could be valuable tools for fundamental studies, disease modeling, and future personalized medicine.

LIST OF ABBREVIATIONS

2D	Two-dimensional
3D	Three-dimensional
ACA	6-amino-n-caproic acid
a-CNC	Aldehyde-cellulose nanocrystals
AFM	Atomic force microscopy
AlgMA	Alginate methacrylate
<i>BIN1</i>	<i>Bridging integrator 1</i>
BSA	Bovine serum albumin
CDK	Cyclin-dependent kinase
CELF1	CUGBP Elav-Like Family Member 1
CMC	Carboxymethylcellulose
CMCMA	Carboxymethylcellulose methacrylate
CNC	Cellulose nanocrystals
dECM	Decellularized extracellular matrix
DM	Differentiation medium
DM1	Myotonic dystrophy type 1
DMD	Duchenne muscular dystrophy
DMEM	Dulbecco's Modified Eagle Medium
DMPK	<i>Dystrophia myotonica protein kinase</i>
ECM	Extracellular matrix
EDC	1-Ethyl-3-(3-dimethylaminopropyl)carbodiimide
ELISA	Enzyme-linked immunosorbent assay
EPS	Electrical pulse stimulation
EthD-1	Ethidium homodimer
FBS	Fetal bovine serum
GelMA	Gelatin methacryloyl
hASCs	Human adipose stem cells
hESCs	Human embryonic stem cells
hiPSCs	Human induced pluripotent stem cells
hPSCs	Human pluripotent stem cells
HRP	Horseradish peroxidase
hTERT	Human telomerase reverse transcriptase

HUgel	Human platelet lysate-based nanocomposite hydrogels
HuMSCs	Human immortalized muscle satellite stem cells
HUVEC	Human umbilical vein endothelial cells
I2959	Irgacure 2959; 2-Hydroxy-4'-(2-hydroxyethoxy)-2-methylpropiophenone
IDA	Interdigitated array
IL	Interleukin
ITO	Indium Tin Oxide
LAP	Lithium phenyl (2,4,6-trimethylbenzoyl) phosphinate
LPS	Lipopolysaccharide
MBNL	Muscleblind-like
MDM	Muscle differentiation medium
MHC	Myosin heavy chain
miRs	microRNAs
MMPs	Matrix metalloproteinases
MRF	Myogenic regulatory factor
MYH	Myosin heavy chain
MyHC	Myosin heavy chain
<i>NFIX</i>	<i>Nuclear Factor I X</i>
NHS	N-hydroxysuccinimide
OOCs	Organs-on-a-chip
PBS	Phosphate buffered saline
PDMS	Polydimethylsiloxane
PEG	Poly(ethylene glycol)
PEGDA	Poly(ethylene glycol) diacrylate
PFOTS	Trichloro(1H,1H,2H,2H-perfluorooctyl)silane
PL	Platelet lysate
RGD	Arg-Gly-Asp; arginine-glycine-aspartate
SAA	Sarcomeric alpha-actinin
SEM	Scanning force microscopy
SPGE	Screen-printed gold electrode
<i>SPTAN1</i>	<i>Spectrin Alpha Non-Erythrocytic 1</i>
SSCs	Satellite stem cells
TBS	Tris-buffered saline
TMSPMA	3-(trimethoxysilyl)propyl methacrylate
TNF- α	Tumor necrosis factor-alpha

Chapter 1. INTRODUCTION

1.1. Tissue engineering for *in vitro* research

Tissue engineering is a complex interdisciplinary field that comprises from molecular level studies in developmental biology and genetics to whole organ engineering. In principle, living cells are associated with a specifically designed matrix or scaffold, which guides new tissue development [1]. In this field, the knowledge gained in cell biology, biochemistry, and molecular biology is applied to the engineering of new tissues. Simultaneously, recent advances in materials science, nanotechnology, and bioengineering allow the application of engineering principles to these artificial living systems [1,2].

Historically, tissue engineering emerged in the context of treating organ loss or failure by replacing damaged tissue with new biological substitutes that restore, maintain, or improve tissue function [3,4]. However, the applications of this field have expanded to address other research and clinical needs, not only for regenerative medicine but also as diagnostic or drug screening tools. In fact, a significant part of the progress in tissue engineering over the last decades has been generated through the development of 3D *in vitro* cell culture platforms for cell biology studies, disease modeling, drug testing, and precision medicine [2].

1.1.1. The basic paradigm of tissue engineering

The basic paradigm of tissue engineering consists of three fundamental elements: the cells that make up the tissue of interest, a 3D scaffold that supports the cells, and signals that stimulate and guide tissue development (**Figure 1.1**) [5]. The cells can be stem cells, progenitor cells, or differentiated cells. Importantly, their behavior in normal morphogenesis and wound healing should be comprehensively studied, as these are the conditions where cells create or recreate functional structures [1]. The cells are usually encapsulated within a 3D scaffold designed for the specific tissue engineering application. This scaffold is made of a biomaterial of natural or synthetic origin, or a mixture of both. Besides, the biomaterial must be carefully selected to have the optimal chemical and physical properties that allow interaction with living cells. Altogether, the cells are influenced by signals or cues present in their microenvironment, such as biochemical factors, mechanical properties, or external stimuli.

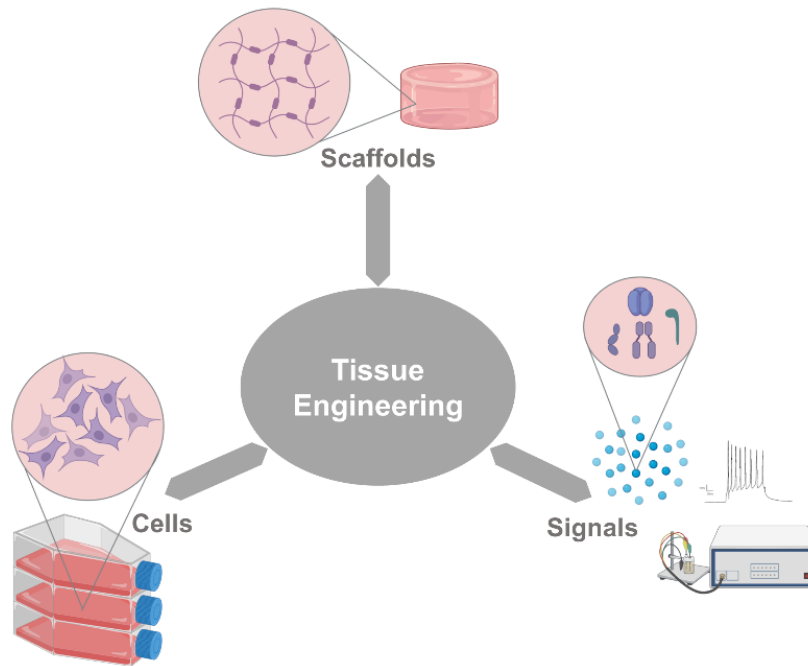


Figure 1.1. The basic paradigm of tissue engineering. Cells are expanded and encapsulated within a biocompatible 3D scaffold. The encapsulated cells are influenced by microenvironmental signals or external stimuli.

To achieve this, it is essential to understand the fundamental and developmental biology of the tissue of interest. Only then can we establish strategies to provide a suitable microenvironment for the cells and control the biological processes for generating new tissues.

The native extracellular matrix

In vivo, most cell types reside within a complex environment that contains multiple extracellular matrix (ECM) components, mixed cell types, and cell-secreted factors. The native ECM is a natural 3D scaffold that supports cells and influences several aspects of their behavior. It is made of structural fibrous proteins (e.g., collagen, fibronectin, vitronectin, elastin, and laminin), proteoglycans, and soluble molecules (e.g., growth factors, small integrin-binding glycoproteins (SIBLINGS), and small matricellular proteins). However, the exact composition changes depending on each tissue [6]. The mechanical properties of the ECM are dictated mainly by the structural proteins and sensed by the cells through adhesions between cell surface integrins and binding motifs (adhesion sites) of the matrix. Proteoglycans fill the interstitial spaces of the structural protein backbone and sequester soluble molecules [7].

The native ECM's dynamic microenvironment is continuously remodeled by cells. They deposit ECM components and degrade the matrix through the action of ECM-cleaving proteins, such as matrix metalloproteinases (MMPs). This constant restructuring is vital for tissue homeostasis. Therefore, the misregulation of this process can cause ECM damage, which is a common factor of many diseases [6]. Understanding the ECM's general composition and remodeling during tissue development is essential for designing engineered tissues because the ideal 3D scaffolds should mimic these native matrices on multiple length scales.

1.1.2. Tissue-engineered 3D cell culture platforms

Besides applications in regenerative medicine, there is a rising paradigm shift for biomedical research and tissue engineering towards developing 3D *in vitro* tissue models as tools for diagnostic and drug screening. These models aim to bridge the gap between traditional cell culture assays and clinical trials, obtaining more physiologically accurate information in the preclinical research stage and reducing the need for animal experimentation.

Conventional cell-based assays and animal models

In vitro cell culture and animal models are routinely employed in tissue physiology studies and as disease models for drug development assays. These techniques have widely contributed to our understanding of biological processes and have been essential for identifying the molecular causes of certain diseases [8]. Still, both types of models have significant shortcomings that make it challenging to obtain physiologically relevant results for humans.

Traditional *in vitro* models involve cell monolayers cultured on flat and rigid substrates, such as tissue culture polystyrene or glass. These 2D cell culture experiments are generally efficient and straightforward. Since cells receive an equal amount of growth factors and nutrients from the medium, there is homogeneous cell growth and proliferation [9]. Notably, 2D cell culture studies have allowed our understanding of fundamental complex biological phenomena, such as stem cell differentiation [10] and tissue morphogenesis [11]. Nonetheless, it has been demonstrated that for most cell types, their characteristics are very different when they are in a monolayer instead of their natural environment (**Figure 1.2**) [7,12,13]. Thus, the majority of 2D models do not come close to emulating the complexity of

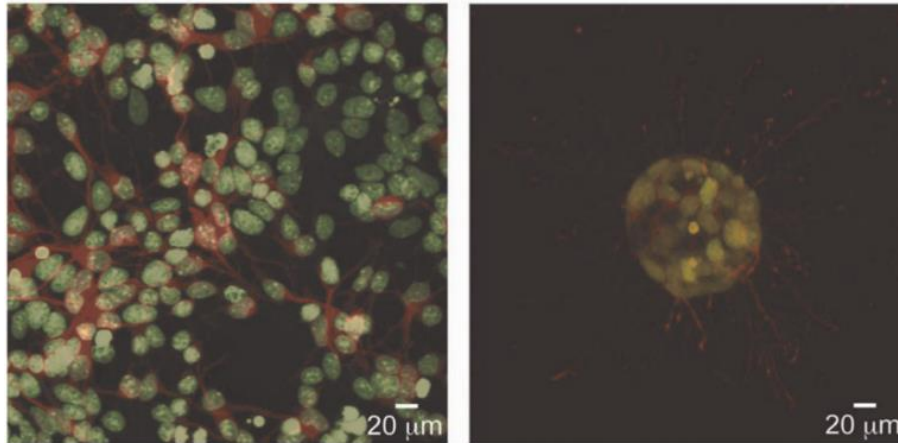


Figure 1.2. Cells experience an entirely different environment between 2D and 3D culture. Neural cells cultured in monolayer (left) are limited to extend processes in the plane of the cell culture surface. Cytoplasm is stained in green and the β -tubulin in axonal extensions is stained in red. When cultured within poly(ethylene glycol) based hydrogels (right) the same cells form neurospheres, extending processes isotropically in 3D. Adapted from Tibitt and Anseth [7].

native tissues with a 3D structural organization of cells surrounded by each other and within an ECM [14]. Therefore, cells in 2D assays for drug development tend to have altered drug responses due to their unnatural microenvironment [15].

On the other hand, functional 3D tissues representing *in vivo* physiology can be found in animal models, from small animals like flies, mice, or rats, to large animal models such as non-human primates. However, the use of animal models in pharmacological research raises several ethical concerns. Moreover, species-specific differences limit the extrapolation of animal data to human conditions [16], and animal models are labor-intensive, time-consuming, and costly. In drug development, 2D *in vitro* cultures are followed by animal experiments before proceeding to clinical trials. Unfortunately, it has been estimated that following this traditional drug development pathway, only around 11.8% of drugs entering clinical trials become approved, generating a cost of billions of dollars for newly authorized medications [17,18]. In fact, most drugs fail during clinical trials because of a lack of clinical efficacy or unacceptable toxicity levels that are not detected with cell and animal models [15]. To overcome these limitations and accelerate preclinical research, *in vitro* studies could be complemented by human 3D cell culture systems. These *in vitro* systems should consist of patient-derived engineered tissues that offer a better representation of the environment of living tissues with a specific 3D architecture.

Microenvironmental cues in 2D vs. 3D cell culture

In 3D cell culture, experiments usually start with cells suspended in a biocompatible liquid precursor, which then solidifies or gels, embedding the cells within the biomaterial matrix. Therefore, more than mere dimensionality, 3D culture can provide adhesive, soluble, mechanical, and topographical microenvironmental cues in a way that differs from 2D settings (**Figure 1.3**) [reviewed in 19]. These variations then result in changes in cell behavior and function.

For instance, cell morphology is remarkably different when adherent cells are cultured in 2D vs. 3D. Since cell adhesions only form in the horizontal plane, cells in 2D are flat and present a forced apical-basal polarity that is abnormal for most mesenchymal cells, affecting intracellular signaling and phenotypic fate. On the contrary, cells cultured in 3D present adhesions in all dimensions, adopting a stellate morphology with no fixed polarity [19]. The forced polarity of cells in 2D also results in unnatural interactions with soluble factors in the medium. Cytokines, growth factors, and nutrients interact homogeneously with the induced apical side of the cell membrane. However, this is different *in vivo* and within 3D scaffolds. The delivery of soluble factors in 3D cultures can be limited, and dynamic spatial gradients can be present due to the physical characteristics of biomaterials, such as scaffold dimensions, pore size, and pore interconnectivity [20,21].

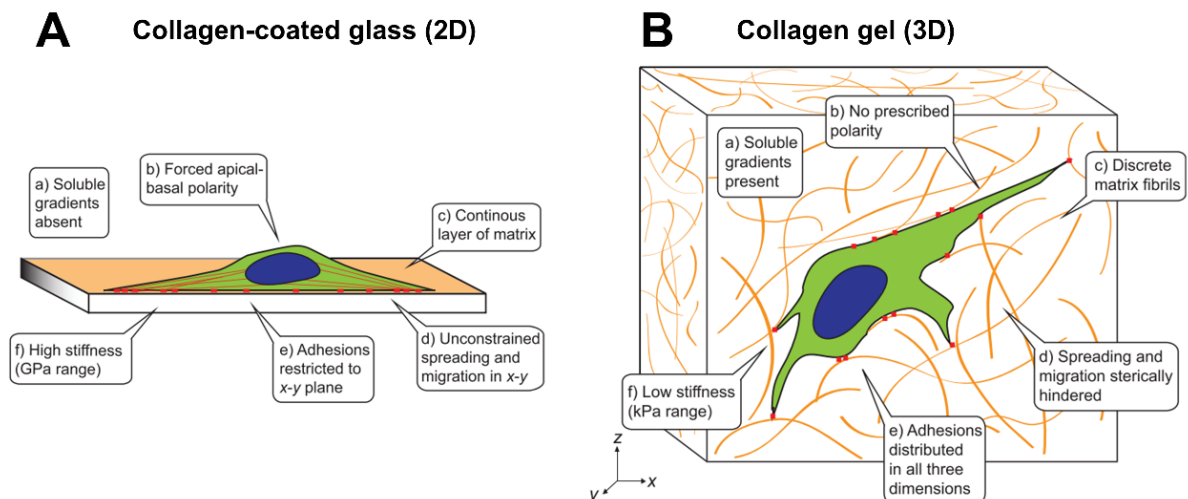


Figure 1.3. Soluble, adhesive, topographical, and mechanical cues in 2D and 3D. The cues encountered by a cell are different between an ECM-coated surface (2D) and a typical 3D ECM (e.g., collagen). Adapted from Baker and Chen [19].

The mechanical forces sensed and exerted by cells represent another critical difference between 2D and 3D cultures. It has been demonstrated that ECM stiffness plays a role in influencing adhesions, morphogenesis, and stem cell differentiation [22,23]. Nevertheless, the vast majority of 2D cell culture surfaces have supraphysiological stiffness values compared to the softer biomaterials for 3D culture. Moreover, conventional 2D culture surfaces tend to be smooth, whereas most biomaterials for 3D cell culture have a heterogeneous fibrous structure. It is well known that the cell-ECM forces depend on the scale and organization of these ECM fibers and whether the cells are physically constrained by the biomaterial [19]. Additionally, cell spreading and migration in 3D scaffolds are significantly slower than in 2D surfaces due to steric hindrance from the scaffold, which creates obstacles for migration and alters cell motility [9]. All these microenvironmental cues depend not only on dimensionality but also on the biomaterials used to create 3D scaffolds. Therefore, these biomaterials should be carefully selected depending on the cell types or 3D tissues developed.

Biomaterials for 3D cell culture

For tissue engineering, cells have been cultured in 3D scaffolds with different architectures, mainly microporous solids, nanofibers, and hydrogels (**Figure 1.4**) [24]. These materials engage cell surface receptors and provide a physical environment to regulate cell function, depending on their architecture and composition, particularly ligand density and composition. Microporous biomaterials, such as cryogels, are appropriate for cell seeding inside the porosities (~100 μm). However, pores are larger than the average cell diameter. Hence, cells effectively sense them as 2D surfaces with curvature [24], and their 3D characteristics would depend on the cell type, cell density, and cell-cell interactions. 3D scaffolds made of nanofibers can have a nanostructured topography similar to the fibrillar native ECM. Yet, these nanofibers are usually rigid with limited water absorption, different from the flexible, bioactive, hydrated fibers of natural ECM [25]. Finally, hydrogels can imitate the hydrated structure and mechanics of the native ECM, while their porosity can be tuned to enable nutrients and waste exchange [26,27].

1.1.3. Hydrogels as scaffolds for tissue engineering

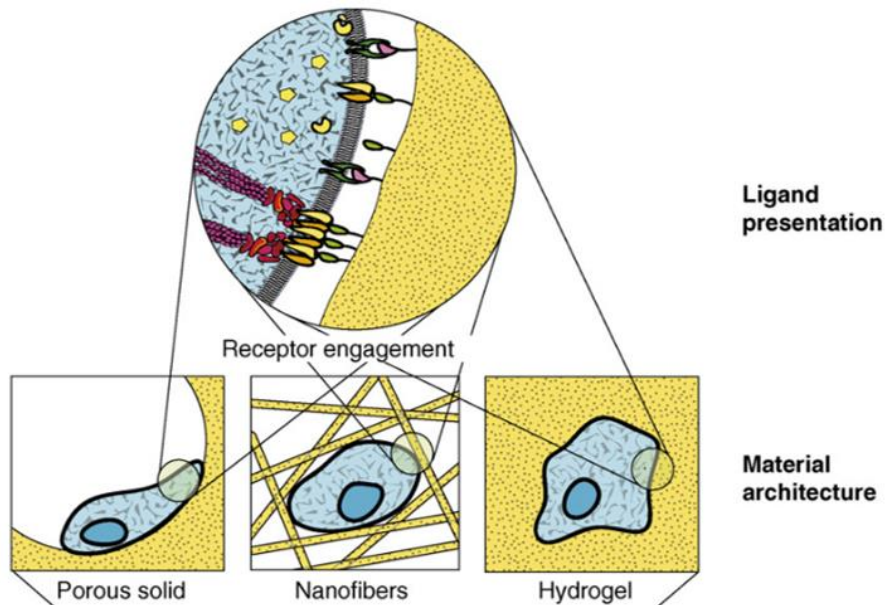


Figure 1.4. Cell receptor–ligand interactions are influenced by biomaterial architectures. These materials can provide a 2D (e.g., flat surfaces, microporous solids) or 3D (e.g., nanofibers, hydrogels) microenvironment for cellular engagement. *Adapted from Saha et al. [24].*

Hydrogels are chemically or physically crosslinked networks of hydrophilic polymers that can absorb from 10-20% up to thousands of times their dry weight in water. These are attractive materials for 3D culture and tissue engineering due to their high water content and because they can be fabricated under biocompatible conditions [26]. The biochemical and physical properties of hydrogels mainly depend on their compositions, crosslinking density, and fabrication methods [28]. Furthermore, hydrogels can be engineered to possess specific physicochemical properties according to the particular tissue requirements [27,29,30].

Hydrogel compositions: natural vs. synthetic

Hydrogels for cell culture can be synthesized from natural materials, synthetic materials, or from a combination of both. Natural hydrogels are inherently biocompatible and primarily derived from the ECM proteins, such as fibrinogen, collagen, and gelatin. These already possess cell adhesion and degradation motifs and many other endogenous factors that promote cell function. Other biological sources include plants or insects, from which biomaterials such as cellulose, alginate, and chitosan are obtained [31]. These natural materials are biocompatible but do not have cell adhesive features. One disadvantage of using natural hydrogels is that the resulting scaffolds could be variable and ill-defined [24]. Moreover, it can be challenging to control their degradation rates and other physicochemical or mechanical properties that are necessary for long-term cell culture [32].

On the other hand, hydrogels formed from inert synthetic molecules, such as poly(ethylene glycol) (PEG) or polylactic acid (PLA), have a well-defined, consistent composition that can be tuned to obtain certain properties. Synthetic biocompatible hydrogels have been shown to maintain the viability of encapsulated cells; however, they do not possess functional motifs for cell interaction, so they are only considered permissive to cell function [19,32]. Nevertheless, these purely synthetic biomaterials can be modified to promote cell adhesion and matrix degradation by introducing RGD peptides and proteolytic or hydrolytic moieties in the polymer network [33,34]. Besides, different materials can be mixed to obtain composite or hybrid hydrogels that combine their respective advantages to resemble the complexity of the native ECM. Usually, natural-natural composite hydrogels are physically blended in a similar ratio to the native ECM composition. On the other hand, natural-synthetic polymers are typically prepared using chemical copolymerization to adjust their mechanical properties and degradability [35].

Critical features of hydrogels for 3D cell culture

The selection or design of hydrogels for cell culture should consider the most relevant features for biomedical applications, including bioadhesion, mechanical properties, transport, and degradation [34]. Bioadhesion is the property that allows cells to attach to hydrogels through cell-binding domains that greatly influence cell shape. As described in **Chapter 1.1.2**, the mechanical properties of the scaffold provide cells with signals through mechanotransduction pathways that regulate cell function and tissue homeostasis [22,23]. Furthermore, the transport of soluble factors through the hydrogel depends on the hydrogel's porosity. This is an essential feature because the hydrogel must allow the transport of oxygen, nutrients, and waste to and from the cells [7]. Additionally, transport can be crucial in drug screening applications of *in vitro* models where drug diffusion through the hydrogel polymer network is required [36]. Finally, cell-mediated hydrogel degradation is necessary for an *in vivo*-like matrix remodeling and can be used to release matrix-bound bioactive factors [37]. As previously discussed, some natural ECM-derived hydrogels, such as collagen, gelatin, and fibrin, already have these cell-adhesion and degradation domains. Furthermore, synthetic hydrogels can be engineered to include cell-adhesive [38] or enzyme-cleavable [39] oligopeptides.

Hydrogel formation: chemical or physical crosslinking

Cell-compatible hydrogels can be formed by several chemical and physical crosslinking strategies (**Figure 1.5**). Physical crosslinking involves non-covalent crosslinks via strong electrostatic interactions, hydrogen bonding, protein

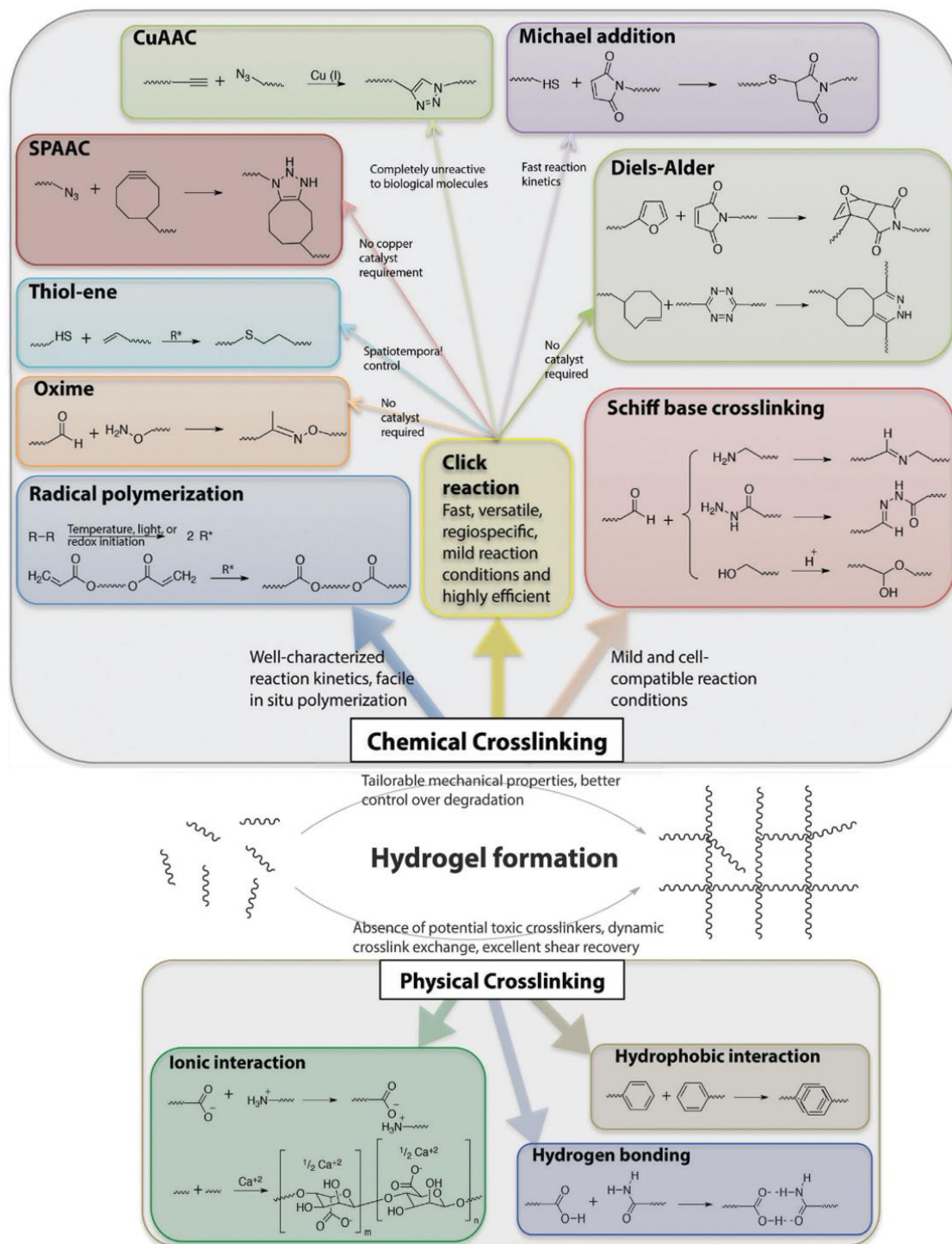


Figure 1.5. Hydrogel formation by chemical or physical crosslinking. The selection functional group for hydrogel formation depends on several factors related to the application of interest, such as the desired initiation mechanism, the specificity and speed of the reaction, and the stability of the resulting bond. *Adapted from Kharkar et al. [29].*

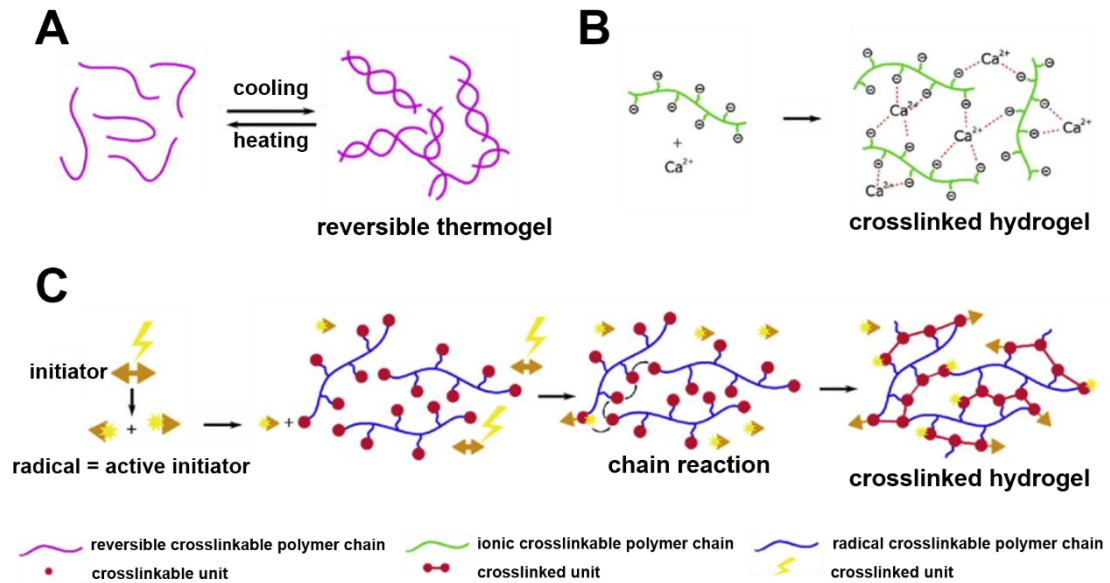


Figure 1.6. Schematic representations of hydrogel formation mechanisms. (A) Reversible thermogel formation. (B) Ionic crosslinking with divalent cations. (C) Radical crosslinking mechanism. UV light activates the initiator generating two radicals, which can react with a functional group of the polymer chain. This causes a chain reaction that crosslinks many functional groups leading to the formation of the hydrogel. *Adapted from Tenje et al. [43].*

interactions, or ionic interactions. For chemical crosslinking, hydrogels can be covalently functionalized to include reactive functional groups for hydrogel polymerization through chain or step growth reactions. The most common are free radical chain polymerization reactions, Schiff base crosslinking reactions, click reactions, and carbodiimide-mediated reactions [29]. Some examples of physical crosslinking can be found in collagen and its denatured form, gelatin, which crosslink with temperature and pH changes forming a thermogel (**Figure 1.6A**) [21]. However, pure gelatin gels are not suitable for cell culture because they are dissolved at cell culture temperatures. Matrigel® and Geltrex™ are commercial hydrogel mixtures of several ECM structural proteins and growth factors [40,41] that are stably crosslinked by temperature. As the last example, alginate hydrogels can be formed by ionic crosslinking with divalent cations, such as Ca^{2+} [42] (**Figure 1.6B**). These reactions are highly biocompatible and straightforward because there is no need for any chemical modifications; nevertheless, temperature or ionic crosslinking cannot be precisely controlled at the microscale.

Chemically crosslinked hydrogels commonly involve modifying the desired natural or synthetic biomaterials with functional groups, such as acrylates, methacrylates, or acrylamides that can undergo radical polymerization reactions in the presence of a photoinitiator and light [29,43] (**Figure 1.6C**). Some polymers that have been functionalized for photopolymerization include poly (ethylene glycol) (PEG) [44], hyaluronic acid (HA) [45], gelatin [46,47], and chitosan [48]. For radical chain polymerization, the most commonly used photoinitiators are 2-hydroxy-4'-(2-hydroxyethoxy)-2-methylpropiophenone (Irgacure 2959) and lithium phenyl-2,4,6-trimethyl-benzoylphosphinate (LAP) [49]. In these reactions, free radicals dissociate from the photoinitiator upon irradiation. Introducing a high dose of cytotoxic free radicals or unnecessarily prolonging exposure may compromise the cytocompatibility of the process. Therefore, it is crucial to optimize their concentration to obtain a good crosslinking efficiency without causing cell damage [50]. Other strategies for chemical crosslinking are carbodiimide-mediated reactions and Schiff base crosslinking reactions. In the first one, 1-ethyl-3-(3-dimethylaminopropyl) carbodiimide (EDC) is typically used to activate the reaction between carboxylic acid groups and amine groups [51]. Finally, Schiff reactions occur between aldehydes and other macromolecules containing amine, hydrazide, or alcohol functional groups. The reaction conditions are mild; therefore, this technique has been used to prepare composite hydrogels for cell encapsulation [52]. The crosslinking degree is one of the main factors that determine several hydrogel properties, such as porosity, diffusivity, elasticity, swelling/shrinking (water content), and degradation rate [29]. These properties are closely related; for example, a less crosslinked biomaterial is more porous, has a lower Young's modulus, and would have a faster degradation rate. Thus, it is crucial to have precise control of the crosslinking reactions and ensure they are carried out under cytocompatible conditions.

Hydrogel microfabrication strategies

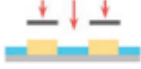



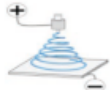

Cell-laden hydrogels can be formed in bulk using the crosslinking strategies mentioned above. However, *in vitro* 3D models have been significantly improved by microfabrication techniques that allow tuning hydrogel properties on the same length scale as the cell microenvironment (around 10-200 μm) [43]. Microengineered hydrogels, in the order of a few microns in at least one dimension, can help build tissue models with higher fidelity and increased control of mechanical and biochemical signals that influence cell behavior [27]. Furthermore, microtechnologies

allow scaling *in vitro* 3D cell culture platforms, offering the possibility to produce high-throughput systems while reducing times and costs [53].

Fabricating microengineered hydrogels requires a controlled crosslinking process that allows precise spatial resolution [27]. Among the most used techniques are photopatterning, soft lithography and micromolding, microfluidics (droplet or fiber spinning systems), electrospinning, and 3D bioprinting [35,43]. Each fabrication strategy results in different types of microengineered hydrogels with distinct key features and applications (**Table 1.1**). Photopatterning, or UV lithography, was first developed for the microelectronics industry [54]. With this microfabrication technique, hydrogel structures are defined by exposing a prepolymer solution to UV light through a patterned mask, crosslinking the exposed regions. Soft lithography implies using elastomeric stamps to define structural or chemical patterns in a material [55]. The stamps are fabricated by cast molding of reusable master molds, which are in turn fabricated by conventional UV lithography techniques. The most common elastomer for soft lithography is polydimethylsiloxane (PDMS), a biocompatible, transparent polymer. The microstructured PDMS stamps can be used to transfer chemical micropatterns to the hydrogels; a technique called microcontact printing (μ CP). In another soft lithography approach, called micromolding, stamps are used as negative molds to replicate features into a hydrogel, obtaining defined blocks.

Microfluidic chips are increasingly used to fabricate hydrogel microstructures with improved control over their final dimensions [43]. Typically, the specifically designed microchannels are filled with hydrogel precursor solutions and crosslinked by mixing with a crosslinking solution inside or outside the chip. This technique has emerged as an alternative to bulk emulsification and extrusion, producing hydrogel microdroplets or microgels and microfibrils. Electrospinning is another fiber-generating approach that combines electrostatic forces and spinning to fabricate fine fibers (from 2 nm to a few μ m in diameter) from polymer solutions or melts [56]. This hydrogel microfabrication technique is very attractive to create fibrous hydrogel scaffolds for tissue engineering. Finally, 3D bioprinting emerged from 3D printing or additive manufacturing as a technique to generate organized 3D scaffolds through the layer-by-layer deposition of bioinks [57]. Bioinks are made of cells suspended in a liquid polymer precursor solution that is printed using extrusion [58]. During or after printing, the bioink is gelled by thermal activation, photocrosslinking, or another cytocompatible process. The final bioink scaffold is a cell-laden hydrogel.

Table 1.1. Current microfabrication technologies to produce diverse hydrogels with flexible functions. Adapted from Liu et al. [35].

Fabrication technology	Commonly used materials	Types of microengineered hydrogels	Key features and applications
Photopatterning 	HA, gelatin, polylysine (PLL), PEG, Polyurethane (PU)	Patterned substrates	-Forming patterned tissues -Generating shape-controlled cell aggregations
Micromolding 	Alginate, agarose, heparin, HA, dextran, collagen, fibrin, gelatin, PEG, polyacrylic acid (PAA)	Defined blocks	-Forming cell aggregations with various shapes -Fabricating assembled tissue models
Droplet microfluidics 	Alginate, agarose, dextran, HA, collagen, gelatin, polyvinyl alcohol (PVA), PEG	Microgels, microdroplets	-Producing multicellular spheroids -Generating compartmentalized tissues
Microfluidic spinning 	Alginate, HA, chitosan, collagen, gelatin, PEG, PU, PAA, PLGA	Microfibers	-Simulating tubular tissues -Producing prevascularized scaffolds
Electrospinning 	Chitosan, collagen, gelatin, fibrin, silk, PCL, PU, PAA, PLGA	Nanofibers	-Guiding cell alignment and migration -Generating fibrous tissues (e.g., nerve)
3D Bioprinting 	Alginate, agarose, HA, gelatin, collagen, gellan, soy protein, fibrin, PEG, polylactic-co-glycolic acid (PLGA), polycaprolactone (PCL)	Flexible scaffolds	-Forming hierarchical tissues -Fabricating prevascularized scaffolds -Building complex devices

1.2. The skeletal muscle tissue

1.2.1. Anatomy and physiology

The skeletal muscle is one of the largest tissues of the human body, constituting approximately 40% of the fat-free body mass [59]. The primary role of the skeletal muscle is to generate contractile forces that are necessary for locomotion, thermogenesis, and metabolism [60]. Therefore, its correct function is essential for maintaining human health. The skeletal muscle tissue is formed by large, multinucleated cells called myofibers. These fibers are characterized by striations, which are seen as thin light and dark bands across the cells when observed under a microscope. Myofibers are organized parallel to each other in bundles, called fascicles. Individual myofibers are surrounded by a thin layer of connective tissue called endomysium, or basement membrane. The perimysium, a thickened connective tissue layer, encapsulates the fascicles, and the epimysium is a dense layer that surrounds the whole muscle (**Figure 1.7**) [61].

Cellular structure of the skeletal muscle

Skeletal muscle fibers are formed by the fusion of several muscle precursor cells during embryogenesis; therefore, they are multinucleated and long. Mature myofibers can be up to a few cm in length and have diameters of approximately 50-70 μm , with their nuclei located along the periphery [62]. The skeletal myofibers have

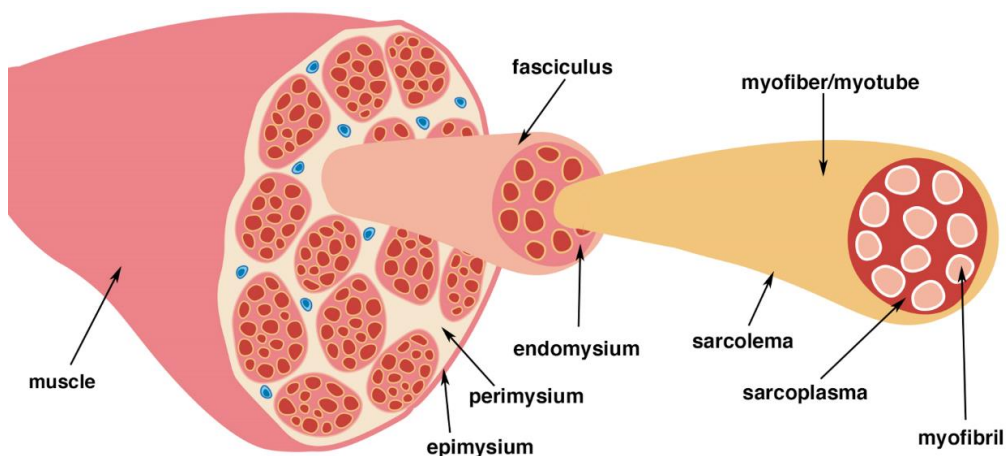


Figure 1.7. Structure of the skeletal muscle anatomy. The epimysium covers the whole muscle. Muscle fibers are grouped in bundles (fascicles). Each fasciculus is surrounded by perimysium while endomysium surrounds the individual myofibers. Each individual myofiber or myotube has a membrane (sarcolemma) and is composed of hundreds of myofibrils. Myofibrils are bundles of organized myofilaments and are surrounded by sarcoplasm. *Adapted from Fernández-Costa et al. [61].*

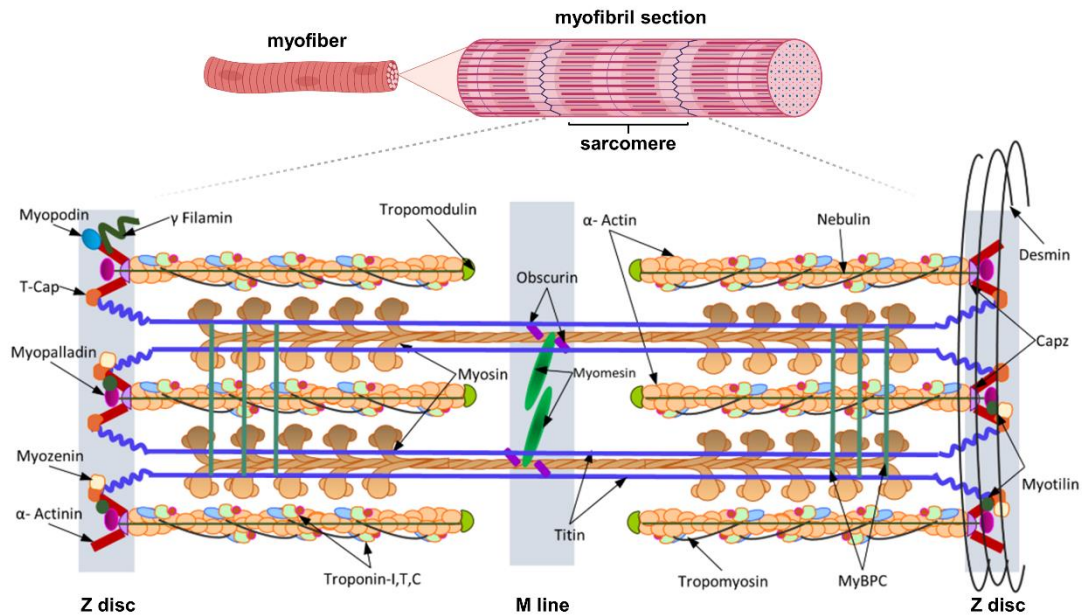


Figure 1.8. Schematic diagram of the sarcomere summarizing organization and location of major sarcomeric proteins. Cytosolic Ca^{2+} causes a conformational change in the structure of troponin C, revealing myosin binding sites. Myosin heads successively bind and move along the length of actin, causing sarcomeric contraction. Titin and nebulin, function as molecular templates maintaining the length of the thick and thin filaments, respectively. The proteins within the M-line and Z-disk function mainly to maintain structural integrity of thick and thin filament lattices, respectively. The desmin intermediate filaments reinforce and integrate the structure of the muscle cell by forming transverse links between adjacent myofibrils. *Adapted from Mukund and Subramaniam [63].*

a highly organized cytoskeleton composed of intracellular contractile proteins assembled into myofilaments. Bundles of organized myofilaments form myofibrils, which are aligned through the whole fiber. Myofibrils are repeating successive sections of the basic contractile unit of skeletal muscle, the sarcomere (**Figure 1.8**) [63].

The sarcomere is a complex unit made of two main myofilaments: thick filaments (myosin and associated proteins) and thin filaments (α -actin and associated proteins), and it is bordered at each end by a line called Z-disk. These myofilaments are in an alternating arrangement that extends parallel to the muscle fiber axis. The striated appearance of skeletal muscle fibers is due to the repetition of the myofilaments and the different ways the light is transmitted in regions containing thick or thin filaments [62]. Thick filaments mostly contain myosin proteins with a head and tail structure. Myosin is considered an enzyme since it hydrolyzes adenosine triphosphate (ATP) (head) and a structural protein (tail). The myosin-associated proteins mainly have structural functions, while others act as regulators

of force generation [63]. Titin is an elastic protein that runs along the thick filament, and its primary role is to guarantee an equal force development through the sarcomere. It also acts as a molecular template for thick filaments [64]. Other proteins, such as myomesin and obscurin, associate myosin with titin. Creatine kinase also binds to myosin, working as a spatial ATP buffer for energy homeostasis. Thin actin filaments are associated with several proteins, such as troponin, tropomyosin, and nebulin. Troponin has different subunits that bind to actin (TNN-I), calcium (TNN-C), or tropomyosin (TNN-T). Tropomyosin stabilizes actin and acts as a scaffold for troponin on the actin filament [65]. Tropomodulin is the capping protein that regulates actin filament length by preventing polymerization or depolymerization. Nebulin has a similar role to titin but for thin filaments. Finally, another essential sarcomeric protein is α -actinin. It is located on the Z-disk and connects titin molecules from opposing sarcomere halves [63].

Contraction and force generation

The sarcomeric contraction involves the movement of the myosin heads (cross-bridges) on actin filaments towards the center of the sarcomere due to a sequence of enzymatic reactions (**Figure 1.9**). Force is generated within each myofibril and collectively experienced by the whole muscle [66]. Briefly, Ca^{2+} is released upon fiber depolarization, raising its concentration in the cytosol and binding to TNN-C. Ca^{2+} binding causes a conformational change in troponin that reveals sites for myosin binding on actin filaments [67]. In each cycle, the cross-bridge attaches to the actin filament, flexes, and then dissociates before returning to its initial configuration and a new binding site on the actin filament [62].

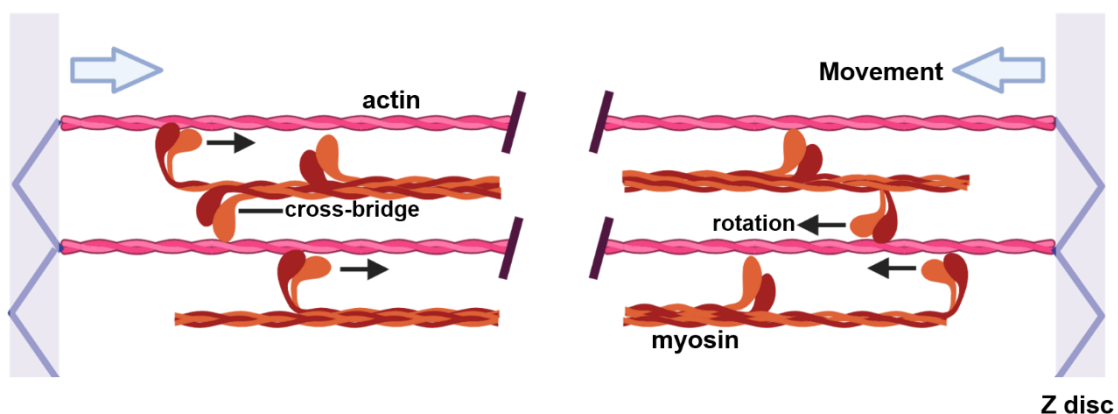


Figure 1.9. Relative movement of actin and myosin filaments. This is achieved by the rotation of the cross-bridge head, which contains the myosin ATPase.

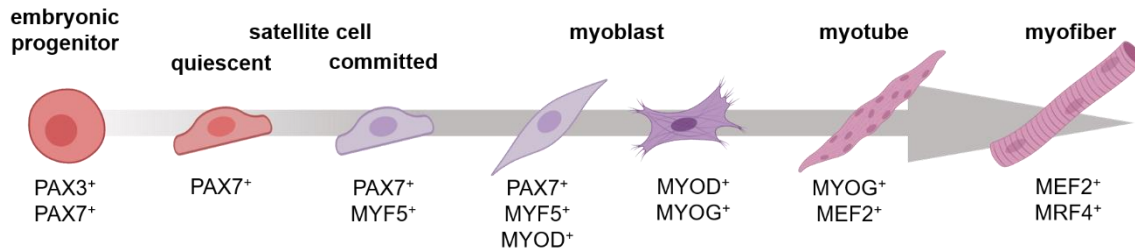


Figure 1.10. Regulation of myogenic differentiation by transcription factors. Satellite cells expressing PAX7 derive from the progenitor cells expressing PAX3/PAX7. Following activation of MYF5 expression in satellite myogenic cells, the myogenic program is activated and myoblasts start expressing MYOD1. Activation of MYOG and MEF2, with downregulation of MYF5 and later MYOD1, marks the start of terminal differentiation into myofibers. Activation of MRF4 occurs several days after the induction of differentiation, following a reduction in MYOG expression.

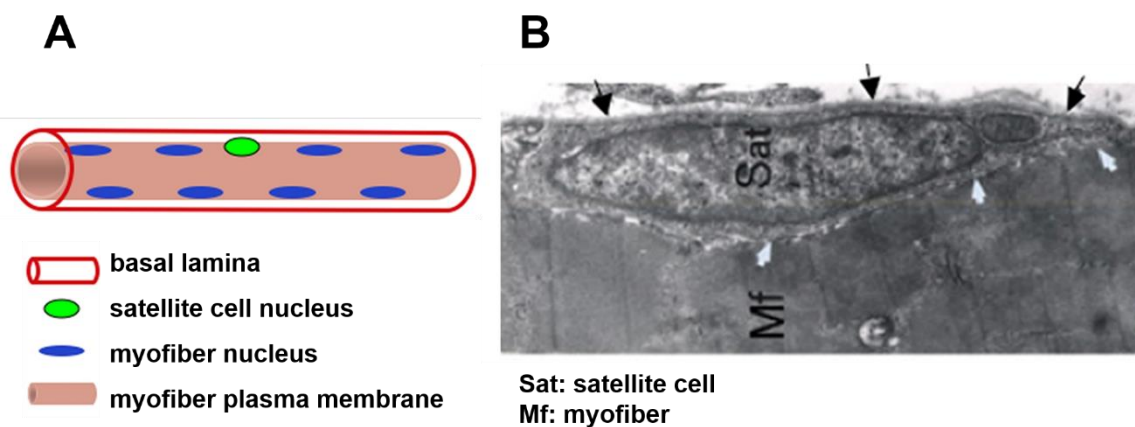


Figure 1.11. Satellite cell location. (A) Healthy adult myofibers present nuclei at the fiber periphery. (B) Electron microscopy image of the satellite cell location. Black arrows depict the basal lamina, and white arrows show satellite cell and myofiber membranes; note the sarcomeric organization within the myofiber. Adapted from Yablonka-Reuveni and Day [70].

1.2.2. Skeletal muscle development

Skeletal muscle fibers are formed by the fusion of muscle precursor cells (myoblasts) to generate multinucleated myotubes, which further mature into myofibers [68]. The development and regeneration of skeletal muscle are regulated by the myogenic regulatory factor (MRF) family of transcription factors [69] (**Figure 1.10**). The only myogenic precursors present after birth in humans are the satellite stem cells (SSCs), located at the periphery of myofibers, on their surface, and beneath their basement membrane (**Figure 1.11**) [70]. These cells are produced by activation of precursor cells expressing PAX3 and PAX7 [71–73]. SSCs are generally quiescent, but during development or after an injury, they are activated by the expression of MYF5 and MYOD1, which induce the myogenic program. SSCs in a proliferative phase are then called myoblasts. The majority of myoblasts proliferates

and differentiates, while the other part goes back to quiescence and restores the pool of SSCs [74]. Myogenesis continues with the activation of MYOG and MEF2, while MYF5 and MYOD1 are downregulated. Then, terminal differentiation of myoblasts into myotubes is induced by activation of a second wave of MRFs (MYOG and MRF4). Mature myotubes present a reduction of MYOG expression. Moreover, they express muscle-specific genes, such as myosin heavy chain (MHC), sarcomeric α -actinin, and titin [75].

1.2.3. Composition of the skeletal muscle extracellular matrix

Myofibers are embedded within a natural 3D scaffold, the skeletal muscle extracellular matrix (ECM), mainly made of collagens, non-collagenous glycoproteins, proteoglycans, and elastin [76]. The skeletal muscle ECM is essential for muscle function since it allows a uniform distribution and transmission of force from muscle to tendon. Besides, the ECM interactions are crucial to maintaining the mechanical homeostasis within the muscle [63]. As described above, the ECM is typically classified into three organized layers: endomysium, perimysium, and epimysium (**Figure 1.7**). Nevertheless, with the increasing knowledge of ECM roles and complexity, it has been argued that a less simplistic skeletal muscle ECM organization should be determined [63,76,77].

Collagens are the most abundant proteins of the skeletal muscle ECM. Glycoproteins are implicated in tissue organization and cell-matrix interactions, and proteoglycans participate in signaling and tissue regeneration [63]. The basement membrane is formed mostly by collagen type IV and laminins, while collagen type I is found mainly in the perimysium and epimysium. All types of collagens in the ECM provide structural support and allow tissue mechanotransduction [78]. In brief, collagen type I fibers provide tensile strength and rigidity. In contrast, collagen type III forms a loose mesh that offers elasticity to the inner layers of the intramuscular connective tissue. Collagen type IV integrates laminins and other proteins into a stable structure, whereas the less abundant collagen type VI is present in all ECM layers [76].

1.2.4. Skeletal muscle metabolism

Energy metabolism

Apart from the biomechanical perspective of skeletal muscle as a tissue responsible for movement generation due to the contraction of its fibers, the skeletal muscle is essential for energy metabolism. The insulin-sensitive glucose transporter type 4 (GLUT4) mediates glucose transport into the muscle. Nutrient increase in the blood after a meal triggers insulin secretion, which regulates the translocation of GLUT4 from intracellular sites to the sarcolemma. Without insulin, most GLUT4 are located in the trans-Golgi network, endosomes, and heterogeneous tubulo-vesicular structures containing specialized GLUT4 storage vesicles (GSVs) and endosomal sorting intermediates. Only around 5% of the total GLUT4 pool is located on the cell surface in the absence of insulin. GSVs translocate to the sarcolemma in response to insulin or exercise, which leads to a 10-fold increase in glucose uptake [79].

Around 80-90% of insulin-stimulated glucose uptake occurs in the skeletal muscle tissue, where glucose is broken down (glycolysis) or stored as glycogen (**Figure 1.12**). Under physiological conditions, roughly two-thirds of all glucose-6-phosphate is turned into glycogen, and one-third enters glycolysis [80]. In glycolysis, glucose is converted into pyruvate, producing energy in the form of ATP and NADH [81]. During the last step of anaerobic glycolysis, pyruvate is converted to lactate. However, during aerobic glycolysis, pyruvate is transported into the mitochondria and converted to acetyl-CoA. Acetyl-CoA enters the tricarboxylic acid (TCA) cycle, producing NADH. Lipids that enter the muscle cell by fatty acid transporters are broken down through β -oxidation of fatty acids and also generate acetyl-CoA, leading to NADH generation. The electron transport chain in the mitochondria uses NADH to produce ATP and water [82].

Insulin resistance and type 2 diabetes

The development of type 2 diabetes occurs in stages. From a general perspective, the onset of the disease involves a reduction in insulin's ability to stimulate glucose uptake in the muscle (clearing glucose from the blood), termed insulin resistance. The failure of GLUT4 translocation to the sarcolemma in response to insulin is considered one of the early steps in developing insulin resistance, which is the hallmark of metabolic syndrome and a precursor of type 2 diabetes [60,79,83].

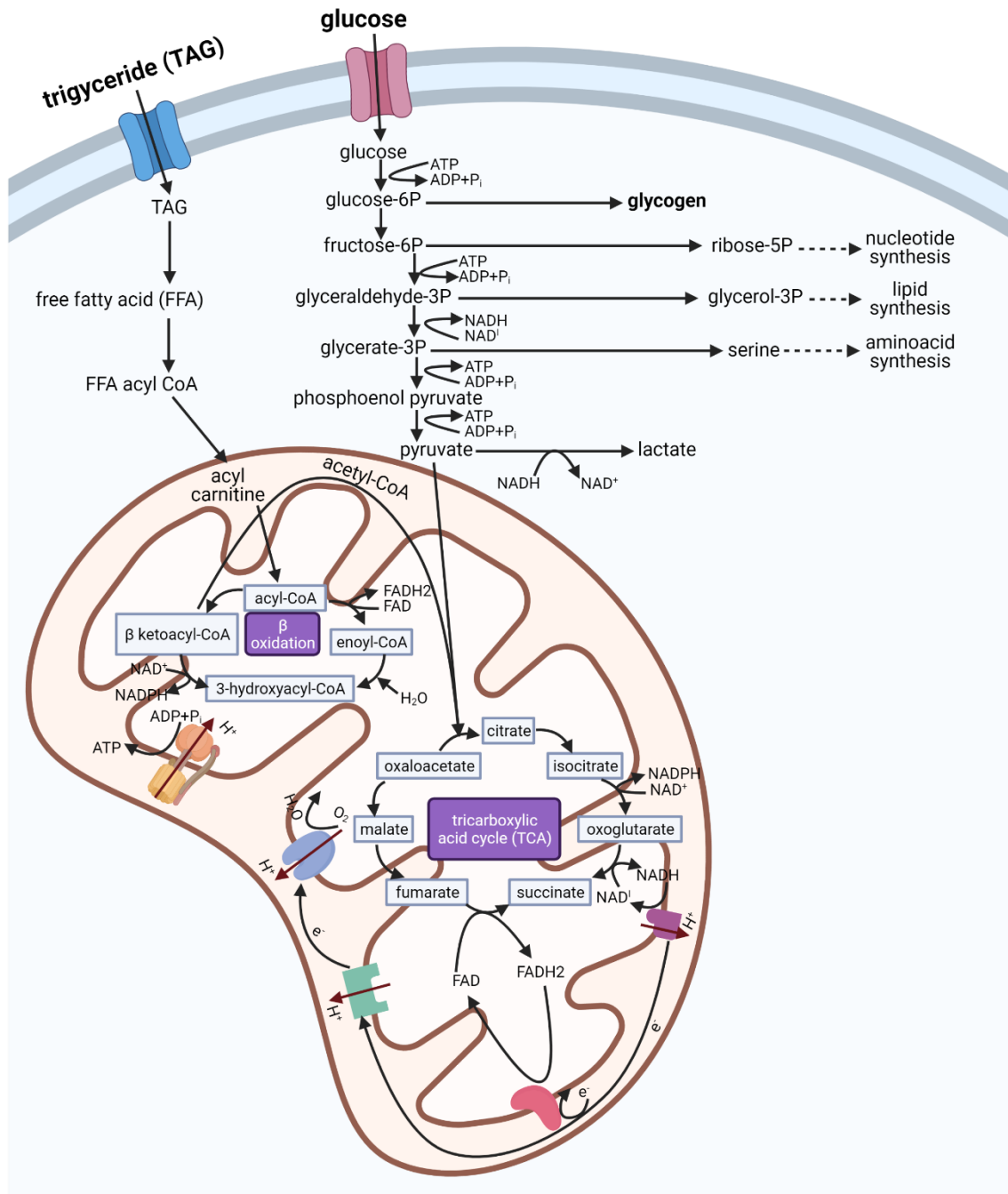


Figure 1.12. Schematic representation of the major pathways involved in muscle energy metabolism. Glycolysis occurs outside the mitochondrion, when a 6-carbon is converted to a 3-carbon pyruvate molecule producing energy in the form of ATP and NADH. Pyruvate is additionally transported into the mitochondrion, where it is converted to acetyl-CoA and enters the tricarboxylic acid (TCA) cycle. Acetyl-CoA is also generated via β -oxidation of lipids in the mitochondrion. The energy generated during TCA (NADH) is used by the electron transport chain, in the cristae of the mitochondrion to generate three ATP molecules and water. In anaerobic glycolysis, the generated NADH is used for lactate production, in contrast to the oxidative phosphorylation system for ATP generation under aerobic conditions. For simplicity, the number of molecules of ATP, NADH, or NAD are not indicated.

Even though pancreatic β -cell failure is required for developing type 2 diabetes, skeletal muscle insulin resistance is considered the primary defect, evident decades before β -cell failure and hyperglycemic symptoms [80].

In the primary phase of insulin resistance, insulin secretion from healthy β -cells is increased to offset the defect in insulin action and maintain normal glucose plasma concentrations. As the syndrome progresses to diabetes, this amplified insulin secretion cannot compensate for the defect in insulin-stimulated glucose uptake, and glucose intolerance arises. In the late stage of diabetes, the pancreatic β -cells lose their extra insulin secretion capacity in response to hyperglycemia [60,80]. As described above, insulin resistance involves the insulin receptor; however, it has been shown that several other hormones and signaling events can weaken insulin action, thus are important in type 2 diabetes [79,83,84].

Skeletal muscle as an endocrine organ

Barely less than two decades ago, the skeletal muscle was identified as an endocrine organ that produces and secretes cytokines and other peptides in response to contraction [85]. These “myokines” exert autocrine metabolic effects

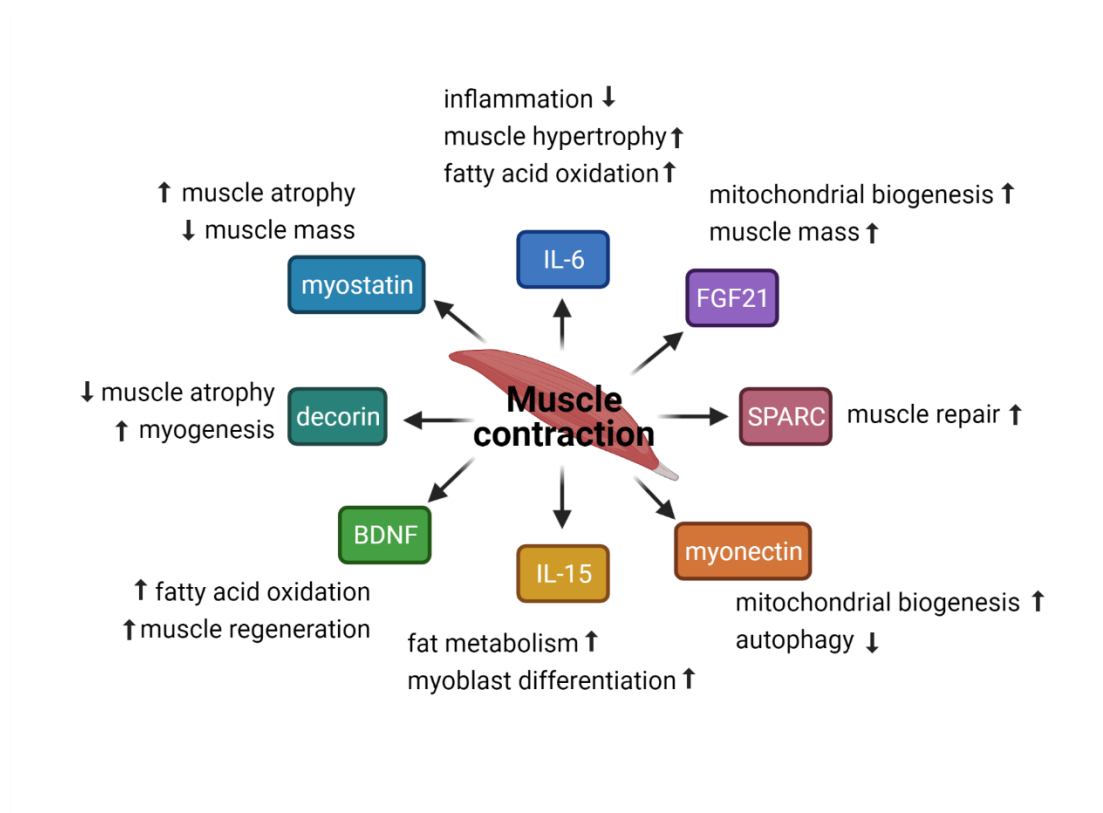


Figure 1.13. The main autocrine effects of skeletal muscle contraction-induced myokines. IL: interleukin; FGF: fibroblast growth factor; SPARC: secreted protein acidic and rich in cysteine; BDNF: brain-derived neurotrophic factor.

(**Figure 1.13**). They are also involved in paracrine and endocrine regulation, affecting other tissues or organs, such as the liver, brain, kidney, pancreas, bone, and adipose tissue (**Figure 1.14**) [84,86].

Muscle-derived interleukin(IL)-6 is the most studied myokine. IL-6 came into focus when it was observed to increase up to 100-fold in circulation during physical exercise [87]. Since then, hundreds of myokines from different families have been discovered by analyzing the secretome of cultured human myocytes [88]. Increasing evidence shows that muscle-derived myokines can improve human health and could alleviate some diseases. However, only a few myokines have been significantly characterized in biological activity and function [89]. For instance, several exercise-induced myokines, such as IL-6, IL-15, and Irisin, are implicated in lipolysis and free fatty acid oxidation [90]. A summary of the myokines and known functions identified to date can be found in **Table 1.2**.

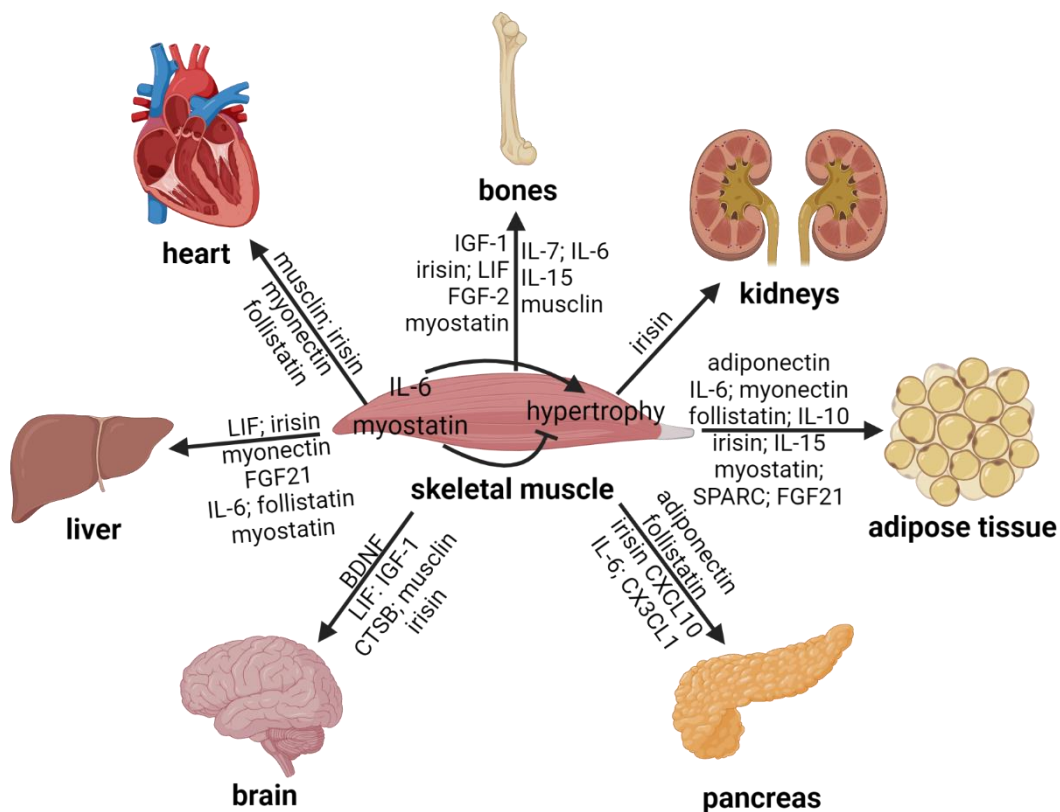


Figure 1.14. The skeletal muscle secretes myokines and communicates with other organs. Myokines mediate the cross talk between skeletal muscle and other organs or tissues by binding to receptors on target cells.

Table 1.2. Myokines and their known metabolic functions. *Adapted from Chen et al. [90].*

Myokine	Target organs or tissues	Metabolic functions
Adiponectin	Adipose tissue, pancreas	Induces anti-inflammatory action and enhances β -cell function
BDNF	Neuronal system, brain, subcutaneous fat, skeletal muscle	Improves learning and memory, induces fat browning, and regulates skeletal muscle metabolism
CTSB	Brain	Enhances memory cognition function, and hippocampal neurogenesis
CX3CL1	Pancreas	Protects β -cells against TNF- α
CXCL10	Pancreas	Critical for exercise-dependent angiogenesis
FGF-2	Bone	Improves bone formation and fracture repair
FGF21	Adipose tissue, liver	Reduces glucose and triglyceride levels and boosts insulin sensitivity and lipolytic response
Follistatin	Liver, heart, pancreas	Stimulates glucose uptake, promotes endothelial cell functions, promotes revascularization, enhances β -cell function, reduces liver fibrosis and functional damage, maintains cardiac growth and development
IGF-1	Bone, brain	Enhances bone remodeling and neuropsychiatric function
IL-6	Liver, skeletal muscle, adipose tissue, pancreas, bone	Modulates muscle growth, maintains glucose homeostasis and lipid metabolism, enhances FFA oxidation and insulin sensitivity, increases osteoblast differentiation
IL-7	Bone	Inhibits bone formation
IL-10	Adipose tissue	Induces anti-inflammatory effects and enhances glucose tolerance
IL-15	Adipocytes, bone, skeletal muscle	Regulates glucose uptake, enhances mitochondrial activity, prevents oxidative stress, and regulates the accumulation of lipids

Irisin	Brain, bone, heart, adipocytes, kidney, blood vessels	Stimulates fat browning, enhances glucose uptake and lipid metabolism, regulates muscle growth, and promotes osteoblast differentiation
LIF	Bone, neurons, liver, skeletal muscle, platelets	Regulates skeletal muscle hypertrophy and regeneration, promotes osteoblast differentiation, inhibits adipocyte differentiation, and protects against cancer cachexia
Musclin	Skeletal muscle, bone, brain, heart	Attenuates glucose uptake and glycogen synthesis, increases exercise capacity, regulates bone growth and brain remodeling, controls blood pressure and vascular contraction
Myonectin	Liver, heart adipocyte, skeletal muscle	Promotes glucose uptake and stimulates fatty acid oxidation
Myostatin	Skeletal muscle, adipose tissue, liver, bone	Modulates muscle growth, attenuates obesity and insulin resistance, regulates bone remodeling, induces energy expenditure and adipocyte browning
SPARC	Adipocytes, skeletal muscle	Modulates skeletal muscle tissue remodeling, inhibits adipogenesis, and enhances systemic glucose tolerance

Interleukin-6 and exercise

Interleukin (IL)-6 is part of the granulocyte colony-stimulating factor-like protein family of cytokines. This cytokine is known to have different immunomodulatory functions that may be anti-inflammatory, pro-inflammatory, or both, depending on the tissue where it is produced [91]. Nowadays, it is known that IL-6 can be produced by immune system cells, adipocytes, and muscle fibers. When synthesized by the immune system cells and adipocytes, IL-6 has a pro-inflammatory function [92]. However, when secreted by muscle fibers, IL-6 appears to have a contradictory role [93]. In skeletal muscle, IL-6 can be synthesized through the macrophages' initial infiltration in the muscle, leading to pro-inflammatory effects [92,94] or produced by myofibers, triggering anti-inflammatory effects [95]. It has been demonstrated that IL-6 is acutely synthesized and secreted post-exercise and has an insulin-like effect on glucose metabolism, increasing insulin-stimulated glucose consumption in human skeletal muscle [88]. Furthermore, the most recent research has shown that the release of contraction-induced IL-6 triggers positive

effects on mitochondrial health and bones and helps control low-grade chronic inflammation through lipid oxidation and IL-6 anti-inflammatory effects [96–98]. For example, exercise and muscle-produced IL-6 inhibit endotoxin-induced tumor necrosis factor-alpha (TNF- α) production in humans [99], and elevated levels of TNF- α , a pro-inflammatory cytokine, are associated with low-grade inflammation, insulin resistance, and atherosclerosis. Nonetheless, these IL-6 anti-inflammatory effects are only significant in individuals with low baseline plasma IL-6 values. Therefore, it is suggested that high plasma levels of IL-6 in the absence of exercise are more closely related to obesity and metabolic syndrome [100,101].

1.2.5. Muscular dystrophies

The skeletal muscle tissue can be affected by several neuromuscular or degenerative disorders, such as myasthenia gravis [102], McArdle disease [103], and muscular dystrophies [104]. Muscular dystrophies are genetically inherited degenerative diseases that share muscle weakness and wasting as common symptoms. Nevertheless, these are very heterogeneous disorders, varying in the age of onset, progression rate, inheritance pattern, and type of affected muscles [104–106]. Rare muscular dystrophy variants are continuously identified. These disorders are usually grouped into the following types: myotonic, Duchenne, Becker, Limb-girdle, facioscapulohumeral, congenital, oculopharyngeal, distal, and Emery-Dreifuss [106]. Myotonic dystrophies are the most frequent in the adult population, affecting between 1 per 3000 and 1 per 8000 adults [107]. Instead, Duchenne muscular dystrophy is the most common in children and is found in approximately 1 per 5000 boys [108]. While individually muscular dystrophies are considered rare diseases, the overall prevalence of combined muscular dystrophies is around 16.14 per 100,000 [109]. Thus, they have a significant impact on society.

Some palliative treatments are available for these diseases, but there is currently no cure for any muscular dystrophy. The underlying heterogeneity of these diseases represents a significant challenge in developing new treatments because it is highly expected that each patient would have a different response to a particular therapy. Remarkably, some drugs for specific muscular disorders have been developed in the last decade, including small molecules and antisense oligonucleotides [110–114]. Still, these therapies must be validated for efficacy and safety in the clinical phases before being widely used in patients.

Myotonic dystrophy type 1

Myotonic dystrophy type 1 (DM1) is a life-threatening, chronically debilitating disorder and the most prevalent hereditary myopathy in adults (for a recent review of DM1 hallmarks, see [115]). Although it is a multisystemic disease, the characteristic feature of DM1 is progressive muscle atrophy, which is a reduction in the size of the skeletal muscle tissue due to protein, cytoplasm, and organelle loss that cause myofiber shrinking [116]. Muscle atrophy usually presents in a distal pattern; therefore, the forearms, hands, ankles, tongue, jaw, and neck muscles are affected more frequently [117]. Moreover, another common symptom of DM1 patients is myotonia (difficulty relaxing a contracted muscle) [118]. As observed in skeletal muscle biopsies from healthy tissues and DM1 patients, DM1 tissues present a significant increase in central nuclei, pyknotic nuclear clumps, ringed fibers, irregular nuclei shape, and myofiber size variability (**Figure 1.15**) [115].

The molecular cause of DM1 is a dynamic mutation that expands the cytosine-thymine-guanine (CTG) triplet repeat in the 3' non-translated region of the *Dystrophia Myotonica Protein Kinase (DMPK)* gene [119]. CTG varies between 5 and 37 repeats in healthy conditions but becomes pathogenic at >50 repeats. The resulting expanded Cytosine-uracil-guanine (CUG) repeat RNAs (CUG^{exp}) accumulate in ribonuclear foci, consisting of hairpin structures that sequester RNA-binding proteins (**Figure 1.16**) [120]. This mutant *DMPK* RNA causes toxic gene misregulation events at the level of gene expression [121,122], translation [123],

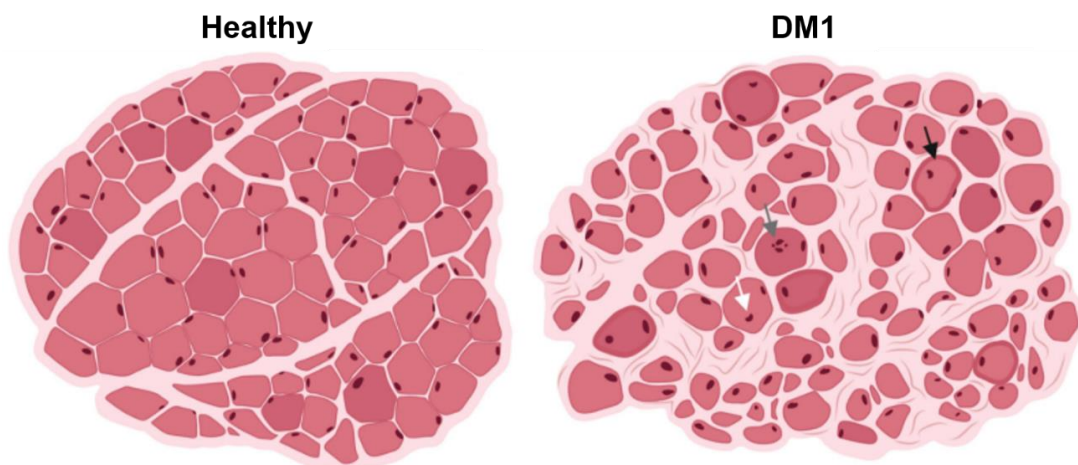


Figure 1.15. Healthy and myotonic dystrophy type 1 (DM1) human skeletal muscle histopathology. Key histopathological signs of DM1, including central nuclei (white arrow), pyknotic nuclear clumps (grey arrow), and ringed fibers (black arrow). Irregularities in fiber shape and size can also be observed. *Adapted from Ozimski et al. [115].*

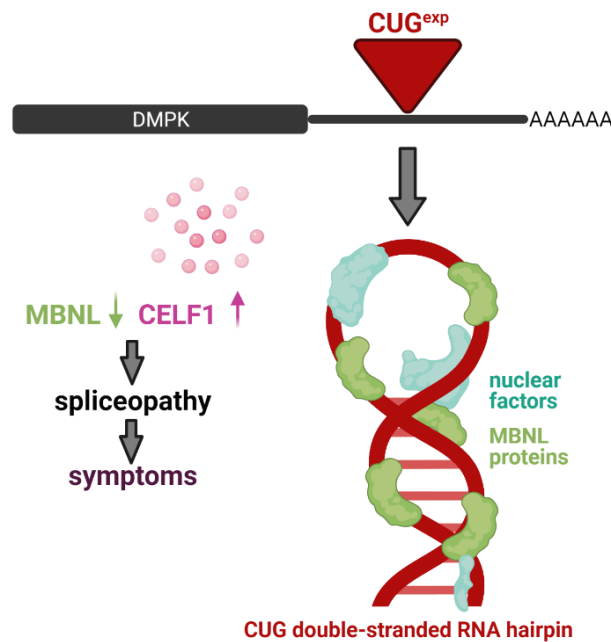


Figure 1.16. RNA toxicity model for DM1 pathogenesis. CUG^{exp} repeat RNAs accumulate in ribonuclear foci forming hairpin structures that sequester RNA-binding proteins, such as proteins of the Muscleblind-like (MBNL) family. MBNL proteins are sequestered (toxic loss-of-function) while CUGBP Elav-like family member 1 (CELF1) is abnormally upregulated (toxic gain-of-function).

Transcriptional silencing

- ① Inhibition of RNA polymerase co-factors
- ② Small molecules that bind to GC-rich repeats

Post-transcriptional silencing

- ③ Antisense oligonucleotides
- ④ Small RNAs targeting CUG repeats

Inhibiting interactions between MBNL and toxic RNA

- ⑤ Small molecules - monomers and polymers
- ⑥ Peptides

Targeting pathways downstream of RNA toxicity

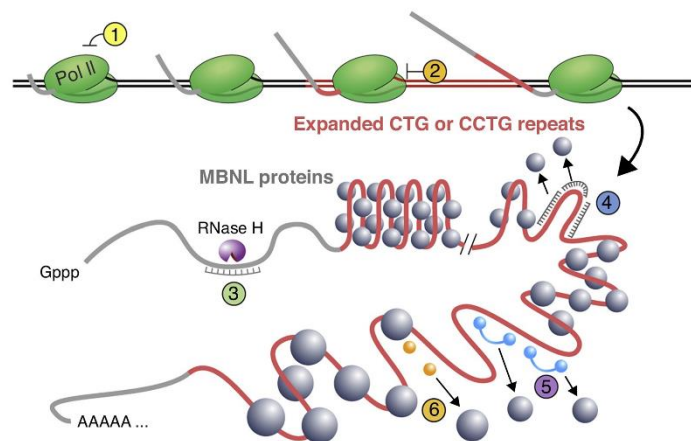


Figure 1.17. Strategies for treating myotonic dystrophy. Adapted from Thornton et al. [142].

gene silencing [124–127], alternative splicing [128–130], and polyadenylation of subsets of transcripts [131]. Proteins of the Muscleblind-like (MBNL) family (such as MBNL1 and MBNL2) and the CUGBP Elav-like family member 1 (CELF1) are the most affected by the CUG^{exp} foci. MBNL proteins are sequestered in these CUG foci and depleted, impairing their molecular function [132]. In contrast, CELF1 is abnormally stabilized. These proteins are critical regulators in RNA splicing, polyadenylation, stability, and translation [133]. Therefore, at a molecular level, DM1 is characterized by a loss-of-function of MBNL1–2 and a gain-of-function of CELF1 [117,120].

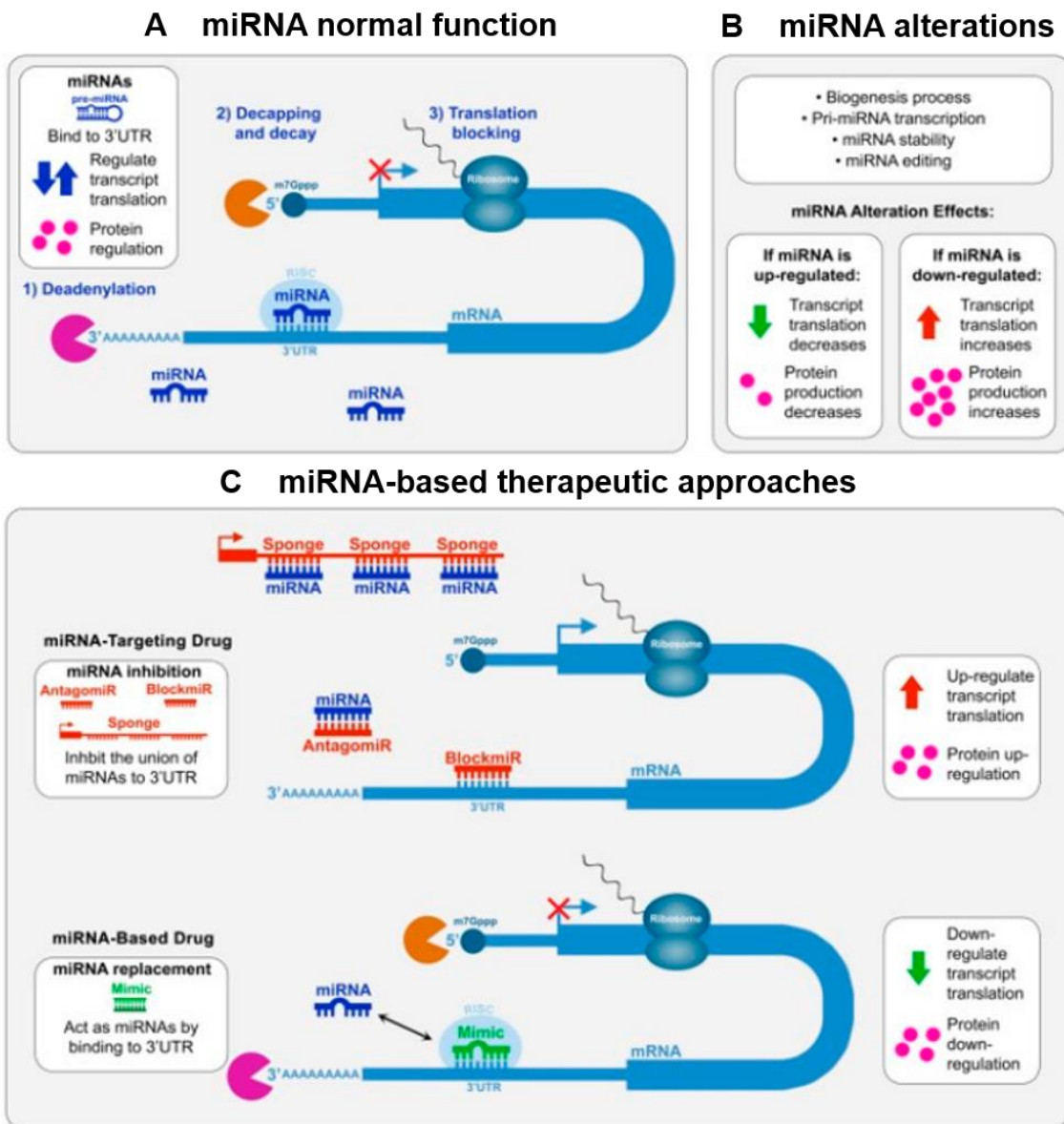


Figure 1.18. MicroRNA (miRNA) mechanisms for mRNA translation, regulation, and therapeutic intervention. (A) *miRNA normal function.* The interaction between miRNA and mRNA targets triggers different mechanisms for transcript regulation in order to reach normal cellular protein levels. (B) *Causes of miRNA dysregulation.* Alterations in miRNA biogenesis, editing, or in its biological stability may cause pathological upregulation or downregulation, which lead to decreased or increased target transcript translation regulation and final protein levels, respectively. (C) *miRNA-based technologies.* (Upper panel in C) When a miRNA is upregulated, inhibition is achieved by using anti-miR products (in red) after miRNA-targeting drug development. AntagomiR synthetic molecules are antisense oligonucleotides (ASOs) perfectly complementary to the specific miRNA target. BlockmiRs are designed to have a sequence that is complementary to one of the mRNA sequences that serve as a binding site for a microRNA. miRNA sponges contain several tandemly arranged miRNA target sequences usually embedded in the 3'UTR of a reporter gene for assessing the activity. (Lower panel in C) miRNA replacement is conducted to restore its function by introducing a miRNA mimic product (in green) and, thus, following miRNA-based drug development. Adapted from López-Castel et al. [113].

Although considerable progress has been made in studying the molecular causes of DM1, there is no effective treatment for patients to date. Animal models, such as mouse [134], fly [135–137], and zebrafish [138], have been used to evaluate different therapeutic candidates [110,113,139–142]. Several therapeutic strategies have been designed to target the mutant allele or its RNA product specifically. Other approaches target signaling pathways downstream from CUG^{exp} expression. These strategies are summarized in (**Figure 1.17**) [142]. Among them, therapeutic gene modulation by microRNAs (miRs) is a promising approach that can regulate the endogenous expression of a gene to mitigate a particular disease (**Figure 1.18**) [143]. Following this strategy, it has been demonstrated that miRs that inhibit MBNL translation can be silenced by antisense oligonucleotides (antagomiRs). Concretely, specific blocking of miR-218 and miR-23b has increased MBNL protein levels and rescued mis-splicing events in DM1 human myoblasts [143] and HSA^{LR} DM1 model mice, where low toxicity, high efficacy, and long-lasting biological effects were observed [143,144]. While these are encouraging results, the effectiveness of treatments for DM1 still needs to be investigated in clinical phases. As previously mentioned, the intrinsic heterogeneity of all muscular dystrophies predicts that each patient would have a different response to any given therapy. Consequently, there is a great clinical need for personalized treatments that target these diseases effectively. Due to the advances in tissue engineering, human-derived *in vitro* tissues are emerging as new preclinical research tools [145,146]. In particular, bioengineered *in vitro* skeletal muscle tissues would provide more efficient and predictive models to improve drug development for muscular dystrophies. The most recent advances and techniques for generating *in vitro* models of skeletal muscle tissue are discussed in the next section.

1.3. Skeletal muscle tissue *in vitro* models

The skeletal muscle tissue has a complex, organized architecture that is closely related to muscle function. This tissue is made of aligned multinucleated myofibers formed by the fusion and differentiation of muscle precursor cells. Animal and human cell lines have been extensively used for translational studies and to evaluate and establish different tissue engineering approaches. The most widely used biomaterials for skeletal muscle tissue models are based on microfabricated hydrogels. Due to the importance of cell alignment, the primary fabrication strategies

focus on providing effective topographical cues that guide the alignment and fusion of muscle precursor cells. The most recent skeletal muscle tissue *in vitro* models will be presented in this chapter and are summarized in **Table 1.3**.

Table 1.3. Novel bioengineering approaches to fabricate skeletal muscle tissue models.

Biomaterial	Cell type(s)	Biofabrication technique	Highlights	Reference
Alginate dialdehyde-gelatin	C2C12 myoblasts	3D Bioprinting	Easy method to align cells by combining bioprinting with appropriate shear stress	(Distler <i>et al.</i> , 2020)
Alginate-PEO bioink with PLC	C2C12 myoblasts and HUVEC endothelial cells	3D printing and electrospinning	Biophysical and biochemical cues facilitate myoblast alignment	(Yeo and Kim, 2020)
Collagen	C2C12 myoblasts and Human microvascular endothelial cells	Extrusion technique	Implantation of endothelialized skeletal muscle tissue enhances microvascularization	(Nakayama <i>et al.</i> , 2019)
Collagen	C2C12 myoblasts	Micromolding	Development of a 3D myogenesis approach with a vessel embedded system	(Wan <i>et al.</i> , 2020)

Collagen with gold nanowires	C2C12 myoblasts	3D Bioprinting	New bioink with gold nanowires as cell aligners that improve the cell orientation when applying an electrical field	(Kim, Jang and Kim, 2019)
Collagen-Matrigel®	Primary myoblasts from mdx mouse model	3D Casting	Automated drug screening BAM-based platform	(Vandenburgh <i>et al.</i> , 2008)
Collagen-Matrigel®	Primary human myoblasts	3D Casting	High throughput micro-muscle platform.	(Mills <i>et al.</i> , 2019)
dECM	C2C12 myoblasts	Thermal gelation	New biomaterial that enhances muscle regeneration when transplanted	(Lee <i>et al.</i> , 2020)
dECM	Primary human myoblasts and HUVEC endothelial cells	3D bioprinting	Enhanced muscle regeneration after implantation of prevascularized muscle bundles in a rodent model	(Choi <i>et al.</i> , 2019)
dECM (Methacrylated)	C2C12 myoblasts	3D Bioprinting	Biochemical and topographical cued biomaterial scaffold	(Kim <i>et al.</i> , 2020)

Fibrin	Primary human myoblasts	3D casting	Intramuscular drug delivery <i>in vitro</i> model	(Gholobova <i>et al.</i> , 2018)
Fibrin-alginate	C2C12 myoblasts	Electrospinning	Study of different mechanical strains to improve myogenic outcomes	(Somers <i>et al.</i> , 2019)
Fibrin-Gelatin	C2C12 myoblasts	3D bioprinting	Study of force modulation and adaptability of 3D printed muscles	(Mestre <i>et al.</i> , 2019)
Fibrin-gelatin-HA-glycerol	human primary muscle progenitor cells (hMPCs)	3D bioprinting	Functional recovery after implantation of multilayered bundles in a rodent model	(Kim <i>et al.</i> , 2018)
Fibrin-Geltrex™	Primary human myoblasts and human stem cells-derived motoneurons	Hydrogel casting of bundles attached to Velcro® anchors	Myobundles with neuromuscular junctions in long-lasting cultures	(Bakooshli <i>et al.</i> , 2019)
Fibrin-Matrigel®	iPSCs from DMD, LGMD other CDM patients	3D casting	Mature myotube recapitulates pathogenic hallmarks	(Maffioletti <i>et al.</i> , 2018)

Fibrin-Matrigel®	C2C12 myoblasts	Micromolding	Fabrication of a high-throughput multiassay platform for the generation of engineered contractile muscle bundles	(Christensen <i>et al.</i> , 2020)
Fibrin-Matrigel®	Primary human myoblasts	Hydrogel casting of bundles within nylon frame	First functional engineered skeletal muscle	(Madden <i>et al.</i> , 2015)
Fibrin-Matrigel®	Human induced pluripotent stem cells	Hydrogel casting of bundles within nylon frame	First functional engineered human skeletal muscle from iPSCs	(Rao <i>et al.</i> , 2018)
Fibrin-Matrigel®	Primary human myoblasts	Hydrogel casting of bundles within nylon frame	Engineered myobundles with the highest specific forces reported to date	(Khodabakus <i>et al.</i> , 2019)
Gelatin	C2C12 myoblasts	Micropatterning	Enhancing of the expression sarcomeric genes	(Denes <i>et al.</i> , 2019)
GeIMA	C2C12 myoblasts	Microfluidic extrusion device	Patterned surface fibers enhance myogenic differentiation	(Shi <i>et al.</i> , 2015)(Ebrahimi <i>et al.</i> , 2018)

GelMA	C2C12 myoblasts	3D Casting	Characterization of geometrical confinement and mechanical stiffness of scaffolds	(Costantini, Testa, Fornetti, <i>et al.</i> , 2017)
GelMA and Collagen methacrylate	C2C12 myoblasts, human adipose stem cells, and human primary muscle progenitor cells (hMPCs)	3D bioprinting	Functional GelMA-based bioink for highly aligned scaffolding	(Kim and Kim, 2020)
PEG-fibrin	C2C12 myoblasts	3D bioprinting	Novel approach to generate skeletal muscle using a self-made 3D bioprinting	(Costantini, Testa, Mozetic, <i>et al.</i> , 2017)
Poly(ethylene glycol) (PEG) - poly(3,4-ethylenedioxythiophene) (PEDOT)	C2C12 myoblasts	Micropatterning	Fabrication of a conductive microgrooved hydrogel for myogenic differentiation.	(Gong <i>et al.</i> , 2019)
Polycaprolactone (PCL)	C2C12 myoblasts	E-field assisted 3D printing	New technique to generate highly aligned skeletal muscle tissue	(Kim, Kim and Kim, 2020)

1.3.1. Cell sources

C2C12 murine myoblasts

The C2C12 cell line is a subclone of C2 myoblasts [produced by 147] that were initially isolated from the thigh muscle of a C3H mouse [148]. These cells differentiate fast in culture after serum removal, generating contractile myotubes that express the characteristic skeletal muscle proteins [149]. Before differentiating, C2C12 myoblasts are star-shaped, mononucleated cells. When myogenic differentiation begins and myoblasts start to fuse, there is a progressive cell shape change towards elongated, multinucleated fibers [150]. The C2C12 cell culture methods and differentiation protocol have been established and well-documented for more than two decades [151]. Thus, this cell line has been extensively used in biomedical research to study myogenic differentiation and skeletal muscle metabolism [reviewed in 152]. Mouse and human myoblasts have shared characteristics in morphology and surface markers. Still, some differences have been identified in proliferation and differentiation rates and expression of differentiation factors [153].

Human primary muscle stem cells

Satellite stem cells (SSCs) are considered the only source of expandable primary myogenic cells present in skeletal muscle [154,155]. These cells can be isolated for *in vitro* research by explant culture or by enzymatic digestion. For explant culture methods, the myofibers are carefully dissected to separate them from their ECM. The myofibers are then placed in dishes coated with gelatin, collagen, or another ECM-like material, where the SSCs activate, migrate, and proliferate [155]. The other method consists of releasing SSCs by enzymatic digestion and mechanical dissociation. The cells are subsequently filtered to obtain single cells in suspension for further plating and expansion [155,156]. Freshly isolated cell preparations are referred to as SSCs. Once satellite cells are cultured and in proliferation, the resulting cells are called myogenic precursor cells or myoblasts [154]. Similar to C2C12 cells, primary human myoblasts proliferate in high serum media and fuse forming multinucleated myotubes when cultured in low serum media. Nevertheless, there are several disadvantages of working with these cells. After serial passaging, they become senescent, limiting their proliferative capacity,

decreasing their ability to differentiate, and varying in phenotype due to the progressive accumulation of DNA damage [157].

Immortalized human muscle precursor cells

Immortalized cell lines have been developed to overcome the problems associated with replicative senescence. In myoblasts, replicative senescence mainly occurs due to two mechanisms: 1) progressive shortening of telomeres at each cell division and 2) activation of the p16-mediated cellular stress pathway [157]. Telomere shortening can be stopped by transducing the cells introducing the cDNA coding for the telomerase catalytic subunit (human telomerase reverse transcriptase: hTERT) [158]. In fact, many cell types, such as fibroblasts and endothelial cells, can be immortalized by introducing hTERT cDNA alone. Nevertheless, in human myoblasts, the expression of cyclin-dependent kinase (CDK)-4 is also required to block the p16INK4a-dependent stress pathway [157].

Immortalized myoblasts are even more relevant in the context of muscular dystrophies. The comparatively short proliferative lifespan of primary myoblasts is more reduced in muscular dystrophies after many cycles of degeneration/regeneration occur *in vivo* before cell isolation [159]. Since the development of models for *in vitro* studies requires large cell numbers that are difficult to obtain with primary cultures, immortalized cell lines of muscular dystrophies represent an essential, necessary tool for comprehensive *in vitro* studies of these disorders.

Transdifferentiated human fibroblasts

Skeletal muscle biopsies are invasive and not always available, especially if a preexisting condition compromises the patient's health. For a less invasive approach, skin fibroblasts have been reprogrammed to develop transdifferentiated myoblasts cells [160–162]. In these studies, fibroblasts were transduced with lentiviral vectors to force the overexpression of MYOD1 and obtain easily accessible human cells for skeletal muscle tissue engineering.

Human pluripotent stem cells (hPSCs)-derived myoblasts

Myoblasts have been successfully derived from human pluripotent stem cells (hPSCs), which include human embryonic stem cells (hESCs) [163] and human induced pluripotent stem cells (hiPSCs) [164]. hPSCs are considered a nearly

unlimited cell source with differentiation capability into all three germ layers of the embryo. Their differentiation into myogenic cells has been explored in the last decade by following transgene-dependent and transgene-free approaches. For instance, the overexpression of MYOD1 by transfection has been used to obtain hPSCs-derived myoblasts to study Miyoshi myopathy and Duchenne muscular dystrophy [165,166]. hPSCs-derived myoblasts have also been obtained by the transgenic overexpression of PAX7 (expressed by the SSCs before MYOD1), resulting in expandable cells called iPax7 [167,168]. Finally, hPSCs can be differentiated through transgene-free strategies that simulate complex developmental events using growth factors and other small molecules [169,170]. However, these differentiation protocols are still very long, expensive, and need to be optimized.

1.3.2. Microfabricated topographical cues for 2D cell culture models of skeletal muscle

The simplest *in vitro* assays for skeletal muscle differentiation are performed by seeding myoblasts on culture vessels without any cell alignment. However, microfabrication strategies such as micropatterning, electrospinning, bioprinting, and microfluidic spinning have been used to create cell culture surfaces that provide topographical cues for the 2D culture of aligned myofibers. These models have highlighted the importance of geometrical cues for improving differentiation into aligned myotubes. Recently, RNAseq analyses of C2C12 myotubes cultured on micropatterned gelatin hydrogels demonstrated the positive effect of topographical cues on the maturation of skeletal muscle cells [171]. The results showed that micropatterned cells have an increased capacity to form aligned sarcomeres and present an enhanced contractile protein expression. In another study, poly(ethylene glycol) (PEG)-based microgrooved hydrogels were used to provide topographical and electrical stimuli to the cells [172]. The electrical properties of the hydrogel were enhanced by combining the PEG hydrogel with poly(3,4-ethylenedioxythiophene) (PEDOT), and bioadhesion was possible due to the inclusion of tripeptide Arg-Gly-Asp (RGD) motifs.

Electrospinning is another common valuable technique for cell guidance due to the possibility of cell seeding over electrospun micro- or nanofibers. For example, mature myotubes have been formed over bundles of fibrin microfibers (**Figure 1.19A**) [173]. Here, mechanical strains were applied to enhance the myogenic

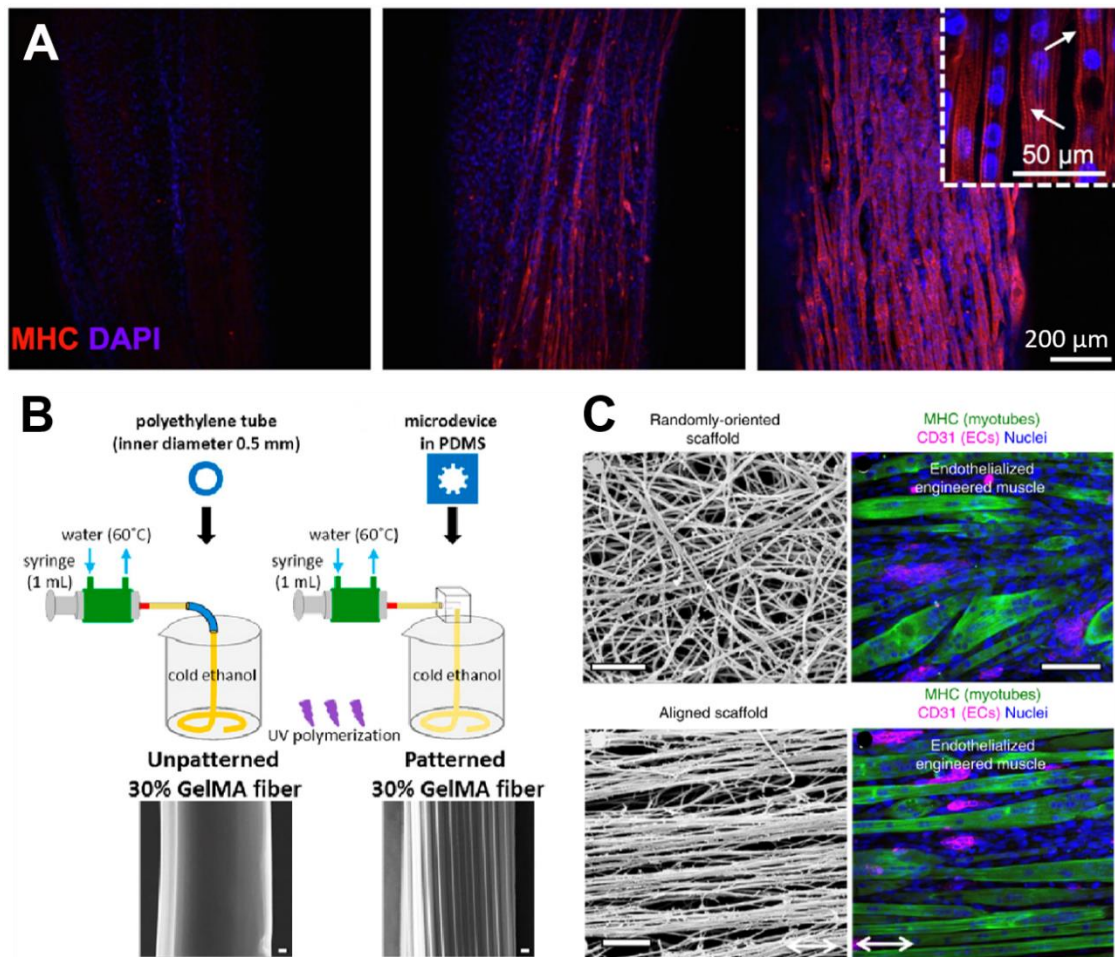


Figure 1.19. Advanced 2D murine skeletal muscle models are fabricated through engineering topographical cues. (A) C2C12 seeded on fibrin microfibers proliferate and mature over 7 days. Nuclei are stained with DAPI (blue). Myotubes present myosin heavy chain (MHC, red) from day 5. *Adapted from Somers et al. [173].* (B) Schematic representation of the fabrication process of unpatterned and micropatterned GelMA fibers. Field emission-scanning electron microscope images showing surface structures of the GelMA fibers. Scale bars: 20 μm . *Adapted from Ebrahimi et al. [177].* (C) Characterization of endothelialized engineered murine muscle. Scanning electron microscopy images of randomly oriented or aligned scaffold nanofibers. Scale bars: 1 μm . Confocal microscopy images showing MHC (green) and CD31 (magenta) staining in differentiated myotubes on randomly oriented or aligned scaffolds. Scale bars: 100 μm . *Adapted from Nakayama et al. [178].*

differentiation of the immature myotubes. In another electrospinning approach, polyvinyl alcohol (PVA)-leached polycaprolactone (PCL) and collagen struts have been used as mechanical supporters with topographical cues for the co-culture of C2C12 myoblasts and human umbilical vein endothelial cells (HUVEC) [174]. HUVECs-laden alginate bioink was uniaxially electrospun on the supporters. C2C12 myoblasts were seeded on the vascularized alginate scaffolds and formed mature myofibers with striated myosin heavy chain (MHC) patterns.

Like electrospinning, bioprinting and microfluidic spinning have been used to generate highly aligned fibers on which cells can be seeded [37–42]. E-field-assisted

3D printing was used to engineer highly hierarchical PCL scaffolds with micro and nanoscale topographical cues [175]. Seeding C2C12 cells on top of these scaffolds enhanced cell alignment and increased myogenic markers. Similarly, microfluidic spun gelatin methacryloyl (GelMA) fibers with a well-defined surface morphology have been fabricated by extrusion through a microgrooved mold (**Figure 1.19B**) [176,177]. The topographical cues on micropatterned GelMA fibers promoted the alignment of seeded C2C12 myoblasts and myotube formation all around the fibers. Combined topographical cues with agrin treatment further enhanced myotube maturation and functionality, as shown by improved contractility under electrical stimulation [177]. Nano-fibrillar collagen fibers generated by extrusion have also been used to give geometrical cues to co-cultured C2C12 and endothelial cells (**Figure 1.19C**) [178]. Scaffold strips made of these nano-fibrillar collagen fibers promoted microvasculature and highly organized myotubes. Altogether, the outcomes of myoblast cell seeding and culture on these different microfabricated structures confirm that geometrical cues are fundamental for engineering mature myotubes *in vitro*.

1.3.3. Tissue-engineered *in vitro* 3D models

Microfabrication approaches in 2D models have highlighted the importance of including topological cues for *in vitro* culture of skeletal muscle tissue. However, topological cues alone cannot resemble the microenvironment of native skeletal muscle tissue. As described earlier (**Chapter 1.1.2**), 3D culture systems can also offer adhesive, soluble, and mechanical microenvironmental cues that influence cell behavior and function. For this reason, 3D scaffolds have become the gold standard for skeletal muscle tissue generation. The primary bioengineering strategy to mimic the extracellular environment and the native cellular morphology consists of encapsulating muscle cell precursors in biocompatible material scaffolds that promote cell alignment and differentiation [179]. These biomaterial scaffolds should provide cells with an appropriate 3D growth environment, optimal oxygen levels, effective nutrient transport, and mechanical integrity over an extended culture period [14]. Hydrogels of natural origin, such as collagen, gelatin, or fibrin, are the most used biomaterials to fabricate scaffolds for engineered skeletal muscle [180]. As previously described (**Chapter 1.1.3**), this is mainly due to their high water content and the presence of cell adhesion and degradation motifs that allow cell growth and

matrix remodeling. 3D bioprinting and hydrogel micromolding have been the most used strategies to fabricate skeletal muscle tissues in the last years.

Murine 3D skeletal muscle models

3D bioprinting is an advantageous technique for the fabrication of skeletal muscle tissue models due to the ability to control fiber alignment and orientation to generate highly ordered scaffolds [181]. Most of the bioprinting designs are based on lines or meshes that guide alignment. For instance, C2C12 cells have recently been embedded in alginate dialdehyde (ADA)-gelatin hydrogels by 3D printing, showing that cells orientate due to shear stress when controlling extrusion pressure through the properly-sized nozzle (**Figure 1.20A**) [182]. In this work, non-degradable

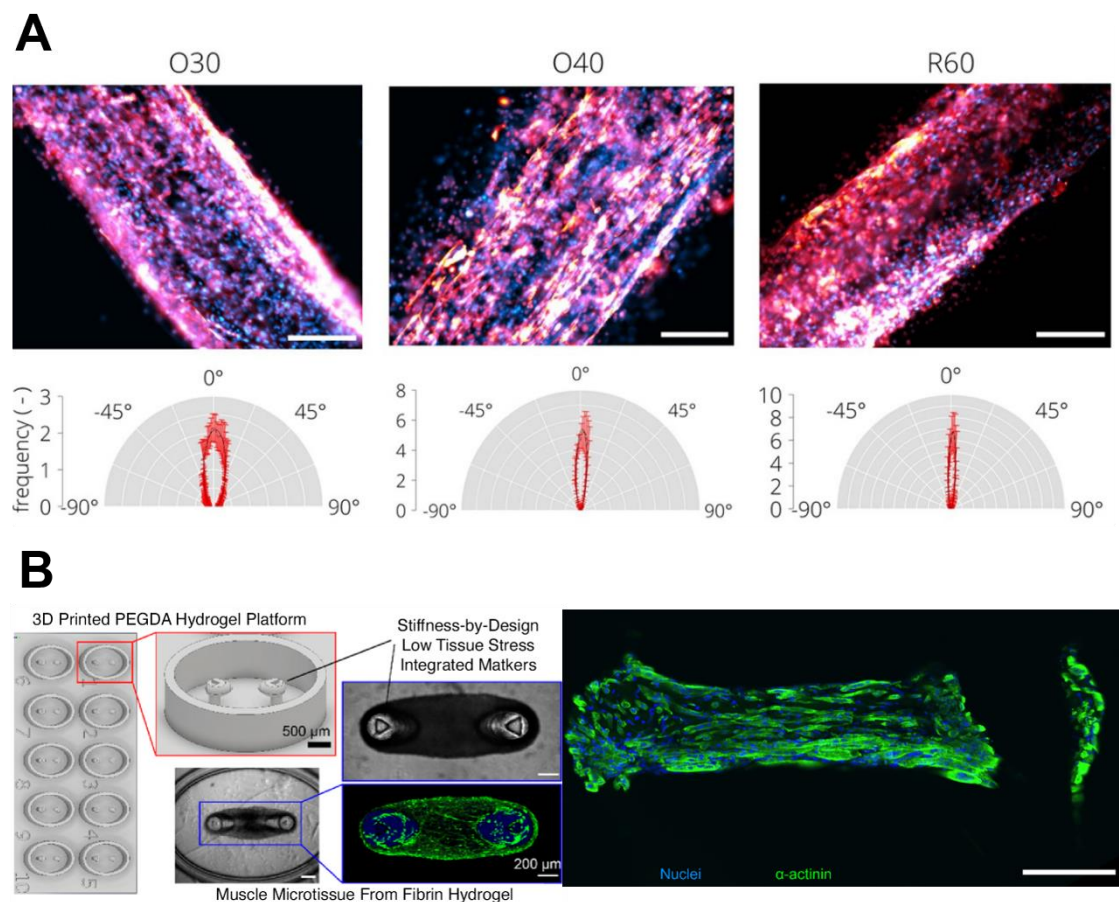


Figure 1.20. Different biofabrication strategies for 3D culture of skeletal muscle cells. (A) Orientation analysis of C2C12 cells encapsulated by 3D bioprinting of cell-laden ADA-GEL bioink. Fluorescence microscopy images of C2C12 cells stained for F-Actin (red) and DAPI (blue). The cells were 3D printed using extrusion nozzles O30 ($d= 330 \mu\text{m}$, $p= 30 \text{ kPa}$), O40 ($d= 330 \mu\text{m}$, $p= 40 \text{ kPa}$), and R60 ($d= 250 \mu\text{m}$, $p= 60 \text{ kPa}$) (scale bars: $200 \mu\text{m}$). The graphs show the corresponding frequency of F-Actin filament orientations depending on extrusion nozzles O30, O40, and R60. A narrowing of the orientation profile is observed. *Adapted from Distler et al. [182].* (B) Multi-assay 3D printed poly(ethylene glycol) diacrylate (PEGDA) hydrogel platforms for casting fibrin hydrogel muscle bundles. Confocal images show cells stained for α -actinin (green) and nuclei (blue). Scale bars: $200 \mu\text{m}$. *Adapted from Christensen et al. [193].*

ADA was combined with gelatin to introduce RGD cell adhesion motifs. The encapsulated cells grow in the printing direction, migrate to the hydrogel surface over time, and differentiate into aligned myotubes. Following a similar approach, C2C12-laden GelMA and collagen methacrylate were bioprinted and photocrosslinked to generate different 3D structures and obtain mature aligned myotubes [183]. Moreover, cell aligners can be added to the bioinks [184]. The authors previously bioprinted collagen along with gold nanowires that aligned following the desired directionality by applying an electric field. Besides, the addition of gold nanowires improved the electrical properties of the scaffolds.

Another combination of natural and synthetic materials for 3D bioprinting was investigated using a custom-made bioprinting system [185]. In this work, aligned C2C12 myoblast-laden hydrogels of PEG-fibrinogen were produced using microfluidic-enhanced 3D bioprinting. Alternatively to the scaffold structures based on 3D bioprinted meshes or lines, hydrogels based on fibrin or collagen can be printed or molded in a cast around flexible posts or pillars. These materials compact when cells remodel the matrix, generating skeletal muscle tissue [186–188]. These platforms allow force measurement of skeletal muscle after electrical stimulation. Myotube contractions result in post bending, and the observed displacement can be used as a proportional measurement of the muscle bundle forces.

Hydrogel micromolding is another common microfabrication technique for skeletal muscle tissue engineering. Usually, PDMS, a biocompatible transparent polymer, is used to create micropatterned molds that transfer the desired features to 3D hydrogels [189,190]. Costantini *et al.* encapsulated C2C12 myoblasts in GelMA hydrogels using PDMS molds with channels of different widths to investigate the effect of geometrical confinement and hydrogel stiffness [191]. The stiffness of these hydrogels was modulated by changing GelMA concentration and UV crosslinking time. The authors concluded that the best alignment and differentiation results were obtained with the narrowest (500 μm) channels and a low stiffness between 1 and 3 kPa. Micromolding can also be used to cast 3D hydrogels around posts or pillars as described above. Recently, this technique was used to develop a new organ-on-a-chip set up with an embedded vessel system [192]. To vascularize the engineered muscle, C2C12 cells were encapsulated in a collagen-Matrigel matrix around PDMS pillars. The researchers used a sacrificial wax template layer to create an embedded channel for HUVEC cell seeding. In another approach, a stereolithographic method

to 3D print poly(ethylene glycol) diacrylate (PEGDA) hydrogels with high precision and high accuracy was developed for more high-throughput studies. This technique allowed the mass-production of structures with posts or cantilevers (**Figure 1.20B**) [193]. The PEGDA platforms were used to cast fibrin hydrogel muscle bundles around the fabricated pillars. In the last couple of years, decellularized ECM (dECM)-derived materials have emerged as attractive natural hydrogels to engineer muscle tissue [194,195]. dECM-derived hydrogels already have tissue-specific biochemical cues, such as growth factors, cytokines, proteoglycans, and structural adhesive proteins [196]. Compared with collagen, C2C12 cells encapsulated in dECM scaffolds resulted in more mature myotubes and better regeneration when implanted in an *in vivo* muscle defect animal model [194]. Furthermore, dECM can be methacrylated to allow bioprinting and photocrosslinking, providing stable topological cues for skeletal muscle engineering [195].

Human 3D skeletal muscle models

In the last decade, skeletal muscle models have mainly been developed with murine myoblasts as a cell model. These studies highlighted critical features for skeletal muscle tissue engineering, such as topological cues, biomaterials, and biochemical factors. The next step is to incorporate human cells to obtain more relevant models that model specific diseases for personalized medicine applications. The first-ever reported 3D skeletal muscle tissues consisted of avian myoblasts encapsulated in a collagen I matrix compacted around pillars [197,198]. The matrix's contraction promotes cell alignment in the direction of the pillars that act as anchoring points, producing long multinucleated myofibers [199]. As described in **Chapter 1.2.3**, collagen I is one of the main components of the skeletal muscle extracellular matrix [76]. However, myogenic maturation and the tissue's contractile force can be diminished due to the relatively high stiffness of collagen hydrogels, especially for large macroscopic scaffolds [14,78]. For this reason, besides collagen, materials with better mechanical properties are being employed. Among them, fibrin composite hydrogels appear to be the most promising materials for fabricating functional skeletal muscles due to their ability to be remodeled by cells and induce ECM synthesis [200].

Functional human skeletal muscle tissues were developed for the first time by the Bursac group using primary human myoblasts. The authors fabricated 3D bundles by casting fibrin-Matrigel® hydrogels within PDMS molds inside a nylon

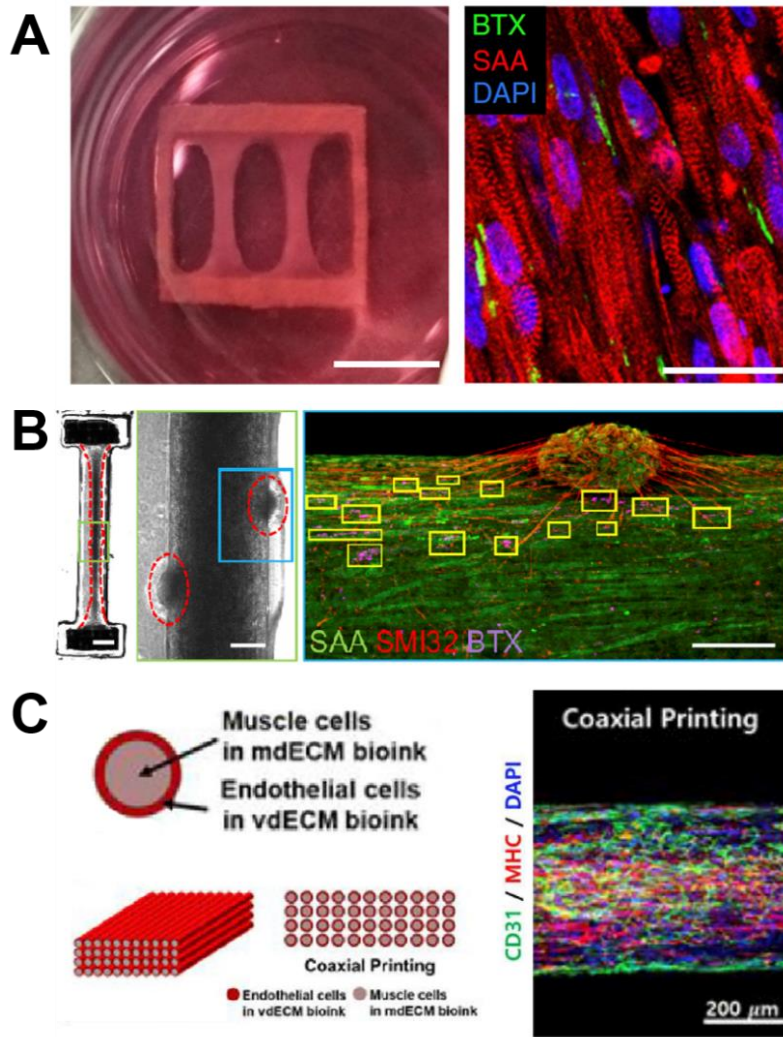


Figure 1.21. Human 3D bioengineered skeletal muscles. (A) Structure of hiPSC-derived muscle bundles anchored within a nylon frame. Scale bar: 5 mm. Representative longitudinal section of 2-week differentiated bundles showing aligned, cross-striated myotubes. SAA= sarcomeric alpha-actinin, BTX= α -bungarotoxin labeling acetylcholine receptors (AChR) and DAPI counterstains myotube nuclei. Scale bar: 25 μ m. *Adapted from Rao et al. [202].* (B) Stitched phase contrast image of a representative 3D skeletal muscle-motor neuron (MN) co-culture. Neuromuscular tissue is outlined with a red dashed line in the left panel. The region outlined in the green box is magnified in the image to the immediate right. Red dashed lines in the right panel outline motoneuron clusters. Scale bars: 2 mm (left panel) and 200 μ m (right panel). *Adapted from Bakooshi et al. [204].* (C) Schematic representation of coaxial printing. Immunofluorescent image of a 3D printed muscle construct. CD31= cluster of differentiation 31, marked endothelial cells, MHC= myosin heavy chain, and DAPI = stained nuclei. The images were taken from the center of the construct. *Adapted from Choi et al. [206].*

frame [201]. Then, active force measurements were performed in response to electrical and biological stimulation. Following the same biofabrication method, the authors generated skeletal muscle tissues derived from direct reprogramming of hiPSCs (**Figure 1.21A**) [202]. Overexpression of PAX7 was induced to obtain satellite cell-like cells (iPax7 cells). Remarkably, the human muscle 3D bundles were

cultured for up to 4 weeks, being the longest culture time reported to the date. The developed myotubes presented a correct membrane localization of dystrophin and generated active twitch and tetanic contractions. The mature tissues retained a pool of PAX7+ cells and MYOG+ myotubes, mimicking the satellite-cells presence in native muscle. Although all these models present different myotube maturation levels, it has been demonstrated that electrical stimulation training enhances myofiber hypertrophy and metabolic flux [203]. One week of an electrical stimulation training regime resulted in an increased myotube diameter by 40%, and the highest specific forces reported to date for an engineered human muscle (19.3 mN mm⁻²). Fibrin-Geltrex™ hydrogels were used to develop a more complex human skeletal muscle model by co-culturing primary human myoblasts with human stem cell-derived motoneurons (**Figure 1.21B**) [204]. The resulting bioengineered human skeletal muscle tissues formed neuromuscular junctions (NMJs) in a long-lasting culture for up to 3 weeks. In the last years, 3D bioprinting has been applied to fabricate human skeletal muscle tissues [205,206]. A cell-laden fibrin bioink was bioprinted with gelatin as a sacrificial material to create organized multilayered muscle bundles [205]. The resulting myofibers were aligned and densely packed. dECM has also been used as a bioink for 3D printing human skeletal muscle bundles (**Figure 1.21C**) [206]. Porcine muscular tissue-derived dECM was used to print primary human myoblasts in granule-based reservoirs. Going a step further, the researchers used coaxial printing of porcine blood vessel-derived dECM with endothelial cells to allow the prevascularization of these muscle tissue.

Engineered human skeletal muscles for drug screening platforms

Engineered skeletal muscles have been recently tested as drug screening platforms. Human myoblasts encapsulated in fibrin hydrogels were integrated with a stereotactic setup that allows modeling intramuscular injection *in vitro* [207]. The release of injected drugs and their metabolites were monitored over time with spectrophotometry and luminescence. Even though these models are helpful for intramuscular drug injection studies, their relatively large size limits their potential as a drug screening platform. These bioartificial fibrin muscles require large numbers of cells, which can be costly and difficult to obtain. Existing microfabrication technologies have permitted these tissues' miniaturization to obtain high-throughput systems [187,208–210]. For example, Mills *et al.* developed a 96-well micro-muscle platform using primary human myoblasts encapsulated in a collagen-Matrigel®

composite matrix around micropillars [208]. The authors affirmed that this microfabrication protocol reduced the size, reagents, and overall compared to the state-of-the-art skeletal muscle bioengineering approaches mentioned above [201,202]. Nevertheless, the reported specific forces and protein expression levels obtained after optogenetic stimulation with this miniaturized system are still equivalent to immature muscle in a fetal-like state. Thus, training and maturation of the micromuscles are needed to create a successful high-throughput screening platform.

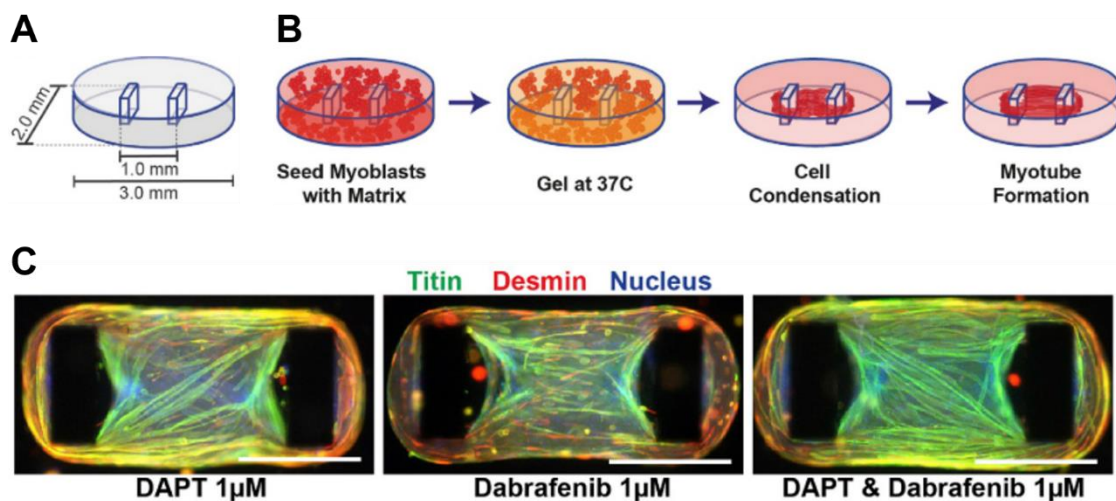


Figure 1.22. Human skeletal micromuscle 96-well platform. (A) Schematic representation of cell culture insert containing an elliptical seeding well with two elastomeric poles. Each well of a 96 well-plate contains an insert. (B) Automatic tissue formation within the micro-muscle platform. Myoblasts are seeded into the elliptical well in combination with matrix and allowed to gel at 37 °C. Cells subsequently condense around the two elastomeric poles. (C) Immunostaining of desmin, titin, and nuclei after a 5-day treatment with DAPT (Notch pathway inhibitor), dabrafenib (kinase inhibitor) or in combination. Scale bars: 500 µm. Adapted from Mills et al. [208].

1.3.4. Modeling muscular dystrophies *in vitro*

Muscular dystrophies are genetically heterogeneous diseases. Therefore, some muscular dystrophies affect each patient in different disease progression rates and severity of the symptoms. For this reason, effective treatments for patients depend on future personalized medicine. The development of *in vitro* bioengineered tissues from patient-derived cells is a great necessity for the research of personalized therapies. Currently, only a few works have been performed with patient-derived cells to create these personalized *in vitro* platforms. In a recent study, hiPSCs derived from patients with different types of muscular dystrophies (Duchenne (DMD), limb-

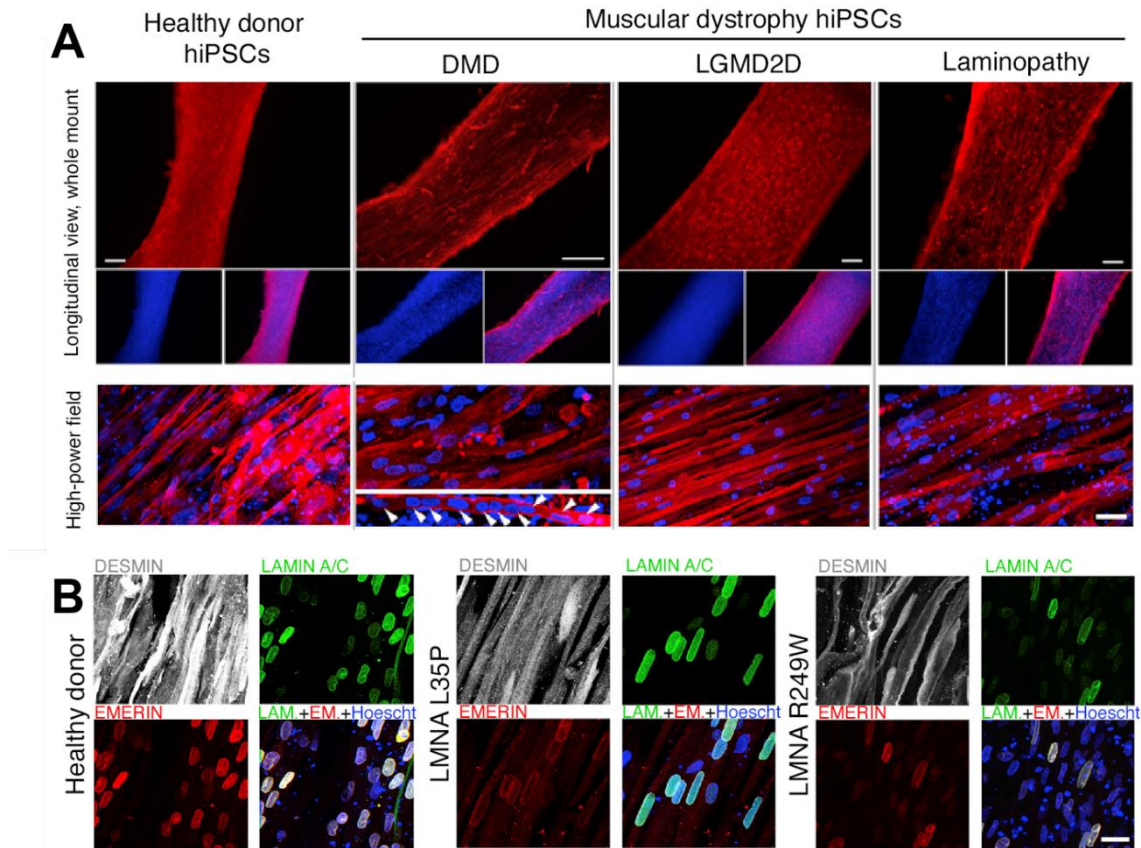


Figure 1.23. Modeling muscular dystrophies using tissue engineering. (A) 3D artificial skeletal muscle constructs derived from healthy and dystrophic hPSCs. Immunofluorescence for myosin heavy chain (MyHC) on muscle constructs derived from hESC and dystrophic hiPSCs (DMD, LGMD2D, and skeletal muscle LMNA) differentiated in 3D for 10 days. Nuclei are counterstained with Hoechst. Arrowheads: multinucleated myotubes. Scale bars: top 250 μ m, bottom 25 μ m. (B) Confocal (z stacks merge) immunofluorescence for DESMIN (myotubes), LAMIN A/C, and EMERIN (nuclear lamina) on hiPSC-derived (healthy and LMNA mutant) artificial muscles. Hoechst: nuclei. Scale bars: 15 μ m. *Adapted from Maffioletti et al. [211].*

gridle, and other congenital muscular dystrophies) were used to generate 3D engineered skeletal muscle tissues (**Figure 1.23A**) [211]. hiPSCs were encapsulated in fibrin hydrogels and cultured under tension to mechanically stimulate myogenic differentiation. Myotubes expressed myogenic maturation markers and displayed the pathogenic characteristics of these muscular dystrophies. Notably, the researchers examined whether the 3D nature of the engineered skeletal muscle tissues would facilitate the recognition of pathological hallmarks that are less evident in traditional 2D cultures. Remarkably, the 3D reconstruction of engineered skeletal muscle models highlighted less prominent features in conventional monolayer cultures (**Figure 1.23B**). The results demonstrated that bioengineered skeletal muscle tissues from patient-derived cells are excellent tools to study the pathogenic pathways of muscular diseases and test potential treatments. However, these patient-derived skeletal muscle tissue platforms have not been used to test potential

drugs for muscular dystrophies yet. In 2009, an automated drug screening platform using contractile muscle tissue engineered from dystrophic murine myoblasts was developed by Vandeburgh and colleagues [210]. Primary myoblasts isolated from the DMD mouse model (mdx mice) were encapsulated in a collagen-Matrigel® matrix and cast around two PDMS pillars to generate miniature bioartificial muscles (mBAMs). The dystrophic mBAMs were electrically stimulated to measure their force generation before and after the administration of potential anti-DMD drugs. Eleven of the 31 tested drugs increased the dystrophic mBAMs tetanic force, obtaining a similar response than DMD patients to many compounds. These results demonstrate the potential of this miniaturized platform as a preclinical model. Nonetheless, mouse-derived cells do not help consider the heterogeneity of muscular dystrophy patients. Therefore, incorporating engineered skeletal muscle tissue from patient-derived cells in these automated drug screening platforms would represent a powerful tool for the preclinical research of these diseases.

Chapter 2. OBJECTIVES

The skeletal muscle tissue has structural, motility, and metabolic functions that are crucial for human health but can be affected by several neuromuscular or metabolic disorders. Research on fundamental skeletal muscle biology and drug screening for new therapies currently rely on performing studies on two-dimensional (2D) *in vitro* cell cultures and *in vivo* animal models. Nevertheless, these methods have significant limitations that affect their relevance to humans. For instance, conventional cell cultures cannot emulate the complex three-dimensional (3D) organization and function of the skeletal muscle tissue, and animal data is often inaccurately extrapolated to human conditions. Therefore, it is necessary to develop alternative strategies that can complement existing *in vitro* and *in vivo* methods in fundamental and preclinical research.

The hypothesis of this thesis is that skeletal muscle precursor cells encapsulated in a suitable microfabricated biomaterial with the appropriate topographical and environmental cues would lead to the formation of functional skeletal muscle tissues that can be used for *in vitro* research. Moreover, employing human cells in skeletal muscle disease models would significantly improve current *in vitro* studies. Following this hypothesis, the main aim of this work is to develop *in vitro* 3D skeletal muscle tissues for the study of muscle metabolism and disease modeling. The specific objectives are the following:

1. To fabricate and characterize composite hydrogels for the encapsulation of skeletal muscle precursor cells in long-lasting scaffolds.
2. To generate functional 3D skeletal muscle tissues and monitor their metabolism using a microfluidic system that includes electrical stimulation and biosensors.
3. To develop a 3D human skeletal muscle tissue model for myotonic dystrophy type 1 using patient-derived cells.
4. To generate functional 3D human skeletal muscle tissues using xeno-free nanocomposite hydrogels.

Chapter 3. MATERIALS AND METHODS

3.1. Cell culture

3.1.1. Murine myoblasts cell culture

Frozen vials containing murine C2C12 myoblasts (CRL1772™, ATCC®) were thawed by gentle agitation in a 37 °C water bath. The vial content was transferred to a 15 mL conical tube containing 9 mL of growth medium warmed at 37 °C. The C2C12 growth medium consisted of Dulbecco's Modified Eagle Medium with 4.5 g L⁻¹ glucose and L-glutamine (DMEM high glucose, Gibco, Thermo Fisher Scientific) supplemented with 10% v/v fetal bovine serum (FBS, Thermo Fisher Scientific) and 1% v/v penicillin/streptomycin (P/S, 10000 U mL⁻¹, Thermo Fisher Scientific). The cell suspension was centrifuged at 200 x g for 5 min, and the supernatant was discarded. The cell pellet was then resuspended in 1 mL of growth medium, and cells were counted using a Neubauer chamber (Thermo Fisher Scientific). Cells were plated in flasks treated for cell culture at a density of 5 x 10³ cells cm⁻² for cell expansion and placed in an incubator. In all cases, cells were grown at 37 °C in a humidified atmosphere containing 5% CO₂. The growth medium was renewed every 2 to 3 days until ~70% confluency was observed. It is crucial that the culture does not become confluent as this will deplete the myoblastic population in the culture.

Once ~70% confluency was reached, cells were detached from the culture flask. The culture medium was removed. The cell layer was then washed with warm 1x Phosphate Buffered Saline (PBS, Thermo Fisher Scientific) and treated with 2 to 3 mL of 0.25% w/v Trypsin 0.53 mM EDTA solution (Thermo Fisher Scientific) for 5 min at 37 °C. Then, 6 to 8 mL of growth medium were added to the flask, and the cell suspension was collected by pipetting. Finally, cells were counted with a Neubauer chamber, and the appropriate aliquots were passaged to new culture flasks for subculturing or used in the experiments. C2C12 cells were used up to passage 8.

To induce C2C12 differentiation into myotubes, cultures were allowed to reach confluency, and the medium was changed to a differentiation medium. The C2C12 differentiation medium consisted of DMEM high glucose, supplemented with 2% v/v horse serum (Thermo Fisher Scientific) and 1% v/v P/S.

3.1.2. Human immortalized fibroblasts cell culture

Immortalized human fibroblasts from a DM1 patient (carrying 1300 CTG repeats quantified in the blood cells) and an unaffected donor (control) [212] were provided by Dr. Denis Furling and Dr. Vincent Mouly (Institute of Myology, Paris, France). Fibroblast cells were grown in DMEM high glucose supplemented with 1% v/v P/S and 15% v/v FBS. We followed the same procedure for cell detaching and subculturing as for C2C12 cells, except fibroblasts were plated at a density of 5.7×10^3 cells cm^{-2} . Also, an automated cell counter (Countess™ II, Applied Biosystems, Thermo Fisher Scientific) was used for all experiments. Human fibroblasts were used up to passage 12. Transdifferentiation into myoblast-like cells was induced by turning on the myogenic program, forcing MyoD expression when culturing cells in muscle differentiation medium (MDM). MDM consisted of DMEM high glucose supplemented with 1% v/v P/S, 2% v/v horse serum, 1% v/v apo-transferrin (10 mg mL^{-1} , Sigma-Aldrich), 0.1% v/v insulin (10 mg mL^{-1} , Sigma-Aldrich), and 0.02% v/v doxycycline (10 mg mL^{-1} , Sigma-Aldrich). For cell differentiation in 2D, fibroblasts were seeded at 1.2×10^4 cells cm^{-2} in 12-well plates containing glass coverslips coated with $50 \mu\text{g mL}^{-1}$ collagen type I (rat tail, Corning) and cultured in growth medium. Once the cells were confluent, the growth medium was replaced by MDM to induce the myogenic program.

3.1.3. Human immortalized muscle satellite stem cells culture

Human immortalized muscle satellite stem cells (HuMSCs) were provided by Dr. Bénédicte Chazaud from the Institute of Myology (Lyon, France). Primary muscle satellite stem cells were previously isolated from a healthy 14-year-old muscle biopsy and immortalized using CDK-4/hTERT expression. Cells expressing PAX7 were grown in Skeletal Muscle Basal Medium (PromoCell), containing skeletal muscle supplemental mix (#C-39365, PromoCell: Calf serum 0.05 mL mL^{-1} , Fetuin (bovine) $50 \mu\text{g mL}^{-1}$, Epidermal Growth Factor (recombinant human) 10 ng mL^{-1} , Basic Fibroblast Growth Factor (recombinant human) 1 ng mL^{-1} , Insulin (recombinant human) $10 \mu\text{g mL}^{-1}$, and Dexamethasone $0.4 \mu\text{g mL}^{-1}$), 1% v/v P/S, and 10% v/v FBS. The protocol for cell detaching and subculturing was slightly modified from the other cell lines. Since this growth medium is a low serum formulation (5% v/v), trypsin is not completely neutralized. Therefore, cells were immediately centrifuged after cell

detaching to remove trypsin. Cells were plated at a density of 5.7×10^3 cells cm^{-2} and used up to passage 30.

The growth medium added after cell encapsulation did not contain FBS but was supplemented with 1 mg mL^{-1} of 6-amino-n-caproic acid (ACA, Sigma-Aldrich). The differentiation medium (HMDM) consisted of DMEM, high glucose, GlutaMAX™ (Gibco, Thermo Fisher Scientific), 1% v/v Penicillin-Streptomycin-Glutamine (P/S-G, 100 X, Gibco, Thermo Fisher Scientific), and 1% v/v Insulin-Transferrin-Selenium-Ethanolamine supplement (ITS-X, 100 X, Gibco, Thermo Fisher Scientific), and 1 mg mL^{-1} of ACA.

3.2. Composite hydrogels as scaffolds for skeletal muscle tissue engineering

3.2.1. Synthesis and characterization of prepolymer precursors

Synthesis of gelatin methacryloyl

Gelatin methacryloyl (GelMA) was synthesized following a previously described protocol [47,213]. Gelatin (Sigma-Aldrich) was dissolved at 10% w/v in 1X PBS at 60 °C. Then, either 1.25% v/v or 5% v/v of methacrylic anhydride (Sigma-Aldrich) was carefully added to the solution drop by drop at a constant rate of $500 \mu\text{L min}^{-1}$, under stirring conditions at 50 °C. The reaction was stopped after 1 h by a 1:5 dilution in warm PBS (40 °C) and dialyzed against Milli-Q water with 6–8 kDa MWCO membranes (Spectra/por, Spectrumlabs). The water was changed every 4 h for 4 days to remove methacrylic acid and salts. After dialysis, GelMA solution was distributed in 50 mL conical tubes and frozen at -80 °C for 2 days. Then, GelMA was placed in a freeze dryer for 5 days before storage at -20 °C until further use.

Synthesis of carboxymethyl cellulose methacrylate

Sodium carboxymethylcellulose (CMC, Sigma-Aldrich) was methacrylated at the maximum degree of methacrylation based on the work by Jeon *et al.* [214]. First, an activating buffer consisting of 50 mM MES hydrate (Sigma) and 0.5 M NaCl (PanReac) in Milli-Q water was prepared, and the pH was adjusted to 6.5. Then, CMC was dissolved (1% w/v) in the activating buffer at 60 °C under stirring conditions. The methacrylation reaction was performed by mixing the CMC solution with 1-Ethyl-3-(3-dimethylaminopropyl)carbodiimide (EDC, 20 Mm, Sigma-Aldrich),

N-hydroxysuccinimide (NHS, 10 mM, Sigma-Aldrich), and 2-aminoethyl methacrylate (10 mM, Sigma-Aldrich). The reaction was stopped after 24 h with excess acetone (Panreac) and filtered using a vacuum flask. The precipitate was dried in an oven at 50 °C and subsequently dissolved in Milli-Q water (1% w/v). The solution was dialyzed against Milli-Q water using 3.5 kDa MWCO membranes (Thermo Fisher Scientific). Finally, the solution of carboxymethyl cellulose methacrylate (CMCMA) was frozen at -80 °C for 2 days and lyophilized for 5 days before storage at -20 °C.

Colorimetric TNBSA assay

2,4,6-Trinitrobenzene Sulfonic Acid (TNBSA, Thermo Fisher Scientific) is a rapid and sensitive assay reagent for the determination of free amino groups [215]. This assay was performed to determine the methacrylation degree of GelMA resulting from the reaction of gelatin and 1.25% or 5% v/v of methacrylic anhydride during its synthesis. Primary amines form a highly chromogenic derivative upon reaction with TNBSA, which can be measured at a wavelength of 335 nm. Therefore, the amount of lysine groups modified from gelatin can be determined [213]. Gelatin and GelMA were dissolved in the reaction buffer (0.1 M sodium bicarbonate, pH 8.5) in a concentration range from 31.25 µg mL⁻¹ to 2000 µg mL⁻¹ and placed in a 96 well-plate (100 µL per well). Five different concentrations were used, and three samples per condition were prepared. Then, 50 µL of a TNBSA 0.01% w/v solution in reaction buffer were added to each well. The reaction was left for 2 h at room temperature and under agitation to ensure all the amino groups react with the TNBSA. The reaction was stopped by adding 25 µL of HCl 1M to each well. Finally, the plate was read using a spectrophotometer to get the absorbance of each concentration at 335 nm.

To calculate the degree of methacrylation, we used the following formula:

$$\% \text{ of methacrylated amines} = \frac{Abs_{gel} - Abs_{GelMA}}{Abs_{GelMA}} \cdot 100$$

Where Abs_{gel} and Abs_{GelMA} represent the absorbance of gelatin or GelMA at a specific concentration.

Nuclear magnetic resonance (NMR)

For $^1\text{H-NMR}$, CMC, and CMCMA were dissolved in D_2O and analyzed on a Varian Inova 500 MHz spectrometer (Varian). All samples were measured with a relaxation delay of 1 s for 64 scans.

3.2.2. Preparation of prepolymer solutions

The polymer precursors were mixed in different concentrations and dissolved in 1X PBS containing the photoinitiator. The final concentrations of photoinitiator, either 2-Hydroxy-4'-(2-hydroxyethoxy)-2-methylpropiophenone (Irgacure, I2959, Sigma-Aldrich) or lithium phenyl (2,4,6-trimethylbenzoyl)phosphinate (LAP, TCI EUROPE N.V.), were fixed at 0.4% or 0.1% w/v. The prepolymers were covered from light and placed in a water bath at 65 °C for 1 h to obtain homogeneous solutions. The solutions were prepared to obtain final concentrations of 5% or 1% w/v GelMA and 1% w/v CMCMA, alginate methacrylate (AlgMA)¹, or polyethylene glycol diacrylate (PEGDA, 4000 Da, Sigma-Aldrich).

3.2.3. Physical characterization of composite hydrogels

Swelling analysis

The prepolymer solutions were prepared as described in **Chapter 3.2.2**. Hydrogels for swelling analysis were fabricated by placing the prepolymer solution in a 48-well plate (300 μL per well). After UV light exposure, hydrogels were carefully removed from the well-plate, rinsed with 1X PBS, and their initial weight was measured. The wet weight was then assessed after 1, 3, and 7 days in PBS, following a quick wipe with tissue paper to remove excess water. The mass increase was calculated by normalizing each wet weight value with the initial weight of the sample. After 7 days, samples were rinsed with Milli-Q water and dried. The swelling ratio, Q , of the hydrogels was determined by:

$$Q = \frac{W_s - W_d}{W_d} \cdot 100$$

¹ AlgMA was synthesized and characterized by Andrea García-Lizarríbar in collaboration with the Nanobioengineering Research Group at the institute for Bioengineering of Catalonia (IBEC).

Here, W_d and W_s represent the weight of dried hydrogels and the weight after swelling in PBS, respectively.

All hydrogels in this work were fabricated using the UV light source of a 3D bioprinter (3D Discovery BioSafety, regenHU; 365 nm, 3 W cm⁻²) or a UV Crosslinker (UVP Crosslinker, model CL-1000L, Analytik Jena; 365 nm, 40 W).

Degradation analysis

Hydrogels were fabricated as described above for the swelling analysis. Subsequently, the samples were transferred from the 48 well-plate to 6 well-plates and left in 1X PBS. After 3 days, each sample was weighed and immersed in 3 mL of a collagenase type II (Thermo Fisher Scientific) solution in PBS. The collagenase type II concentration was 1.5 U mL⁻¹ for hydrogels fabricated using the 3D Bioprinter's UV light source and 0.5 U mL⁻¹ for those fabricated with the UVP crosslinker. Hydrogels were incubated at 37 °C, under shaking conditions (100 rpm). Then, the samples were weighed after 1, 2, 3, 4, and 6 h. The remaining hydrogel mass percentage (% W_r) was determined by:

$$\%W_r = \frac{W_t}{W_i}$$

Here, W_i and W_t represent the weight of the samples at the swelling equilibrium and after collagenase incubation, respectively.

Mechanical analysis

Uniaxial compression tests of all hydrogel formulations were performed using a Zwick Z0.5 TN instrument (Zwick-Roell) with a 5 N load cell. Hydrogels were fabricated following the same protocol as for the swelling analysis. After reaching equilibrium swelling in PBS, cylindrical samples were cut using a 10 mm diameter biopsy punch. The accurate hydrogel diameters and heights were measured before the experiment. Wet hydrogel samples were tested at room temperature up to 30% final strain (deformation), using the following parameters: 0.1 mN preload force and 20% min⁻¹ strain rate. Stress-strain data were obtained from the acquired force–deformation graphs. The compressive modulus values were automatically calculated from the slope of the linear region corresponding to 10-20% deformation (strain) with the TestXpert software (Zwick-Roell).

To obtain Young's modulus of the micropatterned GelMA-CMCMA hydrogels in liquid conditions, samples were photomolded as described later in **Chapter 3.4**. After 24 h of incubation at 37 °C, the stiffness was measured by atomic force microscopy (AFM) following a previously described protocol [216,217]. Briefly, indentation measurements were conducted using a NanoWizard® 4 Bioscience AFM (JPK Instruments) mounted onto a Nikon Ti inverted microscope. Silicon nitride pyramidal tips (NanoWorld) with nominal spring constants of 0.08 Nm⁻¹ were used. Series of 10 indentations at a frequency of 0.05 Hz (10 μm amplitude) were performed in different positions of the GelMA-CMCMA micropatterns. Finally, the Hertz model for a pyramidal tip was fitted to the measured force-distance curves using the JPK data analysis software².

Scanning electron microscopy imaging and pore size analysis

Hydrogels for scanning electron microscopy (SEM) imaging were fabricated following the same protocol for swelling and compression measurements. After 24 h of incubation, the hydrogels were washed with Milli-Q water and fixed for 1 h in a 2.5% glutaraldehyde solution (Sigma-Aldrich). Following several washes, samples were dehydrated by sequential immersion in graded ethanol solutions in Milli-Q water. Washings of 10 min were performed with 50%, 70% (x2), 90% (x3), 96% (x3) and 99.5% (x3) ethanol. To dry the hydrogels without causing their collapse, samples were placed in a critical point drying chamber (K850, Quorum Technologies). Ethanol was completely replaced by liquid CO₂ and gradually heated until CO₂ achieved gas phase equilibrium and was slowly drained. After critical point drying, samples were covered with Au and imaged by ultrahigh-resolution scanning electron microscopy (Nova NanoSEM 230, FEI Company) operating in a low vacuum mode (0.5 mbar of water vapor pressure). SEM images of the hydrogels fabricated using the 3D Bioprinter's UV light source were used to quantify the pore size distribution³ using the Fiji image processing package, a distribution of Image J [218].

² AFM measurements and data analysis were performed by Dr. Jordi Comelles, in collaboration with the Biomimetic Systems for Cell Engineering Research Group at IBEC.

³ Pore size distribution analysis was performed by Andrea García-Lizarrívar, in collaboration with the Nanobioengineering Research Group at IBEC.

3.3. C2C12 cell culture in composite hydrogels for 3D bioprinting of skeletal muscle tissue

3.3.1. Preparation of cell-laden prepolymer solutions

All prepolymer solutions for cell encapsulation were prepared in sterile conditions and mixed in a 1:1 ratio with a cell suspension in growth medium. First, the prepolymers (GelMA, CMCMA, AlgMA, and PEGDA) were weighed in the desired concentrations, sterilized by 15 min of UV exposure inside the biosafety cabinet (Telstar Bio II Advance), and placed inside sterile Eppendorf tubes. The photoinitiators (either I2959 or LAP) were dissolved in sterile 1X PBS (37 °C) and filtered using a 0.22 µm filter. The appropriate volume of this solution was added to the prepolymers. The tubes were covered from light and placed in a water bath at 65 °C for 2 h or until the solution became homogeneous. After this time, the prepolymer solutions were transferred to the 37 °C water bath before cell encapsulation.

C2C12 cells were detached from culture flasks following the protocol from **Chapter 3.1.1**. Cells were counted using a Neubauer chamber and centrifuged for 5 min at 200 x g. Then, cells were resuspended in the appropriate volume of growth medium and carefully mixed with the prepolymer solution for cell encapsulation.

3.3.2. Cell metabolic activity under different GelMA hydrogel fabrication conditions

A multifactorial screening was performed to evaluate the effect of GelMA concentration (1% or 5% w/v), type of photoinitiator (I2959 or LAP), photoinitiator concentration (0.1% or 0.4% w/v), and UV exposure (3 W cm⁻² for 5 s or 25 s) on cell metabolic activity. Cell-laden prepolymer solutions (10⁶ C2C12 cells mL⁻¹) were placed in a 96 well-plate (20 µL per well). After UV exposure using the 3D Bioprinter's UV light source, samples were rinsed with growth medium to remove unreacted reagents and cultured for 24 h. Then, cell-laden hydrogels were incubated with an alamarBlue (Invitrogen, Thermo Fisher Scientific) solution of 10% v/v in growth medium for 3 h at 37 °C, following the manufacturer's protocol. Finally, the absorbance was read at 570 nm (λ_1) and 600 nm (λ_2). The percentage of reduction of alamarBlue, an indicator of cell metabolic activity, was determined by the following equation:

$$\% \text{ Reduction} = \frac{(\varepsilon_{OX})\lambda_2 \cdot A\lambda_1 - (\varepsilon_{OX})\lambda_1 \cdot A\lambda_2}{(\varepsilon_{RED})\lambda_1 \cdot A'_2 - (\varepsilon_{RED})\lambda_2 \cdot A'\lambda_1} \cdot 100$$

Here, ε_{OX} and ε_{RED} represent the molar extinction coefficient of alamarBlue oxidized and reduced form, respectively. A represents the absorbance of the test wells, and A' represents the absorbance of the negative control well.

3.3.3. Cell viability and proliferation in 3D composite hydrogels

The prepolymer concentrations for the following experiments were defined according to the physical characterization results and the cell metabolic activity assay. These final prepolymer solution concentrations were: 5% w/v GelMA with 0.1% w/v of LAP photoinitiator, and with or without 1% w/v CMCMA, AlgMA or PEGDA. Cell-laden prepolymer solutions (10^7 cells mL^{-1}) were placed in cylindrical molds of 6 mm inner diameter and 750 μm height. The samples were photocrosslinked by a 5 s exposure to UV light at 3 W cm^{-2} (3D Bioprinter's UV light source). This procedure was followed by immersion of the cell-laden hydrogels in growth media to remove the unreacted reagents. Finally, samples were placed in an incubator at 37°C and 5% CO_2 atmosphere.

Cell viability assay

C2C12 cells were encapsulated in each hydrogel as described above. The viability was assessed after 1 and 7 days using the Live/Dead™ Viability/Cytotoxicity assay kit (Thermo Fisher Scientific) and Hoescht (Thermo Fisher Scientific) to stain the nuclei. This assay determines live and dead cells simultaneously with two probes that measure recognized cell viability parameters: intracellular esterase activity and plasma membrane integrity. In live cells, esterases convert non-fluorescent calcein acetoxymethyl (calcein AM) to calcein, which produces intense green fluorescence. On the other hand, ethidium homodimer (EthD-1) dye is excluded by live cells. However, EthD-1 can enter cells with a damaged plasma membrane. Its fluorescence is enhanced 40-fold when it binds to nucleic acids, labeling dead cells with bright red fluorescence [219]. Cell-laden hydrogels were washed with warm, sterile PBS to remove FBS esterase activity. Then, we prepared a working solution of $0.5 \mu\text{L mL}^{-1}$ calcein AM, $2 \mu\text{L mL}^{-1}$ EthD-1, and $1 \mu\text{L mL}^{-1}$ Hoescht (Thermo Fisher Scientific) in PBS. Samples were covered from light and incubated for 20 min, at 37°C , under shaking conditions. Finally, cell-laden hydrogels were washed with PBS.

Fluorescence images were captured using confocal microscopy (TCS SPE, Leica) and processed by MATLAB software⁴ (Supporting Information in Appendix A). The cell viability percentage was calculated as the fraction of living cells with respect to the total cell number.

Cell proliferation in 3D composite hydrogels

Cell proliferation within the different composite hydrogels was studied after one week of encapsulation. The growth medium was removed, and cell-laden hydrogels were washed with PBS. Cells were fixed in a 10% formalin solution (Sigma-Aldrich) for 30 min. The samples were then washed with PBS, and cells were permeabilized with 0.1% v/v Triton X-100 (Sigma-Aldrich) in PBS for 15 min. The hydrogels were incubated in 100 nM Rhodamine-Phalloidin 480 (Cytoskeleton) overnight to stain filamentous actin (F-actin). After washing with PBS, nuclei were stained with 300 nM 4',6-diamidino-2-phenylindole (DAPI, Thermo Fisher Scientific) for 15 min. Finally, the cell-laden hydrogels were mounted and observed by confocal microscopy.

3.3.4.3D Bioprinting of cell-laden composite hydrogels and differentiation into myotubes

The 3D bioprinting design was made using the BioCAD v1.0 software (regenHU) as an array of 20 parallel filaments inside a 16 mm diameter circle. The array was designed to consist of two layers of cell-laden hydrogel inside each well of a 6 well-plate. Computer-Aided Design (CAD) files were opened in the 3D DISCOVERY HMI software (regenHU) to use with the bioprinter (3D Discovery BioSafety). Cell-laden prepolymer solutions were prepared as described in **Chapter 3.3.3**. The solutions were then introduced in a 3-cc printing syringe (Nordson Corporation) and placed in the bioprinter's direct dispensing head. 3D printing was performed with a cooling chamber at 10 °C through a 200 µm inner diameter nozzle. The printing rate was fixed at 7 mm s⁻¹, and the printing pressure varied depending on the loaded prepolymer solution. We used 2.5, 2.5, 3, and 5 bar for GelMA, GelMA-CMCMA, GelMA-AlgMA, and GelMA-PEGDA, respectively⁵. After the two layers

⁴ MATLAB code for cell viability was written by Ferran Velasco from the Biosensors for Bioengineering Research Group at IBEC.

⁵ 3D bioprinting was performed in collaboration with Andrea García-Lizarribar from the Nanobioengineering Research Group at IBEC..

were extruded, each well was exposed to 5 s of UV light for hydrogel photocrosslinking. Growth medium was added and replaced every two days. On day 5, the culture medium was switched to differentiation medium. The samples were fixed after 11 days following the procedure from **Chapter 3.3.3**. After permeabilization, the samples were treated with a blocking-permeabilization solution consisting of 0.2% v/v Triton X-100 and 1% w/v bovine serum albumin (BSA, Sigma-Aldrich) in PBS for 1 h. In addition to F-actin and nuclei staining, immunofluorescent staining of myosin heavy chain-4 (MYH4) was performed by incubating the samples in an MF20 Alexa Fluor 488 solution (1:100, eBioscience, Thermo Fisher Scientific) overnight.

3.3.5. Myotube alignment and fusion index analysis

Z-stack images obtained by confocal microscopy were processed using ImageJ software. Myosin heavy chain 4 (MYH4) staining was used to analyze the fusion index and myotube alignment. Myotube alignment was assessed by measuring the angle formed between the myotubes and the longitudinal axis of the printed pattern. The fusion index was calculated by dividing the number of nuclei within the myotubes by the total number of counted nuclei, and this was expressed as a percentage. Three samples for each condition were used, and more than 100 myotubes were analyzed for each sample.

3.3.6. Statistical analysis

All data collected were presented as the mean \pm standard deviation (SD) using GraphPad Prism software (GraphPad). ANOVA and t-tests were performed in StatGraphics Centurion software (StatGraphics) to compare treatments. A *p*-value of 0.05 or less was considered statistically significant.

3.4. Skeletal muscle tissue formation in photomold patterned hydrogels

As an alternative to bioprinting, a photomold patterning technique was used to encapsulate cells in micropatterned hydrogels [220]. This technique allowed the fabrication of skeletal muscle microtissues on any surface that could be placed inside the UVP Crosslinker. In this thesis, the hydrogel micropatterning was performed either on the muscle-on-a-chip microdevice's well or functionalized glass coverslips.

3.4.1. Fabrication of microstructured PDMS stamps

Microstructured PDMS (poly(dimethylsiloxane), Sylgard™ Elastomer base, and curing agent, Dow) stamps were fabricated by replica molding of silicon wafer molds.

Microfabrication of silicon molds

Silicon wafer molds were fabricated by standard photolithography techniques using SU-8 negative photoresist. First, silicon wafers (4" n-type <111>, MicroChemicals GmbH) were cleaned in a plasma chamber for 20 min at 6.8 W. Then, the wafers were heated for 5 min in a hotplate at 95 °C to dehydrate them. Negative resist SU-8 2100 (2100, MicroChem) was spin-coated in 2 steps to obtain structures of 100 μm or 200 μm in height. To make the patterns, a mask aligner (SÜSS Microtec, MJB4) was set to 240 mJ cm⁻² energy radiation at 365 nm. A high-quality emulsion flexible film was used as a photomask (JD Photodata). Irradiation time was set to 20 s. The negative-tone exposed regions of SU-8 were crosslinked by a hotplate cycle of 65 °C and 95 °C for 5 and 20 min, respectively. The labile photoresist was removed by developing the crosslinked patterns immersing the wafer in SU-8 developer (MicroChem) for 10 min. Then, the development was stopped by 2-propanol. After a quick N₂ blow, we heated the molds for 60 min at 120 °C. Finally, the SU-8 patterned silicon molds had to undergo silanization to obtain hydrophobic surfaces and avoid permanent bonding with the PDMS.

Replica molding of microstructured PDMS stamps

The polymer elastomer base and curing agent were weighted in a 10:1 ratio. After mixing thoroughly, we degassed the polymer in a vacuum chamber. PDMS was poured on the patterned silicon substrate and cured at 80 °C for 4 h. Finally, PDMS was detached and cut off using a biopsy punch. We obtained microstructured PDMS stamps of 6 mm in diameter, with channels of 100 μm or 200 μm of width. Finally, PDMS stamps were cleaned by sonication in Milli-Q water and 2-propanol for 5 min and dried using N₂ flow before using them for tissue fabrication.

3.4.2. C2C12 encapsulation in micropatterned hydrogels

Gelatin methacryloyl (GelMA) and carboxymethyl cellulose methacrylate (CMCMA) were synthesized as previously described (**Chapter 3.2.1**). These

prepolymer precursors and the LAP photoinitiator were dissolved in C2C12 growth medium at 65 °C for 2 h in sterile conditions. GelMA, CMCMA and LAP concentrations were fixed to obtain final concentrations of 5%, 1%, and 0.1% w/v, respectively. The prepolymer solution was then mixed with a C2C12 cell suspension to obtain a final cell density of 2.5×10^7 cells mL⁻¹. A drop of cell-laden GelMA-CMCMA prepolymer (20 µL) was placed on the surface of interest (muscle-on-a-chip microdevice with ITO electrodes, **Chapter 4.2**). Then, a microstructured PDMS stamp of 6 mm in diameter (channels of 200 µm width and spacing and 270 µm in height) was pressed lightly on top, filling the microchannels with the solution. The hydrogel was photocrosslinked using a UVP Crosslinker (model CL-1000L, 365 nm, 40 W, from Analytik Jena) with exposure times between 18 s and 120 s. The energy dose for every time point was measured using a wireless power meter (model PM160 Si Sensor Power Meter, 400–1100 nm, 10 nW–200 mW, Thorlabs). Finally, the PDMS stamp was carefully removed, and the 3D micropatterned cell-laden hydrogels remained on the surface. Growth medium was added and renewed every 2 days. After 6 days, the culture medium was switched to differentiation medium to promote the formation of myotubes.

3.4.3. Cell viability and morphology in micropatterned hydrogels

C2C12 cells were encapsulated in GelMA-CMCMA hydrogels at a low cell density (10^6 cells mL⁻¹) to analyze cell viability and morphology after encapsulation with different UV exposure times. Following the procedure from **Chapter 3.3.3**, cell viability was evaluated on days 1, 6, and 10 using the Live/Dead Viability/Cytotoxicity assay kit. Samples were observed with a ZEISS LSM800 confocal laser scanning microscope, and images were captured as Z-stacks. Z-stacks were then processed using a custom MATLAB code. Finally, cell viability percentage was calculated as the fraction of living cells over the total cell number. To assess cell morphology, light microscopy was performed using a Zeiss Axio Observer.Z1/7, and images were obtained 6 days after encapsulation. Finally, bright-field images were analyzed using the ImageJ software to obtain cell descriptor data of the aspect ratio and circularity of encapsulated cells.

3.4.4. Immunofluorescence staining

The microtissues were fixed in a 10% formalin solution (Sigma-Aldrich) 15 days after fabrication. The hydrogels were washed with Tris-buffered saline (TBS, Canvax Biotech). Cells were permeabilized with 0.1% v/v Triton X-100 (Sigma-Aldrich) in TBS for 15 min and blocked with a blocking buffer consisting of 0.3% v/v Triton X-100 and 3% v/v donkey serum (Sigma-Aldrich) in TBS for 2 h. Then, tissues were washed with TBS and incubated in a 100 nM rhodamine-phalloidin 480 (Cytoskeleton) solution overnight to stain F-actin. Myosin heavy chain 4 (MYH4) was stained by incubating in a solution of MF20 Alexa Fluor 488 (1:100, eBioscience, Thermo Fisher Scientific) in blocking buffer. After washing with TBS, nuclei were counterstained with DAPI (1 μ M, Thermo Fisher Scientific) for 15 min. Hydrogels were mounted and stored at 4 °C before observation by confocal microscopy.

3.5. Fabrication of myotonic dystrophy type 1 (DM1) human skeletal muscle microtissues

Human cell-laden 3D microstructured hydrogels were fabricated on top of glass coverslips using a photomold patterning technique, as described in **Chapter 3.4**.

3.5.1. Glass coverslip functionalization

Glass coverslips were treated with 3-(trimethoxysilyl)propyl methacrylate (TMSPMA, Aldrich) (Figure 1 (a)) and coated with a layer of polyethylene glycol diacrylate (PEGDA, MW 4000 Da, Sigma-Aldrich) (**Figure 4.15C**) by free radical polymerization. First, clean glass coverslips were activated by oxygen plasma at 29.6 W for 30 s. Immediately after plasma treatment, the glass surface was covered with a freshly prepared silanization solution (TMSPMA diluted in ethanol at 1:50 and mixed with 3% v/v acetic acid) for 1 h. Then, coverslips were thoroughly washed with ethanol and dried (**Figure 4.15B**).

For PEGDA coating, we prepared a solution of 20% w/v PEGDA and 2% w/v LAP in Milli-Q water by dissolving in a water bath at 60 °C for 30 min. For each coverslip, a 5 μ L drop was placed on a Teflon surface. Then, the silanized side of the coverslip was carefully pressed on top. Finally, samples were exposed to UV for 2

min using a UVP Crosslinker (365 nm, 40 W, Analytik Jena), washed several times with Milli-Q water, and thoroughly dried (**Figure 4.15D**).

3.5.2. Human fibroblasts encapsulation

To encapsulate cells in micropatterned hydrogels, we mixed the prepolymer solution with a cell suspension of either control or DM1 cells in MDM to obtain a final concentration of 2.5×10^7 cells mL⁻¹. Then, an 8 μ L drop of the cell-laden prepolymer was placed on a PEGDA-coated glass coverslip, and a PDMS stamp (100 μ m channels) (**Figure 4.15H**) was pressed lightly on top, filling the microchannels with the solution. The hydrogels were crosslinked by UV exposure of 30 s using the UVP Crosslinker. MDM was added to each sample, and stamps were carefully removed after 20 min of incubation at 37 °C (**Figure 4.15F, I**). Encapsulated cells were differentiated for up to 21 days, with culture media being replaced every two days.

3.5.3. Cell viability assay

Cell viability was evaluated 24 h after encapsulation using the Live/Dead viability/cytotoxicity kit (Invitrogen) following the protocol from **Chapter 3.3.3**. Briefly, samples were washed several times with sterile 1x PBS and incubated for 30 min with a staining solution containing Calcein AM, Ethidium homodimer-1, and Hoechst (Invitrogen) in PBS. Cell viability was calculated as the percentage of living cells with respect to the total cell number analyzed in the 3D reconstruction of confocal Z-stacks using Imaris software (Oxford Instruments).

3.5.4. Antisense oligonucleotide treatment

AntagomiR oligonucleotides (Creative Biogene) were administrated 72 h after DM1 microtissue fabrication. MDM was replaced and supplemented with 100 nM of AntagomiRs for miR-sc (control) or miR-23b-3p. The treatment lasted for 7 days without replacing the culture media. The antagomiR sequences were: 5'-mG*mG*mUmAmAmUmCmCmCmUmGmGmCmAmAmUmGmU*mG*mA*mU*-3'-chol (antagomiR-23b-3p), and 5'-mC*mA*mGmUmAmCmUmUmUmUmGmUmGmUmA*mC*mA*mA*-3'-chol (sc control). Where m denotes 2'-O-methyl-modified phosphoramidites, * denotes phosphorothioate linkages, and chol denotes cholesterol groups.

3.5.5. Fluorescence *in situ* hybridization

Bioengineered 3D skeletal muscle tissues were fixed in 4% paraformaldehyde for 30 min at room temperature and washed with 1X PBS for 10 min. Samples were incubated in the prehybridization buffer (2X saline sodium citrate [SSC], 30% deionized formamide) for 30 min at room temperature and hybridized with a Cy3-(CAG)⁷-Cy3-labeled probe, diluted 1:200 in hybridization buffer (40% deionized formamide, 2X SSC, 10% dextran sulfate, 0.2% BSA, 2 mM Ribonucleoside Vanadyl Complex (Sigma-Aldrich), 1 mg mL⁻¹ *Escherichia coli* tRNA, 1% herring sperm DNA) overnight at 37°C in the dark. After hybridization, samples were washed twice with a prehybridization buffer for 30 min at 42 °C, washed with 1X PBS, and incubated with DAPI for 15 min. All the incubations were performed in a humidity chamber.

3.5.6. Immunofluorescence staining

After fixation, permeabilization, and blocking of cell-laden hydrogels following the procedure from **Chapter 3.4.4**, the samples were incubated with anti-SAA and anti-MYH7 primary antibodies (**Table 3.1**) at 4 °C overnight. After several PBS washes, the samples were incubated for 2 h with the fluorophore-conjugated secondary antibodies (**Table 1**) at RT. Finally, the samples were counterstained with 1 µM DAPI to detect the nuclei.

For MBNL1 detection, after FISH protocol, samples were incubated with the monoclonal anti-MBNL1 primary antibody at 4 °C. The fluorescence signal was amplified using a biotin-conjugated secondary antibody (**Table 3.1**) and the VECTASTAIN® Elite® ABC kit (Vector) for 1 h at RT, followed by PBS washes and incubation with either Dylight®488-FITC (1:200, Vector) for 2 h at RT. Finally, the samples were counterstained with DAPI to detect the nuclei.

Table 3.1. Antibodies

Antibody	Target	Supplier	Technique
Monoclonal Myosin 4, MF20, Alexa Fluor 488-conjugated primary antibody	Myosin heavy chain 4	eBioscience, Thermo Fisher Scientific	If (1:100)
Monoclonal mouse anti-SAA primary antibody	Sarcomeric α -actinin	Sigma-Aldrich	If (1:200)

MATERIALS AND METHODS

Polyclonal rabbit anti-MYH7 primary antibody	Myosin heavy chain 7	Invitrogen	If (1:200)
Polyclonal donkey anti-mouse IgG, Alexa Fluor 488-conjugated secondary antibody	Mouse IgG	Invitrogen	If (1:200)
Polyclonal goat anti-rabbit IgG, Alexa Fluor 568-conjugated secondary antibody	Rabbit IgG	Invitrogen	If (1:200)
Mouse anti-MBNL1, clone MB1a (4A8), primary antibody	Muscleblind-like protein 1	Developmental Studies Hybridoma Bank	If (1:100) Wb (1:200)
Mouse anti-MBNL2, clone MB2a (3B4), primary antibody	Muscleblind-like protein 2	Developmental Studies Hybridoma Bank	Wb (1:100)
Monoclonal mouse anti-GAPDH binding protein-HRP, clone G-9, primary antibody	GAPDH	Santa Cruz Biotechnology	Wb (1:3500)
Anti-mouse IgG, HRP-conjugated secondary antibody	Mouse IgG	Sigma-Aldrich	Wb (1:5000)
Horse anti-mouse-IgG, Biotin-conjugated secondary antibody	Mouse IgG	Vector	If (1:200)

If = immunofluorescence; Wb= western blot

3.5.7. Fusion index and myotube size analysis

Z-stacks were analyzed as 3D images using the Imaris software. Fusion index was determined as the percentage of nuclei in myotubes (≥ 2 myonuclei) with respect to the total number of nuclei in myotubes expressing sarcomeric α -actinin (SAA). The diameter of individual 3D myotubes was obtained by the object-oriented bounding box statistical variable (BoundingBoxOO Length A), which measures the length of the object's shortest principal axis.

3.5.8. RNA extraction, RT-PCR, and real-time PCR

Total RNA from human bioengineered muscles was isolated using Tri-reagent (Sigma) according to the manufacturer's instructions. One microgram of RNA was digested with DNase I (Invitrogen) and reverse-transcribed with SuperScriptTM II (Invitrogen) using random hexanucleotides. qRT-PCR was carried out on one nanogram of cDNA template with the FIREPol[®] EvaGreen[®] qPCR Mix Plus (Solis

Biodyne) and specific primers (**Table 2**). GAPDH and ACTB were used as endogenous controls. miRNA expression was quantified using specific miRCURY LNA microRNA PCR primers (Qiagen) according to the manufacturer's instructions. Relative gene expression was normalized to the miR-103 expression [221]. Expression levels were measured using the QuantStudio 5 Applied Biosystems Real-Time PCR System. Expression relative to the endogenous genes and control group was calculated using the $2^{-\Delta\Delta Ct}$ method. Pairs of samples were compared using two-tailed Student t-tests ($\alpha=0.05$), applying Welch's correction when necessary. For splicing analyses, 20 ng of cDNA were used in a standard PCR reaction with GoTaq polymerase (Promega). Specific primers were used to analyze alternative splicing of BIN1, NFIX, and SPTAN1 (**Table 3.2**).

Table 3.2. Sequences of oligonucleotides used for real-time RT-PCR

Gene	Primer
GAPDH	GTCTCCTCTGACTTCAACAGCG
	ACCACCCTGTTGCTGTGCCAA
MBNL1	CTGCATCTGTCTATGCCAAACT
	GGGAATCTCCTCACAGCTGAAT
MBNL2	CCACCACGCCTGTTATTGTT
	CAGTCCTGAGAAGTTTCTGAGTTG
BIN1	CTCAACCAGAACCTCAATGATGTG
	CTGAGATGGGGACTTGGGGAG
NFIX	GAGCCCTGTTGATGACGTGTTCTA
	CTGCACAAACTCCTTCAGTGAGTC
SPTAN1	GATTGGTGGAAGTGGAAGTGAACGAT
	TGATCCATTGCTGTAGTTCATTCCG

3.5.9. Western blotting

For total protein extraction, samples were homogenized in RIPA buffer (150 mM NaCl, 1% IGEPAL, 0.5% sodium deoxycholate, 0.1% SDS, 50 mM Tris-HCl pH 8.0) supplemented with protease and phosphatase inhibitor cocktails (Roche Applied Science). Total proteins were quantified with a BCA (Bicinchonin acid) protein assay kit (Pierce) using bovine serum albumin as the standard concentration range. For the immunodetection assay, 20 µg of samples were denatured for 5 min at 100°C, electrophoresed on 12% SDS-PAGE gels, transferred onto nitrocellulose membranes 0.45 µm (GE Healthcare), and blocked with 5% non-fat dried milk in 1X PBS with 0.05% Tween 20 at pH 7.4. Membranes were incubated overnight at 4°C with primary mouse anti-MBNL1 (1:200, clone MB1a (4A8), Developmental Studies Hybridoma Bank) or mouse anti-MBNL2 (1:100, clone MB2a (3B4), Developmental Studies Hybridoma Bank). anti-GAPDH-binding protein-HRP antibody (1 h, 1:3500, clone G-9, Santa Cruz) as a loading control. All primary antibodies were detected using horseradish peroxidase (HRP)-conjugated anti-mouse-IgG secondary antibody (1h, 1:5000, Sigma-Aldrich). Immunoreactive bands were detected using ECL Western Blotting Substrate (Pierce), and images were acquired with an AMERSHAM ImageQuant 800 (GE Healthcare). Quantification was performed using ImageJ software. The statistical differences were estimated by the Student's *t*-test ($p < 0.05$) on normalized data⁶.

3.5.10. Statistical analysis

All group data are expressed as mean ± SEM. The comparisons between groups were performed using Prism 8 software (GraphPad) by two-tailed Student *t*-test ($\alpha = 0.05$), applying Welch's correction when necessary. Differences between groups were considered significant when $p < 0.05$ (* $p < 0.05$; ** $p < 0.01$; *** $p < 0.001$; **** $p < 0.0001$).

⁶ The molecular validation for antagomiR treatments was performed by Dr. Estefanía Cerro-Herreros as part of our collaboration with the Translational Genomics Group, InCliva Health Research Institute from Valencia, Spain.

3.6. Human platelet lysate-based nanocomposite hydrogels for skeletal muscle tissue engineering

3.6.1. Fabrication of the hydrogel casting platforms

The hydrogel casting platforms were designed using Fusion 360 software (Autodesk) as circular chips (8 mm diameter) with a rectangular well of 35 μ L volumetric capacity, containing two T-shaped posts (diameter: 0.8 mm; height: 3.25 mm) (**Figure 4.23A**). In this protocol, polydimethylsiloxane (PDMS) replicas of a 3D printed master mold were obtained by Ecoflex™ (00-30, Smooth-On) negative intermediary molds.⁷

Fabrication of the master mold

First, the master mold was generated by transforming the platform design into an STL file for projector-based stereolithography 3D printing using a Solus DLP 3D Printer (Reify 3D) with an opaque orange resin (SolusProto, Reify 3D) that withstands high temperatures. The hard 3D printed molds were silanized by chemical vapor deposition (CVD) of trichloro(1H,1H,2H,2H-perfluorooctyl)silane (PFOTS, Sigma-Aldrich). Briefly, the surface of 3D printed molds was activated with oxygen plasma for 30 s and immediately placed in a vacuum desiccator with 5 drops of PFOTS for 1 h. After deposition, the silanized 3D printed master mold was left in an oven for 1 h at 80 °C.

Fabrication of the negative mold

The Ecoflex™ negative mold was made by mixing the two prepolymers (1A:1B, approximately 15 g of each prepolymer). Before beginning, prepolymer B had to be thoroughly pre-mixed. Then, A and B were thoroughly mixed for 3 minutes. The mixture was placed in a vacuum desiccator for 5 min to remove entrapped air. After, the liquid prepolymer was poured on the 3D printed master mold and degassed inside the vacuum desiccator for 15 minutes. The Ecoflex™ was cured at room temperature overnight. Finally, the cured polymer was carefully peeled off from the 3D printed master mold, washed with ethanol, and dried with N₂ flow and on a hot

⁷ Hydrogel casting platforms were designed by Dr. Juan M Fernández-Costa and fabricated by Lluís Mangas from the Biosensors for Bioengineering Research Group at IBEC.

plate (90 °C, 10 min) before silanization with PFOTS (following the same procedure as with the 3D printed master mold).

Replica molding of PDMS platforms

The polymer elastomer base and curing agent were weighted in a 10:1 ratio. After thoroughly mixing, we degassed the polymer in a vacuum desiccator. The uncured PDMS was poured on the Ecoflex™ mold (placed in a glass Petri dish), and the trapped air in the post area was removed with a syringe. Then, the mold was left inside a vacuum desiccator until all the trapped air was removed. After, the PDMS was cured at 80 °C for 6 h. Before demolding, PDMS was left for additional curing at room temperature overnight. PDMS was then detached from the Ecoflex™ and cleaned by sonication in Milli-Q water and 2-propanol for 5 min. Then, individual PDMS platforms were cut using an 8 mm diameter biopsy punch. Finally, a cover glass was bonded to each platform base by activating the two surfaces (glass and PDMS platform base) with UV plasma for 15 min before joining the two surfaces. Before cell encapsulation, platforms were washed with isopropanol and water.

3.6.2. Preparation of the nanocomposite hydrogel (HUGel)

Preparation of HUGel precursors

Human platelet lysate (PL) was purchased from STEMCELL™ Technologies. Aldehyde-cellulose nanocrystals (a-CNC) were prepared at the Research Institute on Biomaterials, Biodegradables, and Biomimetics (i3Bs, University of Minho, Portugal) [222,223]. Cellulose nanocrystals (CNC) were extracted from microcrystalline cellulose powder (Sigma-Aldrich) by sulphuric acid hydrolysis⁸. Briefly, concentrated sulphuric acid (Sigma-Aldrich) was added dropwise to the microcrystalline cellulose powder up to a final concentration of 64% w/v. The obtained suspension was heated at 44 °C for 2 h. Then, the suspension was collected and stored at 4 °C. To produce a-CNC, sodium periodate (NaIO₄, Sigma-Aldrich) was added to a 1.5% w/v CNC aqueous suspension in a 1:1 molar ratio (NaIO₄:CNC) for 12 h. Finally, the concentration of the working suspension was adjusted by concentrating it against poly(ethylene glycol) (20.000 kDa, Sigma-Aldrich) using benzoylated cellulose dialysis membranes (2000 Da NMWCO, Sigma-Aldrich). Stock

⁸ CNC were synthesized by Manuel Gomez-Florit in collaboration with the i3Bs Research Group from the University of Minho.

water dispersions of a-CNC were prepared and fully characterized in previous works by researchers from the i3Bs Research Group [222,223].

Cell encapsulation by HUgel casting in PDMS platforms

PDMS casting platforms were treated with 0.2% Pluronic® (F-127, Sigma-Aldrich) for 20 minutes to avoid hydrogel attachment to the PDMS well. After treatment, the platforms were washed 3 times with phosphate buffered saline (PBS) and sterilized with UV light. For cell encapsulation, HuMSCs were detached and resuspended in PL. In these experiments, we worked with final cell densities of 0.5, 1, or 2.5×10^7 cells mL⁻¹. The a-CNC water dispersion was placed in a sterile Eppendorf tube at the desired concentration and sonicated for 5 minutes. Then, the suspension was mixed with thrombin from human plasma (2 U mL⁻¹, Sigma-Aldrich) and CaCl₂ (10 mM, Sigma-Aldrich). The cell suspension in PL was thoroughly mixed in a 1:1 ratio with the suspension containing a-CNC, thrombin (final concentration: 1 U mL⁻¹), and CaCl₂ (final concentration: 5 mM). Finally, a volume of 35 µL of the mixture was carefully placed inside each PDMS platform well (**Figure 4.23B**). The samples were allowed to crosslink at 37 °C for 30 min before adding growth medium. After two days, the medium was switched to differentiation medium. Then, half of the medium was replaced every two days. The 3D culture was carried out under shaking conditions inside an incubator (37 °C, 5% CO₂).

3.6.3. Immunofluorescence staining

The bioengineered human muscle tissues were fixed with 10% formalin solution (Sigma-Aldrich) for 30 min at RT, followed by several washes in PBS. Samples were then permeabilized with PBS-T (0.1% Triton-X (Sigma-Aldrich) in PBS), blocked (0.3% Triton-X, 3% donkey serum (Sigma-Aldrich) in PBS) for 2 h at RT, and incubated with monoclonal mouse anti-sarcomeric α -actinin (SAA) primary antibody (1:200, Sigma-Aldrich) at 4 °C overnight. After several PBS-T washes, the samples were incubated for 2 h with polyclonal donkey anti-mouse IgG, Alexa Fluor 488-conjugated secondary antibody (1:200, Invitrogen), and rhodamine-phalloidin (1:200, Cytoskeleton) to stain F-actin, at RT. Finally, the samples were counterstained with DAPI (4',6-diamidino-2-phenylindole, Life Technologies) to detect the nuclei. The complete protocol was performed under shaking conditions.

3.6.4. Electrical Pulse Stimulation

After 7 days in differentiation medium, the bioengineered 3D human skeletal muscle tissues were subjected to electrical pulse stimulation (EPS). EPS was performed with a custom-made stimulation plate consisting of graphite electrodes assembled on a 12-well plate lid. First, the stimulation plate containing the tissues was placed inside a Zeiss Axio Observer.Z1/7 microscope outfitted with the XL S1 cell incubator at 37 °C and on a 5% CO₂ atmosphere. Then, the electrodes were connected to a multifunction generator (NF Corporation), and the frequency and amplitude of the signals were confirmed using a digital oscilloscope (QUIMAT). Finally, the muscle tissues were subjected to a stimulation regime of square pulses with a 10% duty cycle, an electrical field strength of 1 V/mm, and frequencies from 1 to 50 Hz to evaluate tissue response (see **Figure 4.27A**).⁹

3.6.5. Imaging

Live-cell imaging was performed with the Zeiss Axio Observer.Z1/7 microscope outfitted with the XL S1 cell incubator. All images were taken at 37 °C and on a 5% CO₂ atmosphere and processed using the Fiji image processing package, a distribution of ImageJ [218,224]. In addition, fluorescence images were taken with a ZEISS LSM800 confocal laser scanning microscope and analyzed using the Imaris microscope image analysis software (Oxford instruments).

3.6.6. Force measurements

The post deflections during tissue contractions were recorded and analyzed using Fiji. The force-displacement relationship for the posts was estimated using linear bending theory based on previously published protocols (**Figure 4.22**) [188,209]. The Young's modulus of the PDMS (10:1) was previously measured as $E=1.6 \pm 0.1$ MPa. Considering the posts' geometry and dimensions, we calculated a spring constant (k) of 3.54 N/m. The spring constant was used to transform the recorded post deflections (d) into the force generated by the bioengineered 3D skeletal muscle tissues (F).

⁹ The electrical stimulation well-plate was custom-made by Dr. José Yeste from the Biosensors for Bioengineering Research Group at IBEC.

$$F = \frac{6\pi ED^4}{64a^2(3L - a)} \cdot d = k \cdot d$$

Here, D is the diameter of the posts, L is the total length, and a is the length from the bottom of the post to the centroid of the cap.

3.6.7. Statistical analysis

All group data are expressed as mean \pm SEM. The comparisons between groups were performed using Prism 8 software (GraphPad) by two-tailed Student t-test ($\alpha = 0.05$), applying Welch's correction when necessary. Differences between groups were considered significant when $p < 0.05$ (* $p < 0.05$; ** $p < 0.01$; *** $p < 0.001$; **** $p < 0.0001$).

Chapter 4. RESULTS

4.1. Composite Biomaterials as Long-Lasting Scaffolds for 3D Bioprinting of Highly Aligned Muscle Tissue

The first part of this thesis involved studying different gelatin-based composite hydrogels as bioprinted cell-laden scaffolds for engineered skeletal muscle tissue¹⁰. Gelatin methacryloyl (GelMA) is a common biomaterial for tissue engineering. It is obtained by functionalizing natural gelatin with methacrylate groups that can undertake radical polymerization reactions in the presence of a photoinitiator and UV light. However, it is challenging to obtain long-lasting GelMA scaffolds for 3D cell culture due to their poor mechanical properties and high enzymatic degradability. In this work, GelMA was synthesized and combined with three other photocrosslinkable biomaterials that are not degradable by mammalian cells. These biomaterials consisted of commercially available poly(ethylene glycol)diacrylate (PEGDA) and two polysaccharides: alginate and carboxymethyl cellulose (CMC), which were functionalized to obtain alginate methacrylate (AlgMA) and carboxymethyl cellulose methacrylate (CMCMA).

GelMA was combined with either PEGDA, AlgMA, or CMCMA under various fabrication conditions, such as material concentration, type of photoinitiator, photoinitiator concentration, and UV exposure time. Then, the physical and biological properties of the resulting composite hydrogels were extensively characterized and compared to select the optimal conditions for the development of bioprinted skeletal muscle fibers from C2C12 murine cells. The results demonstrated that the composite hydrogels have a higher resistance to degradation than GelMA hydrogels. Thus, the bioprinted scaffolds maintained their 3D structure over a prolonged culture period. Altogether, the properties of the composite hydrogels, scaffold geometry, and bioprinting conditions promoted the alignment of muscle cells and supported their differentiation into multinucleated myotubes expressing myosin heavy chain protein.

¹⁰ This work has been published as:

García-Lizarribar A*, **Fernández-Garibay X***, Velasco-Mallorquí F, Castaño A G, Samitier J, and Ramon-Azcon J 2018 Composite Biomaterials as Long-Lasting Scaffolds for 3D Bioprinting of Highly Aligned Muscle Tissue. *Macromol. Biosci.* **18** 1800167.

*Authors contributed equally to this work.

4.1.1. Introduction

Engineered muscle tissues (skeletal and cardiac muscle) have *in vivo* regenerative medicine applications that involve harvesting cells from the patient, growing them within a suitable scaffolding material, and reintroducing them into the patient [225–227]. Moreover, these engineered tissues also have *in vitro* applications for drug screening, bioactuators, and biosensors [228–232]. Especially interesting is the use of engineered muscle tissues as bioactuators. As intrinsically biocompatible materials, such tissues can be integrated into biomedical devices to harvest energy and produce microcontrolled actuators. Specific examples include the application of skeletal muscle tissue on a Si–MEMS device to act as a micro-bioactuator for energy harvesting [233], bioactuators operated by self-assembled insect muscle tissue [234], or integration of optogenetic myotubes with MEMS systems [235]. In all of these systems, the contractile ability of muscle tissue is needed and can only be obtained with a correct microarchitecture of the tissue, superior adaptable mechanical properties of the material where the tissue is attached, and a stable 3D structure. Important advances have been made in this area. Still, one of the major obstacles in engineering 3D complex tissues such as muscle is the need to encapsulate the cells in a long-lasting biocompatible 3D environment with adaptable mechanical properties [236]. To date, many technologies, including photolithography, electrospinning, and bioprinting [236–240], have been adopted for the fabrication of 3D tissue constructs. Among them, bioprinting shows exciting potential as it is able to provide precise spatial manipulation of living cells with a suitable 3D growth environment, optimal oxygen levels, and effective nutrient transport, as well as mechanical integrity.

Cell responsive bioinks are a critical component in bioprinting technology. Hydrogel-based bioinks encapsulating living cells and bioactive components are commonly used for bioprinting. Currently, natural materials derived from mammalian animals (e.g., collagen, gelatin, and fibrin) are more suitable for engineering skeletal muscle due to higher cell attachment density, greater rates of cell proliferation, gel compaction (resulting in greater final cell density), and endogenous provision of growth factors and biological signals for differentiation [241,242]. So far, a range of natural hydrogels, including gels such as collagen/gelatin [243], gelatin methacryloyl (GelMA) [244,245], alginate [246], fibrin [247], and hyaluronic acid (HA) [248], have been used in bioprinting. Still, none of these materials have fulfilled all the

requirements for engineering muscle tissue bioactuators, such as good mechanical properties and the formation of stable and durable structures. These 3D natural scaffolds are degraded by mammalian cells, and the structural functionality of the bioactuator is finally lost [249].

To overcome the lack of 3D geometry over time and obtain long-lasting architectures, composite materials can be obtained through the combination of degradable and non-degradable materials of both synthetic [238,249–251] and natural origin [214,248,252–254]. Among the distinct types of natural non-biodegradable biomaterials, polysaccharides have attracted considerable attention in biomedical and pharmaceutical applications due to their biocompatibility and chemical properties [255,256]. Carboxymethyl cellulose (CMC) is a water-soluble and biocompatible derivative of cellulose, and it is derived from abundant renewable resources. CMC hydrogels are not biodegradable by mammalian cells and, for this reason, they can be used as a natural biocompatible material to produce non-degradable structures [257]. Only a few applications use it to encapsulate cells [253,258], and CMC methacrylate (CMCMA) combined with GelMA has never been tested in tissue engineering applications. Alginate is a more widely used polysaccharide in tissue engineering applications. Alginate is a linear unbranched polysaccharide derived from seaweed containing repeating units of 1,4-linked β -D-mannuronic acid and α -L-guluronic acid. It gels in the presence of divalent cations, such as calcium, barium, and magnesium [259]. Alginate without any modification has been used in combination with GelMA [252], and it has also been methacrylated and used to encapsulate chondrocyte cells [214]. In addition, GelMA and AlgMA have already been combined to encapsulate human osteoblast-like cells and human umbilical cord vein endothelial cells [260]. Although previous studies have reported promising results, there is still limited control over the mechanical properties, swelling ratios, and the consequent effects on the cell differentiation process of these polysaccharides and their respective composite biomaterials with GelMA. Finally, poly(ethylene glycol) diacrylate (PEGDA) is one of the most popular synthetic non-degradable materials used in tissue engineering applications [261] because of its high hydrophilicity, bioinert structure, and lack of toxic or immunogenic responses. Also, PEG-based hydrogels provide adjustable mechanical properties as their elastic modulus can be tuned over a broad range of values to mimic the moduli of soft tissues [262]. In bioprinting applications, it has been used in combination with natural hydrogels to produce composite hydrogel formulations [251].

Here, we report evaluation of three photocrosslinkable composite materials (i.e., GelMA-alginate-methacrylate [GelMA-AlgMA], GelMA-carboxymethyl cellulose-methacrylate [GelMA-CMCMA]) and GelMA-PEGDA, as bioinks for engineering skeletal muscle tissue. By employing GelMA gels in combination with different non-biodegradable materials (i.e., alginate, cellulose, and PEGDA), we obtained composite materials for direct bioprinting 3D cell-laden skeletal muscle constructs with high structural fidelity, enhanced bioactivity, and long-lasting structures. We formulated a library of composite hydrogel prepolymer solutions with different prepolymer concentrations, UV dosage, and two different UV photoinitiators. Photopolymerizable hydrogels show a close relationship between their mechanical properties and their crosslinking density [49,263] and stiffness of hydrogels strongly affects cell behavior and can induce or inhibit cell differentiation toward different phenotypes [191,262,264,265]. We tuned the mechanical properties of the resulting hydrogels by varying the time of UV-induced crosslinking and photoinitiator concentration. We hypothesized that pore size frequency distribution also has a significant impact on cell behavior [254]. The diffusion of nutrients inside the structures can be reduced, and extremely packed structures limit cell migration and growth. After thorough cell viability and mechanical characterization, we used those formulations to prepare cell-laden hydrogels in combination with C2C12 murine myoblasts. Moreover, we evaluated the maturation of myotube structures by fluorescence microscopy. To this end, we used C2C12-laden composite hydrogels as a system to demonstrate the feasibility of the proposed technique in bioprinting constructs with preserved 3D structures over time. It was vital to match not only the morphology of the functional skeletal muscle fibers but also the cellular arrangement. Control of the hydrogel properties, such as mechanical stiffness, swelling, degradation, and porosity, was critical to obtain proper cellular function and tissue morphogenesis.

4.1.2. Experimental procedure

Synthesis of polymer precursors

Gelatin (Sigma-Aldrich, USA) was modified to a 40% degree of methacrylation as previously described [238]. Briefly, gelatin was dissolved in PBS 10 mM at a concentration of 10% w/v, and methacrylic anhydride (Sigma-Aldrich, USA) was carefully added to the solution drop by drop. One hour later, the reaction

was stopped by adding an excess of PBS 10 mM and dialyzed against Milli-Q water with 6–8 kDa MWCO membranes (Spectra/por, Spectrumlabs, USA). Water was changed every 4 h during 4 days. Gelatin methacryloyl (GelMA) was lyophilized and stored at $-20\text{ }^{\circ}\text{C}$. Sodium carboxymethyl cellulose (CMC) and sodium alginate (alginate, Alg) (Sigma-Aldrich) were methacrylated at a maximum degree of methacrylation as previously described [262]. The methacrylation reaction was performed by mixing a solution of 1% w/v of the polymer in 50 mM MES buffer at pH 6.5 with 20 mM EDC, 10 mM N-hydroxysuccinimide, and 10 mM 2-aminoethylmethacrylate (Sigma-Aldrich). The reaction was stopped after 24 h with the addition of acetone (Panreac, Spain) and filtered using a vacuum flask. The precipitate was dissolved in PBS 10 mM and dialyzed against Milli-Q water with 3.5 kDa MWCO membranes (Thermofisher, USA). Finally, the solutions of methacrylated polymers (CMCMA and AlgMA) were lyophilized and stored at $-20\text{ }^{\circ}\text{C}$.

Nuclear Magnetic Resonance

For $^1\text{H-NMR}$, gelatin, GelMA, CMC, CMCMA, alginate, and AlgMA were dissolved in D_2O and analyzed on a Varian Inova 500 (Varian, USA). All samples were measured with a relaxation delay of 1 s for 64 scans.

Preparation of prepolymer solutions

The polymer precursors (GelMA, CMCMA, AlgMA, and PEGDA) were mixed in different concentrations and diluted in PBS 10 mM containing the photoinitiator. Final concentrations of photoinitiator, either 2-hydroxy-4'-(2-hydroxyethoxy)-2-methylpropiophenone (I2959) (Sigma-Aldrich) or lithium phenyl (2,4,6-trimethylbenzoyl)phosphinate (LAP) (TCI EUROPE N.V., Belgium), were fixed at 0.4% or 0.1% w/v. Polymer solutions were placed at $65\text{ }^{\circ}\text{C}$ for 1 h to obtain homogeneous solutions. Polymer solutions were prepared to obtain final concentrations of 5% or 1% w/v GelMA and 1% w/v CMCMA, AlgMA, or PEGDA. All hydrogels were fabricated using a 3D bioprinter (3DDiscovery BioSafety, regenHU, Switzerland; 365 nm , 3 W cm^{-2}) with the UV light source.

Multifactorial analysis to assess cell viability under 3D bioprinting conditions

The alamarBlue assay (Thermofisher) was performed by following the manufacturer's protocols. A multifactorial screening was assessed to test the

synergic effect of GelMA concentration, photoinitiator concentration of both I2959 and LAP, and UV exposure time on the cell viability. Prepolymers were prepared at 1% or 5% w/v of GelMA. Photoinitiators were used at 0.1% and 0.4% w/v. Cell-laden hydrogels (20 μL amounts) (10^6 C2C12 cells mL^{-1}) were poured into wells of a 96 well-plate. After UV exposure, samples were rinsed with growth medium to remove unreacted reagents and cultured for 24 h. Then, samples were incubated with alamarBlue solution at 10% v/v in growth media for 3 h at 37 °C. Finally, the absorbance was read at 570 nm (λ_1) and 600 nm (λ_2). The percentage of reduction (cell viability) was determined by the following equation:

$$\% \text{ Reduction} = \frac{(\varepsilon_{OX})\lambda_2 \cdot A\lambda_1 - (\varepsilon_{OX})\lambda_1 \cdot A\lambda_2}{(\varepsilon_{RED})\lambda_1 \cdot A'_2 - (\varepsilon_{RED})\lambda_2 \cdot A'\lambda_1} \cdot 100$$

Here, ε_{OX} and ε_{RED} represent the molar extinction coefficient of alamarBlue oxidized form. A and A', represent the absorbance of the samples and the negative control, respectively. Statistical comparison was performed using a 24 ANOVA multifactorial analysis by StatGraphics Centurion software (**Supporting Information**).

Swelling analysis of composite hydrogels

The prepolymer solutions were prepared as described above. Samples for swelling analysis were prepared by placing 300 μL of the prepolymer solution in a 48 well-plate. After exposing the prepolymer solution to UV light, hydrogels were rinsed with PBS, and their initial weight was measured. Then, the wet weight was determined after 1, 3, and 7 days in PBS, after a wipe with tissue paper to remove the excess water. The wet weight increase ratio (ΔW) of the hydrogels was determined by the following equation:

$$\Delta W = \frac{W_s - W_i}{W_i} \cdot 100$$

Here, W_i and W_s represent the weight of composite hydrogels after fabrication and the weight after swelling in PBS, respectively. To calculate the mass increase, each water content value was normalized with the initial weight of the sample.

Degradation of composite hydrogels

Hydrogels were fabricated as described above for the swelling analysis. Hydrogels were removed from the 48 well-plate and left swelling for 3 days in a 6 well-plate. A total of 3 mL of 1.5 U mL⁻¹ of collagenase type II (Thermofisher) in PBS was added on the hydrogels, and they were incubated at 37 °C, under 100 rpm shaking conditions. Then, hydrogels were weighted after 1, 2, and 4 h. The percent hydrogel remaining (%W_r) was determined by the following equation:

$$\%W_r = \frac{W_t}{W_i} \cdot 100$$

Here, W_t represents the weight of hydrogel composites after collagenase incubation.

Analysis of the mechanical properties of composite hydrogels

Uniaxial compression tests of hydrogels were performed using a Zwick Z0.5 TN instrument (Zwick-Roell, Germany) with a 5 N load cell. Hydrogels were fabricated following the same procedure as for the swelling analysis. After reaching equilibrium swelling, cylindrical hydrogels were cut using a 10 mm diameter biopsy punch. Real hydrogel diameters and heights were measured prior to the experiment. Samples were tested at room temperature up to 30% final strain (deformation), using the following parameters: 0.1 mN preload force and 20% min⁻¹ strain rate. Stress-strain graphs were obtained from load-deformation measurements. Values for the compressive modulus were calculated from the slope of the linear region corresponding to 10–20% strain. For each hydrogel formulation, three samples were prepared, and measurements were performed in triplicate.

Pore size quantification

Cylinder-shaped hydrogels, 10 mm in diameter, were fabricated as described above for pore size quantification. Then, they were left swelling in Milli-Q water for 3 days to reach the same hydrogel architecture as cell encapsulation experiments and be comparable with them. After that, dehydration was carried out by sequential immersion in graded ethanol solutions in Milli-Q water: 30%, 50%, 70%, 80%, 90%, and 96% v/v for 5–15 min each and twice for 100% ethanol. Then, samples were placed in the chamber of a critical point dryer (K850, Quorum Technologies, UK), sealed, and cooled. Ethanol was replaced completely by liquid CO₂ and by slowly

heating. CO₂ achieved gas phase equilibrium at 35 °C and 85.06 atm and was slowly drained. This technique allowed dehydration of the hydrogels while avoiding their collapse. After critical point drying, hydrogels were imaged by ultrahigh-resolution scanning electron microscopy (Nova NanoSEM 230, FEI Company, The Netherlands) operating in low vacuum mode (0.5 mbar of water vapor pressure). Scanning electron microscopy (SEM) images were used to quantify the pore size distribution using ImageJ free software (<http://rsb.info.nih.gov/sire.ub.edu/ij>, National Institutes of Health, USA).

3D culture of C2C12 myoblasts embedded in the composite hydrogels

C2C12 myoblasts from *Mus musculus* were purchased from ATCC and expanded in a growth medium based in Dulbecco Modified Eagle Medium (DMEM high glucose, L-glutamine, Gibco, Thermofisher) supplemented with 10% fetal bovine serum (Thermofisher) and 1% penicillin/streptomycin (Thermofisher) at 37 °C and 5% CO₂ atmosphere. To promote myotube formation, differentiation medium was used, based on DMEM high glucose and L-glutamine, supplemented with 2% Horse Serum (HS) (Thermofisher), 1% Penicillin/Streptomycin, and 2.5% HEPES (Thermofisher).

To fabricate cell-laden hydrogels, one volume of prepolymer solutions of the different composite hydrogels was mixed with one volume of a suspension of C2C12 cells to a final density of 1×10^7 cells mL⁻¹. Blends of prepolymer and cells were then placed in a cylindrical mold of 6 mm inner diameter and 750 μm height. Cell-laden solutions were photocrosslinked by 5 s or 25 s exposure to UV light at 3 W cm⁻². This was followed by immersion of the cell-laden hydrogels in growth media to remove the unreacted reagents.

C2C12 survival in the composite hydrogels

C2C12 cells were encapsulated in each hydrogel as described previously. The viability was studied after 1 and 7 days using the Live/Dead assay kit and Hoechst (Thermofisher). Fluorescence images were captured using confocal microscopy (TCS SPE, Leica, Germany) and processed by MATLAB software (**Supporting Information**). Survival percentage was calculated as the fraction of living cells in respect to the total cell number. Additionally, cell morphology within the hydrogels was studied through the immunostaining of nuclei and filamentous actin

(F-actin). For this purpose, hydrogels were fixed in 10% formalin solution (Sigma-Aldrich) 7 days after fabrication. Then, hydrogels were washed with PBS, and cells were permeabilized with Block-Perm solution: 0.2% v/v Triton X-100 (Sigma-Aldrich) and 1% w/v BSA (Sigma-Aldrich) in PBS for 1 h. Afterward, hydrogels were washed in PBS and incubated in 100 nm Rhodamine Phalloidin 480 (Cytoskeleton, USA) solution overnight. After washing with PBS, nuclei were counterstained with DAPI (300 nm, Thermofisher) for 15 min. Hydrogels were mounted and stored at 4 °C before observation by confocal microscopy.

C2C12-laden composite hydrogels bioprinting and C2C12 differentiation into myotubes

Prepolymer solutions and C2C12 cell suspension were mixed as previously described to obtain a 5% w/v GelMA solution with or without 1% w/v of either PEGDA, CMCMA, or AlgMA in PBS containing 0.1% w/v LAP. Solutions were introduced in a 3-cc printing syringe (Nordson Corporation, USA) and placed in the direct dispensing head of the bioprinter (3DDiscovery BioSafety). All of the printing processes were performed in a cooling chamber at 10 °C. The printing rate was 7 mm s⁻¹ and printing pressure varied depending on the loaded prepolymer solution: 2.5, 2.5, 3, and 5 bar in the case of GelMA, GelMA-CMCMA, GelMA-AlgMA, and GelMA-PEGDA, respectively. To promote myotube formation and alignment, cell-laden hydrogel architecture was designed as an array of 20 filaments in a 16 mm diameter circle (BioCAD v1.0 software, regenHU Ltd., Switzerland) and converted to computer-aided design (CAD) files (**Supporting Information**). CAD files were opened in the 3D DISCOVERY HMI software interface (regenHU Ltd., Switzerland). Constructs were made by the extrusion of two layers, through a nozzle of 200 µm inner diameter, and then were photocrosslinked by a 5 s exposure to UV light (365 nm) into a 6 well-plate. After that, hydrogels were immersed in the growth medium and changed three times to remove unreacted reagents. After 5 days, growth medium was switched to differentiation medium. Samples were fixed at 11 days, and F-actin and nuclei were stained as described previously. In addition, staining of myosin heavy chain was performed by incubating the samples in a 5 µg mL⁻¹ MF20 Alexa Fluor 488 (eBioscience, Thermofisher) solution overnight.

Myotube alignment and fusion index analysis

Z-stack images obtained by confocal microscopy were processed using ImageJ software. Myosin heavy chain (MHC) staining was used to analyze the fusion

index and myotube alignment. Myotube alignment was assessed by measuring the angle formed between the myotubes and the longitudinal axis of the printed pattern. The fusion index was calculated by dividing the number of nuclei within the myotubes by the total number of counted nuclei, and this was expressed as a percentage. Three samples for each condition were used, and more than 100 myotubes were analyzed for each sample.

Statistical analysis

All data collected were presented as the mean \pm standard deviation (SD) using GraphPad Prism software (GraphPad, USA). ANOVA and t-tests were performed in StatGraphics Centurion software (StatGraphics, Spain) to compare treatments. A *p*-value of 0.05 or less was considered statistically significant.

4.1.3. Results and discussion

Synthesis and characterization of methacrylated polymers

Our three composite bioinks incorporated four different photocrosslinkable materials (**Figure 4.1**). GelMA emulates the ECM for various cell types [47] in combination with the non-biodegradable materials alginate (Alg), carboxymethyl cellulose (CMC), and PEGDA. GelMA is a photocrosslinkable hydrogel derived from natural gelatin. Gelatin was functionalized with methacrylic anhydride as previously described [47], and the methacrylation was characterized by a colorimetric assay. Hydrogels were finally fabricated using GelMA with a 40% degree of methacrylation (**Table S1, Supporting Information**). Alginate was methacrylated following the protocol described by Jeon *et al.* [214]. In addition, CMC was functionalized using 2-aminoethylmethacrylate and EDC/NHS using carboxylic acids as anchorage points. The number of methacrylate groups was directly verified by ¹H-NMR and was in close agreement with previous works (**Figures S1 and S2, Supporting Information**) [214,257]. Following the reported protocol, we assumed that alginate and CMC achieved a theoretical and real degree of methacrylation of about 45% and 25%,

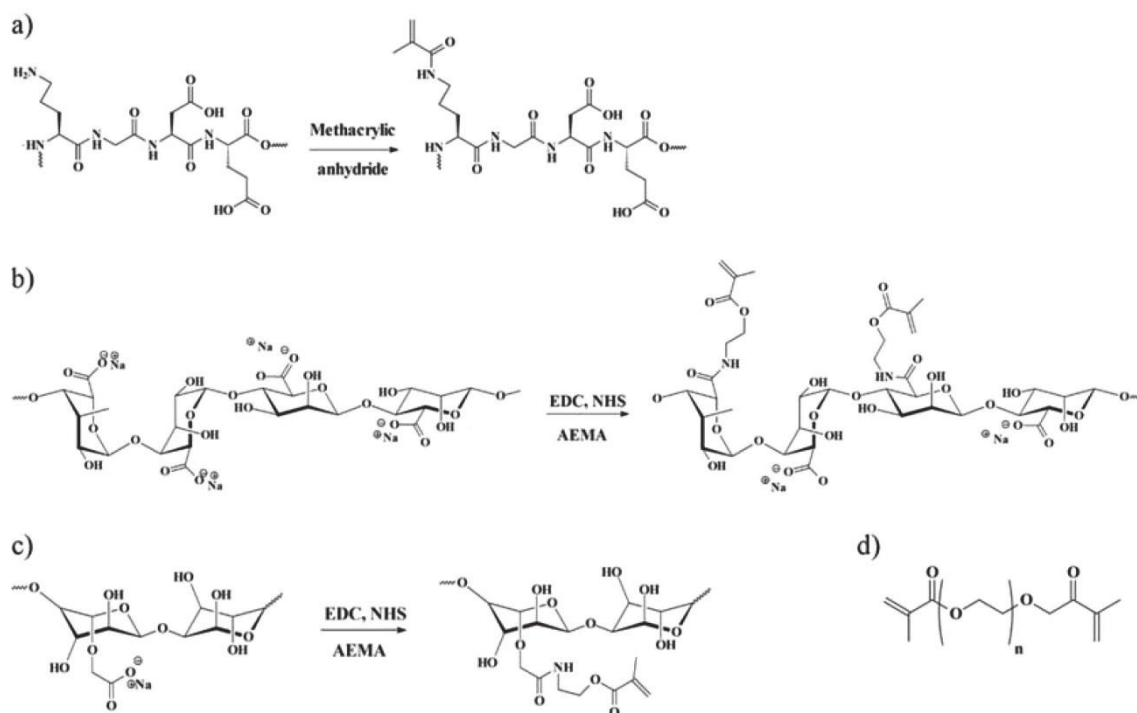


Figure 4.1. Covalent functionalization of the photocrosslinkable materials. (A) gelatin methacryloyl (GelMA), (B) alginate methacrylate (AlgMA), (C) carboxymethyl cellulose methacrylate (CMCMA), and (D) poly(ethylene glycol)diacrylate (PEGDA).

respectively [214,257]. Finally, PEGDA, which already has two end acrylate groups, was obtained from a commercial supplier.

Assessment of optimal C2C12 survival after encapsulation in composite hydrogels

Cell viability after encapsulation in photocrosslinkable bioinks is under the influence of several factors, such as material concentration [266], functionalization degree (amount of functional methacrylates/methacrylamides conjugated onto the polymer) [47], UV exposure time, type of photoinitiator, and photoinitiator concentration [49]. For this reason, the limits of these factors controlling printing capabilities were assessed based on cell viability. To determine the most relevant factors acting on cell viability, C2C12 myoblasts were encapsulated using different biomaterial concentrations, photoinitiator concentrations, and UV exposure times. Two different photoinitiators were used, 2-hydroxy-4'-(2-hydroxyethoxy)-2-methylpropiophenone (I2959) and LAP. To assess all these parameters, a 24 ANOVA multifactorial analysis of cell viability assay was designed using 96 well-plates. Cell viability was determined 24 h after cell printing by an alamarBlue commercial kit. Percentage reduction of alamarBlue reagent is related to cell metabolism; thus, high values of reduction mean high cell viability. Due to the

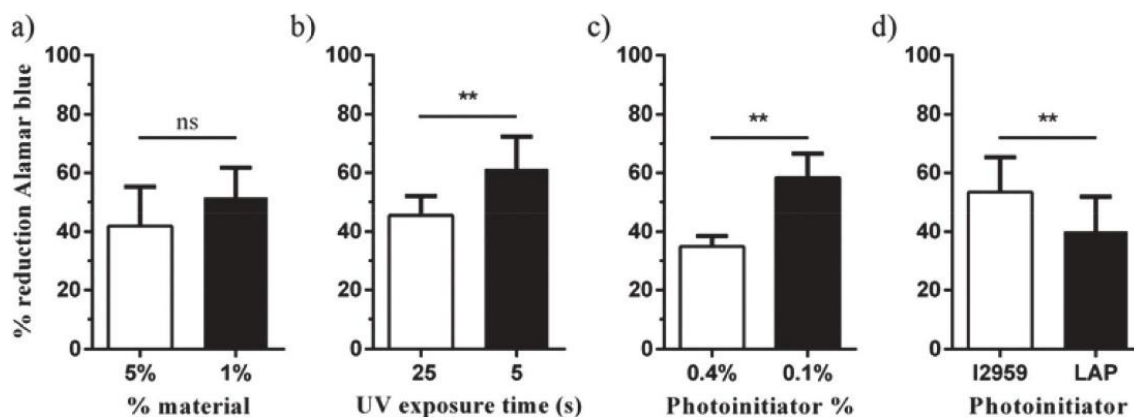


Figure 4.2. Effect of (A) GelMA concentration, (B) UV exposure time, (C) photoinitiator concentration, and (D) photoinitiator type on the C2C12 cell viability. C2C12 cells were encapsulated in GelMA hydrogels at 10^6 cells mL^{-1} and cultured for 24 h. Polymer solutions were prepared containing either I2959 or LAP photoinitiator at 0.1% or 0.4% w/v. Cell-laden prepolymers were photopolymerized under 25 s or 5 s of UV light. Cell viability was examined using the alamarBlue test. Values are represented as percentage reduction (mean \pm standard deviation, *t*-test ***p*-value <0.01, *n* = 12).

bioprinter equipment used in this work, UV light intensity could not be adjusted, but the effects of this parameter were incorporated in exposure time. It was possible to increase or reduce the UV dosage by using longer or shorter exposure times.

The full statistical dataset is shown in the Supporting Information (ANOVA multifactorial analysis of the viability assay). By extracting relevant information, it was possible to define the limits of the bioprinting system. In all samples, composites irradiated for less than 5 s were unable to crosslink. In addition, we found that cell viability was strongly affected by the exposure time, and 25 s of UV drastically reduced cell survival (**Figure 4.2B**). Photoinitiator concentration strongly affects cell viability because the free radicals produced after UV exposure are cytotoxic. **Figure 4.2C** shows the mean cell survival of all samples fabricated with 0.1% and 0.4% w/v of photoinitiator (LAP or I2959). This graph demonstrates that increasing the photoinitiator concentration from 0.1% to 0.4% w/v dramatically decreased cell survival. As was previously reported, LAP has a higher extinction coefficient at 365 nm than I2959 [49], and more radicals are generated using the same concentration. This fact influences cell viability and could explain why I2959 was less toxic than LAP (**Figure 4.2D**). In contrast, the concentration of biomaterial did not have a significant effect on cell viability after printing. Below 1% w/v, the obtained structures were not consistent enough to be useful, and above 7% w/v, the high viscosity clogged the bioprinter's nozzle orifice.

Considering the alamarBlue assay results and the 3D structure of the hydrogels, we concluded that it was possible to work within the 5–25 s range of UV exposure time. Both types of photoinitiators could be used at a maximum concentration of 0.1% w/v, and finally, the methacrylated biomaterials could be printed at a concentration of 5–7% w/v, in agreement with previous findings [191].

Hydrogel swelling and degradation

To study the stability of the different hydrogels over time, different samples were prepared in concordance with the previous viability assay results. The fabrication conditions were the following: 5% w/v of GelMA with 1% w/v of non-biodegradable biomaterial, 5 s of UV exposure, and a 0.1% w/v photoinitiator concentration. As noted in the previous section, photoinitiator concentrations above 0.1% w/v were discarded as unviable because of high cytotoxicity. Below 0.1% w/v, we observed high variability in the formation of the crosslinked scaffolds. **Figure 4.3A-B** shows pictures of the fabricated cylinder-shaped hydrogels. Samples obtained with I2959 were too weak to maintain cylindrical shape, especially compared to hydrogels fabricated with LAP.

Wet weight increased as a function of time in composite hydrogels made with both photoinitiators, I2959 and LAP (**Figure 4.3C**). Samples were weighted right after fabrication and after 1, 2, and 7 days. Photoinitiator molar extinction coefficient, ϵ , determines the generation of free radicals as a function of the wavelength. I2959 has a weak molar absorptivity ($\epsilon = 4 \text{ M}^{-1}\text{cm}^{-1}$) at 365 nm [49,267], and composite hydrogels fabricated with I2959 had a wet weight increase close to 0% or even less, meaning a loss of mass. Thus, with 5 s of UV exposure, these hydrogels showed low crosslinking. The apparent low crosslinking resulted in a loss of material and poorly manageable hydrogels. This behavior occurred due to the pore dilation after water absorption. Therefore, the negative values of wet weight increase are explained by the loss of material, which was greater than the absorbed water content. This effect was not observed in the case of composite hydrogels made with LAP, which were easy to handle and showed wet weight increases >25%. LAP has about 50-fold higher molar absorptivity ($\epsilon = 218 \text{ M}^{-1} \text{ cm}^{-1}$) at 365 nm than I2959 [49], explaining the results. Therefore, the hydrogels containing LAP showed normal swelling behavior, and after 7 days, all reached the swelling equilibrium.

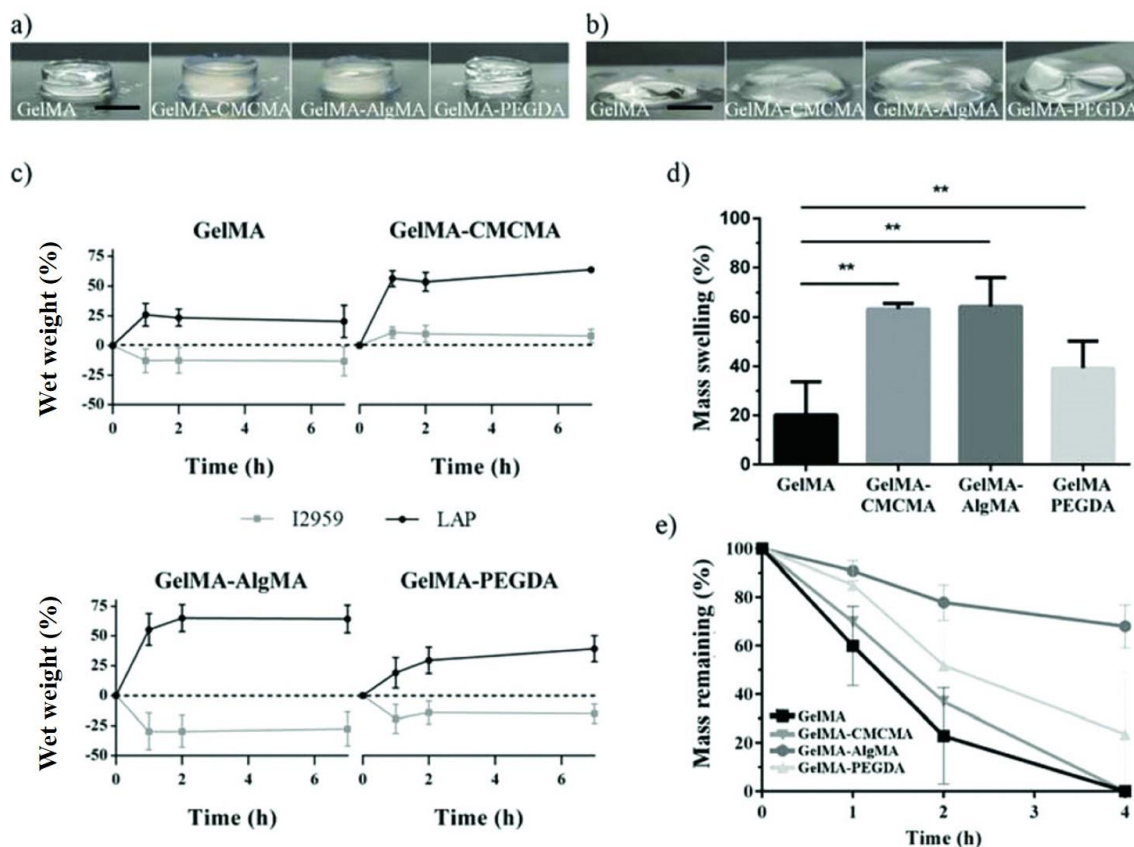


Figure 4.3. Effect of composites on the swelling and degradation of 5% GelMA hydrogels. Disc-shaped hydrogels fabricated using (A) LAP or (B) I2959 as a photoinitiator, under 5 s of UV light exposure. (C) Swelling was studied as the change in wet weight and (D) differences in mass were found in the case of CMCMA, PEGDA, and AlgMA (mean \pm standard deviation, ** p -value < 0.01 , $n = 6$) at the equilibrium swelling. (E) Percentage mass of the remaining profile showing the effect of the composite on the decrease in the wet weight of hydrogels (mean \pm standard deviation, $n = 4$) incubated in a 1.5 U mL^{-1} collagenase type II solution. GelMA (■), GelMA-CMCMA (▼), GelMA-AlgMA (●), GelMA-PEGDA (▲).

The negative effect on shape fidelity when using I2959 (**Figure 4.3B**) could also be attributed to oxygen inhibition in the polymerization system [268]. Lim *et al.* proved that shape fidelity is improved by increasing photoinitiator concentration or UV dosage. In our case, by changing to LAP, its higher molar absorptivity produced the same effect on the photopolymerization yield and resulted in high fidelity, thickness, and mechanical stability (**Figure 4.3A**). Combinations of GelMA with the other hydrophilic photopolymerizable polymers increased the final wet weight. Composite blends containing 1% w/v of CMCMA (p -value < 0.001), AlgMA (p -value = 0.013), or PEGDA (p -value = 0.04) presented significant differences and scaffolds with high water content and swelling were obtained (**Figure 4.3D**). The differences in the water uptake could be attributed to the highly hydrophilic structure of the polysaccharides. In the case of GelMA-AlgMA, the increase in swelling was in concordance with recent publications [260].

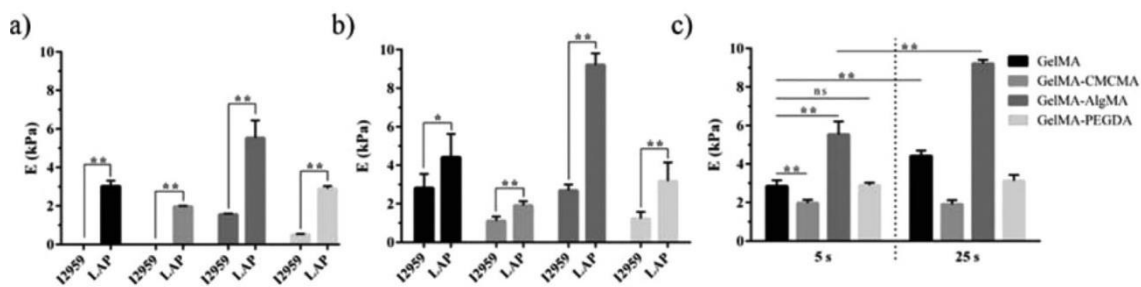


Figure 4.4. Characterization of the mechanical properties of the composite hydrogels. Young's moduli of GelMA and the three composites photocrosslinked with I2959 and LAP during (A) 5 s and (B) 25 s. (C) Comparative Young's modulus of hydrogels photocrosslinked with LAP during 5 s and 25 s. Values are plotted as the mean \pm standard deviation, ** p -value < 0.01 , $n = 3$.

To study the effect of polymer composition on the degradation of composite hydrogels, collagenase II (1.5 U mL^{-1}), which degrades gelatin fraction, was used. Samples were weighed after 1, 2, and 4 h. Hydrogels made with I2959 were completely degraded after 1 h due to their poorly crosslinked structure. For this reason, only the results of the degradation of the materials obtained with LAP are plotted (**Figure 4.3E**). Compared with pristine GelMA, the composite hydrogels showed more resistance to degradation. The addition of 1% w/v PEGDA (p -value = 0.046) and AlgMA (p -value = 0.016) significantly decreased the degradation rate. In particular, more than half of the mass (68%) remained for GelMA-AlgMA hydrogels after 4 h of enzymatic degradation. The results showed increased resistance to degradation of composite hydrogels by adding a small percentage of non-mammalian-derived polymers because alginate, CMC, and PEGDA are not degradable by mammalian cells [257,269,270] and provide stability to the composite hydrogels. Moreover, it is important to note the better mechanical stability and long-lasting structures when fabricated with LAP.

Composite hydrogels with tunable mechanical properties

After swelling, hydrogels were punched to get 10 mm diameter cylinders, and stress-strain curves were obtained by dynamic mechanical analysis. Young's modulus was determined using a compressive modulus and calculated as the slope of the linear part of the stress-strain curves. As the swelling results show (**Figure 4.3C**), hydrogels made with the photoinitiator I2959 under 5 s of UV exposure were extremely weak, and it was not possible to perform the mechanical measurements in some of them (**Figure 4.4A**). In contrast, all the samples made with LAP under 5 s of UV exposure were easy to handle, and Young's modulus values were significantly higher (p -value < 0.005) than those with I2959. It was clear that I2959

needs high UV dosages to develop adequately crosslinked hydrogels. Therefore, 25 s of UV exposure was used (**Figure 4.4B**). With i2959 and this UV dosage, it was possible to fabricate stable hydrogels. However, this long exposure time reduced C2C12 viability (**Figure 4.2B**).

An increase in the polymer concentration, in particular GelMA, increases the stiffness properties of the hydrogel [267]. With the optimized conditions (using LAP and 5 s of UV exposure), Young's modulus was determined to be 3.02 ± 1.13 kPa for 5% w/v of GelMA. These values are similar to the reported by Nichol *et al.* (≈ 2 kPa), Camci-Unal *et al.* (3.4 kPa), and Costantini *et al.* (2.45–5.81 kPa), where similar polymer percentage and degree of methacrylation are used [47,191,271]. **Figure 4.4C** shows that the material stiffness had different behavior with the addition of 1% w/v of PEGDA, CMCMA, and AlgMA. The addition of PEGDA (2.89 ± 0.46 kPa for GelMA-PEGDA) did not cause significant changes. However, adding CMCMA caused a significant reduction in the compressive moduli to 1.96 ± 0.16 kPa (p -value < 0.05). With AlgMA, we observed the opposite effect, with the stiffness increasing significantly to 5.53 ± 2.01 kPa (p -value < 0.05). In all cases, GelMA-AlgMA hydrogels showed the highest compressive modulus compared to the other composites. The mild gelation of alginate by divalent cations such as Ca^{2+} is widely used in biomedical applications. We could assume that the relevant differences of GelMA-AlgMA over the other composites are due to a secondary ionotropic gelation because of divalent ions contained in the polymer solution or the PBS during the swelling.

The stiffness of composite hydrogels can be related to their resistance to collagenase degradation. GelMA-AlgMA hydrogels had the highest resistance and the lowest degradation, followed by GelMA-PEGDA and GelMA-CMCMA hydrogels. These results suggest that the crosslinking density of hydrogels depends on the composite material, UV dosage, and type of photoinitiator. Furthermore, as previously indicated, the mechanical properties of hydrogels strongly impact muscle function and phenotype [14,191,262,264,265]. Therefore, it is of great interest to make hydrogels mimicking the biological scaffolds with tunable mechanical properties. The Young's modulus of hydrogels can be increased by increasing the hydrogel concentration, the UV dosage, or the photoinitiator. However, these modifications may reduce cell viability and the porosity and interconnectivity of hydrogels, affecting the hydrogel's performance [272]. For example, it has been

demonstrated that increasing the mechanical stiffness of GelMA hydrogels by increasing its concentration and/or molecular weight of methacrylate limited cell viability and growth, morphogenesis, and cell migration [273]. In this regard, non-degradable materials hold a great promise as supplementary materials to tune their mechanical properties of hydrogels. Due to their different chemical structures, a small amount of these non-degradable materials is sufficient to considerably change the mechanical properties of composite hydrogels with a minor effect on encapsulated cells. Finally, all of the composite hydrogels showed viscoelastic behavior in the range of the stiffness to promote myotube differentiation in 3D (1–3 kPa) [191] and in 2D structures (8–11 kPa) [23,274]; therefore, all of them could be ideal scaffolds for soft tissues, such as skeletal muscle.

Pore size and pore size distribution

The pore size of composite hydrogels was analyzed using SEM. The images revealed that the fibrillar structure of gelatin was not affected by the addition of the other polymers (**Figure 4.5A-D**). These images were therefore used to determine the pore size distribution (**Figure 4.5E**). Among the different composite hydrogels, no significant differences were found in the range of the small pores (<20 nm), which could limit the passage of nutrients and proteins [275]. However, GelMA-PEGDA hydrogels showed a significant reduction in the number of pores with diameters larger than 200 nm ($5 \times 10^5 \text{ nm}^2$). The GelMA-PEGDA hydrogels presented a homogenous structure in terms of pores size and pores distribution. The structure was more packed, as we can see in **Figure 4.5D**, and the total amount of pores larger than 200 nm was below 0.05% of the total pores (**Figure 4.5F**). This porosity range between 200 and 600 nm is where cells can best spread and extrude their filopodia [276–278]. Therefore, having a very low number of pores around this size could reduce cell viability because of the limited cell spreading. Furthermore, the absence of these pores can negatively affect skeletal muscle differentiation, where myoblast spreading and cell-cell contact play a key role in myotube formation [237].

In this work, we kept the concentrations of CMCMA, AlgMA, and PEGDA constant, but it is expected that increasing this concentration would affect the physicochemical properties of the composite hydrogels. Swelling behavior should show an increase [257], and then a decay because of increasing the polymer concentration. Moreover, the composite hydrogels would be even more resistant to

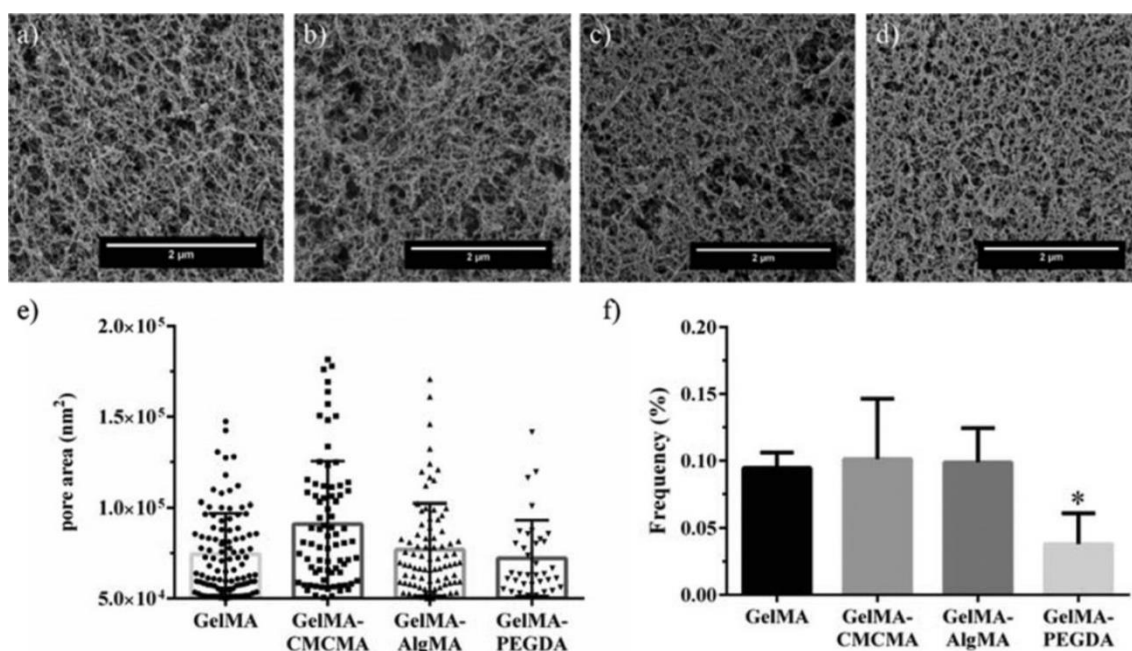


Figure 4.5. Scanning electron microscopy (SEM) images of (A) GelMA, (B) GelMA-CMCMA, (C) GelMA-AlgMA, and (D) GelMA-PEGDA. The aqueous part of composite hydrogels was removed after critical point drying and the fibrillar structure of the hydrogel was left behind. (E) Pore size distribution above 200 nm in diameter and (F) their fraction of the total pore population, expressed as percentages (mean \pm standard deviation, * p -value < 0.05).

biodegradation [271]. Compressive moduli and pore size would also be affected by increasing the non-degradable compounds' concentration. For instance, it has been published that an increase in AlgMA content makes the hydrogels stiffer and reduces the pore size [260]. In the case of CMCMA, it seems to induce, first, a softening of the hydrogels, but the further increase of polymer concentration should lead to a stiffening effect.

Long-term C2C12 viability and proliferation within composite hydrogels

In this study, we compared the long-term viability of C2C12 encapsulated in the composite hydrogels using GelMA as the positive benchmark. To study the long-term viability and proliferation of C2C12 cells, 5% w/v GelMA was dissolved in PBS buffer, with 0.1% w/v LAP and 1% w/v of either PEGDA, CMCMA, AlgMA was added to the polymer solutions corresponding to composites. Cells were trypsinized, and the cell suspension was prepared in growth medium. The biomaterial and the cell suspension were mixed in a 1:1 proportion, and a drop of the resulting solution was

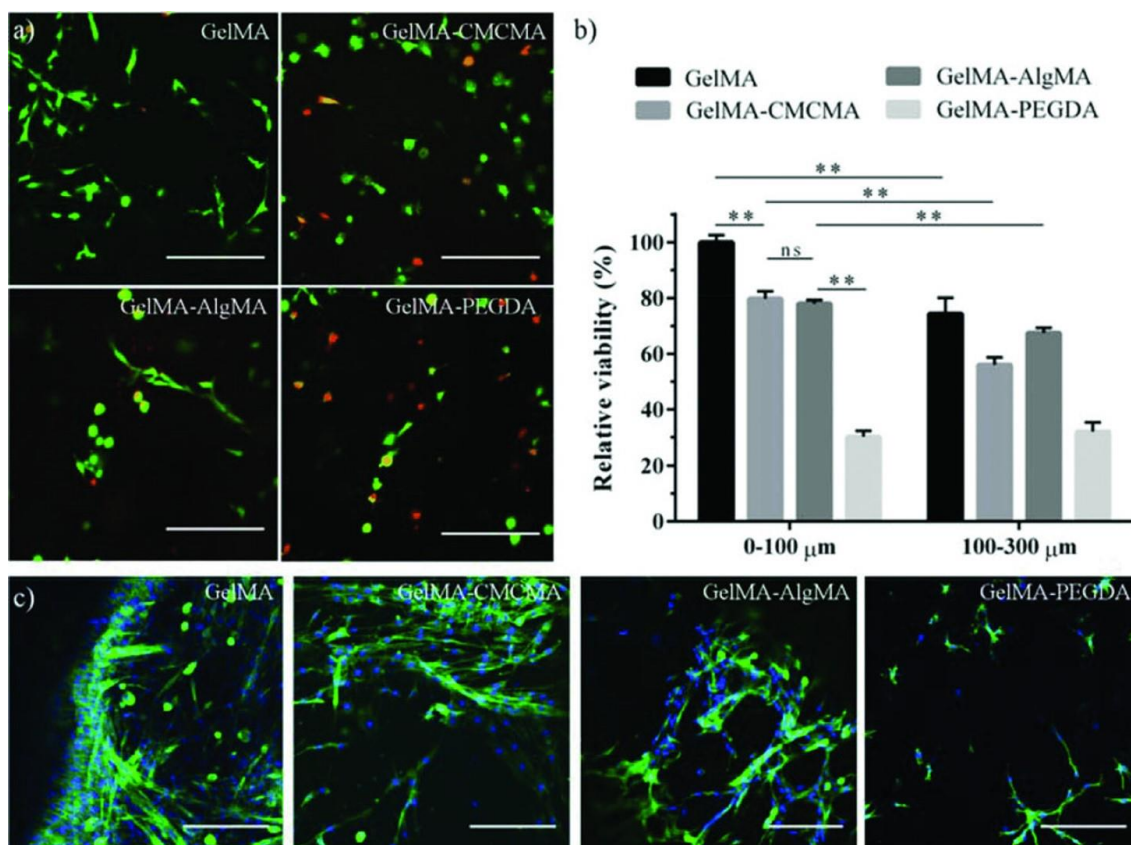


Figure 4.6. C2C12 viability and proliferation in the composite hydrogels after 7 days. (A) Representative images of the live/dead staining (dead in red and live in green) in the range of the first 100 μm depth. (B) Cell viability in composite hydrogels represented as the living cells over the total cell number (mean ± standard deviation, ** p -value < 0.01) relative to GelMA hydrogels. (C) Confocal microscopy pictures of C2C12 cells inside composite hydrogels. F-actin in green and nuclei in blue. Scale bar = 200 μm.

immediately placed in a previously mounted PDMS mold. The samples were irradiated for 5 s under UV light and allowed to swell in the growth medium. The final structures, after demolding, had a 6 mm diameter size and 750 μm height.

The percentage of living cells in the hydrogels was determined using the live/dead staining kit at 1 and 7 days. The viability obtained in the GelMA hydrogels was about 80% after 1 day, in agreement with previous studies [279], and about 60% for GelMA-CMCMA and GelMA-AlgMA hydrogels. These composite hydrogels showed a similar slight decrease in the cell viability at day 7 (**Figure 4.6A-B**). The chemical structures of CMC and alginate do not promote cell attachment to the surface, so they usually show lower cell survival values [258,263]. However, in the composite materials, the viability was still high, and the values were similar to GelMA. Moreover, the percentage of living cells with respect to the total cell number increased after 7 days (**Figure 4.6A-B**). In contrast, the number of living cells in GelMA-PEGDA composites decreased dramatically after 1 day, and low levels of

viable cells remained up to 7 days. These results could be explained by the low number of pores larger than 200 nm in the GelMA-PEGDA hydrogels. Thus, a more significant number of cells remained immobilized from the first moments of encapsulation, and their limited spread affected cell survival and produced low viability values.

We also observed that the number of dead cells increased in the deepest regions of the 3D structures. GelMA, GelMA-CMCMA, and GelMA-AlgMA had significant differences between the number of live cells counted within the first 100 μm from the surface and the ones from 100 μm to 300 μm (**Figure 4.6B**). The porosity of the materials determines the diffusion of nutrients inside the hydrogel. If nutrient uptake is faster than nutrient renewal by diffusion of the medium inside the hydrogel, a lack of nutrients increases with the material depth.

The ability of cells to attach, spread, and grow on hydrogels is important for tissue development [53,280]. To assess the proliferation, cell morphology, and distribution in the composites, staining of F-actin and nuclei (phalloidin and DAPI) was performed after 7 days. **Figure 4.6C** shows cells spreading inside the hydrogels. C2C12 cells in GelMA-PEGDA were less spread than within the other composites, with slight cytoskeleton protrusions, which indicated that PEGDA impairs cell spreading. In contrast, in GelMA, GelMA-CMCMA, and GelMA-AlgMA, C2C12 cells were elongated inside the hydrogels and interconnected with each other. These results indicated that GelMA-PEGDA was the less suitable candidate to promote C2C12 cell growth and spreading, compared to the pristine GelMA and those hydrogels containing CMCMA and AlgMA.

Stiffer materials in 2D are known to promote cell proliferation and attachment [249,280]. Another critical factor is the presence of cell adhesion sequences such as arginylglycylaspartic acid [249]. In 2D, stiffness is a key factor, but in 3D, the porosity also influences cell proliferation and spreading. In our results, GelMA-PEGDA and pristine GelMA had no significant Young's moduli differences between them (**Figure 4.4C**), but cell behavior in the hydrogels was the opposite. Even though GelMA-CMCMA composites were softer than GelMA-PEGDA composites, proliferation and cell adhesion were improved in GelMA-CMCMA. Altogether, the results were consistent with previous studies demonstrating that in 3D, muscular cells can spread, proliferate, and present better myogenesis than in less packed structures [191]. Our

data suggested that stiffness is not the main factor affecting cell behavior in 3D, but rather the critical factor is to obtain less packed structures with a good distribution of big pores. Here, we have obtained a library of composite materials with a good balance between the mechanical properties and mass transport function. As a result, we can choose between scaffolds with similar Young's moduli values but with different pore sizes frequency.

Composite hydrogels as a bioink for muscle tissue bioprinting

Hydrogel patterning is widely used to align cells. Here, extrusion bioprinting was used to build 3D scaffolds of C2C12 embedded in composite hydrogels. A C2C12 cell suspension was first mixed with the prepolymer solutions. The effect on cell alignment inside GelMA filaments below 200 μm in width has already been reported [273,281]. For this reason, the mixture was introduced into a printing syringe, and a nozzle of ± 200 μm inner diameter was used to print the selected design, which consisted of several parallel filaments drawn inside a circle (**Figure 4.7A**). To achieve a relevant height (about 200 μm), two layers were printed. In extrusion bioprinting, inner nozzle diameter, printing pressure, and rate can determine the width and the thickness of the printed bioink. Printing fidelity was evaluated as the percentage change in width compared to inner nozzle diameter (**Figure 4.7B**). After printing, filament width differed with respect to the inner nozzle diameter about 30%, but this fact did not impair the fabrication of isolated filaments (**Figure 4.7C, D**). With this method, bioprinted structures were successfully made using GelMA, GelMA-CMCMA, GelMA-AlgMA, and GelMA-PEGDA. Filaments of ± 200 μm in height and about 250 μm in width were achieved, and these could avoid the problem of low nutrient diffusion in thick hydrogels.

Cells were cultured in the growth medium until high confluence was reached (5 days), and then, the growth medium was switched to a differentiation medium. After 11 days, GelMA scaffolds were nearly flat, and the structure was lost due to cell activity (degradation) while the composite hydrogels preserved their 3D structure. To observe the morphology of the cells and distribution in the hydrogels, cells were stained with phalloidin and DAPI, and also stained with anti-myosin heavy chain (MHC), a protein overexpressed only in differentiated striated muscle. In all cases, C2C12 cells were able to proliferate embedded in the composites and displayed myotube formation (**Figure 4.7E**). The effect of the 3D structures on guiding cell alignment was confirmed by the analysis of myotube orientation (**Figure 4.7G**).

Patterned composite hydrogels exhibited unidirectional orientation of myotubes instead of a random, unorganized mesh, as seen in the images obtained from the unpatterned hydrogels (**Figure 4.6C**). Quantitative analysis of the cell alignment showed that cells in the patterned GelMA hydrogels also exhibited a high degree of alignment but significantly lower than in the composite hydrogels (**Figure 4.7H**). These results are in concordance with the degradability test and sustain the protection against degradability of composite hydrogels. Wider filaments were also fabricated, and it was observed that cell alignment reduced considerably in the filament direction (**Figure S7, Supporting Information**). In agreement, it has been reported that cells confined in GelMA hydrogels, with a geometry constraint below 200 μm induce high cell alignment [273]. Recently, the effect of 3D scaffolds with anisotropic morphology on cell alignment has also been demonstrated, where more than 60% alignment efficacy along 14 days of cell culture was proved [281]. In addition, shear stress generated in the nozzle helped the polymer chains redirect parallel to the longitudinal axis of the bioink stream and promote the alignment of cell adhesion motifs.

Confocal images showed that MHC was present in all the constructs, indicating that it was possible to obtain differentiated myotubes (**Figure 4.7I**). To evaluate the quality of differentiation in the patterned scaffolds, the fusion index was determined as the percentage of nuclei associated with myotubes compared to the total number of nuclei in each sample [282,283]. As expected, C2C12 fused into myotubes in GelMA hydrogel after 11 days of culture. GelMA-CMCMA and GelMA-AlgMA also promoted myogenesis (**Figure 4.7J**). Furthermore, the fusion index of those composites was slightly higher than GelMA. As previously mentioned, GelMA 3D structures tended to degrade after several days due to cell metabolism, making it difficult to find significant 3D areas comparable with the scaffolds made of composite materials. The fusion index corresponding to GelMA-PEGDA hydrogels was similar to the other composites, although immunofluorescence images indicated that the number of myotubes was significantly lower (**Figure 4.7J**).

After all, the applicability of these composite hydrogels in skeletal muscle tissue engineering has been proved. Importantly, for the first time, GelMA-CMCMA composite hydrogels have been successfully used to fabricate skeletal muscle

RESULTS

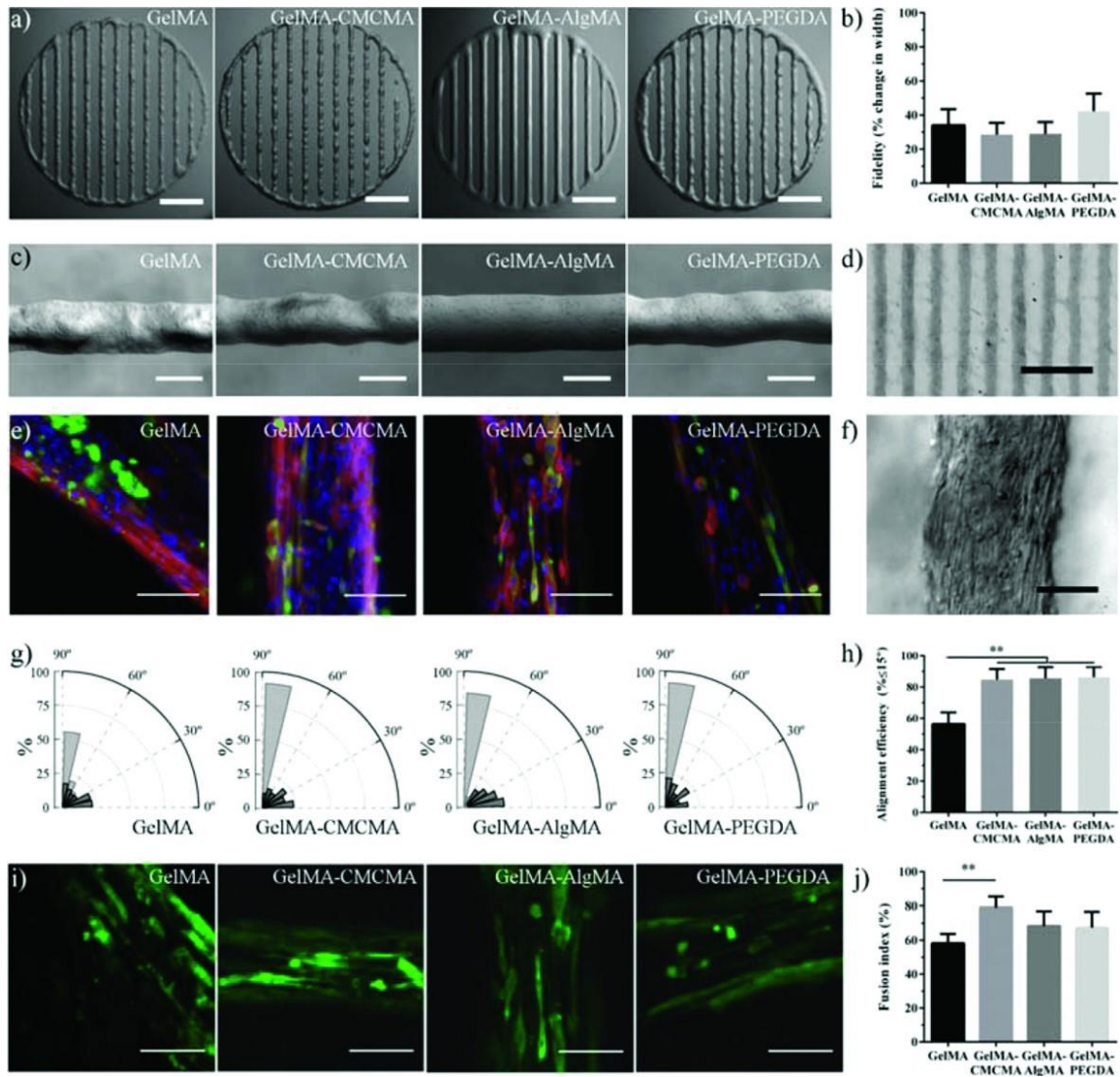


Figure 4.7. C2C12 myotube formation in bioprinted composite hydrogels. (A) Top view images of the bioprinted composite hydrogels after fabrication. Scale bar = 2 mm. (B) Percentage change in width of composite hydrogels after printing compared to nozzle inner diameter. (C) Magnification of the filaments containing C2C12 cells. Scale bar = 250 μ m. (D) 3D structure was successfully printed and remained stable after swelling. Scale bar = 2 mm. (E) Confocal microscopy pictures of C2C12 cells encapsulated in the composite hydrogel structures after 11 days of culture. F-actin in red, MHC in green, and nuclei in blue. Scale bar = 200 μ m. (F) Bright-field image of elongated cells encapsulated in composite hydrogels. Scale bar = 200 μ m. (G) Normalized histograms (bin = 10°) depicting the distribution of the angles between cell cytoskeleton fibers (light gray) inside non-patterned hydrogels (dark gray), and in 3D printed hydrogels. C2C12 inside the bioprinted hydrogels show high degree of alignment (>75%) following the pattern direction, while inside cylinder-shaped hydrogels are randomly distributed. (H) Quantitative analysis of cell alignment efficiency (mean \pm standard deviation, ** p -value < 0.01). (I) Confocal microscopy images showing the expression of MHC (green) in the C2C12 myotubes inside 3D bioprinted composite hydrogels. Scale bar = 200 μ m. (J) Fusion index percentage (mean \pm standard deviation, ** p -value < 0.01) of the C2C12 myotubes encapsulated in the bioprinted composite hydrogels.

constructs. Considering the adjustability of the physical properties, these composite hydrogels can be used in other tissue engineering applications such as heart,

cartilage, or bone, as other authors have demonstrated by using GelMA and AlgMA [255,260].

4.1.4. Conclusions

3D bioprinter technologies have emerged as a great system to fabricate complex tissues. Therefore, bioinks play a key role in the success of using such technologies. In this work, the influence of mechanical stiffness and geometrical confinement on the 3D culture of myoblast-laden GelMA photocrosslinkable composite hydrogels was evaluated in terms of *in vitro* myogenesis. We fabricated new composite hydrogels (GelMA-CMCMA and GelMA-AlgMA) to print stable and non-biodegradable skeletal muscle structures with tunable properties to allow high cell viability and myogenesis. Compared with non-degradable previously described composite hydrogels, such as GelMA-PEGDA, we obtained higher cell proliferation and viability. We demonstrated that the frequency and presence of pores with diameters larger than 200 nm ($5 \times 10^5 \text{ nm}^2$) are crucial factors in the design of 3D scaffolds and 3D cell encapsulation, even in hydrogels with different stiffness. The use of GelMA-CMCMA and GelMA-AlgMA composites with bioprinting methods allowed us to efficiently obtain durable 3D structures of differentiated and aligned muscle fibers. In contrast to GelMA, they are long-lasting materials and good candidates as hydrogels for *in vitro* applications and bioactuators.

4.2. Muscle-on-a-chip with an on-site multiplexed biosensing system for *in situ* monitoring of secreted IL-6 and TNF- α

In this work, GelMA-CMCMA was used to develop skeletal muscle microtissues for *in vitro* monitoring of muscle-secreted cytokines in a muscle-on-a-chip device¹¹. The cell-laden hydrogels were fabricated using photomold patterning with a UV crosslinker. Using this technique, we could obtain 3D structures by exposing the cell-laden photocrosslinkable material to UV light through a micropatterned polydimethylsiloxane (PDMS) stamp. The fabrication conditions, such as type of photoinitiator, photoinitiator concentration, and material concentration, were selected according to the results obtained in our previous work (**Chapter 4.1**). The resulting micropatterned geometry acts as a topographical cue to confine cells and promote their alignment and fusion into myotubes. The physical properties of composite hydrogels fabricated under a range of UV exposure times were characterized. Moreover, we analyzed the viability and morphology of C2C12 myoblasts encapsulated in these biomaterials. The UV exposure time was selected according to the crosslinking condition with the optimal cell morphology results. Aligned fibers could be observed by bright-field microscopy after six days of culture. The presence of long, multinucleated myotubes was confirmed by the expression of myosin heavy chain. Image analyses demonstrated that fibers were oriented following the pattern direction with a high fusion index.

The skeletal muscle microtissues were directly fabricated inside a microfluidic PDMS chip. After differentiation, the 3D microtissues were either electrically or biologically stimulated inside the microdevice. The myokines secreted to the culture medium in response to this stimulation were delivered by a microfluidic network to a screen-printed gold electrode (SPGE) amperometric sensing system for IL-6 and TNF- α detection. Altogether, these results demonstrated that the muscle-on-a-chip biosensing system described in this work could be used to study the *in vitro* skeletal muscle metabolic response upon exercise and under the administration of a chemical compound.

¹¹ This work has been published as:

Ortega M A, **Fernández-Garibay X**, Castaño A G, De Chiara F, Hernández-Albors A, Balaguer-Trias J and Ramón-Azcón J 2019 Muscle-on-a-chip with an on-site multiplexed biosensing system for *in situ* monitoring of secreted IL-6 and TNF- α . *Lab Chip* **19** 2568–80.

4.2.1. Introduction

In vitro biomimetic tissue models with physiological functions can be used to assess biological phenomena in an easy, accurate, and controllable manner. Currently, *in vitro* tissues are useful for studying both the molecular and the cellular bases of physiological and pathological responses of biological processes. To this end, microscale fabrication technologies have emerged as useful tools in tissue engineering and biological applications [284]. Further, these models promise to replace corresponding animal experiments, which are costly, labor-intensive, and beset with serious ethical issues regarding their biological relevance to humans [285].

In addition, almost 40% of total body mass is skeletal muscle (SM) tissue. Although people associate it with strength and movement, its functions range from controlling facial expressions to helping respiratory and blood circulation. The skeletal muscle tissue contains numerous quiescent mononucleated satellite cells which undergo intense proliferation after tissue damage to self-repair. This capacity is impaired or even lost in patients with congenital defects, diabetes, cancer, and/or after traumatic injuries and protracted denervation [286]. According to the American Medical Association, there is no specialized clinical doctor for the treatment of muscular diseases, such as Duchenne muscular dystrophy and inflammatory myopathy, hence the necessity to fill the gap between muscle disorders and *ad hoc* therapies. Moreover, no or too little knowledge is present about the source and auto-paracrine impact of cytokine release such as IL-6 and TNF- α in tissue regeneration. To this end, tissue engineering represents a fascinating and affordable approach to shed light on understanding the mechanisms and factors involved in the development of muscular disease.

In addition, in the field of biomimetic tissues, the need to incorporate biosensing for *in situ* monitoring of the status or the secretion regimes of *in vitro* microtissues is increasingly recognized [287,288]. Additionally, the capability to miniaturize biosensor systems and advanced tissue fabrication procedures have enabled researchers to create multiple tissues on a chip with a high degree of control over experimental variables for high-content screening applications [289]. While recent organs-on-a-chip (OOCs) can model native-organ microstructures for understanding disease mechanisms, current OOCs still lack the precise temporal control needed to study processes such as delayed cell response to treatment and

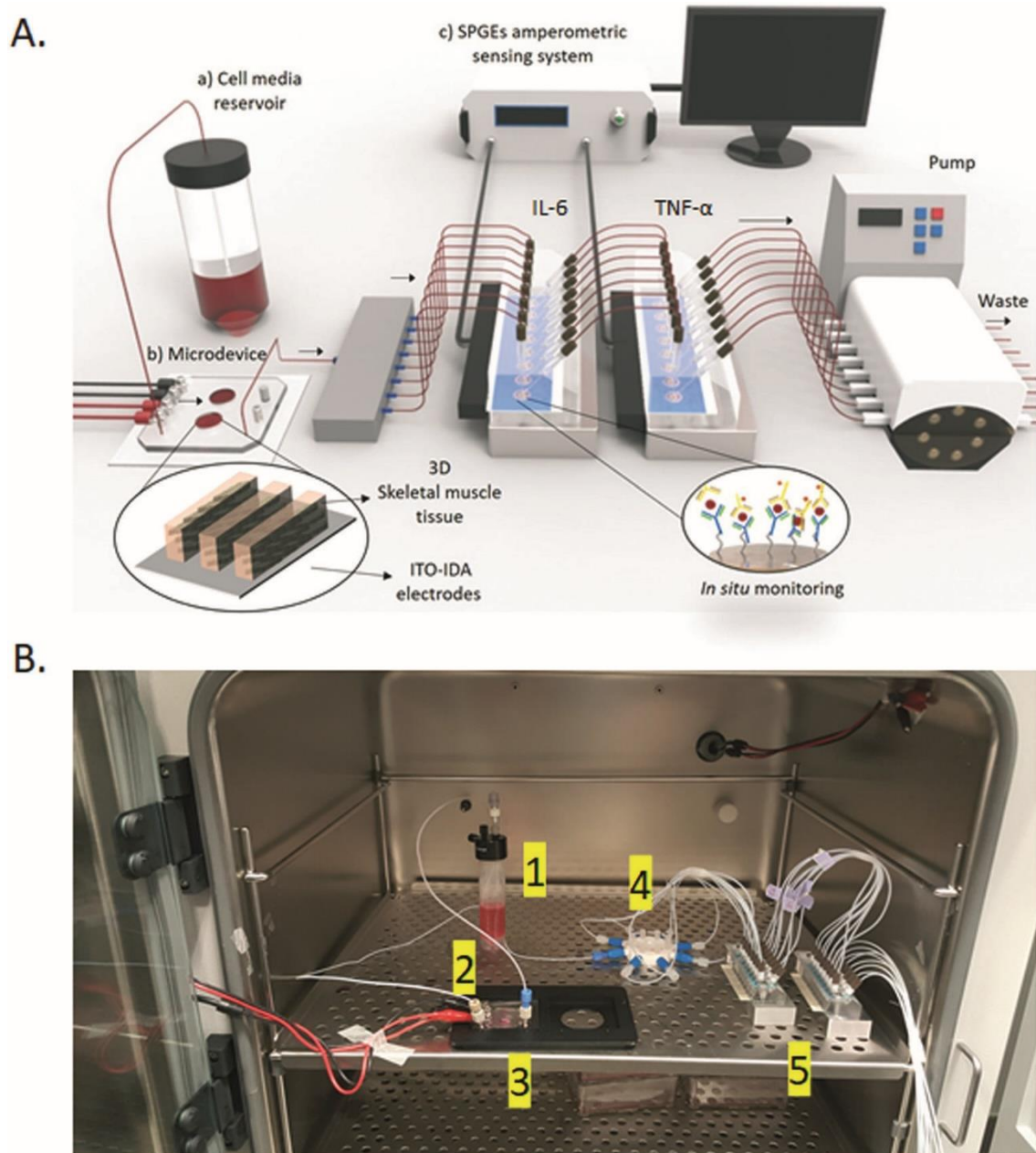


Figure 4.8. Schematic overview of the configuration and function of the muscle-on-a-chip. (A) The flow passes through the microdevice where 3D SM tissue is electrically (ITO-IDA electrodes) or biologically (LPS) stimulated. The outlet flow containing the IL-6 and TNF- α goes directly to an 8-way microfluidic distributor to reach the SPGE sensing system. A peristaltic pump generates negative pressures that pull the medium through the microdevice as well as the detection system (SPGEs). (a) Reservoir containing cell media connected with a (b) custom-made microdevice containing the 3D SM tissue. (c) Multiplexed high-sensitivity platform containing functionalized SPGEs. (B) Physical arrangement: (1) cell medium reservoir; (2) 3D engineered muscle microtissue cultured on the microdevice; (3) microdevice support; (4) 8-way flow distributor; (5) SPGE functionalized sensing system.

chronic effects caused by long-term drug stimulation. Specifically, the difficulty arises when integrating the capability of stimulating the cells of interest with the capability of monitoring individual analytes released *in situ*. For example, OOCs that utilize

magnetic particles [290], or impedimetric sensors [285,287,288] to facilitate analyte detection, are either time-sensitive or unstable under changing medium composition.

Here, we present a cost-effective integrated microdevice capable of simultaneous, *in situ* cell stimulation and analyte detection that is stable over time. We demonstrate this using a microdevice that targets 3D skeletal-muscle tissue known to release cytokines under external stimulations. With this setup, we can provide either electrical stimulation using indium tin oxide (ITO)-interdigitated array (IDA) electrodes or biological stimulation using lipopolysaccharide (LPS) solutions. Simultaneously, we can achieve multiplexed continual *in situ* measurements of secreted myokines using functionalized high-sensitivity screen-printed gold electrodes (SPGEs) (**Figure 4.8**). Our setup demonstrates that microfluidics combined with tissue engineering and biosensing is an affordable approach to determining the response upon external stimuli. This device can be involved in the study of various muscular disease progression, furthering the understanding and treatment of muscular metabolic disorders.

4.2.2. Experimental procedure

Cell culture

Murine C2C12 skeletal myoblasts (CRL-1772, ATCC, Virginia, USA) were expanded in growth medium, which consisted of Dulbecco's Modified Eagle Medium (DMEM high glucose, l-glutamine) (11965092, Gibco, Thermofisher, Massachusetts, USA) supplemented with fetal bovine serum (10% v/v, FBS) (16000044, Thermofisher, Massachusetts, USA) and penicillin/streptomycin (1% v/v) (15140122, Thermofisher, Massachusetts, USA) at 37 °C and a 5% CO₂ atmosphere. To induce differentiation into myotubes, the medium was changed to a differentiation medium, consisting of DMEM high glucose, supplemented with horse serum (2% v/v) (HS) (26050088, Thermofisher, Massachusetts, USA) and 1% v/v penicillin/streptomycin.

Synthesis of prepolymer precursors

Gelatin methacryloyl (GelMA) was synthesized with a 40% degree of methacrylation as previously described [291]. The material was then dialyzed in Milli-Q water with 6–8 kDa MWCO membranes (08-700-142, Spectrumlabs, San Francisco, USA) for 4 days. Sodium carboxymethyl cellulose (CMC) (419273, Sigma Aldrich Co., St. Louis, MO, USA) was methacrylated at a maximum degree of

methacrylation as previously described [291]. The reaction was performed by mixing a solution of the polymer (1% w/v) in MES buffer (50 mM, pH 6.5) with a mix of EDC (20 mM), N-hydroxysuccinimide (10 mM) (130672, Sigma Aldrich Co., St. Louis, MO, USA) and 2-aminoethyl methacrylate (10 mM) (479659, Sigma Aldrich Co., St. Louis, MO, USA). The reaction was stopped after 24 h with the addition of acetone (161007, Panreac, Barcelona, Spain) and filtered using a vacuum flask. The precipitate was dissolved in PBS (10 mM) and dialyzed in Milli-Q water with 3.5 kDa MWCO membranes (68035, Thermofisher, Massachusetts, USA). Finally, the solutions of methacrylated polymers (GelMA and CMCMA) were lyophilized and stored at $-20\text{ }^{\circ}\text{C}$.

Preparation of prepolymer solutions

The prepolymer precursors (GelMA and CMCMA) were dissolved in growth medium containing the photoinitiator lithium phenyl(2,4,6-trimethylbenzoyl)phosphinate (LAP) (L0290, TCI EUROPE N.V, Zwijndrecht, Belgium) at $65\text{ }^{\circ}\text{C}$ for 3 h to obtain a homogeneous solution. The concentrations of GelMA, CMCMA, and LAP were fixed to obtain final concentrations of 5%, 1%, and 0.1% w/v, respectively.

Hydrogel characterization

Swelling analysis

The prepolymer solutions were prepared as described above. Samples for swelling analysis were fabricated by placing the prepolymer solution (300 μL) in a 48-well plate. After exposing the prepolymer solution to UV light (UVP Crosslinker, model CL-1000L, 365 nm, 40 W, from Analytik Jena US, Upland, USA), hydrogels were rinsed with PBS, and their initial weight was measured. Then, the wet weight was determined after 1, 3, and 7 days in PBS (10 mM) after wiping with tissue paper to remove the excess water. To calculate the mass increase, each water content value was normalized with the initial weight of the sample. After day 7, samples were rinsed with Milli-Q water and dried. The swelling ratio, Q , of the hydrogels was determined by:

$$Q = \frac{W_s - W_d}{W_d} \cdot 100$$

Here, W_d and W_s represent the weight of dried hydrogels and the weight after swelling in PBS, respectively.

Mechanical analysis

Uniaxial compression tests of hydrogels were performed using a Zwick Z0.5 TN instrument (058993, Zwick-Roell, Berlin, Germany) with a 5 N load cell. Hydrogels were fabricated following the same procedure as for the swelling analysis. After reaching equilibrium swelling in PBS, cylindrical hydrogels were cut using a 10 mm diameter biopsy punch. Real hydrogel diameters and heights were measured prior to the experiment. Wet samples were tested at room temperature up to 30% final strain (deformation), using the following parameters: 0.1 mN preload force and 20% min^{-1} strain rate. Stress-strain data were obtained from force–deformation graphs (**Figure S2A†**). Values for the compressive modulus were calculated from the slope of the linear region corresponding to 10–20% strain. With uniaxial compressive testing, the testXpert software (Zwick Roell) converts the load-deformation data to stress-strain data using simple geometrical relationships (from measured hydrogel disks), and Young's modulus E is reported [292]. For each hydrogel formulation, three samples were prepared, and measurements were performed in triplicate.

Degradation analysis

Hydrogels were fabricated as described above for the swelling analysis. The hydrogels were removed from the 48-well plate and left to swell for 3 days in a 6-well plate. A total of 3 mL of collagenase type II (0.5 U mL^{-1}) (17101015, Thermofisher, Massachusetts, USA) in PBS was added to the hydrogels, and they were incubated at 37 °C under 100 rpm shaking conditions. Then, the hydrogels were weighed after 1, 2, 3, 4, and 4 h. The percent of hydrogel remaining (W_r) was determined by:

$$\%W_r = \frac{W_t}{W_i} \cdot 100$$

Here, W_t and W_i represent the weight of hydrogel composites at the swelling equilibrium and after collagenase incubation, respectively.

Cell encapsulation in 3D micropatterns

To encapsulate the cells in micropatterns, a photomold patterning technique was used [220]. For that, one volume of prepolymer solution was mixed with one volume of C2C12 cell suspension to obtain a final cell density of 2.5×10^7 cells per

mL. Then, a drop of cell-laden prepolymer (15 μ L) was placed in the bioreactor well. A micro-structured PDMS stamp of 6 mm in diameter (**Figure 4.11A**) was pressed lightly on the top (grooves of 200 μ m and 270 μ m in height, and ridges of 200 μ m, with a length of 6 mm approximately), filling the microchannels with the solution. The hydrogel was photo-crosslinked using a UVP Crosslinker (model CL-1000L, 365 nm, 40 W, from Analytik Jena US, Upland, USA) with exposure times between 18 s and 120 s. The energy dose for every time point was measured using a wireless power meter (model PM160 Si Sensor Power Meter with Bluetooth and USB operation, 400–1100 nm, 10 nW–200 mW, Thorlabs, CA, USA). After carefully removing the stamp, the microdevice was sealed with a cover glass slide. The micro-structured cell-laden hydrogels were incubated inside the microdevice with growth medium for 6 days. Then, the culture medium was switched to differentiation medium (DM) to promote the formation of myotubes. All subsequent experiments were performed in DM cell medium.

C2C12 morphology and viability in composite hydrogels

C2C12 cells were encapsulated in GelMA-CMCMA hydrogels at a low cell density (10^6 cells per mL) using a previously described protocol [291]. Bright-field microscopy images obtained after 6 days of encapsulation were analyzed using ImageJ software to obtain cell descriptor data of the aspect ratio and circularity of cells encapsulated in composite hydrogels with different exposure times. Cell viability was evaluated after 1, 6, and 10 days using the Live/Dead Viability/Cytotoxicity assay kit (L3224, ThermoFisher, Massachusetts, USA). Confocal microscopy images were obtained and processed using a custom MATLAB software code used in our previous work [291]. Cell viability percentage was calculated as the fraction of living cells over the total cell number.

Immunofluorescence staining

The tissues were fixed in a formalin solution (10%) (HT501128, Sigma Aldrich Co., St. Louis, MO, USA) 15 days after fabrication. Then the hydrogels were washed with Tris-buffered saline (TBS, BR0042, Canvax Biotech, Spain). Cells were permeabilized with Triton X-100 (0.1% v/v) (X100, Sigma Aldrich Co., St. Louis, MO, USA) in TBS for 15 min and blocked with a blocking buffer consisting of Triton X-100 (0.3% v/v) and donkey serum (3% v/v) (D9663, Sigma Aldrich Co., St. Louis, MO, USA) in TBS for 2 h. Afterward, tissues were washed with TBS and incubated in rhodamine-phalloidin 480 (100 nM) (PHDR1, Cytoskeleton Inc., Colorado, USA)

solution overnight to stain filamentous actin (F-actin). Additional overnight staining for myosin heavy chain (MHC) was performed by incubating in a solution of MF20 Alexa Fluor 488 (5 $\mu\text{g mL}^{-1}$) (53-6503-82, eBioscience, Thermofisher, Massachusetts, USA) in blocking buffer. After washing with TBS, nuclei were counterstained with DAPI (1 μM , D1306, Thermofisher, Massachusetts, USA) for 15 min. Hydrogels were mounted and stored at 4 °C before observation by confocal microscopy.

Microdevice fabrication

ITO-IDA electrode fabrication

Glass substrates with indium tin oxide (ITO) were commercial (CEC020S, 100 nm thickness, 20 ohms sq^{-1} , Präzisions Glas & Optik, Iserlohn, Germany), with dimensions of 60 mm \times 60 mm \times 1.1 mm of length, width, and thickness, respectively. The interdigitated electrodes were patterned on the ITO-glass substrates by a conventional photolithography procedure. Initially, the ITO glass slides were cleaned by a standard glass cleaning process, 5 min of sonication in DIW, acetone, and 2-propanol in this order. Finally, the substrates were dried under N_2 flow for 3 minutes. They then were activated using a plasma cleaner for 20 min at 6.8 W (Expanded Plasma Cleaner, PCD-002-CE Model, Harrick Scientific Corporation, NY, USA) and heated at 95 °C for 1 min using a hot plate. AZ1512Hs positive resist (MicroChemical GmbH, Ulm, Germany) was spun on the substrate in two steps to obtain a final resist thickness of 2 μm (Spinner model WS-650MZ, Laurell Technologies Corporation, North Wales, USA). A soft bake at 95 °C for 2 min is performed to remove solvents from the resist and improve adhesion. The IDA pattern was stamped on a chromium mask fabricated by direct lithography using a direct-write laser (DWL) machine (DWL 66FS model, 405 nm, 50 mW, Heidelberg Instruments Mikrotechnik GmbH, Heidelberg, Germany). In order to transfer the mask pattern to the resist, the coated substrates were placed under a UV light ($\lambda = 305\text{--}450$ nm) in a UV photolithography mask aligner (SÜSS Microtec, Germany) at 25 mW cm^{-2} for 5 seconds (125 mJ cm^{-2}). The patterned resist was developed for 1 min using an aqueous solution of the AZ400K developer (MicroChemicals GmbH, Ulm, Germany) in a 4:1 ratio and rinsed with distilled water followed by a hard bake at 120 °C for 1 h. Thickness was characterized using a profilometer (DEKTAK 6 M, Veeco Instruments, NY, USA). Then, a wet etching procedure was performed to etch the ITO not protected by resist. The substrates were submerged in a 6 M solution of an HNO_3/HCl mix and heated

at 50 °C for 2 min. Finally, the substrates were sonicated for 5 min in acetone and IPA and then dried with a N₂ flow.

PDMS chip fabrication

Silicon wafer molds were created through a two-layer process using negative photoresist SU8-2100 (MicroChem, Westborough, MA, USA). A microfluidic chip design was printed on a high-quality acetate film to be used as a mask. Finally, a micro featured master mold was obtained by contact photolithography. To obtain a polydimethylsiloxane (PDMS) fluidic chip, a mixture of the prepolymer with a curing agent (Sylgard 184, Dow Corning, Midland, USA) was prepared at a 10:1 ratio, degassed in a vacuum chamber for 1 h, and poured on the SU8 master mold. After overnight incubation at 50 °C, the PDMS replica was cured and carefully peeled off from the mold, followed by a hole punch process. Once the PDMS chip was obtained, a bonding step to the ITO-IDA electrode substrate was performed through oxygen plasma activation for 30 s at 10.5 W (Expanded Plasma Cleaner, PCD-002-CE Model, Harrick Scientific Corporation, NY, USA). Then the final microdevice was heated at 80°C for 2 h.

Fabrication of the biosensing platform

Chemicals and immunochemicals

Phosphate-buffered saline (PBS) was phosphate buffer (0.01 M), potassium chloride (0.0027 M) and sodium chloride (0.137 M) at pH 7.2. MES buffer was prepared from MES hydrate salt (4-morpholineethanesulfonic acid) and adjusted to pH 5.0 (M5287, Sigma Aldrich Co., St. Louis, MO, USA). Purified rat anti-mouse IL-6 (ref. 554400, clone MP5-20F3, capture antibody), biotin rat anti-mouse IL-6 (ref. 554402, clone MP5-32C11, detection antibody), purified rat anti-mouse TNF- α (ref. 551225, clone G281-2626, capture antibody), and biotin rat anti-mouse TNF- α (ref. 554415, clone MP6-XT3, detection antibody) were purchased from BD Biosciences (Barcelona, Spain). Recombinant mouse IL-6 (ref. 200-02, 100 μ g) and recombinant mouse TNF- α (ref. 200-31, 100 μ g) were purchased from CliniSciences S.L. (Nanterre, France). SAV-polyHRP used in the final step was purchased from Pierce ThermoFisher (21140, Barcelona, Spain). For electrochemical measurements, citrate buffer (0.04 M, pH 5.5) (S4641, Sigma Aldrich Co., St. Louis, MO, USA) was used, and a substrate solution was also prepared containing TMB (0.0001%) (3,3',5,5'-tetramethylbenzidine) and H₂O₂ (0.0004%) in citrate buffer.

Functionalization protocol

To specifically capture the secreted IL-6 and TNF- α , it was necessary to first functionalize the surface of SPGE sensors by using a self-assembled monolayer (SAM). To create a uniform SAM, (20-11-mercaptoundecanoyl)-3,6,9,12,18-hexaoxaicosanoic acid (TH003-m11.n3-0.5, Prochimia Surfaces, Sopot, Poland) was used. First, the gold SPGE sensors were cleaned using a UV/ozone cleaner (ProCleanerTM, BioForce Nanosciences, Utah, USA) for 15 min. Afterward, an ethanolic solution of SH-PEG-acid (5 mM) was prepared freshly using 99.5% EtOH HPLC grade (161086.1211, PanReac AppliChem, Barcelona, Spain). The SAM formation step was made under static conditions using a PMMA static cell specially designed for this step (**Figure S3B†**). The SPGE sensor was coupled with PMMA cells, and 50 μ L of the SH-PEG acid molecule was added into each individual reservoir and left overnight at RT. After SAM formation, the electrodes were rinsed in EtOH. In order to facilitate the linkage of protein, carbodiimide chemistry was used using EDC (200 mM) (E7750, Sigma Aldrich Co., St. Louis, MO, USA) mixed 1:1 with N-hydroxysulfosuccinimide sodium salt (sNHS) (200 mM) in H₂O (56485, Sigma Aldrich Co., St. Louis, MO, USA) and MES buffer (M5287, Sigma Aldrich Co., St. Louis, MO, USA). Once activation was performed, capture antibody (100 μ L) in PBS buffer was added and incubated for 2 h at RT. Afterward, two washes with PBS (10 mM) were performed, and the electrodes were passivated using PBS (10 mM, 1% BSA) for 1 h at RT to avoid non-specific binding. The SPGE electrode was implanted under microfluidic conditions throughout all the experiments. As a final step, the SPGE electrode was removed and placed into a static PMMA cell to be processed. At this point, binding of secondary biotinylated antibody was performed, followed by the addition of SA_v-polyHRP, both steps for 1 h at RT. Finally, the SPGE electrodes were connected to the potentiostat, and the amperometric signal was recorded. Electrical stimulation was performed using a wave generator (200 MHz multifunction generator, WF19478, NF Corporation, Yokohama, Japan) connected to a microdevice using metallic connections assembled to it. To evaluate the accuracy in our experiments, blind spiked samples were prepared in DM and measured directly using our optimized immunoassays. The accuracy for both immunoassays was evaluated by establishing a linear regression between spiked and measured values. Analyses were made in triplicate.

Amperometric detection measurements

Amperometric measurements were performed with a μ STAT 200 potentiostat (Metrohm-Dropsens, Herisau, Switzerland). Screen-printed gold electrodes (SPGEs) (Au DRP-220AT, Metrohm-Dropsens, Herisau, Switzerland) consisting of a 4 mm smooth working electrode, an Au counter electrode, and a Ag pseudo-reference electrode were used. A flow cell (DRP-FLWCL, Metrohm-Dropsens, Herisau, Switzerland) for SPGE was used together with the microdevice for the experiments under flow conditions. To integrate both systems and control the delivery of the cell medium containing the secreted myokines to the SPGE sensors, we used an 8-way flow and pressure control microfluidic distributor (part no. 001103, Kinesis, Cambridgeshire, UK). The peristaltic pump used in the experiments was coupled with a multi-channel pump-head, allowing 8 independent parallel tubing setups (Model MCP Process, Cole-Parmer GmbH, Wertheim, Germany). The microfluidic tubing used in all processes was made of PTFE with dimensions of 1/16" OD \times 1/32" ID (Darwin Microfluidics, Paris, France). Once detection was performed, amperometric signals were measured at an applied potential of -0.20 V vs. the Ag pseudo-reference electrode for 250 s. The amperometric signals were acquired under static conditions using the static PMMA cell. The recorded signal was the mean value of the current obtained in the last 10 s when the steady-state was reached. The specific signal produced for detecting proteins is translated by the difference between the original base of the citrate buffer and the signal obtained when the substrate solution is added. The intensity registered due to this electron transfer is directly related to the amount of HRP and, consequently, with the concentration of the IL-6/TNF- α of the analyzed sample through calibration curves [293]. Cyclic voltammetry (CV) measurements were carried out after deposition of $[\text{Fe}(\text{CN})_6]^{3-/4-}$ (50 μL , 5 mM) redox probe solution onto the surface of the modified Au electrode. CV in the range of -0.25 to 0.50 V at a scan rate of 100 mV s^{-1} was used to monitor the SAM formation on the gold electrode surface.

Statistical analysis

Statistical analysis was performed using Graph Prism software (GraphPad Software, San Diego, CA, USA). All data collected were presented as the mean \pm standard deviation (SD). Continuous variables were analyzed using the Kruskal–Wallis rank test. When significant, *post hoc* tests for continuous variables were

performed among groups using the Mann–Whitney test. p values <0.05 were considered statistically significant.

4.2.3. Results and discussion

Description of the integrated platform

In the recently emerged field of organ-on-a-chip, the need to incorporate biosensing for *in situ* monitoring of the status or metabolic behavior of biomimetic organs is increasingly being recognized. In order to fill this gap, we have developed an integrated platform constituted by a custom-made microdevice hosting a skeletal muscle microtissue coupled with a functionalized SPGE biosensing system for high-sensitivity detection of secreted factors such as IL-6 and TNF- α .

The cell medium reservoir containing 20 mL of DM cell medium (**Figure 4.8Aa**) is connected with a miniaturized device containing the 3D muscle microtissue, forming the “muscle-on-a-chip.” The microdevice is formed by combining an ITO-IDA electrode substrate with a polydimethylsiloxane (PDMS) microfluidic chip (**Figure 4.8Ab**). On top of this system, the skeletal muscle cells embedded in the composite hydrogel are patterned by a molding technique and left to grow, fuse, and differentiate until 3D-aligned muscle fibers are obtained. Inside the microdevice, 3D microtissue is exposed to either electrical stimulation (from ITO-IDA electrodes) or biological stimulation (addition of LPS to DM cell medium).

As a consequence of either form of stimulation, myokines are secreted from the construct to the cell medium and are delivered by a microfluidic network to a highly sensitive SPGE amperometric system (**Figure 4.8Ac**). The SPGEs are functionalized with selective monoclonal antibodies before assembly into the microdevice. Finally, the cell medium delivers secreted myokines directly onto the SPGE sensors. This system is optimized to prevent dilution of the sample, avoiding further manipulation by the operator. The capture of these analytes (myokines) produces changes in amperometric signals, which are directly related to concentration. Negative pressures are applied to the whole system using a peristaltic pump. Our custom-designed microfluidic platform fits in a shelf of standard incubators (**Figure 4.8B**).

Muscle-on-a-chip integrated with an on-site multiplexed sensing system for in situ monitoring of secreted myokines

Muscle-on-a-chip

As a proof-of-concept, we choose a model based on skeletal muscle (SM) tissue, known as a secretory organ. Our target SM tissue is fabricated inside the microdevice, enabling not only the renewal of nutrients but also the electrical stimuli to induce tissue contraction. To fabricate the microdevice, we performed a photolithography procedure to obtain an array of ITO-IDA with reference electrodes on a glass substrate for tissue electrical stimulation. The dimensions of the whole device are 60 mm × 60 mm. The size of the ITO-IDA arrays is 220 μm × 110 μm × 0.1 μm for height, width, and thickness, respectively (**Figure S1A†**). The miniaturized chip is built of PDMS placed on top of the ITO-IDA electrodes (**Figure 4.9A**). The microdevice was designed and fabricated to be used and integrated with biocompatible materials such as gelatin methacryloyl (GelMA), which provide an optimal cell environment. This platform presents high compatibility with standard sterilization protocols. On the other hand, using a microfluidic network provides low-volume consumption (<1 mL), ensuring good nutrient exchange with the SM microtissue. The microdevice is also integrated with interdigitated electrodes set for the electrical stimulation of the microtissue, mimicking an *in vitro* exercise model (**Figure 4.9A**).

The size of the interdigitated electrodes is 50 μm with a gap of 50 μm between electrodes. To simulate the intensity and penetration of the electrical field generated by the electrode array, we used COMSOL Multiphysics® software with an AC/DC module. As we expected, the electric current was inversely proportional to the size of the gap between electrodes (**Figure S1B†**) [294]. We concluded that the 50 μm × 50 μm × 0.1 μm electrode dimensions represent a good compromise between electrical field cell tolerance and penetration through the microtissue construct [295]. To stimulate the cells, we set the limit of 1 Hz/5 V to avoid electrode overburn [296].

To design the PDMS microfluidic chip, we used computer-aided design (CAD) software followed by fabrication with a soft lithography technique. After fabrication, we covalently bonded the PDMS chip on top of the ITO-IDA electrodes through an oxygen plasma process (**Figure 4.9A**). The PDMS chip contains two round wells of 10 mm diameter connected with microchannels of 1 mm height and 0.2 mm width

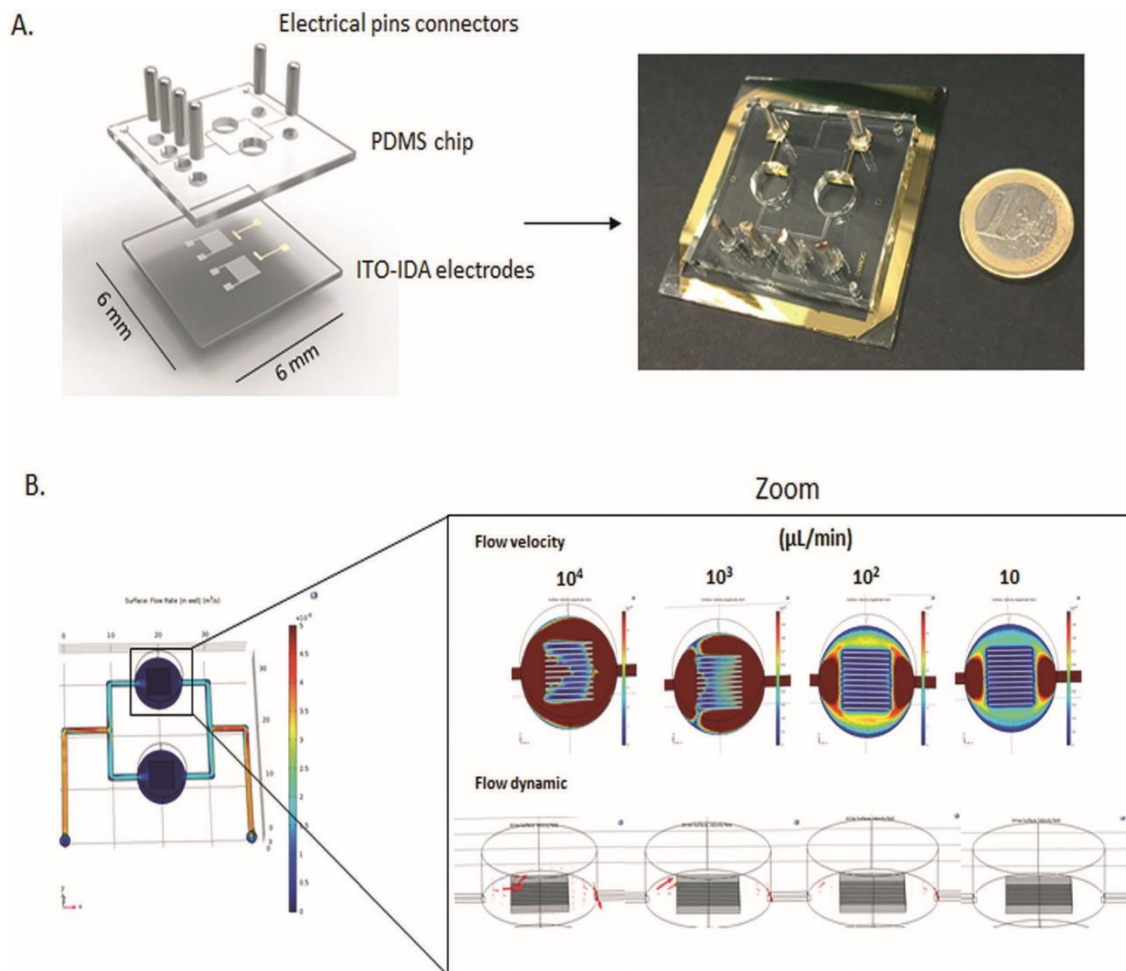


Figure 4.9. Design and fabrication of the microdevice. (A) Schematic image shows the assembly elements and microdevice. (B) COMSOL Multiphysics® simulation of flow velocity and dynamics through a microfluidic network. Various simulations were performed with velocities ranging from 104 to 1 $\mu\text{L min}^{-1}$. Black lines inside the chamber represent the 3D muscle microtissue.

each. The inlet and the outlet were fixed at 2 mm diameter; the electrical pin connectors are fixed at 4 mm (**Figure S1C†**).

To explore the characteristics of the device, we performed theoretical simulations using COMSOL Multiphysics® software (fluid flow module). We used a stationary physics study of various flow rates (from 104 to 10 $\mu\text{L min}^{-1}$) to study the flow behavior within the microchannels. As expected, the flow velocity mirrored the flow rate since the microchannel cross section ($\varnothing = 0.2 \text{ mm}^2$) was fixed (flow rate = cross section \times velocity). The negative pressure gradient from the outlet to the inlet was proportional to the flow rate (**Figure S1D and E†**). To evaluate the flow velocity and dynamics within the microchambers, we included rectangular prisms (grooves) simulating the 3D muscular microtissue. At higher pressure, the fluid escaped towards the wall of the circular chamber, where less resistance is encountered

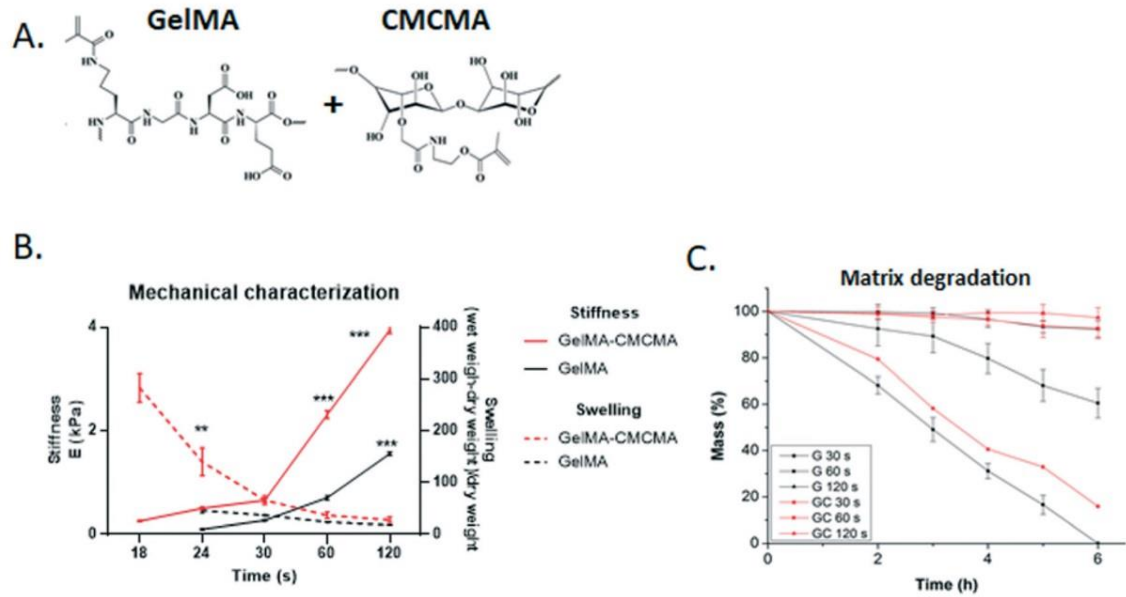


Figure 4.10. (A) Gelatin methacryloyl (GelMA) and carboxymethyl cellulose methacrylate (CMCMA) chemical structures. (B) Mechanical characterization of composite hydrogel GelMA-CMCMA and comparison with only GelMA. (C) Matrix degradation study of GelMA and GelMA-CMCMA hydrogel exposed at different UV times. Data from three different experiments (mean, SD): ** $p < 0.01$; *** $p < 0.001$.

compared with the interspace between the grooves (**Figure 4.9B, zoom**). According to our flow-dynamics simulations in **Figure 4.9B**, we chose $50 \mu\text{L min}^{-1}$ as a working shear flow where random fluid motion and shear stress are minimized. This velocity represents the experimental condition where both nutrient diffusion (laminar flow) and microtissue stability (liquid pressure) are optimized. This condition was made possible by fabricating a 3D SM microtissue inside our microdevice using tissue engineering techniques.

Once we had optimized the working conditions of our microdevice, we fabricated a 3D microarchitecture of the native SM tissue using photopolymerized GelMA hydrogel. Because GelMA-based hydrogels can be degraded by cell metabolism affecting the spatial and physicochemical properties, we added non-biodegradable methacrylate carboxymethyl cellulose (CMCMA) to obtain a hydrogel composite (**Figure 4.10A**) [291]. To characterize the physical and mechanical properties of GelMA and GelMA-CMCMA, we first exposed them to UV light (365 nm) for 18, 24, 30, 60, and 120 seconds. Energy dosage was directly measured with a wireless power meter inside the UVP crosslinker chamber, obtaining energy values of 0.30, 0.37, 0.48, 0.96, and 2.1 J (W s) for 18, 24, 30, 60, and 120 s, respectively. We found that at longer UV light exposure times, the stiffness of both hydrogels

increased (from 0.2 to 1.6 kPa and 0.3 to 3.9 kPa, respectively (**Figure 4.10B**). However, GelMA-CMCMA showed a significantly higher compression modulus than GelMA alone, particularly after 30 seconds of exposure. As expected, we found that the swelling ratio was inversely correlated with stiffness (**Figure 4.10B**). This can be explained by the fact that the longer UV exposure led to an increase in hydrogel crosslinking and a decrease in pore size and water uptake. The magnitude of the change in H₂O uptake is higher in GelMA-CMCMA compared with GelMA alone (from 283 to 58 and from 46 to 18, respectively) (**Figure 4.10B**). Moreover, the presence of CMCMA made the hydrogel more resistant to enzymatic degradation compared with hydrogel without CMCMA (**Figure 4.10C**). From these results, we chose GelMA-CMCMA both for its stability (high stiffness and low enzymatic degradation) and its improved water absorption property (high swelling ratio). The composite hydrogel used to recreate the 3D structure had a stiffness range between 1 and 3 kPa, known to enhance C2C12 3D differentiation [185]. The addition of CMCMA to the hydrogel amplified either the stiffness or the water absorption (high swelling ratio), which are important factors in cell differentiation and nutrient diffusion inside the polymer (**Figure 4.10B**). Moreover, CMCMA increased the enzymatic degradation resistance, which has a significant impact on experimental variability.

To build the encapsulated 3D SM microtissue inside the composite hydrogel, we used a photomold patterning technique. This approach presents numerous advantages such as cost-effectiveness and non-surface dependence and allows fine control over cell alignment, elongation, and maturation without any external stimuli, e.g., mechanical stretch. First, we used a SU-8 mold, fabricated by a photolithography process, to shape the PDMS stamp. Second, the cell-laden hydrogel was micropatterned with the PDMS stamp by UV light exposure (**Figure 4.11A**). We incubated the formed 3D SM microtissue in cell medium for 6 days to allow the cells to adapt to the new settings and stimulate further propagation. At this point, the growth medium (10% fetal bovine serum) was replaced with differentiation medium (2% horse serum).

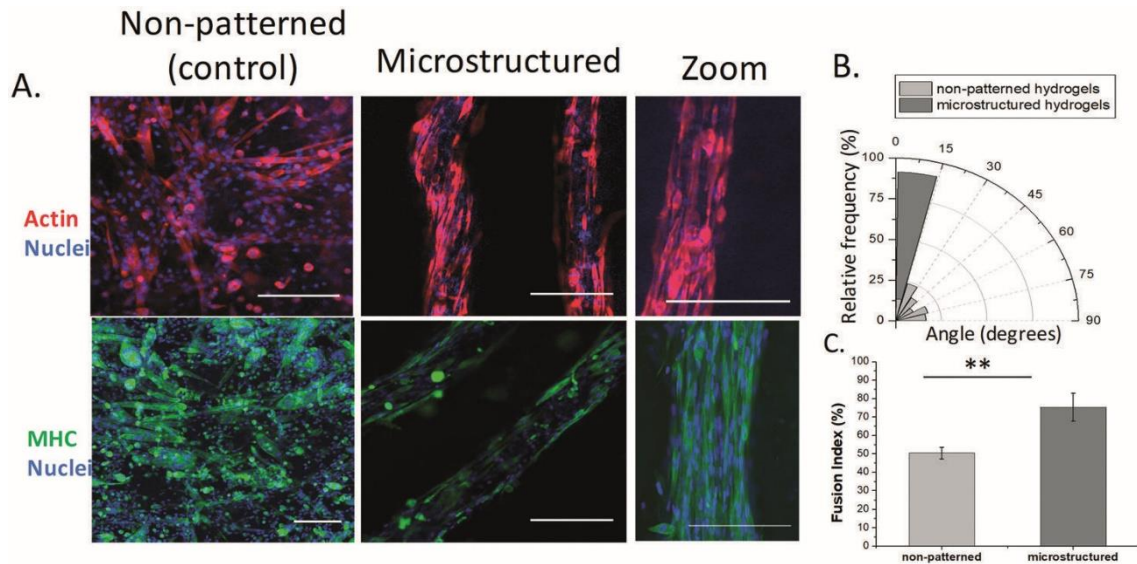


Figure 4.12. (A) Immunostaining for 3D skeletal muscle microtissue for non-patterned (control) and microstructured hydrogels evaluated by phalloidin (red) staining. Cell differentiation was assessed by MHC staining (green). Nuclei were stained by DAPI. Scale bars: 200 μm (B) and (C) cell orientation and fusion index characterization for non-patterned vs. microstructured 3D skeletal muscle tissue. Data from three different experiments (mean, SD): * $p < 0.05$, ** $p < 0.01$; *** $p < 0.001$.

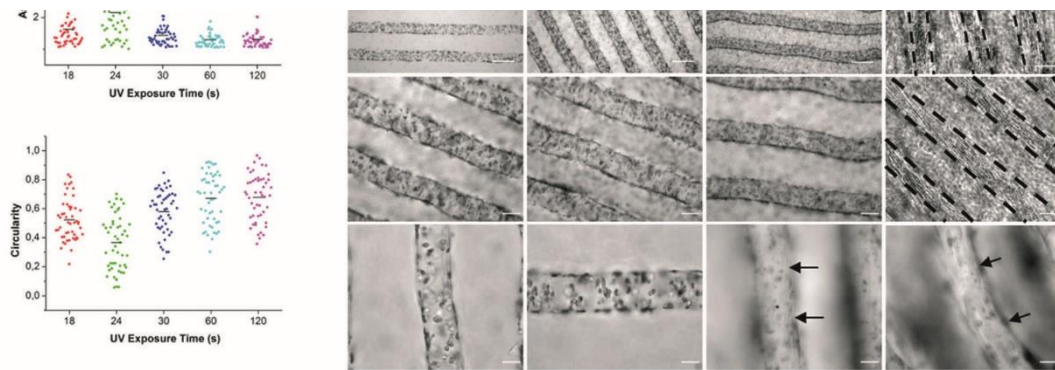


Figure 4.11. Fabrication and characterization of 3D muscle microtissue. (A) Schematic view of the photomold patterning technique used to fabricate the skeletal muscle microtissue. (B) Cell morphology evaluation (circularity and aspect ratio) at different UV exposure times. (C) Bright-field characterization of skeletal muscle cells embedded in 3D composite hydrogel. Dashed lines at 10 days indicate muscular fibers. Black arrows at days 6 and 10 indicate the myotube formation. Scale bars: 200, 100 and 50 μm , top, middle and bottom panel, respectively.

We compared the cell viability of encapsulated cells with 24 s and 60 s of UV exposure. As expected, we observed viable cells throughout the microstructure with 24 seconds of UV exposure at 1, 6 and 10 days of culture compared with 60 seconds (96 \pm 3, 87 \pm 6, 92 \pm 4% and 80 \pm 9, 83 \pm 7, 86 \pm 7%, respectively) (**Figure S2B†**). Moreover, the UV light exposure time of 24 s presented the best cell morphology score, defined by the high aspect ratio (2.149 \pm 0.970) and low circularity (0.366 \pm 0.188) (**Figure 4.11B**). Therefore, we fixed 24 s as the optimal exposure time for the subsequent experiments. Using bright-field microscopy, we observed the homogeneous distribution of the cells at day 1 (24 h post-fabrication) (**Figure 4.11C**).

Progressive cell alignment and elongation towards myotube formation are visible at day 10 (black dashed lines and arrows, **Figure 4.11C**).

To assess the cell differentiation and maturation, we stained cells with F-actin and myosin heavy chain (MHC), respectively. The F-actin stain showed cell elongation and alignment at day 10 throughout the entire thickness of the 3D muscle microtissue compared with random myotube distribution in the non-patterned control group (**Figure 4.12A**). We found that the 3D microgrooves restrict the degree of cell alignment between 0° and 15° , whereas the non-patterned cells are randomly distributed, showing cell alignment ranging from 0 to 90° (**Figure 4.12B**). Furthermore, the 3D muscle microtissue enhanced myotube maturation and cell fusion compared with the 3D non-patterned cells assessed by MHC staining and the fusion index ($75 \pm 7\%$ (patterned) vs. $50 \pm 3\%$ (non-patterned), $p < 0.001$, **Figure 4.12C**). We note that the exposure of the microstructure to UV light for 24 seconds enables precise control of cellular organization in 3D and promoted cell myogenic differentiation and maturation. This *in vivo*-like structure enhanced cell organization with a positive impact on cell viability and function for up to 10 days of culture. Longer UV light exposure of 60 s increased the stiffness of GelMA-CMCMA, reducing cell spatial organization, but did not affect the viability (**Figure S2A†**). The control of the hydrogel microgeometry (microgrooves) is the main factor that improves cell maturation and alignment, pushing engineered tissue one step closer towards the creation of functional *in vitro* tissue [297].

On-site multiplexed sensing system

After fabrication and characterization, the muscle-on-a-chip was connected to a high-sensitivity cytokine biosensing system (**Figure 4.13A-B**) to monitor the release of myokines. In this work, the medium flow coming from the 3D SM tissue passes through the on-site multiplexed sensing system (**Figure 4.8B, number 5**). The commercial SPGEs, where we previously immobilized antibodies against IL-6 and TNF- α , bind the cytokines present in the medium. Once the binding is performed, the SPGE electrodes were finally located in the static PMMA cell, and the secondary antibody and enzymatic tracer were added. The enzymatic reaction produces changes in the electrode current density on the surface directly related to the amount of cytokines detected by the primary antibody.

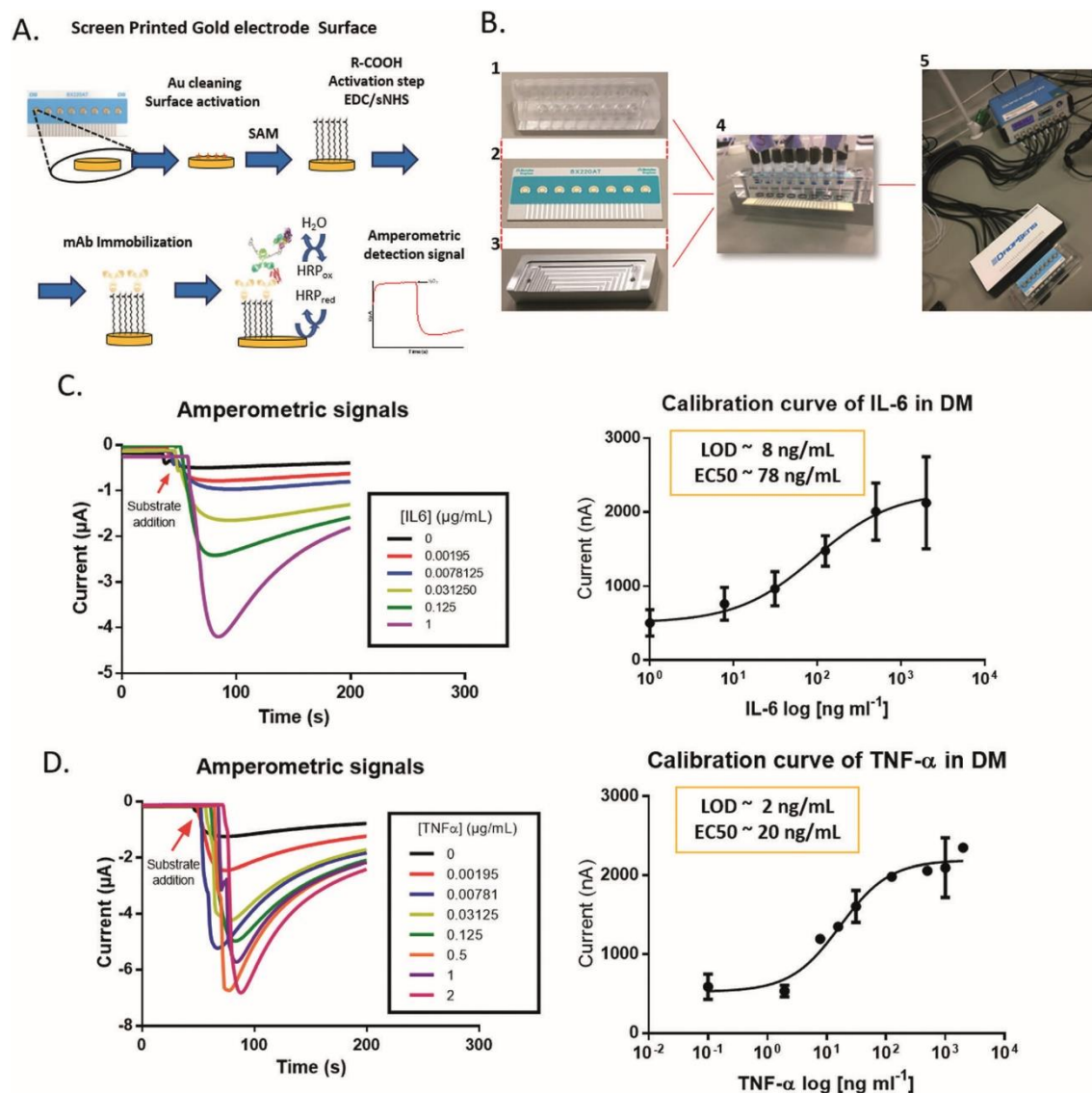


Figure 4.13. On-site multiplexed sensing system description and characterization. (A) Schematic representation of steps for sandwich immunoassay as detection mechanism. (B) Biosensing system physical arrangement: (1) PMMA microfluidic cell cover; (2) SPGE functionalized electrode; (3) stainless steel electrode support case; (4) cell detection chamber coupled with microfluidic connectors; (5) potentiostat. (C) and (D) Raw amperometric signals and calibration curves performed in differentiation medium and under fluidic conditions for IL-6 and TNF- α . Curves show limits of detection of 8 ng mL⁻¹ and 2 ng mL⁻¹ for IL-6 and TNF- α , respectively.

For signal transduction, we chose commercial SPGEs because of their numerous advantages such as favorable electron transfer kinetics, good stability, and convenient covalent bonding with functional groups such as thiol-containing molecules (through the formation of gold (Au)-SH bonds). For detection of secreted myokines in cell medium, the surface of SPGEs was used to anchor IL-6 and TNF- α antibodies. To assess the full coverage of the SPGE surface by the SAM, we used a cyclic voltammogram technique [298]. Briefly, the bare electrode (no SAM layer) showed the typical voltammogram characterized by cathodic and anodic current

peaks for a reversible reaction (dashed line in **Figure S3A†**), whereas with the SPGE surface with a monolayer of SH-PEG-acid, a decrease in the current is observed due to the blocking properties of the monolayer (blue curve in **Figure S3A†**).

The SH-PEG-acid was activated using the EDC/NHS reaction followed by the covalent immobilization of primary IL-6 and TNF- α antibodies. To detect cell-secreted myokines, we used a sandwich immunoassay that involves exposure to biotinylated primary antibodies followed by the streptavidin–horseradish peroxidase (HRP) complex (SAv-polyHRP). The HRP-catalyzed 3,3',5,5'-tetramethylbenzidine (TMB) reaction is recorded via amperometric signals (**Figure 4.13A**). The on-site multiplexed sensing system for each cytokine is constituted by 5 parts: (1) polymethyl methacrylate (PMMA) microfluidic cell cover; (2) SPGE functionalized electrodes; (3) stainless steel electrode support case; (4) cell detection chamber coupled with microfluidic connectors; (5) potentiostat (**Fig. 4.13B**). Before connecting this sensing system to the muscle-on-a-chip through an 8-way flow distributor, we optimized the immunoassay parameters one by one.

First, we performed enzyme-linked immunosorbent assays (ELISAs) to validate the two commercial antibodies used in this study. We observed a limit of detection (LOD) of $0.031 \pm 0.010 \text{ ng mL}^{-1}$ with a slope of 0.726 ± 0.008 and LOD of $0.060 \pm 0.020 \text{ ng mL}^{-1}$ with slope 0.498 ± 0.012 for IL-6 and TNF- α , respectively (**Figure S3C†**). Second, we validated the primary antibody anchorage on the SH-PEG-acid/Au surface using a static PMMA case (**Figure S3B†**). Here, we observed a saturation plateau at 1.5 and 10 $\mu\text{g mL}^{-1}$ for IL-6 and TNF- α , respectively (**Figure S3D†**). Third, the optimal concentrations of secondary biotinylated antibodies found were 5 and 40 $\mu\text{g mL}^{-1}$ for IL-6 and TNF- α , respectively (**Figure S3E†**). **Figure S3F†** shows the optimal attachment kinetics of the SAv-polyHRP to the secondary antibody at 1 $\mu\text{g mL}^{-1}$ for both systems. We set at 160 s the time of HRP-catalyzed TMB oxidation. Finally, these optimized values were used in the later determination of calibration curves, which represent the working conditions to obtain the lowest LOD. Calibration curves under fluidic conditions showed a LOD of $\sim 8 \text{ ng mL}^{-1}$ and $\sim 2 \text{ ng mL}^{-1}$ with effective concentration 50 (EC50) of $\sim 78 \text{ ng mL}^{-1}$ and $\sim 20 \text{ ng mL}^{-1}$ for IL-6 and TNF- α , respectively, with no matrix effect and a high signal/noise ratio (**Figure 4.13C-D**). Moreover, four-parameter logistic regression of the data showed slopes and R2 of 0.92 ± 0.39 (mean \pm SD) and 0.8386 for IL-6 and 1.04 ± 0.31 and 0.9497 for TNF- α . Previous experiments demonstrated no cross-reactivity between

IL-6 and TNF- α (data not shown). Both assays showed a satisfactory accuracy (slope close to 1, **Figure S3G†**).

To note, a few examples can be found in the literature that incorporate a microfluidic platform with a biosensing system to study the metabolism of various tissues [287,288]. For instance, the use of non-label transduction in the case of the impedance allows simple acquisition, but in this case, without an enzymatic amplification, the technique is less robust and very sensitive to changes in medium composition, especially with high ionic buffers. On the other hand, magnetic particles offer an easy system to regenerate the sensors, but the number of possible acquisitions is reduced, and only daily measurements can be performed, which is not informative enough for metabolic studies. The transduction system used in this study was not affected by any medium under investigation and was successfully employed as an *in vitro* model of exercise where electrical stimulation with several measures per hour was needed.

In situ monitoring of secreted myokines upon electrical and biological stimulation

For the final part of this study, the microdevice, the 3D muscle microtissue, and the on-site multiplexed sensing system were assembled through a microfluidic network to measure the release of factors upon electrical and biological stimulation. SM tissue has been identified as an endocrine organ that produces and releases cytokines, which have been named myokines [85]. These compounds such as IL-6 and TNF- α play important roles in biological processes such as energy metabolism, angiogenesis, myogenesis, and muscle repair [299–302].

The system is assembled through a microfluidic network, as can be seen in **Figure 4.8A-B**. The flow passes through the chip where the 3D SM tissue is electrically or biologically stimulated. The outlet flow goes directly to an 8-way microfluidic distributor to reach the SPGE sensing system. A peristaltic pump generates negative pressures that pull the medium to the SPGEs. After binding, the SPGEs are removed and processed separately.

The focal points of this work were the investigation of the source and secretion regime of IL-6 and TNF- α either in muscle stress or during the inflammatory process. Firstly, to find the most responsive biological stimulus for IL-6 and TNF- α secretion, 2D monolayers of differentiated myotubes were incubated in cell culture plates with

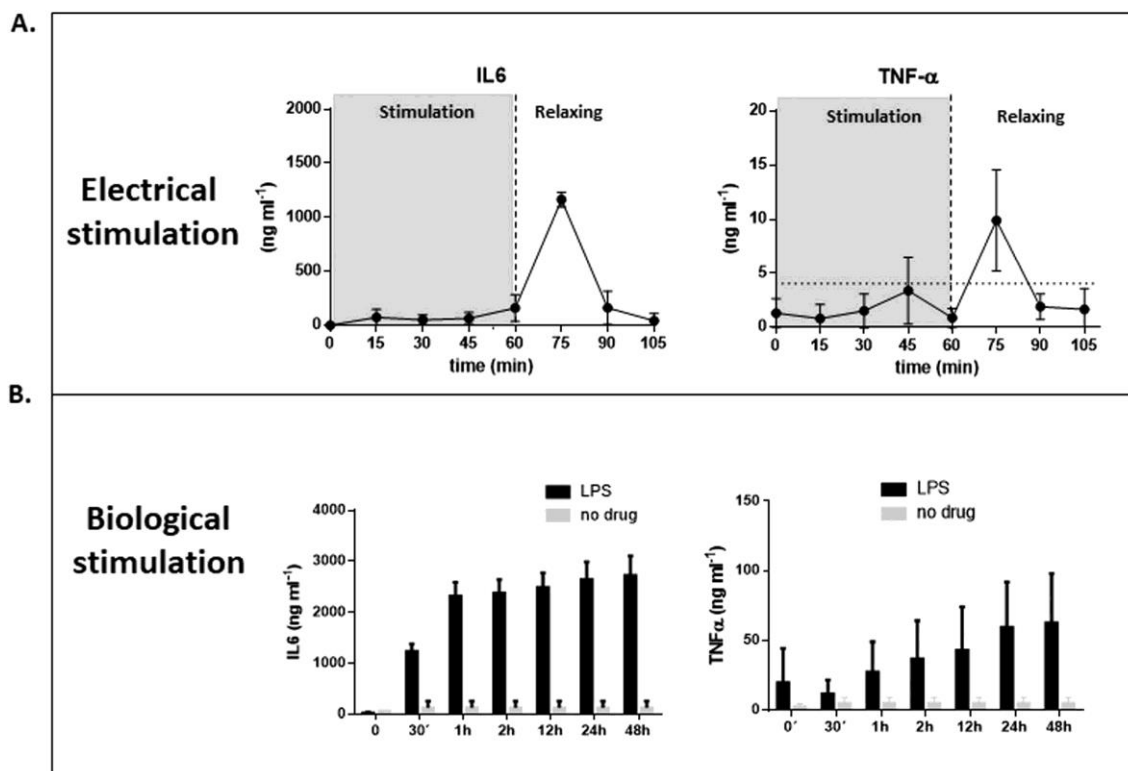


Figure 4.14. IL-6 and TNF- α detection by *in situ* monitoring upon either (A) electrical stimulation (cycle 5 V/1 Hz for 105 min, with a 15 min interval) or (B) LPS stimulation ($10 \mu\text{g mL}^{-1}$) for 48 hours of 3D cultured skeletal muscle cell.

caffeine, dexamethasone, and LPS [303–305]. After determining the cytokine secretion levels by ELISA, LPS, caffeine, and dexamethasone showed the highest release of IL-6 in the medium, whereas similar values among the conditions were obtained with TNF- α release (**Figure S4A†**). TNF- α values did not show significant changes under all the treatments (**Figure S4B†**). According to these results, LPS was used as a biological agent to induce cytokine release in our integrated sensing system.

We performed continual electrical stimulation using a wave generator connected with the muscle-on-a-chip through electrical pins operating at 5 V (peak-peak) at a frequency of 1 Hz with a width of 2 ms for 60 min. We measured the release of myokines every 15 min (switching the 8-way flow distributor) during 1 hour of stimulation phase followed by 1 hour of relaxation phase (i.e., without stimulation). The control group did not receive any electrical stimulation. **Figure 4.14** shows the monitoring of IL-6 and TNF- α concentrations at each period for both stimulation regimes. With this fast acquisition system, we detected up to $1 \mu\text{g mL}^{-1}$ for IL-6 and 10 ng mL^{-1} for TNF- α in DM during the relaxation time after the electrical stimulus was ended (mimicking exercise training) (**Figure 4.14A**). **Figure 4.14B**

demonstrates the release of myokines after supplementation of the medium with $10 \mu\text{g mL}^{-1}$ LPS for 48 h. In the case of IL-6, the maximum detectable peak was reached within 1 hour of stimulation, and then it remained almost constant. IL-6 concentrations over $2.5 \mu\text{g mL}^{-1}$ were detected ($\sim 3 \text{ pg mL}^{-1}$ per cell, calculated using an estimation of 840 000 encapsulated cells per microdevice, **Figure S4C†**) after 1 hour of LPS addition. Conversely, we observed a slow but constant increase of TNF- α throughout all the experiments, reaching over 50 ng mL^{-1} ($\sim 0.07 \text{ pg mL}^{-1}$ per cell, calculated using an estimation of 840 000 encapsulated cells per microdevice, **Figure S4D†**) in 48 hours (**Figure 4.14B**).

Here, we have demonstrated that the secretion of these cytokines in engineered SM is regulated by exercise stress. The study of SM metabolism lies in the timing of the release of those factors, which took place 15 min after the end of electrical stimulation. Even more interesting is the quicker and higher release of these factors from cells as a consequence of LPS stimulation compared with electrical stimulus only (~ 2 times for IL-6 and TNF- α at 1 hour of stimulation) (**Figure 4.14B**). These facts might reshape the role of SM cells in response to bacterial toxins. As such, the development of this novel technology applied to this particular system represents a further and important step for the development of biomimetic muscle platforms to monitor skeletal muscle cytokine functions for quantitative exploration of inflammatory and regenerative processes strongly interconnected with myopathy disease. Nevertheless, promising applications in other organ systems (individually or combination or various) are open to better understanding the biological mechanisms needed for a continual *in situ* monitoring of secreted factors.

In addition, IL-6 and TNF- α are pleiotropic cytokines with multiple effects on immune and non-immune cells. Among those effects, these myokines can play an important role in regulating protein and glucose metabolism during tissue injury. In the case of SM cells, these soluble factors are a fast way of communication not only between the cells of the same organ but also between the cells of different organs. This platform can help us to understand the magnitude and the timing of response upon different chemical and physical stimuli in order to identify a window for therapy.

4.2.4. Conclusions

We have developed an innovative, cost-effective platform capable of simultaneous, *in situ* cell stimulation and analyte detection over time. Our custom-

made microdevice was fabricated and used to host a mature and highly aligned SM tissue obtained using GelMA-CMCMA hydrogels. This 3D *in vivo*-like tissue, known to release cytokines under external stimulations (electrical stimulation using ITO-IDA electrodes or biological stimulation supplementing cell medium with LPS), was combined with a highly controlled flow platform and integrated with a high-sensitive *in situ* sensing system. We functionalized our sensing system with the purpose of achieving multiplexed continual *in situ* measurements of secreted myokines. This unique approach allowed us to detect the release of two important cytokines such as IL-6 and TNF- α , from 3D muscle tissue. We conclude that skeletal muscle cells can express and release these factors in response to electrical stimuli and LPS administration. We are currently working on optimizing this platform for in-depth investigation of the myogenic process and inflammatory response. This revolutionary technology can be exported to any laboratory environment and can have a huge impact on the drug screening process.

4.3. Bioengineered *in vitro* 3D model of myotonic dystrophy type 1 human skeletal muscle

This work describes the first *in vitro* 3D model of myotonic dystrophy type 1 (DM1) human skeletal muscle¹². DM1 is a rare neuromuscular disease that currently has no cure. The disease model was developed with transdifferentiated myoblasts derived from a DM1 patient's fibroblasts. The skeletal muscle microtissue fabrication protocol from **Chapter 4.2** was optimized to encapsulate these human cells in GelMA-CMCMA hydrogels. Briefly, the width of micropatterned filaments was reduced to 100 μm to enhance cell alignment and fusion. In addition, cell-laden hydrogels were fabricated on top of PEGDA-coated cover glass to reduce the unwanted 2D cell attachment to the substrate.

The biofabrication protocol was highly biocompatible; therefore, cell viability remained high after encapsulation in soft hydrogels. In addition, the DM1 cells presented molecular alterations detected in patient biopsies. Cells were cultured for up to three weeks, resulting in aligned multinucleated myotubes from healthy (control) and DM1 cells. We showed that micropatterning improved DM1 myotube formation compared to standard 2D cell cultures, in which DM1 myoblast fusion is not efficient. Notably, the analysis of 3D reconstructions resulted in detecting a new structural phenotype, the reduced thickness of DM1 myotubes compared to healthy control myotubes. Therefore, we evaluated the therapeutic effect of antagomiR-23b on bioengineered DM1 skeletal muscles. We demonstrated that antagomiR treatment for miR-23b could rescue both molecular DM1 hallmarks and structural phenotype, restoring myotube diameter to healthy control sizes with these proof-of-concept experiments. Overall, we showed that this new 3D model represents an improvement over conventional cell culture. Thus, the bioengineered human DM1 skeletal microtissues can be used to test drug efficacy at preclinical levels.

¹² This work has been published as:

Fernández-Garibay X, Ortega M A, Cerro-Herreros E, Comelles J, Martínez E, Artero R, Fernández-Costa J M and Ramón-Azcón J 2021 Bioengineered *in vitro* 3D model of myotonic dystrophy type 1 human skeletal muscle. *Biofabrication* **13** 035035.

4.3.1. Introduction

The skeletal muscle tissue is one of the largest organs of the human body, and it is crucial for locomotion, thermogenesis, and metabolism maintenance [76]. This tissue can be affected by several neuromuscular or metabolic disorders, such as myasthenia gravis [102], McArdle disease [103], type 2 diabetes [80,306], and muscular dystrophies [104]. Muscular dystrophies are genetically inherited degenerative disorders for most of which there is no cure to date. These disorders share muscle weakness and wasting as common symptoms; however, muscular dystrophies are very heterogeneous, differing in age of onset, rate of progression, inheritance pattern, and type of muscles that are affected [104–106]. The intrinsic heterogeneity of these diseases makes the development of new therapies especially challenging since it is expected that each patient would have a different response to treatments.

Drug development for new muscular dystrophy therapies usually involves the use of *in vitro* cell culture assays and *in vivo* animal models in phases before clinical trials. These strategies have long contributed to drug discovery by analyzing specific features of biological processes and identifying the molecular causes of certain diseases [8]. Still, both have significant shortcomings that make it challenging to obtain physiologically relevant results for humans. For instance, conventional *in vitro* models involve 2D cell monolayers cultured on flat and rigid substrates. These models do not emulate the complexity of real tissues, which have a three-dimensional (3D) structural organization of cells surrounded by each other and an extracellular matrix [14]. On the other hand, functional 3D tissues representing tissue physiology can be found in animal models. The use of animal models in pharmacological research raises several ethical concerns. Moreover, *in vivo* models often fail to predict the clinical efficacy of drugs. This is due to species-specific differences that limit the extrapolation of animal data to human conditions [16]. It has been estimated that following this drug development pathway, only 11.8% of drugs entering clinical trials become approved, generating a cost of billions of dollars for newly authorized drugs [17,18]. To accelerate preclinical research, *in vitro* studies could be complemented by human 3D culture systems. These *in vitro* systems consist of patient-derived bioengineered skeletal muscle tissues that offer a better representation of the environment of living tissues with a particular 3D architecture [307].

Skeletal muscle architecture is characterized by bundles of aligned muscle fibers (myofibers). These fibers are formed by the fusion of muscle precursor cells (myoblasts) into multinucleated myotubes, which later become mature myofibers [68]. Because of this complex architecture, engineering skeletal muscle tissues requires a specific organization of muscle precursor cells. These are usually embedded in a suitable biomaterial scaffold, promoting differentiation of myoblasts to form aligned myotubes [179]. Moreover, the biomaterial should provide cells with an appropriate 3D growth environment, optimal oxygen levels, effective nutrient transport, and mechanical integrity over an extended culture period [14]. Hydrogels of natural origin, such as collagen, gelatin, or fibrin, have been widely used as biomaterial scaffolds for engineered skeletal muscle [180]. This is due to their high water content and the presence of cell adhesion and degradation motifs, which allow cell growth and matrix remodeling. Among these hydrogels, gelatin methacryloyl (GelMA) and other methacrylated biomaterials have been used to encapsulate cells in defined 3D structures due to their photocrosslinkable properties [308]. Also, these hydrogels can further be combined with non-degradable biomaterials, such as alginate or carboxymethyl cellulose. The addition of these polysaccharides to GelMA composite hydrogels enhances their mechanical properties and supports long-term culture of myotubes [249,291,309].

In this work, we focused on developing the first bioengineered 3D model of myotonic dystrophy type 1 (DM1) human skeletal muscle tissue. DM1 is a life-threatening and chronically debilitating disorder, which is the most common hereditary myopathy in adults (for a recent review of DM1 hallmarks, see [115]). The genetic cause of DM1 is a dynamic mutation that expands the cytosine-thymine-guanine (CTG) triplet repeat in the 3' non-translated region of the *Dystrophia Myotonica Protein Kinase (DMPK)* gene [119]. Cytosine-uracil-guanine (CUG) repeat RNAs accumulate in nuclear foci. This mutant *DMPK* RNA causes toxic gene misregulation events at the level of gene expression [121,122], translation [123], gene silencing [124–126], alternative splicing [128–130], and polyadenylation of subsets of transcripts [131]. Muscleblind-like (MBNL) proteins, a family of alternative splicing regulators, are sequestered in these CUG foci, and concomitantly their molecular function is impaired [132]. This results in abnormal alternative splicing events directly related to several disease characteristic symptoms, such as muscle weakness and hyper contraction.

Although significant advances have been made in studying the molecular causes of DM1, there is still no effective treatment for patients. Animal models, such as mouse [134], fly [135–137], and zebrafish [138], have been used to evaluate different therapeutic candidates [110,113,139–141]. Among these, therapeutic gene modulation is a promising strategy that has the objective of regulating the endogenous expression of a gene to mitigate a certain disease [143]. Following this approximation, it has been demonstrated that microRNAs (miRs) that inhibit MBNL translation can be silenced by antisense oligonucleotides (antagomiRs). Concretely, specific blocking of miR-218 and miR-23b has resulted in increased MBNL protein levels and rescue of mis-splicing events in DM1 human myoblasts [143] and HSA^{LR} DM1 model mice, where low toxicity, high efficacy, and long-lasting biological effects were observed [143,144]. While these are encouraging results, the effectiveness of treatments for DM1 still needs to be investigated in clinical phases.

Here, we describe a method to fabricate a bioengineered 3D DM1 skeletal muscle tissue model using transdifferentiated myoblasts from patient-derived fibroblasts. These cells were encapsulated in micropatterned GelMA-carboxymethyl cellulose methacrylate (CMCMA) hydrogels on top of functionalized glass coverslips. Cells were cultured for up to three weeks obtaining aligned myotubes with disease-associated molecular and structural phenotypic features. Remarkably, cell encapsulation in micropatterns improved DM1 myotube formation compared to traditional 2D cultures. Moreover, the analysis of 3D reconstructed myotubes showed that DM1 myotubes have a thinner phenotype than myotubes from healthy control cells. Additionally, as a proof-of-concept, we showed that antagomiR treatment for miR-23b could rescue MBNL expression and myotube diameter in 3D DM1 human myotubes. Overall, we demonstrate that patient-derived bioengineered DM1 skeletal muscle microtissues represent valuable *in vitro* tools for preclinical research. Finally, the developed fabrication method for DM1 could easily be translated for drug development and other studies on muscular dystrophies.

4.3.2. Experimental procedure

Cell culture

Immortalized human fibroblasts from unaffected control and DM1 patient (carrying 1300 CTG repeats quantified in the blood cells) [162] were kindly provided by Dr. Denis Furling and Dr. Vincent Mouly (Institute of Myology, Paris). Fibroblast

cells were grown in Dulbecco's modified eagle medium (DMEM, 4.5 g L⁻¹ glucose, Gibco) supplemented with 1% penicillin-streptomycin (P/S, 10 000 U mL⁻¹, Thermofisher) and 15% fetal bovine serum (Gibco). Transdifferentiation into myoblast-like cells was induced by turning on the myogenic program, forcing MyoD expression when culturing cells in muscle differentiation medium (MDM). MDM consisted of DMEM with 4.5 g L⁻¹ glucose, 1% P/S, 2% horse serum, 1% apo-transferrin (10 mg mL⁻¹), 0.1% insulin (10 mg mL⁻¹), and 0.02% doxycycline (10 mg mL⁻¹). In all cases, cells were grown at 37 °C in a humidified atmosphere containing 5% CO₂. For cell differentiation in 2D, fibroblasts were seeded at 12 000 cells cm⁻² in 12-well plates containing glass coverslips coated with 50 µg mL⁻¹ collagen type I and were cultured in growth medium. Once the cells were confluent, the growth medium was replaced by MDM to induce the myogenic program. Fusion index was analyzed in cultures differentiated for seven days.

Microstructured stamps fabrication

Microstructured poly(dimethylsiloxane) (PDMS, Sylgard™ Elastomer base and curing agent) stamps were fabricated by replica molding of silicon wafer molds.

Microfabrication of silicon molds

Silicon wafer molds were fabricated by standard photolithography techniques using SU-8 negative photoresist. Briefly, silicon wafers (4" n-type <111>, MicroChemicals GmbH) were cleaned in a plasma chamber for 20 min at 6.8 W. After that, wafers were heated for 5 min in a hotplate at 95 °C to dehydrate them. Negative resist SU-8 2100 (2100, MicroChem) was spin-coated in two steps to obtain structures of 100 µm in height. To make the patterns, a mask aligner (SÜSS Microtec, MJB4) was set to 240 mJ cm⁻² energy radiation at 365 nm, and a high-quality emulsion flexible film was used as a photomask (JD Photodata, UK). Irradiation time was set to 20 s. Cross-linkage of negative-tone exposed regions of SU-8 was subject to a hotplate cycle of 65 °C and 95 °C for 5 and 20 min, respectively. The labile photoresist was removed by developing the crosslinked patterns immersing the wafer in SU-8 developer (MicroChem) for 10 min. Then, the action of 2-propanol stopped development. After a quick N₂ blow, we heated the molds for 60 min at 120 °C. As a final step, the SU-8 patterned silicon molds had to undergo silanization to obtain hydrophobic surfaces and avoid permanent bonding with the PDMS.

Replica molding of microstructured PDMS stamps

The polymer elastomer base and curing agent were weighted in a 10:1 ratio to obtain microstructured stamps of 6 mm in diameter, with channels of 100 μm and 200 μm of width and height. After mixing thoroughly, we degassed the polymer in a vacuum chamber. PDMS was poured on the patterned silicon substrate and cured at 80 °C for 4 h. Finally, PDMS was detached and cut off using a 5 mm biopsy punch. PDMS stamps were cleaned by sonication in Milli-Q water and 2-propanol for 5 min and dried using N_2 flow before using them for tissue fabrication.

Prepolymer preparation

GelMA (**Figure 4.15E**) and CMCMA (**Figure 4.15G**) were synthesized as previously described [291]. These prepolymer precursors and the photoinitiator lithium phenyl (2,4,6-trimethylbenzoyl) phosphinate (LAP, TCI Europe N.V.) were dissolved in MDM at 65 °C for 2 h. The concentrations of GelMA, CMCMA, and LAP were fixed to obtain final concentrations of 5%, 1%, and 0.1% w/v, respectively.

Cell encapsulation in 3D microstructured hydrogels

Cell-laden 3D microstructured hydrogels were fabricated on top of glass coverslips using a photomold patterning technique, as described in [309].

Glass coverslip functionalization

Glass coverslips were previously treated with 3-(trimethoxysilyl)propyl methacrylate (TMSPMA, Aldrich) (**Figure 4.15A**) and coated with a layer of poly(ethylene glycol) diacrylate (PEGDA, MW 4000 Da, Sigma-Aldrich) (**Figure 4.15C**) by free radical polymerization. First, clean glass coverslips were activated by oxygen plasma at 29.6 W for 30 s. Immediately after plasma treatment, the glass surface was covered with a freshly prepared silanization solution (TMSPMA diluted in ethanol at 1:50 and mixed with 3% acetic acid) for 1 h. Then, coverslips were thoroughly washed with ethanol and dried (**Figure 4.15B**).

For PEGDA coating, we prepared a solution of 20% w/v PEGDA and 2% w/v LAP in Milli-Q water by dissolving in a water bath at 60 °C for 30 min. For each coverslip, a 5 μl drop was placed on a Teflon surface. Then, the silanized side of the coverslip was carefully pressed on top. Finally, samples were exposed to UV for 2 min using a UVP Crosslinker (model CL-1000 I, 365 nm, 40 W, Analytik Jena US), washed several times with Milli-Q water, and thoroughly dried (**Figure 4.15D**).

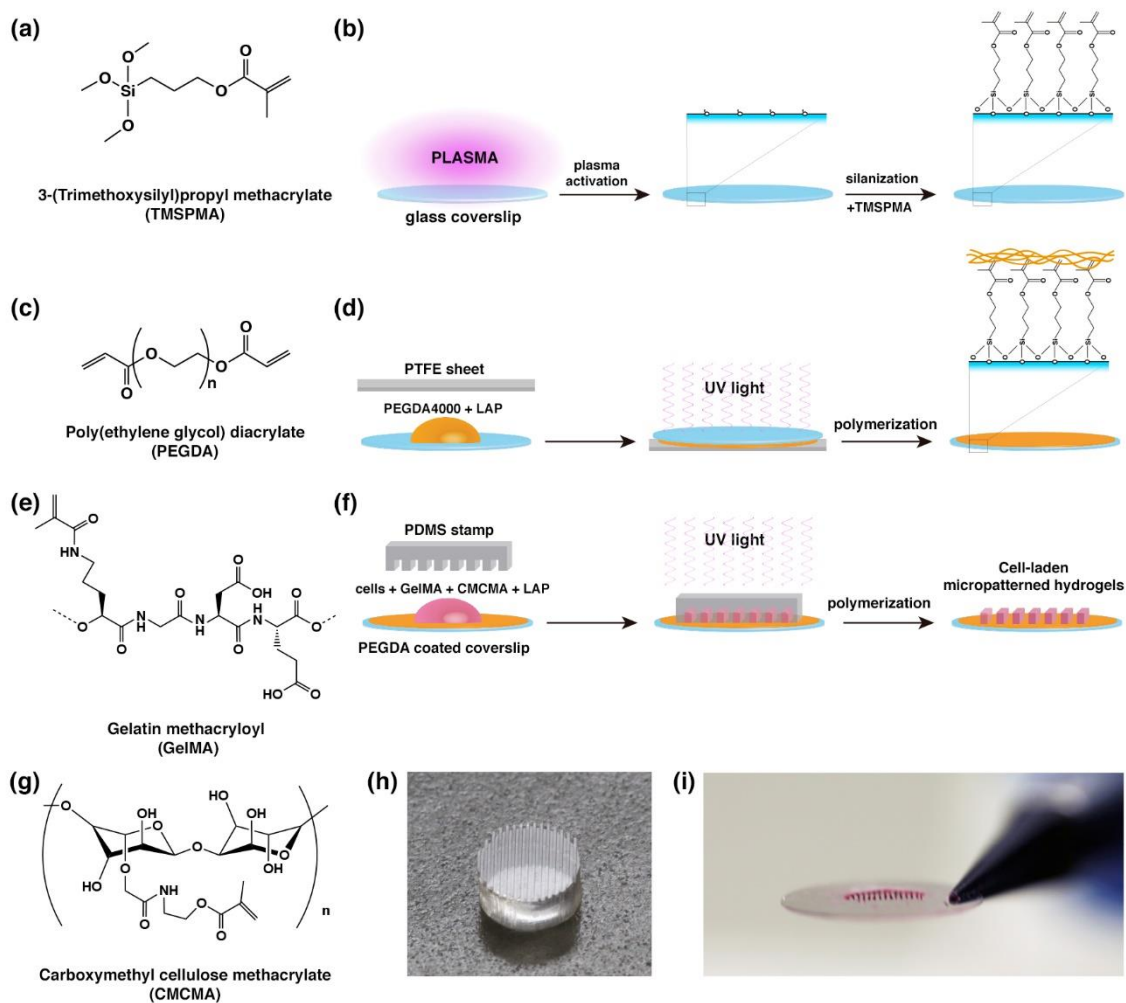


Figure 4.15. Fabrication protocol to obtain 3D skeletal muscle microtissues. (A), (C), (E), (G) Chemical structures of (A) 3-(trimethoxysilyl)propyl methacrylate (TMSPMA), (C) poly(ethylene glycol) diacrylate (PEGDA), (E) gelatin methacryloyl (GelMA), and (G) carboxymethyl cellulose methacrylate (CMCMA). (B) Schematic of silanization of glass coverslips by plasma activation and treatment with TMSPMA. (D) Silanized coverslips were coated with a PEGDA layer. PEGDA was polymerized by UV light exposure in the presence of a photoinitiator, lithium phenyl (2,4,6-trimethylbenzoyl) phosphinate (LAP). (F), (H), (I) Photomold patterning of cell-laden GelMA-CMCMA hydrogels. A microstructured poly(dimethylsiloxane) (PDMS) stamp (H) was used to fabricate cell-laden micropatterned hydrogels on top of PEGDA-coated glass coverslips (I) by polymerization with UV light.

Cell encapsulation

To encapsulate cells in micropatterned hydrogels, we mixed the prepolymer solution with a cell suspension of either control or DM1 cells in MDM to obtain a final concentration of 2.5×10^7 cells mL^{-1} . Then, an 8 μl drop of the cell-laden prepolymer was placed on a PEGDA-coated glass coverslip, and a PDMS stamp (**Figure 4.15H**) was pressed lightly on top, filling the microchannels with the solution. The hydrogels were crosslinked by UV exposure of 30 s using the UVP Crosslinker. MDM was added to each sample, and stamps were carefully removed after 20 min of incubation

at 37 °C (**Figures 4.15F, I**). Encapsulated cells were differentiated for up to 21 days, with culture media being replaced every two days.

Hydrogel characterization

Stiffness measurements

The bulk stiffness of GelMA-CMCMA hydrogels was analyzed by uniaxial compression tests using a Zwick Z0.5 TN instrument (Zwick-Roell, Germany) with a 5 N load cell. Hydrogels were fabricated as described in [309]. For each sample, 300 μ l of the prepolymer solution were placed in a 48-well plate and exposed to UV light for 30 s. Cylindrical samples were cut using a 10 mm diameter biopsy punch. Samples were tested at room temperature (RT) up to 30% final strain (deformation), using the following parameters: 0.1 mN preload force and 20% min^{-1} strain rate. Force-deformation graphs were obtained using the TestXpert (Zwick-Roell) software. Values for the compressive modulus were automatically calculated from the slope of the linear region corresponding to 10%–20% deformation (strain) with the TestXpert software.

To obtain Young's modulus of the micropatterned GelMA-CMCMA hydrogels in liquid conditions, samples were photomolded as described before. After 24 h of incubation at 37 °C, the stiffness was measured by atomic force microscopy (AFM) following a previously described protocol [216,217]. Briefly, indentation measurements were conducted using a NanoWizard® 4 Bioscience AFM (JPK Instruments) mounted onto a Nikon Ti inverted microscope. Silicon nitride pyramidal tips (NanoWorld) with nominal spring constants of 0.08 Nm^{-1} were used. Series of ten indentations at a frequency of 0.05 Hz (10 μ m amplitude) were performed in different positions of the GelMA-CMCMA micropatterns. Finally, the Hertz model for a pyramidal tip was fitted to the measured force-distance curves, using the JPK data analysis software.

Scanning electron microscopy (SEM) imaging

Hydrogels for SEM imaging were fabricated following the same protocol as for compression measurements. After 24 h of incubation, the hydrogels were washed with Milli-Q water and fixed for 1 h in a 2.5% glutaraldehyde solution (Sigma-Aldrich). Following several washes, samples were dehydrated by sequential immersion in graded ethanol solutions in Milli-Q water. Washings of 10 min were performed with 50%, 70% ($\times 2$), 90% ($\times 3$), 96% ($\times 3$), and 99.5% ($\times 3$) ethanol. To dry the hydrogels

without causing their collapse, samples were placed in a critical point drying chamber (K850, Quorum Technologies, UK), where ethanol was completely replaced by liquid CO₂ and gradually heated until CO₂ achieved gas phase equilibrium and was slowly drained. After critical point drying, microstructured hydrogels were covered with Au and imaged by ultrahigh-resolution SEM (Nova NanoSEM 230, FEI Company, The Netherlands) operating in a low vacuum mode (0.5 mbar of water vapor pressure).

Cell viability assay

Cell viability was evaluated 24 h after encapsulation using the Live/Dead viability/cytotoxicity kit (Invitrogen). Briefly, samples were washed several times with sterile 1× phosphate buffered saline (PBS) and incubated for 30 min with a staining solution containing Calcein AM, Ethidium homodimer-1, and Hoechst (Invitrogen) in PBS. Cell viability was calculated as the percentage of living cells with respect to the total cell number analyzed in the 3D reconstruction of confocal Z-stacks using Imaris software.

Antisense oligonucleotide treatment

AntagomiR oligonucleotides (Creative Biogene) were administrated 72 h after DM1 microtissue fabrication. MDM was replaced and supplemented with 100 nM of AntagomiRs for miR-sc (control) or miR-23b-3p. The treatment lasted for seven days without replacing the culture media. The antagomiR sequences were: 5'-mG*mG*mUmAmAmUmCmCmCmUmGmGmCmAmAmUmGmU*mG*mA*mU*-3'-chol (antagomiR-23b-3p), and 5'-mC*mA*mGmUmAmCmUmUmUmUmGmUmGmUmA*mC*mA*mA*-3'-chol (sc control). Where m denotes 2'-O-methyl-modified phosphoramidites, * denotes phosphorothioate linkages, and chol denotes cholesterol groups.

Fluorescence in situ hybridization (FISH)

Bioengineered 3D skeletal muscle tissues were fixed in 4% paraformaldehyde for 30 min at RT and washed with 1× PBS for 10 min. Samples were incubated in the prehybridization buffer (2× saline sodium citrate [SSC], 30% deionized formamide) for 30 min at RT and hybridized with a Cy3-(CAG)₇-Cy3-labeled probe, diluted 1:200 in hybridization buffer (40% deionized formamide, 2× SSC, 10% dextran sulfate, 0.2% BSA, 2 mM Ribonucleoside Vanadyl Complex (Sigma-Aldrich), 1 mg mL⁻¹ *Escherichia coli* tRNA, 1% herring sperm DNA) overnight at 37 °C in the dark. After hybridization, samples were washed twice with a prehybridization buffer for 30 min

at 42 °C, washed with 1× PBS, and incubated with DAPI for 15 min. All the incubations were performed in a humidity chamber.

Immunofluorescence staining

Bioengineered muscle tissues were fixed with 10% formalin solution (Sigma-Aldrich) for 30 min at RT, followed by several washes in PBS. Samples were then permeabilized with PBS-T (0.1% Triton-X (Sigma-Aldrich) in PBS), blocked (0.3% Triton-X, 3% donkey serum (Sigma-Aldrich) in PBS) for 2 h at RT, and incubated with primary antibody (**Supplementary Table 1**) at 4 °C overnight. After several PBS-T washes, the samples were incubated for 2 h with the fluorophore-conjugated secondary antibody (**Supplementary Table 1**) at RT. Finally, the samples were counterstained with DAPI (4',6-diamidino-2-phenylindole, Life Technologies) to detect the nuclei.

For MBNL1 detection, after FISH protocol, samples were incubated with the monoclonal anti-MBNL1 primary antibody at 4 °C. The fluorescence signal was amplified using a biotin-conjugated secondary antibody (**Supplementary Table 1**) and the VECTASTAIN® Elite® ABC kit (Vector) for 1 h at RT, followed by PBS-T washes and incubation with either Dylight®488-FITC (1:200, Vector) for 2 h at RT. Finally, the samples were counterstained with DAPI to detect the nuclei.

Imaging

Light microscopy and live-cell imaging of myotubes were performed using a Zeiss Axio Observer.Z1/7 outfitted with the XL S1 cell incubator. Imaging was performed at 37 °C and 5% CO₂. Fluorescence images were taken as Z-stacks with a ZEISS LSM800 confocal laser scanning microscope and analyzed using the Imaris microscope image analysis software (Oxford instruments) and the Fiji image processing package, a distribution of ImageJ [218,224].

Fusion index and myotube size analysis

Z-stacks were analyzed as 3D images using the Imaris software. Fusion index was determined as the percentage of nuclei in myotubes (≥ 2 myonuclei) with respect to the total number of nuclei, in myotubes expressing sarcomeric α -actinin (SAA). The diameter of individual 3D myotubes was obtained by the object-oriented bounding box statistical variable (BoundingBoxOO Length A), which measures the length of the object's shortest principal axis.

RNA extraction, RT-PCR and real-time PCR

Total RNA from human bioengineered muscles was isolated using Tri-reagent (Sigma) according to the manufacturer's instructions. One microgram of RNA was digested with DNase I (Invitrogen) and reverse-transcribed with SuperScript™ II (Invitrogen) using random hexanucleotides. qRT-PCR was carried out on one nanogram of cDNA template with the FIREPol® EvaGreen® qPCR Mix Plus (Solis Biodyne) and specific primers (supplementary table 2). *GAPDH* and *ACTB* were used as endogenous controls. miRNA expression was quantified using specific miRCURY LNA microRNA PCR primers (Qiagen) according to the manufacturer's instructions. Relative gene expression was normalized to miR-103 expression [221]. Expression levels were measured using the QuantStudio 5 Applied Biosystems Real-Time PCR System. Expression relative to the endogenous genes and control group was calculated using the $2^{-\Delta\Delta Ct}$ method. Pairs of samples were compared using two-tailed Student *t*-tests ($\alpha = 0.05$), applying Welch's correction when necessary. For splicing analyses, 20 ng of cDNA were used in a standard PCR reaction with GoTaq polymerase (Promega). Specific primers were used to analyze alternative splicing of *Bridging integrator 1 (BIN1)*, *Nuclear Factor I X (NFIX)*, and *Spectrin Alpha Non-Erythrocytic 1 (SPTAN1)* (**Supplementary Table 2**).

Western blotting

For total protein extraction, samples were homogenized in RIPA buffer (150 mM NaCl, 1.0% IGEPAL, 0.5% sodium deoxycholate, 0.1% SDS, 50 mM Tris-HCl pH 8.0) supplemented with protease and phosphatase inhibitor cocktails (Roche Applied Science). Total proteins were quantified with a BCA protein assay kit (Pierce) using bovine serum albumin as the standard concentration range. For the immunodetection assay, 20 μ g of samples were denatured for 5 min at 100 °C, electrophoresed on 12% SDS-PAGE gels, transferred onto nitrocellulose membranes 0.45 μ m (GE Healthcare), and blocked with 5% non-fat dried milk in PBS-T (1 \times PBS; 0.05% Tween 20, pH 7.4). Membranes were incubated overnight at 4 °C with primary mouse anti-MBNL1 (1:200, clone MB1a (4A8), Developmental Studies Hybridoma Bank) or mouse anti-MBNL2 (1:100, clone MB2a (3B4), Developmental Studies Hybridoma Bank). Anti-GAPDH-binding protein-horseradish peroxidase (HRP) antibody (1 h, 1:3500, clone G-9, Santa Cruz) as a loading control. All primary antibodies were detected using HRP-conjugated anti-mouse-IgG secondary antibody (1 h, 1:5000, Sigma-Aldrich). Immunoreactive bands were

detected using ECLTM Western blotting substrate (Pierce), and images were acquired with an AMERSHAM ImageQuant 800 (GE Healthcare). Quantification was performed using ImageJ software. The statistical differences were estimated by the Student's *t*-test ($p < 0.05$) on normalized data.

Statistical analysis

All group data are expressed as mean \pm SEM. The comparisons between groups were performed using Prism 8 software (GraphPad) by two-tailed Student *t*-test ($\alpha = 0.05$), applying Welch's correction when necessary. Differences between groups were considered significant when $P < 0.05$ (* $P < 0.05$; ** $P < 0.01$; *** $P < 0.001$; **** $P < 0.0001$).

4.3.3. Results and discussion

A fabrication protocol to obtain 3D skeletal muscle microtissues

The skeletal muscle is a highly organized tissue made up of arrays of aligned, multinucleated myofibers. This complex architecture should be mimicked *in vitro* to obtain 3D models that accurately represent the basic features of skeletal muscle tissue. Multinucleated myofibers are formed by fusion and differentiation of muscle precursor cells; therefore, fabrication strategies for tissue engineering should provide effective topographical cues that favor myoblast alignment and fusion. Among these biofabrication techniques to engineer topographical cues, the most used are micropatterning, micromolding, electrospinning, and 3D bioprinting [61]. Previous studies have shown that cells with a tendency to align *in vivo* (e.g., fibroblasts, murine myoblasts, and endothelial cells) can elongate and align *in vitro* if they are geometrically confined within a suitable biomaterial [273]. Accordingly, our fabrication protocol was designed to encapsulate human muscle precursor cells in micropatterned hydrogels, which confine cells in narrow hydrogel filaments and induce the formation of elongated myotubes.

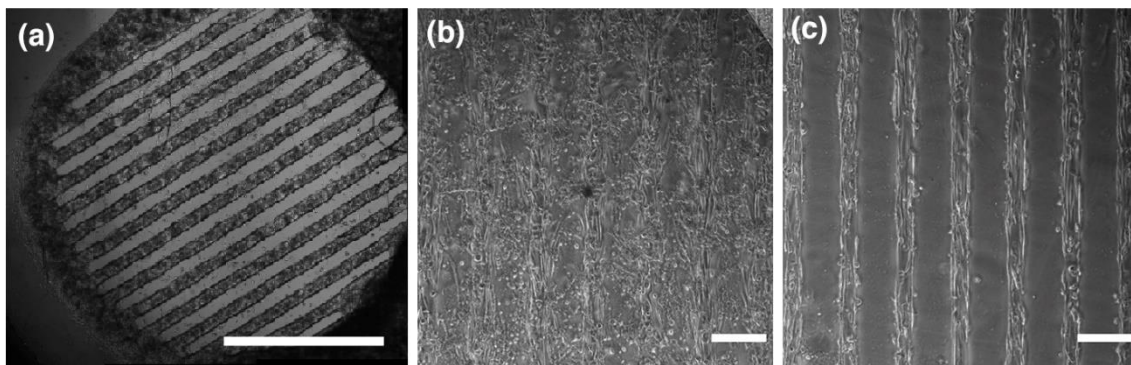


Figure 4.16. Effect of PEGDA coating on micromolded hydrogels. (A) Phase contrast image of cell-laden micropatterned hydrogels (scale bar: 2.5 mm). (B), (C) Representative phase contrast images of cell-laden hydrogels without (B) and with (C) PEGDA coating (scale bars: 200 μm).

As previously described, we used photomold patterning to transfer the features of microstructured PDMS stamps into photocrosslinkable GelMA-CMCMA hydrogels (**Figures 4.15 and 4.16A**). We fabricated stamps with channels of 200 μm (data not shown) or 100 μm of width, height, and spacing. We observed better cell alignment when cells were confined in smaller structures. This was in agreement with other studies where cell alignment and myotube formation were enhanced in the thinnest structures [191]. Besides alignment being favored in narrower patterns, there are other limitations to the dimensions of hydrogels for cell encapsulation. As some studies point out, there is a limited diffusion of oxygen and nutrients in engineered tissues at around 200 μm of depth due to the lack of vascularization [291,310,311]. Therefore, we fabricated smaller structures to overcome this limitation. Consequently, we decided to use the microstructured stamps with smaller features to fabricate hydrogel filaments of 100 μm in width and 5 mm in length on top of glass coverslips.

Using glass as our substrate, we noticed that some cells adhered to the flat surface between hydrogel filaments outside of the 3D structure (**Figure 4.16B**). This was an unwanted effect since cells in 2D would grow and differentiate at a different speed, creating two separate cell populations. To ensure that cells remained confined within the 3D GelMA-CMCMA hydrogel, the glass surface was previously silanized and coated with a thin layer of PEGDA hydrogel. PEGDA is hydrophilic and inert to protein adsorption [312]; hence, this surface modification highly reduced undesired 2D cell attachment outside the GelMA-CMCMA microfilaments fabricated on top of the PEGDA layer (**Figure 4.16C**). Furthermore, GelMA-CMCMA was covalently attached to PEGDA, which gave more stability to the micropatterned structures [47].

Cell encapsulation in photocrosslinkable hydrogels is achieved by free radical polymerization in the presence of a photoinitiator and UV light. Therefore, after this procedure, cell survival strongly depends on critical factors, including UV wavelength, energy dose, and photoinitiator concentration. When cells are exposed to a low dose of long-wave UV light, the procedure is considered biocompatible [313]. As has been reported, LAP photoinitiator has a high extinction coefficient at 365 nm, which makes it more efficient than other commonly used compounds, such as Irgacure 2659 [49,291]. This efficiency allowed crosslinking composite hydrogels with a very low photoinitiator concentration and short exposure times (low energy dose). To confirm this, we measured the energy dose received by cells during 30 s of UV exposure using a wireless power-meter inside the UVP crosslinking chamber, obtaining 0.48 J cm^{-2} (16 mW cm^{-2} during 30 s). This energy dose is very low, considering cell-laden GelMA hydrogels have been crosslinked with energy doses ranging from 0.3 J cm^{-2} to 36 J cm^{-2} [314,315]. Moreover, cell cytotoxicity assays (**Figure 4.17A-H**) showed that more than 88% of encapsulated cells remained viable 24 h after UV exposure (**Figure 4.17I**).

Although both 3D bioprinting and photomold patterning are valuable biofabrication strategies for generating cell-laden hydrogel filaments, photomold patterning offered several advantages compared to our previous 3D bioprinted model [291], such as reproducibility, amount of material required, or the final cost of the procedure.

Human skeletal muscle tissue models have been developed from primary and immortalized human myoblasts and human induced pluripotent stem cells [155]. Bioengineered 3D *in vitro* models require large numbers of cells, especially for high-throughput drug screening platforms. This represents a challenge for developing disease models, where it is necessary to incorporate patient cells coming from muscle biopsies. A major problem of using primary myoblasts from adult DM1 patients is their limited proliferative capacity due to premature replicative senescence [316]. Besides, muscle biopsies are invasive and not always available. Arandel *et al.*

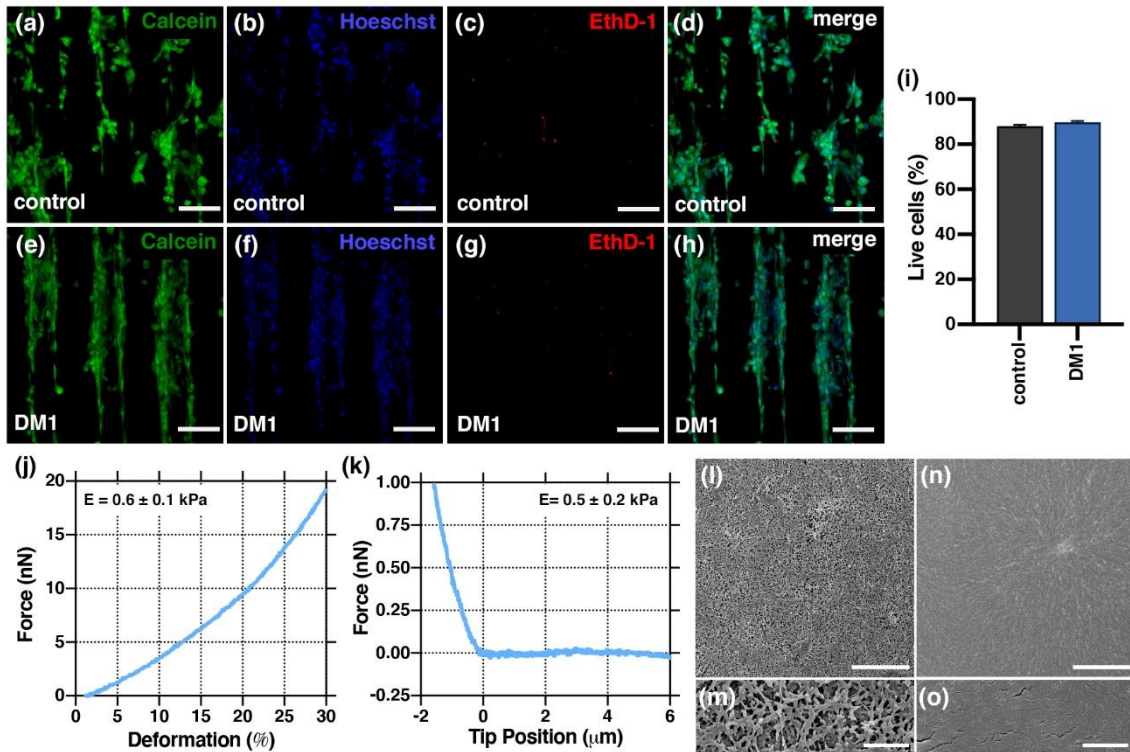


Figure 4.17. (A–H) Representative images of live/dead staining from healthy control (A–D) and DM1 cells (E–H) 24 h after cell encapsulation. Live cells were stained with Calcein AM (green), nuclei were stained by Hoeschst (blue), and dead cells (red) were stained with Ethidium homodimer-1 (EthD-1) (Scale bars: 100 μm). (I) Graph showing the cell viability in micromolded hydrogels represented as the live cells over the total cell number (mean ± SEM). (J) Example of a typical force–deformation curve obtained by uniaxial compression tests on bulk GelMA-CMCMA hydrogels. Young's modulus (E) = 0.6 ± 0.1 kPa (k) typical force–displacement curves of the AFM tip indenting the surface of the GelMA-CMCMA microstructured hydrogels. $E = 0.5 \pm 0.2$ kPa (Mean values ± SEM). (L–O) Scanning electron microscopy (SEM) images of GelMA-CMCMA (L), (M) and PEGDA (N), (O) hydrogels. Scale bars: (L), (N) 5 μm, (M), (O) 1 μm.

overcame these limitations by developing transdifferentiated myotubes cell lines [162]. These cell lines consisted of immortalized skin fibroblasts that were converted into myoblasts by forcing the overexpression of the myogenic regulator factor MYOD1. Here, we fabricated 3D skeletal muscle microtissues from immortalized fibroblasts obtained from a healthy control individual and a DM1 patient. Cell-laden hydrogels were cultured in MDM containing doxycycline and a low serum concentration from the moment of encapsulation. With this culture media, doxycycline activated the myogenic program and transdifferentiation into myoblast-like cells. Additionally, the reduced serum concentration slowed down cell proliferation, inducing a shift to a differentiation state. Furthermore, myoblasts need to be close to recognize each other and fuse into myotubes. Since cell proliferation was limited by the MDM, working with a high cell density (2.5×10^7 cells mL^{-1}) was key in obtaining multinucleated myotubes. In summary, we have developed a reproducible method to generate 3D skeletal muscle microtissues from human cells.

In this protocol, we applied a photomold patterning technique to encapsulate cells in GelMA-CMCMA hydrogel scaffolds.

Physical properties of GelMA-CMCMA hydrogels

Skeletal muscle tissue engineering requires culture time for myoblast fusion and myotube maturation. Additionally, engineered tissues should remain viable for several weeks to be valuable for drug screening applications. For these reasons, the biomaterials used as scaffold need to resist enzymatic degradation by encapsulated cells and other stress cues. We previously showed that degradation of GelMA hydrogels could be slowed down by fabricating composites that include a small percentage of a non-degradable polymer [291]. GelMA contains cell adhesion and degradation sites that allow cells to attach and remodel the matrix, a necessary feature for cell spreading and fusion. CMCMA is a biocompatible cellulose derivate that is non-degradable by mammalian cells [257]. Therefore, its incorporation into the hydrogel formulation provided more structural stability over time. In fact, in our previous works, we have demonstrated that this composite hydrogel allowed long-lasting culture and differentiation of murine skeletal muscle cells [309,317].

The bulk stiffness of GelMA-CMCMA hydrogels was measured using uniaxial compression tests, obtaining a Young's modulus of 0.6 ± 0.1 kPa (**Figure 4.17J**). To calculate the stiffness of our micropatterned hydrogels in liquid conditions, we performed AFM microindentation measurements (**Figure 4.17K**). The obtained values were comparable ($E = 0.5 \pm 0.2$ kPa), corresponding to soft hydrogels in the range of 0.5–0.7 kPa. Some studies suggest that the optimal stiffness for myotube maturation is higher, being closer to the native skeletal muscle tissue (~12 kPa) [274,318]. However, these experiments were performed by seeding cells on top of 2D substrates. In contrast, the stiffness of hydrogels for 3D skeletal muscle models varies depending on the biomaterials used but lean towards softer hydrogels. For instance, the encapsulation of human myoblasts in fibrin-based hydrogels is performed in biomaterials with Young's modulus of 1 ± 0.1 kPa [200]. Similarly, 3D studies performed with GelMA and C2C12 murine cells indicated that softer hydrogels in the range of 1–3 kPa lead to more elongated cell morphology, better cell spreading, and greater differentiation in 3D structures [191,309]. In the case of micropatterned GelMA-based hydrogels, stiffer hydrogels can be obtained by modifying fabrication conditions to increase the crosslinking degree. We previously studied cell morphology and spreading in micropatterned GelMA-CMCMA hydrogels

with different stiffness values [309]. Stellate morphology indicates that cells can move better within the material, which is essential for cell fusion. We observed that cells had a stellate morphology in softer hydrogels, while most cells were round when encapsulated using longer UV exposure times. Furthermore, longer UV exposure times or higher photoinitiator concentration may affect cell viability. Moreover, highly crosslinked hydrogels result in densely packed fibrillar structures that reduce water uptake and hinder nutrient diffusion and transport [291,319,320]. The fibrillar nanostructure of our photomolded GelMA-CMCMA hydrogels was observed using SEM (**Figure 4.17L-M**). The images showed an interconnected porous network that allows the diffusion of growth factors and other biological substances through the hydrogel. Conversely, PEGDA hydrogel analysis in SEM microscopy revealed that it is formed by a dense non-porous matrix (**Figure 4.17N-O**). This characteristic structure in the PEGDA layer helps to avoid cell growth and improves the adhesion and attachment of the GelMA-CMCMA scaffold. Altogether, the physical properties of GelMA-CMCMA hydrogel scaffolds are appropriate for supporting long-term cell culture of skeletal muscle tissue.

3D model of DM1 retains molecular features of the disease and provides a new structural phenotype for preclinical research

In this work, we fabricated 3D skeletal muscle tissue from human immortalized transdifferentiated myoblast-like cells that present molecular and phenotypical features of DM1. By evaluating 2D cell cultures, Arandel *et al.* confirmed that patient-derived cells present nuclear RNA aggregates (foci) of expanded CUG repeats, a hallmark feature of DM1. They also showed that DM1 cells had a reduced fusion capability and formed smaller myotubes compared to healthy controls in 2D [162]. To validate the use of this cell line for our bioengineered DM1 model, we analyzed if nuclear RNA aggregates were also observed in 3D. By performing FISH and immunofluorescence analyses, we demonstrated the presence of CUGexp-RNA foci and their colocalization with MBNL1 (**Figure 4.18**), confirming that these cells retain DM1-associated molecular characteristics and are suitable for generating *in vitro* 3D models for the disease.

To evaluate fusion capability in 3D, we assessed confocal images of 2D cultures and bioengineered microtissues from both control and DM1 myotubes. After seven days in differentiation conditions, we performed immunofluorescence stainings for myosin heavy chain 7, SAA, and nuclei (**Figure 4.19A-P**). Then, we

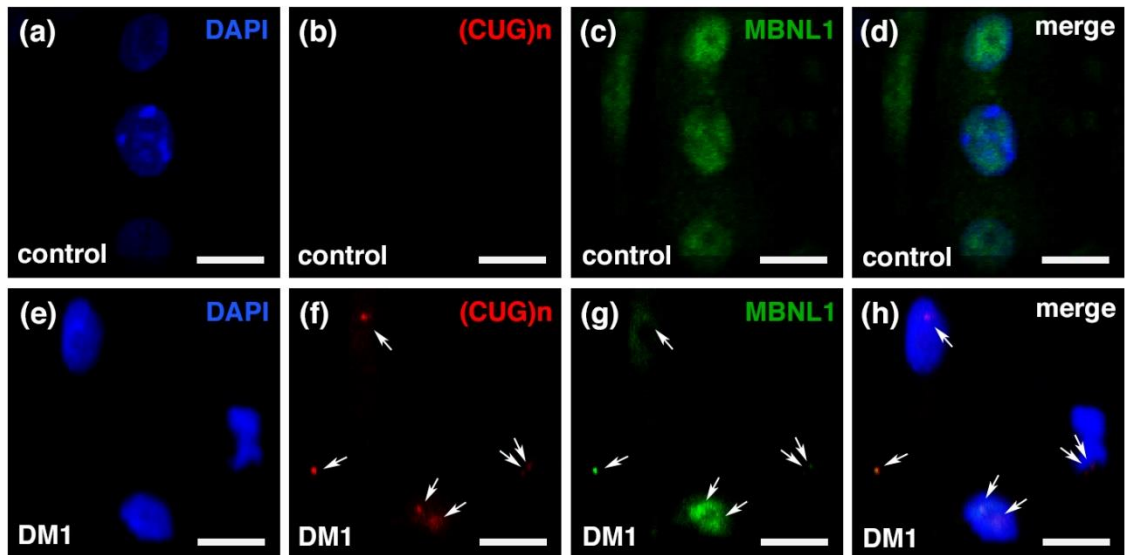


Figure 4.18. Encapsulated DM1 cells present disease-associated molecular phenotypes. Representative confocal images of (A–D) control and (E–H) DM1 immortalized transdifferentiated myoblast-like cells encapsulated in GelMA-CMCMA hydrogels. (A), (E) Nuclei were stained with DAPI (blue). (B), (F) Nuclear RNA aggregates of expanded-CUG repeats (white arrows) were only present in DM1 cells and detected by FISH using a Cy3-(CAG)₇-Cy3 probe (red). (C), (G) MBNL1 stainings (green) showing a reduced expression of MBNL1 in DM1 cells compared to controls. (D), (H) Merged images showing colocalization of MBNL1 with nuclear CUG_{exp}-RNA aggregates in DM1 transdifferentiated myoblast-like cells (Scale bars: 10 μ m).

used confocal images to calculate the fusion index, which is an indicator of differentiation quality in skeletal muscle cell cultures [321]. As expected, DM1 myoblasts in 2D culture had a significantly lower fusion index than healthy controls. Unexpectedly, when cells were encapsulated in 3D GelMA-CMCMA hydrogels, there were no differences in differentiation between healthy controls and DM1 cells, obtaining high fusion index values for both cases (**Figure 4.19Q**). Remarkably, 3D micropatterning resulted in the formation of long, multinucleated myotubes from DM1 patient-derived cells after seven days of culture, which is not possible to generate in standard cell cultures.

Although the fusion index of 3D DM1 myotubes was comparable to healthy myotubes, we observed structural differences, which prompted us to analyze the myotube diameter. Bioengineered skeletal muscle microtissues were differentiated for 7, 14, or 21 days before immunostaining for confocal imaging. Then, the 3D reconstructions of myotubes expressing SAA (**Figure 4.20A-F**) were used to

measure the individual diameter of control and DM1 myotubes over time. Several works have quantified myotube diameter in 2D for different purposes; for example, to characterize patient cells [322], test different culture conditions [323], evaluate the influence of topography in differentiation [324], or to study the effect of administrating

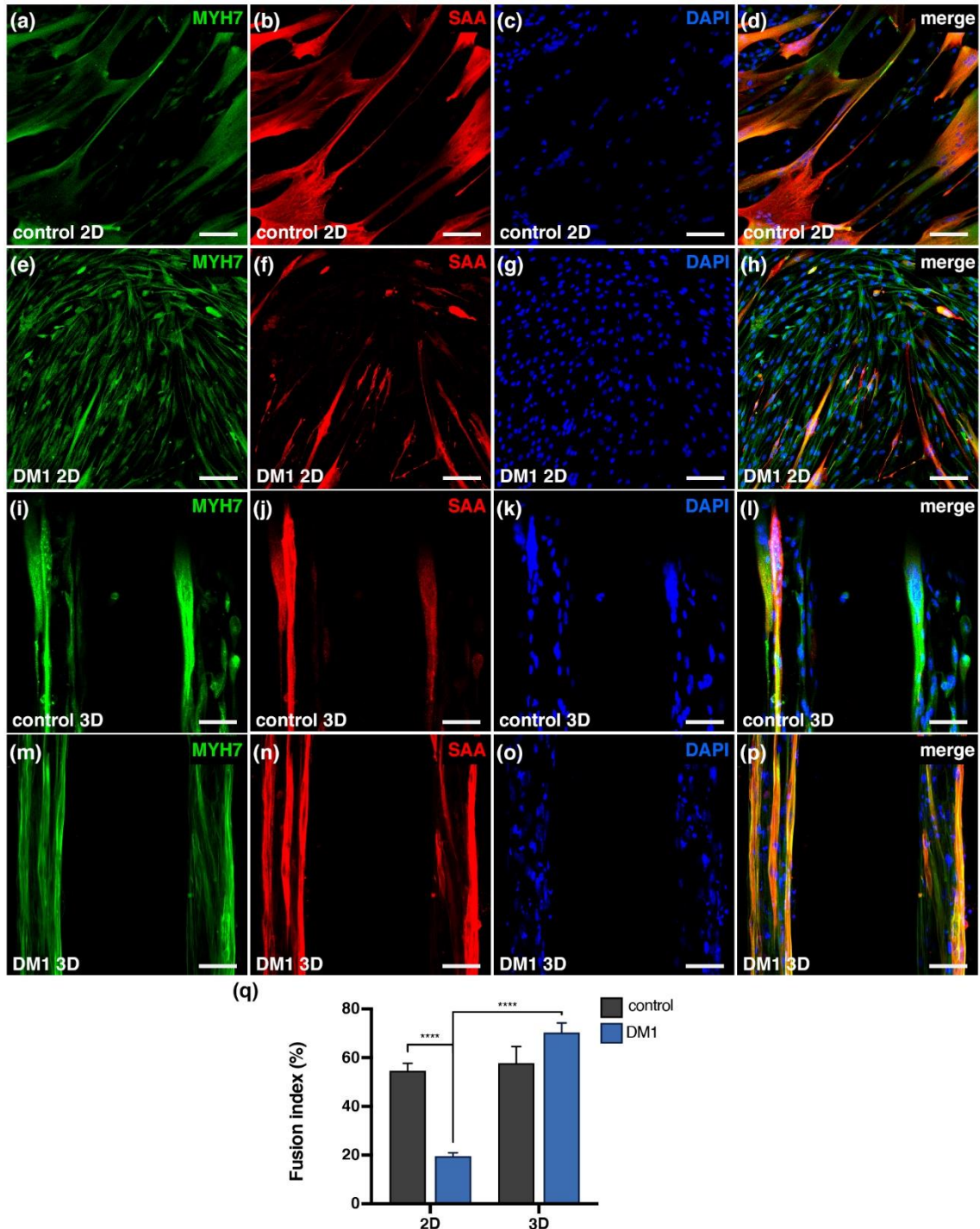


Figure 4.19. Cell differentiation is improved in 3D cultures. (A–P) Representative confocal images of 2D (A–H) and 3D (I–P) cultures stained for myosin heavy chain 7 (MYH7, green), sarcomeric α -actinin (SAA, red), and nuclei (DAPI, blue) after seven days in differentiation conditions (scale bars: 50 μ m). (Q) Graph showing comparison of fusion index expressed as the percentage of differentiated myotubes with respect to the total cell number. **** $p < 0.0001$.

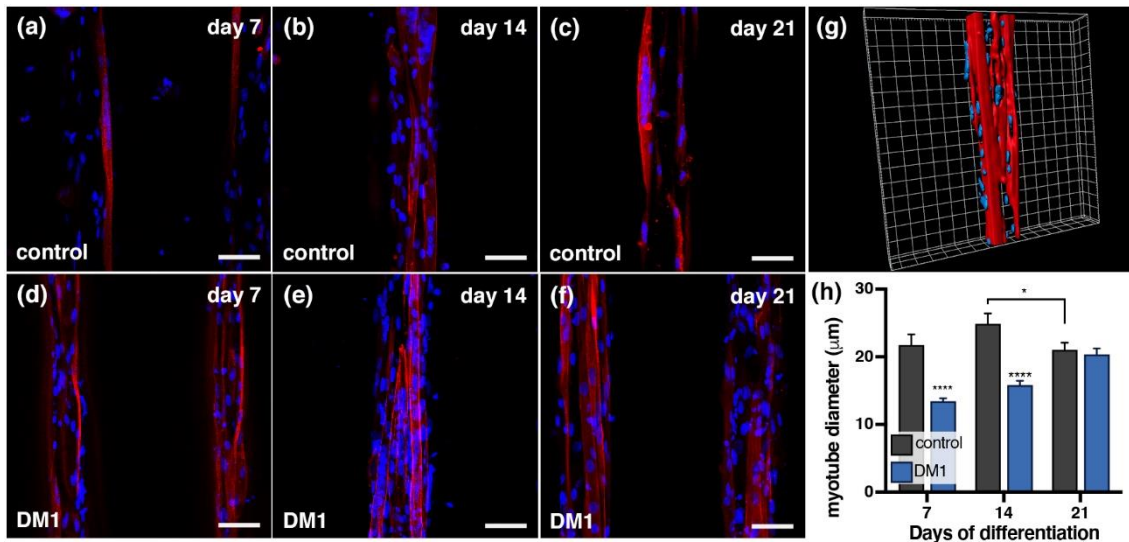


Figure 4.20. 3D DM1 myotubes have a reduced myotube diameter. (A–F) Representative confocal images of bioengineered 3D human skeletal muscle microtissues from healthy control (A–C) and DM1 (D–F) cells cultured for up to 21 days (Scale bars: 50 μm). Myotubes expressing SAA were stained in red and nuclei were counterstained with DAPI (blue). The 3D reconstruction of DM1 microtissues (G) was used to measure the individual diameter of myotubes over culture time (H). * $p < 0.05$ and **** $p < 0.0001$.

a given compound to myotubes [325]. Myotube diameter has also been measured in 3D cultures; for instance, Khodabukus *et al.* compared myotube cross-sections to analyze the maturation of electrically stimulated constructs [203]. Measurements in all these cases were carried out manually, using tools from ImageJ software. In contrast, our measurements were obtained by a 3D reconstruction using Imaris software (**Figure 4.20G**). With this reconstruction, each myotube diameter was automatically obtained with surface analysis tools. We found that 3D DM1 myotubes have a reduced diameter compared to healthy control myotubes (13.4 vs. 21.7 μm) after the first week of 3D culture (**Figure 4.20H**). After two weeks of culture, both types of myotubes increased in size, but DM1 myotubes continue to show a reduced diameter compared to control myotubes. On the contrary, after three weeks of culture, we did not detect differences between the size of 3D myotubes. Nevertheless, this observation might not be due to a DM1 phenotype, but the healthy myotubes have a reduced size after three weeks as a potential senescence of the cultures. For this reason, assays with these 3D muscle models should be performed in myotubes cultured for less than three weeks.

Previous works in DM1 cell models have described deficient muscle differentiation. A reduced fusion potential has been observed in 2D studies with myoblasts from transgenic mice [326] and myogenic satellite cells from DM1 patients [327]. As an indicator of muscle differentiation, the fusion index has been used to

investigate some aspects of DM1 molecular pathology [328,329]. It has also been applied to compare DM1 vs. control cells while establishing cell lines [162] and test if proposed treatments could restore muscle differentiation [330]. Notably, we demonstrated that 3D micropatterning improves the differentiation of DM1 cells, obtaining fusion index values that are similar to healthy controls. Thus, this indicator cannot be applied to evaluate phenotype rescue by a given therapy. Instead, we found a significant difference in the diameter of 3D myotubes from DM1 and control cells. DM1 usually presents in adulthood, when tissue is already formed. Therefore, from a drug development perspective, the reduced myotube diameter in 3D is a more physiologically relevant phenotype than impaired fusion in 2D cultures. Considering these results, we propose that this new structural phenotype would be a better indicator to assess the effects of DM1 therapies in preclinical research.

AntagomiR treatments rescue bioengineered 3D DM1 muscle phenotypes

Antisense oligonucleotides for specific blocking of miR-23b (antagomiRs) have already shown efficacy to increase MBNL protein levels in 2D DM1 myoblasts [143] as well as to rescue molecular pathology, splicing events, and functional phenotypes in a mouse model [143,144]. To demonstrate the application of our bioengineered *in vitro* model of DM1 in preclinical research, we evaluated the effect of this antagomiR in our 3D cell cultures.

AntagomiR against miR-23b (α -miR-23b) or a scrambled control (sc-control) antagomiR were administered to bioengineered DM1 microtissues by gymnotic delivery at a concentration of 100 nM. Of note, cells were already orientated along the micropatterns and transdifferentiated into myoblast-like cells at the moment of antagomiRs administration. The treatment lasted for seven days. To determine the success of the treatment, we analyzed the expression levels of miR-23b by real-time PCR (**Figure 4.21A**). We observed a reduction of miR-23b expression in DM1 3D muscles treated with α -miR-23b compared to the DM1 3D muscles treated with sc-control antagomiR. Next, we investigated if silencing miR-23b enhanced MBNL transcripts in the bioengineered 3D microtissues. We found an increase in MBNL2 transcripts in 3D DM1 myotubes treated with α -miR-23b compared to sc-control-treated tissues. However, MBNL1 was not increased at the transcriptional level (**Figure 4.21B**). Of note, western blot quantification showed an increase in both

MBNL1-2 proteins in bioengineered microtissues treated with α -miR-23b (**Figures 4.21C-D**).

To determine if the increase of MBNL proteins rescue characteristic DM1 spliceopathy, we analyzed the exon inclusion (Percentage Spliced In; PSI) of two MBNL1-dependent splicing events: *BIN1* and *NFIX*; and one MBNL2-dependent splicing event: *SPTAN1*. Remarkably, the exon inclusion was significantly rescued for the three splicing events (**Figures 4.21E-F**). These rescue levels are lower than those obtained by transfection of antagomiRs in 2D myoblasts in previous studies [143]. This can be explained by the different delivery strategies used. Gene silencing by oligonucleotides usually requires a delivery vehicle to perform cell transfection. This requirement comes with several challenges that can complicate the development of oligonucleotide therapies [331]. As an alternative, gymnotic delivery ('naked' delivery of oligonucleotides to cells) has been promising in recent years. With this delivery approach, cells in culture are exposed to a constant concentration of oligonucleotides, similar to what happens *in vivo* when plasma and tissues are exposed to saline-formulated oligonucleotides. Transfection strategy allows the internalization of large amounts of oligonucleotides. Nevertheless, gymnotic delivery remains a more physiologically relevant delivery approach, and its effects can be improved by dosage optimization in future assays.

Finally, to assess the effect of antagomiRs on the DM1 3D structural phenotype, we measured the diameter of 3D myotubes treated with α -miR-23b and compared them to sc-control-treated myotubes (**Figure 4.21G**). After seven days of treatment, we found that sc-control-treated microtissues had a mean myotube diameter of 14.4 μm , similar to DM1 myotubes without any treatment. Remarkably, upon treatment with α -miR-23b, myotubes reached a mean diameter of 21.9 μm (**Figure 4.21H**), comparable to the diameter of myotubes from healthy control cells (**Figure 4.20H**). Altogether, these results highlight the application of our bioengineered *in vitro* 3D model to assess DM1 therapies. Other antisense oligonucleotides and other potential therapies like small molecules or peptides can be tested on this platform. Furthermore, drug effects can be analyzed at different levels, including transcriptional, post-transcriptional, and structural phenotype changes.

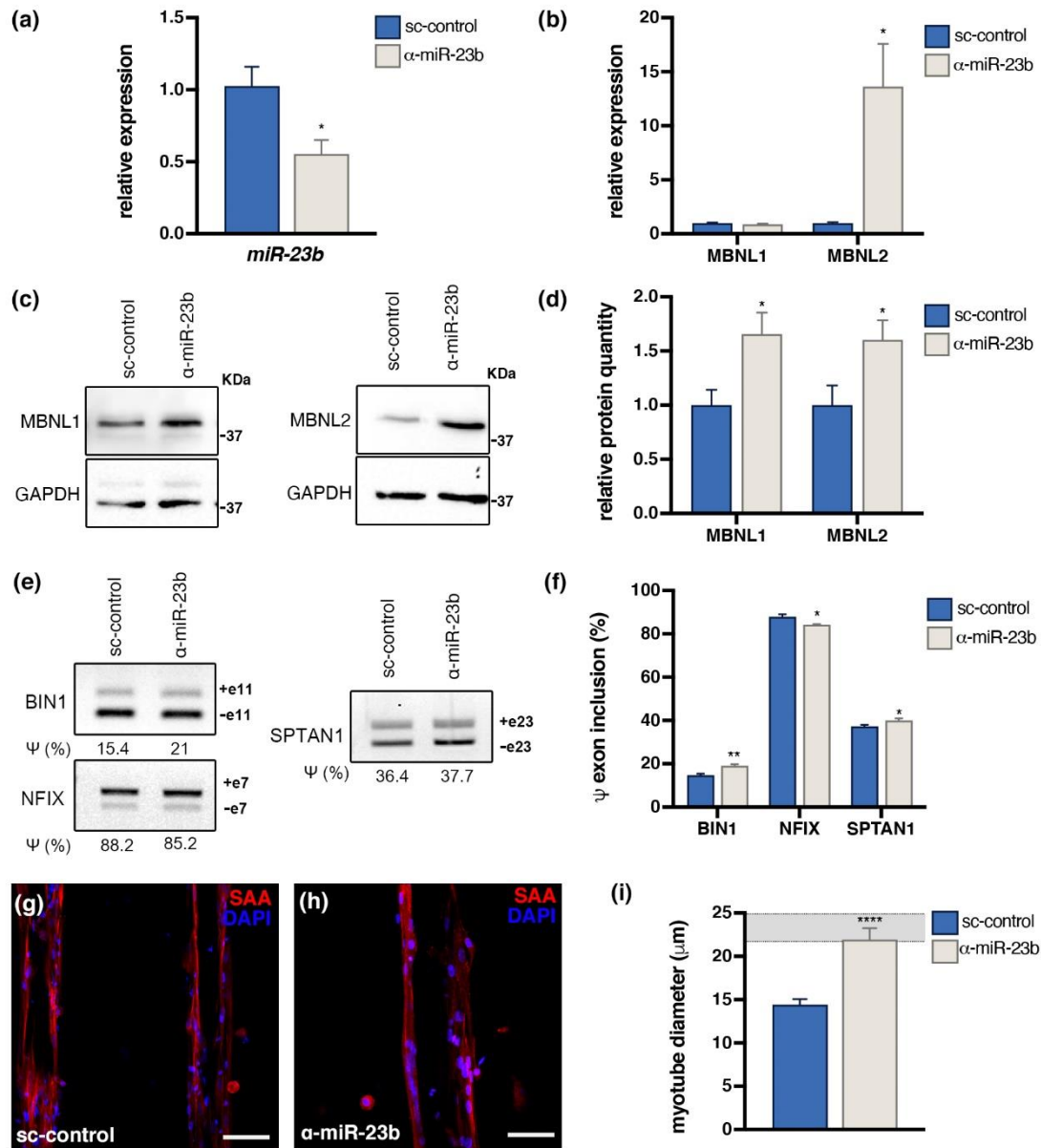


Figure 4.21. Therapeutic effect of antagomiR-23b on a bioengineered *in vitro* 3D model of DM1 human skeletal muscle. (A) Real-time PCR quantification of miR-23b expression after seven days of treatment with 100 nM of antagomiR-23b (α -miR-23b) or scrambled control antagomiR (sc-control). U1 and U6 snRNAs were used as reference genes. (B) qRT-PCR quantification of MBNL1 and MBNL2 expression relative to GAPDH and ACTB genes. (C), (D) Western blot quantification of MBNL1 and MBNL2 protein expression levels in 3D DM1 myotubes seven days after treatment with 100 nM of α -miR-23b or sc-control. GAPDH expression was used as endogenous control. (E), (F) RT-PCR analyses of splicing events altered in BIN1, NFIX, and SPTAN1 in 3D DM1 myotubes. (G-H) Confocal images of DM1 myotubes after treatment with sc-control (G) or α -miR-23b (H). Myotubes expressing SAA were stained in red and nuclei were counterstained with DAPI (blue) (scale bars: 50 μ m). (I) Quantification of the diameter of 3D DM1 myotubes treated with sc-control or α -miR-23b. The shaded area corresponds to the mean of myotube diameter of healthy control myotubes after 7 (bottom limit) and 14 days (top limit) of differentiation. * $p < 0.05$, ** $p < 0.01$ and **** $p < 0.0001$.

4.3.4. Conclusions

In this work, we described a detailed protocol for fabricating 3D skeletal muscle microtissues that can be maintained in long-lasting cultures. This micromolding technique is cheap and can be easily reproduced. Importantly, cell encapsulation in GelMA-CMCMA micropatterned hydrogels produce highly aligned multinucleated myotubes. Using this protocol, we generated for the first time a bioengineered human 3D skeletal muscle model for myotonic dystrophy. Remarkably, this protocol can be applied to cells from patients for different muscle diseases (i.e., other muscular dystrophies) to obtain patient-specific models. DM1 patient-derived cells encapsulated in GelMA-CMCMA hydrogels present DM1 molecular characteristics and correctly differentiated into multinucleated myotubes. A reduced fusion index, an indicator of muscle differentiation, is a typical feature of DM1 standard 2D cultures. Notably, the fusion index is restored to control values in DM1 3D myotubes. However, DM1 3D microtissues display a new structural phenotype; the 3D diameter of myotubes is significantly thinner than control myotubes. Therefore, this more physiological phenotype of the bioengineered 3D DM1 myotubes can be used for drug screening studies of DM1. To evaluate the applicability of this *in vitro* model in evaluating therapeutic compounds, we treated the bioengineered 3D microtissues with antisense oligonucleotides against miR-23b. Our findings indicated that antagomiRs for miR-23b are able to rescue molecular and structural phenotypes of DM1 disease when administrated to bioengineered 3D muscle. Overall, we demonstrated that our patient-derived 3D model is a relevant alternative to the existing *in vitro* and animal models. These bioengineered 3D skeletal muscle microtissues could be useful in a preclinical platform for DM1 drug development.

4.4. Human platelet lysate-based nanocomposite hydrogels for skeletal muscle tissue engineering

The last part of the doctoral thesis was dedicated to developing a xeno-free 3D human skeletal muscle tissue model¹³. Xeno-free biomaterials would represent a more relevant approach in tissue engineering for human disease modeling or regenerative medicine. In this work, the biomaterial scaffold consisted of human platelet lysate-based nanocomposite hydrogels (HUgel) instead of GelMA-CMCMA, which has animal-derived components. This nanocomposite hydrogel was previously developed at the Institute for Biomaterials, Biodegradables, and Biomimetics (i3Bs Research Institute) from the University of Minho in Portugal.

Platelet lysate (PL) is mainly composed of fibrinogen and is rich in growth factors. Although PL gels have a fibrillar structure that can mimic the extracellular matrix, they have poor mechanical properties that limit their use for tissue engineering. Therefore, researchers at i3Bs have reinforced these biomaterials by developing a nanocomposite hydrogel containing functionalized cellulose nanocrystals (a-CNC). The resulting nanocomposite hydrogels have tunable mechanical, structural, and biochemical properties optimal for stem cell 3D culture. However, HUgel has never been used for skeletal muscle tissue engineering before.

Here, we fabricated hydrogel casting platforms to encapsulate human muscle precursor cells in HUgel. The a-CNC content was modulated to enhance matrix remodeling, uniaxial tension, and self-organization of the cells, resulting in the formation of highly aligned, long myotubes expressing SAA. Moreover, the bioengineered human muscles were subjected to electrical stimulation, and the exerted contractile forces were measured in a non-invasive manner. Notably, we found that 0.2% w/v of a-CNC resulted in high matrix compaction without compromising tissue stability and durability. Finally, our preliminary results demonstrated that the bioengineered human skeletal muscles could be used in xeno-free cell culture platforms to assess tissue functionality, which is promising for drug development applications.

¹³ The following are unpublished results from a manuscript in preparation.

4.4.1. Introduction

Engineered human skeletal muscle tissues are promising new tools to accelerate the drug development process of muscle-related diseases, such as muscular dystrophies. In particular, these engineered tissues represent more efficient and predictive *in vitro* models that can be used in preclinical research stages, complementing traditional 2D assays and reducing the need for animal models [61,146]. Advances generated in this field could also be applied to regenerative medicine. Concretely, tissue replacements could be engineered at a larger scale to treat volumetric muscle loss [178,307]. Native skeletal muscle tissue comprises aligned multinucleated fibers formed by the fusion and differentiation of muscle precursor cells [63,68]. Therefore, tissue engineering strategies are based on encapsulating muscle precursor cells in a suitable biomaterial scaffold that mimics the extracellular matrix (ECM) 3D architecture and provides topographical and microenvironmental cues to guide cell alignment and fusion [61].

Nowadays, the most common biomaterials used for skeletal muscle tissue engineering are gelatin methacryloyl (GelMA) [176,177,183,191,291,309,332], collagen [178,184,192,208], and fibrin [173,186,193,201–205,207,211,333]. These natural biomaterials are usually modified or reinforced to improve their mechanical or biological properties. For instance, photocrosslinkable GelMA has been combined with other biomaterials such as cellulose, alginate, or poly(ethylene glycol) (PEG), to generate long-lasting micropatterned composite hydrogels with a slower degradation rate [291,309,332]. On the other hand, collagen and fibrin have been widely combined with Matrigel® [193,201–203,208,211] or Geltrex™ [204,333], which are commercial basement membrane ECM products derived from the Engelbreth–Holm–Swarm (EHS) murine tumor cells. Matrigel® and Geltrex™ contain various structural proteins, including laminin, collagens (mainly collagen IV), entactin, and the heparin sulfate proteoglycan perlecan [334]. Moreover, these EHS matrices have several tumor-derived growth factors, cytokines, and enzymes contributing to their biological function [335,336]. Although these have been useful materials for 3D cell culture, their complex, ill-defined, and highly variable batch-to-batch composition compromises the reproducibility and accuracy of cell-based assays [335,337,338]. Furthermore, these materials are not xeno-free. Nearly all 3D models of human skeletal muscle published to date have used materials derived from xenogenic tissues, such as gelatin from porcine skin [183,205,332], collagen from rat tail

[183,208], fibrinogen from bovine plasma [201–204,333], or decellularized ECM (dECM) from porcine muscle [206]. This limits any clinical application of engineered tissues in regenerative medicine due to the possible presence of xenogenic contaminants from animal-derived ECM [339,340]. Moreover, animal-derived serum in culture media could reduce sensitivity to drug toxicity within *in vitro* testing platforms [14].

Platelet lysate (PL) from human plasma is an attractive alternative biomaterial for xeno-free scaffold formation. PL formulations are prepared by freeze/thaw cycles or by ultrasounds that cause platelet disruption without adding any clot activator to release PL content, resulting in a reproducible batch-to-batch composition [341–343]. Apart from a rich environment of growth factors and cytokines, PL contains ECM precursors like fibrinogen and vitronectin. Hence, PL hydrogels can be formed through thrombin-activated induction of the coagulation cascade, obtaining fibrin-based fibrillar gels [344]. Although these are interesting materials, their potential as scaffolds for 3D cell culture is restricted by their poor structural stability and mechanical properties [345]. Additionally, the intrinsic PL growth factors and cytokines are not well-retained in PL gels [344]. To overcome these limitations, PL gels can be reinforced with nanomaterials that provide additional functionalities. Mendes and colleagues have developed a nanocomposite fibrillar hydrogel (HUGel) based on the induction of the human PL coagulation cascade while incorporating cellulose nanocrystals modified with surface aldehyde groups (a-CNC) [222]. In this material, the a-CNC act as nanofillers that are entrapped in the PL fibril structure, crosslinked through reversible Schiff base bonds with the amine groups of the PL proteins. The resulting nanocomposite hydrogels have tunable mechanical and biochemical properties that can help modulate the behavior of encapsulated stem cells, such as human adipose-derived stem cells (hASCs). It has been demonstrated that increasing a-CNC content in PL hydrogels causes an increase in fiber diameter, interfibrillar porosity, and stiffness. Moreover, a-CNC loading hinders the typical fast clot retraction and improves bioactive molecule retention, controlling the 3D cell microenvironment. HUGel has also been used as bioink for bioprinting hierarchical fibrillar structures for stem cell 3D cell culture without the need for animal-derived serum supplementation [223]. Remarkably, the serum-free cell culture of hASCs in HUGel was compared to GelMA and alginate bioinks. The results showed that, in contrast to the other polymers, HUGel enhances cell spreading and proliferation, and stimulates the production of cell-secreted ECM.

Here, we employed this human platelet lysate-based nanocomposite hydrogel as a scaffold for the 3D culture of human muscle satellite stem cells. This model was developed by encapsulating human muscle satellite stem cells in HUgel around a pair of flexible posts in hydrogel casting platforms. The a-CNC content was modulated to favor uniaxial tension, self-organization, cell fusion, and differentiation into long multinucleated myotubes. Furthermore, the functionality of the bioengineered human skeletal muscle tissues was demonstrated by force measurements of the electrical stimulation-induced contractions. Overall, these preliminary results indicate the great potential of human platelet lysate-based nanocomposite hydrogels for *in vitro* models of skeletal muscle tissue. These bioengineered human tissues could be used as drug screening platforms for muscular dystrophies by incorporating patient-derived satellite cells. Remarkably, the xeno-free characteristics of this *in vitro* 3D model could enable the transition into clinical applications for regenerative medicine.

4.4.2. Experimental procedure

Cell culture

Human immortalized muscle satellite stem cells (HuMSCs) were provided by Dr. Bénédicte Chazaud from the Institute of Myology (Lyon, France). Primary muscle satellite stem cells were previously isolated from a healthy 14-year-old muscle biopsy and immortalized using CDK-4/hTERT expression. Cells expressing PAX7 were grown in Skeletal Muscle Basal Medium (PromoCell), containing skeletal muscle supplemental mix (#C-39365, PromoCell), 1% v/v penicillin/streptomycin (P/S, 10000 U mL⁻¹, Thermo Fisher Scientific), and 10% v/v fetal bovine serum (FBS, Thermo Fisher Scientific). The growth medium added after cell encapsulation did not contain FBS but was supplemented with 1 mg mL⁻¹ of 6-amino-n-caproic acid (ACA, Sigma-Aldrich). The differentiation medium (HMDM) consisted of DMEM, high glucose, GlutaMAX™ (Gibco, Thermo Fisher Scientific), 1% v/v Penicillin-Streptomycin-Glutamine (P/S-G, 100 X, Gibco, Thermo Fisher Scientific), 1% v/v Insulin-Transferrin-Selenium-Ethanolamine supplement (ITS-X, 100 X, Gibco, Thermo Fisher Scientific), and 1 mg mL⁻¹ of ACA.

Fabrication of the hydrogel casting platforms

The hydrogel casting platforms were designed using Fusion 360 software (Autodesk) as circular chips (8 mm diameter) with a rectangular well of 35 μ L

volumetric capacity, containing two T-shaped posts (diameter: 0.8 mm; height: 3.25 mm) (**Figure 4.23A**). In this protocol, polydimethylsiloxane (PDMS) replicas of a 3D printed master mold were obtained by Ecoflex™ (00-30, Smooth-On) negative intermediary molds.¹⁴

Fabrication of the master mold

First, the master mold was generated by transforming the platform design into an STL file for projector-based stereolithography 3D printing using a Solus DLP 3D Printer (Reify 3D) with an opaque orange resin (SolusProto, Reify 3D) that withstands high temperatures. The hard 3D printed molds were silanized by chemical vapor deposition (CVD) of trichloro(1H,1H,2H,2H-perfluorooctyl)silane (PFOTS, Sigma-Aldrich). Briefly, the surface of 3D printed molds was activated with oxygen plasma for 30 s and immediately placed in a vacuum desiccator with 5 drops of PFOTS for 1 h. After deposition, the silanized 3D printed master mold was left in an oven for 1 h at 80 °C.

Fabrication of the negative mold

The Ecoflex™ negative mold was made by mixing the two prepolymers (1A:1B, approximately 15 g of each prepolymer). Before beginning, prepolymer B had to be thoroughly pre-mixed. Then, A and B were thoroughly mixed for 3 minutes. The mixture was placed in a vacuum desiccator for 5 min to remove entrapped air. After, the liquid prepolymer was poured on the 3D printed master mold and degassed inside the vacuum desiccator for 15 minutes. The Ecoflex™ was cured at room temperature overnight. Finally, the cured polymer was carefully peeled off from the 3D printed master mold, washed with ethanol, and dried with N₂ flow and on a hot plate (90 °C, 10 min) before silanization with PFOTS (following the same procedure as with the 3D printed master mold).

Replica molding of PDMS platforms

The PDMS polymer elastomer base and curing agent were weighted in a 10:1 ratio. After thoroughly mixing, we degassed the polymer in a vacuum desiccator. The uncured PDMS was poured on the Ecoflex™ mold (placed in a glass Petri dish), and the trapped air in the post area was removed with a syringe. Then, the mold was left inside a vacuum desiccator until all the trapped air was removed. After, the PDMS

¹⁴ Hydrogel casting platforms were designed by Dr. Juan M. Fernández-Costa and fabricated by Lluís Mangas from the Biosensors for Bioengineering Research Group at IBEC.

was cured at 80 °C for 6 h. Before demolding, PDMS was left for additional curing at room temperature overnight. PDMS was then detached from the Ecoflex™ and cleaned by sonication in Milli-Q water and 2-propanol for 5 min. Then, individual PDMS platforms were cut using an 8 mm diameter biopsy punch. Finally, a cover glass was bonded to each platform base by activating the glass and PDMS platform base with UV plasma for 15 min before joining the two surfaces. Before cell encapsulation, platforms were washed with 2-propanol and water.

Preparation of the nanocomposite hydrogel (HUGel)

Preparation of HUGel precursors

Human platelet lysate (PL) was purchased from STEMCELL™ Technologies. Aldehyde-cellulose nanocrystals (a-CNC) were prepared at the Research Institute on Biomaterials, Biodegradables, and Biomimetics (i3Bs, University of Minho, Portugal) [222,223]. Cellulose nanocrystals (CNC) were extracted from microcrystalline cellulose powder (Sigma-Aldrich) by sulphuric acid hydrolysis. Briefly, concentrated sulphuric acid (Sigma-Aldrich) was added dropwise to the microcrystalline cellulose powder up to a final concentration of 64% w/v. The obtained suspension was heated at 44 °C for 2 h. Then, the suspension was collected and stored at 4 °C. To produce a-CNC, sodium periodate (NaIO₄, Sigma-Aldrich) was added to a 1.5% w/v CNC aqueous suspension in a 1:1 molar ratio (NaIO₄:CNC) for 12 h. Finally, the concentration of the working suspension was adjusted by concentrating it against poly(ethylene glycol) (20.000 kDa, Sigma-Aldrich) using benzoylated cellulose dialysis membranes (2000 Da NMWCO, Sigma-Aldrich). Stock water dispersions of a-CNC were prepared and fully characterized in previous works by researchers from the i3Bs Research Group [222,223].

Cell encapsulation by HUGel casting in PDMS platforms

PDMS casting platforms were treated with 0.2% Pluronic® (F-127, Sigma-Aldrich) for 20 minutes to avoid hydrogel attachment to the PDMS well. After treatment, the platforms were washed 3 times with phosphate buffered saline (PBS) and sterilized with UV light. For cell encapsulation, HuMSCs were detached and resuspended in PL. In these experiments, we worked with final cell densities of 0.5, 1, or 2.5 x 10⁷ cells mL⁻¹. The a-CNC water dispersion was placed in a sterile Eppendorf tube at the desired concentration and sonicated for 5 minutes. Then, the suspension was mixed with thrombin from human plasma (2 U mL⁻¹, Sigma-Aldrich)

and CaCl₂ (10 mM, Sigma-Aldrich). The cell suspension in PL was thoroughly mixed in a 1:1 ratio with the suspension containing a-CNC, thrombin, and CaCl₂. Finally, a volume of 35 μ L of the mixture was carefully placed inside each PDMS platform well (**Figure 4.23B**). The samples were allowed to crosslink at 37 °C for 30 min before adding growth medium. After two days, the medium was switched to differentiation medium. Then, half of the medium was replaced every two days. The 3D culture was carried out under shaking conditions inside an incubator (37 °C, 5% CO₂).

Immunofluorescence staining

The bioengineered human muscle tissues were fixed with 10% formalin solution (Sigma-Aldrich) for 30 min at RT, followed by several washes in PBS. Samples were then permeabilized with PBS-T (0.1% Triton-X (Sigma-Aldrich) in PBS), blocked (0.3% Triton-X, 3% donkey serum (Sigma-Aldrich) in PBS) for 2 h at RT, and incubated with monoclonal mouse anti-sarcomeric α -actinin (SAA) primary antibody (1:200, Sigma-Aldrich) at 4 °C overnight. After several PBS-T washes, the samples were incubated for 2 h with polyclonal donkey anti-mouse IgG, Alexa Fluor 488-conjugated secondary antibody (1:200, Invitrogen), and rhodamine-phalloidin (1:200, Cytoskeleton) to stain F-actin, at RT. Finally, the samples were counterstained with DAPI (4',6-diamidino-2-phenylindole, Life Technologies) to detect the nuclei. The complete protocol was performed under shaking conditions.

Electrical Pulse Stimulation

After 7 days in differentiation medium, the bioengineered 3D human skeletal muscle tissues were subjected to electrical pulse stimulation (EPS). EPS was performed with a custom-made stimulation plate consisting of graphite electrodes assembled on a 12-well plate lid. First, the stimulation plate containing the tissues was placed inside a Zeiss Axio Observer.Z1/7 microscope outfitted with the XL S1 cell incubator at 37 °C and on a 5% CO₂ atmosphere. Then, the electrodes were connected to a multifunction generator (NF Corporation), and the frequency and amplitude of the signals were confirmed using a digital oscilloscope (QUIMAT). Finally, the muscle tissues were subjected to a stimulation regime of square pulses with a 10% duty cycle, an electrical field strength of 1 V/mm, and frequencies from 1 to 50 Hz to evaluate tissue response (see **Figure 4.27A**).¹⁵

¹⁵ The electrical stimulation well-plate was custom-made by Dr. José Yeste from the Biosensors for Bioengineering Research Group at IBEC.

Imaging

Live-cell imaging was performed with the Zeiss Axio Observer.Z1/7 microscope outfitted with the XL S1 cell incubator. All images were taken at 37 °C and on a 5% CO₂ atmosphere and processed using the Fiji image processing package, a distribution of ImageJ [218,224]. In addition, fluorescence images were taken with a ZEISS LSM800 confocal laser scanning microscope and analyzed using the Imaris microscope image analysis software (Oxford instruments).

Force measurements

The post deflections during tissue contractions were recorded and analyzed using Fiji. The force-displacement relationship for the posts was estimated using linear bending theory based on previously published protocols (**Figure 4.22**) [188,209]. The Young's modulus of the PDMS (10:1) was previously measured as 1.6 ± 0.1 MPa. Considering the posts' geometry and dimensions, we calculated a spring constant (k) of 3.54 N/m. The spring constant was used to transform the recorded post deflections (d) into the force generated by the bioengineered 3D skeletal muscle tissues (F).

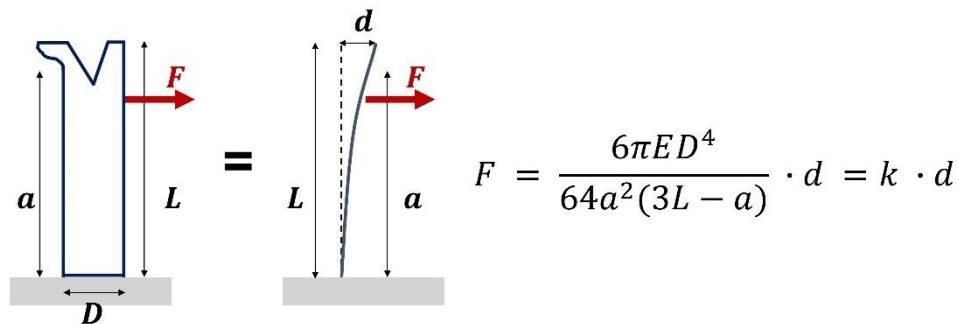


Figure 4.22. Characterization of the post mechanical properties. The force exerted by the skeletal muscle tissues is calculated from the post geometry and mechanics. Diameter (D), total length (L), length from the bottom of the post to the centroid of the cap (a), deflection (d), and Young's modulus of the PDMS (E).

Statistical analysis

All group data are expressed as mean \pm SEM. The comparisons between groups were performed using Prism 8 software (GraphPad) by a two-tailed Student t-test ($\alpha = 0.05$), applying Welch's correction when necessary. Differences between groups were considered significant when $p < 0.05$.

4.4.3. Results and discussion

Human skeletal muscle tissue formation in hydrogel casting platforms

Efficient myotube formation in engineered skeletal muscle tissues requires adequate topographical and microenvironmental signals that favor cell alignment and fusion. When scaffolds are made of compactable biomaterials, such as collagen, EHS matrices, or fibrin, the most common fabrication approach consists of introducing tendon-like attachment points to provide uniaxial tension during ECM remodeling [187]. Following this strategy, fibrin-Matrigel® and fibrin-Geltrex™ hydrogels have been cast in silicone molds with nylon frames or hooks as anchor points [201–204]. The resulting muscle tissue bundles needed to be manipulated and transferred to a different platform for stimulation and force measurements. Another widely used method involves cell-laden matrix compaction around a pair of flexible silicone posts [186,193,204,208,333]. Besides providing uniaxial tension, these hydrogel casting systems allow *in situ* tracking of post deflection due to tissue contraction. Furthermore, these deflections can be transformed into force measurements. Considering these advantages, we fabricated hydrogel casting platforms containing two flexible posts as anchor points (**Figure 4.23A**). The final PDMS platforms were fabricated by replica molding of 3D printed master molds, using Ecoflex™ as reusable intermediary negative molds. Ecoflex™ is a platinum-catalyzed silicone, which is cured at room temperature, resulting in a highly stretchable material that can be applied as a fully deformable elastic mold [346]. The individual platforms were designed as circular chips that fit inside 48-well plates. Each platform has a rectangular casting well with a volumetric capacity of 35 μL and contains a pair of posts that direct tissue formation. Crucially, to ensure that tissues are retained under tension, we designed hook-like features on the top of each post.

Human platelet lysate-based nanocomposite hydrogels (HUgel) were fabricated following a previously published protocol based on the formation of fibrin-based scaffolds [222]. In this work, human immortalized muscle satellite stem cells (HuMSCs) expressing PAX7 were encapsulated in HUgel by hydrogel casting in the two-post PDMS platforms (**Figure 4.23B**). Briefly, a suspension of HuMSCs in PL was mixed with α -CNC water dispersions containing thrombin and calcium ions. The mixture was carefully pipetted into the rectangular PDMS wells and crosslinked for 30 minutes at 37 °C before adding cell culture media. We fixed the concentrations of

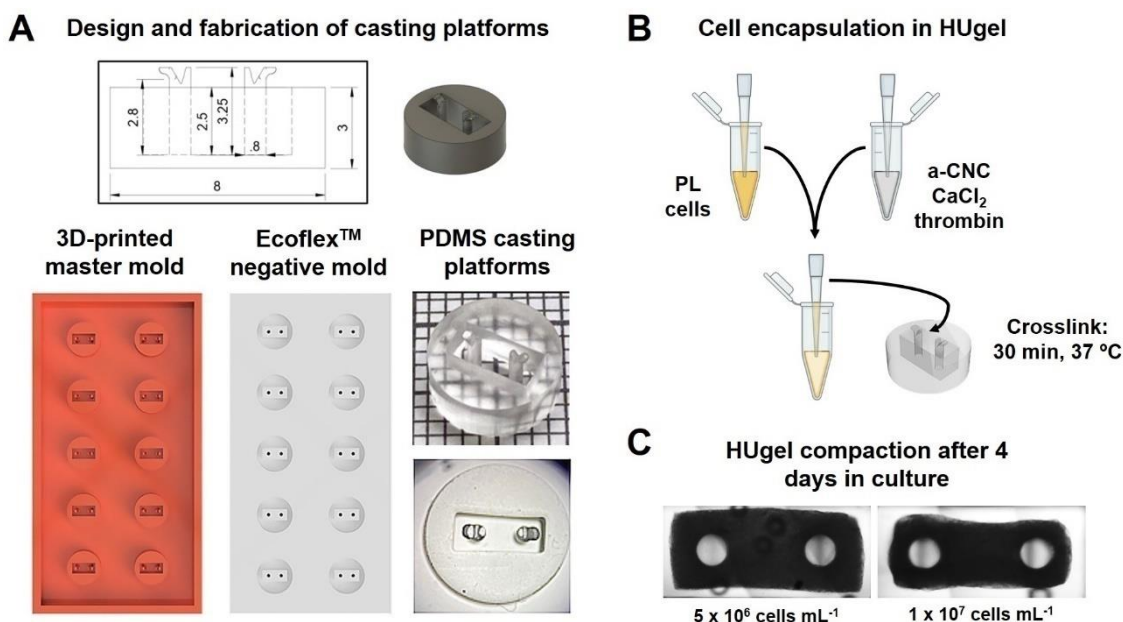


Figure 4.23. Human muscle satellite stem cells encapsulation in a human platelet lysate-based nanocomposite hydrogel (HUgel). (A) Two-post platforms were designed and fabricated by 3D printing and PDMS replica molding, using Ecoflex™ as reusable negative intermediary molds. (B) Schematic of preparation of the HUgel and cell encapsulation. Cells are resuspended in human platelet lysate (PL) at the appropriate cell density. Then, the PL is mixed with the aldehyde cellulose nanocrystals (a-CNC) water dispersion containing CaCl_2 and thrombin. The mix is then pipetted into the two-post platforms and allowed to crosslink for 30 min at 37 °C. Finally, growth medium is added to the platforms. (C) Bright-field images of HUgel compaction after 4 days in culture with cell densities of $5 \times 10^6 \text{ cells mL}^{-1}$ and $1 \times 10^7 \text{ cells mL}^{-1}$.

thrombin (1 U mL^{-1}) and CaCl_2 (5 mM) according to the previous study by Mendes *et al.* [342]. For the initial experiments, a-CNC was mixed at a final concentration of 0.5% w/v, and cells were encapsulated at a density of 5×10^6 and $1 \times 10^7 \text{ cells mL}^{-1}$ (Figure 4.23C). We observed that the cell-laden HUgel matrix started to detach slowly from the PDMS after two days of culture. Hydrogel compaction due to matrix remodeling by the encapsulated cells could be observed after four days. At this time, tissues containing $1 \times 10^7 \text{ cells mL}^{-1}$ were more compacted than those with fewer cells. Matrix remodeling is essential in these casting systems to implement uniaxial tension and induce self-organization during tissue formation [333,347]. Consequently, cell density was increased to $2.5 \times 10^7 \text{ cells mL}^{-1}$ for future experiments.

a-CNC content can be modulated to promote myotube formation

The physical and biological properties of nanocomposite hydrogels with varying α -CNC content have been extensively characterized in previous studies [222,223]. Significantly, researchers found that increasing α -CNC content hampers the typical fast densification of the fibrin matrix, which is referred to as clot retraction. In some tissue engineering applications (e.g., for space-filling of wounded tissues), extensive clot retraction is considered an undesirable hydrogel effect. Nevertheless, for skeletal muscle tissue formation, the contractile effect of the cell-laden matrix contributes to implementing uniaxial tension that facilitates the self-organization and alignment of myoblasts. At the same time, the matrix compaction favors myoblast fusion into myotubes. Here, we modified the content of α -CNC to obtain long-lasting scaffolds with high clot retraction properties that promote skeletal muscle tissue formation (**Figure 4.24A**). Encapsulating human skeletal muscle satellite stem cells in a high density of 2.5×10^7 cells mL^{-1} resulted in HUgel detachment from the PDMS casting platforms within a few hours of culture. The matrix compaction after 12 h was calculated as the percentage of reduction in tissue width (**Figure 4.24B**). We found that the initial working concentration of 0.5% w/v α -CNC resulted in $25.7 \pm 1.6\%$ of matrix compaction, whereas the tissues without α -CNC presented extensive compaction of $66.4 \pm 4.3\%$. However, the lack of mechanical reinforcement from α -CNC caused hydrogel degradation, so the samples broke and collapsed between 12-60 h after cell encapsulation. On the other hand, hydrogels with a low content of

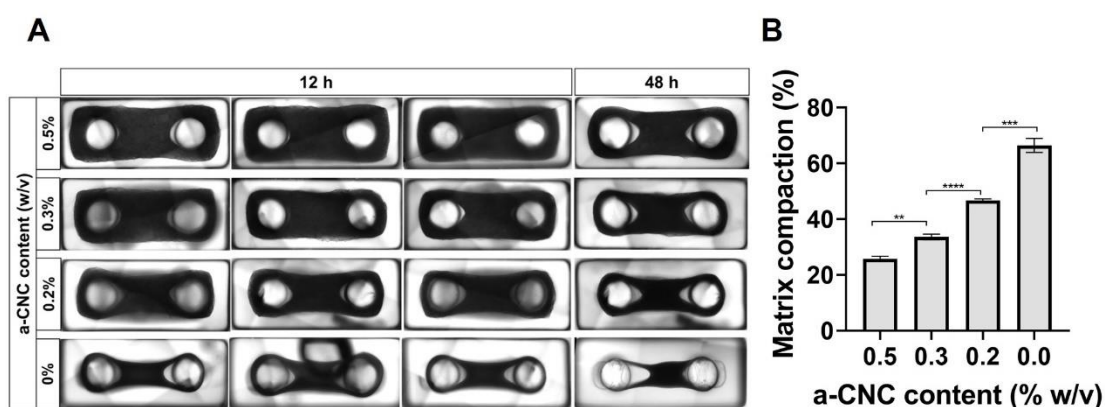


Figure 4.24. HUgel clot retraction increases with decreasing α -CNC content. (A) Representative bright-field images of cell-laden hydrogels after 12 h and 48 h. Human muscle satellite stem cells (HuMSCs) were encapsulated at a density of 2.5×10^7 cells mL^{-1} . α -CNC content was modulated between 0 and 0.5% w/v. (B) Bar graph quantification of matrix compaction measured as the percentage of reduction of tissue width after 12 h of HuMSCs encapsulation. ** $p < 0.01$; *** $p < 0.001$; **** $p < 0.0001$.

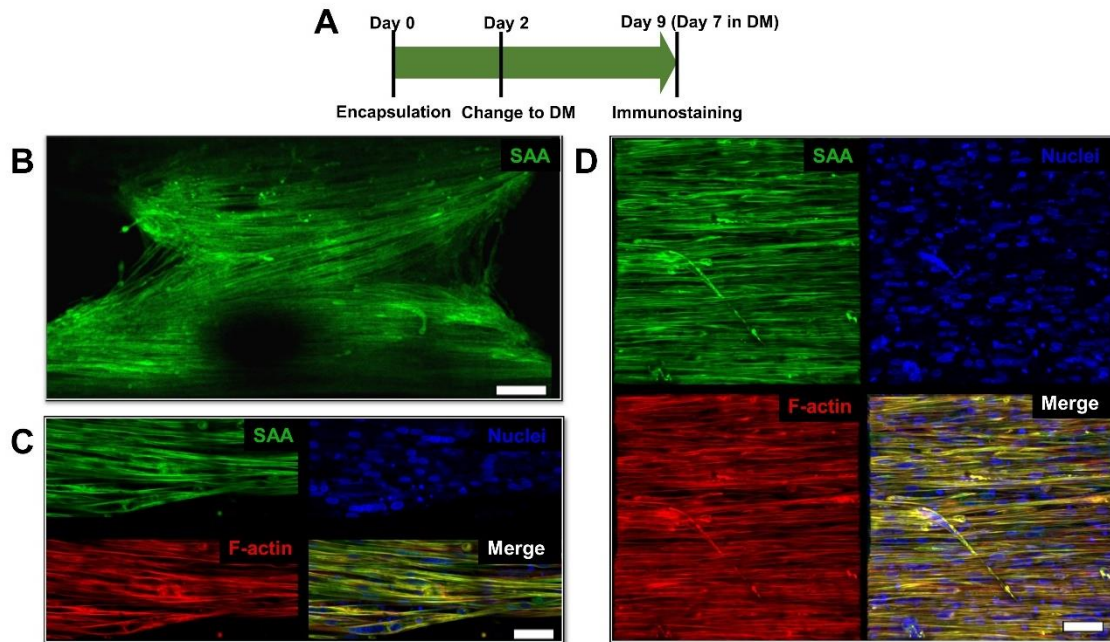


Figure 4.25. Bioengineered *in vitro* 3D model of human skeletal muscle tissue in a xeno-free culture system. (A) Timeline of the experiments. (B-D) Representative confocal images showing long, aligned myotubes expressing sarcomeric α -actinin (SAA, green) in nanocomposite hydrogels containing 0.2% w/v a-CNC. F-actin is stained in red and nuclei in blue. Scale bars: (B): 200 μm , (C-D): 100 μm .

a-CNC (0.3 and 0.2% w/v) offered a high retraction from the beginning of the culture ($33.6 \pm 2\%$ and $46.7 \pm 1.1\%$, respectively) and were stable for at least two weeks.

PL gels are attractive scaffolding materials for stem cell encapsulation because PL contains structural proteins like fibrinogen, as well as growth factors and cytokines that stimulate cell growth and proliferation [342,345]. However, PL gels alone do not retain these growth factors within the scaffold during culture. Therefore, the impact of a-CNC content on the sequestering and release profile of proteins from the HUgel scaffolds was previously investigated [222]. The results indicated that the a-CNC play an important role in growth factor retention within the HUgel scaffolds due to the formation of a protein corona on the CNC surface. Nevertheless, the precise mechanisms and interactions need to be further studied. Notably, nanocomposite hydrogels with high a-CNC content (at least 0.61% w/v) are optimal for hASCs cell encapsulation, where proliferation during cell culture is desired [222,223]. On the contrary, in skeletal muscle tissue engineering, differentiation of muscle precursor stem cells requires that cells stop proliferating and exit the cell cycle in order to fuse and differentiate into multinucleated myotubes. In fact, all cell culture protocols for differentiating skeletal muscle cells involve removing growth

factors and reducing the animal serum present in the basal media [14]. Thus, a microenvironment rich in growth factors could hinder adequate differentiation.

Considering the matrix compaction properties and the expected growth factor release profiles, we selected a-CNC content of 0.2% w/v for the following experiments with HuMSCs. The growth medium was replaced by a serum-free differentiation media (DM) 48 h after cell encapsulation (**Figure 4.25A**). After one week in differentiation media, samples were fixed, and the xeno-free bioengineered muscle tissues were stained for sarcomeric α -actinin (SAA, green), F-actin (red), and nuclei (blue) (**Figure 4.25B-D**). The confocal images showed long, highly aligned, multinucleated myotubes expressing SAA (**Figure 4.25B**).

Nanocomposite hydrogels support the formation of functional human skeletal muscle tissues in a xeno-free cell culture system

The functionality of bioengineered muscle tissues was assessed by their response to electrical pulse stimulation (EPS). As described above, one of the advantages offered by hydrogel casting around two flexible posts is performing *in situ* force measurements. In these systems, characterization of the posts' mechanics allows the conversion of the post deflections (caused by contractile tissues) into force measurements [333,348]. Therefore, measurements are non-invasive and compatible with cell culture conditions.

We performed EPS using graphite electrodes fixed on a modified 12-well plate lid. Bioengineered muscle tissues were subjected to EPS after one week in differentiation conditions (**Figure 4.26A**). At this time, myotubes in tissue borders could be observed through bright-field microscopy. We did not observe any spontaneous contractions without electrical stimulation. However, the bioengineered human skeletal muscle tissues responded to electrical stimulation, presenting twitch or tetanic contractions depending on the applied frequencies (**Figure 4.26B**). Furthermore, immunostaining of electrically stimulated and control (non-stimulated) tissues was performed after the experiments. Confocal images of SAA stainings showed the presence of striations (white arrows in **Figure 4.27**), indicating myotube maturation in some of the myotubes after only 7 days of differentiation. Notably, these striated myotubes were only present in electrically stimulated tissues. Nonetheless,

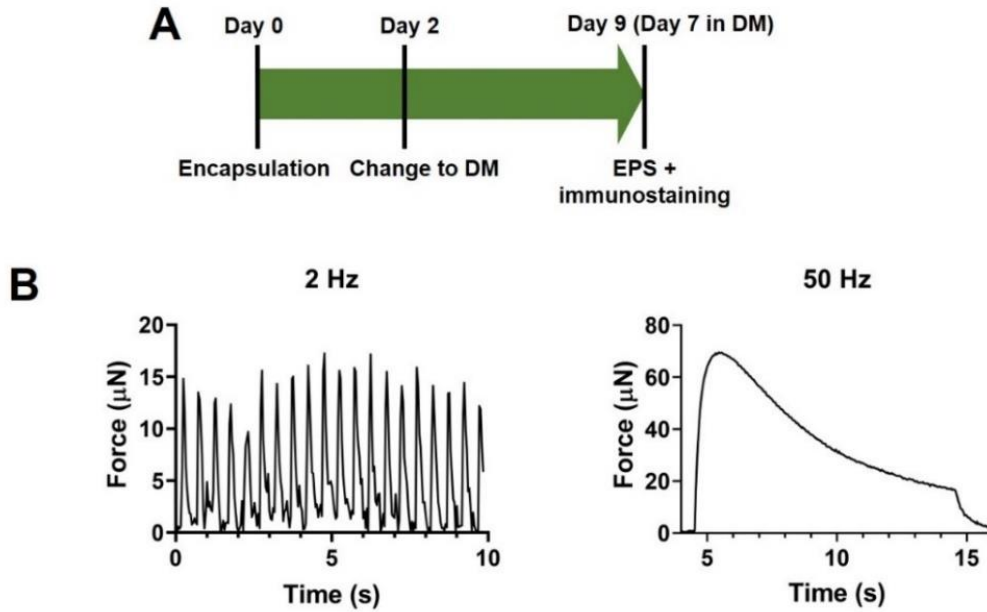


Figure 4.26. Bioengineered 3D human skeletal muscle tissues respond to electrical pulse stimulation (EPS). (A) Timeline of the experiments. (B) Representative force measurement line graphs obtained for the EPS of tissues containing 0.2 % w/v a-CNC show twitch (left) and tetanus (right) contractions with applied frequencies of 2 Hz and 50 Hz, respectively.

we expect extended culture periods combined with electrical stimulation training regimes would improve myotube maturation, obtaining uniformly striated myotubes.

Finally, the bioengineered human skeletal muscle tissues were subjected to a frequency sweep EPS regime going from low to high frequencies, according to the scheme in **Figure 4.28A**. As a proof-of-concept to compare tissue functionality between different conditions, force measurements were performed for HUGel formulations containing 0.3 and 0.2% w/v a-CNC. Remarkably, increasing a-CNC content led to a significant force reduction, and the maximum tetanus contractile force with 0.3% a-CNC was approximately four times lower than with 0.2% a-CNC. The differences in generated tissue force could be explained by the enhanced myotube differentiation and maturation resulting from the uniaxial tension during matrix compaction in 0.2% a-CNC HUGel. Moreover, increasing a-CNC content protects against growth factor release from the hydrogel during culture. As explained above, this continuous growth factor presentation is not suitable for skeletal muscle differentiation; nevertheless, further studies need to be performed to confirm this hypothesis.

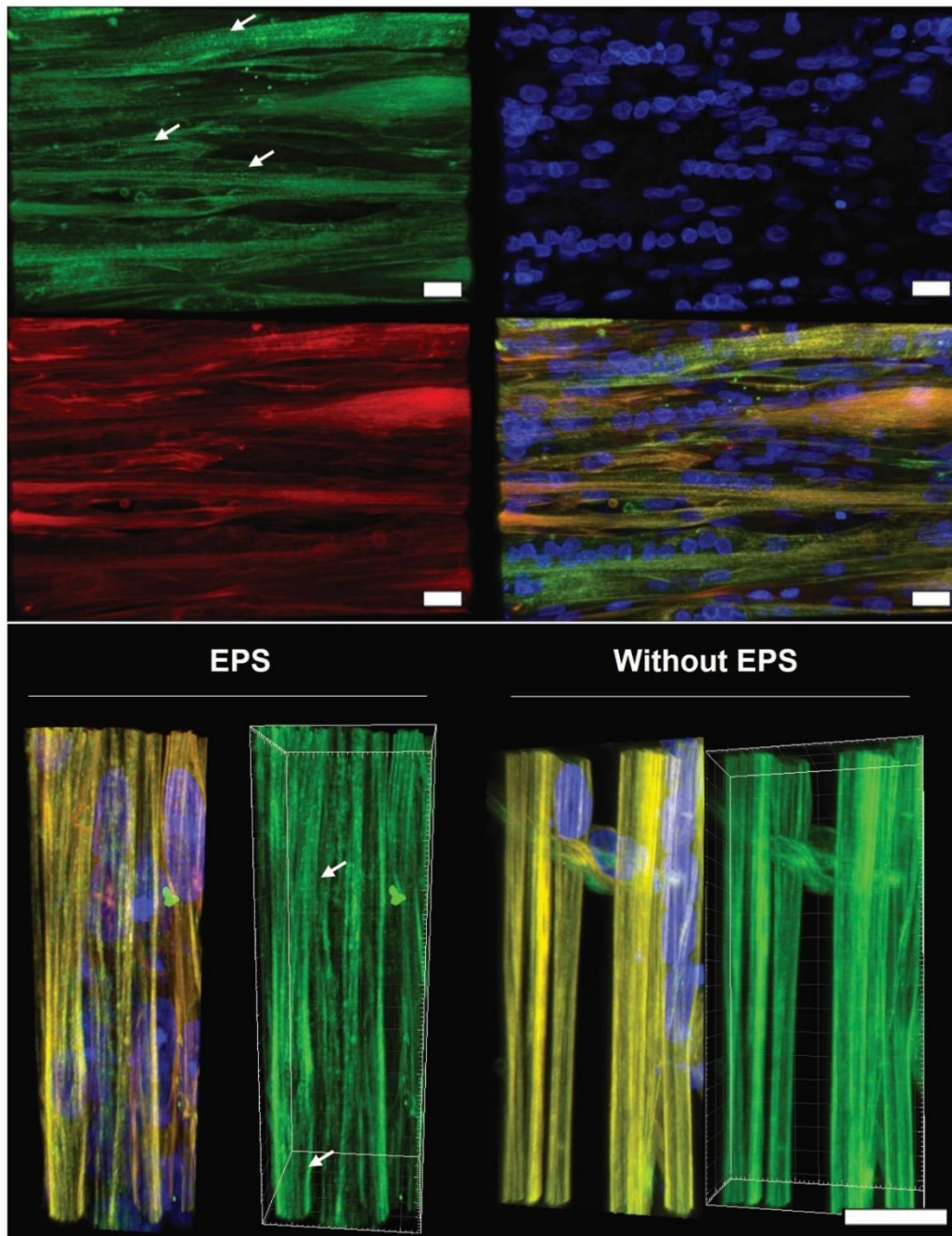


Figure 4.27. Electrically stimulated myotubes present striations after one week of differentiation. Upper panel: Representative confocal images of electrically stimulated bioengineered human skeletal muscle tissues fabricated with 0.2% w/v a-CNC. White arrows point to striated myotubes. Bottom panel: 3D reconstructions of electrically stimulated myotubes (left) vs myotubes without EPS (right). Striations are only observed in electrically stimulated myotubes. SAA is stained green, F-actin in red, and nuclei in blue. Scale bars: 20 μm .

Perspectives of this work

Altogether, these preliminary results highlight the potential of platelet lysate-based nanocomposite hydrogels to develop bioengineered skeletal muscle tissues as functional xeno-free *in vitro* models. Taking advantage of the tunable physical and biological properties of these nanocomposite hydrogels, we optimized HUgel's formulation to generate contractile human skeletal muscle tissues. As mentioned

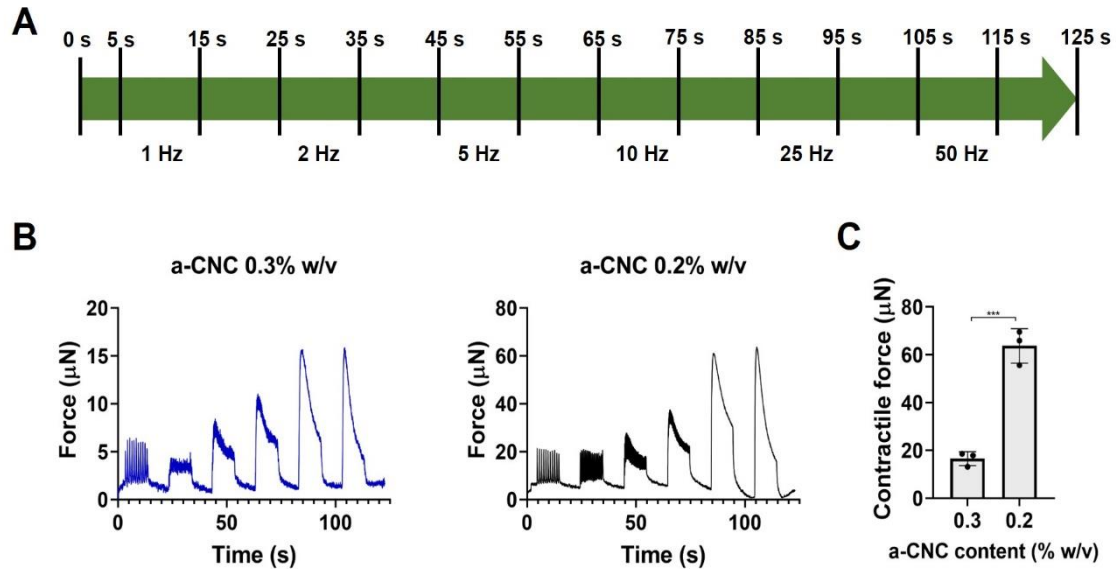


Figure 4.28. Electrical pulse stimulation (EPS) and force measurement graphs. (A) EPS scheme. (B) EPS response from bioengineered human skeletal muscle tissues fabricated with nanocomposite hydrogels containing 0.3% (left) and 0.2% w/v (right) a-CNC. Lower a-CNC content lead to stronger bioengineered skeletal muscles. Line graphs represent mean force values ($n = 3$). (C) Bar graph quantification of the maximum tetanus contractile forces generated by the bioengineered human skeletal muscle tissues with 0.3 and 0.2% w/v a-CNC. *** $p < 0.001$.

above, the maturation of these bioengineered tissues could be enhanced by increasing culture time and by electrical stimulation training. Moreover, an in-depth characterization of the obtained myotubes will be performed in the subsequent experiments, including gene expression analyses to study the difference in maturation between a-CNC loadings.

The application of this biomaterial for the 3D cell culture of human adipose stem cells has been explored in previous works [222,223]. However, at present, HUgel has not been used for the generation of any tissue models. Furthermore, the use of this biomaterial would offer several advantages for skeletal muscle tissue engineering, such as the low batch-to-batch variability of its components and its xeno-free characteristics. In fact, there are no xeno-free skeletal muscle tissue models reported to date. For drug development applications, xeno-free tissue models could provide increased relevance by eliminating animal-derived materials and reagents that could reduce sensitivity to drug effects. Additionally, the nature of these nanocomposite hydrogels offers excellent potential to develop personalized tissues that could be used for *in vitro* studies, and at the same time, could have a more straightforward translation from bench to bedside.

4.4.4. Conclusions

In this work, for the first time, a human platelet lysate-based nanocomposite hydrogel (HUGel), consisting of platelet lysate and cellulose nanocrystals, was used as a scaffold to develop *in vitro* functional human skeletal muscle tissues in a xeno-free system. The previously reported tunability of the mechanical, biochemical, and structural properties of the HUGel, enabled the generation of long, aligned multinucleated human myotubes in a custom 3D cell culture platform. In addition, this *in vitro* system provided electrical stimulation and supported force measurements of contractile bioengineered human skeletal muscle tissues. Overall, we showed that HUGel has a great potential in skeletal muscle tissue engineering for *in vitro* disease modeling. Remarkably, the xeno-free conditions could also enable future clinical applications in regenerative medicine.

Chapter 5. GENERAL RESULTS AND DISCUSSION

The skeletal muscle has a crucial role in thermogenesis, locomotion, and metabolism maintenance. This tissue is composed of bundles of aligned and multinucleated myofibers formed by the fusion of muscle precursor cells during myogenesis [68]. The complex molecular architecture of the skeletal muscle can be affected during exercise, aging, or by pathological conditions, influencing its functionality [349]. Studying skeletal muscle in physiology or pathology involves *in vitro* and *in vivo* models. These strategies have several limitations. For instance, *in vitro* studies are traditionally performed on 2D cell cultures, where precursor cells are seeded and differentiated on flat, rigid substrates far from mimicking the native muscle microenvironment [14]. Furthermore, *in vivo* animal models are limited by species-specific differences with humans [8,350], and the use of animals presents several ethical issues [351]. In contrast, 3D cell culture platforms consist of engineered skeletal muscle tissues that can better emulate the *in vivo* muscle environment and could help reducing animal experimentation [352]. Hence, there is great interest in developing *in vitro* tissue-engineered 3D culture platforms to complement the standard research models.

In recent years, technological advances in biofabrication have enabled an improved spatial organization in engineered tissues compared to traditional models [350]. Moreover, microfabricated engineered tissues can be integrated with microfluidic chips and biosensing systems to develop microphysiological platforms or organs-on-a-chip (OOCs) devices [180,353,354]. These microphysiological platforms enable *in situ* monitoring of tissue behavior under various circumstances, including drug administration and other microenvironmental conditions. Thus, OOCs have broad applications in precision medicine, drug screening, and toxicology [355]. Additionally, generating human skeletal muscle tissue models from the patients' cells would significantly advance the drug development process for muscle-related diseases [155,307]. Considering the potential impact in this field, the main objective of this doctoral thesis was to develop 3D skeletal muscle tissues for *in vitro* studies of muscle metabolism and disease modeling.

Skeletal muscle tissue engineering requires encapsulation of muscle precursor cells (myoblasts) in a suitable biomaterial scaffold [14,68,226,242]. Therefore, the first task of this work was fabricating and characterizing long-lasting biomaterials for the 3D cell culture of skeletal muscle cells. This biomaterial should have adequate porosity, biochemical signals, and topographical cues to guide *in vitro*

myogenesis [179]. Some of these characteristics influence other physicochemical properties, such as degradability and mechanical stiffness, which are important for long-lasting 3D skeletal muscle models. Hydrogels derived from mammalian animals, such as collagen and fibrin, are widely used for tissue engineering due to the intrinsic presence of cell adhesion motifs (RGD sequences) and degradation sites. Among these, we selected gelatin methacryloyl (GelMA) hydrogels. GelMA is derived from gelatin, which is denaturalized collagen [245]. Compared to other natural hydrogels, GelMA offers several advantages; for instance, it also contains methacrylate and methacrylamide functional groups that enable photopolymerization. Notably, combining photopolymerization with biofabrication strategies, such as 3D bioprinting or micromolding, allows precise control of the hydrogel's topography. As a photocrosslinkable hydrogel, GelMA has shown outstanding biocompatibility for cell seeding and encapsulation [47,213,273]. However, cell-mediated degradation of pristine GelMA scaffolds can compromise their mechanical integrity and durability [249]. To address this issue, we copolymerized GelMA with other photocrosslinkable biomaterials that are not degradable by mammalian cells, obtaining long-lasting composite hydrogels.

GelMA was mixed with a synthetic biomaterial, poly(ethylene glycol)diacrylate (PEGDA), and two polysaccharides: alginate methacrylate (AlgMA) and carboxymethyl cellulose methacrylate (CMCMA). Although GelMA has previously been copolymerized with PEGDA [356] and AlgMA [260] for tissue engineering applications, GelMA-CMCMA composite hydrogels had not been studied before this work. First, GelMA, AlgMA, and CMCMA were synthesized, and the methacrylation of the three prepolymer precursors was confirmed by ¹H-NMR. PEGDA was obtained from a commercial supplier. In addition, we worked with the C2C12 murine myoblasts cell line, which has well-established culture protocols for skeletal muscle studies [151,152]. Then, GelMA-AlgMA, GelMA-PEGDA, and GelMA-CMCMA composite hydrogels were fabricated, characterized, and compared to pristine GelMA in terms of cell viability and physicochemical properties. Finally, their application for 3D bioprinting of skeletal muscle tissue was evaluated.

Cell encapsulation in photocrosslinkable hydrogels is accomplished by free radical polymerization in the presence of a photoinitiator and UV light. Thus, after this procedure, cell survival depends on different critical factors, such as UV wavelength, energy dose, type of photoinitiator, and photoinitiator concentration. To

guarantee the biocompatibility of our protocol, we designed a multifactorial analysis for the evaluation of cell metabolic activity under different fabrication conditions. We fabricated pristine GelMA and GelMA-based composite hydrogels with the UV module (365 nm) of our 3D bioprinter. The encapsulation procedure is considered biocompatible when cells are exposed to a low dose of long-wave UV light [313]. Since the UV light intensity could not be adjusted, the received energy dose depended on the UV exposure time. Our analysis indicated that a short exposure time (5 s) and low photoinitiator concentration (0.1% w/v) resulted in significantly higher cell viability than 25 s and 0.4%, respectively. This result can be explained because the free radicals dissociating from the photoinitiator after UV exposure can be cytotoxic [50]. For this reason, photoinitiator concentration also requires careful optimization to obtain adequate crosslinking without causing cell damage. Additionally, we compared two photoinitiators, 2-hydroxy-4'-(2-hydroxyethoxy)-2-methylpropiophenone (I2959) and lithium phenyl(2,4,6-trimethylbenzoyl)phosphinate (LAP). Cell viability was significantly lower with LAP than I2959. This could be explained because LAP has a higher molar extinction coefficient at 365 nm than I2959 [49]. The photoinitiator molar extinction coefficient determines the generation of free radicals as a function of the wavelength; therefore, more free radicals were produced with LAP, generating cytotoxicity at high concentrations. Considering these findings, we fixed the following fabrication conditions: 5 s of UV exposure and 0.1% w/v of photoinitiator. Due to printability limits, the material concentration was established as 5% w/v of GelMA and 1% w/v of PEGDA, AlgMA, or CMCMA.

Myoblast fusion and subsequent myotube maturation require a long culture time, going from a few days to a couple of weeks. Moreover, engineered tissues should remain viable for several weeks to be helpful for drug screening applications. Therefore, the scaffolds need to be stable and present some resistance to cell-mediated remodeling, which occurs by enzymatic degradation. Regarding scaffold stability, cylindrical hydrogels fabricated with I2959 were too weak to maintain their shape unless UV exposure was increased. Nevertheless, this was not desirable because prolonged UV exposure would reduce cell viability. As mentioned above, LAP generates more free radicals than I2959 [49]. This results in more efficient crosslinking with a very low concentration and low energy dose, obtaining stable structures. In fact, only the samples fabricated with LAP presented a typical swelling behavior. Swelling is an important property that refers to the hydrogel's ability to

uptake water [357]. Since the skeletal muscle's ECM has a water content of approximately 75% [358], water absorption and retention are considered desirable hydrogel properties to mimic the native microenvironment. Due to poor crosslinking, the mass loss of I2959-containing samples was more significant than their water uptake. On the other hand, using LAP, we found that incorporating PEGDA, AlgMA, or CMCMA significantly increased water content compared to pristine GelMA hydrogels. This effect was due to the highly hydrophilic structure of these polymers, especially of the polysaccharides [260]. Furthermore, we showed that incorporating 1% w/v of PEGDA, AlgMA, or CMCMA in composite hydrogels led to a slower enzymatic degradation rate than GelMA hydrogels. The durability of composite hydrogels is attributed to the fact that these polysaccharides and synthetic PEGDA are not degraded by mammalian cells [257,269,270]. Remarkably, the resistance to degradation was pronounced in GelMA-AlgMA, where around 68% of initial mass remained after 4 h of incubation with collagenase type II (1.5 U mL^{-1}), compared to 21% of initial GelMA-PEGDA mass. At this time point, GelMA and GelMA-CMCMA hydrogels had completely degraded. Nevertheless, since CMCMA is not degradable by mammalian cells [257], GelMA-CMCMA degradation could be explained by the high collagenase concentration used in the experiments that completely degraded the gelatin fraction. Therefore, we expected that reducing the collagenase concentration would reveal a slower degradation rate in these composite hydrogels.

The mechanical stiffness of the ECM can influence cell morphogenesis, phenotype, and function [22,23]. Here, we investigated the modulation of the mechanical properties of GelMA hydrogels by incorporating 1% w/v of PEGDA, CMCMA, or AlgMA. Although adding PEGDA had no effect, the incorporation of CMCMA or AlgMA caused a significant change in the compressive modulus. We hypothesized that adding CMCMA resulted in a less packed hydrogel network with more water uptake capacity; therefore, Young's modulus was lower than that of GelMA hydrogels. Regarding GelMA-AlgMA, the higher values could be due to a secondary ionic crosslinking of alginate by the divalent cations present in the PBS and culture media [42]. Altogether, we obtained composite hydrogels with tunable compressive moduli in the range of $1.96 \pm 0.16 \text{ kPa}$ to $5.53 \pm 2.01 \text{ kPa}$, under the previously established fabrication conditions. Engler and colleagues demonstrated that C2C12 myotubes have optimal differentiation when seeded on 2D substrates with tissue-like stiffness (8-11 kPa) [274]. However, this is not the case for 3D cell cultures. For example, Costantini *et al.* used increasing GelMA concentrations to

modulate hydrogel stiffness and showed that as the stiffness of GelMA increased, the encapsulated C2C12 cells lost the ability to undergo rapid and efficient myogenesis [191]. Thus, they obtained the best outcome for hydrogels with the lowest stiffness (1-3 kPa). It is important to note that myoblasts in 3D culture need to spread and partially digest the surrounding matrix to fuse with neighboring cells. Therefore, the negative impact on differentiation could be more related to the material concentration (high matrix densities) than to the high stiffness of the hydrogel. Moreover, stiffer hydrogels could be obtained by increasing polymer concentration or UV exposure time. Nonetheless, this would result in more packed hydrogel networks with reduced water uptake that could also hinder nutrient diffusion and transport [319,320].

Scanning electron microscopy (SEM) analysis demonstrated that GelMA's fibrillar nanostructure was preserved in composite hydrogels, displaying an interconnected porous network. Notably, GelMA-PEGDA hydrogels appeared more densely packed than GelMA and the other composites. Besides, pore size distribution analysis showed that the fraction of pores with diameters larger than 200 nm was significantly reduced in GelMA-PEGDA compared to the other formulations. Pores larger than 200 nm in diameter are required for cell spreading and fusion within the matrix, as this is the minimum size for cells to extrude their filopodia [276–278]. In agreement, cell viability assays indicated an approximate 70% reduction in viability within GelMA-PEGDA than pristine GelMA, suggesting that the lack of bigger pores led to cell death. Importantly, we also found that cell viability was higher within the first 100 μm from the surface in all formulations, compared to deeper regions of the hydrogel samples. As various studies point out, the absence of vascularization in engineered tissues results in limited diffusion of oxygen and nutrients around 200 μm of depth [310,311]. Another factor that mildly affected cell viability with respect to pristine GelMA was the absence of cell adhesion sites in PEGDA, CMCMA, and AlgMA structures. Nevertheless, the mean values remained high for GelMA-CMCMA and GelMA-AlgMA. Furthermore, F-actin staining confirmed that cells could elongate, spread and grow within these composite hydrogels. In contrast, cells in GelMA-PEGDA remained mostly round with only some slight protrusions, indicating that the GelMA-PEGDA network was the least suitable for C2C12 growth and proliferation. It is important to note that although GelMA-PEGDA and GelMA-CMCMA hydrogels had similar Young's modulus values, their structure resulted in different cell behavior. Altogether, these findings proved that even though substrate

stiffness remains a crucial factor in 2D studies, porosity might play a more critical role in 3D hydrogels, influencing cell proliferation and spreading.

Next, we evaluated the GelMA-based composite hydrogels as cell-laden bioinks for 3D bioprinting of skeletal muscle tissue. 3D bioprinting is one of the most powerful biofabrication techniques for controlling the spatial organization of cell-laden hydrogels. Since introducing topological cues that guide cell alignment and fusion is essential for skeletal muscle tissue engineering [14,61,359], 3D bioprinting is a promising tool. It has been shown that cells with a tendency to align *in vivo* (e.g., fibroblasts, murine myoblasts, and endothelial cells) can elongate and align *in vitro* if they are geometrically confined within a suitable biomaterial [273,281]. For this reason, we printed arrays of thin filaments to promote skeletal muscle tissue formation. With extrusion bioprinting, filament thickness depends on nozzle diameter, pressure, and printing rate. Therefore, we used a 200 μm nozzle to avoid diffusion limits. Lastly, we obtained filaments of ~ 250 μm width and 200 μm height, dimensions that helped to confine myoblasts and promote their alignment and fusion into myotubes.

Unlike stable composite hydrogels, pristine GelMA hydrogels lost their 3D shape after 11 days of culture due to enzymatic degradation. We studied cell morphology and differentiation by fluorescence staining of F-actin, nuclei, and myosin heavy chain (MHC), a protein expressed in multinucleated myotubes. 3D printed composite hydrogel filaments displayed a high degree of cell alignment compared to non-patterned 3D hydrogels. Apart from geometrically confining the cells, 3D bioprinting favors alignment by generating shear stress in the nozzle [182], which results in the alignment of the polymer chains, thus aligning their RGD cell adhesion sites. Finally, the differentiation quality within the filaments was evaluated by calculating the fusion index, using MHC as an indicator of myotube formation. Fusion index was similar among GelMA, GelMA-AlgMA, and GelMA-PEGDA (~ 60 -70%). Nevertheless, the images showed that myotubes in GelMA filaments were damaged and lacked 3D shape. Furthermore, GelMA-PEGDA hydrogels appeared to contain a lower number of myotubes due to the lower number of viable cells before differentiation. In contrast, GelMA-CMCMA hydrogels presented the highest differentiation levels with a fusion index of around 80%. These results proved that it is possible to engineer skeletal muscle using any of the fabricated composite hydrogels. The outstanding differentiation within GelMA-CMCMA hydrogels could be

explained by their pore size distribution, which presented the least packed fibrillar nanostructures and the highest percentage of larger pores (>200 nm in diameter). Furthermore, GelMA-CMCMA hydrogels were less resistant to matrix remodeling by the encapsulated cells than the other composite hydrogels, enhancing cell spreading and fusion without losing scaffold integrity.

Skeletal muscle contraction is associated with several exercise-mediated health benefits, such as increased insulin sensitivity and glucose uptake [360,361]. Furthermore, the skeletal muscle was recently identified as a secretory organ that produces and releases myokines in response to contractile activity under different physiological conditions [85]. These myokines have hormone-like effects on several organs, including the muscle itself. One of the first discovered myokines was interleukin (IL)-6, which was observed to increase up to 100-fold in circulation after exercise [87]. Currently, hundreds of exercise-regulated myokines have been discovered by secretome analysis of skeletal muscle 2D cell cultures after applying electrical pulse stimulation (EPS) [362,363]. While EPS has been employed in 3D-engineered skeletal muscle tissue models to induce contractile activity [reviewed in 364], all these models focus on the forces generated by contractions and not on the skeletal muscle's endocrine function. Therefore, the second part of this thesis consisted of developing skeletal muscle microtissues in a muscle-on-a-chip for *in vitro* monitoring of muscle-secreted cytokines. Our goal was to fabricate 3D skeletal muscle microtissues in a microfluidic device capable of providing electrical or biological stimulation and simultaneously detecting cell-secreted factors. Considering our earlier work, we decided to continue working with C2C12 cells and GelMA-CMCMA composite hydrogels with the same prepolymer and photoinitiator concentrations (5% w/v GelMA, 1% w/v CMCMA, and 0.1% w/v LAP).

Although 3D bioprinting is a valuable biofabrication tool, photomold patterning was selected as an alternative strategy to generate cell-laden GelMA-CMCMA hydrogel filaments. Using photomold patterning, 3D structures can be obtained by exposing the cell-laden photocrosslinkable prepolymer to UV light through a micropatterned polydimethylsiloxane (PDMS) stamp [220]. The PDMS stamps were fabricated using conventional photolithography and soft lithography techniques, creating a reproducible pattern of microgrooves or channels with the following dimensions: 200 μm width, 270 μm height, and 200 μm of spacing. This technique offered several advantages compared to bioprinting. For example,

photopolymerization was performed using a UV crosslinker device that is more portable and cheaper than 3D bioprinters. Furthermore, our 3D bioprinter required the creation of a specific CAD file depending on the printing substrate. In contrast, photomold patterning was more straightforward since the design was incorporated in the microstructured PDMS stamps. Thus, hydrogels could potentially be fabricated on a wider variety of substrates without the need for any software, so we could directly fabricate them inside the microfluidic device. Moreover, the filament's dimensions depended on the microstructured stamp and not on other factors (e.g., pressure or printing rate), which increased reproducibility. Additionally, photomold patterning required significantly less volume of cell-laden prepolymer solution and a lower amount of cells needed per experiment, reducing the final cost of the procedure. Lastly, the UV crosslinker device had a lower UV light intensity that allowed a finer tuning of the hydrogels' physical properties using low energy doses ($0.3\text{-}2.1\text{ J cm}^{-2}$) without compromising cell viability.

The physical properties of GelMA-CMCMA hydrogels fabricated with UV exposure times from 18 to 120 s were characterized and compared to pure GelMA. In this system, the obtained Young's moduli went from 0.3 to 3.9 kPa, while pure GelMA hydrogels presented lower values in the range of 0.2 to 1.6 kPa. Furthermore, the stiffness of GelMA-CMCMA hydrogels was inversely correlated to water uptake (swelling), confirming that prolonged UV exposure led to increased matrix crosslinking and smaller pores. Moreover, degradation experiments with a low concentration of collagenase type II (0.5 U mL^{-1}) demonstrated that CMCMA incorporation results in a slower enzymatic degradation rate. Afterward, we analyzed the viability and morphology of encapsulated C2C12 cells. As expected, prolonged UV exposure led to a slight decrease in cell viability compared to short exposure times. However, after 10 days of culture, mean viability values remained high, obtaining $86 \pm 7\%$ with 60 s of exposure, compared to $92 \pm 4\%$ with 24 s of exposure. These results indicated that the photomold patterning procedure was biocompatible within our experimental conditions. As explained above, myoblasts need to elongate, spread, and sense neighboring cells to fuse into myotubes. Therefore, cell morphology becomes a more relevant factor among biocompatible hydrogels with high cell viability. Stellate morphology indicates that cells are able to move better within the hydrogel, which is essential for cell fusion. We assessed cell morphology using two cell shape descriptors, aspect ratio and circularity. The analysis showed that the cells encapsulated in softer hydrogels presented the highest aspect ratio and

lower circularity, indicating more active cell spreading in these hydrogels. Consequently, we established an exposure time of 24 s for the formation of skeletal muscle microtissues. Additionally, we increased cell density to 2.5×10^7 cells mL⁻¹ to improve cell fusion. Unlike extrusion printing, photomold patterning does not provide cell prealignment (e.g., nozzle shear stress). Nonetheless, the geometrical confinement in the micropatterned filaments was sufficient to obtain highly oriented fibers following the pattern direction. In addition, this procedure resulted in a fusion index of ~75%, indicating an efficient differentiation into MHC-expressing myotubes.

The skeletal muscle microtissues were fabricated inside microfluidic PDMS devices to form the muscle-on-a-chip platforms. The device substrate consisted of glass containing ITO-IDA electrodes to provide EPS, mimicking an *in vitro* exercise model once the tissues were formed [363,365]. As a proof of concept, we examined the myofiber release of IL-6 and tumor necrosis factor-alpha (TNF- α) upon exercise or an inflammatory process. To this end, the muscle-on-a-chip was connected to a multiplexed, high-sensitivity screen-printed gold electrode (SPGE) amperometric sensing system. The SPGEs were previously functionalized with selective monoclonal antibodies for IL-6 and TNF- α capture, which resulted in current changes directly related to cytokine concentration with low limits of detection (IL-6: 8 ng mL⁻¹; TNF- α : 2 ng mL⁻¹). In this way, we could perform *in situ* stimulation and multiplexed detection of the analytes. There are other examples in the literature where sensing systems have been coupled with microfluidic platforms to assess the metabolism of engineered tissues [287,288]. Still, the employed sensing systems only allowed daily measurements, which would not give enough information to obtain a useful *in vitro* exercise model.

IL-6 levels increase acutely following prolonged exercise in humans [87]. Initial studies pointed to a pro-inflammatory role of this cytokine as an immune response due to local damage in the muscles after contraction [92,366]. Nevertheless, it was later discovered that this acute release comes from myofibers and not immune cells [367]. Furthermore, it is now clear that the role of IL-6 depends on the cells where it is produced. When produced by myofibers, this cytokine has anti-inflammatory action [95,368]. For instance, muscle-derived IL-6 enhances insulin-stimulated glucose consumption, muscle hypertrophy, and free fatty acid oxidation, explaining some of the health benefits of exercising [88,96,98]. Additionally, exercise and muscle-produced IL-6 inhibit endotoxin-induced TNF- α

production in humans [99]. TNF- α is a major pro-inflammatory cytokine associated with skeletal muscle insulin resistance and is mainly produced by activated macrophages [369]. However, it can also be produced by myofibers at increased levels during muscle injury [370] or after highly strenuous exercise, such as marathon running [367].

In this work, we performed continuous EPS of the skeletal muscle microtissues for 1 h (5 V, 1 Hz, 2 ms) followed by a relaxation period of 1 h. The results showed a peak for IL-6 and TNF- α levels after 75 minutes (15 minutes after stopping electrical stimulation, during the relaxation phase). Then, the signals stabilized to basal levels. Notably, TNF- α release was minimal compared to IL-6 (10 ng mL⁻¹ and 1 mg mL⁻¹, respectively). The trends observed in our results correlate with *in vivo* studies with humans under physiological exercise conditions [368] and with *in vitro* assays using 2D cultures of primary human myotubes [363]. First, Steensberg *et al.* measured plasma levels of IL-6 and TNF- α of healthy individuals every 60 minutes during 3 h of continuous exercise [368]. While IL-6 showed a marked increase, reaching the maximum values after 3 h, TNF- α plasma concentration did not significantly change compared to rest levels. Then, Scheler *et al.* performed immunoassays on the culture medium of primary human myotubes in 2D after 24 h of EPS [363]. Likewise, TNF- α was detected at low levels before EPS and did not significantly change after 24 h of stimulation. On the other hand, IL-6 had a pronounced increase, demonstrating the myofiber release of this myokine after EPS-induced contraction with no cell damage and without immune cells, similar to our results. As previously mentioned, increased levels of skeletal muscle-secreted TNF- α have only been seen upon muscle injury or highly strenuous exercise [367,370]. Hence, it is possible that a more intense EPS regime in our experiments would lead to higher cytokine levels than those obtained.

Finally, to examine the skeletal muscle microtissue response to endotoxin-induced inflammation, we added *Escherichia coli* lipopolysaccharide (LPS, 10 μ g mL⁻¹) to the culture medium and measured cytokine release for 48 h (without EPS). Prior 2D assays showed that LPS treatment resulted in IL-6 release from the C2C12 monolayer, but we observed no changes in TNF- α . In contrast, applying the same treatment in the 3D muscle-on-a-chip device, we could detect a slow but constant release of TNF- α up to ~2-fold basal levels. With IL-6, the strongest secretion levels were reached at 1 h of treatment, staying constant for 48 h. These results are in

agreement with a previous study with humans by Starkie and colleagues, where volunteers received a bolus of LPS to induce low-grade inflammation. Notably, their results also indicated that when the subjects were in resting conditions, LPS administration stimulated TNF- α secretion up to 2-fold [99]. Likewise, in their *in vivo* experiments, endotoxin-induced IL-6 levels were increased without exercising and stayed constant throughout the experiment. However, IL-6 only increased 10-fold after LPS administration, whereas exercise resulted in a 19-fold increase. In contrast to the study by Starkie and colleagues, we observed a higher increase in endotoxin-induced IL-6 secretion compared to EPS experiments. This difference might be attributed to the high LPS dose, which could be optimized to mimic low-grade inflammation and would result in a reduced IL-6 secretion. Altogether, the results demonstrated that the 3D skeletal muscle microtissues generated by photomold patterning are suitable for applications in muscle-on-a-chip platforms. In particular, our platform offered simultaneous *in situ* stimulation of engineered tissues and multiplexed detection of secreted cytokines over time. Using this system, we obtained *in vivo*-like metabolic responses from 3D skeletal muscle tissues. Furthermore, these muscle-on-a-chip devices could provide more insight into the timing of cytokine release than the equivalent *in vivo* experiments, which would require several invasive blood tests per hour.

The C2C12 cell line has been successfully employed for decades in biomedical research due to the similarities between murine and human myoblasts [151,152]. The high proliferation rate and well-established protocols for C2C12 culture make it a useful cell line to develop tissue engineering strategies before using human myoblasts, which are not as easy to obtain in large quantities. However, engineered tissues from murine cells still lack physiological relevance to humans [153]. For this reason, it is of great interest to create 3D models of human skeletal muscle tissue, especially for disease modeling. The skeletal muscle can be affected by several disorders. Among these, muscular dystrophies are a group of hereditary diseases with variable phenotypes, all characterized by muscle weakness and atrophy [104,109]. Research on efficient therapies is ongoing; however, there is still no cure for most of these diseases. Besides, the intrinsic genetic variability of muscular dystrophies makes it difficult to predict individual responses to therapies. For these reasons, human skeletal muscles generated from patients' cells are necessary to accelerate preclinical research. However, only a couple of research

groups have introduced patient-derived cells in 3D cell cultures to model human muscular dystrophies [211,347].

Myotonic dystrophy type 1 (DM1) is the most common hereditary myopathy in adults, characterized by progressive skeletal muscle degeneration that results in severe disability. The pathogenic molecular mechanisms of DM1 have been widely researched, allowing the testing of new therapeutic strategies that have promising preliminary results in 2D cell cultures and animal models [371]. However, these models cannot replicate the biological complexity of the disease. Thus, to complement current preclinical research strategies, the third part of this thesis consisted of developing the first *in vitro* 3D model of DM1 human skeletal muscle. The human skeletal muscle microtissues were fabricated through photomold patterning of cell-laden GelMA-CMCMA hydrogels on top of functionalized glass coverslips. Furthermore, we modified the previous protocol to optimize it for human cells. We first observed undesired cell growth on the glass substrate between GelMA-CMCMA filaments, resulting in a separate cell population in 2D. Therefore, the coverslips were silanized and coated with a thin PEGDA layer before photomold patterning. As previously discussed, PEGDA lacks cell adhesion motifs and is inert to protein adsorption [312], which reduced cell adhesion on the substrate. Additionally, GelMA-CMCMA hydrogels were covalently attached to PEGDA [47], which increased the stability of the micropatterns over time. Although cells were mostly aligned within 200 μm wide hydrogel filaments, we observed a marked improvement in cell orientation when confining them in hydrogels with smaller features. Thus, we fabricated micromolded cell-laden hydrogel filaments of 100 μm width, height, and spacing. However, with these thinner filaments, UV exposure of 24 s was insufficient to obtain stable structures that would not break after removing the PDMS stamp.

To improve the strength of the filaments, we increased exposure time to 30 s. The received energy dose remained low (0.48 J cm^{-2}) compared to 5 s of UV exposure using our 3D bioprinter (15 J cm^{-2}) and other works where cell-laden GelMA hydrogels have been crosslinked with higher energy doses up to 36 J cm^{-2} [315]. Also, we confirmed the biocompatibility of the protocol with cell cytotoxicity assays that showed more than 88% of viable cells 24 h after encapsulation. As previously discussed, the optimal stiffness for myoblasts encapsulation mostly depends on the biomaterial used but leans toward soft hydrogels. For instance, human myoblasts

have been encapsulated in fibrin-based hydrogels with Young's modulus of 1 ± 0.1 kPa [200]. The mechanical characterization of these GelMA-CMCMA hydrogels was performed using uniaxial compression tests and AFM microindentation measurements, obtaining Young's modulus values in the range of 0.5-0.7 kPa. Furthermore, the fibrillar nanostructure of photomolded hydrogels was analyzed by SEM and compared to the PEGDA hydrogel layer. While PEGDA images revealed a dense, non-porous matrix, GelMA-CMCMA presented an interconnected porous network that could support oxygen and nutrient diffusion through the hydrogel.

One of the main challenges of tissue-engineered 3D cell culture models is the large number of cells required for their development. In skeletal muscle disease models, cells are obtained from muscle biopsies of patients, which are invasive and not always available. Moreover, primary DM1 myoblasts have a limited proliferative capacity due to premature senescence [316]. To overcome these limitations, we used transdifferentiated myoblasts cell lines established at the Institute of Myology (Paris) [162]. These cell lines consisted of immortalized fibroblasts from skin biopsies which could be converted to myoblasts through the overexpression of MYOD1. We first confirmed that encapsulated patient-derived cells presented hallmark features of DM1, such as nuclear RNA aggregates (foci) of expanded CUG repeats which were colocalized with MBNL1 [115,162]. Bioengineered skeletal muscle microtissues were generated from DM1 patient-derived cells or healthy donor cells (control). Then, 3D cultures were differentiated for 7, 14, or 21 days before immunostainings for myosin heavy chain 7 (MYH7) and sarcomeric α -actinin (SAA). In agreement with previous reports, we observed that DM1 cells in 2D cell culture have a low fusion index compared to controls. In contrast, long-multinucleated DM1 myotubes expressing MYH7 and SAA were formed after 7 days of 3D cell culture, demonstrating that 3D micropatterning enhanced the fusion capability of DM1 cells.

Although the fusion index in bioengineered microtissues was similar between DM1 and control microtissues, we observed some structural differences. Therefore, we analyzed myotube diameters over time using 3D reconstructions of confocal z-stack images. As expected, the diameter increased between one and two weeks of culture owing to myotube maturation. However, after three weeks, the diameter of control myotubes did not increase, possibly due to cell senescence. Therefore, we determined that further assays with these skeletal muscle microtissues should be performed before three weeks of culture. Remarkably, the analysis of 3D

reconstructions revealed that DM1 myotubes had a reduced diameter compared to healthy controls (13.4 vs. 21.7 μm) after 7 days of differentiation. Since impaired differentiation has been reported in myoblasts from transgenic DM1 mice [326] and DM1 patients [327], fusion index had been used to investigate some aspects of DM1 pathology [328,329], characterize cell lines [162], and test potential treatments that could restore differentiation [330]. However, DM1 presents in adulthood when tissues are already formed but present myofiber size reduction, among other characteristics [115]. Therefore, we proposed that the reduced myotube diameter in DM1 should be used instead of the fusion index as a new *in vitro* 3D phenotype due to its increased physiological relevance.

The genetic cause of DM1 is a dynamic mutation in the *Dystrophia myotonica protein kinase (DMPK)* gene [119]. Briefly, mutant CUG repeat RNAs accumulate in nuclear foci [120], sequestering proteins of the Muscleblind-like (MBNL) family and causing their loss of function [132]. Thus, one of the most promising therapeutic strategies for DM1 is using antisense oligonucleotides (antagomiRs) which can silence microRNAs (miRs) that inhibit MBNL translation. Treatment with antagomiR-23b has successfully increased MBNL protein levels and rescued mis-splicing events in 2D cultures of human DM1 myoblasts [143] and the HSA^{LR} DM1 model mice [144]. In these works, long-lasting biological effects were observed, with high efficacy and low toxicity. Therefore, we evaluated the therapeutic effect of antagomiR-23b (α -miR-23b) on bioengineered DM1 skeletal muscles. After three days of culture, once cells were aligned and started to fuse, we added α -miR-23b or scramble control antagomiR (sc-control) to the culture media. The treatment lasted for seven days before analyzing its molecular and structural effects on the 3D DM1 human skeletal muscle microtissues.

Our results demonstrated a reduction of miR-23b expression in DM1 muscles treated with α -miR-23b compared to sc-control. Although miR-23b silencing only enhanced MBNL2 and not MBNL1 transcripts, western blot quantification showed an increase in MBNL1-2 protein levels upon α -miR-23b treatments. Moreover, we demonstrated that the increase of MBNL1-2 protein levels rescues characteristic DM1 spliceopathy for three splicing events: *BIN1*, *NFIX*, and *SPTAN1*. However, rescue levels were lower than those obtained in previous 2D studies [143]. The differences could be attributed to the different antagomiR delivery strategies. While 2D myoblasts in those studies were transfected, we used gymnotic delivery.

Transfection allows the internalization of large amounts of oligonucleotides by using a delivery vehicle [331]. Nevertheless, gymnotic delivery is more physiologically relevant. With this approach, 'naked' delivery of oligonucleotides is performed by exposing cells to a constant oligonucleotide concentration, resembling *in vivo* treatments where plasma and tissues are exposed to saline-formulated oligonucleotides. Nevertheless, the dosage could be optimized to improve the antagomiR therapeutic effects for future assays. Finally, we evaluated the structural changes of DM1 myotubes upon α -miR-23b treatment. Remarkably, we found that myotube diameter was restored to healthy control sizes after seven days of treatment, obtaining mean myotube diameters of 14.4 or 21.9 μm for sc-control or α -miR-23b treatment, respectively. Overall, we proved that this patient-derived 3D model could complement existing *in vitro* and *in vivo* models. This model could be a useful platform for preclinical research of different DM1 therapies. Furthermore, we could assess drug effects at different levels, such as transcriptional, post-transcriptional, and structural phenotype effects. Altogether, the developed protocol for this disease could be easily translated for studies on other muscular dystrophies.

One of the next steps in human skeletal muscle tissue engineering involves improving biomaterial formulations. Nearly all biomaterials used as scaffolds nowadays include animal-derived components. The most common are gelatin from porcine skin, collagen from rat tail, and fibrinogen from bovine plasma [reviewed in 61]. These are often combined with murine tumor cell-derived matrices, such as Matrigel[®] or Geltrex[™]. Some of these biomaterials have ill-defined or highly variable batch-to-batch compositions that can limit the reproducibility and accuracy of cell-based assays [335,337,338]. Moreover, from a regenerative medicine perspective, the possible presence of xenogenic contaminants makes it difficult to consider their future translation as tissue replacements [339,340]. To this date, the only published 3D human skeletal muscle study where the biomaterial was non-xenogenic still used animal-derived serum in the culture media [207]. Although animal serum is typically used in cell culture, some studies have shown that it could reduce sensitivity to drug toxicity within *in vitro* testing platforms [14,372,373]. For these reasons, the last part of this doctoral thesis focused on creating a xeno-free 3D skeletal muscle tissue model.

In this work, we used a human platelet lysate-based nanocomposite hydrogel (HUgel). HUgel is a xeno-free biomaterial with tunable structural, mechanical, and

biochemical properties developed by researchers from the i3Bs Research Institute at the University of Minho [222]. These nanocomposite hydrogels were formed by inducing the human platelet lysate (PL) coagulation cascade while incorporating cellulose nanocrystals modified with surface aldehyde groups (a-CNC). Since PL mostly contains fibrinogen, its self-assembly can be induced by mixing with thrombin and/or calcium ions, obtaining fibrin-based scaffolds [374]. The physical and biological properties of HUgel were extensively characterized by Mendes *et al.*, displaying their outstanding tunability. Moreover, the researchers applied this hydrogel as a scaffold for serum-free culture of human adipose stem cells [223]. Their results showed that HUgel remarkably enhanced cell spreading and proliferation compared to GelMA and alginate in serum-free cell culture. Adding to these features, the compactable nature of HUgel makes it an attractive biomaterial for cell encapsulation in hydrogel casting systems that provide uniaxial tension during matrix compaction. Considering these characteristics and previous works in the field [186,188,193,204,208,209,235,333], we fabricated hydrogel casting platforms containing two flexible PDMS posts as anchor points. These systems also permit *in situ* monitoring of posts deflections caused by tissue contractions, which can be transformed into force measurements.

To generate skeletal muscle tissues, we encapsulated human immortalized skeletal muscle satellite stem cells in HUgel. In these hydrogel casting techniques, matrix compaction is key to provide uniaxial tension and promote myoblasts' organization during tissue formation. Our initial results demonstrated that one factor influencing HUgel compaction was matrix remodeling by the encapsulated cells. Therefore, we fixed a high cell density of 2.5×10^7 cells mL⁻¹ to increase matrix compaction. Another factor affecting HUgel compaction was the a-CNC content. The compaction of the fibrin matrix (clot retraction) can be hindered with increasing a-CNC loadings, as has been described by Mendes *et al.* [222]. Although this reduction in gel volume is undesired for other tissue engineering applications [375], cell organization due to the generated uniaxial tension can favor myoblast fusion from early cell culture stages. Thus, we modulated a-CNC content to obtain long-lasting hydrogels with high clot retraction properties. Notably, PL gels without a-CNC resulted in the highest matrix compaction after 12 h of culture (~66.4%). Nevertheless, tissues collapsed within the first days due to the lack of mechanical reinforcement from the a-CNC. In contrast, nanocomposite hydrogels with only 0.2% w/v of a-CNC were stable for at least two weeks with matrix compaction of

approximately 46.7% after the first 12 h of culture. Besides structural functions, a-CNC content in nanocomposite hydrogels can regulate growth factor retention within the scaffolds due to the formation of a protein corona on the a-CNC surface [222,223,376]. This means that increasing a-CNC loadings results in greater growth factor retention in the hydrogels. Slow growth factor release from the scaffolds is beneficial for other 3D cell culture applications that involve maintaining cell stemness, proliferation, or directed wound healing [377–379]. However, it is well known that *in vitro* skeletal muscle differentiation would be impaired by a microenvironment rich in growth factors [14]. Taken together, we proposed that HUgel formulations containing a low percentage of a-CNC (0.2% w/v) are the most suitable for skeletal muscle tissue engineering.

Long, highly aligned, multinucleated myotubes expressing SAA could be observed after one week of serum-free differentiation. At this time, we evaluated the functionality of human skeletal muscles by assessing their contractile response upon EPS. Different from our previous models, hydrogel casting enabled the measurement of contractile forces. Here, the posts deflection caused by tissue contractions could be transformed into forces by taking into account the geometry, dimensions, and Young's modulus of the PDMS posts [209,235]. Upon EPS, the bioengineered tissues exhibited twitch or tetanic contractions depending on the applied frequencies. The presence of sarcomeric structures is an indicator of myotube maturation. These structures were not present after one week of differentiation in non-stimulated tissues. However, after applying EPS, we could observe these structures in the form of striations in some myotubes. Generally, myotubes require longer culture periods to obtain a more uniform maturation throughout the samples. Moreover, it has been shown that EPS training regimes successfully enhance the maturation of engineered skeletal muscles [186,203]. Therefore, we expected that further optimization of our protocol would significantly improve the maturation of our tissues.

Force measurements in this system could be useful for comparing tissue functionality between different cell lines (e.g., healthy vs. dystrophic) or analyzing the response to a particular treatment. In this work, we compared the tissue response between different nanocomposite hydrogel formulations containing 0.3 and 0.2% w/v of a-CNC. We performed a frequency sweep EPS regime from low to high frequencies and observed that tissues containing 0.3% w/v of a-CNC had a significantly reduced force along the frequency sweep. Notably, a-CNC content of

0.3% w/v led to an approximately four-fold decrease in the maximum tetanus contractile force, compared to 0.2% w/v. We hypothesized that the differences in tissue forces could be explained by the superior myotube differentiation and maturation on 0.2% a-CNC HUGel. Our results showed that this HUGel formulation resulted in greater matrix compaction, which induced uniaxial tension on the tissues. Besides, as mentioned above, higher a-CNC loadings result in a continuous growth factor presentation that could hamper skeletal muscle differentiation. Nevertheless, our next task will be to perform a thorough characterization of the obtained myotubes, including gene expression analyses, to study the difference in myotube differentiation and maturation between a-CNC loadings. Altogether, these preliminary results demonstrated the potential of tunable HUGel to develop a xeno-free human skeletal muscle tissue model. The elimination of animal-derived components from *in vitro* skeletal muscle models provides an increased relevance for human studies. Furthermore, the knowledge acquired with these systems would be easier to translate into regenerative medicine applications.

The results presented in this doctoral thesis highlight the application of microfabricated composite hydrogels as biomaterials for skeletal muscle tissue engineering. Overall, skeletal muscle precursor cells were encapsulated in these biomaterials employing different hydrogel microfabrication techniques, such as 3D bioprinting and hydrogel micromolding, to introduce topographical cues that supported the formation of 3D skeletal muscle tissues. Photomold patterning of GelMA-CMCMA composite hydrogels allowed differentiation of myoblasts into highly aligned, multinucleated myotubes expressing sarcomeric proteins. The bioengineered skeletal muscle microtissues supported long-term culture without losing mechanical stability. Notably, the endocrine function of these tissues was monitored in a muscle-on-a-chip device, obtaining *in vivo*-like responses upon electrical or biological stimulation. Furthermore, the optimized biofabrication protocol was applied to develop the first *in vitro* 3D model of myotonic dystrophy type 1 (DM1) human skeletal muscle. Remarkably, we proved that these bioengineered microtissues could be useful for drug screening applications in which drug effects can be assessed on molecular and structural levels. Lastly, a human platelet lysate-based nanocomposite hydrogel (HUGel) was used for the fabrication of functional human skeletal muscle microtissues in a xeno-free cell culture platform capable of *in situ* force measurements. Altogether, these *in vitro* 3D models represent significant

advances with respect to traditional cell cultures and animal models for studies of muscle physiology or disease modeling.

Chapter 6. CONCLUSIONS

1. Photocrosslinkable GelMA-based composite hydrogels were evaluated as biomaterials for the encapsulation and differentiation of skeletal muscle precursor cells. The incorporation of PEGDA, AlgMA, or CMCMA resulted in long-lasting 3D scaffolds with a slower enzymatic degradation rate and tunable mechanical properties. Our results showed that although mechanical stiffness is a key property in 2D skeletal muscle studies, pore size distribution may play a more critical role for cell spreading and elongation in 3D culture. Together with the composite hydrogel's properties, 3D bioprinting conditions and scaffold geometry promoted the alignment of myoblasts and supported differentiation into multinucleated myotubes.

2. Murine or human 3D skeletal muscle microtissues were fabricated by photomold patterning of cell-laden GelMA-CMCMA composite hydrogels. The presented protocols are biocompatible and can be easily reproduced. Importantly, the geometrical confinement in micropatterned hydrogel filaments produced highly aligned myotubes expressing sarcomeric proteins. These muscle microtissues could be maintained in long-lasting cell cultures.

3. Murine skeletal muscle microtissues were fabricated in a muscle-on-a-chip microfluidic device for *in vitro* monitoring of muscle-secreted cytokines. The platform was capable of *in situ* electrical or biological stimulation and simultaneous multiplexed detection of IL-6 and TNF- α . The obtained metabolic responses emulated previously reported *in vivo* experiments on exercise and endotoxin-induced inflammation.

4. We developed the first *in vitro* 3D model of myotonic dystrophy type 1 (DM1) human skeletal muscle. Patient-derived cells encapsulated in GelMA-CMCMA hydrogels presented the molecular characteristics of DM1. We demonstrated that 3D micropatterning significantly improved DM1 myotube formation compared to traditional 2D cultures. A new 3D structural phenotype was detected, the reduced thickness of DM1 myotubes compared to healthy control myotubes. Notably, proof-of-concept experiments demonstrated that treatment with antagomiR-23b resulted in the rescue of both molecular DM1 hallmarks and structural phenotype, restoring myotube diameter to healthy control sizes.

5. Human platelet lysate-based nanocomposite hydrogels (HUgel) were used as scaffolds to develop *in vitro* functional human skeletal muscle tissues in xeno-free cell culture. The content of cellulose nanocrystals was modulated to favor uniaxial tension, self-organization, cell fusion, and differentiation into long multinucleated myotubes expressing sarcomeric α -actinin. This *in vitro* system allowed *in situ* force measurements of the electrical stimulation-induced contractions.
6. Overall, the 3D skeletal muscle tissues presented in this thesis represent an improvement over conventional cell culture. The biofabrication protocols can be employed to model other muscular dystrophies by incorporating patient-derived cells. These functional bioengineered skeletal muscle tissues could be useful for fundamental studies and test drug efficacy at preclinical levels.

REFERENCES

- [1] Vacanti J P and Vacanti C A 2014 The History and Scope of Tissue Engineering *Principles of Tissue Engineering* ed R Lanza, R Langer and J Vacanti (Boston: Academic Press) pp 3–8
- [2] Wobma H and Vunjak-Novakovic G 2016 Tissue Engineering and Regenerative Medicine 2015: A Year in Review *Tissue Eng. Part B Rev.* **22** 101–13
- [3] Langer R and Vacanti J 1993 Tissue engineering *Science (80-.)*. **260** 920–6
- [4] Vacanti J P and Langer R 1999 Tissue engineering: The design and fabrication of living replacement devices for surgical reconstruction and transplantation *Lancet* **354** 32–4
- [5] Nerem R M and Schutte S C 2014 The Challenge of Imitating Nature *Principles of Tissue Engineering* ed R Lanza, R Langer and J Vacanti (Boston: Elsevier) pp 9–24
- [6] Daley W P, Peters S B and Larsen M 2008 Extracellular matrix dynamics in development and regenerative medicine *J. Cell Sci.* **121** 255–64
- [7] Tibbitt M W and Anseth K S 2009 Hydrogels as extracellular matrix mimics for 3D cell culture *Biotechnol. Bioeng.* **103** 655–63
- [8] Bersini S, Arrigoni C, Lopa S, Bongio M, Martin I and Moretti M 2016 Engineered miniaturized models of musculoskeletal diseases *Drug Discov. Today* **21** 1429–36
- [9] Duval K, Grover H, Han L-H H, Mou Y, Pegoraro A F, Fredberg J and Chen Z 2017 Modeling Physiological Events in 2D vs. 3D Cell Culture *Physiology* **32** 266–77
- [10] Jaiswal N, Haynesworth S E, Caplan A I and Bruder S P 1997 Osteogenic differentiation of purified, culture-expanded human mesenchymal stem cells in vitro. *J. Cell. Biochem.* **64** 295–312
- [11] Schnaper H W, Grant D S, Stetler-Stevenson W G, Fridman R, D'Orazi G, Murphy A N, Bird R E, Hoythya M, Fuerst T R, French D L, Quigley J P and Kleinman H K 1993 Type IV collagenase(s) and TIMPs modulate endothelial cell morphogenesis in vitro *J. Cell. Physiol.* **156** 235–46
- [12] Petersen O W, Ronnov-Jessen L, Howlett A R and Bissell M J 1992 Interaction with basement membrane serves to rapidly distinguish growth and differentiation pattern of normal and malignant human breast epithelial cells. *Proc. Natl. Acad. Sci.* **89** 9064–8
- [13] Tanaka H, Murphy C L, Murphy C, Kimura M, Kawai S and Polak J M 2004 Chondrogenic differentiation of murine embryonic stem cells: Effects of culture

- conditions and dexamethasone *J. Cell. Biochem.* **93** 454–62
- [14] Khodabukus A and Baar K 2016 Factors that affect tissue-engineered skeletal muscle function and physiology *Cells Tissues Organs* **202** 159–68
- [15] Edmondson R, Broglie J J, Adcock A F and Yang L 2014 Three-Dimensional Cell Culture Systems and Their Applications in Drug Discovery and Cell-Based Biosensors *Assay Drug Dev. Technol.* **12** 207–18
- [16] Taylor M J, Tanna S and Sahota T 2010 In Vivo Study of a Polymeric Glucose-Sensitive Insulin Delivery System Using a Rat Model *J. Pharm. Sci.* **99** 4215–27
- [17] DiMasi J A, Grabowski H G and Hansen R W 2016 Innovation in the pharmaceutical industry: New estimates of R&D costs *J. Health Econ.* **47** 20–33
- [18] Dowden H and Munro J 2019 Trends in clinical success rates and therapeutic focus *Nat. Rev. Drug Discov.* **18** 495–6
- [19] Baker B M and Chen C S 2012 Deconstructing the third dimension-how 3D culture microenvironments alter cellular cues *J. Cell Sci.* **125** 3015–24
- [20] Ashe H L and Briscoe J 2004 The interpretation of morphogen gradients *Development* **133** 385–94
- [21] Ramanujan S, Pluen A, McKee T D, Brown E B, Boucher Y and Jain R K 2002 Diffusion and Convection in Collagen Gels: Implications for Transport in the Tumor Interstitium *Biophys. J.* **83** 1650–60
- [22] Eyckmans J, Boudou T, Yu X and Chen C S 2011 A Hitchhiker's Guide to Mechanobiology *Dev. Cell* **21** 35–47
- [23] Engler A J, Sen S, Sweeney H L and Discher D E 2006 Matrix Elasticity Directs Stem Cell Lineage Specification *Cell* **126** 677–89
- [24] Saha K, Pollock J F, Schaffer D V. and Healy K E 2007 Designing synthetic materials to control stem cell phenotype *Curr. Opin. Chem. Biol.* **11** 381–7
- [25] Wade R J, Bassin E J, Rodell C B and Burdick J A 2015 Protease-degradable electrospun fibrous hydrogels *Nat. Commun.* **6** 6639
- [26] Hoffman A S 2002 Hydrogels for biomedical applications *Adv. Drug Deliv. Rev.* **54** 3–12
- [27] Khademhosseini A and Langer R 2007 Microengineered hydrogels for tissue engineering *Biomaterials* **28** 5087–92

- [28] Yue K, Trujillo-de Santiago G, Alvarez M M M, Tamayol A, Annabi N and Khademhosseini A 2015 Synthesis, properties, and biomedical applications of gelatin methacryloyl (GelMA) hydrogels *Biomaterials* **73** 254–71
- [29] Kharkar P M, Kiick K L and Kloxin A M 2013 Designing degradable hydrogels for orthogonal control of cell microenvironments *Chem. Soc. Rev.* **42** 7335–72
- [30] Xiao S, Zhao T, Wang J, Wang C, Du J, Ying L, Lin J, Zhang C, Hu W, Wang L and Xu K 2019 Gelatin Methacrylate (GelMA)-Based Hydrogels for Cell Transplantation: an Effective Strategy for Tissue Engineering *Stem Cell Rev. Reports* **15** 664–79
- [31] Dawson E, Mapili G, Erickson K, Taqvi S and Roy K 2008 Biomaterials for stem cell differentiation *Adv. Drug Deliv. Rev.* **60** 215–28
- [32] Cushing M C and Anseth K S 2007 Hydrogel Cell Cultures *Science (80-.)*. **316** 1133–4
- [33] Park K, Na K and Chung H 2005 Enhancement of the adhesion of fibroblasts by peptide containing an Arg-Gly-Asp sequence with poly(ethylene glycol) into a thermo-reversible hydrogel as a synthetic extracellular matrix *Biotechnol. Lett.* **27** 227–31
- [34] Seliktar D 2012 Designing Cell-Compatible Hydrogels for Biomedical Applications *Science (80-.)*. **336** 1124–8
- [35] Liu H, Wang Y, Cui K, Guo Y, Zhang X and Qin J 2019 Advances in Hydrogels in Organoids and Organs-on-a-Chip *Adv. Mater.* **31** 1–28
- [36] Lin C-C C and Metters A T 2006 Hydrogels in controlled release formulations: Network design and mathematical modeling *Adv. Drug Deliv. Rev.* **58** 1379–408
- [37] Lutolf M P and Hubbell J A 2005 Synthetic biomaterials as instructive extracellular microenvironments for morphogenesis in tissue engineering *Nat. Biotechnol.* **23** 47–55
- [38] Martino M M, Mochizuki M, Rothenfluh D A, Rempel S A, Hubbell J A and Barker T H 2009 Controlling integrin specificity and stem cell differentiation in 2D and 3D environments through regulation of fibronectin domain stability *Biomaterials* **30** 1089–97
- [39] Lutolf M P, Lauer-Fields J L, Schmoekel H G, Metters A T, Weber F E, Fields G B and Hubbell J A 2003 Synthetic matrix metalloproteinase-sensitive hydrogels for the conduction of tissue regeneration: Engineering cell-invasion characteristics *Proc. Natl. Acad. Sci.* **100** 5413–8
- [40] Murphy M P, Niedziela D A and Keane O M 2017 EHS matrix incubated in media containing penicillin retains sufficient concentrations of antibiotic to inhibit growth of susceptible microorganisms *J. Microbiol. Methods* **139** 103–6

- [41] Miller J S, Stevens K R, Yang M T, Baker B M, Nguyen D-H T, Cohen D M, Toro E, Chen A A, Galie P A, Yu X, Chaturvedi R, Bhatia S N and Chen C S 2012 Rapid casting of patterned vascular networks for perfusable engineered three-dimensional tissues *Nat. Mater.* **11** 768–74
- [42] Drury J L, Dennis R G and Mooney D J 2004 The tensile properties of alginate hydrogels *Biomaterials* **25** 3187–99
- [43] Tenje M, Cantoni F, Porras Hernández A M, Searle S S, Johansson S, Barbe L, Antfolk M and Pohlit H 2020 A practical guide to microfabrication and patterning of hydrogels for biomimetic cell culture scaffolds *Organs-on-a-Chip* **2** 100003
- [44] HAHN M, TAITE L, MOON J, ROWLAND M, RUFFINO K and WEST J 2006 Photolithographic patterning of polyethylene glycol hydrogels *Biomaterials* **27** 2519–24
- [45] Khetan S and Burdick J A 2010 Patterning network structure to spatially control cellular remodeling and stem cell fate within 3-dimensional hydrogels *Biomaterials* **31** 8228–34
- [46] Van Den Bulcke A I, Bogdanov B, De Rooze N, Schacht E H, Cornelissen M and Berghmans H 2000 Structural and Rheological Properties of Methacrylamide Modified Gelatin Hydrogels *Biomacromolecules* **1** 31–8
- [47] Nichol J W, Koshy S T, Bae H, Hwang C M, Yamanlar S and Khademhosseini A 2010 Cell-laden microengineered gelatin methacrylate hydrogels *Biomaterials* **31** 5536–44
- [48] Kufelt O, El-Tamer A, Sehring C, Meißner M, Schlie-Wolter S and Chichkov B N 2015 Water-soluble photopolymerizable chitosan hydrogels for biofabrication via two-photon polymerization *Acta Biomater.* **18** 186–95
- [49] Fairbanks B D, Schwartz M P, Bowman C N and Anseth K S 2009 Photoinitiated polymerization of PEG-diacrylate with lithium phenyl-2,4,6-trimethylbenzoylphosphinate: polymerization rate and cytocompatibility *Biomaterials* **30** 6702–7
- [50] Mironi-Harpaz I, Wang D Y, Venkatraman S and Seliktar D 2012 Photopolymerization of cell-encapsulating hydrogels: Crosslinking efficiency versus cytotoxicity *Acta Biomater.* **8** 1838–48
- [51] Rowley J A, Madlambayan G and Mooney D J 1999 Alginate hydrogels as synthetic extracellular matrix materials *Biomaterials* **20** 45–53
- [52] Tan H, Chu C R, Payne K A and Marra K G 2009 Injectable in situ forming biodegradable chitosan–hyaluronic acid based hydrogels for cartilage tissue engineering *Biomaterials* **30** 2499–506

- [53] Chen C S, Mrksich M, Huang S, Whitesides G M and Ingber D E 1997 Geometric Control of Cell Life and Death *Science* (80-.). **276** 1425–8
- [54] Romankiw L T 1997 A path: from electroplating through lithographic masks in electronics to LIGA in MEMS *Electrochim. Acta* **42** 2985–3005
- [55] Xia Y and Whitesides G M 1998 SOFT LITHOGRAPHY *Annu. Rev. Mater. Sci.* **28** 153–84
- [56] Bhardwaj N and Kundu S C 2010 Electrospinning: A fascinating fiber fabrication technique *Biotechnol. Adv.* **28** 325–47
- [57] Levato R, Visser J, Planell J, Engel E, Malda J and Mateos-Timoneda M A 2014 Biofabrication of tissue constructs by 3D bioprinting of cell-laden microcarriers. *Biofabrication* **6** 035020
- [58] Stanton M M, Samitier J and Sánchez S 2015 Bioprinting of 3D hydrogels *Lab Chip* **15** 3111–5
- [59] Frontera W R and Ochala J 2015 Skeletal muscle: a brief review of structure and function. *Calcif. Tissue Int.* **96** 183–95
- [60] Wolfe R R 2006 The underappreciated role of muscle in health and disease *Am. J. Clin. Nutr.* **84** 475–82
- [61] Fernández-Costa J M, Fernández-Garibay X, Velasco-Mallorquí F and Ramón-Azcón J 2021 Bioengineered in vitro skeletal muscles as new tools for muscular dystrophies preclinical studies *J. Tissue Eng.* **12** 204173142098133
- [62] Petersen O H 2012 Chapter 5. Muscle *Lecture Notes. Human Physiology* ed O H Petersen (Liverpool, UK: Blackwell Publishing) pp 95–121
- [63] Mukund K and Subramaniam S 2019 Skeletal muscle: A review of molecular structure and function, in health and disease *Wiley Interdiscip. Rev. Syst. Biol. Med.* **12** e1462
- [64] Linke W A 2018 Titin Gene and Protein Functions in Passive and Active Muscle *Annu. Rev. Physiol.* **80** 389–411
- [65] Zot A S and Potter J D 1987 Structural Aspects of Troponin-Tropomyosin Regulation of Skeletal Muscle Contraction *Annu. Rev. Biophys. Biophys. Chem.* **16** 535–59
- [66] Fitts R H 2008 The cross-bridge cycle and skeletal muscle fatigue *J. Appl. Physiol.* **104** 551–8
- [67] Galińska-Rakoczy A, Engel P, Xu C, Jung H S, Craig R, Tobacman L S and Lehman W

2008 Structural Basis for the Regulation of Muscle Contraction by Troponin and Tropomyosin *J. Mol. Biol.* **379** 929–35

- [68] Chal J and Pourquié O 2017 Making muscle: skeletal myogenesis in vivo and in vitro *Development* **144** 2104–22
- [69] Zammit P S 2017 Function of the myogenic regulatory factors Myf5, MyoD, Myogenin and MRF4 in skeletal muscle, satellite cells and regenerative myogenesis *Semin. Cell Dev. Biol.* **72** 19–32
- [70] Yablonka-Reuveni Z 2011 The skeletal muscle satellite cell: still young and fascinating at 50. *J. Histochem. Cytochem. Off. J. Histochem. Soc.* **59** 1041–59
- [71] Buckingham M 2007 Skeletal muscle progenitor cells and the role of Pax genes *C. R. Biol.* **330** 530–3
- [72] Yin H, Price F and Rudnicki M A 2013 Satellite Cells and the Muscle Stem Cell Niche *Physiol. Rev.* **93** 23–67
- [73] Zammit P S, Partridge T A and Yablonka-Reuveni Z 2006 The skeletal muscle satellite cell: the stem cell that came in from the cold *J. Histochem. Cytochem.* **54** 1177–91
- [74] Bencze M, Riederer I, Butler-Browne G S, Savino W and Mouly V 2013 *Stem Cells: Current Challenges and New Directions* ed K Turksen (New York, NY: Springer New York)
- [75] Sanger J W, Chowrashi P, Shaner N C, Spalhoff S, Wang J, Freeman N L and Sanger J M 2002 Myofibrillogenesis in Skeletal Muscle Cells *Clin. Orthop. Relat. Res.* **403** S153–62
- [76] Csapo R, Gumpenberger M and Wessner B 2020 Skeletal Muscle Extracellular Matrix – What Do We Know About Its Composition, Regulation, and Physiological Roles? A Narrative Review *Front. Physiol.* **11** 1–15
- [77] Gillies A R and Lieber R L 2011 Structure and function of the skeletal muscle extracellular matrix *Muscle Nerve* **44** 318–31
- [78] Hinds S, Bian W, Dennis R G and Bursac N 2011 The role of extracellular matrix composition in structure and function of bioengineered skeletal muscle *Biomaterials* **32** 3575–83
- [79] Leto D and Saltiel A R 2012 Regulation of glucose transport by insulin: traffic control of GLUT4 *Nat. Rev. Mol. Cell Biol.* **13** 383–96
- [80] DeFronzo R A and Tripathy D 2009 Skeletal Muscle Insulin Resistance Is the Primary

Defect in Type 2 Diabetes *Diabetes Care* **32** S157–63

- [81] Stump C S, Henriksen E J, Wei Y and Sowers J R 2006 The metabolic syndrome: Role of skeletal muscle metabolism *Ann. Med.* **38** 389–402
- [82] Eaton S, Bartlett K B and POURFARZAM M 1996 Mammalian mitochondrial β -oxidation *Biochem. J.* **320** 345–57
- [83] Saltiel A R and Kahn C R 2001 Insulin signalling and the regulation of glucose and lipid metabolism. *Nature* **414** 799–806
- [84] Pedersen B K, Åkerström T C A, Nielsen A R and Fischer C P 2007 Role of myokines in exercise and metabolism *J. Appl. Physiol.* **103** 1093–8
- [85] Pedersen B K and Febbraio M A 2008 Muscle as an Endocrine Organ: Focus on Muscle-Derived Interleukin-6 *Physiol. Rev.* **88** 1379–406
- [86] Carson B P 2017 The Potential Role of Contraction-Induced Myokines in the Regulation of Metabolic Function for the Prevention and Treatment of Type 2 Diabetes *Front. Endocrinol. (Lausanne)*. **8** 1–8
- [87] Steensberg A, Febbraio M A, Osada T, Schjerling P, Hall G, Saltin B and Pedersen B K 2001 Interleukin-6 production in contracting human skeletal muscle is influenced by pre-exercise muscle glycogen content *J. Physiol.* **537** 633–9
- [88] Lee J H and Jun H S 2019 Role of myokines in regulating skeletal muscle mass and function *Front. Physiol.* **10** 1–9
- [89] Ma J and Chen K 2021 The role of Irisin in multiorgan protection *Mol. Biol. Rep.* **48** 763–72
- [90] Chen W, Wang L, You W and Shan T 2021 Myokines mediate the cross talk between skeletal muscle and other organs *J. Cell. Physiol.* **236** 2393–412
- [91] Brocker C, Thompson D, Matsumoto A, Nebert D W and Vasiliou V 2010 Evolutionary divergence and functions of the human interleukin (IL) gene family *Hum. Genomics* **5** 30–55
- [92] Coppack S W 2001 Pro-inflammatory cytokines and adipose tissue *Proc. Nutr. Soc.* **60** 349–56
- [93] Rogeri P S, Gasparini S O, Martins G L, Costa L K F, Araujo C C, Lugaresi R, Kopfler M and Lancha A H 2020 Crosstalk Between Skeletal Muscle and Immune System: Which Roles Do IL-6 and Glutamine Play? *Front. Physiol.* **11** 1–11

- [94] Tominaga T, Ma S, Saitou K and Suzuki K 2019 Glucose Ingestion Inhibits Endurance Exercise-Induced IL-6 Producing Macrophage Infiltration in Mice Muscle *Nutrients* **11** 1496
- [95] Pillon N J, Bilan P J, Fink L N and Klip A 2013 Cross-talk between skeletal muscle and immune cells: muscle-derived mediators and metabolic implications *Am. J. Physiol. Metab.* **304** E453–65
- [96] Fix D K, VanderVeen B N, Counts B R and Carson J A 2019 Regulation of Skeletal Muscle DRP-1 and FIS-1 Protein Expression by IL-6 Signaling ed I G Fatouros *Oxid. Med. Cell. Longev.* **2019** 8908457
- [97] Cornish S M, Chilibeck P D and Candow D G 2020 Potential Importance of Immune System Response to Exercise on Aging Muscle and Bone *Curr. Osteoporos. Rep.* **18** 350–6
- [98] Wedell-Neergaard A-S, Lehrskov L L, Pedersen B K and Ellingsgaard H 2019 Exercise-Induced Changes in Visceral Adipose Tissue Mass Are Regulated by IL-6 Signaling : A Clinical and Translational Report Exercise-Induced Changes in Visceral Adipose Tissue Mass Are Regulated by IL-6 Signaling : A R *Cell Metab.* **29** 844-855.e3
- [99] Starkie R, Ostrowski S R, Jauffred S, Febbraio M, Klarlund B, Copenhagen T and Pedersen B K 2003 Exercise and IL-6 infusion inhibit endotoxin-induced TNF-alpha production in humans. *FASEB J.* **17** 884–6
- [100] Bruun J M, Helge J W, Richelsen B and Stallknecht B 2006 Diet and exercise reduce low-grade inflammation and macrophage infiltration in adipose tissue but not in skeletal muscle in severely obese subjects. *Am. J. Physiol. Endocrinol. Metab.* **290** E961-7
- [101] Fischer C P, Berntsen A, Perstrup L B, Eskildsen P and Pedersen B K 2007 Plasma levels of interleukin-6 and C-reactive protein are associated with physical inactivity independent of obesity. *Scand. J. Med. Sci. Sports* **17** 580–7
- [102] Meriggioli M N and Sanders D B 2009 Autoimmune myasthenia gravis: emerging clinical and biological heterogeneity *Lancet Neurol.* **8** 475–90
- [103] Kaczor J J, Robertshaw H A and Tarnopolsky M A 2017 Higher oxidative stress in skeletal muscle of McArdle disease patients *Mol. Genet. Metab. Reports* **12** 69–75
- [104] Mercuri E, Bönnemann C G and Muntoni F 2019 Muscular dystrophies *Lancet* **394** 2025–38
- [105] Benarroch L, Bonne G, Rivier F and Hamroun D 2019 The 2020 version of the gene table of neuromuscular disorders (nuclear genome) *Neuromuscul. Disord.* **29** 980–1018

- [106] Carter J C, Sheehan D W, Prochoroff A and Birnkrant D J 2018 Muscular Dystrophies *Clin. Chest Med.* **39** 377–89
- [107] Vydra D G and Rayi A 2021 *Myotonic Dystrophy* (Treasure Island (FL))
- [108] Yiu E M and Kornberg A J 2015 Duchenne muscular dystrophy. *J. Paediatr. Child Health* **51** 759–64
- [109] Mah J K, Korngut L, Fiest K M, Dykeman J, Day L J, Pringsheim T and Jette N 2016 A Systematic Review and Meta-analysis on the Epidemiology of the Muscular Dystrophies *Can. J. Neurol. Sci. / J. Can. des Sci. Neurol.* **43** 163–77
- [110] Overby S J, Cerro-Herreros E, Llamusi B and Artero R 2018 RNA-mediated therapies in myotonic dystrophy *Drug Discov. Today* **23** 2013–22
- [111] Verhaart I E C and Aartsma-Rus A 2019 Therapeutic developments for Duchenne muscular dystrophy. *Nat. Rev. Neurol.* **15** 373–86
- [112] Reddy K, Jenquin J R, Cleary J D and Berglund J A 2019 Mitigating RNA Toxicity in Myotonic Dystrophy using Small Molecules *Int. J. Mol. Sci.* **20** 4017
- [113] López Castel A, Overby S J and Artero R 2019 MicroRNA-Based Therapeutic Perspectives in Myotonic Dystrophy *Int. J. Mol. Sci.* **20** 5600
- [114] Datta N and Ghosh P S 2020 Update on Muscular Dystrophies with Focus on Novel Treatments and Biomarkers. *Curr. Neurol. Neurosci. Rep.* **20** 14
- [115] Ozimski L L, Sabater-Arcis M, Bargiela A and Artero R 2021 The hallmarks of myotonic dystrophy type 1 muscle dysfunction *Biol. Rev.* **96** 716–30
- [116] Bonaldo P and Sandri M 2013 Cellular and molecular mechanisms of muscle atrophy *Dis. Model. Mech.* **6** 25–39
- [117] Thornton C A 2014 Myotonic Dystrophy *Neurol. Clin.* **32** 705–19
- [118] Meola G 2013 Clinical aspects, molecular pathomechanisms and management of myotonic dystrophies. *Acta Myol. myopathies cardiomyopathies Off. J. Mediterr. Soc. Myol.* **32** 154–65
- [119] Udd B and Krahe R 2012 The myotonic dystrophies: molecular, clinical, and therapeutic challenges *Lancet Neurol.* **11** 891–905
- [120] LoRusso S, Weiner B and Arnold W D 2018 Myotonic Dystrophies: Targeting Therapies for Multisystem Disease *Neurotherapeutics* **15** 872–84

- [121] Wang E T, Treacy D, Eichinger K, Struck A, Estabrook J, Olafson H, Wang T T, Bhatt K, Westbrook T, Sedehizadeh S, Ward A, Day J, Brook D, Berglund J A, Cooper T, Housman D, Thornton C and Burge C 2019 Transcriptome alterations in myotonic dystrophy skeletal muscle and heart *Hum. Mol. Genet.* **28** 1312–21
- [122] Ebralidze A 2004 RNA Leaching of Transcription Factors Disrupts Transcription in Myotonic Dystrophy *Science (80-.).* **303** 383–7
- [123] Jones K, Wei C, Iakova P, Bugiardini E, Schneider-Gold C, Meola G, Woodgett J, Killian J, Timchenko N A and Timchenko L T 2012 GSK3 β mediates muscle pathology in myotonic dystrophy *J. Clin. Invest.* **122** 4461–72
- [124] Rau F, Freyermuth F, Fugier C, Villemain J-P, Fischer M-C, Jost B, Dembele D, Gourdon G, Nicole A, Duboc D, Wahbi K, Day J W, Fujimura H, Takahashi M P, Auboeuf D, Dreumont N, Furling D and Charlet-Berguerand N 2011 Misregulation of miR-1 processing is associated with heart defects in myotonic dystrophy *Nat. Struct. Mol. Biol.* **18** 840–5
- [125] Krol J, Fiszler A, Mykowska A, Sobczak K, de Mezer M and Krzyzosiak W J 2007 Ribonuclease Dicer Cleaves Triplet Repeat Hairpins into Shorter Repeats that Silence Specific Targets *Mol. Cell* **25** 575–86
- [126] Fernandez-Costa J M, Garcia-Lopez A, Zuñiga S, Fernandez-Pedrosa V, Felipe-Benavent A, Mata M, Jaka O, Aiastui A, Hernandez-Torres F, Aguado B, Perez-Alonso M, Vilchez J J, Lopez de Munain A and Artero R D 2013 Expanded CTG repeats trigger miRNA alterations in *Drosophila* that are conserved in myotonic dystrophy type 1 patients *Hum. Mol. Genet.* **22** 704–16
- [127] Kalsotra A, Singh R K, Gurha P, Ward A J, Creighton C J and Cooper T A 2014 The Mef2 Transcription Network Is Disrupted in Myotonic Dystrophy Heart Tissue, Dramatically Altering miRNA and mRNA Expression *Cell Rep.* **6** 336–45
- [128] Du H, Cline M S, Osborne R J, Tuttle D L, Clark T A, Donohue J P, Hall M P, Shiue L, Swanson M S, Thornton C A and Ares M 2010 Aberrant alternative splicing and extracellular matrix gene expression in mouse models of myotonic dystrophy *Nat. Struct. Mol. Biol.* **17** 187–93
- [129] Charizanis K, Lee K-Y, Batra R, Goodwin M, Zhang C, Yuan Y, Shiue L, Cline M, Scotti M M, Xia G, Kumar A, Ashizawa T, Clark H B, Kimura T, Takahashi M P, Fujimura H, Jinnai K, Yoshikawa H, Gomes-Pereira M, Gourdon G, Sakai N, Nishino S, Foster T C, Ares M, Darnell R B and Swanson M S 2012 Muscleblind-like 2-Mediated Alternative Splicing in the Developing Brain and Dysregulation in Myotonic Dystrophy *Neuron* **75** 437–50

- [130] Goodwin M, Mohan A, Batra R, Lee K-Y, Charizanis K, Gómez F J F, Eddarkaoui S, Sergeant N, Buée L, Kimura T, Clark H B, Dalton J, Takamura K, Weyn-Vanhentenryck S M, Zhang C, Reid T, Ranum L P W, Day J W and Swanson M S 2015 MBNL Sequestration by Toxic RNAs and RNA Misprocessing in the Myotonic Dystrophy Brain *Cell Rep.* **12** 1159–68
- [131] Batra R, Charizanis K, Manchanda M, Mohan A, Li M, Finn D J, Goodwin M, Zhang C, Sobczak K, Thornton C A and Swanson M S 2014 Loss of MBNL Leads to Disruption of Developmentally Regulated Alternative Polyadenylation in RNA-Mediated Disease *Mol. Cell* **56** 311–22
- [132] Fernandez-Costa J M, Llamusi M B, Garcia-Lopez A and Artero R 2011 Alternative splicing regulation by Muscleblind proteins: from development to disease *Biol. Rev.* **86** 947–58
- [133] Michel L, Huguet-Lachon A and Gourdon G 2015 Sense and Antisense DMPK RNA Foci Accumulate in DM1 Tissues during Development ed R Artero *PLoS One* **10** e0137620
- [134] Gomes-Pereira M, Cooper T A and Gourdon G 2011 Myotonic dystrophy mouse models: towards rational therapy development *Trends Mol. Med.* **17** 506–17
- [135] Cerro-Herreros E, Fernandez-Costa J M, Sabater-Arcis M, Llamusi B and Artero R 2016 Derepressing muscleblind expression by miRNA sponges ameliorates myotonic dystrophy-like phenotypes in *Drosophila* *Sci. Rep.* **6** 36230
- [136] Bargiela A, Cerro-Herreros E, Fernandez-Costa J M, Vilchez J J, Llamusi B and Artero R 2015 Increased autophagy and apoptosis contribute to muscle atrophy in a myotonic dystrophy type 1 *Drosophila* model *Dis. Model. Mech.* **8** 679–90
- [137] Garcia-Lopez A, Monferrer L, Garcia-Alcover I, Vicente-Crespo M, Alvarez-Abril M C and Artero R D 2008 Genetic and Chemical Modifiers of a CUG Toxicity Model in *Drosophila* ed A Lewin *PLoS One* **3** e1595
- [138] Todd P K, Ackall F Y, Hur J, Sharma K, Paulson H L and Dowling J J 2014 Transcriptional changes and developmental abnormalities in a zebrafish model of myotonic dystrophy type 1 *Dis. Model. Mech.* **7** 143–55
- [139] Chen G, Masuda A, Konishi H, Ohkawara B, Ito M, Kinoshita M, Kiyama H, Matsuura T and Ohno K 2016 Phenylbutazone induces expression of MBNL1 and suppresses formation of MBNL1-CUG RNA foci in a mouse model of myotonic dystrophy *Sci. Rep.* **6** 25317
- [140] Konieczny P, Selma-Soriano E, Rapisarda A S, Fernandez-Costa J M, Perez-Alonso M

- and Artero R 2017 Myotonic dystrophy: candidate small molecule therapeutics *Drug Discov. Today* **22** 1740–8
- [141] Huang K, Masuda A, Chen G, Bushra S, Kamon M, Araki T, Kinoshita M, Ohkawara B, Ito M and Ohno K 2020 Inhibition of cyclooxygenase-1 by nonsteroidal anti-inflammatory drugs demethylates MeR2 enhancer and promotes Mbnl1 transcription in myogenic cells *Sci. Rep.* **10** 2558
- [142] Thornton C A, Wang E and Carrell E M 2017 Myotonic dystrophy: approach to therapy *Curr. Opin. Genet. Dev.* **44** 135–40
- [143] Cerro-Herreros E, Sabater-Arcis M, Fernandez-Costa J M, Moreno N, Perez-Alonso M, Llamusi B and Artero R 2018 miR-23b and miR-218 silencing increase Muscleblind-like expression and alleviate myotonic dystrophy phenotypes in mammalian models *Nat. Commun.* **9** 2482
- [144] Cerro-Herreros E, González-Martínez I, Moreno-Cervera N, Overby S, Pérez-Alonso M, Llamusi B and Artero R 2020 Therapeutic Potential of AntagomiR-23b for Treating Myotonic Dystrophy *Mol. Ther. - Nucleic Acids* **21** 837–49
- [145] Kankala R K, Wang S-B and Chen A-Z 2019 Microengineered Organ-on-a-chip Platforms towards Personalized Medicine *Curr. Pharm. Des.* **24** 5354–66
- [146] Martinez E, St-Pierre J-P and Variola F 2019 Advanced bioengineering technologies for preclinical research *Adv. Phys. X* **4** 1622451
- [147] Blau H, Pavlath G, Hardeman E, Chiu C, Silberstein L, Webster S, Miller S and Webster C 1985 Plasticity of the differentiated state *Science (80-.)*. **230** 758–66
- [148] YAFFE D and SAXEL O 1977 Serial passaging and differentiation of myogenic cells isolated from dystrophic mouse muscle *Nature* **270** 725–7
- [149] Yoshida N, Yoshida S, Koishi K, Masuda K and Nabeshima Y 1998 Cell heterogeneity upon myogenic differentiation: down-regulation of MyoD and Myf-5 generates “reserve cells”. *J. Cell Sci.* **111** 769–79
- [150] Burattini S, Ferri P, Battistelli M, Curci R, Luchetti F and Falcieri E 2004 C2C12 murine myoblasts as a model of skeletal muscle development: morpho-functional characterization *Eur. J. Histochem.* **48** 223–34
- [151] McMahon D K, Anderson P A, Nassar R, Bunting J B, Saba Z, Oakeley A E and Malouf N N 1994 C2C12 cells: biophysical, biochemical, and immunocytochemical properties. *Am. J. Physiol.* **266** C1795-802

- [152] Wong C Y, Al-Salami H and Dass C R 2020 C2C12 cell model: its role in understanding of insulin resistance at the molecular level and pharmaceutical development at the preclinical stage *J. Pharm. Pharmacol.* **72** 1667–93
- [153] Mierzejewski B, Archacka K, Grabowska I, Florkowska A, Ciemerych M A and Brzoska E 2020 Human and mouse skeletal muscle stem and progenitor cells in health and disease *Semin. Cell Dev. Biol.* **104** 93–104
- [154] Danoviz M E and Yablonka-Reuveni Z 2012 Skeletal Muscle Satellite Cells: Background and Methods for Isolation and Analysis in a Primary Culture System *Myogenesis: Methods and Protocols* ed J X DiMario (Totowa, NJ: Humana Press) pp 21–52
- [155] Wang J, Khodabukus A, Rao L, Vandusen K, Abutaleb N and Bursac N 2019 Engineered skeletal muscles for disease modeling and drug discovery *Biomaterials* **221** 119416
- [156] Bonavaud S, Thibert P, Gherardi R K and Barlovatz-Meimon G 1997 Primary human muscle satellite cell culture: Variations of cell yield, proliferation and differentiation rates according to age and sex of donors, site of muscle biopsy, and delay before processing *Biol. Cell* **89** 233–40
- [157] Mamchaoui K, Trollet C, Bigot A, Negroni E, Chaouch S, Wolff A, Kandalla P K, Marie S, Di Santo J, St Guily J L, Muntoni F, Kim J, Philippi S, Spuler S, Levy N, Blumen S C, Voit T, Wright W E, Aamiri A, Butler-Browne G and Mouly V 2011 Immortalized pathological human myoblasts: towards a universal tool for the study of neuromuscular disorders. *Skelet. Muscle* **1** 34
- [158] Zhu C-H, Mouly V, Cooper R N, Mamchaoui K, Bigot A, Shay J W, Di Santo J P, Butler-Browne G S and Wright W E 2007 Cellular senescence in human myoblasts is overcome by human telomerase reverse transcriptase and cyclin-dependent kinase 4: consequences in aging muscle and therapeutic strategies for muscular dystrophies. *Aging Cell* **6** 515–23
- [159] Bigot A, Jacquemin V, Debacq-Chainiaux F, Butler-Browne G S, Toussaint O, Furling D and Mouly V 2008 Replicative aging down-regulates the myogenic regulatory factors in human myoblasts. *Biol. cell* **100** 189–99
- [160] Boularaoui S M, Abdel-Raouf K M A, Alwahab N S A, Kondash M E, Truskey G A, Teo J C M and Christoforou N 2018 Efficient transdifferentiation of human dermal fibroblasts into skeletal muscle *J. Tissue Eng. Regen. Med.* **12** e918–36
- [161] Ito N, Kii I, Shimizu N, Tanaka H and Takeda S 2017 Direct reprogramming of fibroblasts into skeletal muscle progenitor cells by transcription factors enriched in undifferentiated subpopulation of satellite cells *Sci. Rep.* **7** 8097

- [162] Arandel L, Polay Espinoza M, Matloka M, Bazinet A, De Dea Diniz D, Naouar N, Rau F, Jollet A, Edom-Vovard F, Mamchaoui K, Tarnopolsky M, Puymirat J, Battail C, Boland A, Deleuze J-F, Mouly V, Klein A F and Furling D 2017 Immortalized human myotonic dystrophy muscle cell lines to assess therapeutic compounds *Dis. Model. Mech.* **10** 487–97
- [163] Thomson J A, Itskovitz-Eldor J, Shapiro S S, Waknitz M A, Swiergiel J J, Marshall V S and Jones J M 1998 Embryonic Stem Cell Lines Derived from Human Blastocysts *Science (80-.)*. **282** 1145 LP – 1147
- [164] Takahashi K, Tanabe K, Ohnuki M, Narita M, Ichisaka T, Tomoda K and Yamanaka S 2007 Induction of pluripotent stem cells from adult human fibroblasts by defined factors. *Cell* **131** 861–72
- [165] Tanaka A, Woltjen K, Miyake K, Hotta A, Ikeya M, Yamamoto T, Nishino T, Shoji E, Sehara-Fujisawa A, Manabe Y, Fujii N, Hanaoka K, Era T, Yamashita S, Isobe K-I, Kimura E and Sakurai H 2013 Efficient and reproducible myogenic differentiation from human iPS cells: prospects for modeling Miyoshi Myopathy in vitro. *PLoS One* **8** e61540
- [166] Abujarour R, Bennett M, Valamehr B, Lee T T, Robinson M, Robbins D, Le T, Lai K and Flynn P 2014 Myogenic differentiation of muscular dystrophy-specific induced pluripotent stem cells for use in drug discovery. *Stem Cells Transl. Med.* **3** 149–60
- [167] Darabi R, Arpke R W, Irion S, Dimos J T, Grskovic M, Kyba M and Perlingeiro R C R 2012 Human ES- and iPS-derived myogenic progenitors restore DYSTROPHIN and improve contractility upon transplantation in dystrophic mice. *Cell Stem Cell* **10** 610–9
- [168] Shelton M, Metz J, Liu J, Carpenedo R L, Demers S-P, Stanford W L and Skerjanc I S 2014 Derivation and expansion of PAX7-positive muscle progenitors from human and mouse embryonic stem cells. *Stem cell reports* **3** 516–29
- [169] Borchin B, Chen J and Barberi T 2013 Derivation and FACS-mediated purification of PAX3+/PAX7+ skeletal muscle precursors from human pluripotent stem cells. *Stem cell reports* **1** 620–31
- [170] Barberi T, Bradbury M, Dincer Z, Panagiotakos G, Socci N D and Studer L 2007 Derivation of engraftable skeletal myoblasts from human embryonic stem cells. *Nat. Med.* **13** 642–8
- [171] Denes L T, Riley L A, Mijares J R, Arboleda J D, McKee K, Esser K A and Wang E T 2019 Culturing C2C12 myotubes on micromolded gelatin hydrogels accelerates myotube maturation *Skelet. Muscle* **9** 17
- [172] Gong H Y, Park J, Kim W, Kim J, Lee J Y and Koh W-G 2019 A Novel Conductive and

- Micropatterned PEG-Based Hydrogel Enabling the Topographical and Electrical Stimulation of Myoblasts *ACS Appl. Mater. Interfaces* **11** 47695–706
- [173] Somers S M, Zhang N Y, Morrisette-McAlmon J B F, Tran K, Mao H Q and Grayson W L 2019 Myoblast maturity on aligned microfiber bundles at the onset of strain application impacts myogenic outcomes *Acta Biomater.* **94** 232–42
- [174] Yeo M and Kim G H 2020 Micro/nano-hierarchical scaffold fabricated using a cell electrospinning/3D printing process for co-culturing myoblasts and HUVECs to induce myoblast alignment and differentiation *Acta Biomater.* **107** 102–14
- [175] Kim J, Kim W and Kim G 2020 Scaffold with micro/nanoscale topographical cues fabricated using E-field-assisted 3D printing combined with plasma-etching for enhancing myoblast alignment and differentiation *Appl. Surf. Sci.* **509** 145404
- [176] Shi X, Ostrovidov S, Zhao Y, Liang X, Kasuya M, Kurihara K, Nakajima K, Bae H, Wu H and Khademhosseini A 2015 Microfluidic spinning of cell-responsive grooved microfibers *Adv. Funct. Mater.* **25** 2250–9
- [177] Ebrahimi M, Ostrovidov S, Salehi S, Kim S B, Bae H and Khademhosseini A 2018 Enhanced skeletal muscle formation on microfluidic spun gelatin methacryloyl (GelMA) fibres using surface patterning and agrin treatment *J. Tissue Eng. Regen. Med.* **12** 2151–63
- [178] Nakayama K H, Quarta M, Paine P, Alcazar C, Karakikes I, Garcia V, Abilez O J, Calvo N S, Simmons C S, Rando T A and Huang N F 2019 Treatment of volumetric muscle loss in mice using nanofibrillar scaffolds enhances vascular organization and integration *Commun. Biol.* **2** 170
- [179] Smoak M M M and Mikos A G G 2020 Advances in biomaterials for skeletal muscle engineering and obstacles still to overcome *Mater. Today Bio* **7** 100069
- [180] Zhang Y S and Khademhosseini A 2017 Advances in engineering hydrogels *Science (80-.)*. **356** eaaf3627
- [181] Potyondy T, Uquillas J A, Tebon P J, Byambaa B, Hasan A, Tavafoghi M, Mary H, Aninwene G E, Pountos I, Khademhosseini A and Ashammakhi N 2021 Recent advances in 3D bioprinting of musculoskeletal tissues *Biofabrication* **13** 022001
- [182] Distler T, Solisito A A, Schneidereit D, Friedrich O, Detsch R and Boccaccini A R 2020 3D printed oxidized alginate-gelatin bioink provides guidance for C2C12 muscle precursor cell orientation and differentiation via shear stress during bioprinting *Biofabrication* **12**

- [183] Kim W and Kim G 2020 3D bioprinting of functional cell-laden bioinks and its application for cell-alignment and maturation *Appl. Mater. Today* **19** 100588
- [184] Kim W J, Jang C H and Kim G H 2019 A Myoblast-Laden Collagen Bioink with Fully Aligned Au Nanowires for Muscle-Tissue Regeneration *Nano Lett.* **19** 8612–20
- [185] Costantini M, Testa S, Mozetic P, Barbetta A, Fuoco C, Fornetti E, Tamiro F, Bernardini S, Jaroszewicz J, Świążkowski W, Trombetta M, Castagnoli L, Seliktar D, Garstecki P, Cesareni G, Cannata S, Rainer A and Gargioli C 2017 Microfluidic-enhanced 3D bioprinting of aligned myoblast-laden hydrogels leads to functionally organized myofibers in vitro and in vivo *Biomaterials* **131** 98–110
- [186] Mestre R, Patiño T, Barceló X, Anand S, Pérez-Jiménez A and Sánchez S 2019 Force Modulation and Adaptability of 3D-Bioprinted Biological Actuators Based on Skeletal Muscle Tissue *Adv. Mater. Technol.* **4** 1–13
- [187] Vandenburg H, Shansky J, Benesch-Lee F, Barbata V, Reid J, Thorrez L, Valentini R and Crawford G 2008 Drug-screening platform based on the contractility of tissue-engineered muscle *Muscle and Nerve* **37** 438–47
- [188] Kalman B, Picart C and Boudou T 2016 Quick and easy microfabrication of T-shaped cantilevers to generate arrays of microtissues *Biomed. Microdevices* **18** 43
- [189] Tanaka N, Ota H, Fukumori K, Miyake J, Yamato M and Okano T 2014 Micro-patterned cell-sheets fabricated with stamping-force-controlled micro-contact printing *Biomaterials* **35** 9802–10
- [190] Bettadapur A, Suh G C, Geisse N A, Wang E R, Hua C, Huber H A, Viscio A A, Kim J Y, Strickland J B and McCain M L 2016 Prolonged Culture of Aligned Skeletal Myotubes on Micromolded Gelatin Hydrogels *Sci. Rep.* **6** 28855
- [191] Costantini M, Testa S, Fornetti E, Barbetta A, Trombetta M, Cannata S M, Gargioli C and Rainer A 2017 Engineering Muscle Networks in 3D Gelatin Methacryloyl Hydrogels: Influence of Mechanical Stiffness and Geometrical Confinement *Front. Bioeng. Biotechnol.* **5** 1–8
- [192] Wan L, Flegle J, Ozdoganlar B and LeDuc P 2020 Toward Vasculature in Skeletal Muscle-on-a-Chip through Thermo-Responsive Sacrificial Templates *Micromachines* **11** 907
- [193] Christensen R K, Von Halling Laier C, Kiziltay A, Wilson S and Larsen N B 2020 3D Printed Hydrogel Multiassay Platforms for Robust Generation of Engineered Contractile Tissues *Biomacromolecules* **21** 356–65

- [194] Lee H, Ju Y M, Kim I, Elsangedy E, Lee J H, Yoo J J, Atala A and Lee S J 2020 A novel decellularized skeletal muscle-derived ECM scaffolding system for in situ muscle regeneration *Methods* **171** 77–85
- [195] Kim W, Lee H, Lee J, Atala A, Yoo J J, Jin S, Hyung G, Lee S J and Kim G H 2020 Efficient myotube formation in 3D bioprinted tissue construct by biochemical and topographical cues *Biomaterials* **230** 119632
- [196] BADYLAK S, FREYTES D and GILBERT T 2009 Extracellular matrix as a biological scaffold material: Structure and function *Acta Biomater.* **5** 1–13
- [197] Okano T 1998 Tissue Engineered Skeletal Muscle: Preparation of Highly Dense, Highly Oriented Hybrid Muscular Tissues *Cell Transplant.* **7** 71–82
- [198] Vandenburg H H, Karlisch P and Farr L 1988 Maintenance of highly contractile tissue-cultured avian skeletal myotubes in collagen gel *Vitr. Cell. Dev. Biol.* **24** 166–74
- [199] Powell C A, Smiley B L, Mills J and Vandenburg H H 2002 Mechanical stimulation improves tissue-engineered human skeletal muscle *Am. J. Physiol. Physiol.* **283** C1557–65
- [200] Chiron S, Tomczak C, Duperray A, Lainé J, Bonne G, Eder A, Hansen A, Eschenhagen T, Verdier C and Coirault C 2012 Complex Interactions between Human Myoblasts and the Surrounding 3D Fibrin-Based Matrix ed M Parsons *PLoS One* **7** e36173
- [201] Madden L, Juhas M, Kraus W E, Truskey G A and Bursac N 2015 Bioengineered human myobundles mimic clinical responses of skeletal muscle to drugs *Elife* **2015** 1–14
- [202] Rao L, Qian Y, Khodabukus A, Ribar T and Bursac N 2018 Engineering human pluripotent stem cells into a functional skeletal muscle tissue *Nat. Commun.* **9** 126
- [203] Khodabukus A, Madden L, Prabhu N K, Koves T R, Jackman C P, Muoio D M and Bursac N 2019 Electrical stimulation increases hypertrophy and metabolic flux in tissue-engineered human skeletal muscle *Biomaterials* **198** 259–69
- [204] Afshar Bakooshli M, Lippmann E S, Mulcahy B, Iyer N, Nguyen C T, Tung K, Stewart B A, van den Dorpel H, Fuehrmann T, Shoichet M, Bigot A, Pegoraro E, Ahn H, Ginsberg H, Zhen M, Ashton R S and Gilbert P M 2019 A 3D culture model of innervated human skeletal muscle enables studies of the adult neuromuscular junction *Elife* **8** 1–29
- [205] Kim J H, Seol Y-J, Ko I K, Kang H-W, Lee Y K, Yoo J J, Atala A and Lee S J 2018 3D Bioprinted Human Skeletal Muscle Constructs for Muscle Function Restoration *Sci. Rep.* **8** 12307

- [206] Choi Y-J, Jun Y-J, Kim D Y, Yi H-G, Chae S, Kang J, Lee J, Gao G, Kong J-S, Jang J, Chung W K, Rhie J-W, Cho D-W, Yeon D, Yi H-G, Chae S, Rhie J-W and Cho D-W 2019 A 3D cell printed muscle construct with tissue-derived bioink for the treatment of volumetric muscle loss *Biomaterials* **206** 160–9
- [207] Gholobova D, Gerard M, Decroix L, Desender L, Callewaert N, Annaert P and Thorrez L 2018 Human tissue-engineered skeletal muscle: a novel 3D in vitro model for drug disposition and toxicity after intramuscular injection *Sci. Rep.* **8** 1–14
- [208] Mills R J, Parker B L, Monnot P, Needham E J, Vivien C J, Ferguson C, Parton R G, James D E, Porrello E R and Hudson J E 2019 Development of a human skeletal micro muscle platform with pacing capabilities *Biomaterials* **198** 217–27
- [209] Ramade A, Legant W R, Picart C, Chen C S and Boudou T 2014 Microfabrication of a Platform to Measure and Manipulate the Mechanics of Engineered Microtissues *Methods in Cell Biology* vol 121 (Elsevier Inc.) pp 191–211
- [210] Vandeburgh H, Shansky J, Benesch-Lee F, Skelly K, Spinazzola J M, Saponjian Y and Tseng B S 2009 Automated drug screening with contractile muscle tissue engineered from dystrophic myoblasts *FASEB J.* **23** 3325–34
- [211] Maffioletti S M, Sarcar S, Henderson A B H, Mannhardt I, Pinton L, Moyle L A, Steele-Stallard H, Cappellari O, Wells K E, Ferrari G, Mitchell J S, Tyzack G E, Kotiadis V N, Khedr M, Ragazzi M, Wang W, Duchen M R, Patani R, Zammit P S, Wells D J, Eschenhagen T and Tedesco F S 2018 Three-Dimensional Human iPSC-Derived Artificial Skeletal Muscles Model Muscular Dystrophies and Enable Multilineage Tissue Engineering *Cell Rep.* **23** 899–908
- [212] Arandel L, Polay Espinoza M, Matloka M, Bazinet A, De Dea Diniz D, Naouar N, Rau F, Jollet A, Edom-Vovard F, Mamchaoui K, Tarnopolsky M, Puymirat J, Battail C, Boland A, Deleuze J-F, Mouly V, Klein A F and Furling D 2017 Immortalized human myotonic dystrophy muscle cell lines to assess therapeutic compounds *Dis. Model. Mech.* **10** 487–97
- [213] Benton J A, DeForest C A, Vivekanandan V and Anseth K S 2009 Photocrosslinking of Gelatin Macromers to Synthesize Porous Hydrogels That Promote Valvular Interstitial Cell Function *Tissue Eng. Part A* **15** 3221–30
- [214] Jeon O, Bouhadir K H, Mansour J M and Alsberg E 2009 Photocrosslinked alginate hydrogels with tunable biodegradation rates and mechanical properties *Biomaterials* **30** 2724–34
- [215] Habeeb A F S A 1966 Determination of free amino groups in proteins by trinitrobenzenesulfonic acid *Anal. Biochem.* **14** 328–36

- [216] Alcaraz J, Buscemi L, Grabulosa M, Trepas X, Fabry B, Farré R and Navajas D 2003 Microrheology of Human Lung Epithelial Cells Measured by Atomic Force Microscopy *Biophys. J.* **84** 2071–9
- [217] Comelles J, Fernández-Majada V, Berlanga-Navarro N, Acevedo V, Paszkowska K and Martínez E 2020 Microfabrication of poly(acrylamide) hydrogels with independently controlled topography and stiffness *Biofabrication* **12** 025023
- [218] Schindelin J, Arganda-Carreras I, Frise E, Kaynig V, Longair M, Pietzsch T, Preibisch S, Rueden C, Saalfeld S, Schmid B, Tinevez J-Y, White D J, Hartenstein V, Eliceiri K, Tomancak P and Cardona A 2012 Fiji: an open-source platform for biological-image analysis *Nat. Methods* **9** 676–82
- [219] Kaneshiro E S, Wyder M A, Wu Y-P and Cushion M T 1993 Reliability of calcein acetoxymethyl ester and ethidium homodimer or propidium iodide for viability assessment of microbes *J. Microbiol. Methods* **17** 1–16
- [220] Occhetta P, Sadr N, Piraino F, Redaelli A, Moretti M and Rasponi M 2013 Fabrication of 3D cell-laden hydrogel microstructures through photo-mold patterning *Biofabrication* **5** 035002
- [221] Peltier H J and Latham G J 2008 Normalization of microRNA expression levels in quantitative RT-PCR assays: Identification of suitable reference RNA targets in normal and cancerous human solid tissues *RNA* **14** 844–52
- [222] Mendes B B, Gómez-Florit M, Pires R A, Domingues R M A, Reis R L and Gomes M E 2018 Human-based fibrillar nanocomposite hydrogels as bioinstructive matrices to tune stem cell behavior *Nanoscale* **10** 17388–401
- [223] Mendes B B, Gómez-Florit M, Hamilton A G, Detamore M S, Domingues R M A, Reis R L and Gomes M E 2020 Human platelet lysate-based nanocomposite bioink for bioprinting hierarchical fibrillar structures *Biofabrication* **12**
- [224] Schneider C A, Rasband W S and Eliceiri K W 2012 NIH Image to ImageJ: 25 years of image analysis *Nat. Methods* **9** 671–5
- [225] Ahadian S, Sadeghian R B, Salehi S, Ostrovidov S, Bae H, Ramalingam M and Khademhosseini A 2015 Bioconjugated Hydrogels for Tissue Engineering and Regenerative Medicine. *Bioconjug. Chem.* **26** 1984–2001
- [226] Ostrovidov S, Hosseini V, Ahadian S, Fujie T, Parthiban S P, Ramalingam M, Bae H, Kaji H and Khademhosseini A 2014 Skeletal muscle tissue engineering: methods to form skeletal myotubes and their applications. *Tissue Eng. Part B. Rev.* **20** 403–36

- [227] Grasman J M, Zayas M J, Page R L and Pins G D 2015 Biomimetic scaffolds for regeneration of volumetric muscle loss in skeletal muscle injuries. *Acta Biomater.* **25** 2–15
- [228] Banerjee P and Bhunia A K 2009 Mammalian cell-based biosensors for pathogens and toxins *Trends Biotechnol.* **27** 179–88
- [229] Fernandes T G, Diogo M M, Clark D S, Dordick J S and Cabral J M S 2009 High-throughput cellular microarray platforms: applications in drug discovery, toxicology and stem cell research *Trends Biotechnol.* **27** 342–9
- [230] Kim S B, Bae H, Cha J M, Moon S J, Dokmeci M R, Cropek D M and Khademhosseini A 2011 A cell-based biosensor for real-time detection of cardiotoxicity using lensfree imaging *Lab Chip* **11** 1801
- [231] Misawa N, Mitsuno H, Kanzaki R and Takeuchi S 2010 Highly sensitive and selective odorant sensor using living cells expressing insect olfactory receptors *Proc. Natl. Acad. Sci.* **107** 15340–4
- [232] Bhise N S, Ribas J, Manoharan V, Zhang Y S, Polini A, Massa S, Dokmeci M R and Khademhosseini A 2014 Organ-on-a-chip platforms for studying drug delivery systems *J. Control. Release* **190** 82–93
- [233] Fujita H, Van Dau T, Shimizu K, Hatsuda R, Sugiyama S and Nagamori E 2011 Designing of a Si-MEMS device with an integrated skeletal muscle cell-based bio-actuator. *Biomed. Microdevices* **13** 123–9
- [234] Baryshyan A L, Domigan L J, Hunt B, Trimmer B A and Kaplan D L 2014 Self-assembled insect muscle bioactuators with long term function under a range of environmental conditions. *RSC Adv.* **4** 39962–8
- [235] Sakar M S, Neal D, Boudou T, Borochin M A, Li Y, Weiss R, Kamm R D, Chen C S, Asada H H and Manuscript A 2012 Formation and Optogenetic Control of Engineered 3D Skeletal Muscle Bioactuators *Lab Chip* **12** 4976
- [236] Ramón-Azcón J, Ahadian S, Estili M, Liang X, Ostrovidov S, Kaji H, Shiku H, Ramalingam M, Nakajima K, Sakka Y, Khademhosseini A and Matsue T 2013 Dielectrophoretically aligned carbon nanotubes to control electrical and mechanical properties of hydrogels to fabricate contractile muscle myofibers *Adv. Mater.* **25** 4028–34
- [237] Ramón-Azcón J, Ahadian S, Obregón R, Camci-Unal G, Ostrovidov S, Hosseini V, Kaji H, Ino K, Shiku H, Khademhosseini A and Matsue T 2012 Gelatin methacrylate as a promising hydrogel for 3D microscale organization and proliferation of dielectrophoretically patterned cells *Lab Chip* **12** 2959

- [238] Visser J, Melchels F P W, Jeon J E, van Bussel E M, Kimpton L S, Byrne H M, Dhert W J A, Dalton P D, Hutmacher D W and Malda J 2015 Reinforcement of hydrogels using three-dimensionally printed microfibrils. *Nat. Commun.* **6** 6933
- [239] Bajaj P, Schweller R M, Khademhosseini A, West J L and Bashir R 2014 3D biofabrication strategies for tissue engineering and regenerative medicine. *Annu. Rev. Biomed. Eng.* **16** 247–76
- [240] Huang Z-M, Zhang Y-Z, Kotaki M and Ramakrishna S 2003 A review on polymer nanofibers by electrospinning and their applications in nanocomposites *Compos. Sci. Technol.* **63** 2223–53
- [241] Cummings C L, Gawlitta D, Nerem R M and Stegemann J P 2004 Properties of engineered vascular constructs made from collagen, fibrin, and collagen-fibrin mixtures. *Biomaterials* **25** 3699–706
- [242] Kwee B J and Mooney D J 2017 Biomaterials for skeletal muscle tissue engineering. *Curr. Opin. Biotechnol.* **47** 16–22
- [243] Smith C M, Stone A L, Parkhill R L, Stewart R L, Simpkins M W, Kachurin A M, Warren W L and Williams S K 2004 Three-dimensional bioassembly tool for generating viable tissue-engineered constructs. *Tissue Eng.* **10** 1566–76
- [244] Loessner D, Meinert C, Kaemmerer E, Martine L C, Yue K, Levett P A, Klein T J, Melchels F P W, Khademhosseini A and Hutmacher D W 2016 Functionalization, preparation and use of cell-laden gelatin methacryloyl-based hydrogels as modular tissue culture platforms *Nat. Protoc.* **11** 727–46
- [245] Yue K, Li X, Schrobback K, Sheikhi A, Annabi N, Leijten J, Zhang W, Zhang Y S, Hutmacher D W, Klein T J and Khademhosseini A 2017 Structural analysis of photocrosslinkable methacryloyl-modified protein derivatives. *Biomaterials* **139** 163–71
- [246] Gao Q, He Y, Fu J, Liu A and Ma L 2015 Coaxial nozzle-assisted 3D bioprinting with built-in microchannels for nutrients delivery. *Biomaterials* **61** 203–15
- [247] Nakamura M, Iwanaga S, Henmi C, Arai K and Nishiyama Y 2010 Biomaterials and biomaterials for future developments of bioprinting and biofabrication. *Biofabrication* **2** 14110
- [248] Ouyang L, Highley C B, Rodell C B, Sun W and Burdick J A 2016 3D Printing of Shear-Thinning Hyaluronic Acid Hydrogels with Secondary Cross-Linking. *ACS Biomater. Sci. Eng.* **2** 1743–51
- [249] Hutson C B, Nichol J W, Aubin H, Bae H, Yamanlar S, Al-Haque S, Koshy S T and

- Khademhosseini A 2011 Synthesis and Characterization of Tunable Poly(Ethylene Glycol): Gelatin Methacrylate Composite Hydrogels *Tissue Eng. Part A* **17** 1713–23
- [250] Bertassoni L E, Cecconi M, Manoharan V, Nikkhah M, Hjortnaes J, Cristino A L, Barabaschi G, Demarchi D, Dokmeci M R, Yang Y and Khademhosseini A 2014 Hydrogel bioprinted microchannel networks for vascularization of tissue engineering constructs *Lab Chip* **14** 2202–11
- [251] Jia W, Gungor-Ozkerim P S, Zhang Y S, Yue K, Zhu K, Liu W, Pi Q, Byambaa B, Dokmeci M R, Shin S R and Khademhosseini A 2016 Direct 3D bioprinting of perfusable vascular constructs using a blend bioink. *Biomaterials* **106** 58–68
- [252] X. Chen Y, Cain B and Soman P 2017 Gelatin methacrylate-alginate hydrogel with tunable viscoelastic properties *AIMS Mater. Sci.* **4** 363–9
- [253] Kageyama T, Osaki T, Enomoto J, Myasnikova D, Nittami T, Hozumi T, Ito T and Fukuda J 2016 In Situ Cross-Linkable Gelatin-CMC Hydrogels Designed for Rapid Engineering of Perfusable Vasculatures. *ACS Biomater. Sci. Eng.* **2** 1059–66
- [254] Murphy C M and O'Brien F J 2010 Understanding the effect of mean pore size on cell activity in collagen-glycosaminoglycan scaffolds. *Cell Adh. Migr.* **4** 377–81
- [255] Devi N and Maji T K 2009 Preparation and evaluation of gelatin/sodium carboxymethyl cellulose polyelectrolyte complex microparticles for controlled delivery of isoniazid. *AAPS PharmSciTech* **10** 1412–9
- [256] Shi C, Zhuang C, Cui Y and Tao F 2017 Preparation and characterization of gelatin film modified by cellulose active ester *Polym. Bull.* **74** 3505–25
- [257] Reeves R, Ribeiro A, Lombardo L, Boyer R and Leach J B 2010 Synthesis and Characterization of Carboxymethylcellulose-Methacrylate Hydrogel Cell Scaffolds *Polymers (Basel)*. **2** 252–64
- [258] Ke Y, Liu G S, Wang J H, Xue W, Du C and Wu G 2014 Preparation of carboxymethyl cellulose based microgels for cell encapsulation *Express Polym. Lett.* **8** 841–9
- [259] Ribeiro C C, Barrias C C and Barbosa M A 2004 Calcium phosphate-alginate microspheres as enzyme delivery matrices. *Biomaterials* **25** 4363–73
- [260] Wei D, Xiao W, Sun J, Zhong M, Guo L, Fan H and Zhang X 2015 A biocompatible hydrogel with improved stiffness and hydrophilicity for modular tissue engineering assembly. *J. Mater. Chem. B* **3** 2753–63
- [261] Hutanu D, Frishberg M D, Guo L and Darie C C 2014 Recent Applications of

- [262] Kloxin A M, Tibbitt M W and Anseth K S 2010 Synthesis of photodegradable hydrogels as dynamically tunable cell culture platforms *Nat. Protoc.* **5** 1867–87
- [263] Zimmermann H, Hillgärtner M, Manz B, Feilen P, Brunnenmeier F, Leinfelder U, Weber M, Cramer H, Schneider S, Hendrich C, Volke F and Zimmermann U 2003 Fabrication of homogeneously cross-linked, functional alginate microcapsules validated by NMR-, CLSM- and AFM-imaging. *Biomaterials* **24** 2083–96
- [264] Zhang Y S, Arneri A, Bersini S, Shin S-R, Zhu K, Goli-Malekabadi Z, Aleman J, Colosi C, Busignani F, Dell’Erba V, Bishop C, Shupe T, Demarchi D, Moretti M, Rasponi M, Dokmeci M R, Atala A and Khademhosseini A 2016 Bioprinting 3D microfibrillar scaffolds for engineering endothelialized myocardium and heart-on-a-chip. *Biomaterials* **110** 45–59
- [265] Nishiyama Y, Nakamura M, Henmi C, Yamaguchi K, Mochizuki S, Nakagawa H and Takiura K 2009 Development of a three-dimensional bioprinter: construction of cell supporting structures using hydrogel and state-of-the-art inkjet technology. *J. Biomech. Eng.* **131** 35001
- [266] Liu W, Heinrich M A, Zhou Y, Akpek A, Hu N, Liu X, Guan X, Zhong Z, Jin X, Khademhosseini A and Zhang Y S 2017 Extrusion Bioprinting of Shear-Thinning Gelatin Methacryloyl Bioinks *Adv. Healthc. Mater.* **6** 1601451
- [267] Bédier A, Braschler T, Peric O, Fantner G E, Mosser S, Fraering P C, Benchérif S, Mooney D J and Renaud P 2015 A compressible scaffold for minimally invasive delivery of large intact neuronal networks. *Adv. Healthc. Mater.* **4** 301–12
- [268] Lim K S, Schon B S, Mekhileri N V, Brown G C J, Chia C M, Prabakar S, Hooper G J and Woodfield T B F 2016 New Visible-Light Photoinitiating System for Improved Print Fidelity in Gelatin-Based Bioinks. *ACS Biomater. Sci. Eng.* **2** 1752–62
- [269] Lee K Y and Mooney D J 2012 Alginate: properties and biomedical applications. *Prog. Polym. Sci.* **37** 106–26
- [270] Zhu J 2010 Bioactive modification of poly(ethylene glycol) hydrogels for tissue engineering. *Biomaterials* **31** 4639–56
- [271] Camci-Unal G, Cuttica D, Annabi N, Demarchi D and Khademhosseini A 2013 Synthesis and Characterization of Hybrid Hyaluronic Acid-Gelatin Hydrogels *Biomacromolecules* **14** 1085–92
- [272] Lutolf M P, Gilbert P M and Blau H M 2009 Designing materials to direct stem-cell fate.

- [273] Aubin H, Nichol J W, Hutson C B, Bae H, Sieminski A L, Cropek D M, Akhyari P and Khademhosseini A 2010 Directed 3D cell alignment and elongation in microengineered hydrogels *Biomaterials* **31** 6941–51
- [274] Engler A J, Griffin M A, Sen S, Bönnemann C G, Sweeney H L and Discher D E 2004 Myotubes differentiate optimally on substrates with tissue-like stiffness *J. Cell Biol.* **166** 877–87
- [275] Ralla K, Sohling U, Riechers D, Kasper C, Ruf F and Scheper T 2010 Adsorption and separation of proteins by a smectitic clay mineral. *Bioprocess Biosyst. Eng.* **33** 847–61
- [276] Kim M-C, Silberberg Y R, Abeyaratne R, Kamm R D and Asada H H 2018 Computational modeling of three-dimensional ECM-rigidity sensing to guide directed cell migration. *Proc. Natl. Acad. Sci. U. S. A.* **115** E390–9
- [277] Pertz O 2011 Filopodia: Nanodevices that sense nanotopographic ECM cues to orient neurite outgrowth. *Commun. Integr. Biol.* **4** 436–9
- [278] Evers J F, Muench D and Duch C 2006 Developmental relocation of presynaptic terminals along distinct types of dendritic filopodia. *Dev. Biol.* **297** 214–27
- [279] Yin J, Yan M, Wang Y, Fu J and Suo H 2018 3D Bioprinting of Low-Concentration Cell-Laden Gelatin Methacrylate (GelMA) Bioinks with a Two-Step Cross-linking Strategy. *ACS Appl. Mater. Interfaces* **10** 6849–57
- [280] Zhao X, Lang Q, Yildirimer L, Lin Z Y, Cui W, Annabi N, Ng K W, Dokmeci M R, Ghaemmaghami A M and Khademhosseini A 2016 Photocrosslinkable Gelatin Hydrogel for Epidermal Tissue Engineering. *Adv. Healthc. Mater.* **5** 108–18
- [281] Wu Y, Wang Z, Fuh J Y H, Wong Y S, Wang W and Thian E S 2016 Mechanically-enhanced three-dimensional scaffold with anisotropic morphology for tendon regeneration. *J. Mater. Sci. Mater. Med.* **27** 115
- [282] Agrawal G, Aung A and Varghese S 2017 Skeletal muscle-on-a-chip: An in vitro model to evaluate tissue formation and injury *Lab Chip* **17** 3447–61
- [283] Bajaj P, Reddy Jr. B, Millet L, Wei C, Zorlutuna P, Bao G and Bashir R 2011 Patterning the differentiation of C2C12 skeletal myoblasts *Integr. Biol.* **3** 897–909
- [284] Khademhosseini A, Langer R, Borenstein J and Vacanti J P 2006 Microscale technologies for tissue engineering and biology. *Proc. Natl. Acad. Sci. U. S. A.* **103** 2480–7

- [285] Wu M-H, Huang S-B and Lee G-B 2010 Microfluidic cell culture systems for drug research *Lab Chip* **10** 939
- [286] Bian W and Bursac N 2008 Tissue engineering of functional skeletal muscle: challenges and recent advances. *IEEE Eng. Med. Biol. Mag. Q. Mag. Eng. Med. Biol. Soc.* **27** 109–13
- [287] Skardal A, Murphy S V, Devarasetty M, Mead I, Kang H, Seol Y, Shrike Zhang Y, Shin S, Zhao L, Aleman J, Hall A R, Shupe T D, Kleensang A, Dokmeci M R, Jin Lee S, Jackson J D, Yoo J J, Hartung T, Khademhosseini A, Soker S, Bishop C E and Atala A 2017 Multi-tissue interactions in an integrated three-tissue organ-on-a-chip platform *Sci. Rep.* **7** 8837
- [288] Zhang Y S, Aleman J, Shin S R, Kilic T, Kim D, Mousavi Shaegh S A, Massa S, Riahi R, Chae S, Hu N, Avci H, Zhang W, Silvestri A, Sanati Nezhad A, Manbohi A, De Ferrari F, Polini A, Calzone G, Shaikh N, Alerasool P, Budina E, Kang J, Bhise N, Ribas J, Pourmand A, Skardal A, Shupe T, Bishop C E, Dokmeci M R, Atala A and Khademhosseini A 2017 Multisensor-integrated organs-on-chips platform for automated and continual in situ monitoring of organoid behaviors. *Proc. Natl. Acad. Sci. U. S. A.* **114** E2293–302
- [289] Grosberg A, Alford P W, McCain M L and Parker K K 2011 Ensembles of engineered cardiac tissues for physiological and pharmacological study: Heart on a chip *Lab Chip* **11** 4165–73
- [290] Riahi R, Shaegh S A M, Ghaderi M, Zhang Y S, Shin S R, Aleman J, Massa S, Kim D, Dokmeci M R and Khademhosseini A 2016 Automated microfluidic platform of bead-based electrochemical immunosensor integrated with bioreactor for continual monitoring of cell secreted biomarkers. *Sci. Rep.* **6** 24598
- [291] García-Lizarribar A, Fernández-Garibay X, Velasco-Mallorquí F, Castaño A G, Samitier J and Ramon-Azcon J 2018 Composite Biomaterials as Long-Lasting Scaffolds for 3D Bioprinting of Highly Aligned Muscle Tissue *Macromol. Biosci.* **18** 1800167
- [292] Oyen M L 2014 Mechanical characterisation of hydrogel materials *Int. Mater. Rev.* **59** 44–59
- [293] Fanjul-Bolado P, González-García M B and Costa-García A 2005 Amperometric detection in TMB/HRP-based assays. *Anal. Bioanal. Chem.* **382** 297–302
- [294] Van Gerwen P, Laureyn W, Laureys W, Huyberegts G, Op De Beeck M, Baert K, Suls J, Sansen W, Jacobs P, Hermans L and Mertens R 1998 Nanoscaled interdigitated electrode arrays for biochemical sensors *Sensors Actuators B Chem.* **49** 73–80

- [295] Ahadian S, Ramón-Azcón J, Ostrovidov S, Camci-Unal G, Hosseini V, Kaji H, Ino K, Shiku H, Khademhosseini A and Matsue T 2012 Interdigitated array of Pt electrodes for electrical stimulation and engineering of aligned muscle tissue *Lab Chip* **12** 3491
- [296] Evers-van Gogh I J A, Alex S, Stienstra R, Brenkman A B, Kersten S and Kalkhoven E 2015 Electric Pulse Stimulation of Myotubes as an In Vitro Exercise Model: Cell-Mediated and Non-Cell-Mediated Effects. *Sci. Rep.* **5** 10944
- [297] Hosseini V, Ahadian S, Ostrovidov S, Camci-Unal G, Chen S, Kaji H, Ramalingam M and Khademhosseini A 2012 Engineered contractile skeletal muscle tissue on a microgrooved methacrylated gelatin substrate *Tissue Eng Part A* **18** 2453–65
- [298] Campuzano S, Pedrero M, Montemayor C, Fatás E and Pingarrón J M 2006 Characterization of alkanethiol-self-assembled monolayers-modified gold electrodes by electrochemical impedance spectroscopy *J. Electroanal. Chem.* **586** 112–21
- [299] Li J, King N C and Sinoway L I 2003 ATP concentrations and muscle tension increase linearly with muscle contraction. *J. Appl. Physiol.* **95** 577–83
- [300] Muñoz-Cánoves P, Scheele C, Pedersen B K and Serrano A L 2013 Interleukin-6 myokine signaling in skeletal muscle: a double-edged sword? *FEBS J.* **280** 4131–48
- [301] Ost M, Coleman V, Kasch J and Klaus S 2016 Regulation of myokine expression: Role of exercise and cellular stress. *Free Radic. Biol. Med.* **98** 78–89
- [302] Yoon J H, Kim J, Song P, Lee T G, Suh P-G and Ryu S H 2012 Secretomics for skeletal muscle cells: a discovery of novel regulators? *Adv. Biol. Regul.* **52** 340–50
- [303] Egawa T, Ohno Y, Goto A, Sugiura T, Ohira Y, Yoshioka T, Hayashi T and Goto K 2016 Caffeine Affects Myotube Size As Well As Regulates Protein Degradation and Protein Synthesis Pathways in C2C12 Skeletal Muscle Cells *J. Caffeine Res.* **6** 88–96
- [304] Shimizu K, Genma R, Gotou Y, Nagasaka S and Honda H 2017 Three-Dimensional Culture Model of Skeletal Muscle Tissue with Atrophy Induced by Dexamethasone *Bioengineering* **4** 56
- [305] Frost R A, Nystrom G J and Lang C H 2002 Lipopolysaccharide regulates proinflammatory cytokine expression in mouse myoblasts and skeletal muscle. *Am. J. Physiol. Regul. Integr. Comp. Physiol.* **283** R698-709
- [306] Corcoran M P, Lamon-Fava S and Fielding R A 2007 Skeletal muscle lipid deposition and insulin resistance: Effect of dietary fatty acids and exercise *Am. J. Clin. Nutr.* **85** 662–77

- [307] Moyle L A, Jacques E and Gilbert P M 2020 Engineering the next generation of human skeletal muscle models: From cellular complexity to disease modeling *Curr. Opin. Biomed. Eng.* **16** 9–18
- [308] Ahadian S, Ramón-Azcón J, Estili M, Liang X, Ostrovidov S, Shiku H, Ramalingam M, Nakajima K, Sakka Y, Bae H, Matsue T and Khademhosseini A 2015 Hybrid hydrogels containing vertically aligned carbon nanotubes with anisotropic electrical conductivity for muscle myofiber fabrication *Sci. Rep.* **4** 4271
- [309] Ortega M A, Fernández-Garibay X, Castaño A G, De Chiara F, Hernández-Albors A, Balaguer-Trias J and Ramón-Azcón J 2019 Muscle-on-a-chip with an on-site multiplexed biosensing system for in situ monitoring of secreted IL-6 and TNF- α *Lab Chip* **19** 2568–80
- [310] Kang H W, Lee S J, Ko I K, Kengla C, Yoo J J and Atala A 2016 A 3D bioprinting system to produce human-scale tissue constructs with structural integrity *Nat. Biotechnol.* **34** 312–9
- [311] Rouwkema J, Koopman B F J M, Blitterswijk C A Van, Dhert W J A and Malda J 2009 Supply of Nutrients to Cells in Engineered Tissues *Biotechnol. Genet. Eng. Rev.* **26** 163–78
- [312] Peter M and Tayalia P 2016 An alternative technique for patterning cells on poly(ethylene glycol) diacrylate hydrogels *RSC Adv.* **6** 40878–85
- [313] Wong D Y, Ranganath T and Kasko A M 2015 Low-dose, long-wave UV light does not affect gene expression of human mesenchymal stem cells *PLoS One* **10** 1–21
- [314] Ouyang L, Highley C B, Sun W and Burdick J A 2017 A Generalizable Strategy for the 3D Bioprinting of Hydrogels from Nonviscous Photo-crosslinkable Inks *Adv. Mater.* **29**
- [315] Boere K W M, Visser J, Seyednejad H, Rahimian S, Gawlitta D, Van Steenbergen M J, Dhert W J A, Hennink W E, Vermonden T and Malda J 2014 Covalent attachment of a three-dimensionally printed thermoplast to a gelatin hydrogel for mechanically enhanced cartilage constructs *Acta Biomater.* **10** 2602–11
- [316] Bigot A, Klein A F, Gasnier E, Jacquemin V, Ravassard P, Butler-Browne G, Mouly V and Furling D 2009 Large CTG Repeats Trigger p16-Dependent Premature Senescence in Myotonic Dystrophy Type 1 Muscle Precursor Cells *Am. J. Pathol.* **174** 1435–42
- [317] Hernández-Albors A, Castaño A G, Fernández-Garibay X, Ortega M A, Balaguer J and Ramón-Azcón J 2019 Microphysiological sensing platform for an in-situ detection of tissue-secreted cytokines *Biosens. Bioelectron. X* **2** 100025

- [318] Gilbert P M, Havenstrite K L, Magnusson K E G, Sacco A, Leonardi N A, Kraft P, Nguyen N K, Thrun S, Lutolf M P and Blau H M 2010 Substrate Elasticity Regulates Skeletal Muscle Stem Cell Self-Renewal in Culture *Science (80-.)*. **329** 1078–81
- [319] Van Vlierberghe S, Cnudde V, Dubruel P, Masschaele B, Cosijns A, De Paepe I, Jacobs P J S, Van Hoorebeke L, Remon J P and Schacht E 2007 Porous gelatin hydrogels: 1. Cryogenic formation and structure analysis *Biomacromolecules* **8** 331–7
- [320] Miri A K, Hosseinabadi H G, Cecen B, Hassan S and Zhang Y S 2018 Permeability mapping of gelatin methacryloyl hydrogels *Acta Biomater.* **77** 38–47
- [321] Monge C, Ren K, Berton K, Guillot R, Peyrade D and Picart C 2012 Engineering Muscle Tissues on Microstructured Polyelectrolyte Multilayer Films *Tissue Eng. Part A* **18** 1664–76
- [322] Pomiès P, Rodriguez J, Blaquière M, Sedraoui S, Gouzi F, Carnac G, Laoudj-Chenivresse D, Mercier J, Préfaut C and Hayot M 2015 Reduced myotube diameter, atrophic signalling and elevated oxidative stress in cultured satellite cells from COPD patients *J. Cell. Mol. Med.* **19** 175–86
- [323] Archer-Lahlou E, Lan C and Jagoe R T 2018 Physiological culture conditions alter myotube morphology and responses to atrophy treatments: implications for in vitro research on muscle wasting *Physiol. Rep.* **6** e13726
- [324] Almonacid Suarez A M, Zhou Q, Rijn P and Harmsen M C 2019 Directional topography gradients drive optimum alignment and differentiation of human myoblasts *J. Tissue Eng. Regen. Med.* **13** 2234–45
- [325] Ohno Y, Oyama A, Kaneko H, Egawa T, Yokoyama S, Sugiura T, Ohira Y, Yoshioka T and Goto K 2018 Lactate increases myotube diameter via activation of MEK/ERK pathway in C2C12 cells *Acta Physiol.* **223** e13042
- [326] Timchenko N A, Patel R, Iakova P, Cai Z J, Quan L and Timchenko L T 2004 Overexpression of CUG Triplet Repeat-binding Protein, CUGBP1, in Mice Inhibits Myogenesis *J. Biol. Chem.* **279** 13129–39
- [327] Furling D, Lemieux D, Taneja K and Puymirat J 2001 Decreased levels of myotonic dystrophy protein kinase (DMPK) and delayed differentiation in human myotonic dystrophy myoblasts *Neuromuscul. Disord.* **11** 728–35
- [328] Peng X, Shen X, Chen X, Liang R, Azares A R and Liu Y 2015 Celf1 regulates cell cycle and is partially responsible for defective myoblast differentiation in myotonic dystrophy RNA toxicity *Biochim. Biophys. Acta - Mol. Basis Dis.* **1852** 1490–7

- [329] Beaulieu D, Thebault P, Pelletier R, Chapdelaine P, Tarnopolsky M, Furling D and Puymirat J 2012 Abnormal prostaglandin E2 production blocks myogenic differentiation in myotonic dystrophy *Neurobiol. Dis.* **45** 122–9
- [330] François V, Klein A F, Beley C, Jollet A, Lemerrier C, Garcia L and Furling D 2011 Selective silencing of mutated mRNAs in DM1 by using modified hU7-snrRNAs *Nat. Struct. Mol. Biol.* **18** 85–7
- [331] Soifer H S, Koch T, Lai J, Hansen B, Hoeg A, Oerum H and Stein C A 2012 Silencing of Gene Expression by Gymnotic Delivery of Antisense Oligonucleotides *Functional Genomics: Methods and Protocols* ed M Kaufmann and C Klinger (New York, NY: Springer New York) pp 333–46
- [332] Fernández-Garibay X, Ortega M A, Cerro-Herreros E, Comelles J, Martínez E, Artero R, Fernández-Costa J M and Ramón-Azcón J 2021 Bioengineered in vitro 3D model of myotonic dystrophy type 1 human skeletal muscle *Biofabrication* **13** 035035
- [333] Afshar M E, Abraha H Y, Bakooshli M A, Davoudi S, Thavandiran N, Tung K, Ahn H, Ginsberg H J, Zandstra P W and Gilbert P M 2020 A 96-well culture platform enables longitudinal analyses of engineered human skeletal muscle microtissue strength *Sci. Rep.* **10** 1–16
- [334] Aisenbrey E A and Murphy W L 2020 Synthetic alternatives to Matrigel *Nat. Rev. Mater.* **5** 539–51
- [335] Talbot N C and Caperna T J 2015 Proteome array identification of bioactive soluble proteins/peptides in Matrigel: relevance to stem cell responses *Cytotechnology* **67** 873–83
- [336] Higuchi A, Ling Q-D, Ko Y-A, Chang Y and Umezawa A 2011 Biomaterials for the Feeder-Free Culture of Human Embryonic Stem Cells and Induced Pluripotent Stem Cells *Chem. Rev.* **111** 3021–35
- [337] Polykandriotis E, Arkudas A, Horch R E, Kneser U and Mitchell G 2008 To Matrigel or Not to Matrigel *Am. J. Pathol.* **172** 1441–2
- [338] Vukicevic S, Kleinman H K, Luyten F P, Roberts A B, Roche N S and Reddi A H 1992 Identification of multiple active growth factors in basement membrane matrigel suggests caution in interpretation of cellular activity related to extracellular matrix components *Exp. Cell Res.* **202** 1–8
- [339] Kenar H, Ozdogan C Y, Dumlu C, Doger E, Kose G T and Hasirci V 2019 Microfibrillar scaffolds from poly(l-lactide-co-ε-caprolactone) blended with xeno-free collagen/hyaluronic acid for improvement of vascularization in tissue engineering

applications *Mater. Sci. Eng. C* **97** 31–44

- [340] Parenteau-Bareil R, Gauvin R and Berthod F 2010 Collagen-Based Biomaterials for Tissue Engineering Applications *Mater.* **3**
- [341] Fekete N, Gadelorge M, Fürst D, Maurer C, Dausend J, Fleury-Cappellesso S, Mailänder V, Lotfi R, Ignatius A, Sensebé L, Bourin P, Schrezenmeier H and Rojewski M T 2012 Platelet lysate from whole blood-derived pooled platelet concentrates and apheresis-derived platelet concentrates for the isolation and expansion of human bone marrow mesenchymal stromal cells: production process, content and identification of active com *Cytotherapy* **14** 540–54
- [342] Mendes B B, Gómez-Florit M, Babo P S, Domingues R M, Reis R L and Gomes M E 2018 Blood derivatives awaken in regenerative medicine strategies to modulate wound healing. *Adv. Drug Deliv. Rev.* **129** 376–93
- [343] Crespo-Diaz R, Behfar A, Butler G W, Padley D J, Sarr M G, Bartunek J, Dietz A B and Terzic A 2011 Platelet Lysate Consisting of a Natural Repair Proteome Supports Human Mesenchymal Stem Cell Proliferation and Chromosomal Stability *Cell Transplant.* **20** 797–812
- [344] Fortunato T M, Beltrami C, Emanuelli C, De Bank P A and Pula G 2016 Platelet lysate gel and endothelial progenitors stimulate microvascular network formation in vitro: tissue engineering implications *Sci. Rep.* **6** 25326
- [345] Sadeghi-Ataabadi M, Mostafavi-Pour Z, Vojdani Z, Sani M, Latifi M and Talaei-Khozani T 2017 Fabrication and characterization of platelet-rich plasma scaffolds for tissue engineering applications. *Mater. Sci. Eng. C. Mater. Biol. Appl.* **71** 372–80
- [346] Iuliano A, van der Wal E, Ruijmbek C W B, in 't Groen S L M, Pijnappel W W M P, de Greef J C and Saggiomo V 2020 Coupling 3D Printing and Novel Replica Molding for In House Fabrication of Skeletal Muscle Tissue Engineering Devices *Adv. Mater. Technol.* **5** 1–9
- [347] Ebrahimi M, Lad H, Fusto A, Tiper Y, Datye A, Nguyen C T, Jacques E, Moyle L A, Nguyen T, Musgrave B, Chávez-Madero C, Bigot A, Chen C, Turner S, Stewart B A, Pegoraro E, Vitiello L and Gilbert P M 2021 De novo revertant fiber formation and therapy testing in a 3D culture model of Duchenne muscular dystrophy skeletal muscle *Acta Biomater.*
- [348] Boudou T, Legant W R, Mu A, Borochin M A, Thavandiran N, Radisic M, Zandstra P W, Epstein J A, Margulies K B and Chen C S 2012 A microfabricated platform to measure and manipulate the mechanics of engineered cardiac microtissues. *Tissue Eng. Part A* **18** 910–9

- [349] Otten E 1988 Concepts and models of functional architecture in skeletal muscle *Exerc. Sport Sci. Rev.* **16** 89–137
- [350] Arrigoni C, Petta D, Bersini S, Mironov V, Candrian C and Moretti M 2019 Engineering complex muscle-tissue interfaces through microfabrication *Biofabrication* **11** 032004
- [351] Levy N 2012 The use of animal as models: ethical considerations. *Int. J. Stroke* **7** 440–2
- [352] Khodabukus A, Prabhu N, Wang J and Bursac N 2018 In Vitro Tissue-Engineered Skeletal Muscle Models for Studying Muscle Physiology and Disease *Adv. Healthc. Mater.* **7** 1701498
- [353] Truskey G A, Achneck H E, Bursac N, Chan H, Cheng C S, Fernandez C, Hong S, Jung Y, Koves T, Kraus W E, Leong K, Madden L, Reichert W M and Zhao X 2013 Design considerations for an integrated microphysiological muscle tissue for drug and tissue toxicity testing *Stem Cell Res. Ther.* **4** S10
- [354] Henry O Y F, Villenave R, Crounce M J, Leineweber W D, Benz M A and Ingber D E 2017 Organs-on-chips with integrated electrodes for trans-epithelial electrical resistance (TEER) measurements of human epithelial barrier function *Lab Chip* **17** 2264–71
- [355] Wu Q, Liu J, Wang X, Feng L, Wu J, Zhu X, Wen W and Gong X 2020 Organ-on-a-chip: Recent breakthroughs and future prospects *Biomed. Eng. Online* **19** 1–19
- [356] Pedron S and Harley B A C 2013 Impact of the biophysical features of a 3D gelatin microenvironment on glioblastoma malignancy *J. Biomed. Mater. Res. Part A* **101** 3404–15
- [357] Ganji F, Vasheghani-Farahani S and Vasheghani-Farahani E 2010 Theoretical Description of Hydrogel Swelling: A Review *Iran. Polym. J.* **19** 375–98
- [358] McKee T J, Perlman G, Morris M and Komarova S V 2019 Extracellular matrix composition of connective tissues: a systematic review and meta-analysis *Sci. Rep.* **9** 10542
- [359] Zhao Y, Zeng H, Nam J and Agarwal S 2009 Fabrication of skeletal muscle constructs by topographic activation of cell alignment *Biotechnol. Bioeng.* **102** 624–31
- [360] Richter E A and Hargreaves M 2013 Exercise, GLUT4, and Skeletal Muscle Glucose Uptake *Physiol. Rev.* **93** 993–1017
- [361] Maarbjerg S J, Sylow L and Richter E A 2011 Current understanding of increased insulin sensitivity after exercise - emerging candidates *Acta Physiol.* **202** 323–35
- [362] Pourteymour S, Eckardt K, Holen T, Langleite T, Lee S, Jensen J, Birkeland K I, Drevon

- C A and Hjorth M 2017 Global mRNA sequencing of human skeletal muscle: Search for novel exercise-regulated myokines *Mol. Metab.* **6** 352–65
- [363] Scheler M, Irmeler M, Lehr S, Hartwig S, Staiger H, Al-Hasani H, Beckers J, Hrabé de Angelis M, Häring H and Weigert C 2013 Cytokine response of primary human myotubes in an in vitro exercise model *Am. J. Physiol. Physiol.* **305** C877–86
- [364] Mueller C, Trujillo-Miranda M, Maier M, Heath D E, O'Connor A J and Salehi S 2021 Effects of External Stimulators on Engineered Skeletal Muscle Tissue Maturation *Adv. Mater. Interfaces* **8** 2001167
- [365] Carter S and Solomon T P J 2019 In vitro experimental models for examining the skeletal muscle cell biology of exercise: the possibilities, challenges and future developments *Pflügers Arch. - Eur. J. Physiol.* **471** 413–29
- [366] NIEMAN D C, NEHLSSEN-CANNARELLA S L, FAGOAGA O R, HENSON D A, UTTER A, DAVIS J M, WILLIAMS F and BUTTERWORTH D E 1998 Influence of mode and carbohydrate on the cytokine response to heavy exertion *Med. Sci. Sport. Exerc.* **30** 671–8
- [367] Starkie R L, Rolland J, Angus D J, Anderson M J and Febbraio M A 2001 Circulating monocytes are not the source of elevations in plasma IL-6 and TNF- α levels after prolonged running *Am. J. Physiol. Physiol.* **280** C769–74
- [368] Steensberg A, Keller C, Starkie R L, Osada T, Febbraio M A and Pedersen B K 2002 IL-6 and TNF- α expression in, and release from, contracting human skeletal muscle *Am. J. Physiol. Metab.* **283** E1272–8
- [369] Warren G L, Hulderman T, Jensen N, McKinstry M, Mishra M, Luster M I and Simeonova P P 2002 Physiological role of tumor necrosis factor α in traumatic muscle injury *FASEB J.* **16** 1630–2
- [370] Li Y 2003 TNF- α is a mitogen in skeletal muscle *Am. J. Physiol. Physiol.* **285** C370–6
- [371] Pascual-Gilabert M, López-Castel A and Artero R 2021 Myotonic dystrophy type 1 drug development: A pipeline toward the market *Drug Discov. Today*
- [372] Rodrigues M A and Mattei R 1987 The influence of serum substitute Ultrosor G in toxicological evaluations in mammalian cells in vitro. *Ecotoxicol. Environ. Saf.* **14** 269–74
- [373] Karnieli O, Friedner O M, Allickson J G, Zhang N, Jung S, Fiorentini D, Abraham E, Eaker S S, Yong tan K, Chan A, Griffiths S, Wehn A K, Oh S and Karnieli O 2017 A consensus introduction to serum replacements and serum-free media for cellular

therapies *Cytotherapy* **19** 155–69

- [374] Brown A C and Barker T H 2014 Fibrin-based biomaterials: modulation of macroscopic properties through rational design at the molecular level. *Acta Biomater.* **10** 1502–14
- [375] Sahana T G and Rekha P D 2018 Biopolymers: Applications in wound healing and skin tissue engineering *Mol. Biol. Rep.* **45** 2857–67
- [376] Mendes B B, Gómez-Florit M, Osório H, Vilaça A, Domingues R M A, Reis R L and Gomes M E 2020 Cellulose nanocrystals of variable sulfation degrees can sequester specific platelet lysate-derived biomolecules to modulate stem cell response *Chem. Commun.* **56** 6882–5
- [377] Tiffany A S, Dewey M J and Harley B A C 2020 Sequential sequestrations increase the incorporation and retention of multiple growth factors in mineralized collagen scaffolds *RSC Adv.* **10** 26982–96
- [378] Whitaker M J, Quirk R A, Howdle S M and Shakesheff K M 2001 Growth factor release from tissue engineering scaffolds *J. Pharm. Pharmacol.* **53** 1427–37
- [379] Willerth S M, Rader A and Sakiyama-Elbert S E 2008 The effect of controlled growth factor delivery on embryonic stem cell differentiation inside fibrin scaffolds *Stem Cell Res.* **1** 205–18

Appendix A. JOURNAL ARTICLES PRESENTED IN THIS THESIS



Composite Biomaterials as Long-Lasting Scaffolds for 3D Bioprinting of Highly Aligned Muscle Tissue

Andrea García-Lizarribar, Xiomara Fernández-Garibay, Ferran Velasco-Mallorquí, Albert G. Castaño, Josep Samitier,* and Javier Ramon-Azcon*

New biocompatible materials have enabled the direct 3D printing of complex functional living tissues, such as skeletal and cardiac muscle. Gelatinmethacryloyl (GelMA) is a photopolymerizable hydrogel composed of natural gelatin functionalized with methacrylic anhydride. However, it is difficult to obtain a single hydrogel that meets all the desirable properties for tissue engineering. In particular, GelMA hydrogels lack versatility in their mechanical properties and lasting 3D structures. In this work, a library of composite biomaterials to obtain versatile, lasting, and mechanically tunable scaffolds are presented. Two polysaccharides, alginate and carboxymethyl cellulose chemically functionalized with methacrylic anhydride, and a synthetic material, such as poly(ethylene glycol) diacrylate are combined with GelMA to obtain photopolymerizable hydrogel blends. Physical properties of the obtained composite hydrogels are screened and optimized for the growth and development of skeletal muscle fibers from C2C12 murine cells, and compared with pristine GelMA. All these composites show high resistance to degradation maintaining the 3D structure with high fidelity over several weeks. Altogether, in this study a library of biocompatible novel and totally versatile composite biomaterials are developed and characterized, with tunable mechanical properties that give structure and support myotube formation and alignment.

Moreover, these engineered tissues also have in vitro applications such as drug screening, bioactuators, and biosensors.^[4–8] Especially interesting is the use of engineered muscle tissues as bioactuators. As intrinsically biocompatible materials, such tissues can be integrated in biomedical devices to harvest energy and produce microcontrolled actuators. Specific examples include the application of skeletal muscle tissue on a Si–MEMS device to act as a micro-bioactuator for energy harvesting,^[9] bioactuators operated by self-assembled insect muscle tissue,^[10] or integration of optogenetic myotubes with MEMS systems.^[11] In all of these systems, the contractile ability of muscle tissue is needed and can only be obtained with a correct microarchitecture of the tissue, superior adaptable mechanical properties of the material where the tissue is attached, and a stable 3D structure. Important advances have been made in this area, but one of the major obstacles in engineering 3D complex tissues such as muscle is the need to encapsulate the cells in a long-lasting biocompatible 3D environment with adaptable mechanical properties.^[12] To date, many technologies, including photolithography, electrospinning, and bioprinting,^[12–16] have been adopted for the fabrication of 3D tissue constructs. Among them, bioprinting shows exciting potential as it is able to provide precise spatial manipulation of living cells with a suitable 3D growth environment, optimal oxygen levels, and effective nutrient transport, as well as mechanical integrity.

Cell responsive bioinks are a critical component in bioprinting technology. Hydrogel-based bioinks encapsulating living cells and bioactive components are commonly used for bioprinting. Currently, natural materials derived from mammalian animals (e.g., collagen, gelatin, and fibrin) are more suitable for engineering skeletal muscle due to higher cell attachment density, greater rates of cell proliferation, gel compaction (resulting in greater final cell density), and endogenous provision of growth factors and biological signals for differentiation.^[17,18] So far, a range of natural hydrogels including gels such as collagen/gelatin,^[19] gelatin-methacryloyl (GelMA),^[20,21] alginate,^[22] fibrin,^[23] and hyaluronic acid (HA)^[24] have been used in bioprinting, but none of these materials have been able

environment with adaptable mechanical properties.^[12] To date, many technologies, including photolithography, electrospinning, and bioprinting,^[12–16] have been adopted for the fabrication of 3D tissue constructs. Among them, bioprinting shows exciting potential as it is able to provide precise spatial manipulation of living cells with a suitable 3D growth environment, optimal oxygen levels, and effective nutrient transport, as well as mechanical integrity.


1. Introduction

Engineered muscle tissues (skeletal and cardiac muscle) have in vivo regenerative medicine applications that involve harvesting cells from the patient, growing them within a suitable scaffolding material, and reintroducing them into the patient.^[1–3]

A. García-Lizarribar, X. Fernández Garibay, F. Velasco Mallorquí, Dr. A. G. Castaño, Prof. J. Samitier, Dr. J. Ramon-Azcon
Institute for Bioengineering of Catalonia
Barcelona Institute of Science and Technology
Baldiri Reixac 10–12, 08028 Barcelona, Spain
E-mail: jsamitier@ibecbarcelona.eu; jramon@ibecbarcelona.eu

A. García-Lizarribar, Prof. J. Samitier
Centro de Investigación Biomédica en Red
28029 Madrid, Spain

Prof. J. Samitier
Department of Electronic and Biomedical Engineering
University of Barcelona, 08028 Barcelona, Spain

 The ORCID identification number(s) for the author(s) of this article can be found under <https://doi.org/10.1002/mabi.201800167>.

DOI: 10.1002/mabi.201800167

to fulfil all the necessary requirements for engineering muscle tissue bioactuators, such as mechanical properties, and formation of stable and durable structures. These 3D natural scaffolds are degraded by mammalian cells and the structural functionality of the bioactuator finally is lost.^[25]

To overcome the lack of 3D geometry along the time and obtain long-lasting architectures, composite materials can be obtained through the combination of degradable and non-degradable materials of both synthetic^[14,25–27] and natural^[24,28–31] origin. Among the distinct types of natural non-biodegradable biomaterials, polysaccharides, due to their biocompatibility and chemical properties, have attracted considerable attention in biomedical and pharmaceutical applications.^[32,33] Carboxymethyl cellulose (CMC) is a water-soluble and biocompatible derivative of cellulose and it is derived from abundant renewable resources. CMC hydrogels are not biodegradable by mammalian cells and, for this reason, they can be used as a natural biocompatible material to produce non-degradable structures.^[34] Only a few applications use it to encapsulate cells^[30,35] and CMC-methacrylate combined with GelMA has never been tested in tissue engineering applications. Alginate is a more widely used polysaccharide in tissue engineering applications. Alginate is a linear unbranched polysaccharide, derived from seaweed, that contains repeating units of 1,4-linked β -D-mannuronic acid and α -L-guluronic acid. It gels in the presence of divalent cations, such as calcium, barium, and magnesium.^[36] Alginate without any modification has been used in combination with GelMA,^[29] and it has also been methacrylated and used to encapsulate chondrocyte cells.^[28] In addition, GelMA and AlgMA have been already combined to encapsulate human osteoblast-like cells and human umbilical cord vein endothelial cells.^[37] Although previous studies have reported promising results, there is still limited control over the mechanical properties, swelling ratios, and the consequent effects on the cell differentiation process of these polysaccharides and their respective composite biomaterials with GelMA. Finally, poly(ethylene glycol) diacrylate (PEGDA) is one of the most popular synthetic non-degradable materials used in tissue engineering applications,^[38] because of its high hydrophilicity, bioinert structure, and lack of toxic or immunogenic responses. Also, PEG-based hydrogels provide adjustable mechanical properties as their elastic modulus can be tuned over a broad range of values to mimic the moduli of soft tissues.^[39] In bioprinting applications, it has been used in combination with natural hydrogels to produce composite hydrogel formulations.^[27]

Here, we report evaluation of three photocrosslinkable composite materials (i.e., GelMA-alginate-methacrylate [GelMA-AlgMA], GelMA-carboxymethyl cellulose-methacrylate [GelMA-CMCMA]) and GelMA-PEGDA, as bioinks for engineering skeletal muscle tissue. Employing GelMA gels in combination with different non-biodegradable materials (i.e., alginate, cellulose, and PEGDA), we obtained composite materials for direct bioprinting of 3D cell-laden skeletal muscle constructs with high structural fidelity, enhanced bioactivity, and long-standing structures. We formulated a library of composite hydrogel prepolymer solutions with different prepolymers concentrations, UV dosage, and two different UV photoinitiators. Photopolymerizable hydrogels show a close relationship between

their mechanical properties and their crosslinking density^[40,41] and stiffness of hydrogels strongly affects cell behavior and can induce or inhibit cell differentiation toward different phenotypes.^[39,42–44] We tuned the mechanical properties of the resulting hydrogels by varying the time of UV-induced crosslinking and photoinitiator concentration. We hypothesized that pore size frequency distribution have also significant impact on cell behavior.^[31] The diffusion of nutrients inside the structures can be reduced and extremely packed structures limit cell migration and growth. After thorough cell viability and mechanical characterization, we used those formulations for the preparation of cell-laden hydrogels in combination with C2C12 murine myoblasts and we evaluated the maturation of myotube structures by fluorescence microscopy. To this end, we used C2C12-laden composite hydrogels as a system to demonstrate the feasibility of the proposed technique in bioprinting constructs with preserved 3D structure over time. It was vital not only to match the morphology of the functional skeletal muscle fibers, but also the cellular arrangement. Control of the hydrogel properties, such as mechanical stiffness, swelling, degradation, and porosity, was critical to obtain proper cellular function and tissue morphogenesis.

2. Experimental Section

2.1. Synthesis of Polymer Precursors

Gelatin (Sigma-Aldrich, USA) was modified to a 40% degree of methacrylation as previously described.^[14] Briefly, gelatin was dissolved in PBS 10 mM at a concentration of 10% w/v, and methacrylic anhydride (Sigma-Aldrich, USA) was carefully added to the solution drop by drop. One hour later, the reaction was stopped by adding an excess of PBS 10 mM and dialyzed against Milli Q water with 6–8 kDa MWCO membranes (Spectra/por, Spectrumlabs, USA). Water was changed every 4 h during a 4 d period. Gelatin-methacryloyl (GelMA) was lyophilized and stored at -20°C . Sodium carboxymethylcellulose (CMC) and sodium alginate (alginate, Alg) (Sigma-Aldrich) were methacrylated at a maximum degree of methacrylation as previously described.^[39] The methacrylation reaction was performed by mixing a solution of 1% w/v of the polymer in 50 mM MES buffer at pH 6.5 with 20 mM EDC, 10 mM *N*-hydroxysuccinimide and 10 mM 2-aminoethylmethacrylate (Sigma-Aldrich). The reaction was stopped after 24 h with the addition of acetone (Panreac, Spain) and filtered using a vacuum flask. The precipitate was dissolved in PBS 10 mM and dialyzed against Milli Q water with 3.5 kDa MWCO membranes (ThermoFisher, USA). Finally, the solutions of methacrylated polymers (CMCMA and AlgMA) were lyophilized and stored at -20°C .

2.2. Nuclear Magnetic Resonance

For $^1\text{H-NMR}$, gelatin, GelMA, CMC, CMCMA, alginate, and AlgMA were dissolved in D_2O and analyzed on a Varian Inova 500 (Varian, USA). All samples were measured with a relaxation delay of 1 s for 64 scans.

2.3. Preparation of Prepolymer Solutions

The polymer precursors (GelMA, CMCMA, AlgMA, and PEGDA) were mixed at different concentrations and diluted in PBS 10 mM containing the photoinitiator. Final concentrations of photoinitiator, either 2-Hydroxy-4'-(2-hydroxyethoxy)-2-methylpropiophenone (I2959) (Sigma-Aldrich) or lithium Phenyl (2,4,6-trimethylbenzoyl)phosphinate (LAP) (TCI EUROPE N.V., Belgium) were fixed at 0.4% or 0.1% w/v. Polymer solutions were placed at 65 °C for 1 h to obtain homogeneous solutions. Polymer solutions were prepared to obtain final concentrations of 5% or 1% w/v GelMA and 1% w/v CMCMA, AlgMA, or PEGDA. All hydrogels were fabricated using a 3D bioprinter (3DDiscovery BioSafety, regenHU, Switzerland; 365 nm, 3 W cm⁻²) with the UV light source.

2.4. Multifactorial Analysis to Assess Cell Viability under 3D Bioprinting Conditions

The alamarBlue assay (ThermoFisher) was performed by following manufacturer's protocols. A multifactorial screening was assessed to test the synergic effect of GelMA concentration, photoinitiator concentration of both I2959 and LAP, and UV exposure time, on the cell viability. Prepolymers were prepared at 1% or 5% w/v of GelMA. Photoinitiators were used at 0.1% and 0.4% w/v. Cell-laden hydrogels (20 µL amounts) (10⁶ C2C12 cells mL⁻¹) were poured into wells of a 96 well-plate. After UV exposure, samples were rinsed with growth medium to remove unreacted reagents and cultured for 24 h. Then, samples were incubated with alamarBlue solution at 10% v/v in growth media for 3 h at 37 °C. Finally, the absorbance was read at 570 nm (λ_1) and 600 nm (λ_2). The percentage of reduction (cell viability) was determined by the following equation:

$$\% \text{ Reduction} = \frac{(\epsilon_{\text{OX}})\lambda_2 \cdot A\lambda_1 - (\epsilon_{\text{OX}})\lambda_1 \cdot A\lambda_2}{(\epsilon_{\text{RED}})\lambda_2 \cdot A\lambda_1 - (\epsilon_{\text{RED}})\lambda_1 \cdot A\lambda_2} \cdot 100 \quad (1)$$

Here, ϵ_{OX} and ϵ_{RED} represent the molar extinction coefficient of alamarBlue oxidized form. A and A', represent the absorbance of the samples and the negative control, respectively. Statistical comparison was performed using a 2⁴ ANOVA multifactorial analysis by StatGraphics Centurion software (Supporting Information).

2.5. Swelling Analysis of Composite Hydrogels

The prepolymer solutions were prepared as described above. Samples for swelling analysis were prepared by placing 300 µL of the prepolymer solution in a 48 well-plate. After exposing the prepolymer solution to UV light hydrogels were rinsed with PBS and their initial weight was measured. Then, the wet weight was determined after 1, 3, and 7 d in PBS, after a wipe with tissue paper to remove the excess water. The wet weight increase ratio (ΔW) of the hydrogels was determined by the following equation:

$$\Delta W = \frac{W_s - W_i}{W_i} \cdot 100 \quad (2)$$

Here, W_i and W_s represent the weight of composite hydrogels after fabrication and the weight after swelling in PBS, respectively. To calculate the mass increase, each water content value was normalized with the initial weight of the sample.

2.6. Degradation of Composite Hydrogels

Hydrogels were fabricated as described above for the swelling analysis. Hydrogels were removed from the 48 well-plate and left swelling for 3 d in a 6 well-plate. A total of 3 mL of 1.5 U mL⁻¹ of collagenase type II (ThermoFisher) in PBS was added on the hydrogels and they were incubated at 37 °C, under 100 rpm shaking conditions. Then, hydrogels were weighted after 1, 2, and 4 h. The percent hydrogel remaining (% W_t) was determined by the following equation:

$$\% W_t = \frac{W_t}{W_i} \cdot 100 \quad (3)$$

Here, W_t represents the weight of hydrogel composites after collagenase incubation.

2.7. Analysis of the Mechanical Properties of Composite Hydrogels

Uniaxial compression tests of hydrogels were performed using a Zwick Z0.5 TN instrument (Zwick-Roell, Germany) with a 5 N load cell. Hydrogels were fabricated following the same procedure as for the swelling analysis. After reaching equilibrium swelling, cylindrical hydrogels were cut using a 10 mm diameter biopsy punch. Real hydrogel diameters and heights were measured prior to the experiment. Samples were tested at room temperature up to 30% final strain (deformation), using the following parameters: 0.1 mN preload force and 20% min⁻¹ strain rate. Stress-strain graphs were obtained from load-deformation measurements. Values for the compressive modulus were calculated from the slope of the linear region corresponding to 10–20% strain. For each hydrogel formulation, three samples were prepared, and measurements were performed in triplicate.

2.8. Pore Size Quantification

Cylinder-shaped hydrogels, 10 mm in diameter, were fabricated as described above for pore size quantification. Then, they were left swelling in Milli-Q water for 3 d to reach the same hydrogel architecture as cell encapsulation experiments and be comparable with them. After that, dehydration was carried out by sequential immersion in graded ethanol solutions in Milli-Q water: 30%, 50%, 70%, 80%, 90%, and 96% v/v for 5–15 min each and twice for 100% ethanol. Then, samples were placed in the chamber of a critical point dryer (K850, Quorum technologies, UK), sealed, and cooled. Ethanol was replaced completely by liquid CO₂, and by slowly heating. CO₂ achieved gas phase equilibrium at 35 °C and 85.06 atm and was slowly drained. This technique allowed dehydration of the hydrogels while avoiding their collapse. After critical point drying, hydrogels were imaged by ultrahigh resolution scanning electron microscopy (Nova

NanoSEM 230, FEI Company, The Netherlands) operating in low vacuum mode (0.5 mbar of water vapor pressure). Scanning electron microscopy (SEM) images were used to quantify the pore size distribution using ImageJ free software (<http://rsb.info.nih.gov/ij>, National Institutes of Health, USA).

2.9. 3D Culture of C2C12 Myoblasts Embedded in the Composite Hydrogels

C2C12 myoblasts from *Mus musculus* were purchased from ATCC and expanded in a growth medium based in Dulbecco Modified Eagle Medium (DMEM high glucose, L-glutamine, Gibco, Thermofisher) supplemented with 10% fetal bovine serum (Thermofisher) and 1% penicillin/streptomycin (Thermofisher) at 37 °C and 5% CO₂ atmosphere. To promote myotube formation, differentiation medium was used, based in DMEM high glucose and L-glutamine, supplemented with 2% Horse Serum (HS) (Thermofisher) 1% Penicillin/Streptomycin, and 2.5% HEPES (Thermofisher).

To fabricate cell-laden hydrogels, one volume of prepolymer solutions of the different composite hydrogels was mixed with one volume of a suspension of C2C12 cells to a final density of 1×10^7 cells mL⁻¹. Blends of prepolymer and cells were then placed in a cylindrical mold of 6 mm inner diameter and 750 μm height. Cell-laden solutions were photocrosslinked by 5 s or 25 s exposure to UV light at 3 W cm⁻². This was followed by immersion of the cell-laden hydrogels in growth media to remove the unreacted reagents.

2.10. C2C12 Survival in the Composite Hydrogels

C2C12 cells were encapsulated in each hydrogel as described previously. The viability was studied after 1 and 7 d using the live/dead assay kit and Hoechst (Thermofisher). Fluorescence images were captured using confocal microscopy (TCS SPE, Leica, Germany) and processed by MATLAB software (Supporting Information). Survival percentage was calculated as the fraction of living cells in respect to the total cell number. Additionally, cell morphology within the hydrogels was studied through the immunostaining of nuclei and filamentous actin (F-actin). For this purpose, hydrogels were fixed in 10% formalin solution (Sigma-Aldrich) 7 d after fabrication. Then, hydrogels were washed with PBS and cells were permeabilized with Block-Perm solution: 0.2% v/v Triton X-100 (Sigma-Aldrich) and 1% w/v BSA (Sigma-Aldrich) in PBS for 1 h. Afterward, hydrogels were washed in PBS and incubated in 100 nM Rhodamine Phalloidin 480 (Cytoskeleton, USA) solution overnight. After washing with PBS, nuclei were counterstained with DAPI (300 nM, Thermofisher) for 15 min. Hydrogels were mounted and stored at 4 °C before observation by confocal microscopy.

2.11. C2C12-Laden Composite Hydrogels Bioprinting and C2C12 Differentiation into Myotubes

Prepolymer solutions and C2C12 cell suspension were mixed as previously described to obtain a 5% w/v GelMA solution

with or without 1% of either PEGDA, CMCMA, or AlgMA in PBS containing 0.1% w/v LAP. Solutions were introduced in a 3-cc printing syringe (Nordson Corporation, USA) and placed in the direct dispensing head of the bioprinter (3DDiscovery BioSafety). All of the printing processes were performed in a cooling chamber at 10 °C. The printing rate was 7 mm s⁻¹ and printing pressure varied depending on the loaded prepolymer solution. 2.5, 2.5, 3, and 5 bar in the case of GelMA, GelMA-CMCMA, GelMA-AlgMA, and GelMA-PEGDA, respectively. To promote myotube formation and alignment, cell-laden hydrogel architecture was designed as an array of 20 filaments in a 16 mm diameter circle (BioCAD v1.0 software, regenHU Ltd., Switzerland), and converted to computer-aided design (CAD) files (Figure S6, Supporting Information). CAD files were opened in the 3D DISCOVERY HMI software interface (regenHU Ltd., Switzerland). Constructs were made by the extrusion of two layers, through a nozzle of 200 μm inner diameter, and then were photocrosslinked by a 5 s exposure to UV light (365 nm) into a 6 well-plate. After that, hydrogels were immersed in the growth medium and changed three times to remove unreacted reagents. After 5 d, growth medium was switched to differentiation medium. Samples were fixed at 11 d and F-actin and nuclei were stained as described previously (Section 4.10). In addition, a staining of myosin heavy chain was performed by incubating the samples in a 5 μg mL⁻¹ MF20 Alexa Fluor 488 (eBioscience, Thermofisher) solution overnight.

2.12. Myotube Alignment and Fusion Index Analysis

Z-stack images obtained by confocal microscopy were processed using ImageJ software. Myosin heavy chain (MHC) staining was used for analysis of the fusion index and myotube alignment. Myotube alignment was assessed by measuring the angle formed between the myotubes and the longitudinal axis of the printed pattern. The fusion index was calculated by dividing the number of nuclei within the myotubes by the total number of counted nuclei and this was expressed as a percentage. Three samples for each condition were used and more than 100 myotubes were analyzed for each sample.

2.13. Statistical Analysis

All data collected were presented as the mean ± standard deviation (SD) using GraphPad Prism software (GraphPad, USA). ANOVA and *t*-tests were performed in StatGraphics Centurion software (StatGraphics, Spain) to compare treatments. A *p*-value of 0.05 or less was considered statistically significant.

3. Results and Discussion

3.1. Synthesis and Characterization of Methacrylated Polymers

Our three composite bioinks incorporate four different photocrosslinkable materials (Figure 1). GelMA emulates the ECM for various cells types^[45] in combination with the non-biodegradable materials Alginate (Alg), carboxymethylcellulose

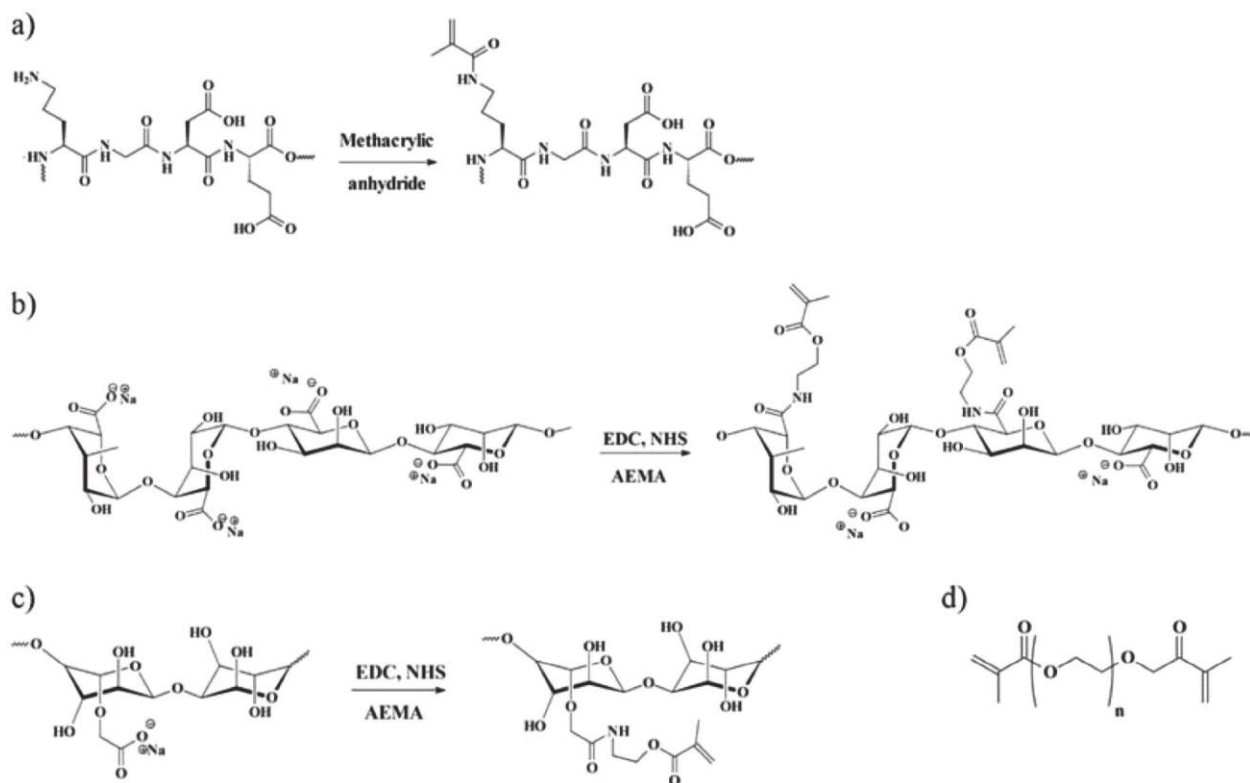


Figure 1. Covalent functionalization of the photocrosslinkable materials: a) methacryloylated gelatin (GelMA), b) alginate-methacrylate (AlgMA), c) microfibrillated cellulose-methacrylate (CMCMA), and d) PEGDA.

(CMC) and PEGDA. GelMA is a photocrosslinkable hydrogel derived from natural gelatin. Gelatin was functionalized with methacrylate anhydride as described previously^[45] and the methacrylation was characterized by a colorimetric assay. Hydrogels were finally fabricated using GelMA with 40% degree of methacrylation (Table S1, Supporting Information). Alginate was methacrylated following the protocol described by Jeon et al.^[28] In addition, for the first time CMC was successfully functionalized using 2-aminoethylmethacrylate and EDC/NHS using carboxylic acids as anchorage points. The number of methacrylate groups was directly verified by ¹H-NMR and was in close agreement (Figures S1 and S2, Supporting Information) with previous work.^[28,34] We assume that following reported protocol Alginate and CMC achieved a theoretical and real degree of methacrylation about 45% and 25%, respectively.^[28,34] Finally, PEGDA, which has already two end acrylate groups, was obtained from a commercial supplier.

3.2. Assessment of Optimal C2C12 Survival After Encapsulation in Composite Hydrogels

Cell viability after encapsulation in photocrosslinkable bioinks, are under the influence of several factors, such as material concentration,^[46] functionalization degree (amount of functional methacrylates/methacrylamides conjugated onto the polymer),^[45] UV exposure time, type of photoinitiator, and photoinitiator concentration.^[40] For this reason, the limits of these

factors controlling printing capabilities were assessed based on cell viability. To determine the most relevant factors acting on cell viability, C2C12 myoblasts were encapsulated using different biomaterial concentration, photoinitiator concentration, and UV exposure time. Two different photoinitiators were used, 2-hydroxy-4'-(2-hydroxyethoxy)-2-methylpropiophenone (I2959) and LAP. To assess all these parameters a 2⁴ ANOVA multifactorial analysis of cell viability assay was designed using 96 well-plates. Cell viability was determined 24 h after cell printing by an alamarBlue commercial kit. Percentage reduction of alamarBlue reagent is related to cell metabolism, in this way high values of reduction mean high cell viability. Due to the bioprinter equipment used in this work the intensity of the UV light could not be adjusted, but the effects of this parameter were incorporated in exposure time. It is possible to increase or reduce the UV dosage by using longer or shorter exposure times, respectively.

The full statistical dataset is shown in the supporting Information (ANOVA multifactorial analysis of the viability assay). By extracting relevant information, it is possible to define the limits of the bioprinting system. In all samples, composites irradiated for less than 5 s were unable to crosslink. In addition, we found that cell viability was strongly affected by the exposure time, and 25 s of UV drastically reduced cell survival (Figure 2b). Photoinitiator concentration has a strong effect on cell viability because the free radicals produced after UV exposure are cytotoxic. Figure 2c shows the mean cell survival of all samples fabricated with 0.1% and 0.4% of photoinitiator

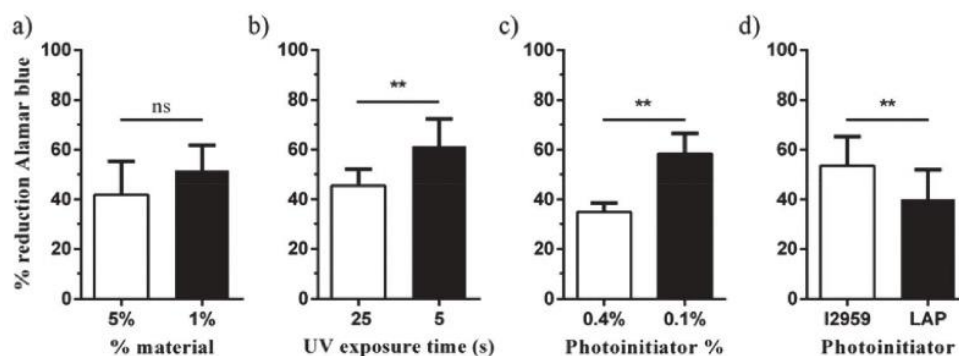


Figure 2. Effect of a) GelMA concentration, b) UV exposure time, c) photoinitiator concentration, and d) photoinitiator type on the C2C12 viability. C2C12 cells were encapsulated in GelMA hydrogels at 10^6 cell mL^{-1} and cultured for 24 h. Polymer solutions were prepared containing either I2959 or LAP photoinitiator at 0.1% or 0.4% w/v. Cell-laden prepolymers were photopolymerized under 25 s or 5 s of UV light. Cell viability was examined using the alamarBlue test. Values are represented as percentage reduction (mean \pm standard deviation, *t*-test ***p*-value < 0.01, *n* = 12).

(LAP or I2959). This graph demonstrates that increasing the photoinitiator concentration (even I2959 or LAP) from 0.1% to 0.4% dramatically decreased cell survival. As was reported previously, LAP has a higher extinction coefficient at 365 nm than I2959,^[40] and more radicals are generated using the same concentration, this fact influences cell viability and could explain why I2959 was less toxic than LAP (Figure 2d). In contrast, the quantity of material did not have a significant effect on the cell viability after printing. Below 1% of the material, the structures obtained were not consistent enough to be useful and above 7% the high viscosity clogged the nozzle orifice.

Taking the alamarBlue assay results and the preservation of the 3D structure of the hydrogels, we concluded that it is possible to work within the 5–25 s range of UV exposure time. It is possible to use both types of photoinitiators at a maximum concentration of 0.1%, and finally work with 5–7% of material using methacrylated biomaterials in agreement with previous findings.^[44]

3.3. Hydrogel Swelling and Degradation

To study the stability of the different hydrogels over time, different samples were prepared in concordance with the previous viability assay conditions. Crosslinking conditions were: 5% of GelMA material with 1% of non-biodegradable methacrylated biomaterial, 5 s of UV dosage and 0.1% photoinitiator concentration. As noted in the previous section, photoinitiator concentrations above 0.1% were discarded as unviable because of high cytotoxicity. Below 0.1%, we observed high variability in the formation of the crosslinked scaffolds. **Figure 3a,b** shows pictures of the fabricated cylinder-shaped hydrogels. Samples obtained with I2959 were too weak to maintain cylindrical shape, especially compared to hydrogels fabricated with LAP.

Wet weight increases as function of time in composite hydrogels made with both photoinitiators, I2959 and LAP (Figure 3c). Samples were weighted after fabrication and after 1, 2, and 7 d. Photoinitiator molar extinction coefficient, ϵ , determines the generation of free radicals as a function of the wavelength. I2959 showed weak molar absorptivity ($\epsilon = 4 \text{ M}^{-1} \text{ cm}^{-1}$) at 365 nm,^[40,47] and composite hydrogels had a wet weight

increase close to 0% or even below, meaning a loss of mass. Thus, with 5 s of UV dosage composite hydrogels showed low crosslinking. The apparent low crosslinking resulted in a loss of material and in poorly manageable hydrogels. This behavior occurred due to the pore dilatation after water absorbance. Therefore, the negative values of wet weight increase are explained due to the loss of material, which was greater than the absorbed water content. This effect was not observed in the case of composite hydrogels made with LAP, which were easy to handle and showed wet weight increases >25%. LAP has about 50-fold higher molar absorptivity ($\epsilon = 218 \text{ M}^{-1} \text{ cm}^{-1}$) at 365 nm than I2959^[40] which explains the results. Thus, the LAP hydrogels showed a normal swelling behavior, and after 7 d all reached the swelling equilibrium.

The dramatic effect on shape fidelity by using I2959 (Figure 3b) could be also attributed to oxygen inhibition in the polymerization system, as has been recently published.^[48] Lim et al. prove that shape fidelity is improved by increasing photoinitiator concentration or UV dosage. In our case, the LAP's higher molar absorptivity produces the same effect on the photopolymerization yield, and resulted in high fidelity, thickness, and mechanical stability (Figure 3a).

Combinations of GelMA with the hydrophilic methacrylated polymers, showed an increase in the final wet weight. Composite blends containing 1% of CMCMA (*p*-value < 0.001), AlgMA (*p*-value = 0.013), or PEGDA (*p*-value = 0.04) showed significant differences and scaffolds with high water content and swelling were obtained (Figure 3d). The differences in the water uptake could be attributed to the highly hydrophilic structure of the polysaccharides. In the case of GelMA-AlgMA, the increase in swelling is in concordance with recent publications.^[37]

To study the effect of polymer composition on the degradation of composite hydrogels collagenase II (1.5 U mL^{-1}), which degrades gelatin fraction, was used. Samples were weighted after 1, 2, and 4 h. Hydrogels made in the presence of I2959 were completely degraded after 1 h due to their low crosslinked structure. For this reason, the results of the degradation of the materials obtained only with LAP are plotted (Figure 3e). Compared with pristine GelMA the composite hydrogels showed more resistance to degradation. The addition of 1% PEGDA

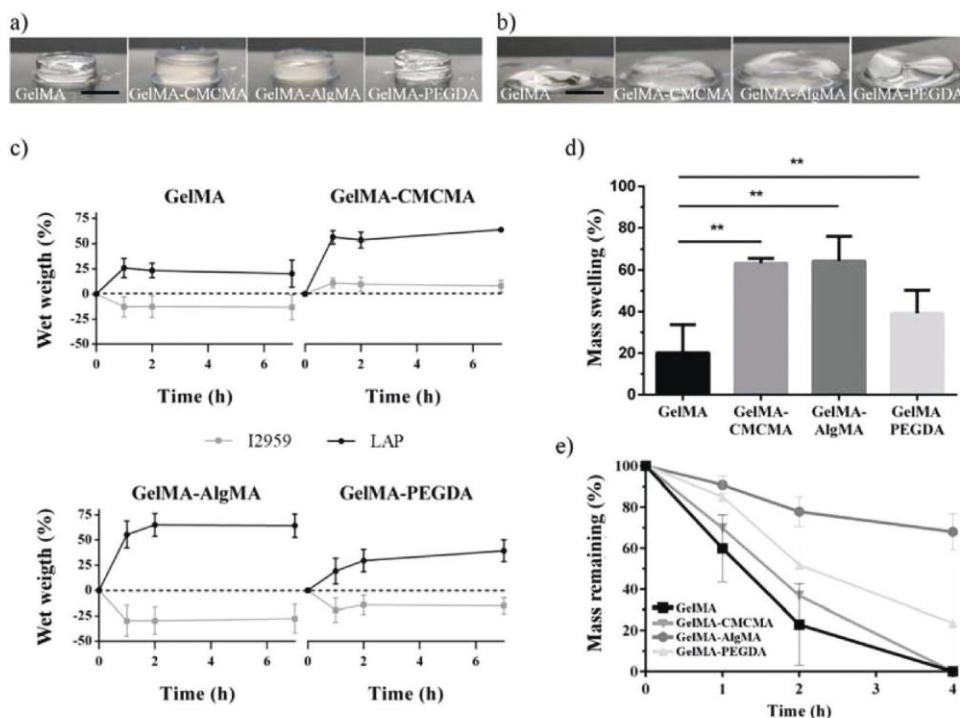


Figure 3. Effect of composites on the swelling and degradation of 5% w/v GelMA hydrogels. Disc-shaped hydrogels fabricated using a) LAP or b) I2959 as a photoinitiator, under 5 s of UV light exposure. c) Swelling was studied as the change in wet weight and d) differences in mass were found in the case of CMCMA, PEGDA, and AlgMA (mean \pm standard deviation, $**p$ -value < 0.01 , $n = 6$) at the equilibrium swelling. e) Percentage mass of the remaining profile showing the effect of the composite on the decrease in the wet weight of hydrogels (mean \pm standard deviation, $n = 4$) incubated in a 1.5 U mL^{-1} collagenase type II solution. GelMA (■), GelMA-CMCMA (▼), GelMA-AlgMA (●), GelMA-PEGDA (▲).

(p -value = 0.046) and AlgMA (p -value = 0.016) significantly decreased the degradation rate. In particular, more than a half of the mass swelling (68%) remained for GelMA-AlgMA hydrogels after 4 h of enzymatic degradation.

The results show the increased resistance to degradation of composite hydrogels by the addition of a small percentage of non-mammalian animal derived polymers. Since Alginate, CMC, and PEGDA are not degradable by mammalian cells^[34,49,50] and provide stability to the composite hydrogels. It is important to note the better mechanical stability and long-lasting structures when fabricated with LAP.

3.4. Composite Hydrogels with Tunable Mechanical Properties

After swelling, hydrogels were punched to obtain 10 mm diameter cylinders and stress-strain curves were measured by dynamic mechanical analysis. Young's modulus was determined using a compressive modulus and was calculated as the slope of the linear part of the stress-strain curves. As the swelling results show (Figure 3c), hydrogels made in the presence of I2959 under 5 s of UV exposure were extremely weak and it was not possible to perform the mechanical measurements in some of them (Figure 4a). In contrast, all the samples made in the presence of LAP under 5 s of UV exposure were easy to handle and the Young's modulus values were significantly higher (p -value < 0.005) than those of I2959. It was clear that I2959 needs high UV dosages to develop adequately

crosslinked hydrogels and, for this reason, 25 s of UV exposure was used (Figure 4b). With this UV dosage it was possible to fabricate stable hydrogels, but this exposure time reduced C2C12 viability (Figure 2b).

Increase in the polymer concentration, in particular GelMA, increases the stiffness properties of the hydrogel.^[47] In our case, in the optimized conditions (using LAP and 5 s of UV exposure) Young's modulus was determined to be $3.02 \pm 1.13 \text{ kPa}$ for 5% GelMA. These values agree with reported by Nichol et al. ($\approx 2 \text{ kPa}$), Camci-Unal et al. (3.4 kPa), and Costantini et al. ($2.45\text{--}5.81 \text{ kPa}$) where similar polymer percentage and degree of methacrylation are used.^[44,45,51] Figure 4c shows that the material stiffness had different behavior with the addition of 1% of PEGDA, CMCMA, and AlgMA. The addition of PEGDA ($2.89 \pm 0.46 \text{ kPa}$ for GelMA-PEGDA) did not cause significant changes. However, addition of CMCMA caused a significant reduction in the compressive moduli to $1.96 \pm 0.16 \text{ kPa}$ (p -value < 0.05). With AlgMA we observed the opposite effect, with the stiffness increasing significantly to $5.53 \pm 2.01 \text{ kPa}$ (p -value < 0.05).

In all cases, GelMA-AlgMA hydrogels showed the highest compressive modulus compared to the other composites. The mild gelation of alginate by the addition of divalent cations such as Ca^{2+} is widely used in biomedical applications. We could assume that the relevant differences of GelMA-AlgMA over the other composites are due to a secondary ionotropic gelation because of divalent ions contained in the polymer solution or in the PBS during the swelling.

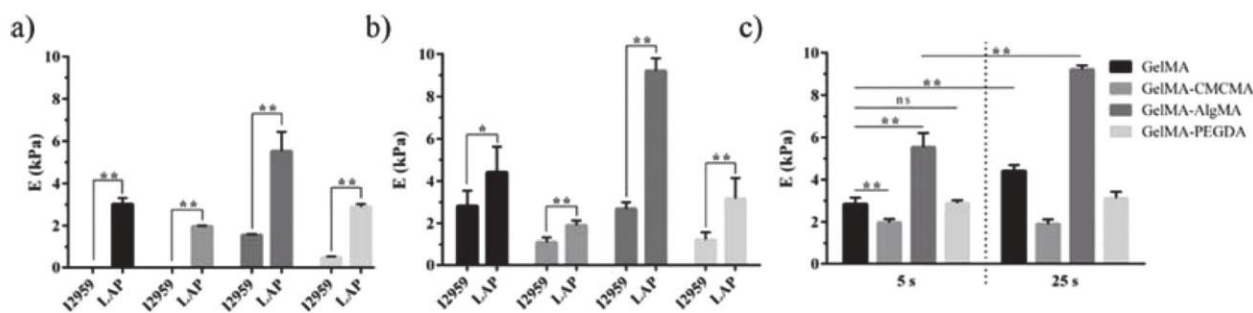


Figure 4. Characterization of the mechanical properties of the composite hydrogels. Young's moduli of GelMA and the three composites photocrosslinked with I2959 and LAP during a) 5 s and b) 25 s. c) Comparative Young's modulus of hydrogels photocrosslinked with LAP during 5 s and 25 s. Values are plotted as the mean \pm standard deviation, ***p*-value < 0.01, *n* = 3.

Stiffness of composite hydrogels can be related to their resistance to collagenase degradation. GelMA-AlgMA hydrogels had the highest resistance and the lowest degradation, followed by GelMA-PEGDA and GelMA-CMCMA hydrogels. These results suggest that the crosslinking density of hydrogels depends on the composite material, UV dosage, and type of photoinitiator. Furthermore, as previously indicated, the mechanical properties of hydrogels strongly impact muscle function and phenotype.^[39,42–44,52] Therefore, it is of great interest to make hydrogels mimicking the biological scaffolds with tunable mechanical properties. It is possible to increase the mechanical properties of hydrogels to increase the hydrogel concentration, the UV dosage, or the photoinitiator. However, these methods may reduce cell viability, as we have demonstrated, and the porosity and interconnectivity of hydrogels and therefore has adverse effects on the performance of hydrogels.^[53] For example, it has been demonstrated that increasing the mechanical properties of GelMA hydrogels by increasing the concentration and/or molecular weight of methacrylate limited cell viability and

growth, morphogenesis, and cell migration.^[54] In this regard, non-degradable materials hold a great promise as a supplementary material for hydrogels to tune their mechanical properties. Due to their different chemical structures, small amount of these non-degradable materials is sufficient to considerably change the mechanical properties of composite hydrogels with minor effect on encapsulated cells. Finally, all composite hydrogels showed viscoelastic behavior in the range of the stiffness to promote myotube differentiation in 3D (1–3 kPa)^[44] and in 2D structures (8–11 kPa);^[55,56] therefore, all of them could be ideal scaffolds for soft tissues, such as skeletal muscle.

3.5. Pore Size and Pore Distribution

The pore size of composite hydrogels was analyzed using SEM. The images revealed that the fibrillar structure of the gelatin was not affected by the addition of the other polymers (Figure 5a–d). These images were therefore used to

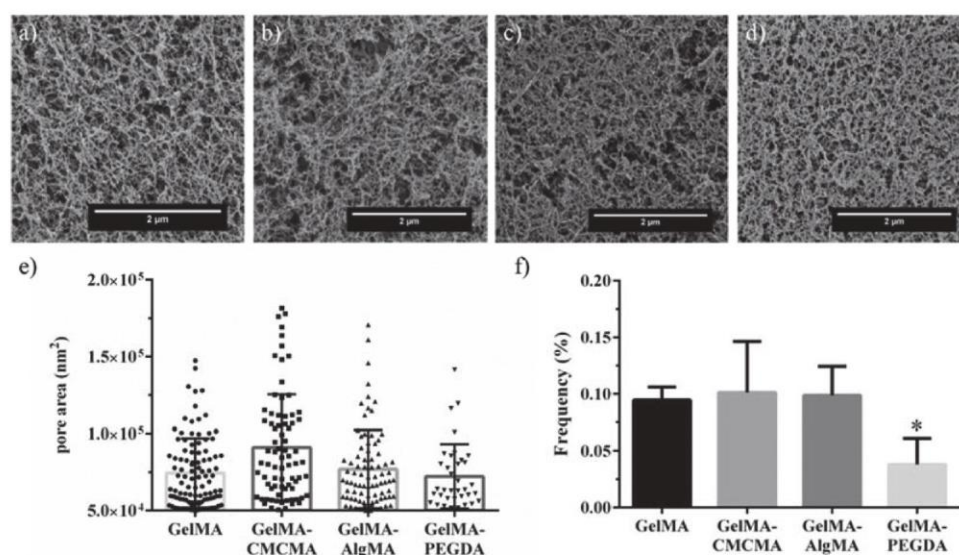


Figure 5. Scanning electron microscopy (SEM) images of a) GelMA, b) GelMA-CMCMA, c) GelMA-AlgMA, and d) GelMA-PEGDA. The aqueous part of composite hydrogels was removed after critical point drying and fibrillar structure of the hydrogel was left behind. e) Pore size distribution above 200 nm in diameter and f) their fraction of the total pore population, expressed as percentages (mean \pm standard deviation, **p*-value < 0.05).

determine the pore size distribution (Figure 5e). Among the different composite hydrogels, no significant differences were found in the range of the small pores (<20 nm), which could limit the passage of nutrients and proteins.^[57] However, GelMA-PEGDA hydrogels showed significant reduction in the number of pores with diameters > 200 nm ($5 \cdot 10^5 \text{ nm}^2$). The GelMA-PEGDA hydrogel presented a homogenous structure in terms of pores size and pores distribution. The structure is more packed as we can see in Figure 5d, and the total amount of pores > 200 nm was below 0.05% of the total pores (Figure 5f). This porosity range between 200 and 600 nm is where cells can best spread and extrude their filopodia.^[58–60] Therefore, very low levels or the nonexistence of pores above this size could reduce cell viability because the limited cell spreading. Furthermore, the absence of these pores can negatively affect skeletal muscle differentiation, where myoblast spreading, and cell–cell contact play key role in myotube formation.^[13]

We kept the concentrations of CMCMA, AlgMA, and PEGDA constant but increasing this concentration would affect the physico-mechanical properties of the composite hydrogels. Swelling behavior should show an increase,^[34] and then a decay because of increasing the polymer concentration. Moreover, composite hydrogels would be more resistant to biodegradation.^[51] Compressive moduli and pore size would also be affected by increasing the non-degradable compounds' concentration. As has been published, an increase on AlgMA content makes the hydrogels stiffer and reduces the pore size.^[37] In the

case of CMCMA, it seems to induce, first, a softening of the hydrogels, but the further increase of polymer concentration should lead to a stiffening effect.

3.6. Long-Term C2C12 Viability and Proliferation within Composite Hydrogels

In this study, we compared the long-term viability of C2C12 encapsulated in the composite hydrogels using GelMA as the positive benchmark. To study the long-term viability and proliferation of C2C12 cells, 5% w/v GelMA was dissolved in PBS buffer, with LAP 0.1% and 1% of either PEGDA, CMCMA, AlgMA was added to the polymer solutions corresponding to composites. Cells were trypsinized and the cell suspension was prepared in the growth medium. The material and the cell suspension were mixed in 1:1 proportion and a drop of the resulting solution was immediately placed in a previously mounted PDMS mold. The samples were irradiated for 5 s under UV light and allowed to swell in the growth medium. The final structures, after demolding, had a 6 mm diameter size and 750 μm height.

The percentage of living cells in the hydrogels was determined using the live/dead staining kit at 1 and 7 d. The viability obtained in the GelMA hydrogels was about 80% at 1 d, in agreement with previous studies,^[61] and about 60% for GelMA-CMCMA and GelMA-AlgMA hydrogels. These composite hydrogels showed a similar slight decrease in the cell viability at day 7 (Figure 6a,b). The chemical structures of CMC

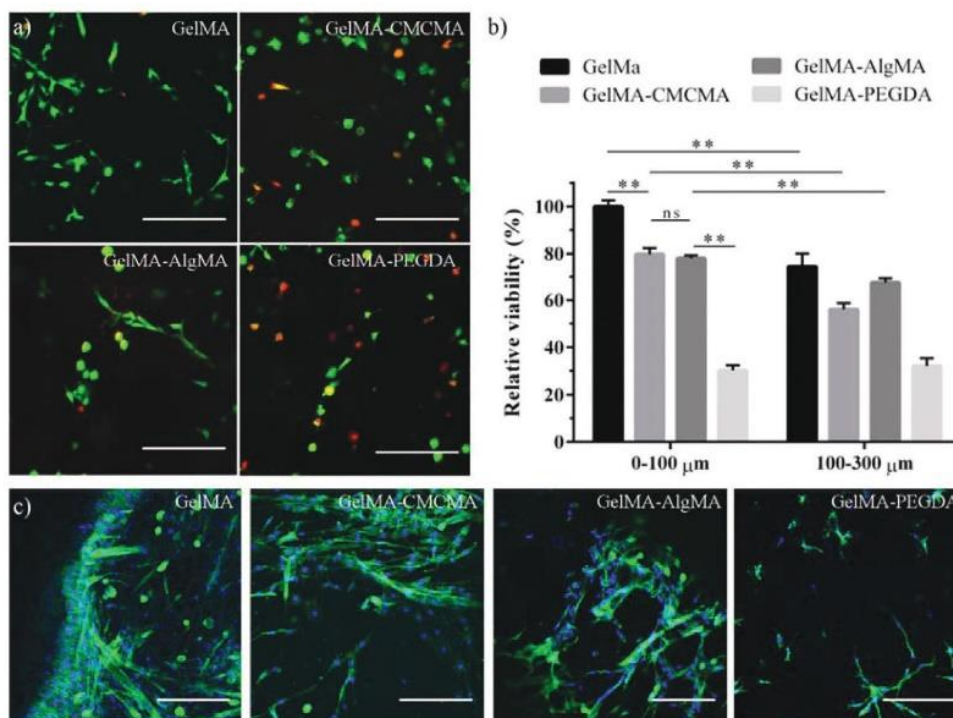


Figure 6. C2C12 viability and proliferation in the composite hydrogels at 7 d. a) Representative images of the live/dead staining (dead in red and live in green) in the range of the first 100 μm depth. b) Cell viability in composite hydrogels represented as the living cells over the total cell number (mean \pm standard deviation, $**p$ -value < 0.01) relative to GelMA hydrogels. c) Confocal microscopy pictures of C2C12 cells inside composite hydrogels. F-actin in green and nuclei in blue. Scale bar = 200 μm .

and Alginate do not promote cell attachment to the surface, so they usually show lower survival values.^[35,41] However, in the composite materials, the viability was still high, and the values were similar to GelMA. Moreover, the percentage of living cells increased at 7 d (Figure 6a,b).

In contrast, the number of living cells in GelMA-PEGDA composites decreased dramatically after 1 d and low levels of living cells remained up to 7 d. These results could be explained by the reduction of the number of pores > 200 nm, in the GelMA-PEGDA hydrogels. Thus, cells remained immobilized after 1 d and their limited spread affected cell survival and produced low viability values.

We also observed that the number of dead cells increased in the deepest regions of the 3D structures. GelMA, GelMA-CMCMA, and GelMA-AlgMA had significant differences between the number of live cells counted within first 100 μm from the surface and the ones below 100 μm (until 300 μm) (Figure 6b). The porosity of the materials determines the diffusion of nutrients inside the hydrogel. If nutrient uptake is faster than nutrient renewal through diffusion of the medium inside the hydrogel, a lack of nutrients results that increases with the material depth.

The ability of cells to attach, spread, and grow on hydrogels is important for tissue development.^[62,63] To check the proliferation, cell morphology, and distribution in the composites, immunofluorescence staining of F-actin and nuclei was performed (phalloidin and DAPI) at 7 d. Figure 6c shows cell spreading inside the hydrogels. C2C12 cells in GelMA-PEGDA were less spread than the other composites, with slight cytoskeleton protrusions, which indicated that PEGDA impairs cell spreading. In contrast, in GelMA, GelMA-CMCMA, and GelMA-AlgMA C2C12 cells elongated inside the hydrogels, the abundant F-actin filaments, and interconnected between them. These results indicated that GelMA-PEGDA is the less suitable candidate to promote C2C12 cell growth and spreading, compared to the pristine GelMA and those that contain CMCMA and AlgMA.

Stiffer materials in 2D are known to promote cell proliferation and attachment.^[25,63] Another important factor is the presence of cell adhesion sequences such as arginylglycylaspartic acid.^[25] In 2D, stiffness is a key factor but in 3D the porosity also influences cell proliferation and spreading as seen in our results. GelMA-PEGDA and pristine GelMA had no significant Young's moduli differences (Figure 4c) but cell behavior in the hydrogel is totally opposite.

Even though GelMA-CMCMA composites are softer than GelMA-PEGDA composites, proliferation and cell adhesion are improved in GelMA-CMCMA. Altogether, the results are consistent with previous studies demonstrating that in 3D, muscular cells can spread, proliferate, and present better myogenesis than in less packed structures.^[44] Our data suggests that stiffness is not the main factor affecting cell behavior in 3D but rather the key factor is to obtain less packed structures with a good distribution of big pores. Here, we have obtained a library of composite materials with a good balance between the mechanical and mass transport function. As a result, we can choose between scaffolds with similar Young's moduli values but with different pore sizes frequency.

3.7. Composite Hydrogels as a Bioink for Muscle Tissue Bioprinting

Hydrogel patterning is widely used to align cells and extrusion bioprinting was used to build 3D scaffolds of C2C12 embedded in composite hydrogels. A C2C12 cell suspension was first mixed with the prepolymer solutions. The effect on cell alignment inside GelMA filaments below 200 μm in width has been already reported,^[54,64] for this reason the mixture was introduced into a printing syringe and a nozzle of $\pm 200 \mu\text{m}$ inner diameter was used. Several filaments were drawn inside a circle (Figure 7a).

To achieve a relevant height (about 200 μm) two layers were printed. In extrusion bioprinting, nozzle inner diameter, printing pressure, and rate can determine the width and the thickness of the printed bioink. Printing fidelity was evaluated as the percentage change in width, compared to nozzle inner diameter (Figure 7b). After printing, filament width differed with respect to the nozzle inner diameter about 30%, but this fact did not impair the fabrication of isolated filaments (Figure 7c,d). With this method, bioprinted structures were successfully made using GelMA, GelMA-CMCMA, GelMA-AlgMA, and GelMA-PEGDA. Filaments of $\pm 200 \mu\text{m}$ in height and about 250 μm in width were achieved and these could avoid the problem of low nutrient diffusion in thick hydrogels.

Cells were cultured in the growth medium until high confluence was reached (5 d) and then, the growth medium was switched to a differentiation medium. At 11 d, GelMA scaffolds were nearly flat, and the structure was lost, due to the cell activity (degradation) while the composite hydrogels preserved their 3D structure. To observe the morphology of the cells and distribution in the hydrogels, cells were stained with phalloidin and DAPI, and also stained with anti-myosin heavy chain (MHC), a protein overexpressed only in differentiated striated muscle. In all cases, C2C12 were able to proliferate embedded in the composites and displayed myotube formation (Figure 7e). The effect of the 3D structures on guiding cell alignment was confirmed by the analysis of myotube orientation (Figure 7g). Patterned composite hydrogels exhibited unidirectional orientation of myotubes instead of a random, unorganized mesh as seen in the images obtained from the unpatterned hydrogels (Figure 6c). Quantitative analysis of the cell alignment shows that cells in the patterned GelMA hydrogels also exhibited high degree of alignment but significantly lower than the composite hydrogels (Figure 7h). These results are in concordance with the degradability test and sustain the protection against degradability of composite hydrogels. Wider filaments were also fabricated and was observed that cell alignment reduced considerably in the filament direction (Figure S7, Supporting Information). In agreement, it has been reported that cells confined in GelMA hydrogels, with a geometry constraint below 200 μm widths induce high cell alignment.^[54] Recently, the effect of 3D scaffolds with anisotropic morphology on cell alignment has also been demonstrated, where more than 60% alignment efficacy along 14 d of cell culture is proved.^[64] In addition, shear stress generated in the nozzle helps the polymer chains to redirect parallel to the longitudinal axis of the bioink stream, and thus may also promote the alignment of cell adhesion motifs.

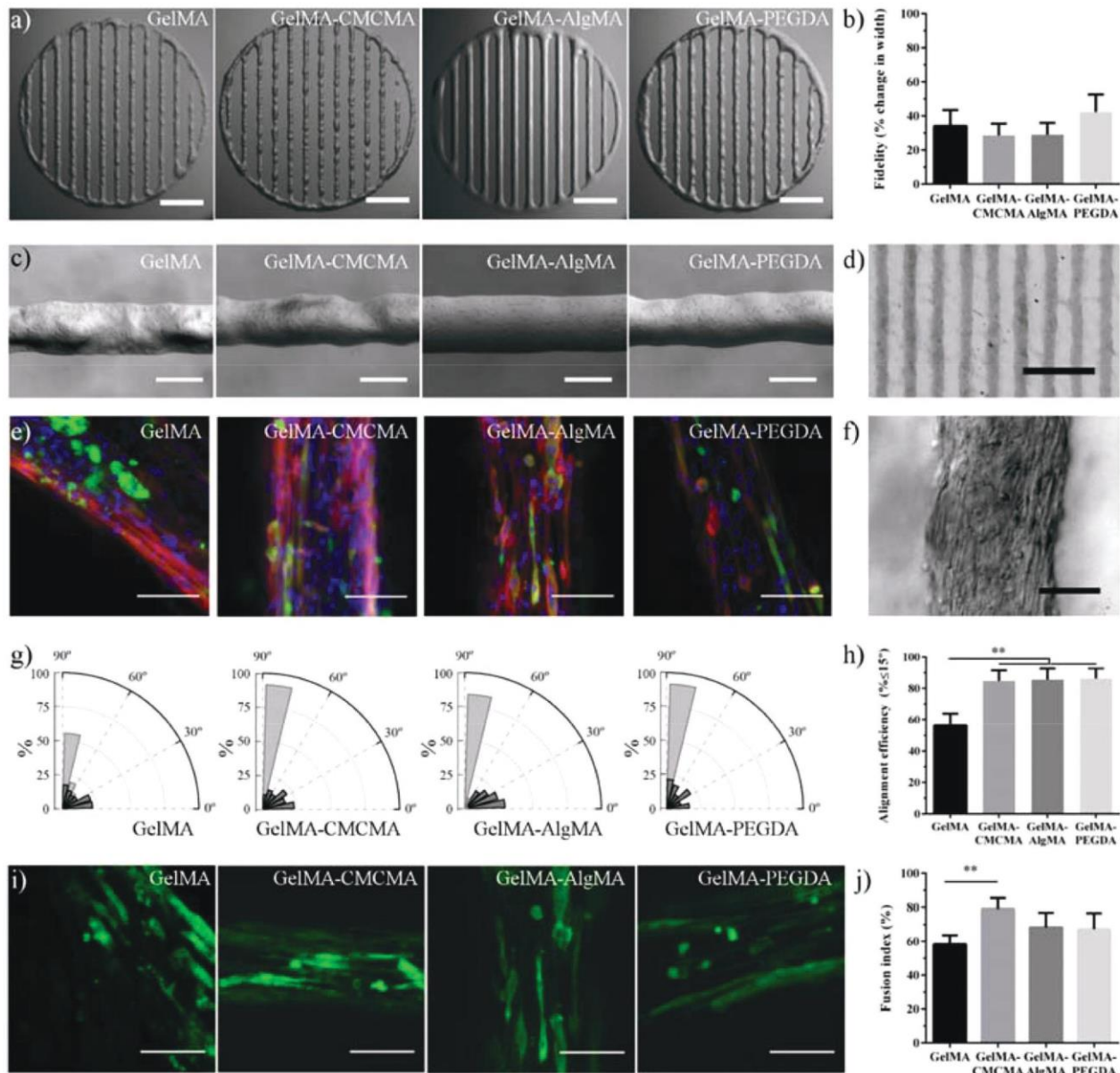


Figure 7. C2C12 myotube formation in bioprinted composite hydrogels. a) Top view images of the bioprinted composite hydrogels after fabrication. Scale bar = 2 mm. b) Percentage change in width of composite hydrogels after printing compared to nozzle inner diameter. c) Magnification of the filaments containing C2C12 cells. Scale bar = 250 μm . d) 3D structure was successfully printed and remained stable after swelling. Scale bar = 2 mm. e) Confocal microscopy pictures of C2C12 cells encapsulated in the composite hydrogel structures after 11 d of culture. F-actin in red, MHC in green, and nuclei in blue. Scale bar = 200 μm . f) Bright field image of elongated cells encapsulated in composite hydrogel. Scale bar = 200 μm . g) Normalized histograms (bin = 10°) depicting the distribution of the angles between cell cytoskeleton fibers (light gray) inside non-patterned hydrogels (dark gray), while inside cylinder-shaped hydrogels are randomly distributed. C2C12 inside the bioprinted hydrogels show high degree of alignment ($>75\%$) following the pattern direction, while inside cylinder-shaped hydrogels are randomly distributed. h) Quantitative analysis of cell alignment efficiency (mean \pm standard deviation, $**p$ -value < 0.01). i) Confocal microscopy images showing the expression of MHC (green) in the C2C12 myotubes inside 3D bioprinted composite hydrogels. Scale bar = 200 μm . j) Fusion index percentage (mean \pm standard deviation, $**p$ -value < 0.01) of the C2C12 myotubes encapsulated in the bioprinted composite hydrogels.

Confocal images showed that MHC was present in all the constructs, indicating that it was possible to obtain differentiated myotubes (Figure 7i). To evaluate the quality of differentiation in the patterned scaffolds, the fusion index was determined as the percentage of nuclei associated with myotubes compared to the total number of nuclei in each sample.^[65,66] As

expected, C2C12 fused into myotubes in GelMA hydrogel after 11 d of culture. GelMA-CMCMA and GelMA-AlgMA also promoted myogenesis (Figure 7j). Furthermore, the fusion index of those composites was slightly higher than GelMA. As previously mentioned, GelMA 3D structures tended to degrade after several days, due to cell metabolism, making it difficult to

find significant 3D areas comparable with the scaffolds made of composite materials. The fusion index corresponding to GelMA-PEGDA hydrogels was similar to the other composites immunofluorescence images indicating that the number of myotubes was significantly lower (Figure 7j).

After all, the applicability of these composite hydrogels in skeletal muscle tissue engineering has been proved and for the first time, GelMA-CMCMA composite hydrogels have been successfully used to fabricate skeletal muscle constructs. Considering the adjustability of the physical properties, these composite hydrogels can be used in other tissue engineering applications: heart, cartilage, or bone as other authors have been demonstrated by using GelMA and AlgMA.^[32,37]

4. Conclusion

3D bioprinter technologies have emerged as a great system to fabricate complex tissues. Therefore, bioinks play a key role to success in the use of such technologies. In this work, the influence of mechanical stiffness and geometrical confinement on the 3D culture of myoblast-laden GelMA photo-crosslinkable composite hydrogels was evaluated in terms of in vitro myogenesis. We compared new composite hydrogels (GelMA-CMCMA and GelMA-AlgMA) to print stable and non-biodegradable skeletal muscle structures, and at the same time with tunable properties to allow high cell viability and myogenesis. Compared with non-degradable previously described composite hydrogels, such as GelMA-PEGDA, we obtained higher cell proliferation and viability. We demonstrated that frequency and presence of pores with diameters > 200 nm ($5 \cdot 10^5 \text{ nm}^2$) are crucial factors in the design of 3D scaffolds and in cell 3D encapsulation, even in hydrogels with different stiffness. The use of GelMA-CMCMA and GelMA-AlgMA composites with bioprinting methods allowed us to efficiently obtain 3D durable structures of differentiated and aligned muscle fibers. In contrast to GelMA, they are long-lasting materials and good candidates as hydrogels for in vitro applications and bioactuators.

Supporting Information

Supporting Information is available from the Wiley Online Library or from the author.

Acknowledgments

A.G.-L. and X.F.-G. contributed equally to this work. Funding for this project was provided by the Ramon y Cajal (RYC-2014-15022) fellowship and Severo Ochoa Program for Centers of Excellence (R&D 2016–2019) funded by the Ministerio de Economía, Industria y Competitividad; an ERC grant (ERC starting grant project-714317-DAMOC); the CERCA Programme/Generalitat de Catalunya (2014-SGR-1442 and 2014-SGR-1460); and the Fundación Bancaria “la Caixa”-Obra Social “la Caixa” (projecte IBEC-La Caixa Healthy Ageing); MINDS project funded by Ministerio de Economía, Industria y Competitividad (TEC2015-70104P) and Biotob TEC2015-72718-EXP.

Conflict of Interest

The authors declare no conflict of interest.

Keywords

3D bioprinting, bioinks, composite hydrogels, skeletal muscle, long-lasting scaffolds

Received: May 2, 2018

Revised: July 3, 2018

Published online: August 29, 2018

- [1] S. Ahadian, R. B. Sadeghian, S. Salehi, S. Ostrovidov, H. Bae, M. Ramalingam, A. Khademhosseini, *Bioconjugate Chem.* **2015**, *26*, 1984.
- [2] S. Ostrovidov, V. Hosseini, S. Ahadian, T. Fujie, S. P. Parthiban, M. Ramalingam, H. Bae, H. Kaji, A. Khademhosseini, *Tissue Eng. Part B-Rev.* **2014**, *20*, 403.
- [3] J. M. Grasman, M. J. Zayas, R. L. Page, G. D. Pins, *Acta Biomaterialia* **2015**, *25*, 2.
- [4] P. Banerjee, A. K. Bhunia, *Trends Biotechnol.* **2009**, *27*, 179.
- [5] T. G. Fernandes, M. M. Diogo, D. S. Clark, J. S. Dordick, J. M. S. Cabral, *Trends Biotechnol.* **2009**, *27*, 342.
- [6] S. B. Kim, H. Bae, J. M. Cha, S. J. Moon, M. R. Dokmeci, D. M. Cropek, A. Khademhosseini, *Lab Chip* **2011**, *11*, 1801.
- [7] N. Misawa, H. Mitsuno, R. Kanzaki, S. Takeuchi, *Proc. Natl. Acad. Sci.* **2010**, *107*, 15340.
- [8] N. S. Bhise, J. Ribas, V. Manoharan, Y. S. Zhang, A. Polini, S. Massa, M. R. Dokmeci, A. Khademhosseini, *J. Controlled Release* **2014**, *190*, 82.
- [9] H. Fujita, V. T. Dau, K. Shimizu, R. Hatsuda, S. Sugiyama, E. Nagamori, *Biomed. Microdevices* **2011**, *13*, 123.
- [10] A. L. Baryshyan, L. J. Domigan, B. Hunt, B. A. Trimmer, D. L. Kaplan, *RSC Adv.* **2014**, *4*, 39962.
- [11] M. S. Sakar, D. Neal, T. Boudou, M. A. Borochin, Y. Li, R. Weiss, R. D. Kamm, C. S. Chen, H. H. Asada, *Lab Chip* **2012**, *12*, 4976.
- [12] J. Ramon-Azcon, S. Ahadian, M. Estili, X. B. Liang, S. Ostrovidov, H. Kaji, H. Shiku, M. Ramalingam, K. Nakajima, Y. Sakka, A. Khademhosseini, T. Matsue, *Adv. Mater.* **2013**, *25*, 4028.
- [13] J. Ramon-Azcon, S. Ahadian, R. Obregon, G. Camci-Unal, S. Ostrovidov, V. Hosseini, H. Kaji, K. Ino, H. Shiku, A. Khademhosseini, T. Matsue, *Lab Chip* **2012**, *12*, 2959.
- [14] J. Visser, F. P. Melchels, J. E. Jeon, E. M. van Bussel, L. S. Kimpton, H. M. Byrne, W. J. Dhert, P. D. Dalton, D. W. Huttmacher, J. Malda, *Nat. Commun.* **2015**, *6*, 6933.
- [15] P. Bajaj, R. M. Schweller, A. Khademhosseini, J. L. West, R. Bashir, *Annu. Rev. Biomed. Eng.* **2014**, *16*, 247.
- [16] Z.-M. Huang, Y. Z. Zhang, M. Kotaki, S. Ramakrishna, *Compos. Sci. Technol.* **2003**, *63*, 2223.
- [17] C. L. Cummings, D. Gawlitta, R. M. Nerem, J. P. Stegmann, *Biomaterials* **2004**, *25*, 3699.
- [18] B. J. Kwee, D. J. Mooney, *Curr. Opin. Biotechnol.* **2017**, *47*, 16.
- [19] C. M. Smith, A. L. Stone, R. L. Parkhill, R. L. Stewart, M. W. Simpkins, A. M. Kachurin, W. L. Warren, S. K. Williams, *Tissue Eng.* **2004**, *10*, 1566.
- [20] D. Loessner, C. Meinert, E. Kaemmerer, L. C. Martine, K. Yue, P. A. Levett, T. J. Klein, F. P. W. Melchels, A. Khademhosseini, D. W. Huttmacher, *Nat. Protoc.* **2016**, *11*, 727.
- [21] K. Yue, X. Li, K. Schrobback, A. Sheikhi, N. Annabi, J. Leijten, W. Zhang, Y. S. Zhang, D. W. Huttmacher, T. J. Klein, A. Khademhosseini, *Biomaterials* **2017**, *139*, 163.
- [22] Q. Gao, Y. He, J. Z. Fu, A. Liu, L. Ma, *Biomaterials* **2015**, *61*, 203.
- [23] M. Nakamura, S. Iwanaga, C. Henmi, K. Arai, Y. Nishiyama, *Biofabrication* **2010**, *2*, 014110.
- [24] L. Ouyang, C. B. Highley, C. B. Rodell, W. Sun, J. A. Burdick, *ACS Biomater. Sci. Eng.* **2016**, *2*, 1743.

- [25] C. B. Hutson, J. W. Nichol, H. Aubin, H. Bae, S. Yamanlar, S. Al-Haque, S. T. Koshy, A. Khademhosseini, *Tissue Eng. Part A* **2011**, *17*, 1713.
- [26] L. E. Bertassoni, M. Cecconi, V. Manoharan, M. Nikkiah, J. Hjortnaes, A. L. Cristino, G. Barabaschi, D. Demarchi, M. R. Dokmeci, Y. Yang, A. Khademhosseini, *Lab Chip* **2014**, *14*, 2202.
- [27] W. Jia, P. S. Gungor-Ozkerim, Y. S. Zhang, K. Yue, K. Zhu, W. Liu, Q. Pi, B. Byambaa, M. R. Dokmeci, S. R. Shin, A. Khademhosseini, *Biomaterials* **2016**, *106*, 58.
- [28] O. Jeon, K. H. Bouhadir, J. M. Mansour, E. Alsberg, *Biomaterials* **2009**, *30*, 2724.
- [29] Y. X. Chen, B. Cain, P. Soman, *AIMS Mater. Sci.* **2017**, *4*, 363.
- [30] T. Kageyama, T. Osaki, J. Enomoto, D. Myasnikova, T. Nittami, T. Hozumi, T. Ito, J. Fukuda, *ACS Biomater. Sci. Eng.* **2016**, *2*, 1059.
- [31] C. M. Murphy, F. J. O'Brien, *Cell Adhes. Migr.* **2010**, *4*, 377.
- [32] N. Devi, T. K. Maji, *AAPS PharmSciTech* **2009**, *10*, 1412.
- [33] C. Zhuang, C. Shi, F. Tao, Y. Cui, *Int. J. Biol. Macromol.* **2017**.
- [34] R. Reeves, A. Ribeiro, L. Lombardo, R. Boyer, J. B. Leach, *Polymers* **2010**, *2*, 252.
- [35] Y. Ke, G. S. Liu, J. H. Wang, W. Xue, C. Du, G. Wu, *eXPRESS Polym. Lett.* **2014**, *8*, 841.
- [36] C. C. Ribeiro, C. C. Barrias, M. A. Barbosa, *Biomaterials* **2004**, *25*, 4363.
- [37] D. Wei, W. Xiao, J. Sun, M. Zhong, L. Guo, H. Fan, X. Zhang, *J. Mater. Chem. B* **2015**, *3*, 2753.
- [38] D. Hutanu, M. D. Frishberg, L. Guo, C. C. Daire, *Mod. Chem. Appl.* **2014**, *2*, 132.
- [39] A. M. Kloxin, J. A. Benton, K. S. Anseth, *Biomaterials* **2010**, *31*, 1.
- [40] B. D. Fairbanks, M. P. Schwartz, C. N. Bowman, K. S. Anseth, *Biomaterials* **2009**, *30*, 6702.
- [41] H. Zimmermann, M. Hillgärtner, B. Manz, P. Feilen, F. Brunnenmeier, U. Leinfelder, M. Weber, H. Cramer, S. Schneider, C. Hendrich, F. Volke, U. Zimmermann, *Biomaterials* **2003**, *24*, 2083.
- [42] Y. S. Zhang, A. Arneri, S. Bersini, S.-R. Shin, K. Zhu, Z. Goli-Malekabadi, J. Aleman, C. Colosi, F. Busignani, V. Dell'Erba, C. Bishop, T. Shupe, D. Demarchi, M. Moretti, M. Rasponi, M. R. Dokmeci, A. Atala, A. Khademhosseini, *Biomaterials* **2016**, *110*, 45.
- [43] Y. Nishiyama, M. Nakamura, C. Henmi, K. Yamaguchi, S. Mochizuki, H. Nakagawa, K. Takiura, *J. Biomech. Eng.* **2008**, *131*, 035001.
- [44] M. Costantini, S. Testa, E. Fornetti, A. Barbetta, M. Trombetta, S. M. Cannata, C. Gargioli, A. Rainer, *Front. Bioeng. Biotechnol.* **2017**, *5*.
- [45] J. W. Nichol, S. T. Koshy, H. Bae, C. M. Hwang, S. Yamanlar, A. Khademhosseini, *Biomaterials* **2010**, *31*, 5536.
- [46] W. Liu, M. A. Heinrich, Y. Zhou, A. Akpek, N. Hu, X. Liu, X. Guan, Z. Zhong, X. Jin, A. Khademhosseini, Y. S. Zhang, *Adv. Healthcare Mater.* **2017**, *6*, 1601451.
- [47] A. Bédurier, T. Braschler, O. Peric, G. E. Fantner, S. Mosser, P. C. Fraering, S. Benchérif, D. J. Mooney, P. Renaud, *Adv. Healthcare Mater.* **2015**, *4*, 301.
- [48] K. S. Lim, B. S. Schon, N. V. Mekhileri, G. C. J. Brown, C. M. Chia, S. Prabakar, G. J. Hooper, T. B. F. Woodfield, *ACS Biomater. Sci. Eng.* **2016**, *2*, 1752.
- [49] K. Y. Lee, D. J. Mooney, *Prog. Polym. Sci.* **2012**, *37*, 106.
- [50] J. Zhu, *Biomaterials* **2010**, *31*, 4639.
- [51] G. Camci-Unal, D. Cuttica, N. Annabi, D. Demarchi, A. Khademhosseini, *Biomacromolecules* **2013**, *14*, 1085.
- [52] A. Khodabukus, K. Baar, *Cells Tissues Organs* **2015**, *202*, 159.
- [53] M. P. Lutolf, P. M. Gilbert, H. M. Blau, *Nature* **2009**, *462*, 433.
- [54] H. Aubin, J. W. Nichol, C. B. Hutson, H. Bae, A. L. Sieminski, D. M. Cropek, P. Akhyari, A. Khademhosseini, *Biomaterials* **2010**, *31*, 6941.
- [55] A. J. Engler, M. A. Griffin, S. Sen, C. G. Bönnemann, H. L. Sweeney, D. E. Discher, *J. Cell Biol.* **2004**, *166*, 877.
- [56] A. J. Engler, S. Sen, H. L. Sweeney, D. E. Discher, *Cell* **2006**, *126*, 677.
- [57] K. Ralla, U. Sohling, D. Riechers, C. Kasper, F. Ruf, T. Scheper, *Bioprocess Biosyst. Eng.* **2010**, *33*, 847.
- [58] M.-C. Kim, Y. R. Silberberg, R. Abeyaratne, R. D. Kamm, H. H. Asada, *Proc. Natl. Acad. Sci.* **2018**, *115*, E390.
- [59] O. Pertz, *Commun. Integr. Biol.* **2011**, *4*, 436.
- [60] J. F. Evers, D. Muench, C. Duch, *Dev. Biol.* **2006**, *297*, 214.
- [61] J. Yin, M. Yan, Y. Wang, J. Fu, H. Suo, *ACS Appl. Mater. Interfaces* **2018**, *10*, 6849.
- [62] C. S. Chen, M. Mrksich, S. Huang, G. M. Whitesides, D. E. Ingber, *Science* **1997**, *276*, 1425.
- [63] X. Zhao, Q. Lang, L. Yildirimer, Z. Y. Lin, W. Cui, N. Annabi, K. W. Ng, M. R. Dokmeci, A. M. Ghaemmaghami, A. Khademhosseini, *Adv. Healthcare Mater.* **2016**, *5*, 108.
- [64] Y. Wu, Z. Wang, J. Y. H. Fuh, Y. S. Wong, W. Wang, E. S. Thian, *J. Mater. Sci.: Mater. Med.* **2016**, *27*, 115.
- [65] G. Agrawal, A. Aung, S. Varghese, *Lab Chip* **2017**, *17*, 3447.
- [66] P. Bajaj, B. Reddy, L. Millet, C. Wei, P. Zorlutuna, G. Bao, R. Bashir, *Integr. Biol.* **2011**, *3*, 897.



Supporting Information

for *Macromol. Biosci.*, DOI: 10.1002/mabi.201800167

Composite Biomaterials as Long-Lasting Scaffolds for 3D Bioprinting of Highly Aligned Muscle Tissue

Andrea García-Lizarribar, Xiomara Fernández-Garibay, Ferran Velasco-Mallorquí, Albert G. Castaño, Josep Samitier,* and Javier Ramon-Azcon*

Supporting Information

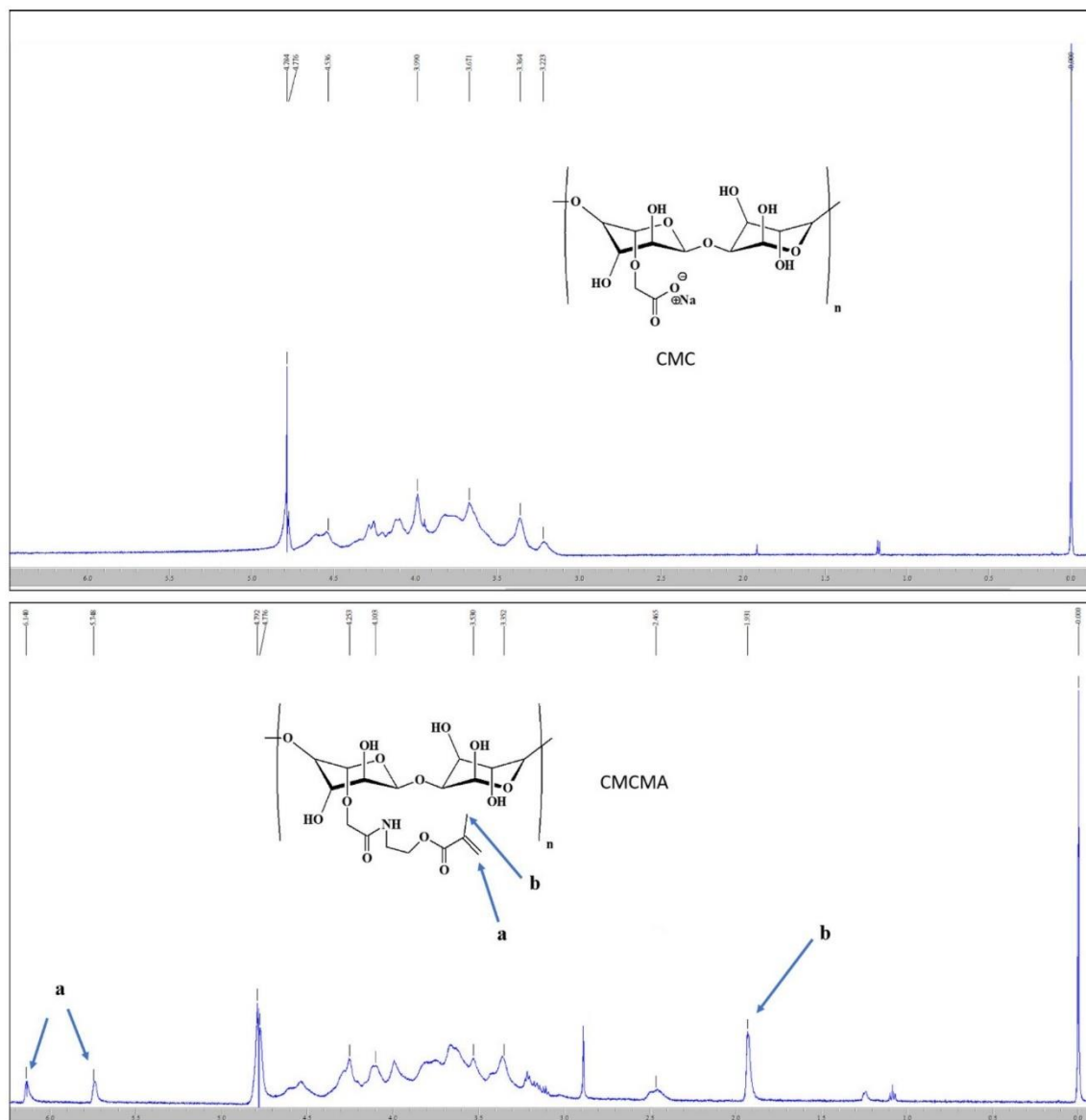
 ^1H RMN spectra

Figure S1. ^1H NMR spectra of methacrylated CMC and CMC without chemical modification in D_2O . By comparison with the spectrum of CMC, new signals were observed at (a) $\delta = 5.748$ ppm and $\delta = 6.140$ ppm in the spectrum of CMCMA, related to the acrylic protons, and a signal at $\delta = 1.931$ ppm (b) related to the methyl protons.

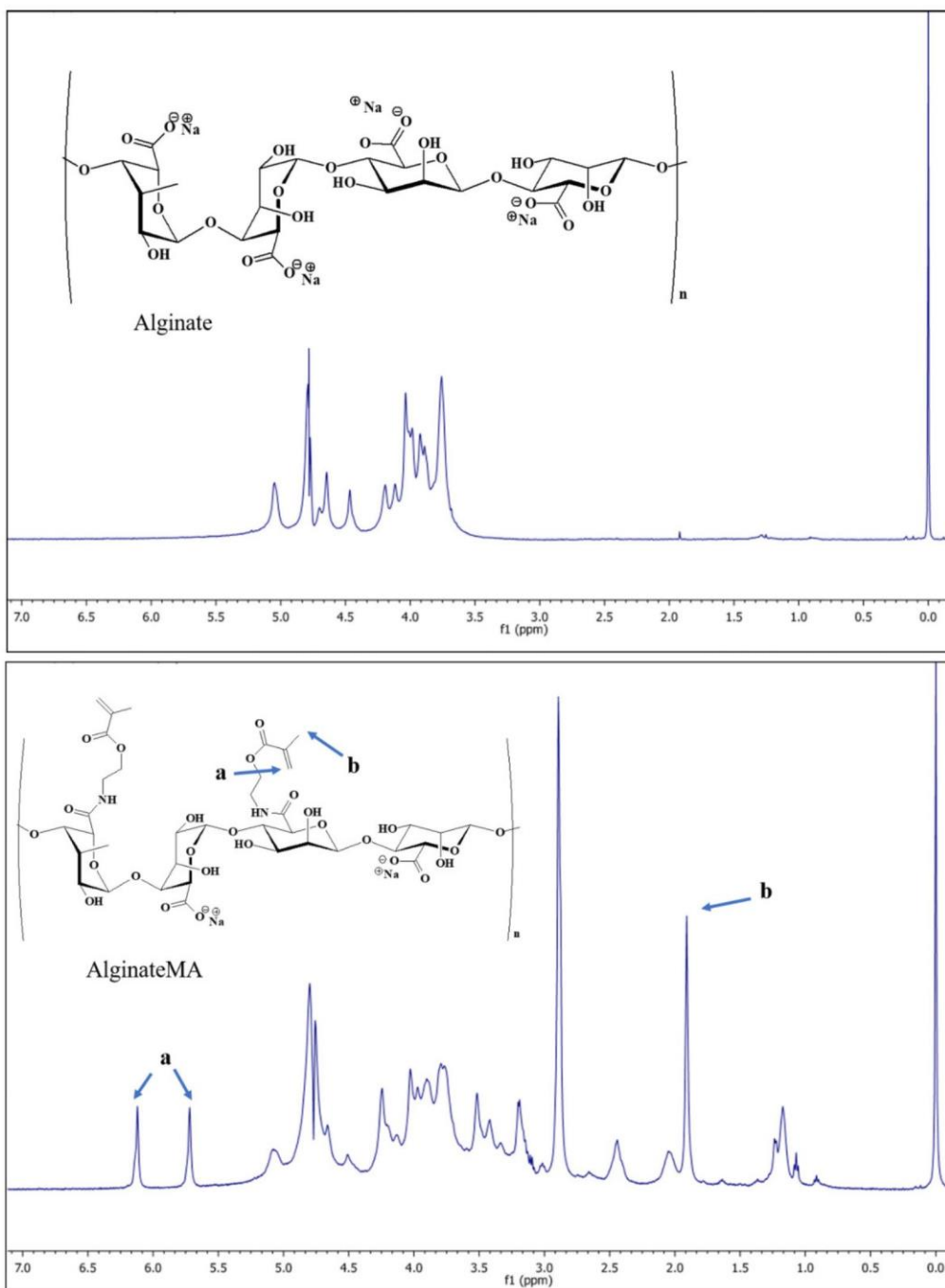


Figure S2. ¹H NMR spectra of methacrylated Alginate and Alginate without chemical modification in D₂O. By comparison with the spectrum of alginate, new signals were observed at (a) $\delta = 5.748$ ppm and $\delta = 6.140$ ppm in the spectrum of AlgMA, related to the acrylic protons, and a signal at $\delta = 1.931$ ppm (b) related to the methyl protons.

Colorimetric TNBS assay

To perform this assay, two different concentrations of previously fabricated methacrylated gelatin were used (for the chemical modification of the gelatin we used 5% and 1,25% concentration of methacrylic anhydre), diluted in different concentrations and a volume of 100 μ l per well. Three samples of each concentration and condition have been measured. Five different concentrations of gelatin 10% (w/v) were placed in the well, in a concentration range from 2000 μ g/ml to 31,25 μ g/ml. Also, 3 samples per concentration were placed. Once all these concentrations are set and placed in the well plate, we added 50 μ L/well of the TNBS 0,01% in bicarbonate buffer and we let 2 hours at room temperature and under agitation, to ensure all the amino groups reacted with the TNBS. To stop the reaction, we added 25 μ L/well of HCl 1M. Once the assay was over, the read out of the plate was done in a spectrophotometer to get the absorbance of each concentration at a wavelength of 335 nm.

To calculate the degree of methacrylation we used the following definition:

$$\% \text{ of methacrylated amines} = \frac{Abs_{gel} - Abs_{GelMa}}{Abs_{GelMa}} * 100$$

Where:

Abs_{gel} = Absorbance of the gelatin at specific concentration

Abs_{GelMa} = Absorbance of the methacrylated gelatin at specific concentration

Knowing this definition, we calculated the relative absorbance. The results obtained are in the Table S1.

Table S1. Results of the % of methacrylated amines at two different concentrations of methacrylic anhydre.

Concentration of methacrylic anhydre	5,00%	1,25%
Relative methacrylation of the GelMA	82%	40%

ANOVA multi factorial analysis of the viability assay

The analysis of variance (ANOVA) is used to detect significant factors in a multi-factor model. In this multi-factor model, we analyze one variable, the viability and four factors: a) degree of methacrylation, 40-82%; b) amount of material, 1-5%; c) percentage of photoinitiator, 0.1-0.4%; d) time of UV exposure, 5-25 seconds. We performed one experiment with LAP and another with I2959 photoinitiators.

We presented first the analysis for the LAP photoinitiator.

Table S2. Estimated effects for cell viability using LAP as photoinitiator.

Parameter	Estimated	Error SD	V.I.F.
Average	40,1459	0,414117	
A:%_Methacrylation	1,77806	0,828235	1,0
B:%_GelMA	2,20221	0,828235	1,0
C:%_LAP	-15,1813	0,828235	1,0
D:Time_UV	-9,9957	0,828235	1,0
AB	-6,01625	0,828235	1,0
AC	1,11564	0,828235	1,0
AD	-6,78512	0,828235	1,0
BC	-4,88792	0,828235	1,0
BD	2,21203	0,828235	1,0
CD	5,32844	0,828235	1,0
ABC	3,84148	0,828235	1,0
ABD	0,835602	0,828235	1,0
ACD	4,40073	0,828235	1,0
BCD	1,09107	0,828235	1,0

Standard errors based on total error with 33 DOF

This table shows the estimates for each of the estimated effects and interactions. The standard error of each of these effects is also shown, which measures its sampling error. Note also that the largest variance inflation factor (V.I.F.) is equal to 1.0. For a perfectly orthogonal design, all factors would be equal to 1. Factors of 10 or more are usually interpreted as indicative of serious confusion between effects. These factors are plotted in the figure 2b in the main manuscript.

Table S3. Table of analysis of variance for cell viability using LAP as photoinitiator.

Parameter	Square summatory	DOF	Mean square	F factor	P-value
A:%_Methacrylation	37,9379	1	37,9379	4,61	0,0393
B:%_GelMA	58,1965	1	58,1965	7,07	0,0120
C:%_LAP	2765,65	1	2765,65	335,98	0,0000
D:Time_UV	1198,97	1	1198,97	145,65	0,0000
AB	434,343	1	434,343	52,76	0,0000
AC	14,9357	1	14,9357	1,81	0,1872
AD	552,454	1	552,454	67,11	0,0000
BC	286,701	1	286,701	34,83	0,0000
BD	58,717	1	58,717	7,13	0,0117
CD	340,708	1	340,708	41,39	0,0000
ABC	177,083	1	177,083	21,51	0,0001
ABD	8,37876	1	8,37876	1,02	0,3204
ACD	232,397	1	232,397	28,23	0,0000
BCD	14,2853	1	14,2853	1,74	0,1968
Error total	271,645	33	8,23167		
Total (corr.)	6452,4	47			

R-squared = 95,79 %

R-square (ajusted for g.l.) = 94,00 %

Standard error of the estimated = 2,87

Absolute mean error = 1,74

The S3 table partitions the variability of viability percentage into separate pieces for each of the effects, then test the statistical significance of each effect by comparing its mean square against an estimate of experimental error. In this case, 11 effects have a P-value of less than 0.05, indicating that they are significantly different from zero with a confidence level of 95.0%.

The R-squared statistic indicates that the model, thus adjusted, explains 95.79% of the variability in viability percentage. The adjusted R-squared statistic, which is more adequate to compare models with different number of independent variables, is 94.00%. The standard error of the estimate shows that the standard deviation of the residues is 2.87. The absolute mean error of 1.74 is the average value of the residuals.

We presented the analysis for I2959.

Table S4. Estimated effects for cell viability using Irgacure2959 as a photoinitiator.

Parameter	Estimated	Error SD	V.I.F.
Average	73,8756	0,646776	
A:%_Methacrylation	-11,0284	1,28592	1,06366
B:%_GelMA	-14,3333	1,28592	1,06366
C:%_Irgacure	-19,2262	1,29355	1,07207
D:Time_UV	-24,786	1,28592	1,06366
AB	-14,5773	1,29355	1,07207
AC	15,8097	1,28592	1,06366
AD	-3,75476	1,29355	1,07207
BC	2,22693	1,28592	1,06366
BD	4,17098	1,29355	1,07207
CD	-5,72849	1,28592	1,06366
ABC	3,49247	1,29355	1,07207
ABD	6,88013	1,28592	1,06366
ACD	-2,50225	1,29355	1,07207
BCD	2,46957	1,29355	1,07207

Standard errors based on total error with 30 DOF

Table S5. Table of analysis of variance for cell viability using Irgacure2959 as a photoinitiator.

Parameter	Square summatory	DOF	Mean square	F factor	P-value
A:%_Methacrylation	1285,75	1	1285,75	73,55	0,0000
B:%_GelMA	2171,84	1	2171,84	124,24	0,0000
C:%_Irgacure	3861,7	1	3861,7	220,91	0,0000
D:Time_UV	6494,53	1	6494,53	371,52	0,0000
AB	2219,96	1	2219,96	126,99	0,0000
AC	2642,29	1	2642,29	151,15	0,0000
AD	147,285	1	147,285	8,43	0,0069
BC	52,4258	1	52,4258	3,00	0,0936
BD	181,748	1	181,748	10,40	0,0030
CD	346,907	1	346,907	19,85	0,0001
ABC	127,427	1	127,427	7,29	0,0113
ABD	500,411	1	500,411	28,63	0,0000
ACD	65,4117	1	65,4117	3,74	0,0625
BCD	63,7144	1	63,7144	3,64	0,0658
Error total	524,424	30	17,4808		
Total (corr.)	22355,3	44			

R-squared = 97,65 %

R-square (ajusted for g.l.) = 96,56 %

Standard error of the estimated = 4,18

Absolute mean error = 2,66

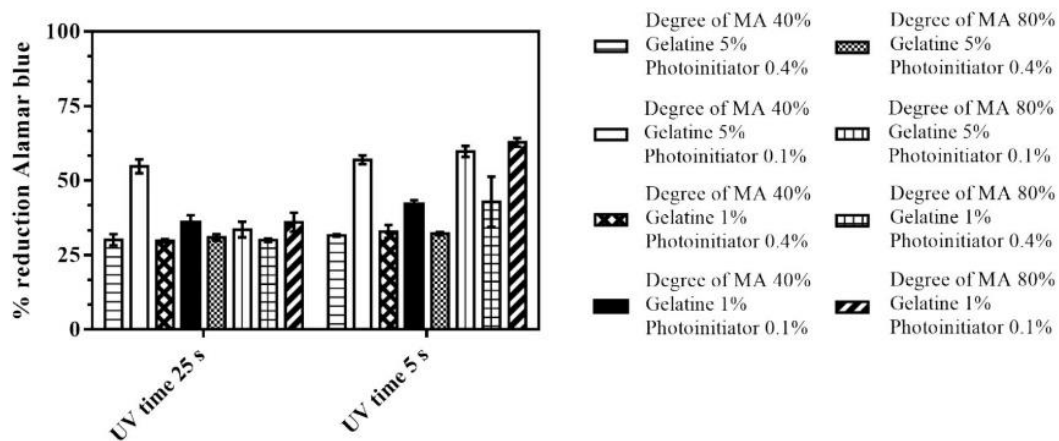


Figure S3. Histogram of Alamar blue reduction of C2C12 cells using LAP as photoinitiator

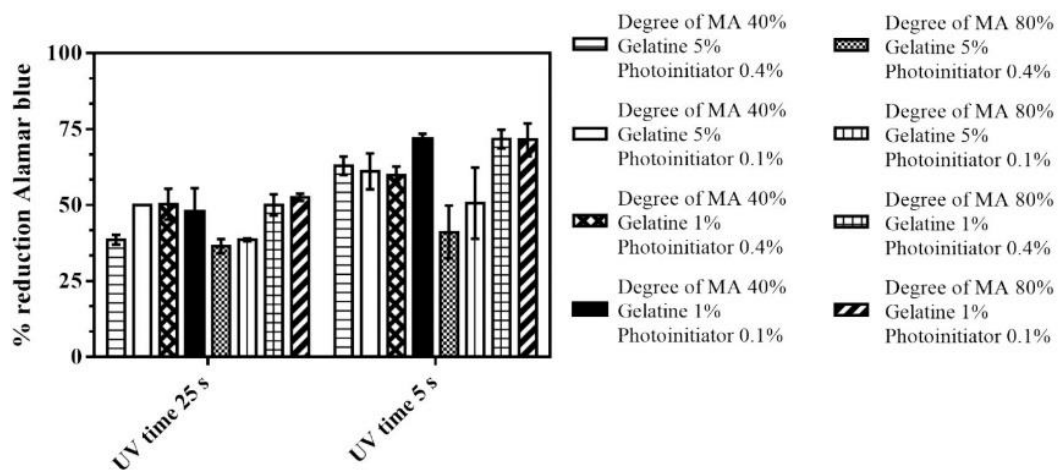


Figure S4. Histogram of Alamar blue reduction of C2C12 cells using Irigacure2959 as photoinitiator.

Finally, we present here the effect of the A: methacrylation degree of GelMA, B: GelMA concentration in composites, C: Photoinitiator concentration and D: UV light exposure time (s) on C2C12 viability in 3D cultures using a) Irgacure 2959 or b) LAP as photoinitiators. Black bars represent a negative effect and white bars a positive effect. Those bars overtaking $p < 0.05$ line have a significative effect.

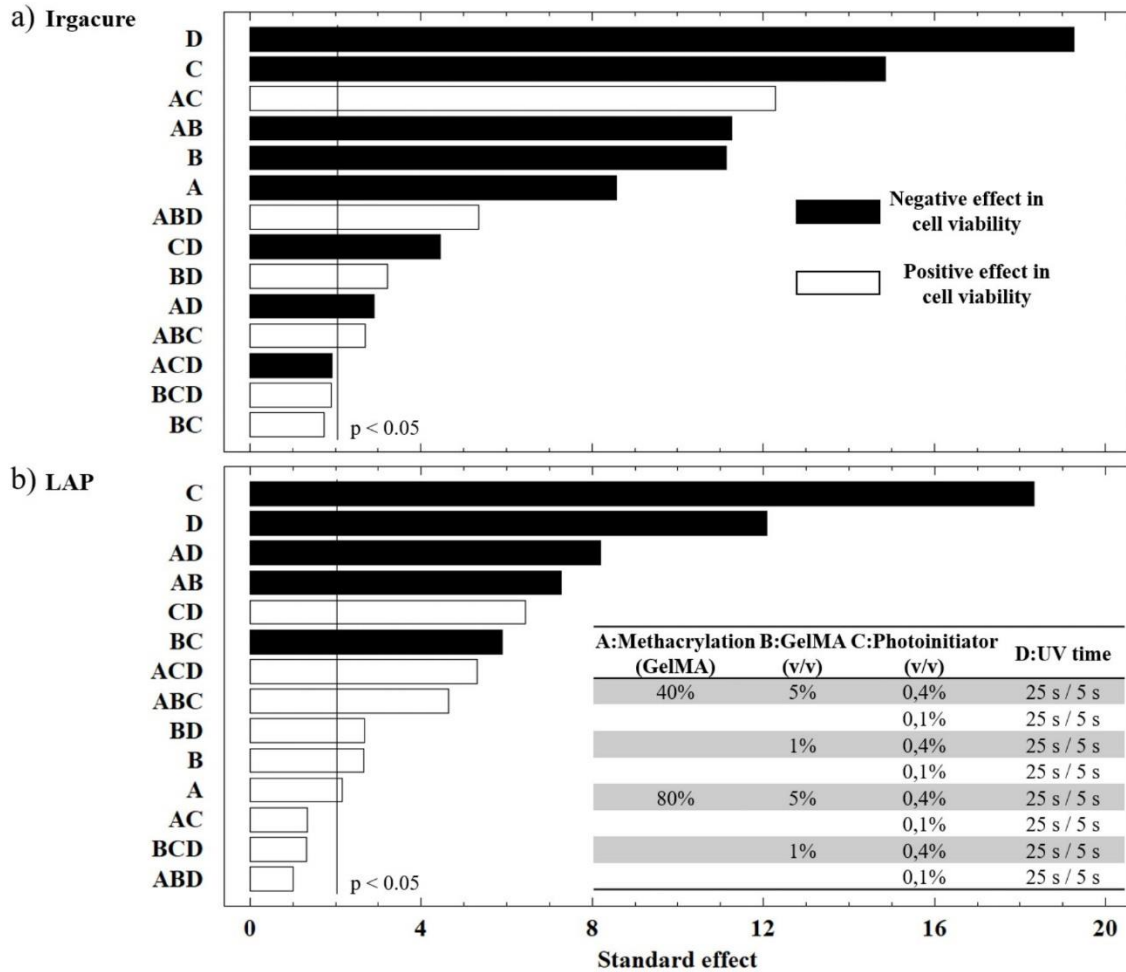


Figure S5. Histogram representing the F factors of a) Alamar blue reduction of C2C12 cells using Irgacure2959 as photoinitiator and of b) Alamar blue reduction of C2C12 cells using LAP as photoinitiator.

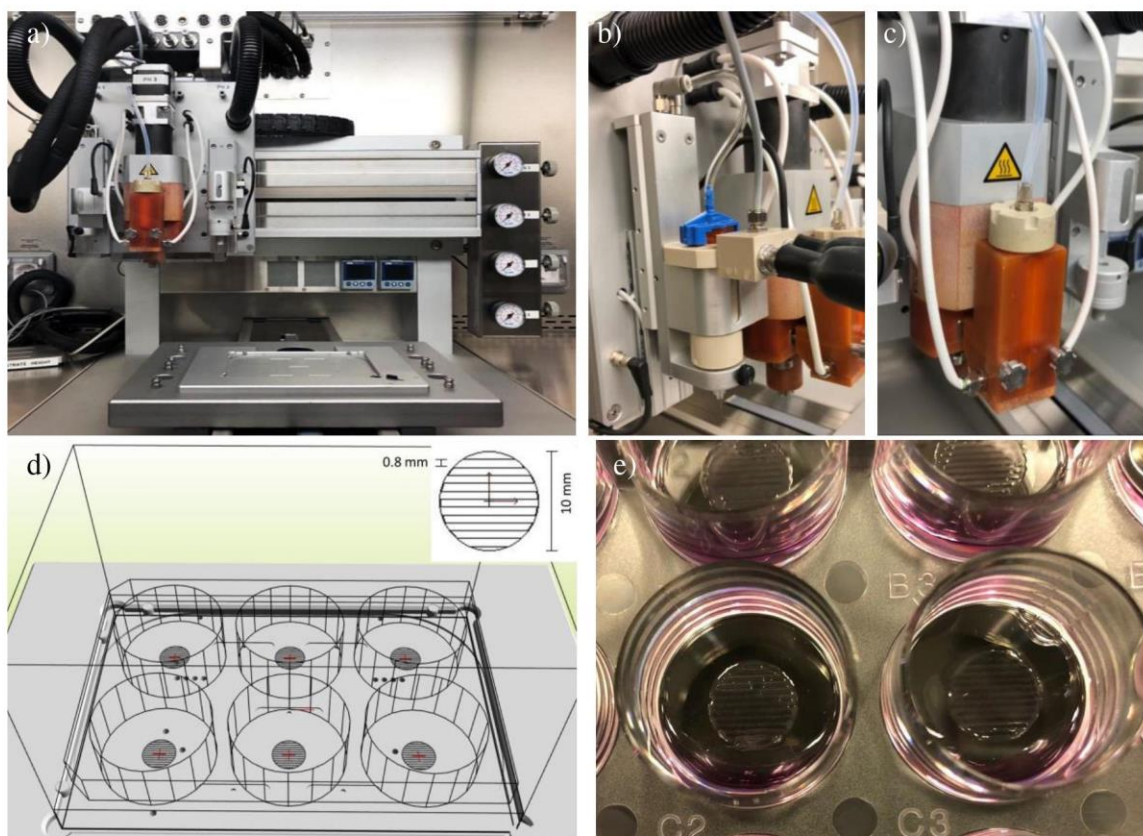


Figure S6. a) Schematics of the bioprinter, b) extruder or printhead, c) UV source. d) Hydrogels architecture design in the 3D DISCOVERY HMI software interface. e) Picture of the printed composite hydrogels in a 12 well plate

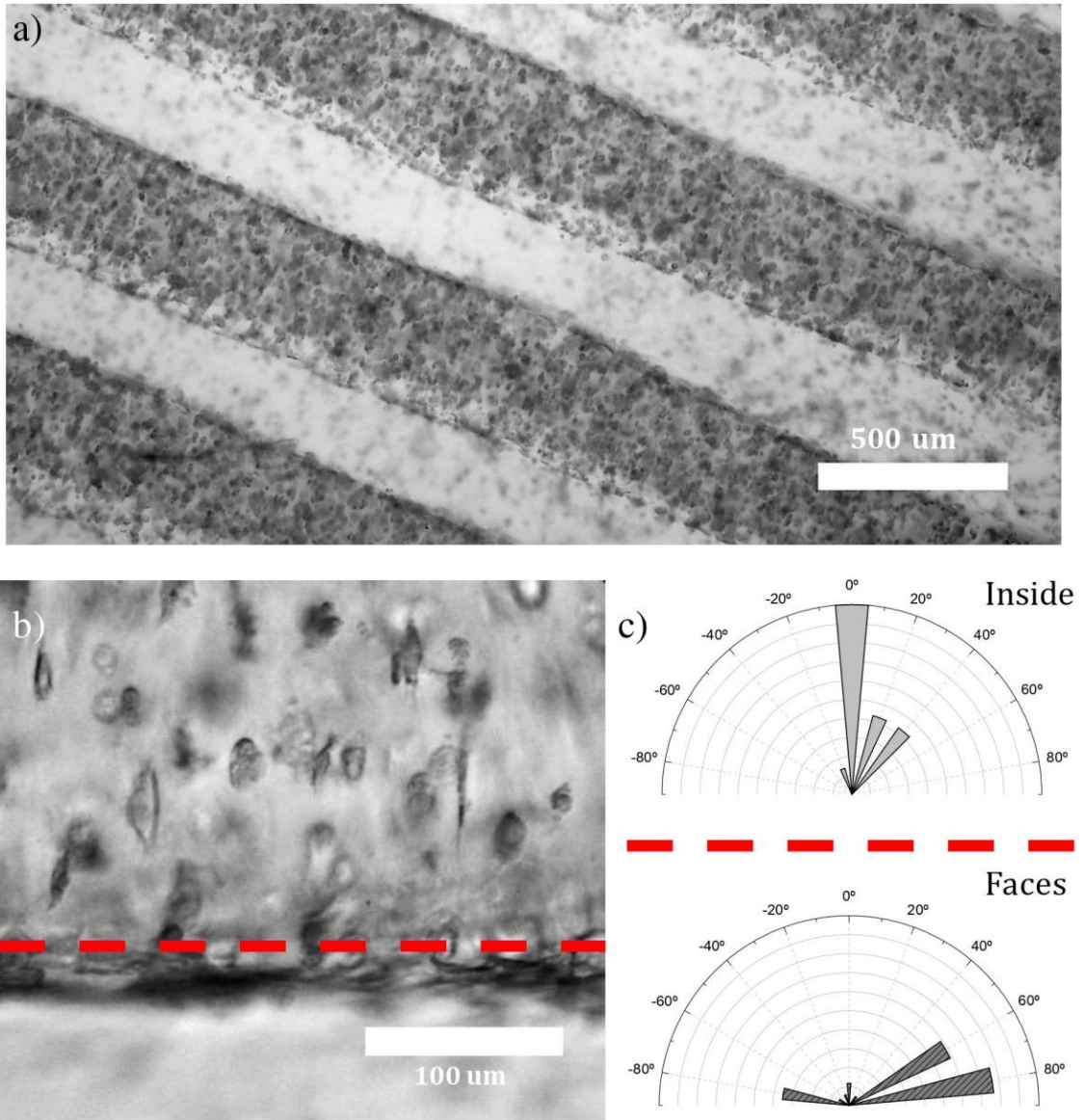


Figure S7. C2C12 cell alignment in composite hydrogel (GelMA-CMCMA) filaments of 400 μm in width. a) Top view of the filaments. b) Detail of cells inside the filament. c) Angle distribution histograms of the cells inside the filament and at the faces, showing the loss of cell alignment in the filament direction due to the filament width.

MATLAB code to calculate the number of live/dead cells in 3D scaffolds

```
clc;
clear all;

totalLive = [];
totalDead = [];
totalDeadPercent = [];
totalLivePercent = [];
c = 1;

for i = 11:4:67
    f = imread ('C:\Users\usuari\Desktop\LiveDead assays\LiveDead_d1\Gelatin12.tif', i);

    fb = f(:,:,1);
    fg = f(:,:,2);
    fr = f(:,:,3);

    mediana2r = medfilt2(fr,[10 10]);
    mediana2g = medfilt2(fg,[10 10]);
    mediana2b = medfilt2(fb,[10 10]);

    figure(1);subplot(1,2,1),imshow(fr),title('Red channel')
    subplot(1,2,2);imshow(mediana2r),title('Red channel filtered')
    figure(2);subplot(1,2,1),imshow(fg),title('Green channel')
    subplot(1,2,2);imshow(mediana2g),title('Green Channel filtered')
    figure(3);subplot(1,2,1),imshow(fb),title('Blue channel')
    subplot(1,2,2);imshow(mediana2b),title('Blue channel filtered')

    % RED
    llind_r=quantile2(mediana2r(:),0.95); mediana2ro=mediana2r;
    mediana2r(mediana2r<llind_r)=0;
    mediana2r(mediana2r>=llind_r)=1;

    Red_c=mediana2r.*1;

    % GREEN
    llind_g=quantile2(mediana2g(:),0.95);mediana2go=mediana2g;
    mediana2g(mediana2g<llind_g)=0;
    mediana2g(mediana2g>=llind_g)=1;

    Green_c=mediana2g.*1;

    % BLUE
    llind_b=quantile2(mediana2b(:),0.98);mediana2bo=mediana2b;
    mediana2b(mediana2b<llind_b)=0;
```



```

mediana2b(mediana2b>=llind_b)=1;

Blue_c=mediana2b.*1;

Red_c(Red_c>0) = 255;
Green_c(Green_c>0) = 255;
Blue_c(Blue_c>0) = 255;

figure(7);subplot(1,3,1),imshow(Red_c),title('EthD-1 binary')
subplot(1,3,2);imshow(Green_c),title('Calcein binary')
subplot(1,3,3);imshow(Blue_c),title('Dead'),title('Hoechst binary')

Dead=Red_c.*Blue_c;
Live=Green_c.*Blue_c;
LiveError=Dead.*Live;

Dead(Dead>0) = 255;
Live(Live>0) = 255;
LiveError(LiveError>0) = 255;

figure(50);subplot(1,3,1),imshow(Dead),title('Dead')
subplot(1,3,2),imshow(Live),title('Live')
subplot(1,3,3),imshow(LiveError), title('LiveError')

ra = 5;

Dead=imerode(Dead, strel('disk',ra));
Live=imerode(Live, strel('disk',ra));
LiveError=imerode(LiveError, strel('disk',ra));

Dead=imdilate(Dead, strel('disk',ra));
Live=imdilate(Live, strel('disk',ra));
LiveError=imdilate(LiveError, strel('disk',ra));

figure(8);subplot(1,3,1),imshow(Dead),title('Dead')
subplot(1,3,2),imshow(Live),title('Live')
subplot(1,3,3),imshow(LiveError), title('LiveError')

figure(9)

% Live counting
%
[numLive,L] = bwboundaries(Live,'noholes');
map=zeros(length(numLive),3);cmap=colormap(map);
figure(10);imshow(label2rgb(L,cmap, [.5 .5 .5])),title('Live counting')
hold on
for k = 1:length(numLive)

```

```

    boundary = numLive{k};
    plot(boundary(:,2), boundary(:,1), 'r', 'LineWidth', 1)

end
;
numLive = length (numLive);

% Dead counting

[numDead,L] = bwboundaries(Dead,'noholes');
map=zeros(length(numDead),3);cmap=colormap(map);
figure(11);imshow(label2rgb(L,cmap, [.5 .5 .5])),title('Dead counting')
hold on
for k = 1:length(numDead)
    boundary = numDead{k};
    plot(boundary(:,2), boundary(:,1), 'r', 'LineWidth', 1)
end
;
numDead = length (numDead);

% Triple staining

[numLiveError,L] = bwboundaries(LiveError,'noholes');
map=zeros(length(numLiveError),3);cmap=colormap(map);
figure(12);imshow(label2rgb(L,cmap, [.5 .5 .5])),title('LiveError counting')
hold on
for k = 1:length(numLiveError)
    boundary = numLiveError{k};
    plot(boundary(:,2), boundary(:,1), 'r', 'LineWidth', 1)

end
;
numLiveError = length (numLiveError);

totalLive(c) = numLive - numLiveError
totalDead(c) = numDead
totalLivePercent(c) = (totalLive(c) / (totalLive(c)+totalDead(c))) * 100;
totalDeadPercent(c) = (totalDead(c) / (totalLive(c)+totalDead(c))) * 100;
total(c) = totalLive(c) + totalDead (c)
c = c + 1;

break;
end

LivePercent = mean(totalLivePercent)
DeadPercent = mean(totalDeadPercent)

```




Cite this: *Lab Chip*, 2019, 19, 2568

Muscle-on-a-chip with an on-site multiplexed biosensing system for *in situ* monitoring of secreted IL-6 and TNF- α †

María A. Ortega, Xiomara Fernández-Garibay, Albert G. Castaño, Francesco De Chiara, Alejandro Hernández-Albors, Jordina Balaguer-Trias and Javier Ramón-Azcón *

Despite the increasing number of organs-on-a-chip that have been developed in the past decade, limited efforts have been made to integrate a sensing system for *in situ* continual measurements of biomarkers from three-dimensional (3D) tissues. Here, we present a custom-made integrated platform for muscle cell stimulation under fluidic conditions connected with a multiplexed high-sensitivity electrochemical sensing system for *in situ* monitoring. To demonstrate this, we use our system to measure the release levels and release time of interleukin 6 and tumor necrosis factor alpha *in vitro* by 3D muscle microtissue under electrical and biological stimulations. Our experimental design has enabled us to perform multiple time point measurements using functionalized screen-printed gold electrodes with sensitivity in the ng mL⁻¹ range. This affordable setup is uniquely suited for monitoring factors released by 3D single cell types upon external stimulation for metabolic studies.

Received 27th March 2019,
Accepted 19th June 2019

DOI: 10.1039/c9lc00285e

rscl/loc

1. Introduction

In vitro biomimetic tissue models with physiological functions can be used to assess biological phenomena in an easy, accurate, and controllable manner. Currently, *in vitro* tissues are useful for studying both the molecular and the cellular bases of physiological and pathological responses of biological processes. To this end, microscale fabrication technologies have emerged as useful tools in tissue engineering and biological applications.¹ Further, these models promise to replace corresponding animal experiments, which are costly, labor-intensive, and beset with serious ethical issues regarding their biological relevance to humans.²

In addition, almost 40% of total body mass is skeletal muscle (SM) tissue. Although people associate it with strength and movement, its functions range from controlling facial expressions to helping respiratory and blood circulation. The skeletal muscle tissue contains numerous quiescent mononucleated satellite cells which undergo intense proliferation after tissue damage to self-repair. This capacity is impaired or even lost in patients with congenital defects, diabetes, and cancer and/or after traumatic injuries and protracted

denervation.³ According to the American Medical Association, there is no specialized clinical doctor for the treatment of muscular diseases, such as Duchenne muscular dystrophy and inflammatory myopathy, hence the necessity to fill the gap between muscle disorders and *ad hoc* therapies. Moreover, no or too little knowledge is present about the source and auto-paracrine impact of cytokine release such as IL-6 and TNF- α in tissue regeneration. To this end, tissue engineering represents a fascinating and affordable approach to shed light on understanding the mechanisms and factors involved in the development of muscular disease.

In addition, in the field of biomimetic tissues, the need to incorporate biosensing for *in situ* monitoring of the status or the secretion regimes of *in vitro* microtissues is increasingly recognized.^{4,5} Additionally, the capability to miniaturize biosensor systems and advanced tissue fabrication procedures have enabled researchers to create multiple tissues on a chip with a high degree of control over experimental variables for high-content screening applications.⁶ While recent organs-on-a-chip (OOCs) can model native-organ microstructures for understanding disease mechanisms, current OOCs still lack the precise temporal control needed to study processes such as delayed cell response to treatment and chronic effects caused by long-term drug stimulation. Specifically, the difficulty arises when integrating the capability of stimulating the cells of interest with the capability of monitoring individual analytes released *in situ*. For example, OOCs that utilize

Institute for Bioengineering of Catalonia (IBEC), The Barcelona Institute of Science and Technology (BIST), Baldri I Reixac, 10-12, 08028, Barcelona, Spain.
E-mail: jramon@ibecbarcelona.eu

† Electronic supplementary information (ESI) available. See DOI: 10.1039/c9lc00285e

magnetic particles,⁷ or impedimetric sensors^{2,4,5} to facilitate analyte detection, are either time-sensitive or unstable under changing medium composition.

Here, we present a cost-effective integrated microdevice capable of simultaneous, *in situ* cell stimulation and analyte detection that is stable over time. We demonstrate this using a microdevice that targets 3D skeletal-muscle tissue known to release cytokines under external stimulations. With this setup, we can provide either electrical stimulation using indium tin oxide (ITO)-interdigitated array (IDA) electrodes or biological stimulation using lipopolysaccharide (LPS) solutions. Simultaneously, we can achieve multiplexed continual *in situ* measurements of secreted myokines using functional-

ized high-sensitivity screen-printed gold electrodes (SPGEs) (Fig. 1). Our setup demonstrates that microfluidics combined with tissue engineering and biosensing is an affordable approach in determining the response upon external stimuli. This device can be involved in the study of various muscular disease progression, furthering the understanding and treatment of muscular metabolic disorders.

2. Materials and methods

2.1 Cell culture

Murine C2C12 skeletal myoblasts (CRL-1772, ATCC, Virginia, USA) were expanded in growth medium, which consisted of

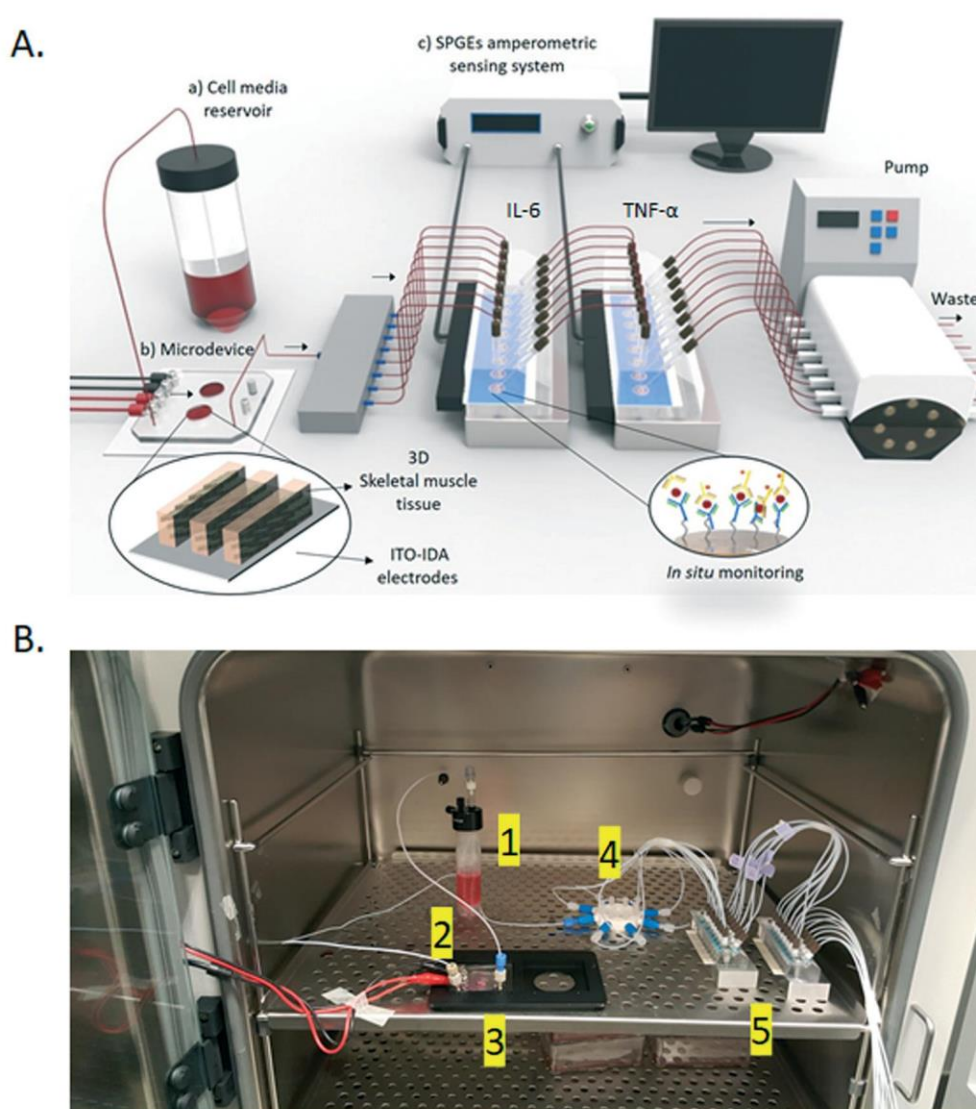


Fig. 1 Schematic overview of the configuration and function of the muscle-on-a-chip. (A) The flow passes through the microdevice where 3D SM tissue is electrically (ITO-IDA electrodes) or biologically (LPS) stimulated. The outlet flow containing the IL-6 and TNF- α goes directly to an 8-way microfluidic distributor to reach the SPGE sensing system. A peristaltic pump generates negative pressures that pull the medium through the microdevice as well as the detection system (SPGEs). (a) Reservoir containing cell media connected with a (b) custom-made microdevice containing the 3D SM tissue. (c) Multiplexed high-sensitivity platform containing functionalized SPGEs. (B) Physical arrangement: (1) cell medium reservoir; (2) 3D engineered muscle microtissue cultured on the microdevice; (3) microdevice support; (4) 8-way flow distributor; (5) SPGE functionalized sensing system.

Dulbecco's Modified Eagle Medium (DMEM high glucose, L-glutamine) (11965092, Gibco, Thermofisher, Massachusetts, USA) supplemented with fetal bovine serum (10%, FBS) (16000044, Thermofisher, Massachusetts, USA) and penicillin/streptomycin (1%) (15140122, Thermofisher, Massachusetts, USA) at 37 °C and a 5% CO₂ atmosphere. To induce differentiation into myotubes, the medium was changed to a differentiation medium, consisting of DMEM high glucose, supplemented with horse serum (2%) (HS) (26050088, Thermofisher, Massachusetts, USA) and 1% penicillin/streptomycin.

2.2 Synthesis of prepolymer precursors

Gelatin methacryloyl (GelMA) was synthesized with a 40% degree of methacrylation as previously described.⁸ The material was then dialyzed in Milli-Q water with 6–8 kDa MWCO membranes (08-700-142, Spectrumlabs, San Francisco, USA) for 4 days. Sodium carboxymethylcellulose (CMC) (419273, Sigma Aldrich Co., St. Louis, MO, USA) was methacrylated at a maximum degree of methacrylation as previously described.⁸ The reaction was performed by mixing a solution of the polymer (1% w/v) in MES buffer (50 mM, pH 6.5) with a mix of EDC (20 mM), *N*-hydroxysuccinimide (10 mM) (130672, Sigma Aldrich Co., St. Louis, MO, USA) and 2-aminoethyl methacrylate (10 mM) (479659, Sigma Aldrich Co., St. Louis, MO, USA). The reaction was stopped after 24 h with the addition of acetone (161007, Panreac, Barcelona, Spain) and filtered using a vacuum flask. The precipitate was dissolved in PBS (10 mM) and dialyzed in Milli-Q water with 3.5 kDa MWCO membranes (68035, Thermofisher, Massachusetts, USA). Finally, the solutions of methacrylated polymers (GelMA and CMCMA) were lyophilized and stored at -20 °C.

2.3 Preparation of prepolymer solutions

The prepolymer precursors (GelMA and CMCMA) were dissolved in growth medium containing the photoinitiator lithium phenyl(2,4,6-trimethylbenzoyl)phosphinate (LAP) (L0290, TCI EUROPE N.V, Zwijndrecht, Belgium) at 65 °C for 3 h to obtain a homogeneous solution. The concentrations of GelMA, CMCMA and LAP were fixed to obtain final concentrations of 5%, 1% and 0.1% (w/v), respectively.

2.4 Hydrogel characterization

2.4.1 Swelling analysis. The prepolymer solutions were prepared as described above. Samples for swelling analysis were fabricated by placing the prepolymer solution (300 μL) in a 48-well plate. After exposing the prepolymer solution to UV light (UVP Crosslinker, model CL-1000L, 365 nm, 40 W, from Analytik Jena US, Upland, USA), hydrogels were rinsed with PBS and their initial weight was measured. Then, the wet weight was determined after 1, 3, and 7 days in PBS (10 mM) after wiping with tissue paper to remove the excess water. To calculate the mass increase, each water content value was normalized with the initial weight of the sample. After day

7, samples were rinsed with Milli-Q water and dried. The swelling ratio, Q , of the hydrogels was determined by

$$Q = \frac{W_s - W_d}{W_d} \times 100 \quad (1)$$

Here, W_d and W_s represent the weight of dried hydrogels and the weight after swelling in PBS, respectively.

2.4.2 Mechanical analysis. Uniaxial compression tests of hydrogels were performed using a Zwick Z0.5 TN instrument (058993, Zwick-Roell, Berlin, Germany) with a 5 N load cell. Hydrogels were fabricated following the same procedure as for the swelling analysis. After reaching equilibrium swelling in PBS, cylindrical hydrogels were cut using a 10 mm diameter biopsy punch. Real hydrogel diameters and heights were measured prior to the experiment. Wet samples were tested at room temperature up to 30% final strain (deformation), using the following parameters: 0.1 mN preload force and 20% min⁻¹ strain rate. Stress-strain data were obtained from force-deformation graphs (Fig. S2A†). Values for the compressive modulus were calculated from the slope of the linear region corresponding to 10–20% strain. With uniaxial compressive testing, the testXpert software (Zwick Roell) converts the load-deformation data to stress-strain data using simple geometrical relationships (from measured hydrogel disks), and the Young's modulus E is reported.⁹ For each hydrogel formulation, three samples were prepared, and measurements were performed in triplicate.

2.4.3 Degradation analysis. Hydrogels were fabricated as described above for the swelling analysis. The hydrogels were removed from the 48-well plate and left to swell for 3 days in a 6-well plate. A total of 3 mL of collagenase type II (0.5 U mL⁻¹) (17101015, Thermofisher, Massachusetts, USA) in PBS was added to the hydrogels and they were incubated at 37 °C under 100 rpm shaking conditions. Then, the hydrogels were weighed after 1, 2, 3, 4, and 4 h. The percent of hydrogel remaining (W_r) was determined by:

$$\%W_r = \frac{W_f}{W_i} \times 100 \quad (2)$$

Here, W_f and W_i represent the weight of hydrogel composites at the swelling equilibrium and after collagenase incubation respectively.

2.5 Cell encapsulation in 3D micropatterns

To encapsulate the cells in micropatterns, a photomold patterning technique was used.¹⁰ For that, one volume of prepolymer solution was mixed with one volume of C2C12 cell suspension to obtain a final cell density of 2.5×10^7 cells per mL. Then, a drop of cell-laden prepolymer (15 μL) was placed in the bioreactor well, and a micro-structured PDMS stamp of 6 mm in diameter (Fig. 4A) was pressed lightly on top (grooves of 200 μm and 270 μm in height, and ridges of 200 μm, with a length of 5 mm approximately), filling the microchannels with

the solution. The hydrogel was photo-crosslinked using a UVP Crosslinker (model CL-1000L, 365 nm, 40 W, from Analytik Jena US, Upland, USA) with exposure times between 18 s and 120 s. The energy dose for every time point was measured using a wireless power meter (model PM160 Si Sensor Power Meter with Bluetooth and USB operation, 400–1100 nm, 10 nW–200 mW, Thorlabs, CA, USA). After carefully removing the stamp, the microdevice was sealed with a cover glass slide. The micro-structured cell-laden hydrogels were incubated inside the microdevice with growth medium for 6 days. Then, the culture medium was switched to differentiation medium (DM) to promote the formation of myotubes. All subsequent experiments were performed in DM cell medium.

2.6 C2C12 morphology and viability in composite hydrogels

C2C12 cells were encapsulated in GelMA-CMCMA hydrogels at a low cell density (1×10^6 cells per mL) using a previously described protocol.⁸ Bright-field microscopy images obtained after 6 days of encapsulation were analyzed using ImageJ software to obtain cell descriptor data of the aspect ratio and circularity of cells encapsulated in composite hydrogels with different exposure times. Cell viability was evaluated after 1, 6 and 10 days using the Live/Dead Viability/Cytotoxicity assay kit (L3224, ThermoFisher, Massachusetts, USA). Confocal microscopy images were obtained and processed using a custom MATLAB software code used in our previous work.⁸ Cell viability percentage was calculated as the fraction of living cells over the total cell number.

2.7 Immunofluorescence staining

The tissues were fixed in a formalin solution (10%) (HT501128, Sigma Aldrich Co., St. Louis, MO, USA) 15 days after fabrication. Then the hydrogels were washed with Tris-buffered saline (TBS, BR0042, Canvax Biotech, Spain). Cells were permeabilized with Triton X-100 (0.1%) (X100, Sigma Aldrich Co., St. Louis, MO, USA) in TBS for 15 min and blocked with a blocking buffer consisting of Triton X-100 (0.3%) and donkey serum (3%) (D9663, Sigma Aldrich Co., St. Louis, MO, USA) in TBS for 2 h. Afterwards, tissues were washed with TBS and incubated in rhodamine-phalloidin 480 (100 nM) (PHDR1, Cytoskeleton Inc., Colorado, USA) solution overnight to stain filamentous actin (F-actin). An additional overnight staining for myosin heavy chain (MHC) was performed by incubating in a solution of MF20 Alexa Fluor 488 ($5 \mu\text{g mL}^{-1}$) (53-6503-82, eBioscience, ThermoFisher, Massachusetts, USA) in blocking buffer. After washing with TBS, nuclei were counterstained with DAPI (1 μM , D1306, ThermoFisher, Massachusetts, USA) for 15 min. Hydrogels were mounted and stored at 4 °C before observation by confocal microscopy.

2.8 Microdevice fabrication

2.8.1 ITO-IDA electrode fabrication. Glass substrates with indium tin oxide (ITO) were commercial (CEC020S, 100 nm thickness, 20 ohms sq^{-1} , Präzisions Glas & Optik, Iserlohn, Germany), with dimensions of 60 mm \times 60 mm \times 1.1 mm for

length, width and thickness, respectively. The interdigitated electrodes were patterned on the ITO-glass substrates by a conventional photolithography procedure. Initially, the ITO glass slides were cleaned by a standard glass cleaning process, 5 min of sonication in DIW, acetone and 2-propanol in this order. Finally, the substrates were dried under N_2 flow for 3 minutes and then were activated using a plasma cleaner for 20 min at 6.8 W (Expanded Plasma Cleaner, PCD-002-CE Model, Harrick Scientific Corporation, NY, USA) and heated at 95 °C for 1 minute using a hot plate. AZ1512Hs positive resist (MicroChemical GmbH, Ulm, Germany) was spun on the substrate in two steps to obtain a final resist thickness of 2 μm (Spinner model WS-650MZ, Laurell Technologies Corporation, North Wales, USA). A soft bake at 95 °C for 2 min is performed to remove solvents from the resist and improve adhesion. The IDA pattern was stamped on a chromium mask fabricated by direct lithography using a direct write laser (DWL) machine (DWL 66FS model, 405 nm, 50 mW, Heidelberg Instruments Mikrotechnik GmbH, Heidelberg, Germany). In order to transfer the mask pattern to the resist, the coated substrates were placed under a UV light ($\lambda = 305\text{--}450$ nm) in a UV photolithography mask aligner (SÜSS Microtec, Germany) at 25 mW cm^{-2} for 5 seconds (125 mJ cm^{-2}). The patterned resist was developed for 1 min using an aqueous solution of the AZ400K developer (MicroChemicals GmbH, Ulm, Germany) in a 4:1 ratio and rinsed with distilled water, followed by a hard bake at 120 °C for 1 h. Thickness was characterized using a profilometer (DEKTAK 6 M, Veeco Instruments, NY, USA). Then, a wet etching procedure was performed to etch the ITO not protected by resist. The substrates were submerged in a 6 M solution of a HNO_3/HCl mix and heated at 50 °C for 2 min. Finally, the substrates were sonicated for 5 min in acetone and IPA and then dried with a N_2 flow.

2.8.2 PDMS chip fabrication. Silicon wafer molds were created through a two-layer process using negative photoresist SU8-2100 (MicroChem, Westborough, MA, USA). A microfluidic chip design was printed on a high-quality acetate film to be used as a mask and finally a micro featured master mold was then obtained by contact photolithography. To obtain a polydimethylsiloxane (PDMS) fluidic chip, a mixture of prepolymer with curing agent (Sylgard 184, Dow Corning, Midland, USA) was prepared at a 10:1 ratio, degassed in a vacuum chamber for 1 h, and poured on the SU8 master mold. After overnight incubation at 50 °C, the PDMS replica was cured and carefully peeled off from the mold, followed by a hole punch process. Once the PDMS chip was obtained, a bonding step to the ITO-IDA electrode substrate was performed through oxygen plasma activation for 30 s at 10.5 W (Expanded Plasma Cleaner, PCD-002-CE Model, Harrick Scientific Corporation, NY, USA). Then the final microdevice was heated at 80 °C for 2 h.

2.9 Fabrication of the biosensing platform

2.9.1 Chemicals and immunochemicals. Phosphate-buffered saline (PBS) is phosphate buffer (0.01 M), potassium

chloride (0.0027 M) and sodium chloride (0.137 M) at pH 7.2. MES buffer was prepared from MES hydrate salt (4-morpholineethanesulfonic acid) and adjusted to pH 5.0 (M5287, Sigma Aldrich Co., St. Louis, MO, USA). Purified rat anti-mouse IL-6 (ref. 554400, clone MP5-20F3, capture antibody), biotin rat anti-mouse IL-6 (ref. 554402, clone MP5-32C11, detection antibody), purified rat anti-mouse TNF- α (ref. 551225, clone G281-2626, capture antibody), and biotin rat anti-mouse TNF- α (ref. 554415, clone MP6-XT3, detection antibody) were purchased from BD Biosciences (Barcelona, Spain). Recombinant mouse IL-6 (ref. 200-02, 100 μ g) and recombinant mouse TNF- α (ref. 200-31, 100 μ g) were purchased from CliniSciences S.L. (Nanterre, France). SAV-polyHRP used in the final step was purchased from Pierce ThermoFisher (21140, Barcelona, Spain). For electrochemical measurements, citrate buffer (0.04 M, pH 5.5) (S4641, Sigma Aldrich Co., St. Louis, MO, USA) was used and substrate solution was also prepared containing TMB (0.0001%) (3,3',5,5'-tetramethylbenzidine) and H₂O₂ (0.0004%) in citrate buffer.

2.9.2 Functionalization protocol. To capture specifically the IL-6 and TNF- α secreted it was necessary to first functionalize the surface of SPGE sensors by using a self-assembled monolayer (SAM). To create a uniform SAM, (20-11-mercaptoundecanoyl)-3,6,9,12,18-hexaoxaicosanoic acid (TH003-m11.n3-0.5, Prochimia Surfaces, Sopot, Poland) was used. First, the gold SPGE sensors were cleaned using an UV/ozone cleaner (ProCleanerTM, BioForce Nanosciences, Utah, USA) for 15 min. Afterwards, an ethanolic solution of SH-PEG-acid (5 mM) was prepared freshly using 99.5% EtOH HPLC grade (161086.1211, PanReac AppliChem, Barcelona, Spain). The SAM formation step was made under static conditions using a PMMA static cell especially designed for this step (Fig. S3b[†]). The SPGE sensor was coupled with PMMA cells and 50 μ L of the SH-PEG acid molecule was added into each individual reservoir and left overnight at RT. After SAM formation, the electrodes were rinsed in EtOH. In order to facilitate the linkage of protein, carbodiimide chemistry was used utilizing EDC (200 mM) (E7750, Sigma Aldrich Co., St. Louis, MO, USA) mixed 1:1 with *N*-hydroxysulfosuccinimide sodium salt (sNHS) (200 mM) in H₂O (56485, Sigma Aldrich Co., St. Louis, MO, USA) and MES buffer (M5287, Sigma Aldrich Co., St. Louis, MO, USA). Once activation is performed, capture antibody (100 μ L) in PBS buffer was added and incubated for 2 h at RT. Afterwards, two washes with PBS (10 mM) are performed and the electrodes are passivated using PBS (10 mM, 1% BSA) for 1 h at RT to avoid non-specific binding. The SPGE electrode is implanted under microfluidic conditions throughout all the experiments. As a final step, the SPGE electrode is removed and placed into a static PMMA cell to be processed. At this point, binding of secondary biotinylated antibody was performed followed by addition of SAV-polyHRP, both steps for 1 h at RT. Finally, the SPGE electrodes are connected to the potentiostat and the amperometric signal was recorded. Electrical stimulation was performed using a wave generator (200

MHz multifunction generator, WF19478, NF Corporation, Yokohama, Japan) connected to a microdevice using metallic connections assembled to it. To evaluate the accuracy in our experiments, blind spiked samples were prepared in DM and measured directly using our optimized immunoassays. The accuracy for both immunoassays was evaluated by establishing a linear regression between spiked and measured values. Analyses were made in triplicate.

2.9.3 Amperometric detection measurements. Amperometric measurements were performed with a μ STAT 200 potentiostat (Metrohm-Dropsens, Herisau, Switzerland). Screen-printed gold electrodes (SPGEs) (Au DRP-220AT, Metrohm-Dropsens, Herisau, Switzerland) consisting of a 4 mm smooth working electrode, an Au counter electrode and a Ag pseudo-reference electrode were used. A flow cell (DRP-FLWCL, Metrohm-Dropsens, Herisau, Switzerland) for SPGE was used together with the microdevice for the experiments under flow conditions. To integrate both systems and to control the delivery of the cell medium containing the secreted myokines to the SPGE sensors, we used an 8-way flow and pressure control microfluidic distributor (part no. 001103, Kinesis, Cambridgeshire, UK). The peristaltic pump used in the experiments was coupled with a multi-channel pump-head, allowing 8 independent parallel tubing setups (Model MCP Process, Cole-Parmer GmbH, Wertheim, Germany). The microfluidic tubing used in all processes was made of PTFE with dimensions of 1/16" OD \times 1/32" ID (Darwin Microfluidics, Paris, France). Once detection was performed, amperometric signals were measured at an applied potential of -0.20 V vs. the Ag pseudo-reference electrode for 250 s. The amperometric signals were acquired under static conditions using the static PMMA cell. The recorded signal was the mean value of the current obtained in the last 10 s when the steady state was reached. The specific signal produced for the detection of proteins is translated by the difference between the original base of the citrate buffer and the signal obtained when the substrate solution is added. The intensity registered due to this electron transfer is directly related with the amount of HRP and, consequently, with the concentration of the IL-6/TNF- α of the analyzed sample through calibration curves.¹¹ Cyclic voltammetry (CV) measurements were carried out after deposition of [Fe(CN)₆]^{3-/4-} (50 μ L, 5 mM) redox probe solution onto the surface of the modified Au electrode. CV in the range of -0.25 to 0.50 V at a scan rate of 100 mV s⁻¹ was used to monitor the SAM formation on the gold electrode surface.

2.10 Statistical analysis

Statistical analysis was performed using Graph Prism software (GraphPad Software, San Diego, CA, USA). All data collected were presented as the mean \pm standard deviation (SD). Continuous variables were analyzed using the Kruskal-Wallis rank test. When significant, *post hoc* tests for continuous variables were performed among groups using the

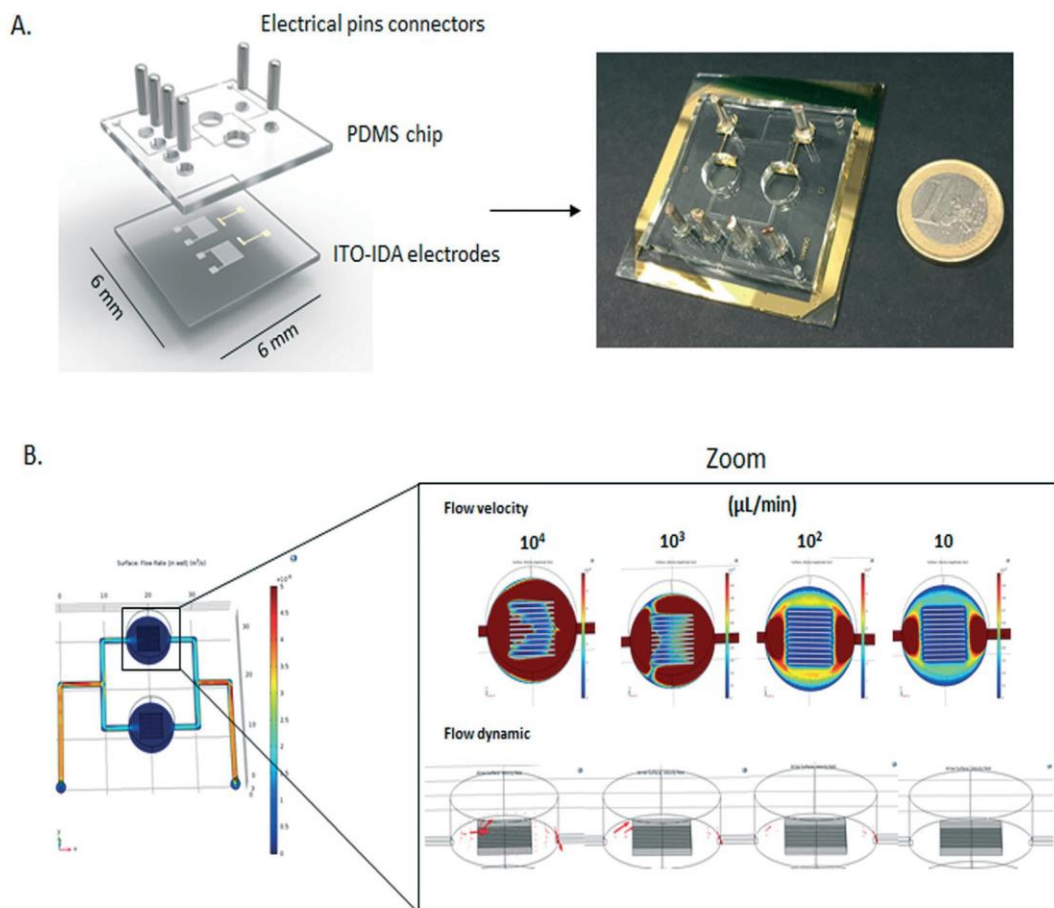


Fig. 2 Design and fabrication of the microdevice. (A) Schematic image shows the assembly elements and microdevice. (B) COMSOL Multiphysics® simulation of flow velocity and dynamics through a microfluidic network. Various simulations were performed with velocities ranging from 10^4 to $1 \mu\text{L min}^{-1}$. Black lines inside the chamber represent the 3D muscle microtissue.

Mann–Whitney test. p values <0.05 were considered statistically significant.

3. Results and discussion

3.1 Description of the integrated platform

In the recently emerged field of organ-on-a-chip the need to incorporate biosensing for *in situ* monitoring of the status or metabolic behavior of biomimetic organs is increasingly being recognized. In order to fill this gap, we have developed an integrated platform constituted by a custom-made microdevice hosting a SM microtissue coupled with a functionalized SPGE biosensing system for high-sensitivity detection of secreted factors such as IL-6 and TNF- α .

The cell medium reservoir containing 20 mL of DM cell medium (Fig. 1Aa) is connected with a miniaturized device containing the 3D muscle microtissue, forming the “muscle-on-a-chip.” The microdevice is formed by a combination of an ITO-IDA electrode substrate with a polydimethylsiloxane (PDMS) microfluidic chip (Fig. 1Ab). On the top of this system, the SM cells embedded in composite hydrogel are patterned by a molding technique and left to grow, fuse and differentiate until 3D aligned muscle fibers are obtained. Inside

the microdevice, 3D microtissue is exposed to either electrical stimulation (from ITO-IDA electrodes) or biological stimulation (addition of LPS to DM cell medium).

As a consequence of either form of stimulation, myokines are secreted from the construct to the cell medium and are delivered by a microfluidic network to a highly sensitive SPGE amperometric system (Fig. 1Ac). The SPGEs are functionalized with selective monoclonal antibodies before assembly into the microdevice. Finally, the cell medium delivers secreted myokines directly onto the SPGE sensors. This system is optimized to not dilute the sample, avoiding further manipulation by the operator. The capture of these analytes (myokines) produces changes in amperometric signals which are directly related with concentration. Negative pressures are applied to the whole system using a peristaltic pump. Our custom-designed microfluidic platform fits in a shelf of standard incubators (Fig. 1B).

3.2 Muscle-on-a-chip integrated with an on-site multiplexed sensing system for *in situ* monitoring of secreted myokines

3.2.1 Muscle-on-a-chip. As a proof-of-concept, we choose a model based on SM tissue, known to be a secretory organ.

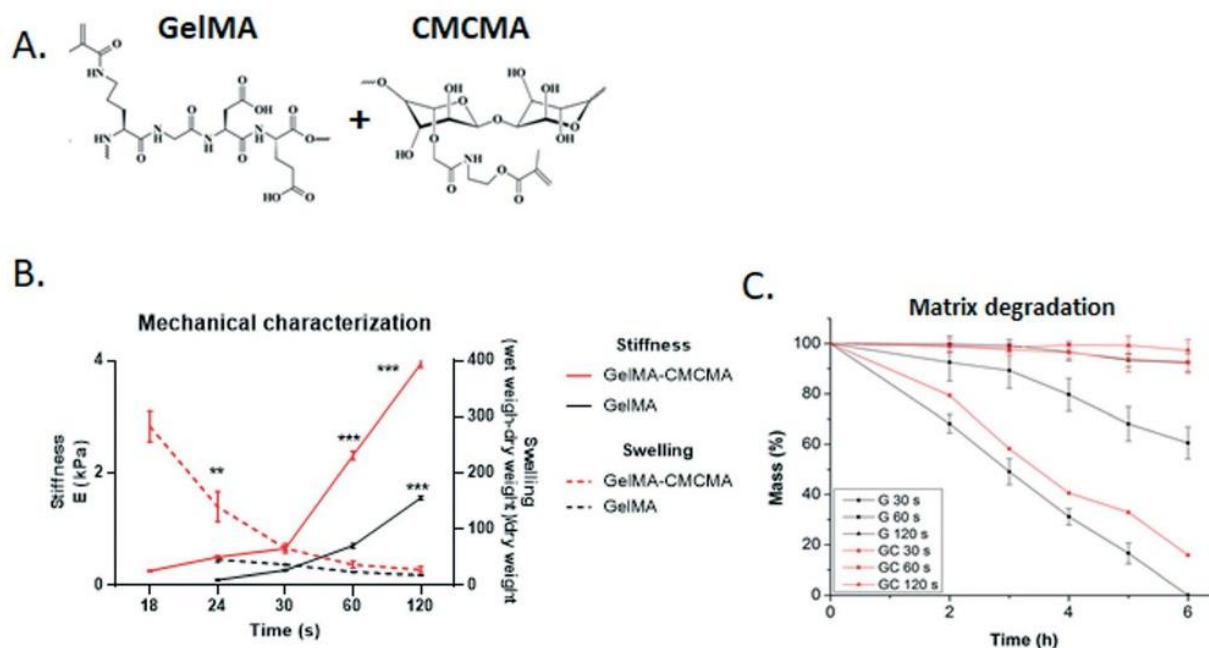


Fig. 3 (A) Gelatin methacryloyl (GelMA) and carboxymethyl cellulose methacrylate (CMCMA) chemical structures. (B) Mechanical characterization of composite hydrogel GelMA-CMCMA and comparison with only GelMA. (C) Matrix degradation study of GelMA and GelMA-CMCMA hydrogel exposed at different UV times. Data from three different experiments (mean, SD): ** $p < 0.01$; *** $p < 0.001$.

Our target SM tissue is fabricated inside the microdevice, enabling not only the renewal of nutrients but also the electrical stimuli to induce tissue contraction. To fabricate the microdevice, we perform a photolithography procedure to obtain an array of ITO-IDA with reference electrodes on a glass substrate for tissue electrical stimulation. The dimensions of the whole device are 60 mm × 60 mm. The size of the ITO-IDA arrays is 220 μm × 110 μm × 0.1 μm for height, width, and thickness, respectively (Fig. S1A†). The miniaturized chip is built of PDMS placed on top of the ITO-IDA electrodes (Fig. 2A). The microdevice is designed and fabricated to be used and integrated with biocompatible materials such as gelatin methacryloyl (GelMA), which provide an optimal cell environment. This platform presents a high compatibility with standard sterilization protocols. On the other hand, using a microfluidic network provides low-volume consumption (<1 mL), ensuring good nutrient exchange with the SM microtissue. The microdevice is also integrated with interdigitated electrodes set for the electrical stimulation of the microtissue, mimicking an *in vitro* exercise model (Fig. 2A).

The size of the interdigitated electrodes is 50 μm with a gap of 50 μm between electrodes. To simulate the intensity and penetration of the electrical field generated by the electrode array, we used COMSOL Multiphysics® software with an AC/DC module. As we expected, the electric current is inversely proportional to the size of the gap between electrodes (Fig. S1B†).¹² We conclude that the 50 μm × 50 μm × 0.1 μm electrode dimensions represent a good compromise between electrical field cell tolerance and penetration through the microtissue construct.¹³ To stimulate the cells, we set the limit of 1 Hz/5 V to avoid electrode overburn.¹⁴

To design the PDMS microfluidic chip, we used computer-aided design (CAD) software followed by fabrication with a soft lithography technique. After fabrication, we covalently bound the PDMS chip on top of the ITO-IDA electrodes through an oxygen plasma process (Fig. 2A). The PDMS chip contains two round wells of 10 mm diameter connected with microchannels of 1 mm height and 0.2 mm width each. Both the inlet and the outlet are fixed at 2 mm diameter; the electrical pin connectors are fixed at 4 mm (Fig. S1C†).

To explore the characteristics of the device, we performed theoretical simulations using COMSOL Multiphysics® software (fluid flow module). We used a stationary physic study of various flow rates (from 10⁴ to 10 μL min⁻¹) to study the flow behavior within the microchannels. As expected, the flow velocity mirrors the flow rate since the microchannel cross section ($\varnothing = 0.2 \text{ mm}^2$) is fixed (flow rate = cross section × velocity). The negative pressure gradient from the outlet to the inlet is present and is proportional to the flow rate (Fig. S1D and E†). To evaluate the flow velocity and dynamics within the microchambers, we included rectangular prisms (grooves) simulating the 3D muscular microtissue. At higher pressure, the fluid escapes towards the wall of the circular chamber where less resistance is encountered compared with the interspace between the grooves (Fig. 2B, zoom). According to our flow-dynamics simulations in Fig. 2B, we chose 50 μL min⁻¹ as a working shear flow where random fluid motion and shear stress are minimized. This velocity represents the experimental condition where both nutrient diffusion (laminar flow) and microtissue stability (liquid pressure) are optimized. This condition is made possible by

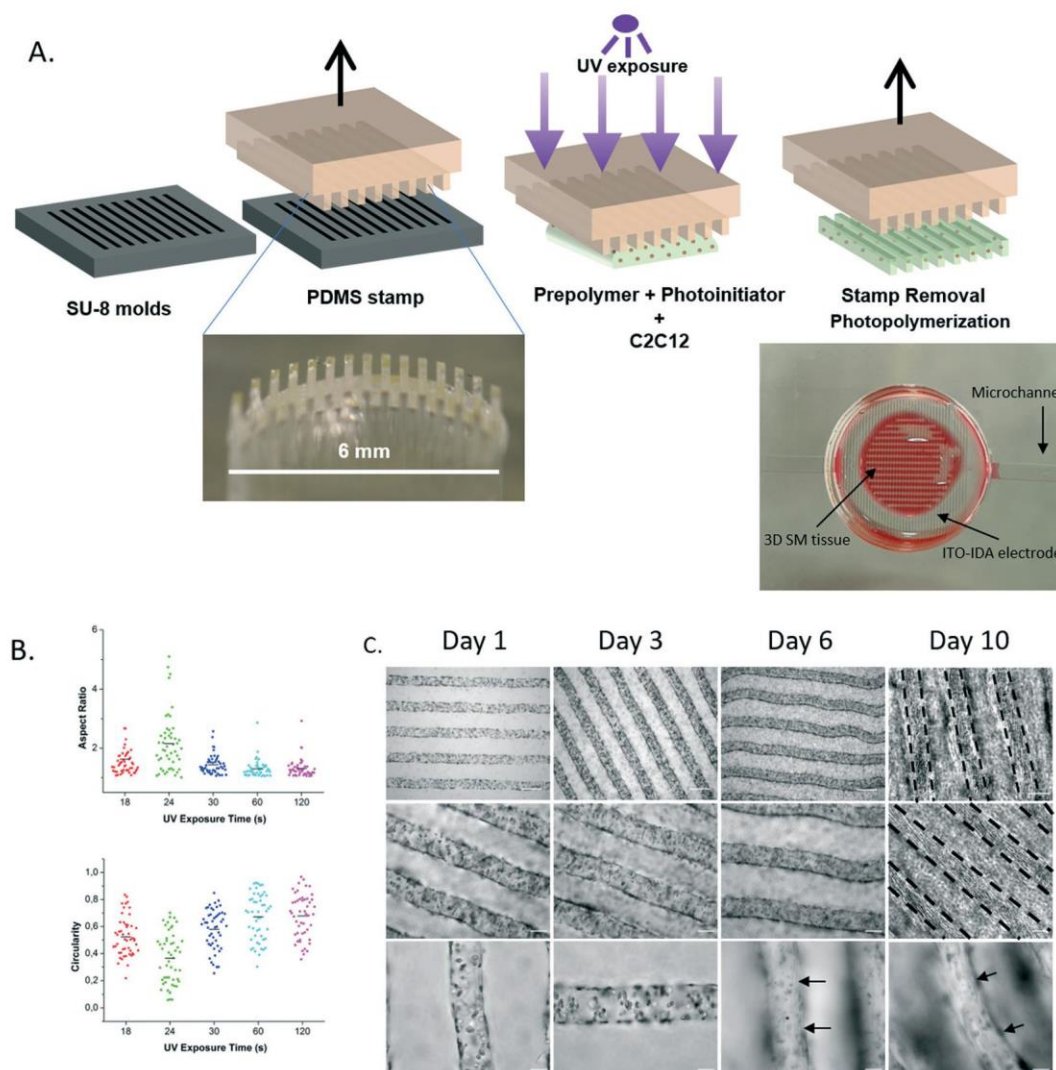


Fig. 4 Fabrication and characterization of 3D muscle microtissue. (A) Schematic view of the photo-mold patterning technique used to fabricate the skeletal muscle microtissue. (B) Cell morphology evaluation (circularity and aspect ratio) at different UV exposure times. (C) Bright-field characterization of skeletal muscle cells embedded in 3D composite hydrogel. Dashed lines at 10 days indicate muscular fibers. Black arrows at days 6 and 10 indicate the microtubule formation. Scale bars: 200, 100 and 50 μm , top, middle and bottom panel, respectively.

fabricating a 3D SM microtissue inside our microdevice using tissue engineering techniques.

Once we have optimized the working conditions of our microdevice, we fabricate a 3D microarchitecture of the native SM tissue using photopolymerized GelMA hydrogel. Because GelMA-based hydrogels can be degraded by cell metabolism, thus affecting the spatial and physicochemical properties, we add non-biodegradable methacrylate carboxy methyl cellulose (CMCMA) to obtain a hydrogel composite (Fig. 3A).⁸ To characterize the physical and mechanical properties of GelMA and GelMA-CMCMA, we first expose them to UV light (365 nm) for 18, 24, 30, 60, and 120 seconds. Energy dosage was directly measured with a wireless power meter inside the UVP crosslinker chamber, obtaining energy values of 0.30, 0.37, 0.48, 0.96 and 2.1 J (W s) for 18, 24, 30, 60 and 120 s, respectively. We find that at longer UV light exposure times, the stiffness of both hydrogels increases (from 0.2 to

1.6 kPa and 0.3 to 3.9 kPa, respectively, Fig. 3B), but GelMA-CMCMA showed a significantly higher compression modulus compared with GelMA alone, in particular after 30 seconds of exposure. As expected, we found that the swelling ratio is inversely correlated with stiffness (Fig. 3B). This can be explained by the fact that the longer UV exposure led to an increase in hydrogel crosslinking and decrease in porous size and water uptake. The magnitude of the change in H_2O uptake is higher in GelMA-CMCMA compared with GelMA alone (from 283 to 58 and from 46 to 18, respectively) (Fig. 3B). Moreover, the presence of CMCMA makes the hydrogel more resistant to enzymatic degradation compared with hydrogel without CMCMA (Fig. 3C). From these results, we chose GelMA-CMCMA both for its stability (high stiffness and low enzymatic degradation) and for its improved water absorption property (high swelling ratio). The composite hydrogel used to recreate the 3D structure shows a stiffness range

between 1 and 3 kPa, which is known to enhance C2C12 3D differentiation.¹⁵ The addition of CMCMA to the hydrogel amplified either the stiffness or the water absorption (high swelling ratio) which are important factors in cell differentiation and nutrient diffusion inside the polymer (Fig. 3B). Moreover, CMCMA increased the enzymatic degradation resistance, which has a significant impact on experimental variability.

To build the encapsulated 3D SM microtissue inside the composite hydrogel, we use a photo-mold patterning technique. This approach presents numerous advantages such as cost-effectiveness and non-surface dependence and allows fine control over cell alignment, elongation and maturation without any external stimuli, *e.g.* mechanical stretch. First, we use an SU-8 mold, fabricated by a photolithography process, to shape the PDMS stamp. Second, cell-laden hydrogel was micropatterned with the PDMS stamp by UV light exposure (Fig. 4A). We incubate the formed 3D SM microtissue in cell medium for 6 days to allow the cells to adapt to the new settings and stimulate further propagation. At this point, the growth medium (10% fetal bovine serum) is replaced with differentiation medium (2% horse serum).

As expected, we observe viable cells throughout the microstructure at 24 seconds of UV exposure at 1, 6 and 10 days of culture compared with 60 seconds (96 ± 3 , 87 ± 6 , $92 \pm 4\%$ and 80 ± 9 , 83 ± 7 , $86 \pm 7\%$, respectively) (Fig. S2B†). Moreover, the UV light exposure time of 24 seconds presents the best cell morphology score, defined by the high aspect ratio (2.149 ± 0.970) and low circularity (0.366 ± 0.188) (Fig. 4B). Therefore, we fix 24 seconds as the optimal exposure time for the subsequent experiments. Using bright-field microscopy, we observe homogeneous distribution of the cells at day 1 (24 h post fabrication) (Fig. 4C). Progressive cell alignment and elongation towards myotube formation are visible at day 10 (black dashed lines and arrows, Fig. 4C).

To assess the cell differentiation and maturation, we stain cells with F-actin and myosin heavy chain (MHC), respectively. The F-actin stain shows cell elongation and alignment at day 10 throughout the entire thickness of the 3D muscle microtissue compared with random myotube distribution in the non-patterned control group (Fig. 5A). We found that the 3D microgrooves restrict the degree of cell alignment between 0° and 15° , whereas the non-patterned cells are randomly distributed showing cell alignment ranging from 0 to 90° (Fig. 5B). Furthermore, the 3D muscle microtissue enhances myotube maturation and cell fusion compared with the three-dimensional non-patterned cells assessed by MHC staining and the fusion index, respectively (75 ± 7 vs. 50 ± 3 , $p < 0.001$, Fig. 5C). We note that the exposure of the microstructure to UV light for 24 seconds enables precise control of cellular organization in 3D and promotes cell myogenic differentiation and maturation. This *in vivo*-like structure enhances cell organization with a positive impact on cell viability and function up to 10 days of culture. Longer UV light exposure increases the stiffness of GelMA-CMCMA, reducing cell spatial organization, but does not affect the viability (Fig. S2A†). The control of the hydrogel microgeometry (microgrooves) is the main factor that improves cell maturation and alignment, pushing engineered tissue one step closer towards the creation of functional *in vitro* tissue.¹⁶

3.2.2 On-site multiplexed sensing system. After fabrication and characterization, the muscle-on-a-chip is connected to a high-sensitivity cytokine biosensing system (Fig. 6A and B) to monitor the release of myokines. In this work, the medium flow coming from the 3D SM tissue passes through the on-site multiplexed sensing system (Fig. 1B, number 5). The commercial SPGEs, where we previously immobilized antibodies against IL-6 and TNF- α , bind the cytokines present in the medium. Once binding is performed, the SPGE electrodes were finally located in the static PMMA cell, and secondary

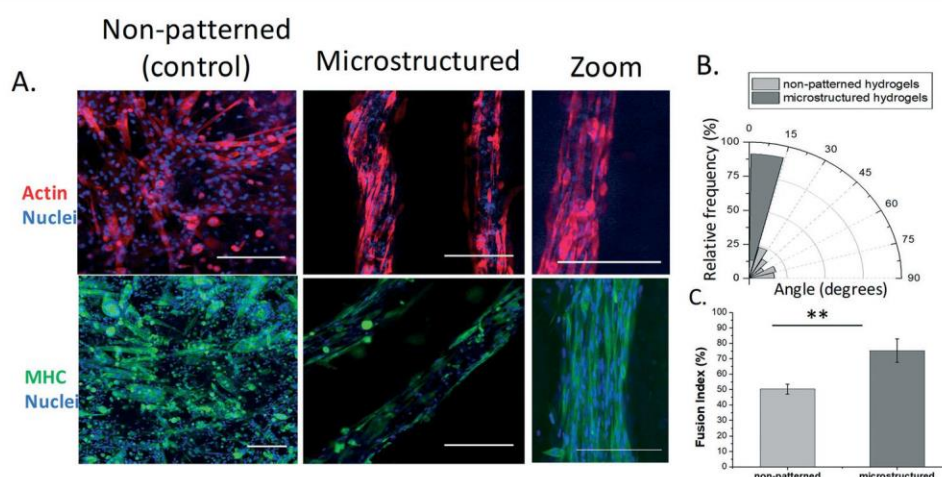


Fig. 5 (A) Immunostaining for 3D skeletal muscle microtissue for non-patterned (control) and microstructured hydrogels evaluated by phalloidin (red) staining. Cell differentiation was assessed by MHC staining (green). Nuclei were stained by DAPI. Scale bars: 200 μ m (B) and (C) cell orientation and fusion index characterization for non-patterned vs. microstructured 3D skeletal muscle tissue. Data from three different experiments (mean, SD): * $p < 0.05$, ** $p < 0.01$; *** $p < 0.001$.

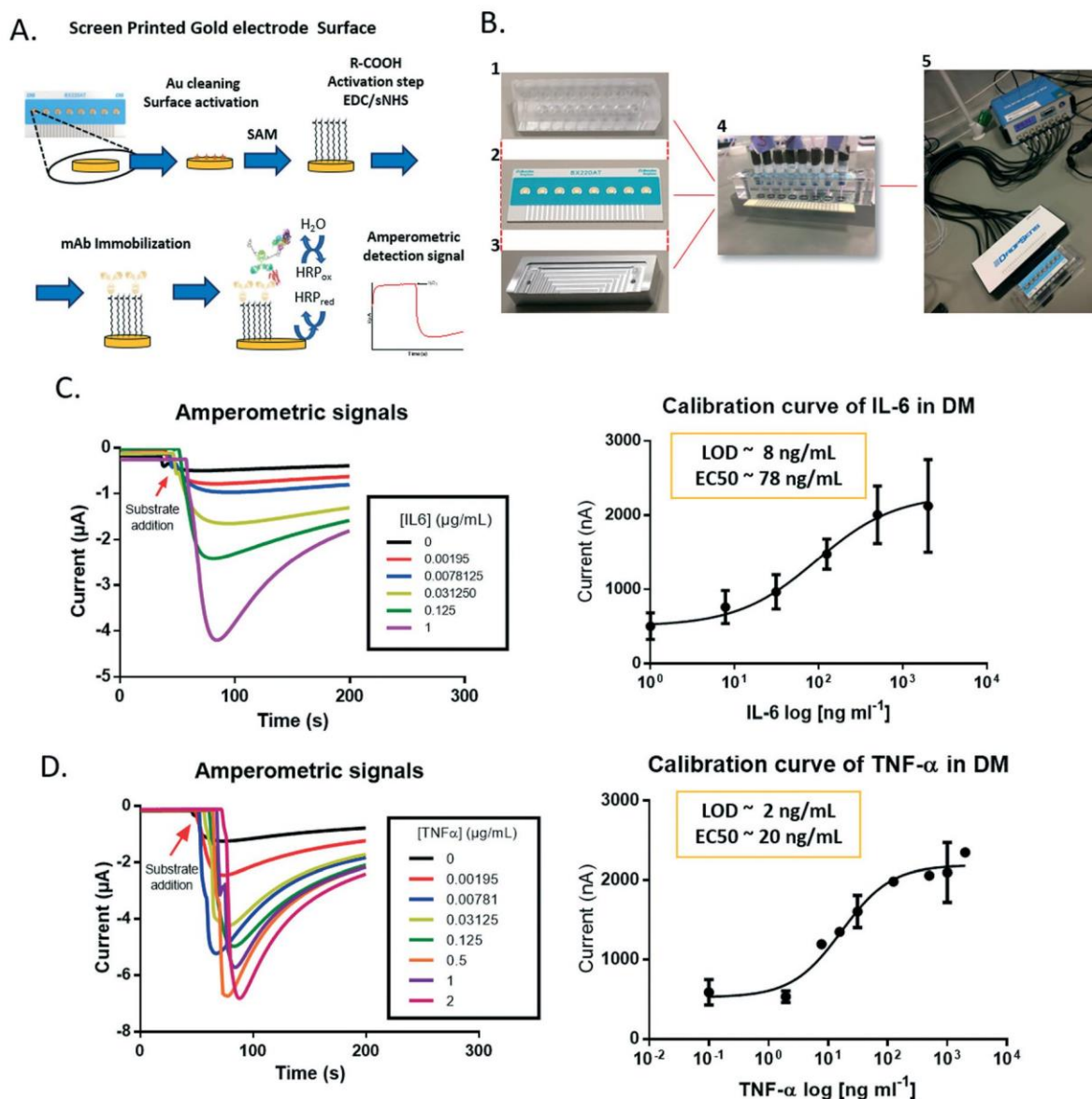


Fig. 6 On-site multiplexed sensing system description and characterization. (A) Schematic representation of steps for sandwich immunoassay as detection mechanism. (B) Biosensing system physical arrangement: (1) PMMA microfluidic cell cover; (2) SPGE functionalized electrode; (3) stainless steel electrode support case; (4) cell detection chamber coupled with microfluidic connectors; (5) potentiostat. (C) and (D) Raw amperometric signals and calibration curves performed in differentiation medium and under fluidic conditions for IL-6 and TNF- α . Curves show limits of detection of 8 ng mL⁻¹ and 2 ng mL⁻¹ for IL-6 and TNF- α , respectively.

antibody and enzymatic tracer were added. The enzymatic reaction produces changes in the electrode current density on the surface that are directly related with the amount of cytokines detected by the primary antibody.

For signal transduction, we chose commercial SPGEs because of their numerous advantages such as favorable electron transfer kinetics, good stability, and convenient covalent bonding with functional groups such as thiol-containing molecules (through the formation of gold (Au)-SH bonds). For detection of secreted myokines in cell medium, the surface of SPGEs was used to anchor IL-6 and TNF- α antibodies. To assess the full coverage of the SPGE surface by the SAM we used a cyclic voltammogram technique.¹⁷ Briefly, the

bare electrode (no SAM layer) showed the typical voltammogram characterized by cathodic and anodic current peaks for a reversible reaction (dashed line in Fig. S3A[†]), whereas with the SPGE surface with a monolayer of SH-PEG-acid a decrease in the current is observed due to the blocking properties of the monolayer (blue curve in Fig. S3A[†]).

The SH-PEG-acid is activated using the EDC/NHS reaction followed by the covalent immobilization of primary IL-6 and TNF- α antibodies. To detect cell secreted myokines, we use a sandwich immunoassay that involves exposure to biotinylated primary antibodies followed by the streptavidin-horseradish peroxidase (HRP) complex (SAV-polyHRP). The HRP-catalyzed 3,3',5,5'-tetramethylbenzidine (TMB) reaction is recorded *via*

amperometric signals (Fig. 6A). The on-site multiplexed sensing system for each cytokine is constituted by 5 parts: (1) poly methyl methacrylate (PMMA) microfluidic cell cover; (2) SPGE functionalized electrodes; (3) stainless steel electrode support case; (4) cell detection chamber coupled with microfluidic connectors; (5) potentiostat (Fig. 6B). Before connecting this sensing system to the muscle-on-a-chip through an 8-way flow distributor, we optimized the immunoassay parameters one by one.

First, we performed enzyme-linked immunosorbent assays (ELISAs) to validate the two commercial antibodies used in this study. We observed a limit of detection (LOD) of $0.031 \pm 0.010 \text{ ng mL}^{-1}$ with a slope of 0.726 ± 0.008 and LOD of $0.060 \pm 0.020 \text{ ng mL}^{-1}$ with slope 0.498 ± 0.012 for IL-6 and TNF- α , respectively (Fig. S3C†). Second, we validated the primary antibody anchorage on the SH-PEG-acid/Au surface using a static PMMA case (Fig. S3B†). Here, we observed a saturation plateau at 1.5 and $10 \mu\text{g mL}^{-1}$ for IL-6 and TNF- α , respectively (Fig. S3D†). Third, the optimal concentrations of secondary biotinylated antibody found were 5 and $40 \mu\text{g mL}^{-1}$ for IL-6 and TNF- α , respectively (Fig. S3E†). Fig. S3F† shows the optimal attachment kinetics of the SAV-polyHRP to the secondary antibody at $1 \mu\text{g mL}^{-1}$ for both systems. We set at 160 seconds the time of HRP-catalyzed TMB oxidation. Finally, these optimized values were used in later determination of calibration curves, which represent the working conditions to obtain the lowest LOD. Calibration curves under fluidic conditions showed a LOD of $\sim 8 \text{ ng mL}^{-1}$ and $\sim 2 \text{ ng mL}^{-1}$ with effective concentration 50 (EC_{50}) of $\sim 78 \text{ ng mL}^{-1}$ and $\sim 20 \text{ ng mL}^{-1}$ for IL-6 and TNF- α , respectively, with no matrix effect and a high signal/noise ratio (Fig. 6C and D). Moreover, four-parameter logistic regression of the data showed slopes and R^2 of 0.92 ± 0.39 (mean \pm SD) and 0.8386 for IL-6 and 1.04 ± 0.31 and 0.9497 for TNF- α . Previous experiments demonstrated no cross reactivity between IL-6 and TNF- α (data not shown). Both assays showed a satisfactory accuracy (slope close to 1, Fig. S3G†).

To note, a few examples can be found in the literature that incorporate a microfluidic platform with a biosensing system to study the metabolism of various tissues.^{4,5} For instance, the use of a non-label transduction in the case of the impedance allows simple acquisition, but in this case without an enzymatic amplification, the technique is less robust and very sensitive to changes in medium composition, especially with high ionic buffers. On the other hand, magnetic particles offer an easy system to regenerate the sensors, but the number of possible acquisitions is reduced and only daily measurements can be performed, which is not informative enough for metabolic studies. The transduction system used in this study was not affected by any medium under investigation and was successfully employed as an *in vitro* model of exercise where electrical stimulation with several measures per hour was needed.

3.3 *In situ* monitoring of secreted myokines upon electrical and biological stimulation

For the final part of this study, the microdevice, the 3D muscle microtissue, and the on-site multiplexed sensing sys-

tem are assembled through a microfluidic network to measure the release of factors upon electrical and biological stimulation.

SM tissues have been identified as an endocrine organ that produces and releases cytokines, which have been named myokines.¹⁸ These compounds such as IL-6 and TNF- α play important roles in biological processes such as energy metabolism, angiogenesis, myogenesis, and muscle repair.^{19–22}

The system is assembled through a microfluidic network as can be seen in Fig. 1A and B. The flow passes through the chip where the 3D SM tissue is electrically or biologically stimulated. The outlet flow goes directly to an 8-way microfluidic distributor to reach the SPGE sensing system. A peristaltic pump generates negative pressures that pull the medium to the SPGEs. After binding the SPGEs are removed and processed separately.

The focal points of this work are the investigation of the source and secretion regime of IL-6 and TNF- α either in muscle stress or during the inflammatory process. Firstly, to find the most responsive biological stimulus for IL-6 and TNF- α secretion, 2D monolayers of differentiated myotubes were incubated in cell culture plates with caffeine, dexamethasone and LPS.^{23–25} After determining the cytokine secretion levels by ELISA, LPS, caffeine and dexamethasone showed the highest release of IL-6 in the medium, whereas similar values among the conditions were obtained with TNF- α release (Fig. S4A†). TNF- α values do not show significant changes under all the treatments (Fig. S4B†). According to these results LPS was used as a biological agent to induce cytokine release in our integrated sensing system.

We performed continual electrical stimulation using a wave generator connected with the muscle-on-a-chip through electrical pins operating at 5 V (peak-peak) at a frequency of 1 Hz with a width of 2 ms for 60 min. We measured the release of myokines every 15 min (switching the 8-way flow distributor) during 1 hour of stimulation phase followed by 1 hour of relaxation phase (*i.e.*, without stimulation). The control group did not receive any electrical stimulation. Fig. 7 shows the monitoring of IL-6 and TNF- α concentrations at each period of time for both stimulation regimes. With this fast acquisition system, we detected up to $1 \mu\text{g mL}^{-1}$ for IL-6 and 10 ng mL^{-1} for TNF- α in DM during the relaxation time after electrical stimulus was ended (mimicking exercise training) (Fig. 7A). Fig. 7B demonstrates the release of myokines after supplementation of the medium with $10 \mu\text{g mL}^{-1}$ LPS for 48 h. In the case of IL-6, the maximum detectable peak is reached within 1 hour of stimulation and then it remained almost constant. IL-6 concentrations over $2.5 \mu\text{g mL}^{-1}$ were detected ($\sim 3 \text{ pg mL}^{-1}$ per cell, calculated using an estimation of 840 000 encapsulated cells per microdevice, Fig. S4C†) after 1 hour of LPS addition. Conversely, we observed a slow but constant increase of TNF- α throughout all the experiments, reaching over 50 ng mL^{-1} ($\sim 0.07 \text{ pg mL}^{-1}$ per cell, calculated using an estimation of 840 000 encapsulated cells per microdevice, Fig. S4D†) in 48 hours (Fig. 7B).

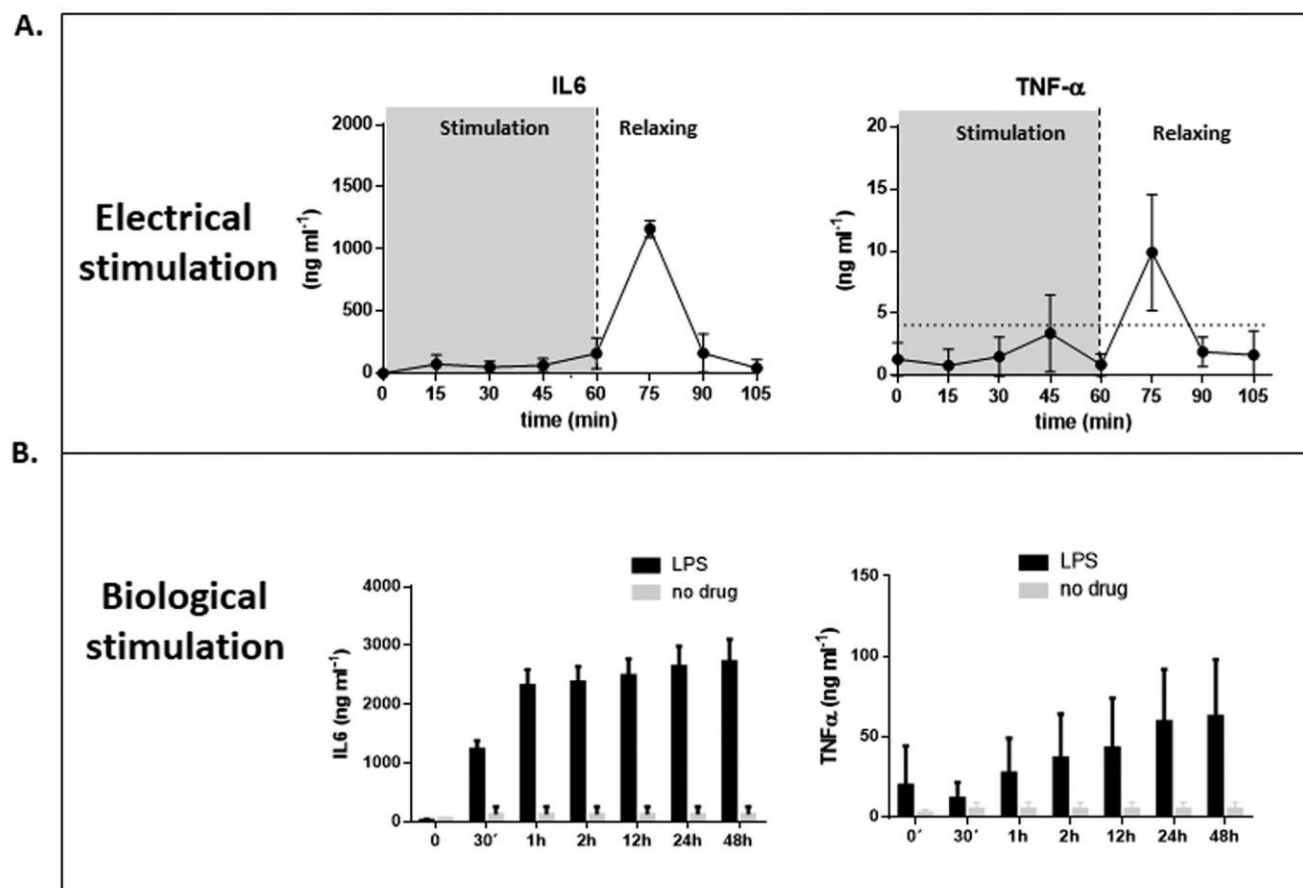


Fig. 7 IL-6 and TNF- α detection by *in situ* monitoring upon either (A) electrical stimulation (cycle 5 V/1 Hz for 105 min, with a 15 min interval) or (B) LPS stimulation ($10 \mu\text{g mL}^{-1}$) for 48 hours of 3D cultured skeletal muscle cell.

Here, we have demonstrated that secretion of these cytokines in SM is regulated by exercise stress. The study of SM metabolism lies in the timing of release of those factors, which takes place 15 minutes after the end of electrical stimulation. These experiments suggest that SM cells might play a potential role in the myogenic process. Even more interesting is the quicker and higher release of these factors from cells as a consequence of LPS stimulation compared with electrical stimulus only (~ 2 times for IL-6 and TNF- α at 1 hour of stimulation) (Fig. 7B). These facts might reshape the role of SM cells in response to bacterial toxins. As such, the development of this novel technology applied to this particular system represents a further and important step for development of biomimetic muscle platforms to monitor skeletal muscle cytokine functions for quantitative exploration of inflammatory and regenerative processes strongly interconnected with myopathy disease. Nevertheless, promising applications in other organs systems (individually or combination or various) are open to best understand the biological mechanisms needed for a continual *in situ* monitoring of secreted factors.

In addition, IL-6 and TNF- α are pleiotropic cytokines with a multiple effect on immune and non-immune cells. Among those effects, these myokines can play an important role in

regulating protein and glucose metabolism during tissue injury. In the case of SM cells these soluble factors are a fast way of communication not only between the cells of the same organ but also between the cells of different organs. This platform can help us to understand the magnitude and the timing of response upon different chemical and physical stimuli in order to identify a window for therapy.

4. Conclusions

We have developed an innovative cost-effective platform capable of simultaneous, *in situ* cell stimulation and analyte detection over time. Our custom-made microdevice was fabricated and used to host a mature and highly aligned SM tissue obtained using GelMA-CMCMA hydrogels. This 3D *in vivo*-like tissue, known to release cytokines under external stimulations (electrical stimulation using ITO-IDA electrodes or biological stimulation supplementing cell medium with LPS) was combined with a highly controlled flow platform, and integrated with a high-sensitive *in situ* sensing system. We functionalized our sensing system with the purpose of achieving multiplexed continual *in situ* measurements of secreted myokines. This unique approach allowed us to detect the release of two important cytokines such as IL-6 and TNF- α .

from 3D muscle tissue. We conclude that skeletal muscle cells can express and release these factors in response to electrical stimuli and LPS administration. We are currently working on optimizing this platform for in-depth investigation of the myogenic process and inflammatory response. This revolutionary technology can be exported to any laboratory environment and can have a huge impact on the drug-screening process.

Author contributions

M. A. O, X. F, A. G. C, A. H and J. R. conceived and planned the experiments. X. F and A. G. C carried out biological experiments related to 3D SM tissue formation and characterization. M. A. O, A. H, and J. B developed the sensing platform. M. A. O and J. B performed integrated experiments and acquisition of data. M. A. O, A. G. C., A. H and J. R contributed to the interpretation of the results. F. D. C. and M. A. O drafted and edited the manuscript. J. R supervised the project. All authors provided critical feedback and helped shape the research, analysis and manuscript.

Conflicts of interest

There are no conflicts to declare.

Acknowledgements

Funding for this project was provided by the Ramon y Cajal (RYC-2014-15022) fellowship and the Severo Ochoa Program for Centers of Excellence (R&D 2016–2019) funded by the Ministerio de Economía, Industria y Competitividad (83716); an ERC grant (ERC starting grant project 714317, DAMOC); the CERCA Programme/Generalitat de Catalunya (2014-SGR-1442 and 2014-SGR-1460); and the Fundación Bancaria “la Caixa” Obra Social (project IBEC-La Caixa Healthy Ageing, MR17-00268). The authors thank Mr. Xavier Menino Pizarro, Engineering Mechanics Head from the Research Technical Support Unit at the Institute of Photonics Sciences (ICFO) for the design and fabrication of the custom-made pieces used in this work. Also, we would like to thank Dr. Minseong Kim for his drawing skill.

References

- 1 A. Khademhosseini, R. Langer, J. Borenstein and J. P. Vacanti, *Proc. Natl. Acad. Sci. U. S. A.*, 2006, **103**, 2480–2487.
- 2 M.-H. Wu, S.-B. Huang and G.-B. Lee, *Lab Chip*, 2010, **10**, 939–956.
- 3 W. Bian and N. Bursac, *IEEE Eng. Med. Biol. Mag.*, 2008, **27**, 109–113.
- 4 A. Skardal, S. V. Murphy, M. Devarasetty, I. Mead, H.-W. Kang, Y.-J. Seol, Y. Shrike Zhang, S.-R. Shin, L. Zhao, J. Aleman, A. R. Hall, T. D. Shupe, A. Kleensang, M. R. Dokmeci, S. Jin Lee, J. D. Jackson, J. J. Yoo, T. Hartung, A. Khademhosseini, S. Soker, C. E. Bishop and A. Atala, *Sci. Rep.*, 2017, **7**, 8837.
- 5 Y. S. Zhang, J. Aleman, S. R. Shin, T. Kilic, D. Kim, S. A. Mousavi Shaegh, S. Massa, R. Riahi, S. Chae, N. Hu, H. Avci, W. Zhang, A. Silvestri, A. Sanati Nezhad, A. Manbohi, F. De Ferrari, A. Polini, G. Calzone, N. Shaikh, P. Alerasool, E. Budina, J. Kang, N. Bhise, J. Ribas, A. Pourmand, A. Skardal, T. Shupe, C. E. Bishop, M. R. Dokmeci, A. Atala and A. Khademhosseini, *Proc. Natl. Acad. Sci. U. S. A.*, 2017, **114**, E2293–E2302.
- 6 A. Grosberg, P. W. Alford, M. L. McCain and K. K. Parker, *Lab Chip*, 2011, **11**, 4165–4173.
- 7 R. Riahi, S. A. M. Shaegh, M. Ghaderi, Y. S. Zhang, S. R. Shin, J. Aleman, S. Massa, D. Kim, M. R. Dokmeci and A. Khademhosseini, *Sci. Rep.*, 2016, **6**, 24598.
- 8 A. García-Lizarribar, X. Fernández-Garibay, F. Velasco-Mallorquí, A. G. Castaño, J. Samitier and J. Ramon-Azcon, *Macromol. Biosci.*, 2018, **18**, 1800167.
- 9 M. L. Oyen, *Int. Mater. Rev.*, 2014, **59**, 44–59.
- 10 P. Occhetta, N. Sadr, F. Piraino, A. Redaelli, M. Moretti and M. Rasponi, *Biofabrication*, 2013, **5**, 035002.
- 11 P. Fanjul-Bolado, M. B. González-García and A. Costa-García, *Anal. Bioanal. Chem.*, 2005, **382**, 297–302.
- 12 P. Van Gerwen, W. Laureyn, W. Laureys, G. Huyberegts, M. Op De Beeck, K. Baert, J. Suls, W. Sansen, P. Jacobs, L. Hermans and R. Mertens, *Sens. Actuators, B*, 1998, **49**, 73–80.
- 13 S. Ahadian, J. Ramón-Azcón, S. Ostrovidov, G. Camci-Unal, V. Hosseini, H. Kaji, K. Ino, H. Shiku, A. Khademhosseini and T. Matsue, *Lab Chip*, 2012, **12**, 3491–3503.
- 14 I. J. A. Evers-van Gogh, S. Alex, R. Stienstra, A. B. Brenkman, S. Kersten and E. Kalkhoven, *Sci. Rep.*, 2015, **5**, 10944.
- 15 M. Costantini, S. Testa, P. Mozetic, A. Barbetta, C. Fuoco, E. Fornetti, F. Tamiro, S. Bernardini, J. Jaroszewicz, W. Swieszkowski, M. Trombetta, L. Castagnoli, D. Seliktar, P. Garstecki, G. Cesareni, S. Cannata, A. Rainer and C. Gargioli, *Biomaterials*, 2017, **131**, 98–110.
- 16 V. Hosseini, S. Ahadian, S. Ostrovidov, G. Camci-Unal, S. Chen, H. Kaji, M. Ramalingam and A. Khademhosseini, *Tissue Eng., Part A*, 2012, **18**, 2453–2465.
- 17 S. Campuzano, M. Pedrero, C. Montemayor, E. Fatás and J. M. Pingarrón, *J. Electroanal. Chem.*, 2006, **586**, 112–121.
- 18 B. K. Pedersen and M. A. Febbraio, *Physiol. Rev.*, 2008, **88**, 1379–1406.
- 19 J. Li, N. C. King and L. I. Sinoway, *J. Appl. Physiol.*, 2003, **95**, 577–583.
- 20 P. Munoz-Canoves, C. Scheele, B. K. Pedersen and A. L. Serrano, *Rev. Geophys.*, 2013, **280**, 4131–4148.
- 21 M. Ost, V. Coleman, J. Kasch and S. Klaus, *Free Radical Biol. Med.*, 2016, **98**, 78–89.
- 22 J. H. Yoon, J. Kim, P. Song, T. G. Lee, P.-G. Suh and S. H. Ryu, *Adv. Biol. Regul.*, 2012, **52**, 340–350.
- 23 T. Egawa, Y. Ohno, A. Goto, T. Sugiura, Y. Ohira, T. Yoshioka, T. Hayashi and K. Goto, *J. Caffeine Res.*, 2016, **6**, 88–96.
- 24 K. Shimizu, R. Genma, Y. Gotou, S. Nagasaka and H. Honda, *Bioengineering*, 2017, **4**, 56–66.
- 25 R. A. Frost, G. J. Nystrom and C. H. Lang, *Am. J. Physiol.*, 2002, **283**, R698–R709.

SUPPORTING INFORMATION

Muscle-on-a-chip with on-site multiplexed biosensing system for in situ-monitoring of secreted IL-6 and TNF- α

María A. Ortega^a, Xiomara Fernández-Garibay^a, Albert G. Castañó^a, Francesco De Chiara^a, Alejandro Hernández-Albors^a, Jordina Balaguer-Trias^a and Javier Ramón-Azcón^a

^aInstitute for Bioengineering of Catalonia (IBEC), The Barcelona Institute of Science and Technology (BIST). Baldori I Reixac, 10-12, 08028, Barcelona, Spain.

Email: jramon@ibecbarcelona.eu

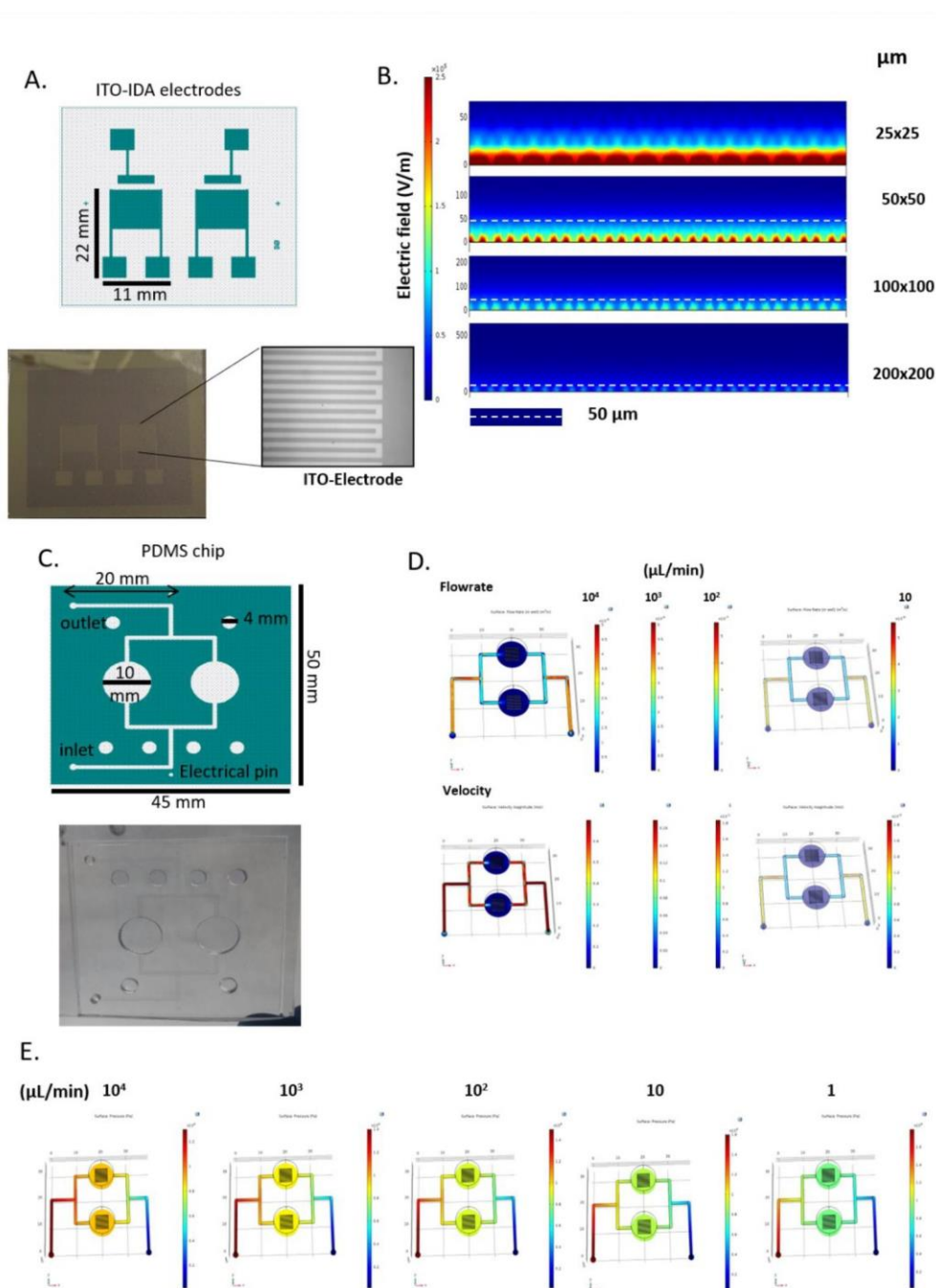


Fig S1. (A) Dimensions of custom-made ITO-IDA electrodes. Real image of electrodes substrate with zoomed view of the interdigitated array. B) COMSOL Multiphysics® simulations of the electrical field behavior at various interelectrode distance. (C) PDMS microfluidic chip dimensions. (D) and (E) COMSOL Multiphysics® simulations of flow rate, velocity and pressure throughout the device respectively.

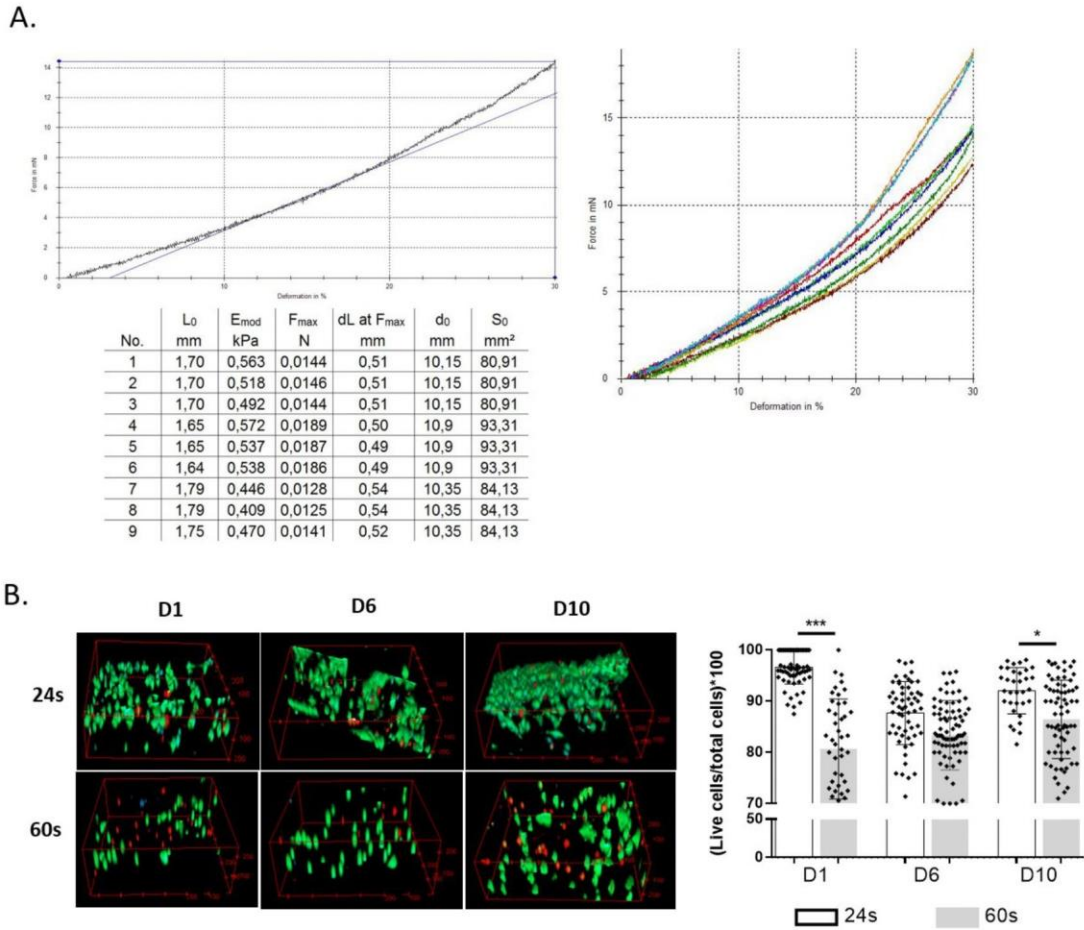


Fig. S2. (A) Force deformation curves and data for uniaxial compression test of GelMA-CMCMA hydrogels photocrosslinked at 24 sec. (B) Live/dead staining to assess cell viability in composite hydrogels fabricated at 24 s and 60 s of UV exposure (live cells in green and dead cells in red) Data from three different experiments (mean, SD): **p<0.01; ***p<0.001.

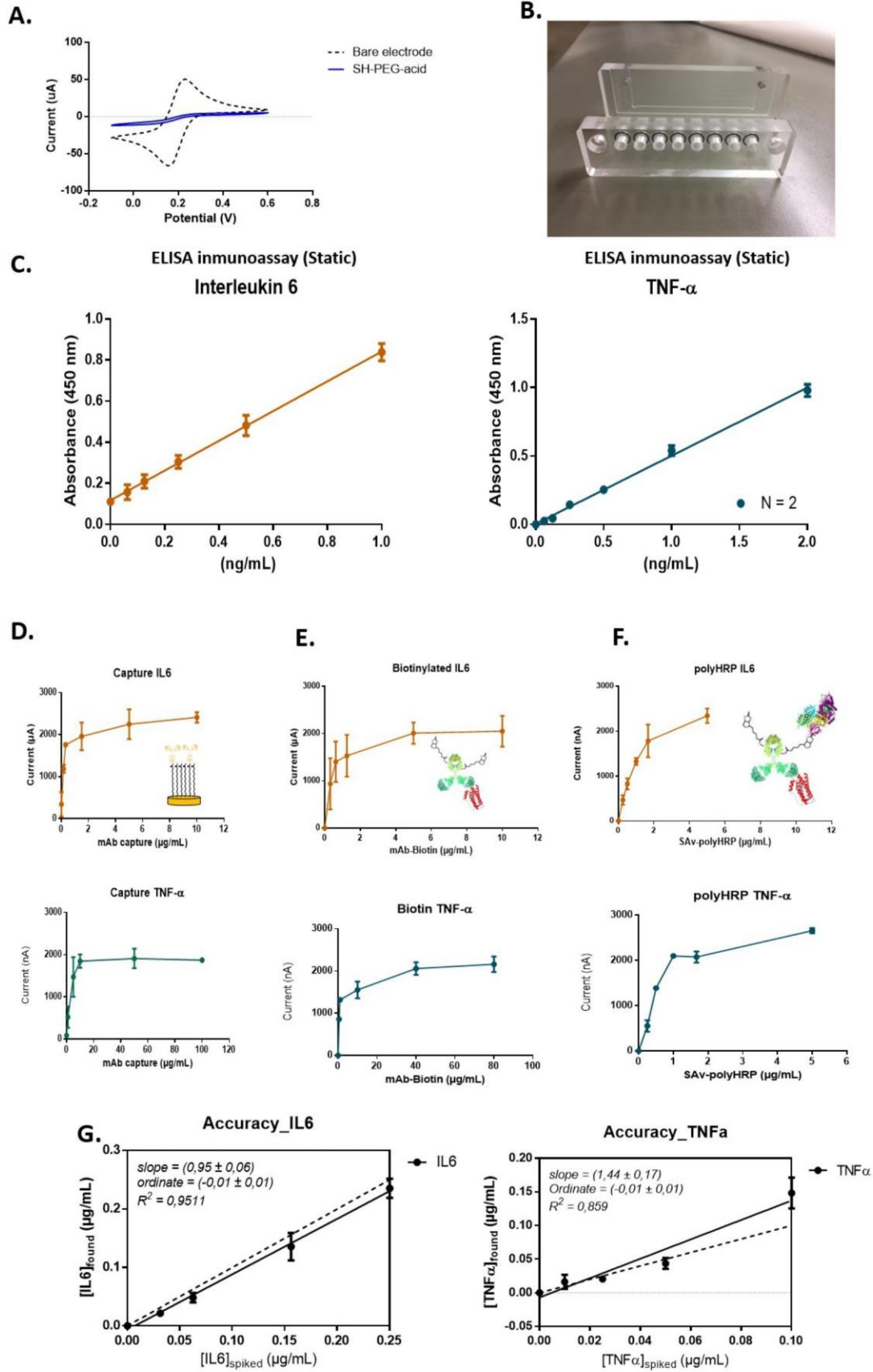


Fig. S3. (A) Cyclic voltammetry applied at 100 mV/s to bare electrode (dashed curve) versus functionalized with SH-PEG-acid (blue line). Changes in signal indicates the coverage of SAM on SPGE surface. (B) In-house PMMA static cells used for SPGEs functionalization protocol. (C) ELISA calibration curves for IL-6 and TNF- α respectively. Optimization of immunoassay on SPGEs surface using 1 $\mu\text{g mL}^{-1}$ of IL-6 and TNF- α during detection step. Saturation levels were reached at 1.5, 5, and 1 $\mu\text{g mL}^{-1}$ for IL6 and 10, 40 and 1 $\mu\text{g mL}^{-1}$ for TNF- α for (D) capture antibody, (E) secondary biotinylated antibody and (F) SAV-polyHRP conjugate, respectively. (G) Accuracy studies made by IL6 and TNF- α , performed using blind spiked samples prepared in differentiation media and used directly in the immunosensor without previous dilution. The data shown correspond to the average of at least two replicates. All data shown by mean \pm SD

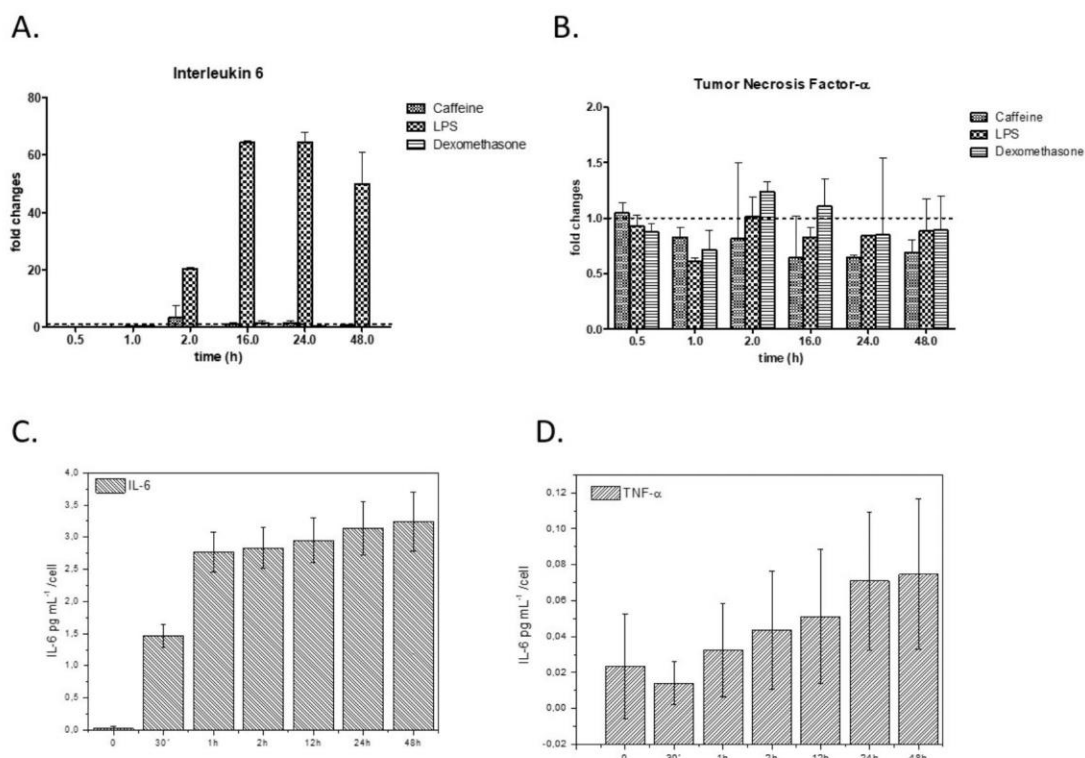


Fig. S4. (A) 2D drug screening assays evaluating IL-6 and (B) TNF- α release induced by caffeine (100 μM), dexamethasone (100 μM) and LPS (10 $\mu\text{g mL}^{-1}$). 2D myotubes were incubated for 0.5, 1, 2, 16, 24 and 48 h, in DM supplemented by the drug. Three replicates for each condition were analyzed. The screening of the cytokine levels was carried out by ELISA technique. (C) and (D) Amount of secreted IL-6 and TNF- α (pg mL $^{-1}$) per cell upon LPS-stimulation inside the microdevice. Calculations were made counting cell nuclei (DAPI immunostaining) inside 3D SM microtissue, with an estimation of 840.000 encapsulated cells.

Biofabrication



PAPER

OPEN ACCESS

RECEIVED

10 November 2020

REVISED

20 March 2021

ACCEPTED FOR PUBLICATION

9 April 2021

PUBLISHED

26 April 2021

Original content from this work may be used under the terms of the [Creative Commons Attribution 4.0 licence](#).

Any further distribution of this work must maintain attribution to the author(s) and the title of the work, journal citation and DOI.



Bioengineered *in vitro* 3D model of myotonic dystrophy type 1 human skeletal muscle

Xiomara Fernández-Garibay¹ , María A Ortega¹, Estefanía Cerro-Herreros^{2,3,4}, Jordi Comelles^{1,5}, Elena Martínez^{1,5,6} , Rubén Artero^{2,3,4}, Juan M Fernández-Costa^{1,*} and Javier Ramón-Azcón^{1,7,*}

¹ Institute for Bioengineering of Catalonia (IBEC), The Barcelona Institute of Science and Technology (BIST), c/Baldiri Reixac 10-12, E08028 Barcelona, Spain

² University Institute for Biotechnology and Biomedicine (BIOTECMED), University of Valencia, Dr Moliner 50, E46100 Burjassot, Valencia, Spain

³ Translational Genomics Group, Incliva Health Research Institute, Dr Moliner 50, E46100 Burjassot, Valencia, Spain

⁴ Joint Unit Incliva- CIPE, Dr Moliner 50, E46100 Burjassot, Valencia, Spain

⁵ Department of Electronics and Biomedical Engineering, University of Barcelona (UB), c/Martí i Franquès 1-11, E08028 Barcelona, Spain

⁶ Centro de Investigación Biomédica en Red (CIBER), Av. Monforte de Lemos 3-5, Pabellón 11, Planta 0, E28029 Madrid, Spain

⁷ Institució Catalana de Reserca i Estudis Avançats (ICREA), Passeig de Lluís Companys, 23, E08010 Barcelona, Spain

* Authors to whom any correspondence should be addressed.

E-mail: jfernandez@ibecbarcelona.eu and jramon@ibecbarcelona.eu

Keywords: myotonic dystrophy, skeletal muscle, tissue engineering, hydrogel micropatterning, 3D cell culture

Supplementary material for this article is available [online](#)

Abstract

Myotonic dystrophy type 1 (DM1) is the most common hereditary myopathy in the adult population. The disease is characterized by progressive skeletal muscle degeneration that produces severe disability. At present, there is still no effective treatment for DM1 patients, but the breakthroughs in understanding the molecular pathogenic mechanisms in DM1 have allowed the testing of new therapeutic strategies. Animal models and *in vitro* two-dimensional cell cultures have been essential for these advances. However, serious concerns exist regarding how faithfully these models reproduce the biological complexity of the disease. Biofabrication tools can be applied to engineer human three-dimensional (3D) culture systems that complement current preclinical research models. Here, we describe the development of the first *in vitro* 3D model of DM1 human skeletal muscle. Transdifferentiated myoblasts from patient-derived fibroblasts were encapsulated in micromolded gelatin methacryloyl-carboxymethyl cellulose methacrylate hydrogels through photomold patterning on functionalized glass coverslips. These hydrogels present a microstructured topography that promotes myoblasts alignment and differentiation resulting in highly aligned myotubes from both healthy and DM1 cells in a long-lasting cell culture. The DM1 3D microtissues recapitulate the molecular alterations detected in patient biopsies. Importantly, fusion index analyses demonstrate that 3D micropatterning significantly improved DM1 cell differentiation into multinucleated myotubes compared to standard cell cultures. Moreover, the characterization of the 3D cultures of DM1 myotubes detects phenotypes as the reduced thickness of myotubes that can be used for drug testing. Finally, we evaluated the therapeutic effect of antagomiR-23b administration on bioengineered DM1 skeletal muscle microtissues. AntagomiR-23b treatment rescues both molecular DM1 hallmarks and structural phenotype, restoring myotube diameter to healthy control sizes. Overall, these new microtissues represent an improvement over conventional cell culture models and can be used as biomimetic platforms to establish preclinical studies for myotonic dystrophy.

1. Introduction

The skeletal muscle tissue is one of the largest organs of the human body, and it is crucial for locomotion, thermogenesis, and metabolism maintenance [1]. This tissue can be affected by several neuromuscular or metabolic disorders, such as myasthenia gravis [2], McArdle disease [3], type 2 diabetes [4, 5], and muscular dystrophies [6]. Muscular dystrophies are genetically inherited degenerative disorders for most of which there is no cure to date. These disorders share muscle weakness and wasting as common symptoms; however, muscular dystrophies are very heterogeneous, differing in age of onset, rate of progression, inheritance pattern, and type of muscles that are affected [6–8]. The intrinsic heterogeneity of these diseases makes the development of new therapies especially challenging since it is expected that each patient would have a different response to treatments.

Drug development for new muscular dystrophy therapies usually involves the use of *in vitro* cell culture assays and *in vivo* animal models in phases before clinical trials. These strategies have long contributed to drug discovery by analyzing specific features of biological processes and identifying the molecular causes of certain diseases [9]. Still, both have significant shortcomings that make it challenging to obtain physiologically relevant results for humans. For instance, conventional *in vitro* models involve 2D cell monolayers cultured on flat and rigid substrates. These models do not emulate the complexity of real tissues, which have a three-dimensional (3D) structural organization of cells surrounded by each other and an extracellular matrix [10]. On the other hand, functional 3D tissues representing tissue physiology can be found in animal models. The use of animal models in pharmacological research raises several ethical concerns. Moreover, *in vivo* models often fail to predict the clinical efficacy of drugs. This is due to species-specific differences that limit the extrapolation of animal data to human conditions [11]. It has been estimated that following this drug development pathway, only 11.8% of drugs entering clinical trials become approved, generating a cost of billions of dollars for newly authorized drugs [12, 13]. To accelerate preclinical research, *in vitro* studies could be complemented by human 3D culture systems. These *in vitro* systems consist of patient-derived bioengineered skeletal muscle tissues that offer a better representation of the environment of living tissues with a particular 3D architecture [14].

Skeletal muscle architecture is characterized by bundles of aligned muscle fibers (myofibers). These fibers are formed by the fusion of muscle precursor cells (myoblasts) into multinucleated myotubes, which later become mature myofibers [15]. Because of this complex architecture, engineering skeletal muscle tissues requires a specific organization of muscle precursor cells. These are usually embedded

in a suitable biomaterial scaffold, promoting differentiation of myoblasts to form aligned myotubes [16]. Moreover, the biomaterial should provide cells with an appropriate 3D growth environment, optimal oxygen levels, effective nutrient transport, and mechanical integrity over an extended culture period [10]. Hydrogels of natural origin, such as collagen, gelatin, or fibrin, have been widely used as biomaterial scaffolds for engineered skeletal muscle [17]. This is due to their high water content and the presence of cell adhesion and degradation motifs, which allow cell growth and matrix remodeling. Among these hydrogels, gelatin methacryloyl (GelMA) and other methacrylated biomaterials have been used to encapsulate cells in defined 3D structures due to their photocrosslinkable properties [18]. Also, these hydrogels can further be combined with non-degradable biomaterials, such as alginate or carboxymethyl cellulose. The addition of these polysaccharides to GelMA composite hydrogels enhances their mechanical properties and supports long-term culture of myotubes [19–21].

In this work, we focused on developing the first bioengineered 3D model of myotonic dystrophy type 1 (DM1) human skeletal muscle tissue. DM1 is a life-threatening and chronically debilitating disorder, which is the most common hereditary myopathy in adults (for a recent review of DM1 hallmarks see [22]). The genetic cause of DM1 is a dynamic mutation that expands the cytosine-thymine-guanine (CTG) triplet repeat in the 3' non-translated region of the *Dystrophia Myotonia Protein Kinase* (*DMPK*) gene [23]. Cytosine-uracil-guanine (CUG) repeat RNAs accumulate in nuclear foci. This mutant *DMPK* RNA causes toxic gene misregulation events at the level of gene expression [24, 25], translation [26], gene silencing [27–30], alternative splicing [31–33], and polyadenylation of subsets of transcripts [34]. Muscleblind-like (MBNL) proteins, a family of alternative splicing regulators, are sequestered in these CUG foci, and concomitantly their molecular function is impaired [35]. This results in abnormal alternative splicing events directly related to several disease characteristic symptoms, such as muscle weakness and hyper contraction.

Although significant advances have been made in studying the molecular causes of DM1, there is still no effective treatment for patients. Animal models, such as mouse [36], fly [37–39], and zebrafish [40], have been used to evaluate different therapeutic candidates [41–45]. Among these, therapeutic gene modulation is a promising strategy that has the objective of regulating the endogenous expression of a gene to mitigate a certain disease [46]. Following this approximation, it has been demonstrated that microRNAs (miRNAs) that inhibit MBNL translation can be silenced by antisense oligonucleotides (antagomiRNAs). Concretely, specific blocking of miR-218 and miR-23b has resulted in increased MBNL protein levels and rescue of

mis-splicing events in DM1 human myoblasts [46] and HSA^{LR} DM1 model mice, where low toxicity, high efficacy, and long-lasting biological effects were observed [46, 47]. While these are encouraging results, the effectiveness of treatments for DM1 still needs to be investigated in clinical phases.

Here, we describe a method to fabricate a bioengineered 3D DM1 skeletal muscle tissue model using transdifferentiated myoblasts from patient-derived fibroblasts. These cells were encapsulated in micro-patterned GelMA-carboxymethyl cellulose methacrylate (CMCMA) hydrogels on top of functionalized glass coverslips. Cells were cultured for up to three weeks obtaining aligned myotubes with disease-associated molecular and structural phenotypic features. Remarkably, cell encapsulation in micropatterns improved DM1 myotube formation compared to traditional 2D cultures. Moreover, the analysis of 3D reconstructed myotubes showed that DM1 myotubes have a thinner phenotype than myotubes from healthy control cells. Additionally, as a proof-of-concept, we showed that antagomiR treatment for miR-23b could rescue MBNL expression and myotube diameter in 3D DM1 human myotubes. Overall, we demonstrate that patient-derived bioengineered DM1 skeletal muscle microtissues represent valuable *in vitro* tools for preclinical research. Finally, the developed fabrication method for DM1 could easily be translated for drug development and other studies on muscular dystrophies.

2. Experimental procedure

2.1. Cell culture

Immortalized human fibroblasts from unaffected control and DM1 patient (carrying 1300 CTG repeats quantified in the blood cells) [48] were kindly provided by Dr Denis Furling and Dr Vincent Mouly (Institute of Myology, Paris). Fibroblast cells were grown in Dulbecco's modified eagle medium (DMEM, 4.5 g l⁻¹ glucose, Gibco) supplemented with 1% penicillin-streptomycin (P/S, 10 000 U ml⁻¹, Thermofisher) and 15% fetal bovine serum (Gibco). Transdifferentiation into myoblast-like cells was induced by turning on the myogenic program, forcing MyoD expression when culturing cells in muscle differentiation medium (MDM). MDM consisted of DMEM with 4.5 g l⁻¹ glucose, 1% P/S, 2% horse serum, 1% apo-transferrin (10 mg ml⁻¹), 0.1% insulin (10 mg ml⁻¹), and 0.02% doxycycline (10 mg ml⁻¹). In all cases, cells were grown at 37 °C in a humidified atmosphere containing 5% CO₂. For cell differentiation in 2D, fibroblasts were seeded at 12 000 cells cm⁻² in 12-well plates containing glass coverslips coated with 50 µg ml⁻¹ collagen type I and were cultured in growth medium. Once the cells were confluent, the growth medium was replaced by MDM to induce

the myogenic program. Fusion index was analyzed in cultures differentiated for seven days.

2.2. Microstructured stamps fabrication

Microstructured poly(dimethylsiloxane) (PDMS), Sylgard™ Elastomer base and curing agent) stamps were fabricated by replica molding of silicon wafer molds.

2.2.1. Microfabrication of silicon molds

Silicon wafer molds were fabricated by standard photolithography techniques using SU-8 negative photoresist. Briefly, silicon wafers (4" n-type <111>, MicroChemicals GmbH) were cleaned in a plasma chamber for 20 min at 6.8 W. After that, wafers were heated for 5 min in a hotplate at 95 °C to dehydrate them. Negative resist SU-8 2100 (2100, MicroChem) was spin-coated in two steps to obtain structures of 100 µm in height. To make the patterns, a mask aligner (SÜSS Microtec, MJB4) was set to 240 mJ cm⁻² energy radiation at 365 nm, and a high-quality emulsion flexible film was used as a photomask (JD Photodata, UK). Irradiation time was set to 20 s. Cross-linkage of negative-tone exposed regions of SU-8 was subject to a hotplate cycle of 65 °C and 95 °C for 5 and 20 min, respectively. The labile photoresist was removed by developing the crosslinked patterns immersing the wafer in SU-8 developer (MicroChem) for 10 min. Then, the action of 2-propanol stopped development. After a quick N₂ blow, we heated the molds for 60 min at 120 °C. As a final step, the SU-8 patterned silicon molds had to undergo silanization to obtain hydrophobic surfaces and avoid permanent bonding with the PDMS.

2.2.2. Replica molding of microstructured PDMS stamps

The polymer elastomer base and curing agent were weighted in a 10:1 ratio to obtain microstructured stamps of 6 mm in diameter, with channels of 100 µm and 200 µm of width and height. After mixing thoroughly, we degassed the polymer in a vacuum chamber. PDMS was poured on the patterned silicon substrate and cured at 80 °C for 4 h. Finally, PDMS was detached and cut off using a 5 mm biopsy punch. PDMS stamps were cleaned by sonication in Milli-Q water and 2-propanol for 5 min and dried using N₂ flow before using them for tissue fabrication.

2.3. Prepolymer preparation

GelMA (figure 1(e)) and CMCMA (figure 1(g)) were synthesized as previously described [19]. These prepolymer precursors and the photoinitiator lithium phenyl (2,4,6-trimethylbenzoyl) phosphinate (LAP, TCI Europe N.V.) were dissolved in MDM at 65 °C for 2 h. The concentrations of GelMA, CMCMA and LAP were fixed to obtain final concentrations of 5%, 1% and 0.1% (w/v), respectively.

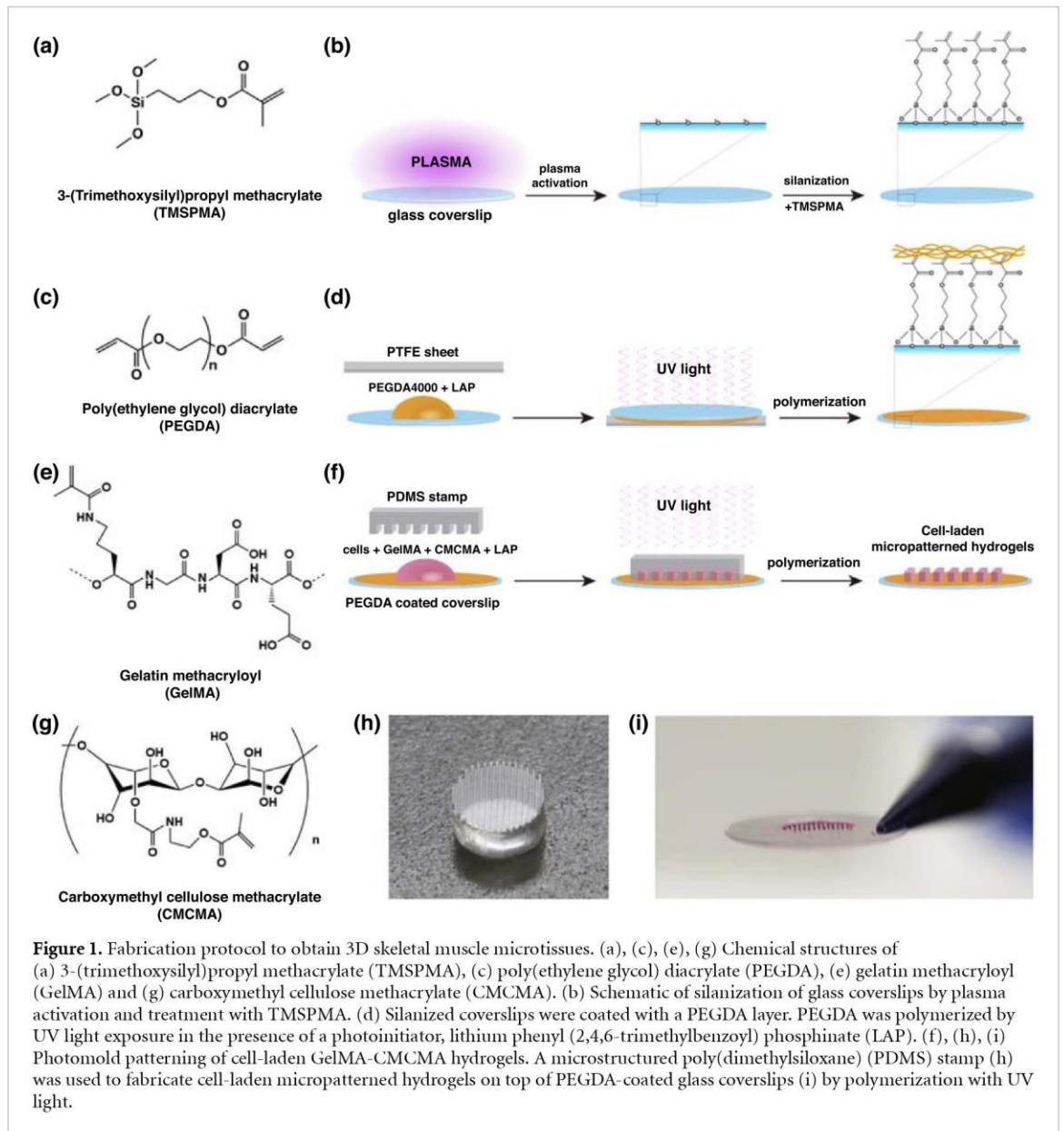


Figure 1. Fabrication protocol to obtain 3D skeletal muscle microtissues. (a), (c), (e), (g) Chemical structures of (a) 3-(trimethoxysilyl)propyl methacrylate (TMSPMA), (c) poly(ethylene glycol) diacrylate (PEGDA), (e) gelatin methacryloyl (GelMA) and (g) carboxymethyl cellulose methacrylate (CMCMA). (b) Schematic of silanization of glass coverslips by plasma activation and treatment with TMSPMA. (d) Silanized coverslips were coated with a PEGDA layer. PEGDA was polymerized by UV light exposure in the presence of a photoinitiator, lithium phenyl (2,4,6-trimethylbenzoyl) phosphinate (LAP). (f), (h), (i) Photomold patterning of cell-laden GelMA-CMCMA hydrogels. A microstructured poly(dimethylsiloxane) (PDMS) stamp (h) was used to fabricate cell-laden micropatterned hydrogels on top of PEGDA-coated glass coverslips (i) by polymerization with UV light.

2.4. Cell encapsulation in 3D microstructured hydrogels

Cell-laden 3D microstructured hydrogels were fabricated on top of glass coverslips using a photomold patterning technique, as described in [20].

2.4.1. Glass coverslip functionalization

Glass coverslips were previously treated with 3-(trimethoxysilyl)propyl methacrylate (TMSPMA, Aldrich) (figure 1(a)) and coated with a layer of poly(ethylene glycol) diacrylate (PEGDA, MW 4000 Da, Sigma-Aldrich) (figure 1(c)) by free radical polymerization. First, clean glass coverslips were activated by oxygen plasma at 29.6 W for 30 s. Immediately after plasma treatment, the glass surface was covered with a freshly prepared silanization solution (TMSPMA diluted in ethanol at 1:50 and mixed with 3% acetic acid) for 1 h. Then, coverslips were thoroughly washed with ethanol and dried (figure 1(b)).

For PEGDA coating, we prepared a solution of 20% (w/v) PEGDA and 2% (w/v) LAP in Milli-Q water by dissolving in a water bath at 60 °C for 30 min. For each coverslip, a 5 μ l drop was placed on a Teflon surface. Then, the silanized side of the coverslip was carefully pressed on top. Finally, samples were exposed to UV for 2 min using a UVP Crosslinker (model CL-1000 I, 365 nm, 40 W, Analytik Jena US), washed several times with Milli-Q water, and thoroughly dried (figure 1(d)).

2.4.2. Cell encapsulation

To encapsulate cells in micropatterned hydrogels, we mixed the prepolymer solution with a cell suspension of either control or DM1 cells in MDM to obtain a final concentration of 2.5×10^7 cells ml^{-1} . Then, an 8 μ l drop of the cell-laden prepolymer was placed on a PEGDA-coated glass coverslip, and a PDMS stamp (figure 1(h)) was pressed lightly on top, filling the microchannels with the solution. The hydrogels were

crosslinked by UV exposure of 30 s using the UVP Crosslinker. MDM was added to each sample, and stamps were carefully removed after 20 min of incubation at 37 °C (figures 1(f) and (i)). Encapsulated cells were differentiated for up to 21 days, with culture media being replaced every two days.

2.5. Hydrogel characterization

2.5.1. Stiffness measurements

The bulk stiffness of GelMA-CMCMA hydrogels was analyzed by uniaxial compression tests using a Zwick Z0.5 TN instrument (Zwick-Roell, Germany) with a 5 N load cell. Hydrogels were fabricated as described in [20]. For each sample, 300 μ l of the prepolymer solution were placed in a 48-well plate and exposed to UV light for 30 s. Cylindrical samples were cut using a 10 mm diameter biopsy punch. Samples were tested at room temperature (RT) up to 30% final strain (deformation), using the following parameters: 0.1 mN preload force and 20% min^{-1} strain rate. Force-deformation graphs were obtained using the TestXpert (Zwick-Roell) software. Values for the compressive modulus were automatically calculated from the slope of the linear region corresponding to 10%–20% deformation (strain) with the TestXpert software.

To obtain Young's modulus of the micropatterned GelMA-CMCMA hydrogels in liquid conditions, samples were photomolded as described before (see section 2.4). After 24 h of incubation at 37 °C, the stiffness was measured by atomic force microscopy (AFM) following a previously described protocol [49, 50]. Briefly, indentation measurements were conducted using a NanoWizard® 4 Bioscience AFM (JPK Instruments) mounted onto a Nikon Ti inverted microscope. Silicon nitride pyramidal tips (NanoWorld) with nominal spring constants of 0.08 Nm^{-1} were used. Series of ten indentations at a frequency of 0.05 Hz (10 μ m amplitude) were performed in different positions of the GelMA-CMCMA micropatterns. Finally, the Hertz model for a pyramidal tip was fitted to the measured force-distance curves, using the JPK data analysis software.

2.5.2. Scanning electron microscopy (SEM) imaging

Hydrogels for SEM imaging were fabricated following the same protocol as for compression measurements. After 24 h of incubation, the hydrogels were washed with Milli-Q water and fixed for 1 h in a 2.5% glutaraldehyde solution (Sigma-Aldrich). Following several washes, samples were dehydrated by sequential immersion in graded ethanol solutions in Milli-Q water. Washings of 10 min were performed with 50%, 70% ($\times 2$), 90% ($\times 3$), 96% ($\times 3$) and 99.5% ($\times 3$) ethanol. To dry the hydrogels without causing their collapse, samples were placed in a critical point drying chamber (K850, Quorum Technologies, UK), where ethanol was completely replaced by

liquid CO_2 and gradually heated until CO_2 achieved gas phase equilibrium and was slowly drained. After critical point drying, microstructured hydrogels were covered with Au and imaged by ultrahigh-resolution SEM (Nova NanoSEM 230, FEI Company, The Netherlands) operating in a low vacuum mode (0.5 mbar of water vapor pressure).

2.6. Cell viability assay

Cell viability was evaluated 24 h after encapsulation using the Live/Dead viability/cytotoxicity kit (Invitrogen). Briefly, samples were washed several times with sterile $1 \times$ phosphate buffered saline (PBS) and incubated for 30 min with a staining solution containing Calcein AM, Ethidium homodimer-1, and Hoescht (Invitrogen) in PBS. Cell viability was calculated as the percentage of living cells with respect to the total cell number analyzed in the 3D reconstruction of confocal Z-stacks using Imaris software.

2.7. Antisense oligonucleotide treatment

AntagomiR oligonucleotides (Creative Biogene) were administrated 72 h after DM1 microtissue fabrication. MDM was replaced and supplemented with 100 nM of AntagomiRs for miR-sc (control) or miR-23b-3p. The treatment lasted for seven days without replacing the culture media. The antagomiR sequences were: 5'-mG*mG*mUmAmAmUmCmCmCmUmGmGmCmAmAmUmGmU*mG*mA*mU*-3'-chol (antagomiR-23b-3p), and 5'-mC*mA*mGmUmAmCmUmUmUmUmGmUmGmUmA*mC*mA*mA*-3'-chol (sc control). Where m denotes 2'-O-methyl-modified phosphoramidites, * denotes phosphorothioate linkages, and chol denotes cholesterol groups.

2.8. Fluorescence in situ hybridization (FISH)

Bioengineered 3D skeletal muscle tissues were fixed in 4% paraformaldehyde for 30 min at RT and washed with $1 \times$ PBS for 10 min. Samples were incubated in the prehybridization buffer ($2 \times$ saline sodium citrate [SSC], 30% deionized formamide) for 30 min at RT and hybridized with a Cy3-(CAG)₇-Cy3-labeled probe, diluted 1:200 in hybridization buffer (40% deionized formamide, $2 \times$ SSC, 10% dextran sulfate, 0.2% BSA, 2 mM Ribonucleoside Vanadyl Complex (Sigma-Aldrich), 1 mg ml^{-1} *Escherichia coli* tRNA, 1% herring sperm DNA) overnight at 37 °C in the dark. After hybridization, samples were washed twice with a prehybridization buffer for 30 min at 42 °C, washed with $1 \times$ PBS, and incubated with DAPI for 15 min. All the incubations were performed in a humidity chamber.

2.9. Immunofluorescence staining

Bioengineered muscle tissues were fixed with 10% formalin solution (Sigma-Aldrich) for 30 min at

RT, followed by several washes in PBS. Samples were then permeabilized with PBS-T (0.1% Triton-X (Sigma-Aldrich) in PBS), blocked (0.3% Triton-X, 3% donkey serum (Sigma-Aldrich) in PBS) for 2 h at RT, and incubated with primary antibody (supplementary table 1 (available online at stacks.iop.org/BF/13/035035/mmedia)) at 4 °C overnight. After several PBS-T washes, the samples were incubated for 2 h with the fluorophore-conjugated secondary antibody (supplementary table 1) at RT. Finally, the samples were counterstained with DAPI (4',6-diamidino-2-phenylindole, Life Technologies) to detect the nuclei.

For MBNL1 detection, after FISH protocol, samples were incubated with the monoclonal anti-MBNL1 primary antibody at 4 °C. The fluorescence signal was amplified using a biotin-conjugated secondary antibody (supplementary table 1) and the VECTASTAIN® Elite® ABC kit (Vector) for 1 h at RT, followed by PBS-T washes and incubation with either Dylight®488-FITC (1:200, Vector) for 2 h at RT. Finally, the samples were counterstained with DAPI to detect the nuclei.

2.10. Imaging

Light microscopy and live-cell imaging of myotubes were performed using a Zeiss Axio Observer.Z1/7 outfitted with the XL S1 cell incubator. Imaging was performed at 37 °C and 5% CO₂. Fluorescence images were taken as Z-stacks with a ZEISS LSM800 confocal laser scanning microscope and analyzed using the Imaris microscope image analysis software (Oxford instruments) and the Fiji image processing package, a distribution of Image J [51, 52].

2.11. Fusion index and myotube size analysis

Z-stacks were analyzed as 3D images using the Imaris software. Fusion index was determined as the percentage of nuclei in myotubes (≥ 2 myonuclei) with respect to the total number of nuclei, in myotubes expressing sarcomeric α -actinin (SAA). The diameter of individual 3D myotubes was obtained by the object-oriented bounding box statistical variable (BoundingBoxOO Length A), which measures the length of the object's shortest principal axis.

2.12. RNA extraction, RT-PCR and real-time PCR

Total RNA from human bioengineered muscles was isolated using Tri-reagent (Sigma) according to the manufacturer's instructions. One microgram of RNA was digested with DNase I (Invitrogen) and reverse-transcribed with SuperScript™ II (Invitrogen) using random hexanucleotides. qRT-PCR was carried out on one nanogram of cDNA template with the FIRE-Pol® EvaGreen® qPCR Mix Plus (Solis Biodyne) and specific primers (supplementary table 2). *GAPDH* and *ACTB* were used as endogenous controls. miRNA

expression was quantified using specific miRCURY LNA microRNA PCR primers (Qiagen) according to the manufacturer's instructions. Relative gene expression was normalized to miR-103 expression [53]. Expression levels were measured using the QuantStudio 5 Applied Biosystems Real-Time PCR System. Expression relative to the endogenous genes and control group was calculated using the $2^{-\Delta\Delta C_t}$ method. Pairs of samples were compared using two-tailed Student *t*-tests ($\alpha = 0.05$), applying Welch's correction when necessary. For splicing analyses, 20 ng of cDNA were used in a standard PCR reaction with GoTaq polymerase (Promega). Specific primers were used to analyze alternative splicing of *Bridging integrator 1 (BIN1)*, *Nuclear Factor I X (NFIX)*, and *Spectrin Alpha Non-Erythrocytic 1 (SPTAN1)* (supplementary table 2).

2.13. Western blotting

For total protein extraction, samples were homogenized in RIPA buffer (150 mM NaCl, 1.0% IGEPAL, 0.5% sodium deoxycholate, 0.1% SDS, 50 mM Tris-HCl pH 8.0) supplemented with protease and phosphatase inhibitor cocktails (Roche Applied Science). Total proteins were quantified with a BCA protein assay kit (Pierce) using bovine serum albumin as the standard concentration range. For the immunodetection assay, 20 μ g of samples were denatured for 5 min at 100 °C, electrophoresed on 12% SDS-PAGE gels, transferred onto nitrocellulose membranes 0.45 μ m (GE Healthcare), and blocked with 5% non-fat dried milk in PBS-T (1 \times PBS; 0.05% Tween 20, pH 7.4). Membranes were incubated overnight at 4 °C with primary mouse anti-MBNL1 (1:200, clone MB1a (4A8), Developmental Studies Hybridoma Bank) or mouse anti-MBNL2 (1:100, clone MB2a (3B4), Developmental Studies Hybridoma Bank). Anti-GAPDH-binding protein-horseradish peroxidase (HRP) antibody (1 h, 1:3500, clone G-9, Santa Cruz) as a loading control. All primary antibodies were detected using HRP-conjugated anti-mouse-IgG secondary antibody (1 h, 1:5000, Sigma-Aldrich). Immunoreactive bands were detected using ECL™ Western blotting substrate (Pierce), and images were acquired with an AMERSHAM ImageQuant 800 (GE Healthcare). Quantification was performed using ImageJ software. The statistical differences were estimated by the Student's *t*-test ($p < 0.05$) on normalized data.

2.14. Statistical analysis

All group data are expressed as mean \pm SEM. The comparisons between groups were performed using Prism 8 software (GraphPad) by two-tailed Student *t*-test ($\alpha = 0.05$), applying Welch's correction when necessary. Differences between groups were considered significant when $P < 0.05$ (* $P < 0.05$; ** $P < 0.01$; *** $P < 0.001$; **** $P < 0.0001$).

3. Results and discussion

3.1. A fabrication protocol to obtain 3D skeletal muscle microtissues

The skeletal muscle is a highly organized tissue made up of arrays of aligned, multinucleated myofibers. This complex architecture should be mimicked *in vitro* to obtain 3D models that accurately represent the basic features of skeletal muscle tissue. Multinucleated myofibers are formed by fusion and differentiation of muscle precursor cells; therefore, fabrication strategies for tissue engineering should provide effective topographical cues that favor myoblast alignment and fusion. Among these biofabrication techniques to engineer topographical cues, the most used are micropatterning, micromolding, electrospinning, and 3D bioprinting [54]. Previous studies have shown that cells with a tendency to align *in vivo* (e.g. fibroblasts, murine myoblasts, and endothelial cells) can elongate and align *in vitro* if they are geometrically confined within a suitable biomaterial [55]. Accordingly, our fabrication protocol was designed to encapsulate human muscle precursor cells in micropatterned hydrogels, which confine cells in narrow hydrogel filaments and induce the formation of elongated myotubes.

As previously described, we used photomold patterning to transfer the features of microstructured PDMS stamps into photocrosslinkable GelMA-CMCMA hydrogels (figures 1 and 2(a)). We fabricated stamps with channels of 200 μm (data not shown) or 100 μm of width, height, and spacing. We observed better cell alignment when cells were confined in smaller structures. This was in agreement with other studies where cell alignment and myotube formation were enhanced in the thinnest structures [56]. Besides alignment being favored in narrower patterns, there are other limitations to the dimensions of hydrogels for cell encapsulation. As some studies point out, there is a limited diffusion of oxygen and nutrients in engineered tissues at around 200 μm of depth due to the lack of vascularization [19, 57, 58]. Therefore, we fabricated smaller structures to overcome this limitation. Consequently, we decided to use the microstructured stamps with smaller features to fabricate hydrogel filaments of 100 μm in width and 5 mm in length on top of glass coverslips.

Using glass as our substrate, we noticed that some cells adhered to the flat surface between hydrogel filaments outside of the 3D structure (figure 2(b)). This was an unwanted effect since cells in 2D would grow and differentiate at a different speed, creating two separate cell populations. To ensure that cells remained confined within the 3D GelMA-CMCMA hydrogel, the glass surface was previously silanized and coated with a thin layer of PEGDA hydrogel. PEGDA is hydrophilic and inert to protein adsorption [59]; hence, this surface modification highly reduced undesired 2D cell attachment outside the

GelMA-CMCMA microfilaments fabricated on top of the PEGDA layer (figure 2(c)). Furthermore, GelMA-CMCMA was covalently attached to PEGDA, which gave more stability to the micropatterned structures [60].

Cell encapsulation in photocrosslinkable hydrogels is achieved by free radical polymerization in the presence of a photoinitiator and UV light. Therefore, after this procedure, cell survival strongly depends on critical factors, including UV wavelength, energy dose, and photoinitiator concentration. When cells are exposed to a low dose of long-wave UV light, the procedure is considered biocompatible [61]. As has been reported, LAP photoinitiator has a high extinction coefficient at 365 nm, which makes it more efficient than other commonly used compounds, such as Irgacure 2659 [19, 62]. This efficiency allowed crosslinking composite hydrogels with a very low photoinitiator concentration and short exposure times (low energy dose). To confirm this, we measured the energy dose received by cells during 30 s of UV exposure using a wireless power-meter inside the UVP crosslinking chamber, obtaining 0.48 J cm^{-2} (16 mW cm^{-2} during 30 s). This energy dose is very low, considering cell-laden GelMA hydrogels have been crosslinked with energy doses ranging from 0.3 J cm^{-2} to 36 J cm^{-2} [63, 64]. Moreover, cell cytotoxicity assays (figures 3(a)–(h)) showed that more than 88% of encapsulated cells remained viable 24 h after UV exposure (figure 3(i)).

Although both 3D bioprinting and photomold patterning are valuable biofabrication strategies for generating cell-laden hydrogel filaments, photomold patterning offered several advantages compared to our previous 3D bioprinted model [19], such as reproducibility, amount of material required, or the final cost of the procedure.

Human skeletal muscle tissue models have been developed from primary and immortalized human myoblasts and human induced pluripotent stem cells [65]. Bioengineered 3D *in vitro* models require large numbers of cells, especially for high-throughput drug screening platforms. This represents a challenge for developing disease models, where it is necessary to incorporate patient cells coming from muscle biopsies. A major problem of using primary myoblasts from adult DM1 patients is their limited proliferative capacity due to premature replicative senescence [66]. Besides, muscle biopsies are invasive and not always available. Arandel *et al* overcame these limitations by developing transdifferentiated myotubes cell lines [48]. These cell lines consisted of immortalized skin fibroblasts that were converted into multinucleated myoblasts by forcing the overexpression of the myogenic regulator factor MYOD1. Here, we fabricated 3D skeletal muscle microtissues from immortalized fibroblasts obtained from a healthy control individual and a DM1 patient. Cell-laden hydrogels were cultured in MDM containing doxycycline and a

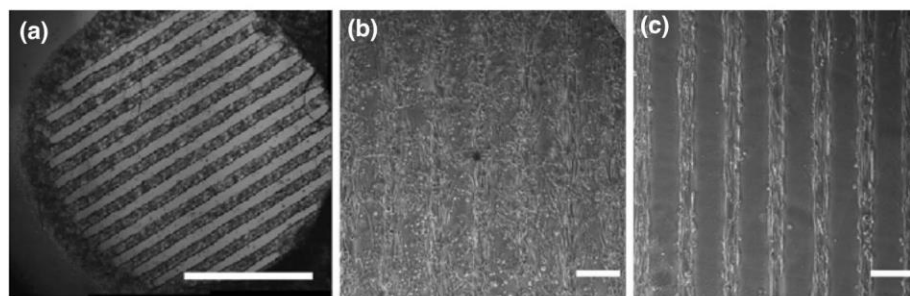


Figure 2. Effect of PEGDA coating on micropatterned hydrogels. (a) Phase contrast image of cell-laden micropatterned hydrogels (scale bar: 2.5 mm). (b), (c) Representative phase contrast images of cell-laden hydrogels without (b) and with (c) PEGDA coating (scale bars: 200 μm).

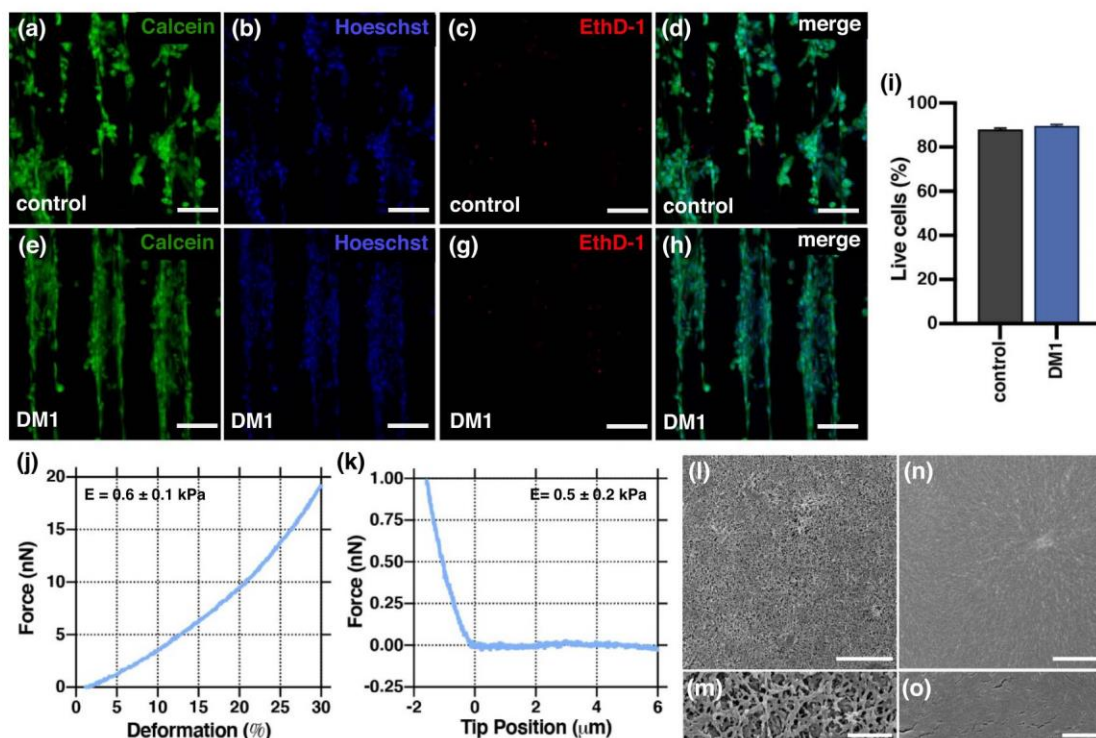


Figure 3. (a)–(h) Representative images of live/dead staining from healthy control (a)–(d) and DM1 cells (e)–(h) 24 h after cell encapsulation. Live cells were stained with Calcein AM (green), nuclei were stained by Hoescht (blue), and dead cells (red) were stained with Ethidium homodimer-1 (EthD-1) (Scale bars: 100 μm). (i) Graph showing the cell viability in micropatterned hydrogels represented as the live cells over the total cell number (mean \pm SEM). (j) Example of a typical force–deformation curve obtained by uniaxial compression tests on bulk GelMA–CMCMA hydrogels. Young’s modulus (E) = 0.6 ± 0.1 kPa (k) typical force–displacement curves of the AFM tip indenting the surface of the GelMA–CMCMA microstructured hydrogels. $E = 0.5 \pm 0.2$ kPa (Mean values \pm SEM). (l)–(o) Scanning electron microscopy (SEM) images of GelMA–CMCMA (l), (m) and PEGDA (n), (o) hydrogels. Scale bars: (l), (n) 5 μm , (m), (o) 1 μm .

low serum concentration from the moment of encapsulation. With this culture media, doxycycline activated the myogenic program and transdifferentiation into myoblast-like cells. Additionally, the reduced serum concentration slowed down cell proliferation, inducing a shift to a differentiation state. Furthermore, myoblasts need to be close to recognize each other and fuse into myotubes. Since cell proliferation was limited by the MDM, working with a high cell density (2.5×10^7 cells ml^{-1}) was key in obtaining multinucleated myotubes. In summary, we have developed a reproducible method to generate 3D skeletal muscle microtissues from human cells. In this

protocol, we applied a photomold patterning technique to encapsulate cells in GelMA–CMCMA hydrogel scaffolds.

3.2. Physical properties of GelMA–CMCMA hydrogels

Skeletal muscle tissue engineering requires culture time for myoblast fusion and myotube maturation. Additionally, engineered tissues should remain viable for several weeks to be valuable for drug screening applications. For these reasons, the biomaterials used as scaffold need to resist enzymatic degradation by encapsulated cells and other stress

cues. We previously showed that degradation of GelMA hydrogels could be slowed down by fabricating composites that include a small percentage of a non-degradable polymer [19]. GelMA contains cell adhesion and degradation sites that allow cells to attach and remodel the matrix, a necessary feature for cell spreading and fusion. CMCMA is a biocompatible cellulose derivative that is non-degradable by mammalian cells [67]. Therefore, its incorporation into the hydrogel formulation provided more structural stability over time. In fact, in our previous works, we have demonstrated that this composite hydrogel allowed long-lasting culture and differentiation of murine skeletal muscle cells [20, 68].

The bulk stiffness of GelMA-CMCMA hydrogels was measured using uniaxial compression tests, obtaining a Young's modulus of 0.6 ± 0.1 kPa (figure 3(j)). To calculate the stiffness of our micropatterned hydrogels in liquid conditions, we performed AFM microindentation measurements (figure 3(k)). The obtained values were comparable ($E = 0.5 \pm 0.2$ kPa), corresponding to soft hydrogels in the range of 0.5–0.7 kPa. Some studies suggest that the optimal stiffness for myotube maturation is higher, being closer to the native skeletal muscle tissue (~ 12 kPa) [69, 70]. However, these experiments were performed by seeding cells on top of 2D substrates. In contrast, the stiffness of hydrogels for 3D skeletal muscle models varies depending on the biomaterials used but lean towards softer hydrogels. For instance, the encapsulation of human myoblasts in fibrin-based hydrogels is performed in biomaterials with Young's modulus of 1 ± 0.1 kPa [71]. Similarly, 3D studies performed with GelMA and C2C12 murine cells indicated that softer hydrogels in the range of 1–3 kPa lead to more elongated cell morphology, better cell spreading, and greater differentiation in 3D structures [20, 56]. In the case of micropatterned GelMA-based hydrogels, stiffer hydrogels can be obtained by modifying fabrication conditions to increase the crosslinking degree. We previously studied cell morphology and spreading in micropatterned GelMA-CMCMA hydrogels with different stiffness values [20]. Stellate morphology indicates that cells can move better within the material, which is essential for cell fusion. We observed that cells had a stellate morphology in softer hydrogels, while most cells were round when encapsulated using longer UV exposure times. Furthermore, longer UV exposure times or higher photoinitiator concentration may affect cell viability (see section 3.1). Moreover, highly crosslinked hydrogels result in densely packed fibrillar structures that reduce water uptake and hinder nutrient diffusion and transport [19, 72, 73]. The fibrillar nanostructure of our photomolded GelMA-CMCMA hydrogels was observed using SEM (figures 3(l) and (m)). The images showed an interconnected porous network that allows the diffusion of growth factors

and other biological substances through the hydrogel. Conversely, PEGDA hydrogel analysis in SEM microscopy revealed that it is formed by a dense non-porous matrix (figures 3(n) and (o)). This characteristic structure in the PEGDA layer helps to avoid cell growth and improves the adhesion and attachment of the GelMA-CMCMA scaffold. Altogether, the physical properties of GelMA-CMCMA hydrogel scaffolds are appropriate for supporting long-term cell culture of skeletal muscle tissue.

3.3. 3D model of DM1 retains molecular features of the disease and provides a new structural phenotype for preclinical research

In this work, we fabricated 3D skeletal muscle tissue from human immortalized transdifferentiated myoblast-like cells that present molecular and phenotypical features of DM1. By evaluating 2D cell cultures, Arandel *et al* confirmed that patient-derived cells present nuclear RNA aggregates (foci) of expanded CUG repeats, a hallmark feature of DM1. They also showed that DM1 cells had a reduced fusion capability and formed smaller myotubes compared to healthy controls in 2D [48]. To validate the use of this cell line for our bioengineered DM1 model, we analyzed if nuclear RNA aggregates were also observed in 3D. By performing FISH and immunofluorescence analyses, we demonstrated the presence of CUG^{exp}-RNA foci and their colocalization with MBNL1 (figure 4), confirming that these cells retain DM1-associated molecular characteristics and are suitable for generating *in vitro* 3D models for the disease.

To evaluate fusion capability in 3D, we assessed confocal images of 2D cultures and bioengineered microtissues from both control and DM1 myotubes. After seven days in differentiation conditions, we performed immunofluorescence stainings for myosin heavy chain 7, SAA, and nuclei (figures 5(a)–(p)). Then, we used confocal images to calculate the fusion index, which is an indicator of differentiation quality in skeletal muscle cell cultures [74]. As expected, DM1 myoblasts in 2D culture had a significantly lower fusion index than healthy controls. Unexpectedly, when cells were encapsulated in 3D GelMA-CMCMA hydrogels, there were no differences in differentiation between healthy controls and DM1 cells, obtaining high fusion index values for both cases (figure 5(q)). Remarkably, 3D micropatterning resulted in the formation of long, multinucleated myotubes from DM1 patient-derived cells after seven days of culture, which is not possible to generate in standard cell cultures.

Although the fusion index of 3D DM1 myotubes was comparable to healthy myotubes, we observed structural differences, which prompted us to analyze the myotube diameter. Bioengineered skeletal muscle microtissues were differentiated for 7, 14, or 21 days before immunostaining for confocal imaging.

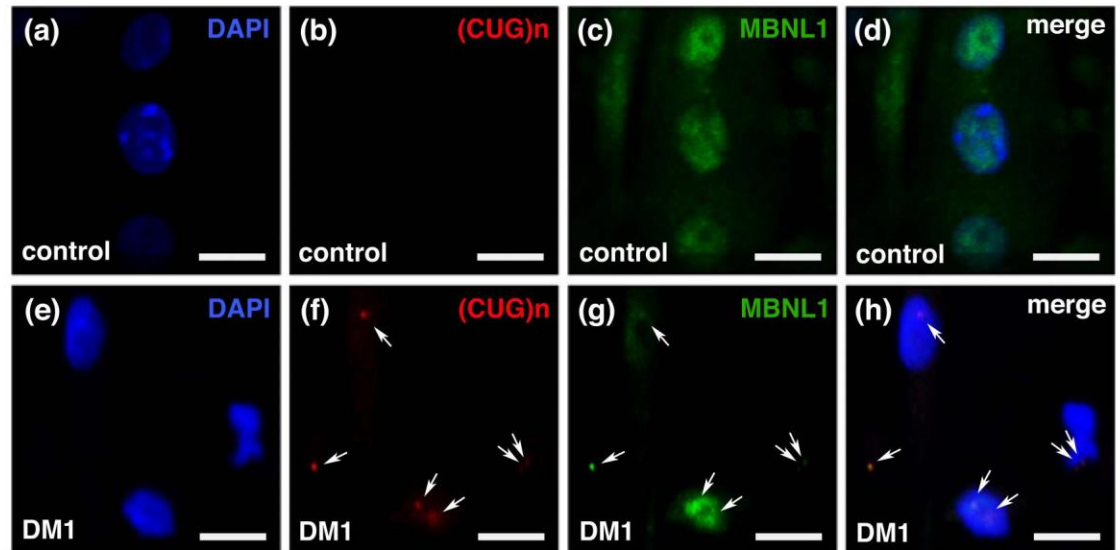


Figure 4. Encapsulated DM1 cells present disease-associated molecular phenotypes. Representative confocal images of (a)–(d) control and (e)–(h) DM1 immortalized transdifferentiated myoblast-like cells encapsulated in GelMA-CMCMA hydrogels. (a), (e) Nuclei were stained with DAPI (blue). (b), (f) Nuclear RNA aggregates of expanded-CUG repeats (white arrows) were only present in DM1 cells and detected by FISH using a Cy3-(CAG)₇-Cy3 probe (red). (c), (g) MBNL1 stainings (green) showing a reduced expression of MBNL1 in DM1 cells compared to controls. (d), (h) Merged images showing colocalization of MBNL1 with nuclear CUGexp-RNA aggregates in DM1 transdifferentiated myoblast-like cells (Scale bars: 10 μm).

Then, the 3D reconstructions of myotubes expressing SAA (figures 6(a)–(f)) were used to measure the individual diameter of control and DM1 myotubes over time. Several works have quantified myotube diameter in 2D for different purposes; for example, to characterize patient cells [75], test different culture conditions [76], evaluate the influence of topography in differentiation [77], or to study the effect of administering a given compound to myotubes [78]. Myotube diameter has also been measured in 3D cultures; for instance, Khodabukus *et al* compared myotube cross-sections to analyze the maturation of electrically stimulated constructs [79]. Measurements in all these cases were carried out manually, using tools from ImageJ software. In contrast, our measurements were obtained by a 3D reconstruction using Imaris software (figure 6(g)). With this reconstruction, each myotube diameter was automatically obtained with surface analysis tools. We found that 3D DM1 myotubes have a reduced diameter compared to healthy control myotubes (13.4 vs. 21.7 μm) after the first week of 3D culture (figure 6(h)). After two weeks of culture, both types of myotubes increased in size, but DM1 myotubes continue to show a reduced diameter compared to control myotubes. On the contrary, after three weeks of culture, we did not detect differences between the size of 3D myotubes. Nevertheless, this observation might not be due to a DM1 phenotype, but the healthy myotubes have a reduced size after three weeks as a potential senescence of the cultures. For this reason, assays with these 3D muscle models should be performed in myotubes cultured for less than three weeks.

Previous works in DM1 cell models have described deficient muscle differentiation. A reduced fusion potential has been observed in 2D studies with myoblasts from transgenic mice [80] and myogenic satellite cells from DM1 patients [81]. As an indicator of muscle differentiation, the fusion index has been used to investigate some aspects of DM1 molecular pathology [82, 83]. It has also been applied to compare DM1 vs. control cells while establishing cell lines [48] and test if proposed treatments could restore muscle differentiation [84]. Notably, we demonstrated that 3D micropatterning improves the differentiation of DM1 cells, obtaining fusion index values that are similar to healthy controls. Thus, this indicator cannot be applied to evaluate phenotype rescue by a given therapy. Instead, we found a significant difference in the diameter of 3D myotubes from DM1 and control cells. DM1 usually presents in adulthood, when tissue is already formed. Therefore, from a drug development perspective, the reduced myotube diameter in 3D is a more physiologically relevant phenotype than impaired fusion in 2D cultures. Considering these results, we propose that this new structural phenotype would be a better indicator to assess the effects of DM1 therapies in preclinical research.

3.4. AntagomiR treatments rescue bioengineered 3D DM1 muscle phenotypes

Antisense oligonucleotides for specific blocking of miR-23b (antagomiRs) have already shown efficacy to increase MBNL protein levels in 2D DM1 myoblasts [46] as well as to rescue molecular pathology, splicing events, and functional phenotypes in a mouse

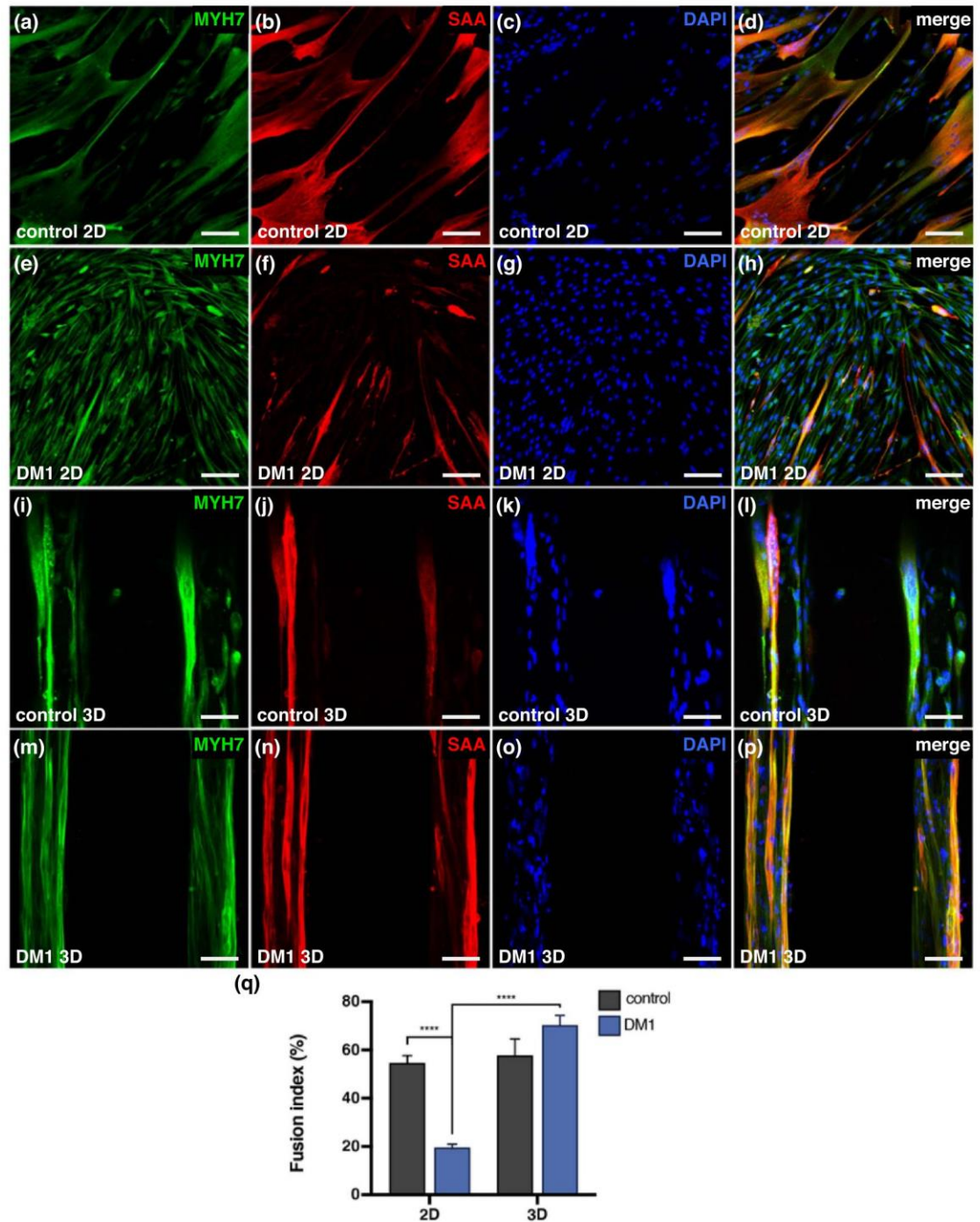


Figure 5. Cell differentiation is improved in 3D cultures. (a)–(p) Representative confocal images of 2D (a)–(h) and 3D (i)–(p) cultures stained for myosin heavy chain 7 (MYH7, green), sarcomeric α -actinin (SAA, red), and nuclei (DAPI, blue) after seven days in differentiation conditions (scale bars: 50 μ m). (q) Graph showing comparison of fusion index expressed as the percentage of differentiated myotubes with respect to the total cell number. **** $p < 0.0001$.

model [46, 47]. To demonstrate the application of our bioengineered *in vitro* model of DM1 in preclinical research, we evaluated the effect of this antagonomiR in our 3D cell cultures.

AntagonomiR against miR-23b (α -miR-23b) or a scrambled control (sc-control) antagonomiR were administered to bioengineered DM1 microtissues by gymnotic delivery at a concentration of 100 nM. Of note, cells were already orientated along the micropatterns and transdifferentiated into

myoblast-like cells at the moment of antagonomiRs administration. The treatment lasted for seven days. To determine the success of the treatment, we analyzed the expression levels of miR-23b by real-time PCR (figure 7(a)). We observed a reduction of miR-23b expression in DM1 3D muscles treated with α -miR-23b compared to the DM1 3D muscles treated with sc-control antagonomiR. Next, we investigated if silencing miR-23b enhanced MBNL transcripts in the bioengineered 3D microtissues. We found an

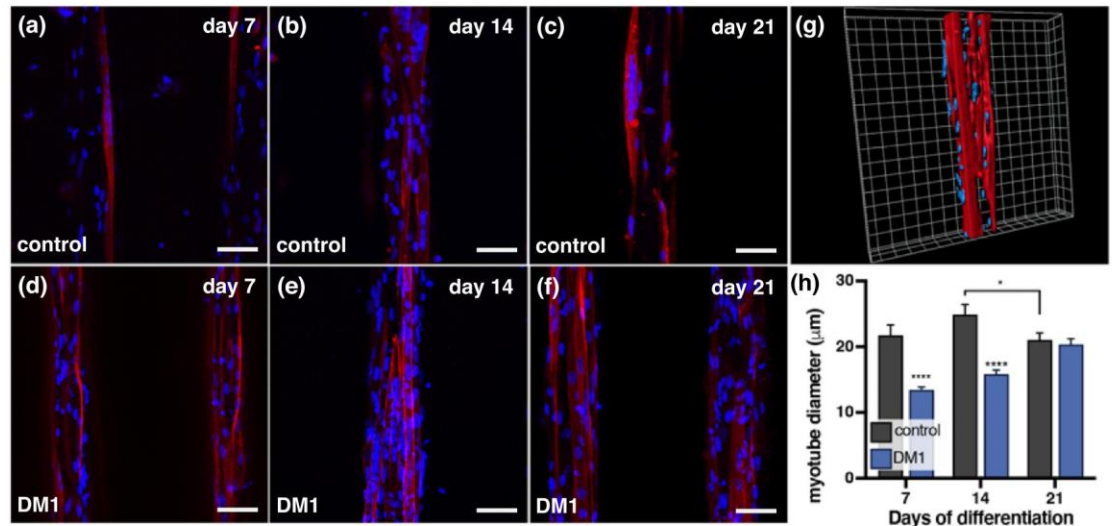


Figure 6. 3D DM1 myotubes have a reduced myotube diameter. (a)–(f) Representative confocal images of bioengineered 3D human skeletal muscle microtissues from healthy control (a)–(c) and DM1 (d)–(f) cells cultured for up to 21 days (Scale bars: 50 μm). Myotubes expressing SAA were stained in red and nuclei were counterstained with DAPI (blue). The 3D reconstruction of DM1 microtissues (g) was used to measure the individual diameter of myotubes over culture time (h). * $p < 0.05$ and **** $p < 0.0001$.

increase in MBNL2 transcripts in 3D DM1 myotubes treated with α -miR-23b compared to sc-control-treated tissues. However, MBNL1 was not increased at the transcriptional level (figure 7(b)). Of note, western blot quantification showed an increase in both MBNL1-2 proteins in bioengineered microtissues treated with α -miR-23b (figures 7(c) and (d)). To determine if the increase of MBNL proteins rescue characteristic DM1 spliceopathy, we analyzed the exon inclusion (Percentage Spliced In; PSI) of two MBNL1-dependent splicing events: *BIN1* and *NFIX*; and one MBNL2-dependent splicing event: *SPTAN1*. Remarkably, the exon inclusion was significantly rescued for the three splicing events (figures 7(e) and (f)). These rescue levels are lower than those obtained by transfection of antagomiRs in 2D myoblasts in previous studies [46]. This can be explained by the different delivery strategies used. Gene silencing by oligonucleotides usually requires a delivery vehicle to perform cell transfection. This requirement comes with several challenges that can complicate the development of oligonucleotide therapies [85]. As an alternative, gymnotic delivery ('naked' delivery of oligonucleotides to cells) has been promising in recent years. With this delivery approach, cells in culture are exposed to a constant concentration of oligonucleotides, similar to what happens *in vivo* when plasma and tissues are exposed to saline-formulated oligonucleotides. Transfection strategy allows the internalization of large amounts of oligonucleotides. Nevertheless, gymnotic delivery remains a more physiologically relevant delivery approach, and its effects can be improved by dosage optimization in future assays.

Finally, to assess the effect of antagomiRs on the DM1 3D structural phenotype, we measured the diameter of 3D myotubes treated with α -miR-23b and compared them to sc-control-treated myotubes (figure 7(g)). After seven days of treatment, we found that sc-control-treated microtissues had a mean myotube diameter of 14.4 μm , similar to DM1 myotubes without any treatment. Remarkably, upon treatment with α -miR-23b, myotubes reached a mean diameter of 21.9 μm (figure 7(h)), comparable to the diameter of myotubes from healthy control cells (figure 6(h)). Altogether, these results highlight the application of our bioengineered *in vitro* 3D model to assess DM1 therapies. Other anti-sense oligonucleotides and other potential therapies like small molecules or peptides can be tested on this platform. Furthermore, drug effects can be analyzed at different levels, including transcriptional, post-transcriptional, and structural phenotype changes.

4. Conclusions

In this work, we described a detailed protocol for fabricating 3D skeletal muscle microtissues that can be maintained in long-lasting cultures. This micro-molding technique is cheap and can be easily reproduced. Importantly, cell encapsulation in GelMA-CMCMA micropatterned hydrogels produce highly aligned multinucleated myotubes. Using this protocol, we generated for the first time a bioengineered human 3D skeletal muscle model for myotonic dystrophy. Remarkably, this protocol can be applied to cells from patients for different muscle diseases

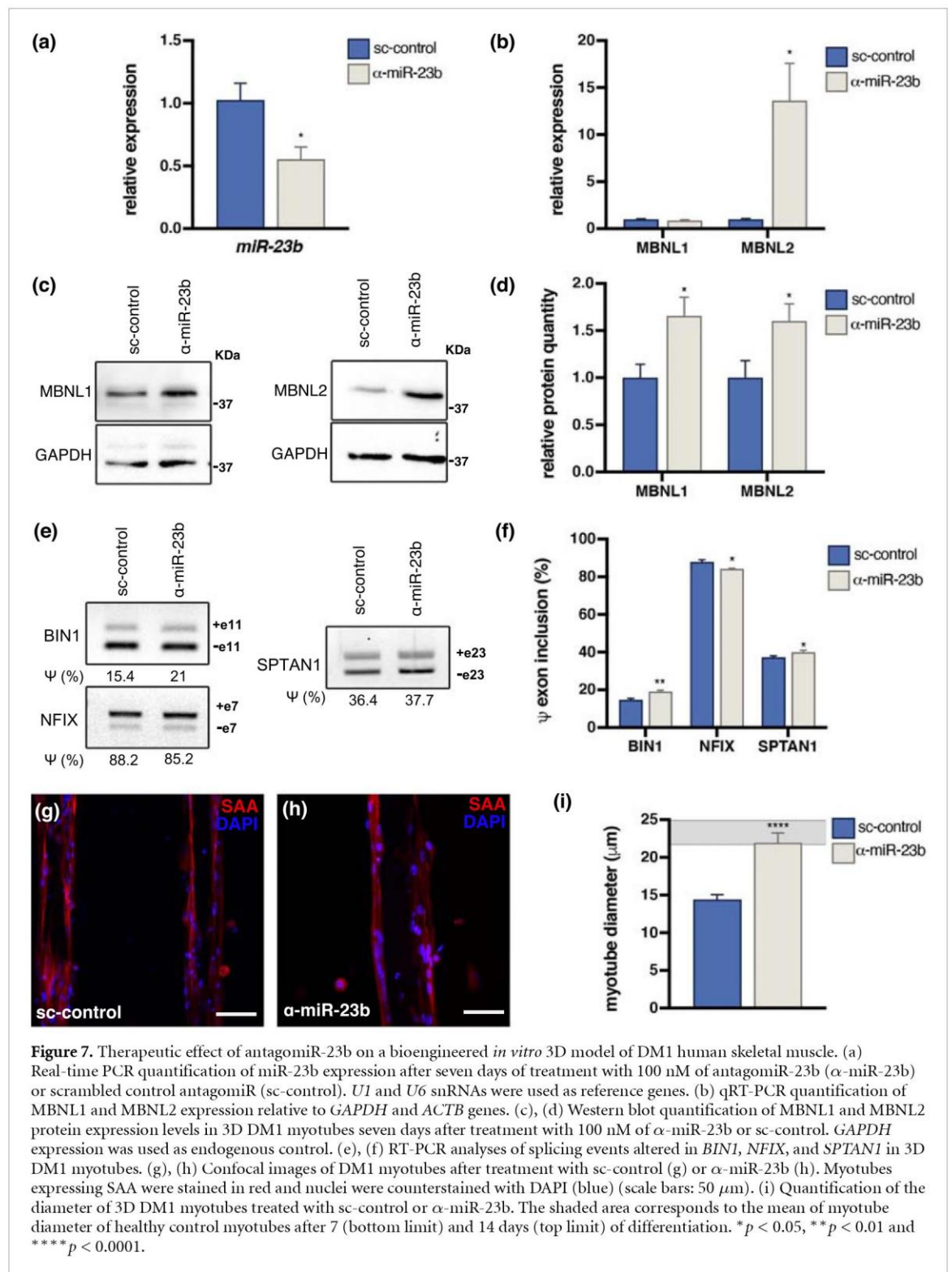


Figure 7. Therapeutic effect of antagomiR-23b on a bioengineered *in vitro* 3D model of DM1 human skeletal muscle. (a) Real-time PCR quantification of miR-23b expression after seven days of treatment with 100 nM of antagomiR-23b (α -miR-23b) or scrambled control antagomiR (sc-control). *U1* and *U6* snRNAs were used as reference genes. (b) qRT-PCR quantification of MBNL1 and MBNL2 expression relative to *GAPDH* and *ACTB* genes. (c), (d) Western blot quantification of MBNL1 and MBNL2 protein expression levels in 3D DM1 myotubes seven days after treatment with 100 nM of α -miR-23b or sc-control. *GAPDH* expression was used as endogenous control. (e), (f) RT-PCR analyses of splicing events altered in *BIN1*, *NFIX*, and *SPTAN1* in 3D DM1 myotubes. (g), (h) Confocal images of DM1 myotubes after treatment with sc-control (g) or α -miR-23b (h). Myotubes expressing SAA were stained in red and nuclei were counterstained with DAPI (blue) (scale bars: 50 μ m). (i) Quantification of the diameter of 3D DM1 myotubes treated with sc-control or α -miR-23b. The shaded area corresponds to the mean of myotube diameter of healthy control myotubes after 7 (bottom limit) and 14 days (top limit) of differentiation. * $p < 0.05$, ** $p < 0.01$ and **** $p < 0.0001$.

(i.e. other muscular dystrophies) to obtain patient-specific models. DM1 patient-derived cells encapsulated in GelMA-CMCMA hydrogels present DM1 molecular characteristics and correctly differentiated into multinucleated myotubes. A reduced fusion index, an indicator of muscle differentiation, is a typical feature of DM1 standard 2D cultures. Notably, the fusion index is restored to control values in DM1 3D myotubes. However, DM1 3D

microtissues display a new structural phenotype; the 3D diameter of myotubes is significantly thinner than control myotubes. Therefore, this more physiological phenotype of the bioengineered 3D DM1 myotubes can be used for drug screening studies of DM1. To evaluate the applicability of this *in vitro* model in evaluating therapeutic compounds, we treated the bioengineered 3D microtissues with anti-sense oligonucleotides against miR-23b. Our findings

indicated that antagomiRs for miR-23b are able to rescue molecular and structural phenotypes of DM1 disease when administrated to bioengineered 3D muscle. Overall, we demonstrated that our patient-derived 3D model is a relevant alternative to the existing *in vitro* and animal models. These bioengineered 3D skeletal muscle microtissues could be useful in a preclinical platform for DM1 drug development.

Data availability statement

All data that support the findings of this study are included within the article (and any supplementary files).

Acknowledgments

The authors thank the technical support of Judith Linacero, from the Microscopy and MicroFab-Space Characterization Facilities (IBEC), for her advice and for performing SEM imaging. This project received financial support from the European Research Council program under Grants ERC-StG-DAMOC (714317), the Spanish Ministry of Economy and Competitiveness, through the ‘Severo Ochoa’ Program for Centres of Excellence in R&D (SEV-2016-2019) and ‘Retos de investigación: Proyectos I+D+i’ (TEC2017-83716-C2-1-R and TEC2017-83716-C2-2-R), the CERCA Programme/Generalitat de Catalunya (2014-SGR-1460) and Fundació Bancaria ‘la Caixa’—Obra Social ‘la Caixa’ (project IBEC-La Caixa Healthy Ageing) to J R-A.

X F-G was supported by a predoctoral fellowship (BES-2016-076681) from the Ministerio de Economía y Competitividad. J M F-C was awarded with postdoctoral fellowship (APOSTD/2017/088) from the Generalitat Valenciana. E C-H was awarded with postdoctoral fellowship (APOSTD/2019/142) from the Generalitat Valenciana. Additional support was received from the Generalitat Valenciana (PROMETEO/2020/081) to R A. Cells used in this study were kindly provided by Dr Denis Furling and Dr Vincent Mouly (Institute of Myology, Paris). Antibody MB1a (4A8) and antibody MB2a (3B4) was provided by MDA Monoclonal Antibody Resources.


Author contributions

X F-G, J M F-C, R A, and J R-A conceived this work. X F-G and J M F-C performed and coordinated the experiments and data analysis. M A O designed and fabricated the micropatterned silicon molds, E C-H did the molecular validation of antagomiR treatments, J C and E M performed the AFM measurements and data analysis. J R-A, R A and E M acquired the funding for this project. X F-G and J M F-C prepared the manuscript with the supervision of J R-A and input from all the authors.

Ethical statement

The authors declared no potential conflicts of interest with respect to the research, authorship, and/or publication of this article.

ORCID iDs

Xiomara Fernández-Garibay 

<https://orcid.org/0000-0002-0697-985X>

Elena Martínez  <https://orcid.org/0000-0002-6585-4213>

Juan M Fernández-Costa  <https://orcid.org/0000-0002-1854-6082>

Javier Ramón-Azcón  <https://orcid.org/0000-0002-3636-8013>

References

- [1] Csapo R, Gumpenberger M and Wessner B 2020 Skeletal muscle extracellular matrix—what do we know about its composition, regulation, and physiological roles? A narrative review *Front. Physiol.* **11** 1–15
- [2] Meriggioli M N and Sanders D B 2009 Autoimmune myasthenia gravis: emerging clinical and biological heterogeneity *Lancet Neurol.* **8** 475–90
- [3] Kaczor J J, Robertshaw H A and Tarnopolsky M A 2017 Higher oxidative stress in skeletal muscle of McArdle disease patients *Mol. Genet. Metab. Rep.* **12** 69–75
- [4] DeFronzo R A and Tripathy D 2009 Skeletal muscle insulin resistance is the primary defect in type 2 diabetes *Diabetes Care* **32** S157–63
- [5] Corcoran M P, Lamon-Fava S and Fielding R A 2007 Skeletal muscle lipid deposition and insulin resistance: effect of dietary fatty acids and exercise *Am. J. Clin. Nutr.* **85** 662–77
- [6] Mercuri E, Bönnemann C G and Muntoni F 2019 Muscular dystrophies *Lancet* **394** 2025–38
- [7] Benarroch L, Bonne G, Rivier F and Hamroun D 2019 The 2020 version of the gene table of neuromuscular disorders (nuclear genome) *Neuromuscul. Disord.* **29** 980–1018
- [8] Carter J C, Sheehan D W, Prochoroff A and Birnkrant D J 2018 Muscular dystrophies *Clin. Chest Med.* **39** 377–89
- [9] Bersini S, Arrigoni C, Lopa S, Bongio M, Martin I and Moretti M 2016 Engineered miniaturized models of musculoskeletal diseases *Drug Discov. Today* **21** 1429–36
- [10] Khodabukus A and Baar K 2016 Factors that affect tissue-engineered skeletal muscle function and physiology *Cells Tissues Organs* **202** 159–68
- [11] Taylor M J, Tanna S and Sahota T 2010 *In vivo* study of a polymeric glucose-sensitive insulin delivery system using a rat model *J. Pharm. Sci.* **99** 4215–27
- [12] DiMasi J A, Grabowski H G and Hansen R W 2016 Innovation in the pharmaceutical industry: new estimates of R&D costs *J. Health Econ.* **47** 20–33
- [13] Dowden H and Munro J 2019 Trends in clinical success rates and therapeutic focus *Nat. Rev. Drug Discov.* **18** 495–6
- [14] Moyle L A, Jacques E and Gilbert P M 2020 Engineering the next generation of human skeletal muscle models: from cellular complexity to disease modeling *Curr. Opin. Biomed. Eng.* **16** 9–18
- [15] Chal J and Pourquié O 2017 Making muscle: skeletal myogenesis *in vivo* and *in vitro* *Development* **144** 2104–22
- [16] Smoak M M and Mikos A G 2020 Advances in biomaterials for skeletal muscle engineering and obstacles still to overcome *Mater. Today Bio* **7** 100069
- [17] Zhang Y S and Khademhosseini A 2017 Advances in engineering hydrogels *Science* **356** eaaf3627

- [18] Ahadian S *et al* 2015 Hybrid hydrogels containing vertically aligned carbon nanotubes with anisotropic electrical conductivity for muscle myofiber fabrication *Sci. Rep.* **4** 4271
- [19] García-Lizarribar A, Fernández-Garibay X, Velasco-Mallorquí F, Castaño A G, Samitier J and Ramon-Azcon J 2018 Composite biomaterials as long-lasting scaffolds for 3D bioprinting of highly aligned muscle tissue *Macromol. Biosci.* **18** 1800167
- [20] Ortega M A, Fernández-Garibay X, Castaño A G, De Chiara F, Hernández-Albors A, Balaguer-Trias J and Ramón-Azcón J 2019 Muscle-on-a-chip with an on-site multiplexed biosensing system for *in situ* monitoring of secreted IL-6 and TNF- α *Lab Chip* **19** 2568–80
- [21] Hutson C B, Nichol J W, Aubin H, Bae H, Yamanlar S, Al-Haque S, Koshy S T and Khademhosseini A 2011 Synthesis and characterization of tunable poly(ethylene glycol): gelatin methacrylate composite hydrogels *Tissue Eng. A* **17** 1713–23
- [22] Ozimki L, Sabater-Arcis M, Bargiela A and Artero R 2020 The hallmarks of myotonic dystrophy type 1 muscle dysfunction *Biol. Rev.* **96** 716–30
- [23] Udd B and Krahe R 2012 The myotonic dystrophies: molecular, clinical, and therapeutic challenges *Lancet Neurol.* **11** 891–905
- [24] Wang E T *et al* 2019 Transcriptome alterations in myotonic dystrophy skeletal muscle and heart *Hum. Mol. Genet.* **28** 1312–21
- [25] Ebraldize A 2004 RNA leaching of transcription factors disrupts transcription in myotonic dystrophy *Science* **303** 383–7
- [26] Jones K, Wei C, Iakova P, Bugiardini E, Schneider-Gold C, Meola G, Woodgett J, Killian J, Timchenko N A and Timchenko L T 2012 GSK3 β mediates muscle pathology in myotonic dystrophy *J. Clin. Invest.* **122** 4461–72
- [27] Rau F *et al* 2011 Misregulation of miR-1 processing is associated with heart defects in myotonic dystrophy *Nat. Struct. Mol. Biol.* **18** 840–5
- [28] Krol J, Fiszler A, Mykowska A, Sobczak K, De Mezer M and Krzyzosiak W J 2007 Ribonuclease dicer cleaves triplet repeat hairpins into shorter repeats that silence specific targets *Mol. Cell* **25** 575–86
- [29] Fernandez-Costa J M *et al* 2013 Expanded CTG repeats trigger miRNA alterations in *Drosophila* that are conserved in myotonic dystrophy type 1 patients *Hum. Mol. Genet.* **22** 704–16
- [30] Kalsotra A, Singh R K, Gurha P, Ward A J, Creighton C J and Cooper T A 2014 The Mef2 transcription network is disrupted in myotonic dystrophy heart tissue, dramatically altering miRNA and mRNA expression *Cell Rep.* **6** 336–45
- [31] Du H *et al* 2010 Aberrant alternative splicing and extracellular matrix gene expression in mouse models of myotonic dystrophy *Nat. Struct. Mol. Biol.* **17** 187–93
- [32] Charizanis K *et al* 2012 Muscleblind-like 2-mediated alternative splicing in the developing brain and dysregulation in myotonic dystrophy *Neuron* **75** 437–50
- [33] Goodwin M *et al* 2015 MBNL sequestration by toxic RNAs and RNA misprocessing in the myotonic dystrophy brain *Cell Rep.* **12** 1159–68
- [34] Batra R *et al* 2014 Loss of MBNL leads to disruption of developmentally regulated alternative polyadenylation in RNA-mediated disease *Mol. Cell* **56** 311–22
- [35] Fernandez-Costa J M, Llamusi M B, Garcia-Lopez A and Artero R 2011 Alternative splicing regulation by Muscleblind proteins: from development to disease *Biol. Rev.* **86** 947–58
- [36] Gomes-Pereira M, Cooper T A and Gourdon G 2011 Myotonic dystrophy mouse models: towards rational therapy development *Trends Mol. Med.* **17** 506–17
- [37] Cerro-Herreros E, Fernandez-Costa J M, Sabater-Arcis M, Llamusi B and Artero R 2016 Derepressing muscleblind expression by miRNA sponges ameliorates myotonic dystrophy-like phenotypes in *Drosophila* *Sci. Rep.* **6** 1–13
- [38] Bargiela A, Cerro-Herreros E, Fernandez-Costa J M, Vilchez J J, Llamusi B and Artero R 2015 Increased autophagy and apoptosis contribute to muscle atrophy in a myotonic dystrophy type 1 *Drosophila* model *DMM Dis. Model. Mech.* **8** 679–90
- [39] Garcia-Lopez A, Monferrer L, Garcia-Alcover I, Vicente-Crespo M, Alvarez-Abril M C and Artero R D 2008 Genetic and chemical modifiers of a CUG toxicity model in *Drosophila* *PLoS One* **3** e1595
- [40] Todd P K, Ackall F Y, Hur J, Sharma K, Paulson H L and Dowling J J 2014 Transcriptional changes and developmental abnormalities in a zebrafish model of myotonic dystrophy type 1 *DMM Dis. Model. Mech.* **7** 143–55
- [41] Chen G, Masuda A, Konishi H, Ohkawara B, Ito M, Kinoshita M, Kiyama H, Matsuura T and Ohno K 2016 Phenylbutazone induces expression of MBNL1 and suppresses formation of MBNL1-CUG RNA foci in a mouse model of myotonic dystrophy *Sci. Rep.* **6** 1–11
- [42] Konieczny P, Selma-Soriano E, Rapisarda A S, Fernandez-Costa J M, Perez-Alonso M and Artero R 2017 Myotonic dystrophy: candidate small molecule therapeutics *Drug Discov. Today* **22** 1740–8
- [43] Huang K, Masuda A, Chen G, Bushra S, Kamon M, Araki T, Kinoshita M, Ohkawara B, Ito M and Ohno K 2020 Inhibition of cyclooxygenase-1 by nonsteroidal anti-inflammatory drugs demethylates MeR2 enhancer and promotes Mbnl1 transcription in myogenic cells *Sci. Rep.* **10** 2558
- [44] Overby S J, Cerro-Herreros E, Llamusi B and Artero R 2018 RNA-mediated therapies in myotonic dystrophy *Drug Discov. Today* **23** 2013–22
- [45] López Castel A, Overby S J and Artero R 2019 MicroRNA-based therapeutic perspectives in myotonic dystrophy *Int. J. Mol. Sci.* **20** 5600
- [46] Cerro-Herreros E, Sabater-Arcis M, Fernandez-Costa J M, Moreno N, Perez-Alonso M, Llamusi B and Artero R 2018 miR-23b and miR-218 silencing increase Muscleblind-like expression and alleviate myotonic dystrophy phenotypes in mammalian models *Nat. Commun.* **9** 2482
- [47] Cerro-Herreros E, González-Martínez I, Moreno-Cervera N, Overby S, Pérez-Alonso M, Llamusi B and Artero R 2020 Therapeutic potential of AntagomiR-23b for treating myotonic dystrophy *Mol. Ther. Nucleic Acids* **21** 837–49
- [48] Arandel L *et al* 2017 Immortalized human myotonic dystrophy muscle cell lines to assess therapeutic compounds *Dis. Model. Mech.* **10** 487–97
- [49] Alcaraz J, Buscemi L, Grabulosa M, Trepax X, Fabry B, Farré R and Navajas D 2003 Microrheology of human lung epithelial cells measured by atomic force microscopy *Biophys. J.* **84** 2071–9
- [50] Comelles J, Fernández-Majada V, Berlanga-Navarro N, Acevedo V, Paszkowska K and Martínez E 2020 Microfabrication of poly(acrylamide) hydrogels with independently controlled topography and stiffness *Biofabrication* **12** 025023
- [51] Schindelin J *et al* 2012 Fiji: an open-source platform for biological-image analysis *Nat. Methods* **9** 676–82
- [52] Schneider C A, Rasband W S and Eliceiri K W 2012 NIH image to ImageJ: 25 years of image analysis *Nat. Methods* **9** 671–5
- [53] Peltier H J and Latham G J 2008 Normalization of microRNA expression levels in quantitative RT-PCR assays: identification of suitable reference RNA targets in normal and cancerous human solid tissues *RNA* **14** 844–52
- [54] Fernández-Costa J M, Fernández-Garibay X, Velasco-Mallorquí F and Ramón-Azcón J 2021 Bioengineered *in vitro* skeletal muscles as new tools for muscular dystrophies preclinical studies *J. Tissue Eng.* **12** 1–19
- [55] Aubin H, Nichol J W, Hutson C B, Bae H, Sieminski A L, Cropek D M, Akhyari P and Khademhosseini A 2010 Directed 3D cell alignment and elongation in microengineered hydrogels *Biomaterials* **31** 6941–51

- [56] Costantini M, Testa S, Fornetti E, Barbetta A, Trombetta M, Cannata S M, Gargioli C and Rainer A 2017 Engineering muscle networks in 3D gelatin methacryloyl hydrogels: influence of mechanical stiffness and geometrical confinement *Front. Bioeng. Biotechnol.* **5** 1–8
- [57] Kang H W, Lee S J, Ko I K, Kengla C, Yoo J J and Atala A 2016 A 3D bioprinting system to produce human-scale tissue constructs with structural integrity *Nat. Biotechnol.* **34** 312–9
- [58] Rouwkema J, Koopman B F J M, C A Van B, Dhert W J A and Malda J 2009 Supply of nutrients to cells in engineered tissues *Biotechnol. Genet. Eng. Rev.* **26** 163–78
- [59] Peter M and Tayalia P 2016 An alternative technique for patterning cells on poly(ethylene glycol) diacrylate hydrogels *RSC Adv.* **6** 40878–85
- [60] Nichol J W, Koshy S T, Bae H, Hwang C M, Yamanlar S and Khademhosseini A 2010 Cell-laden microengineered gelatin methacrylate hydrogels *Biomaterials* **31** 5536–44
- [61] Wong D Y, Ranganath T and Kasko A M 2015 Low-dose, long-wave UV light does not affect gene expression of human mesenchymal stem cells *PLoS One* **10** 1–21
- [62] Fairbanks B D, Schwartz M P, Bowman C N and Anseth K S 2009 Photoinitiated polymerization of PEG-diacrylate with lithium phenyl-2,4,6-trimethylbenzoylphosphine: polymerization rate and cytocompatibility *Biomaterials* **30** 6702–7
- [63] Ouyang L, Highley C B, Sun W and Burdick J A 2017 A generalizable strategy for the 3D bioprinting of hydrogels from nonviscous photo-crosslinkable inks *Adv. Mater.* **29** 1604983
- [64] Boere K W M, Visser J, Seyednejad H, Rahimian S, Gawlitta D, Van Steenberg M J, Dhert W J A, Hennink W E, Vermonden T and Malda J 2014 Covalent attachment of a three-dimensionally printed thermoplastic to a gelatin hydrogel for mechanically enhanced cartilage constructs *Acta Biomater.* **10** 2602–11
- [65] Wang J, Khodabukus A, Rao L, Vandusen K, Abutaleb N and Bursac N 2019 Engineered skeletal muscles for disease modeling and drug discovery *Biomaterials* **221** 119416
- [66] Bigot A, Klein A F, Gasnier E, Jacquemin V, Ravassard P, Butler-Browne G, Mouly V and Furling D 2009 Large CTG repeats trigger p16-dependent premature senescence in myotonic dystrophy type 1 muscle precursor cells *Am. J. Pathol.* **174** 1435–42
- [67] Reeves R, Ribeiro A, Lombardo L, Boyer R and Leach J B 2010 Synthesis and characterization of carboxymethylcellulose-methacrylate hydrogel cell scaffolds *Polymers* **2** 252–64
- [68] Hernández-Albors A, Castaño A G, Fernández-Garibay X, Ortega M A, Balaguer J and Ramón-Azcón J 2019 Microphysiological sensing platform for an *in-situ* detection of tissue-secreted cytokines *Biosens. Bioelectron.* **2** 100025
- [69] Engler A J, Griffin M A, Sen S, Bönnemann C G, Sweeney H L and Discher D E 2004 Myotubes differentiate optimally on substrates with tissue-like stiffness *J. Cell Biol.* **166** 877–87
- [70] Gilbert P M, Havenstrite K L, Magnusson K E G, Sacco A, Leonardi N A, Kraft P, Nguyen N K, Thrun S, Lutolf M P and Blau H M 2010 Substrate elasticity regulates skeletal muscle stem cell self-renewal in culture *Science* **329** 1078–81
- [71] Chiron S, Tomczak C, Duperray A, Lainé J, Bonne G, Eder A, Hansen A, Eschenhagen T, Verdier C and Coirault C 2012 Complex interactions between human myoblasts and the surrounding 3D fibrin-based matrix *PLoS One* **7** 2–9
- [72] Van Vlierberghe S, Cnudde V, Dubruel P, Masschaele B, Cosijns A, De Paepe I, Jacobs P J S, Van Hoorebeke L, Remon J P and Schacht E 2007 Porous gelatin hydrogels: 1. cryogenic formation and structure analysis *Biomacromolecules* **8** 331–7
- [73] Miri A K, Hosseinabadi H G, Cecen B, Hassan S and Zhang Y S 2018 Permeability mapping of gelatin methacryloyl hydrogels *Acta Biomater.* **77** 38–47
- [74] Monge C, Ren K, Berton K, Guillot R, Peyrade D and Picart C 2012 Engineering muscle tissues on microstructured polyelectrolyte multilayer films *Tissue Eng. A* **18** 1664–76
- [75] Pomiès P, Rodriguez J, Blaquièrre M, Sedraoui S, Gouzi F, Carnac G, Laoudj-Chenivesse D, Mercier J, Préfaut C and Hayot M 2015 Reduced myotube diameter, atrophic signalling and elevated oxidative stress in cultured satellite cells from COPD patients *J. Cell. Mol. Med.* **19** 175–86
- [76] Archer-Lahlou E, Lan C and Jagoe R T 2018 Physiological culture conditions alter myotube morphology and responses to atrophy treatments: implications for *in vitro* research on muscle wasting *Physiol. Rep.* **6** e13726
- [77] Almonacid Suarez A M, Zhou Q, Rijn P and Harmsen M C 2019 Directional topography gradients drive optimum alignment and differentiation of human myoblasts *J. Tissue Eng. Regen. Med.* **13** 2234–45
- [78] Ohno Y, Oyama A, Kaneko H, Egawa T, Yokoyama S, Sugiura T, Ohira Y, Yoshioka T and Goto K 2018 Lactate increases myotube diameter via activation of MEK/ERK pathway in C2C12 cells *Acta Physiol.* **223** e13042
- [79] Khodabukus A, Madden L, Prabhu N K, Kovacs T R, Jackman C P, Muoio D M and Bursac N 2019 Electrical stimulation increases hypertrophy and metabolic flux in tissue-engineered human skeletal muscle *Biomaterials* **198** 259–69
- [80] Timchenko N A, Patel R, Iakova P, Cai Z J, Quan L and Timchenko L T 2004 Overexpression of CUG triplet repeat-binding protein, CUGBP1, in mice inhibits myogenesis *J. Biol. Chem.* **279** 13129–39
- [81] Furling D, Lemieux D, Taneja K and Puymirat J 2001 Decreased levels of myotonic dystrophy protein kinase (DMPK) and delayed differentiation in human myotonic dystrophy myoblasts *Neuromuscul. Disord.* **11** 728–35
- [82] Peng X, Shen X, Chen X, Liang R, Azares A R and Liu Y 2015 Celf1 regulates cell cycle and is partially responsible for defective myoblast differentiation in myotonic dystrophy RNA toxicity *Biochim. Biophys. Acta* **1852** 1490–7
- [83] Beaulieu D, Thebault P, Pelletier R, Chapdelaine P, Tarnopolsky M, Furling D and Puymirat J 2012 Abnormal prostaglandin E2 production blocks myogenic differentiation in myotonic dystrophy *Neurobiol. Dis.* **45** 122–9
- [84] François V, Klein A F, Beley C, Jollet A, Lemerrier C, Garcia L and Furling D 2011 Selective silencing of mutated mRNAs in DM1 by using modified hU7-siRNAs *Nat. Struct. Mol. Biol.* **18** 85–7
- [85] Soifer H S, Koch T, Lai J, Hansen B, Hoeg A, Oerum H and Stein C A 2012 Silencing of gene expression by gymnotic delivery of antisense oligonucleotides *Functional Genomics: Methods in Molecular Biology (Methods and Protocols vol 815)* ed M Kaufmann and C Klinger (New York: Springer) pp 333–46

Appendix B. OTHER PUBLICATIONS



Microphysiological sensing platform for an in-situ detection of tissue-secreted cytokines



Alejandro Hernández-Albors¹, Albert G. Castaño¹, Xiomara Fernández-Garibay, María Alejandra Ortega, Jordina Balaguer, Javier Ramón-Azcón*

Institute for Bioengineering of Catalonia (IBEC), The Barcelona Institute of Science and Technology, Baldori Reixac 10-12, 08028, Barcelona, Spain

ARTICLE INFO

Keywords:

Microphysiological tissues
Tissue engineering
Electrochemical, biosensors
Magnetic particles
Skeletal muscle
Electric stimulation

ABSTRACT

Understanding the protein-secretion dynamics from single, specific tissues is critical toward the advancement of disease detection and treatments. However, such secretion dynamics remain difficult to measure *in vivo* due to the uncontrolled contributions from other tissue populations. Here, we describe an integrated platform designed for the reliable, near real-time measurements of cytokines secreted from an *in vitro* single-tissue model. In our setup, we grow 3D biomimetic tissues to discretize cytokine source, and we separate them from a magnetic microbead-based biosensing system using a Transwell insert. This design integrates physiochemically controlled biological activity, high-sensitivity protein detection ($\text{LOD} < 20 \text{ pg mL}^{-1}$), and rapid protein diffusion to enable non-invasive, near real-time measurements. To showcase the specificity and sensitivity of the system, we use our setup to probe the inflammatory process related to the protein Interleukine 6 (IL-6) and to the Tumor Necrosis Factor (TNF- α). We show that our setup can monitor the time-dependence profile of IL-6 and TNF- α secretion that results from the electrical and chemical stimulation of 3D skeletal muscle tissues. We demonstrate a novel and affordable methodology for discretizing the secretion kinetics of specific tissues for advancing metabolic-disorder studies and drug-screening applications.

1. Introduction

Detecting changes in protein secretion with spatiotemporal accuracy remains a fundamental challenge toward understanding the role of proteins in regulating biological processes. For instance, to understand its role in immune and inflammatory responses, (Rothenberg, 2007) protein expressions of cytokine are routinely studied from blood serums using methods such as RNA sequencing, protein microarrays, enzyme-linked immunosorbent assay (ELISA) or mass spectroscopy (MS) (Mukherjee and Mani, 2013). However, because most *in vivo* tissues of interest are composed of a variety of cells, profiling cytokine expressions by specific cells directly from bulk serum samples remains impractical.

Recent studies approach this challenge in two ways, focusing either on maximizing detection sensitivity, or on tailoring the ideal functional-tissue models. The first approach targets real-time analysis and quantification of secreted cytokines using ultrasensitive detection method or imaged-based high-resolution spatiotemporal techniques (Shirasaki et al., 2015; Juan-Colás et al., 2018; Saxena et al., 2018). Here however,

because the techniques involved rely on single-cell secretion, this approach cannot probe cytokine secretion by functional tissues.

The second approach tailors specific, desired functional tissue samples that can be probed by established techniques such as ELISA or MS. Using this approach, cytokine secretions have been analyzed from *in vivo* muscles, *in vitro* contractile myofiber sheets, (Furrer et al., 2017; Takahashi et al., 2018) or even adipose and immune cells co-cultures without unwanted interactions from unknown cells (Kongsuphol et al., 2019). However, because techniques such as ELISA and MS lack temporal resolution, this approach cannot profile cytokine secretion at timescales relevant to biological processes (Zhang et al., 2017; Bruls et al., 2009; Esteban-Fernández de Ávila et al., 2013; Skardal et al., 2017). Here we present an integrated platform designed for reliable, near real-time profiling of cytokine secretions by combining the advantages of both aforementioned approaches: we maximize both the chemical and the time resolution of our detection system, and we tailor tissue samples that are ideal for our measurement. Fig. 1 illustrates our integration concept, which grows the desired 3D skeletal muscle (SM, blue oblongs) sample tissues on the top surface of

* Corresponding author.

E-mail address: jramon@ibecbarcelona.eu (J. Ramón-Azcón).

¹ Both authors have contributed equally in the work.

<https://doi.org/10.1016/j.biosx.2019.100025>

Received 22 May 2019; Received in revised form 8 July 2019; Accepted 25 July 2019

Available online 06 August 2019

2590-1370/© 2019 The Author(s). Published by Elsevier B.V. This is an open access article under the CC BY-NC-ND license (<http://creativecommons.org/licenses/by-nc-nd/4.0/>).

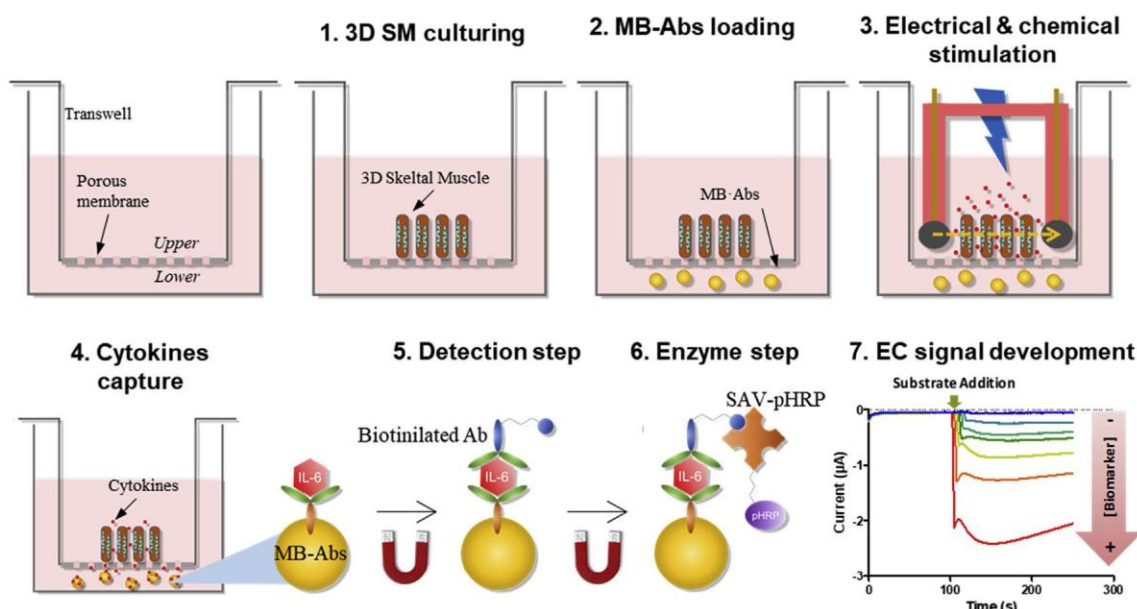


Fig. 1. Schematic illustration of the immunosensor measurement procedure. Firstly, 3D SM is fabricated on the Transwell membrane, then MB-Abs are loaded in the lower compartment. Secreted cytokines, under the chemical and electrical effect, are captured by the MB-Abs. Detection step is followed by the addition of a biotinylated antibody and SAV-pHRP. Finally, MB-Abs are resuspended in enzymatic buffer and captured on the surface of the SPCEs. After addition of the corresponding substrate, EC signal is obtained. The intensity of the current is directly related with the concentration of secreted cytokines.

the porous membrane (dashed lines) of a Transwell insert, in proximity of antibody-bioconjugated magnetic microbead (MB-abs) detectors, located underneath the membrane. Upon electrical and chemical stimulation applied to the SM in the Transwell insert, any secreted cytokine would rapidly diffuse through the porous membrane to be captured by the nearby microbeads. This concept enables our custom-grown in vitro 3D SM tissues (Ortega et al., 1039) to provide the ideal sample for our measurements, while exploiting the magnetic beads' high area to volume ratio and its proximity to the sample maximize chemical and temporal resolutions (20 and 10 pg mL^{-1} , near real-time, respectively).

In this article, we test the validity of our concept by profiling inflammatory process related cytokines: Interleukine 6 (IL-6) and Tumor Necrosis Factor (TNF- α), induced by chemical and electrical stimulation of 3D engineered skeletal muscle tissues. We demonstrate that our integrated system represents a simple and feasible tool profiling the secretion kinetics of specific proteins from specific in vitro tissue models. Our results provide a new strategy toward understanding the role of proteins in both diseased and healthy states and in drug-screening assays.

2. Experimental section

2.1. Materials

Electrochemical measurements were carried out using a Portable multipotentiostat μ STAT 8000P (Metrohm Dropsense AG Herisau, Switzerland). Screen-printed carbon electrodes (SPCEs), were integrated by a Ag/AgCl pseudo-reference electrode and a carbon counter electrode (DRP-8X110, 2.56 mm \varnothing) originally used as working electrodes (Metrohm Dropsense AG Herisau, Switzerland). Round bottom non-treated plates were purchased from Nirco (Barberà del Vallés, Spain). Polystyrene MaxiSorp microtiter plates used to perform ELISA assays were purchased from Nunc (Roskilde, Denmark). Washing steps were carried out using a 405 TS microplate washer (BioTeck Instruments, Winooski, USA). The electrochemical data obtained was analyzed using DropView 8400 software (Metrohm Dropsense AG Herisau, Switzerland). Absorbances were read on Infinite[®] 200 PRO multiplate reader (TEKAN, Männedorf, Switzerland). Digital light

processing (DLP) projector-based stereo-lithography 3D printer (Solus DLP model, Reify3D, CA, USA) was used to fabricate the device for the electrical stimulation. Crosslinking of composite hydrogel were performed by a UVP Crosslinker (CL-1000, Analytik Jena, Germany). Assessment of electrical stimulation was done using grade 1 graphite Rods (Ted Pella, Ca, USA), connected to a multifunctional wave generator (WF1947/WF1948, NF corporation, Japan).

2.1.1. Chemicals and immunochemicals

Recombinant mouse Interleukin 6 (ref. 200-02-100 μg) and recombinant mouse TNF- α (ref. 200-31-100 μg) were purchased from CliniSciences S.L. (Nanterre, France). Purified rat anti-mouse IL-6 (ref. 554400, clone MP5-20F3, capture antibody), biotin rat anti-mouse IL-6 (ref. 554402, clone MP5-32C11, detection antibody), purified rat anti-mouse TNF- α (ref. 551225, clone G281-2626, capture antibody), and biotin rat anti-mouse TNF- α (ref. 554415, clone MP6-XT3, detection antibody) were purchased from BD Biosciences (Barcelona, Spain). Streptavidin-poly Horseradish Peroxidase (SAV-pHRP), MF20 Alexa Fluor 488, DAPI, Tosyl-activated magnetic beads MB Dynabeads[®] MyOne[™], Dulbecco's modified Eagle's medium (DMEM high glucose, L-glutamine, GIBCO, 11965092), trypsin/EDTA, horse serum (HS, 26050088), fetal bovine serum (FBS, 16000044), penicillin/streptomycin (P/S, 15140122), 3.5 kDa MWCO membranes (68035) were purchased from Thermo Fisher (21140, Massachusetts, USA). Bovine serum albumin (BSA, A4737), Dexamethasone (Dex, D4901), Caffeine (C0750) and Lipopolysaccharides from E. Coli O55:B5 (LPS, L6529), Gelatin Type A from porcine skin (G2500), methacrylate anhydride (276685), 10% formalin solution (HT5011), Triton (X-100), 24 mm Transwell with 0.4 μm Pore Polyester Membrane Insert (CLS3450), Sodium carboxymethylcellulose (CMC, 419273), N-(3-Dimethylaminopropyl)-N'-ethylcarbodiimide hydrochloride (EDC, E7750), N-hydroxysuccinimide (NHS, 130672), aminoethylmethacrylate (479659), Trypsin/EDTA (T4049) were purchased from Sigma-Aldrich (Sigma Aldrich Co. St Louis, MO, USA). Tris-buffered saline was purchased from Canvax (TBS, BR0042, Biotech, Spain). Rhodamine-Phalloidin 480 was purchased from Cytoskeleton (PHDR1, USA). The Bradford solution (BIO-RAD protein assay cat No. 500-0006) was purchased from BIO-RAD laboratories GmbH (Munich, Germany). Acetone

was purchased from Panreac (161007, Barcelona, Spain). Polydimethylsiloxane (PDMS) was purchased from Dow Corning (SILPOT 184, Toray, Japan). 6–8 kDa MWCO membranes were purchased from Spectrumlabs (08-700-142, San Francisco, USA). Lithium Phenyl (2,4,6-trimethylbenzoyl)phosphinate (i.e., LAP) was purchased from TCI EUROPE N.V. (Belgium). Murine C2C12 skeletal myoblasts was purchased from American Type Culture Collection (CRL-1772, ATCC, Virginia, USA). Phosphate buffer saline (PBS) was 0.01 mol L⁻¹ phosphate buffer, 0.14 mol L⁻¹ in NaCl and 0.003 mol L⁻¹ in KCl saline solution at pH 7.5. PBST was PBS with 0.05% (v/v) Tween 20. PBST-BSA was PBST with 1% (w/v) BSA. Coating buffer is 0.05 M carbonate-bicarbonate buffer, pH 9.6. Citrate buffer was a 0.04 M solution of sodium citrate, pH 5.5. The substrate solution for optical measurement and used also in the amperometric immunosensor was 0.01% TMB (3,3',5,5'-tetramethylbenzidine) and 0.004% H₂O₂ in citrate buffer. For amperometric measurements, citrate buffer-KCl was prepared with citrate buffer that contains 0.1 mol L⁻¹ KCl. Borate buffer was 0.1 M boric acid (pH 9.5).

2.2. Preparation and optimization of the MB-Abs-based immunosensing platform

The antibody was coupled covalently to the magnetic beads (Supplementary information) according to the supplier protocol but with slight modifications, and the final concentration of the functionalized microbeads (MB-Abs) was 8 mg mL⁻¹. Prior to performing the detection of the secreted cytokines, the immunosensing platform was characterized and optimized (in terms of concentration) by checkboard titration. The incubation time for cytokines detection by MB-Abs was set at 60 min. Subsequent incubation steps for biotinylated antibody and SAV-pHRP bioconjugate were set at 30 min. Interleukin 6 and TNF- α solutions were prepared at 4 ng mL⁻¹ in differentiation media as standard solutions during amperometric optimization measurements. The effects of different parameters, including the MB-Abs quantity, biotinylated antibody, and enzyme tracer concentrations, were analyzed. The effect of each parameter was evaluated individually, and optimized values were used in subsequent experiments. Initially, MB-Abs quantity was optimized in the range of 0.1 μ g–5 μ g. Other parameters including biotinylated antibody and SAV-pHRP concentrations were maintained constant at 1 μ g mL⁻¹ in both cases.

To optimize detection and enzymatic steps, MB-Abs concentration was set, and concentrations of both biotinylated antibodies and SAV-pHRP were evaluated in the range of 0.0625–1 μ g mL⁻¹, following the same procedure as described before.

Related to selectivity studies, cross-reactivity was evaluated for either IL-6 and TNF- α including a negative control (zero point). On the other hand, to evaluate accuracy in our experiments, different blind spiked samples were prepared in differentiation media and measured directly by our optimized immunoassays. Accuracy for both immunoassays was evaluated by establishing a linear regression between spiked and measured values. All experiments were performed in triplicate.

2.3. Cell culture

Murine C2C12 myoblast cells were cultured under a 5% CO₂ atmosphere at 37 °C in growth medium, high glucose DMEM, containing L-Glut, 10% (v/v) FBS, 1% (v/v) P/S. When ~70% confluency was reached, the cells were detached by using trypsin/EDTA and then subcultured or used in the experiment. High glucose DMEM, containing L-Glut, 2% (v/v) HS, and 1% (v/v) P/S was used as differentiation medium (DM) to promote C2C12 differentiation towards myotubes.

2.4. Synthesis and preparation of prepolymer solutions

Gelatin-methacryloyl (GelMA) and carboxymethyl cellulose-

methacrylate (CMCMA) were synthesized according with our previous reported protocol (Supporting Information) (García-lizarribar et al., 2018). Prepolymer solutions were prepared by dissolving polymers and photoinitiator lithium phenyl (2,4,6-trimethylbenzoyl)phosphinate (LAP) in growth medium to obtain final concentrations of 5% (w/v) GelMA, 1% (w/v) CMCMA, and 0.1% (w/v) LAP. Prepolymer solutions were placed at 65 °C for 3 h to obtain homogeneous solutions.

2.5. Fabrication of the 3D SM engineered tissue (3SM)

Polymer solution was mixed with a C2C12 cell suspension to reach the final cell density of 25·10⁶ cell mL⁻¹. 3D skeletal muscle tissues were fabricated by photo-molding technique as we described previously (Ortega et al., 2019). Briefly, 20 μ L of the cell-laden prepolymer were poured on the Transwell insert (24 mm) and a microstructured PDMS stamp was placed onto the prepolymer. The PDMS microgrooves were filled and cell-laden prepolymer was exposed for 24 s under a UV light source (40 W, UVP Crosslinker) (Fig. S2, Supplementary information). After carefully removing the stamp we obtained a 3D cell-microstructured hydrogel anchored on the Transwell membrane. Once 3SM was fabricated, a new cell medium was added on the upper part (1 mL) and the lower part (2 mL) and changed every 2 days. The growth medium was replaced at day 6 with differentiation media (DM). The DM was changed every 2 days until day 14, when the drug assays or electrical assays were carried out.

2.6. Immunostaining

The tissues were fixed in a 10% formalin solution at 15 days after fabrication. Then hydrogels were washed with TBS, cells were permeabilized with 0.1% Triton X-100 in TBS for 15 min and blocked with a blocking buffer consisting of 0.3% Triton X-100 and 3% donkey serum (brand) in TBS for 2 h. Afterwards, tissues were washed with TBS and incubated in 100 nM Rhodamine-Phalloidin 480 solution overnight to stain filamentous actin (F-actin). An additional overnight staining for Myosin Heavy Chain (MHC) was performed by incubating in a solution of 5 μ g/mL MF20 Alexa Fluor 488 in blocking buffer. After washing with TBS, nuclei were counterstained with DAPI 1 μ M for 15 min.

2.7. Immunosensor measurement procedure

Transwell permeable supports were used as a platform to develop the immunosensing measurement procedure, design and operation of the integrated platform is depicted in Fig. 1. 3SM were maintained in culture for up to 14 days and, just before electrical or chemical stimulation, MB-Abs (5 μ g for IL-6 and 10 μ g for TNF- α) were loaded in the lower side of the Transwell, where capture step was performed. Samples were incubated under soft stirring to avoid bead aggregation, inside an incubator at 37 °C and 5% CO₂ atmosphere. During the experiments, upper part and lower part was filled with 1 mL and 2 mL of cell medium, respectively. Secreted cytokines, as a result of either electrical or chemical stimulation, diffused through the Transwell membrane and were captured by the specific antibodies immobilized onto the surface of the beads. MB-Abs were replaced every hour to obtain a continuous monitoring of the secreted cytokines. After this time, MB-Abs were washed (3X) and resuspended in biotinylated antibody 0.125 μ g mL⁻¹ or 0.5 μ g mL⁻¹ (in the case of IL-6 or TNF- α respectively), prepared in PBST-BSA buffer, and leave it under stirring for 30 min to avoid bead aggregation. Then, MB-Abs were washed again and resuspended in SAV-pHRP 0.50 μ g mL⁻¹ (for both cytokines) prepared in PBST-BSA buffer, for 30 min under the same conditions described before. Afterwards, MB-Abs were washed and resuspended in 100 μ L of citrate buffer-KCl and captured onto the surface of the working electrode using a custom-made PMMA cell with magnets located under the SPCEs (Fig. S3 Supporting Information). Finally, amperometric measurements were carried out by applying a constant

potential of -0.2 V vs Ag pseudo-reference electrode. After current stabilization (100 s), $20\ \mu\text{L}$ of substrate solution prepared in citrate buffer-KCl, was added to each well. Electrochemical signals were recorded once the current was again stabilized (250 s).

2.8. Drug stimulation assays

2D Drug stimulation screening assays. Caffeine, Dexamethasone (Dex) and Lipopolysaccharide (LPS) were tested in skeletal myotubes cultured in 2D (well plate configuration) using differentiation media for 7 days, to evaluate the effect of each drug in the cytokine's secretion at different times. Myotubes cultured in 2D were incubated for 0.5, 1, 2, 16, 24 and 48 h, in DM supplemented by the drug. Caffeine was diluted in DM to a concentration of $100\ \mu\text{M}$. Dex, was suspended in absolute ethanol at a concentration of $10\ \text{mM}$ and diluted further in DM to obtain a final concentration of $100\ \mu\text{M}$. LPS was diluted in DM to a concentration of $10\ \mu\text{g mL}^{-1}$. Three replicas for each condition were analyzed. The screening of the cytokine levels was carried out by ELISA (See supporting information).

3SM drug stimulation assay. Mature 3SM at day 14 were incubated in DM supplemented by LPS at different times: 0.5, 1, 2, 4, 8 and 24 h. MBAbs were placed 1 hour before drug treatment in the lower compartment, and after drug treatment the immunoassay was performed as described in section 2.8.

2.9. Electrical pulse stimulation (EPS) assays

In order to stimulate 3SM on the Transwell membrane, a pair of graphite electrodes (3 mm diameter), separated at 1 cm, were used. A custom-made device was designed and fabricated using a DLP projector-based stereo-lithography 3D printer to hold the electrodes and fixed on well plate's lid. Copper wires were assembled to graphite rods and located out of the lid through the device, to permit the connection to a wave generator (Supplementary information). Under this configuration, electrical stimulation on Transwells was carried out in a high reproducible way, allowing the microscope imaging of the tissue. Mature 3SM were subjected to stimulations regimes with 0.25, 1 and 5 V peak-peak at 1 Hz of frequency and a duration of 2 ms during 1 h, to evaluate cell response upon electrical stimuli. To study time-dependent secretion of cytokines, samples were stimulated for seven hours in a continuous EPS, and on the other hand in cycles of 1 h stimulation with and 2 h of relaxing time (stimulation off) for a total of nine hours.

2.10. Data and statistical analysis

The calibration curves fittings and statistical analysis were performed using GraphPad Prims 5.03 (GraphPad Software Inc., San Diego, CA). Data is presented as the mean ($\bar{x} \pm \text{SD}$). A *t*-test was used for statistical analysis of two sample comparison, and ANOVA one-way for statistical evaluation of one factor. A value of $p < 0.05$ was considered statistically significant.

3. Results and discussion

3.1. Immunoassay optimization and analytical features

The conjugation efficiency (coupling of antibody to MB) supernatants after immobilization process were evaluated using Bradford assay. Our results indicate a coupling yield of $94 \pm 8\%$ for all replicates. The functionality of the bioconjugates by the electrochemical immunoassay, MBAbs, biotinylated antibody, and SAV-pHRP concentrations were optimized by checkboard titration assay. Fig. 2a illustrates the effect of MBAbs quantity on the normalized current obtained at -0.2 V applied potential, corresponding to IL 6 (orange circle) and TNF- α (blue squares) detection. The current reaches optimum signal at $5\ \mu\text{g}$ (IL-6) and $10\ \mu\text{g}$ (TNF- α) of MBAbs, with non-

significant enhancement of the signal using higher concentrations. These values of MBAbs were selected for the optimization of the further steps.

Fig. 2b shows the values of the maximum signal performance achieved at different biotinylated antibody concentrations. The current values for IL-6 reach saturation point at $0.125\ \mu\text{g mL}^{-1}$ of biotinylated antibody, while for TNF- α we consider the saturation level above $0.5\ \mu\text{g mL}^{-1}$, setting these values as optimal for further experiments.

Finally, the current response was tested at different concentrations of SAV-pHRP, from 0.0625 to $1\ \mu\text{g mL}^{-1}$. As shown in Fig. 2c, in the case of IL-6, the signal response shows an increment of $50\% \mu\text{A}$ at $0.5\ \mu\text{g mL}^{-1}$, whereas in the case of TNF- α , this improvement takes place at a lower concentration of $0.25\ \mu\text{g mL}^{-1}$, maintaining the same response at higher concentrations of the SAV-pHRP. For these reasons, concentration of $0.5\ \mu\text{g mL}^{-1}$ of SAV-pHRP for both immunoassays were selected, simplifying the experimental procedure of the biosensor for both cytokines. These optimized values were used in later determination of calibrations curves, which represent the working conditions to obtained lowest limit of detection.

The dose-dependence of the magnetic bead-based immunosensors developed was studied for different concentrations of IL-6 and TNF- α in differentiation media. The assay was performed as is shown in Fig. 1, and described in Section 2, by assessing standard solutions of IL-6 and TNF- α (between 0 and $0.5\ \text{ng mL}^{-1}$ in DM). As expected, the current signal recorded was directly proportional to the concentration of the cytokine in the sample in both cases. The limit of detection for IL-6 and TNF- α (Fig. 2d and e) were $40 \pm 10\ \text{pg mL}^{-1}$ and $20 \pm 10\ \text{pg mL}^{-1}$, respectively, which are better than ELISA tests.

Several works that have used magnetic beads to detect secreted biomarkers or cytokines have reported similar LOD's, about tens of pg mL^{-1} . Riahi et al. succeeded on on-chip measurements with a LOD of $30\ \text{pg mL}^{-1}$ by EC detection (Riahi et al., 2016). Other reports are based on the use of on-chip fluorescent bead-based immunoassay, (Cui et al., 2018) or by magnetic beads with the out-chip enzymatic step to monitor cytokine secretion from immune cells with a sensitivity of tens of pg mL^{-1} (Kongsuphol et al., 2016). Also, by a novel optofluidic nanobiosensor, Li et al., have reported a sensitivity of $39\ \text{pg mL}^{-1}$, in the real-time detection of cytokine secretion using nanoplasmonics (Li et al., 2018). Thus, the limit of detection reached by the immunosensor described in this work is considered optimal for our purposes, taking into account the sensitivity reported by recent works, and the reported amount of secreted IL-6 ($\sim 0.05\ \text{ng mL}^{-1}$) without any stimulation in skeletal muscle 2D cultures (Nedachi et al., 2008; Farmawati et al., 2013). Our selectivity studies showed no cross reactivity between IL-6 and TNF- α and the feasibility of the system, while the assays used to study the accuracy in both cases showed a slope close to 1 (Fig. 3f and g), indicating that both immunosensors are high accurate in the working range of our interest.

3.2. 3D SM engineered tissue (3SM) and sensing system integration

To fabricate the 3D skeletal muscle constructs, muscle cells were encapsulated in a 5% w/v Gelatin methacryloyl (GelMA), and 1% w/v carboxy methyl cellulose methacrylate (CMCMA) polymer solution. Gelatin methacryloyl was combined with CMCMA to avoid cell degradation and improve stability, as we previously demonstrated (García-lizarribar et al., 2018). To control the 3D cellular organization of the encapsulated C2C12 cells, photo-mold patterning technique was applied using a microgrooved PDMS stamp and this method was directly carried out on the upper membrane of a Transwell (Fig. 3a-e). (Ortega et al., 1039)

The skeletal muscle constructs were differentiated from day 6 to day 14 and characterized by bright field microscopy during the skeletal muscle cells maturation. At day 14 constructs show aligned fibers (Fig. 3f), which compared to non-patterned samples show a high degree of alignment (Fig. 3g). The myotubes show a high content of myosin

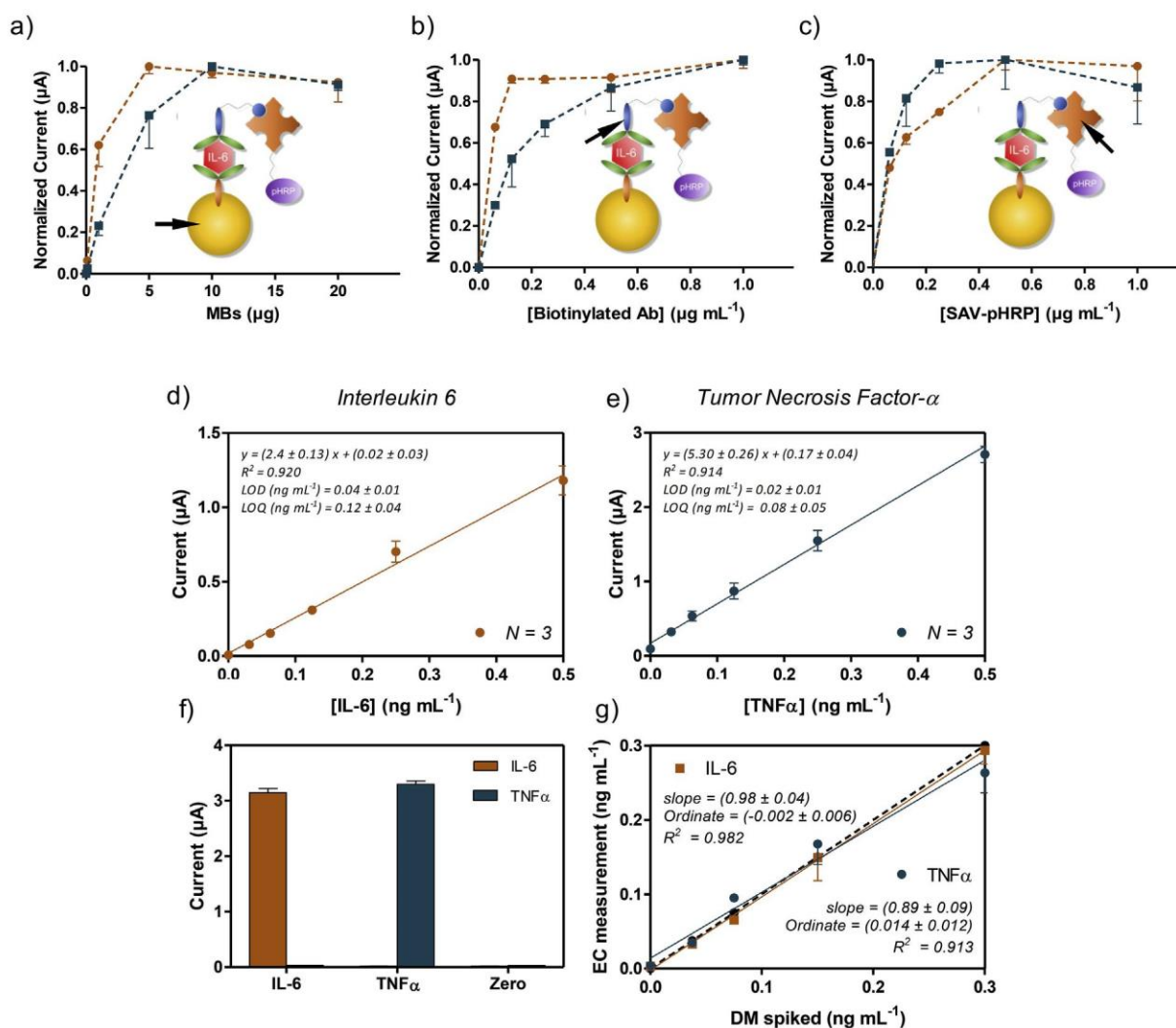


Fig. 2. Optimization of the electrochemical MB-Abs based immunoassay for IL-6 (orange circles) and TNF- α (blue squares) using 4 ng mL^{-1} of each cytokine. Normalized current vs a) the number of microbeads in the 6 well Transwell set up, b) concentration of the biotinylated antibody, and c) SAV-pHRP concentration. Other parameters such as cytokine concentration and incubation time for each step were maintained fixed. Calibration curves for the detection of d) IL-6 and e) TNF- α respectively, in differentiation media and different analytical parameters such as limit of detection and quantification. f) Selectivity studies for both immunoassays, IL-6 and TNF- α at concentration of 4 ng mL^{-1} . g) Accuracy studies performed using spiked samples prepared in differentiation media and used directly in the immunosensor without previous dilution. The data shown correspond to the average of at least two replicates. All data shown by mean \pm SD. (For interpretation of the references to colour in this figure legend, the reader is referred to the Web version of this article.)

heavy chain positive stained cells (Fig. 3h), and a high fusion index compared to non-patterned samples (Fig. 3i). Thus, these results demonstrate the functional C2C12 differentiation towards myotubes and are in concordance with found by Ortega et al. (Ortega et al., 1039) We demonstrate that the reported fabrication method can be used on a permeable membrane without further modifications, and 3SM kept anchored on the membrane for at least 14 days supporting growth and skeletal muscle differentiation. In the present work, we exploit the advantages of Transwell insert membranes, to assess the invasive way of place MB-Abs and 3SM together. To demonstrate cytokine diffusion through the Transwell membrane ($0.4 \mu\text{m}$ pore size), we placed IL-6 solution in the upper compartment. As expected, we found that IL-6 concentration increases with time in the lower compartment, indicating diffusion of cytokines through the porous membrane. Thus, permeable membranes, where 3SM are located, allow the diffusion of the secreted cytokines to the lower compartment where MB-Abs immediately capture the cytokines, but the membrane pore size prevents MB-Abs diffusion to the upper part. In this work, the integrated platform has been designed to monitor the secretion processes over time by the in situ capturing of the released cytokines. Several works have previously used

complex chip arrays or devices to detect cytokines from immune cells by MB-Abs, which were located in separated compartments or chambers to avoid the cell-MB-Abs interaction (Riahi et al., 2016; Cui et al., 2018; Kongsuphol et al., 2016). In addition, previous work has reported complex systems based on fluorescence imaging or nanoplasmonic biosensors, which capture antibodies on the substrate for detecting cytokine secretion of single cells (Juan-Colás et al., 2018; Li et al., 2018; Nedachi et al., 2008; Farmawati et al., 2013; An et al., 2017). These examples have succeeded in “real-time” quantification of cytokine secretion but using single cells or cell solutions. Our platform incorporates the novelty of integrating a 3D tissue-like skeletal muscle instead of isolated cells.

3.3. Drug stimulation assays

To study the viability of the sensor and monitor the response of the skeletal muscle against chemical stimuli, IL-6 and TNF- α secretion were measured. To find the best chemical stimuli for promoting IL-6 secretion, 2D monolayers of differentiated myotubes were incubated with caffeine, which causes effects on muscle size and changes in signaling

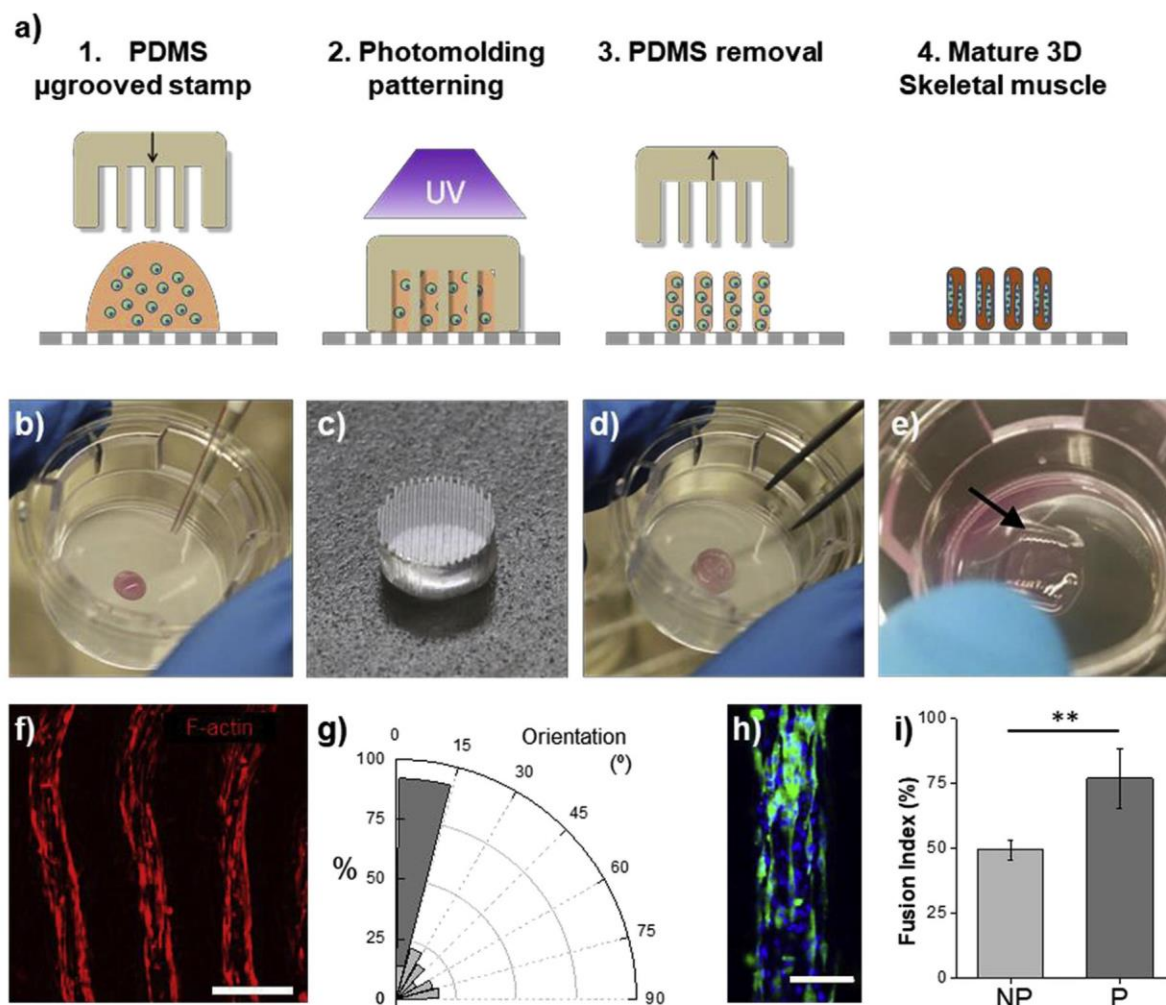


Fig. 3. Fabrication of the 3D skeletal muscle in the integrated platform. a) Schematics of the photo mold patterning on the Transwell. 1. A drop of cell-laden solution is poured on the porous membrane of the Transwell, 2. A microstructured PDMS stamp is placed onto the prepolymer. The PDMS microgrooves were filled and cell-laden prepolymer is exposed under a UV light. 3. After removing the stamp we obtain a 3D cell-microstructured hydrogel anchored on the Transwell membrane. 4. After 14 days we obtain a mature 3D skeletal muscle. Pictures of the fabrication process: b) Cell-laden prepolymer drop onto a Transwell. c) Detail of the microgrooved stamp. d) PDMS microgrooves filled with the prepolymer cell-laden solution. e) Detail of the skeletal muscle tissue (arrow) on the Transwell, after fabrication. f) Confocal microscopy picture of 3SM at day 14, showing elongated cells and myotubes. F-actin in red. Scale bar = 500 μm . g) Normalized histogram (bin = 15°) depicting the distribution of the angles between cell cytoskeleton fibers inside non-patterned hydrogels (NP, light gray) and in the 3SM (dark gray). Inside the 3SM myotubes show high degree of alignment (> 75%) following the pattern direction. h) Confocal image of the one structure of the mature 3SM depicting the cell, showing the presence of MHC positive myotubes (green). Nuclei in blue. Scale bar = 200 μm . i) Fusion index percentage (mean \pm standard deviation, **p-value < 0.01) of the myotubes inside the non-patterned hydrogels (light gray) and in the 3SM (dark gray). (For interpretation of the references to colour in this figure legend, the reader is referred to the Web version of this article.)

pathways, (Egawa et al., 2016) dexamethasone, which is used as a muscle atrophy inducer, (Shimizu et al., 2017) and LPS which stimulates the expression of IL-6 and TNF- α in both skeletal muscles in vivo and C2C12 myoblasts in vitro (Frost et al., 2002).

After we determined cytokine secretion by a in house ELISA, LPS treatment showed the highest secretion of IL-6 with no significant changes under caffeine and Dex treatment (Fig. 4a and b). The TNF- α values do not show significant changes under all the treatments (Fig. 4c and d). Thus, LPS was chosen to be tested in the integrated sensing system.

The 3D skeletal muscle tissues were grown on the Transwell membrane and at day 14 and incubated with differentiation media containing LPS (10 $\mu\text{g mL}^{-1}$). The IL-6 and TNF- α secretions were monitored in function of time for 24 hours. The IL-6 secretion showed an increasing profile along the incubation time as was found in 2D experiments. The TNF- α secretion showed an increasing but no statistically significant trend, and released less protein compared to IL-6 (Fig. 4e and f).

Our results prove that 3SM responds to LPS treatment, and that mature muscle cells secrete IL-6. On the other hand, we have demonstrated the capacity of the integrated system to monitor low concentrations of cytokine levels, immediately following chemical stimuli. After 24 h, we found that the IL-6 expression fold change (20.98 ± 1.61) was at least three times higher than the TNF- α fold change (3.37 ± 4.00); this correlates with the reported differences between IL-6 and TNF- α expression under LPS treatment in mouse (Frost et al., 2002).

3.4. Dependence between contraction/relaxation periods and IL-6 secretion from skeletal muscle

To electrically stimulate the 3SM, we designed and fabricated a device that fits in the Transwell insert containing a pair of graphite rods (Fig. 5a). A function generator was connected to the graphite rods by copper wires in the external part of the well plate's lid (Fig. 5b). The graphite rods are not in direct contact with the 3SM, enabling the

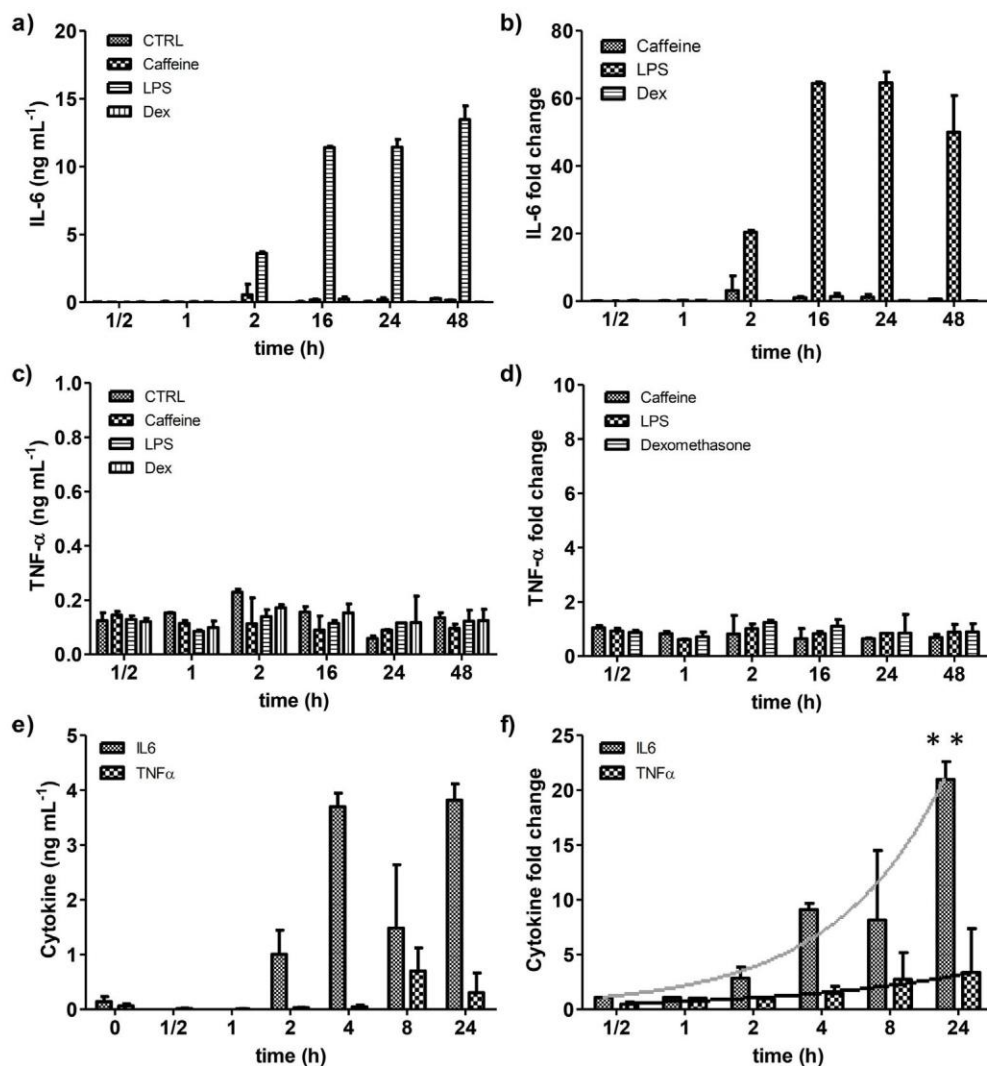


Fig. 4. Monitoring of IL-6 and TNF- α secretion under the effect of chemical stimuli. Cytokine secretion by ELISA test of a) IL-6 concentration and b) normalized values by fold change (Treatment/Ctrol), and c) TNF- α concentration and d) normalized values by fold change of 2D differentiated myotubes under the effect of caffeine, Dex, and LPS. Continuous monitoring in integrated platform of e) IL6 secretion and TNF- α secretion concentration from 3D skeletal muscle constructs exposed to LPS ($10 \mu\text{g mL}^{-1}$) for 24 h. f) Fold change of IL-6 and TNF- α secretion was calculated to assess responsiveness of 3SM to stimulation with LPS. Trend of cytokine secretion drawn as a gray line (IL-6) and a black line (TNF- α). ANOVA test **p-value < 0.01. Data are shown by mean \pm SD, (n = 4–6).

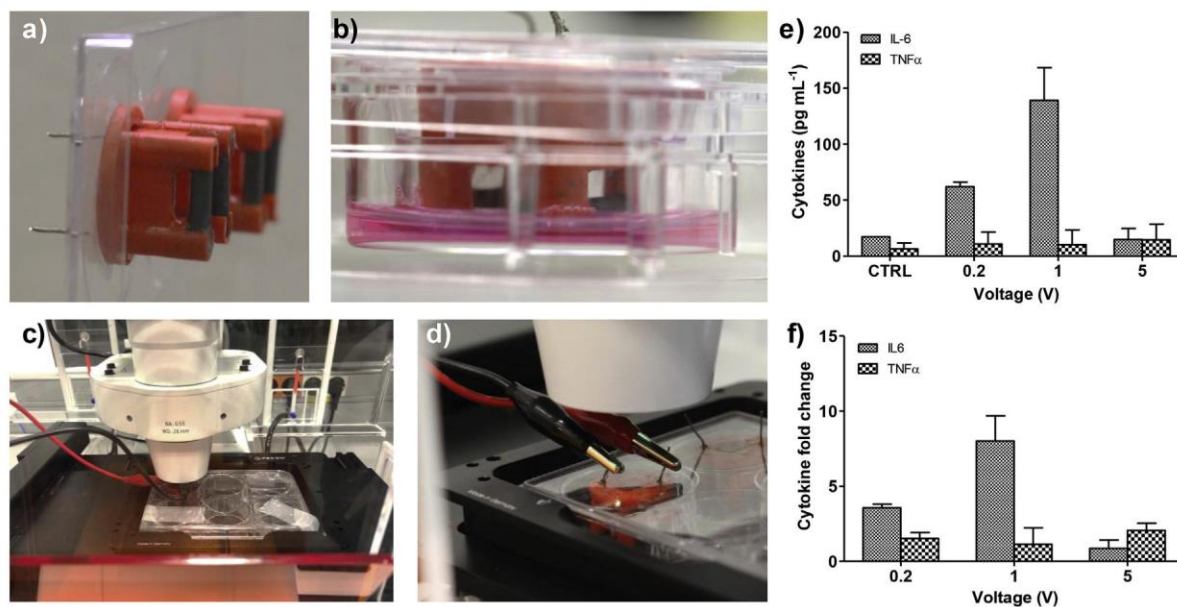


Fig. 5. a) Picture of the tailored device for the electrical stimulation. b) Lateral view of the device inside the Transwell in a well plate. c) Integrated system coupled to a wave generator and located in a microscope. d) Detail of the connection between copper wires and wave generator. e) Effect of EPS regimes on the cytokine secretion, f) fold change in IL-6 and TNF- α secretion was calculated to assess responsiveness of 3SM to EPS regimes. Data are shown by mean \pm SD. (n = 4–6) p < 0.05.

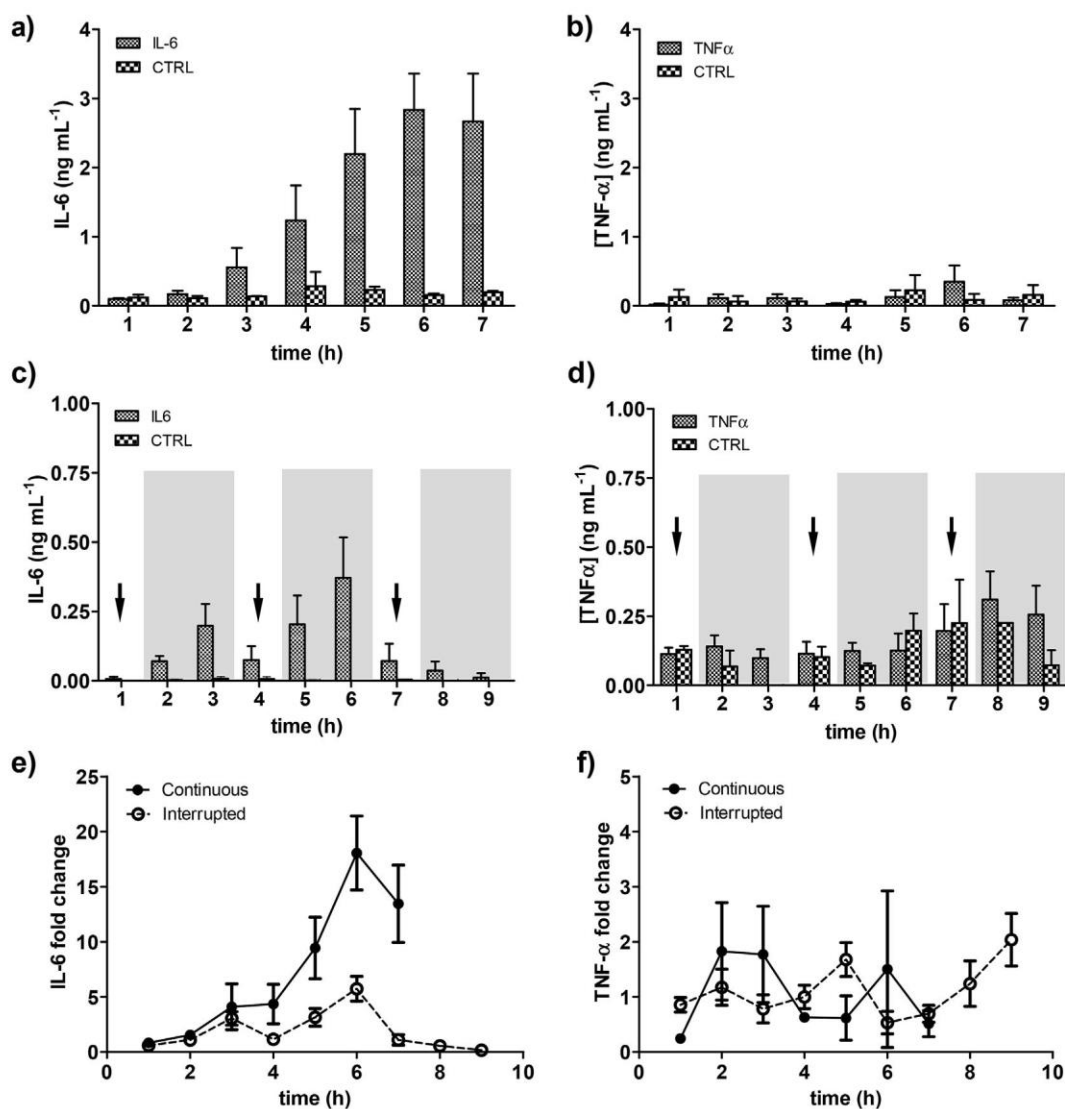


Fig. 6. Monitoring of a) IL-6 secretion and b) TNF- α secretion under continuous EPS. Monitoring of c) IL6 secretion and d) TNF- α secretion under interrupted EPS. Arrows indicate EPS and gray background indicates relax period. Fold change increase in e) IL-6 and f) TNF- α secretion was calculated to assess responsiveness of 3SM to electrical stimulation. Results from continuous EPS (dots-line) and interrupted EPS (empty dots-dash line) show an impact on the IL-6 secretion but not on the TNF- α secretion. Data are shown by mean \pm SD. (n = 4–6).

imaging of the skeletal muscle tissue during the electrical stimulation (Fig. 5c). This compact configuration allows the routine use of culture-well plates inside the incubator.

Previous works have reported that electrical pulse stimulation of in vitro skeletal muscle induced muscle contractions (Ortega et al., 2013; Nedachi et al., 2008; Marotta et al., 2004; Ramón-Azcón et al., 2013; Park et al., 2008; Evers-van Gogh et al., 2015; Banan Sadeghian et al., 2018). Other works have also reported that intense exercise by skeletal muscle increases IL-6 expression and secretion, but not of that of TNF- α (Banan Sadeghian et al., 2018; Bustamante et al., 2014). To obtain an appropriate stimulation regime with the tailored device, we optimized the stimulation regime to obtain high IL-6 secretion with a low TNF- α increase. The skeletal muscle constructs were electrically stimulated under three voltage regimes 0.25 V, 1 V, and 5 V. We found that electrical stimulations led to a significant increase of IL-6 secretion at 0.2 and 1 V, compared to the control, with a maximum level ($0.14 \pm 0.02 \text{ ng mL}^{-1}$) by applying 1V (Fig. 5e). No significant changes in TNF- α secretion were found. Our results suggest a successful EPS-evoked contraction of the 3SM, depicted by the increase of IL-6 expression, without effects on TNF- α release. Normalized values by fold change (EPS/CTRL) (Fig. 5f) confirmed the highest IL-6/TNF- α

signal at 1 V, which was fixed for the next experiments.

Once we fixed the EPS regime at 1 V, 1 Hz, and 0.002 s, we attempted to elucidate the time-dependent secretion of IL-6 from the 3D skeletal muscle tissues. First, we applied continuous EPS for 7 hours, to mimic endurance exercise and our system allows to detect changes in secreted IL-6 at low concentrations ($0.5\text{--}3 \text{ ng mL}^{-1}$). Fig. 6a shows a significant increase of IL-6 from 3 hours after starting EPS, while no significant increase in TNF- α release was observed (Fig. 6b). The effect of electrical stimulation on the IL-6 expression has been demonstrated previously in C2C12 myotubes, rat myotubes, with a peak after 2 hours of EPS, in agreement with our findings (Evers-van Gogh et al., 2015; Bustamante et al., 2014; Peake et al., 2015).

Next, we wanted to mimic interrupted exercise by alternating EPS with relaxed periods and use the biosensor platform to discretize when 3D skeletal muscle releases the cytokines. To this end, we applied stimulation periods of 1 h and relaxation periods of 2 h. First, in the case of IL-6 we observed lower secretion than in continuous EPS (Fig. 6c), while the TNF- α secretion kept similar, under 0.5 ng mL^{-1} , as in the case of continuous EPS (Fig. 6d) without any pattern associated to the stimulation periods.

We also found an unexpected profile in the IL-6 secretion: a

significant increase of secreted IL-6 took place during relaxation periods after 2 and 3 h, and after 5 and 6 h. To compare both regimes, we normalized the cytokine secretion by fold change calculation between stimulated and control samples (EPS/Ctrl). In the case of IL-6, we were able to measure differences based on the different EPS regimes. During the 3 first hours no differences are found in terms of fold change, but after that point, the endurance exercise (continuous EPS) induced higher IL-6 secretion, while alternate exercise produced to a different profile with lower IL-6 secretion levels and the presence of secretion peaks (Fig. 6e). As expected, the TNF- α profiles were similar with random tendencies along the time and low fold change (Fig. 6f). As we showed, the integrated platform allows to monitor the cytokine secretion of the 3D skeletal muscle tissue over the time to discretize the effect of different EPS regimes.

4. Conclusions

In this study, we developed an in vitro integrated platform to monitor the secretion of inflammatory processes related cytokines from single tissue-based models. When functionalized, magnetic beads were coupled with a 3D tissue engineered skeletal muscle, and chemical and electrical stimuli. First, we succeeded in the fabrication of the 3D tissue engineered skeletal muscle on a porous membrane of Transwells, what allowed the diffusion of the secreted cytokines to the lower compartment. Next, magnetic beads assay developed underneath the membrane, allowed amperometric measurements of IL-6 and TNF- α . Changes in the concentrations of IL-6 and TNF- α were measured clearly with limits of detection below of 40 and 20 pg mL⁻¹, respectively. Through this configuration, secretion processes has been monitored by the in situ capturing of the released cytokines in a near real-time. Under proinflammatory drug exposure the expected changes in the cytokine levels were observed, and this effect was further monitored in the 3D tissue engineered skeletal muscle. In addition, this work showed different time-dependent profiles of IL-6 secretion, induced by the electrical stimulation-based contraction. These findings contribute to the better understanding roles of IL-6 in muscle related inflammation process. Therefore, this platform is an attractive candidate for further applications, since it does not require any complex modifications. Future work will involve study of other biomimetic tissues under a wide range of treatments or disorders, as in vitro test to high sensitivity metabolic studies.

CRedit authorship contribution statement

Alejandro Hernández-Albors: Conceptualization, Formal analysis, Writing - original draft, Writing - review & editing, Methodology, Investigation. **Albert G. Castaño:** Conceptualization, Methodology, Investigation, Writing - original draft. **Xiomara Fernández-Garibay:** Formal analysis, Writing - original draft, Conceptualization, Methodology, Investigation. **María Alejandra Ortega:** Conceptualization, Methodology, Investigation. **Jordina Balaguer:** Formal analysis, Investigation. **Javier Ramón-Azcón:** Conceptualization, Writing - review & editing, Methodology, Investigation, Supervision.

Acknowledgements

Funding for this project was provided by the Ramon y Cajal (RYC-2014-15022) fellowship and Severo Ochoa Program for Centers of Excellence (R&D 2016–2019) funded by the Ministerio de Economía, Industria y Competitividad; an ERC grant (ERC starting grant project – 714317 – DAMOC); the CERCA Programme/Generalitat de Catalunya (2014-SGR-1442 and 2014-SGR-1460); and the Fundación Bancaria "la Caixa" - Obra Social "la Caixa" (projecte IBEC-La Caixa Healthy Ageing).

The authors thank Micro-Nano Technology Unit (U2 of the ICTS "NANBIOSIS") from Institute of Microelectronics of Barcelona (IMB-CNM, Barcelona, Spain), for the design and fabrication of the several custom-made pieces used in this work. We thank Patrick Han at SayEdit.com for help with English editing.

Appendix A. Supplementary data

Supplementary data to this article can be found online at <https://doi.org/10.1016/j.biosx.2019.100025>.

References

- An, X., Sendra, V.G., Liadi, I., Ramesh, B., Romain, G., Haymaker, C., Martínez-Paniagua, M., Lu, Y., Radvanyi, L.G., Roysam, B., Varadarajan, N., 2017. *PLoS One* 12, e0181904.
- Banan Sadeghian, R., Ebrahimi, M., Salehi, S., 2018. *J. Tissue Eng. Regen. Med.* 12, 912–922.
- Bruls, D.M., Evers, T.H., Kahlman, J.A.H., van Lankvelt, P.J.W., Ovsyanko, M., Pelssers, E.G.M., Schleipen, J.J.H.B., de Theije, F.K., Verschuren, C.A., van der Wijk, T., van Zon, J.B.A., Dittmer, W.U., Immink, A.H.J., Nieuwenhuis, J.H., Prins, M.W.J., 2009. *Lab Chip* 9, 3504.
- Bustamante, M., Fernández-Verdejo, R., Jaimovich, E., Buvinic, S., 2014. *Am. J. Physiol. Metab.* 306, E869–E882.
- Cui, X., Liu, Y., Hu, D., Qian, W., Tin, C., Sun, D., Chen, W., Lam, R.H.W., 2018. *Lab Chip* 18, 522–531.
- Egawa, T., Ohno, Y., Goto, A., Sugiura, T., Ohira, Y., Yoshioka, T., Hayashi, T., Goto, K., 2016. *J. Caffeine Res.* 6, 88–96.
- Esteban-Fernández de Ávila, B., Escamilla-Gómez, V., Campuzano, S., Pedrero, M., Salvador, J.-P., Marco, M.-P., Pingarrón, J.M., 2013. *Sens. Actuators B Chem.* 188, 212–220.
- Evers-van Gogh, I.J.A., Alex, S., Stienstra, R., Brenkman, A.B., Kersten, S., Kalkhoven, E., 2015. *Sci. Rep.* 5, 10944.
- Farmawati, A., Kitajima, Y., Nedachi, T., Sato, M., Kanzaki, M., Nagatomi, R., 2013. *Endocr. J.* 137–147.
- Frost, R.A., Nystrom, G.J., Lang, C.H., 2002. *Am. J. Physiol. Integr. Comp. Physiol.* 283, R698–R709.
- Furrer, R., Eisele, P.S., Schmidt, A., Beer, M., Handschin, C., 2017. *Sci. Rep.* 7, 40789.
- García-lizarribar, A., Fernández-garibay, X., Velasco-mallorquí, F., Castaño, A.G., 2018. *J. Samitier J. Ramon-azcon* 1800167, 1–13.
- Juan-Colás, J., Hitchcock, I.S., Coles, M., Johnson, S., Krauss, T.F., 2018. *Proc. Natl. Acad. Sci.* 115, 13204–13209.
- Kongsuphol, P., Liu, Y., Ramadan, Q., 2016. *Biomed. Microdevices* 18, 93.
- Kongsuphol, P., Gupta, S., Liu, Y., Bhuvanendran Nair Gourikuttu, S., Biswas, S.K., Ramadan, Q., 2019. *Sci. Rep.* 9, 4887.
- Li, X., Soler, M., Szydzik, C., Khoshmanesh, K., Schmidt, J., Coukos, G., Mitchell, A., Altug, H., 2018. *Small* 14, 1800698.
- Marotta, M., Bragós, R., Gómez-Foix, A.M., 2004. *Biotechniques* 36, 68–73.
- Mukherjee, P., Mani, S., 2013. *Biochim. Biophys. Acta - Proteins Proteomics* 1834, 2226–2232.
- Nedachi, T., Fujita, H., Kanzaki, M., 2008. *Am. J. Physiol. Metab.* 295, E1191–E1204.
- M. A. Ortega, X. Fernández-Garibay, A. G. Castaño, F. De Chiara, A. Hernández-Albors, J. Balaguer-Trias and J. Ramón-Azcón, *Lab Chip*, DOI:10.1039/C9LC00285E.
- Park, H., Bhalla, R., Saigal, R., Radisic, M., Watson, N., Langer, R., Vunjak-Novakovic, G., 2008. *J. Tissue Eng. Regen. Med.* 2, 279–287.
- Peake, J.M., Della Gatta, P., Suzuki, K., Nieman, D.C., 2015. *Exerc. Immunol. Rev.* 21, 8–25.
- Ramón-Azcón, J., Ahadian, S., Estili, M., Liang, X., Ostrovidov, S., Kaji, H., Shiku, H., Ramalingam, M., Nakajima, K., Sakka, Y., Khademhosseini, A., Matsue, T., 2013. *Adv. Mater.* 25, 4028–4034.
- Riahi, R., Shaegh, S.A.M., Ghaderi, M., Zhang, Y.S., Shin, S.R., Aleman, J., Massa, S., Kim, D., Dokmeci, M.R., Khademhosseini, A., 2016. *Sci. Rep.* 6, 24598.
- Rothenberg, E.V., 2007. *Nat. Immunol.* 8, 441–444.
- Saxena, A., Dagur, P.K., Desai, A., McCoy, J.P., 2018. *Front. Immunol.* <https://doi.org/10.3389/fimmu.2018.02462>.
- Shimizu, K., Genma, R., Gotou, Y., Nagasaka, S., Honda, H., 2017. *Bioengineering* 4, 56.
- Shirasaki, Y., Yamagishi, M., Suzuki, N., Izawa, K., Nakahara, A., Mizuno, J., Shoji, S., Heike, T., Harada, Y., Nishikomori, R., Ohara, O., 2015. *Sci. Rep.* 4, 4736.
- Skardal, A., Murphy, S.V., Devarasetty, M., Mead, I., Kang, H.-W., Seol, Y.-J., Shrike Zhang, Y., Shin, S.-R., Zhao, L., Aleman, J., Hall, A.R., Shupe, T.D., Kleensang, A., Dokmeci, M.R., Jin Lee, S., Jackson, J.D., Yoo, J.J., Hartung, T., Khademhosseini, A., Soker, S., Bishop, C.E., Atala, A., 2017. *Sci. Rep.* 7, 8837.
- Takahashi, H., Shimizu, T., Okano, T., 2018. *Sci. Rep.* 8, 13932.
- Zhang, Y.S., Aleman, J., Shin, S.R., Kilic, T., Kim, D., Mousavi Shaegh, S.A., Massa, S., Riahi, R., Chae, S., Hu, N., Avci, H., Zhang, W., Silvestri, A., Sanati Nezhad, A., Manbohi, A., De Ferrari, F., Polini, A., Calzone, G., Shaikh, N., Alerasool, P., Budina, E., Kang, J., Bhise, N., Ribas, J., Pourmand, A., Skardal, A., Shupe, T., Bishop, C.E., Dokmeci, M.R., Atala, A., Khademhosseini, A., 2017. *Proc. Natl. Acad. Sci.* 114, E2293–E2302.

Bioengineered *in vitro* skeletal muscles as new tools for muscular dystrophies preclinical studies

Journal of Tissue Engineering
Volume 12: 1–19
© The Author(s) 2021
Article reuse guidelines:
sagepub.com/journals-permissions
DOI: 10.1177/2041731420981339
journals.sagepub.com/home/tej



Juan M. Fernández-Costa , Xiomara Fernández-Garibay ,
Ferran Velasco-Mallorquí  and Javier Ramón-Azcón 

Abstract

Muscular dystrophies are a group of highly disabling disorders that share degenerative muscle weakness and wasting as common symptoms. To date, there is not an effective cure for these diseases. In the last years, bioengineered tissues have emerged as powerful tools for preclinical studies. In this review, we summarize the recent technological advances in skeletal muscle tissue engineering. We identify several ground-breaking techniques to fabricate *in vitro* bioartificial muscles. Accumulating evidence shows that scaffold-based tissue engineering provides topographical cues that enhance the viability and maturation of skeletal muscle. Functional bioartificial muscles have been developed using human myoblasts. These tissues accurately responded to electrical and biological stimulation. Moreover, advanced drug screening tools can be fabricated integrating these tissues in electrical stimulation platforms. However, more work introducing patient-derived cells and integrating these tissues in microdevices is needed to promote the clinical translation of bioengineered skeletal muscle as preclinical tools for muscular dystrophies.

Keywords

Skeletal muscle, tissue engineering, muscular dystrophy, biomaterials, drug screening platforms

Date received: received: 30 July 2020; accepted: 26 November 2020

Introduction

Muscular dystrophies (MD) are a group of genetically inherited muscle degenerative disorders characterized by muscle weakness and wasting.¹ The disorders differ in the age of onset, rate of progression, pattern of inheritance, and the type of muscles that are affected (Table 1). Depending on the type of muscular dystrophy, axial, limb, or facial muscles could be affected by a different degree of muscle degeneration and weakness. In specific MDs, other muscles such as cardiac and respiratory are also involved. Moreover, the pathology of some MD disorders has an impact on other organs and tissues as the brain, the skin, the testis, or the eyes. Very rare muscular dystrophies variants are continually identified. To date, more than 50 genes have been determined to be involved in more than 70 inherited muscular dystrophies.² These disorders are usually classified into nine main categories or types: myotonic, Duchenne, Becker, Limb-girdle, facioscapulohumeral, congenital, oculopharyngeal, distal, and Emery-Dreifuss.³

Myotonic syndromes are the most common form in the adult population affecting 1 per 3000 people.⁴ In contrast, Duchenne muscular dystrophy is the most prevalent in childhood and is found in roughly 1 per 5000 boys.⁵ Although individually muscular dystrophies are considered

Biosensors for Bioengineering, Institute for Bioengineering of Catalonia (IBEC), The Barcelona Institute of Science and Technology (BIST), Barcelona, Spain

Corresponding authors:

Juan M. Fernández-Costa, Biosensors for Bioengineering, Institute for Bioengineering of Catalonia (IBEC), The Barcelona Institute of Science and Technology (BIST), Parc Científic de Barcelona (PCB) Edifici Clúster, c/Baldiri i Reixac, 10-12, Barcelona E08028, Spain.
Email: jfernandez@ibecbarcelona.eu

Javier Ramón-Azcón, Biosensors for Bioengineering, Institute for Bioengineering of Catalonia (IBEC), The Barcelona Institute of Science and Technology (BIST), Parc Científic de Barcelona (PCB) Edifici Clúster, c/Baldiri i Reixac, 10-12, Barcelona E08028, Spain.
Email: jramon@ibecbarcelona.eu



Creative Commons Non Commercial CC BY-NC: This article is distributed under the terms of the Creative Commons Attribution-NonCommercial 4.0 License (<https://creativecommons.org/licenses/by-nc/4.0/>) which permits non-commercial use, reproduction and distribution of the work without further permission provided the original work is attributed as specified on the SAGE and Open Access pages (<https://us.sagepub.com/en-us/nam/open-access-at-sage>).

Table 1. Muscular dystrophies classification.

Disease name	Age of onset	Pattern of inheritance (gene affected)	Muscle affected
Duchenne muscular dystrophy (DMD) (OMIM #310200)	Early childhood	XR (DMD; Entrez #1756)	Proximal muscles
Myotonic dystrophies (DM)			
DM1 (OMIM #160900)	Mostly young adulthood, also congenital and childhood-on set	AD (DMPK; Entrez #1760)	Distal muscles
DM2 (OMIM #602668)	Adulthood	AD (CNBP; Entrez #7555)	Proximal muscles
Becker muscular dystrophy (BMD) (OMIM #300376)	Childhood and adulthood	XR (DMD; Entrez #1756)	Proximal muscles
Congenital muscular dystrophies (CMD)			
Bethlem myopathy 1 (BTHLM1) (OMIM #158810)	Congenital	AD (COL6A1; Entrez #1291; COL6A2; Entrez #1292; COL6A3; Entrez #1293)	Proximal muscles
Bethlem myopathy 2 (BTHLM2) (OMIM #616471)	Congenital	AD (COL12A1; Entrez #1303)	Distal muscles
Fukuyama CMD or MD-dystroglycanopathy type A4 (MDDGA4) (OMIM #253800)	Congenital	AR (FKTN; Entrez #2218)	Generalized muscle weakness
MD-dystroglycanopathy type B4 (MDDGB4) (OMIM #613152)	Congenital	AR (FKTN; Entrez #2218)	Generalized muscle weakness
LGMD-dystroglycanopathy type C4 (MDDGC4) (OMIM #611588)	Congenital or early childhood	AR (FKTN; Entrez #2218)	Proximal muscles
CMD with merosin deficiency (MDC1A) (OMIM #607855)	Congenital	AR (LAMA2; Entrez #3908)	Generalized muscle weakness
CMD1B (OMIM #604801)	Congenital	AR (Unknown)	Proximal muscles
CMD1C (OMIM #606612)	Congenital	AR (FKRP; Entrez #79147)	Proximal muscles
CMD1D (OMIM #608840)	Congenital	AR (LARGE1; Entrez #9215)	Generalized muscle weakness
MD-dystroglycanopathy type A1 (MDDGA1) (OMIM #236670)	Congenital-death in the 1st year of life	AR (POMT1; Entrez #10585)	Generalized muscle weakness
MD-dystroglycanopathy type A2 (MDDGA2) (OMIM #613150)	Congenital-death in the 1st year of life	AR (POMT2; Entrez #29954)	Generalized muscle weakness
MD-dystroglycanopathy type A3 (MDDGA3) (OMIM #253080)	Congenital-death in the 1st year of life	AR (POMGNT1; Entrez #55624)	Generalized muscle weakness
MD-dystroglycanopathy type A4 (MDDGA4) (OMIM #253800)	Congenital-death in the 1st year of life	AR (FKTN; Entrez #2218)	Generalized muscle weakness
MD-dystroglycanopathy type A5 (MDDGA5) (OMIM #613153)	Congenital-death in the 1st year of life	AR (FKRP; Entrez #79147)	Generalized muscle weakness
MD-dystroglycanopathy type A6 (MDDGA6) (OMIM #613154)	Congenital-death in the 1st year of life	AR (LARGE1; Entrez #9215)	Generalized muscle weakness
MD-dystroglycanopathy type A7 (MDDGA7) (OMIM #614643)	Congenital-death in the 1st year of life	AR (CRPPA; Entrez #729920)	Generalized muscle weakness
MD-dystroglycanopathy type A8 (MDDGA8) (OMIM #614830)	Congenital-death in the 1st year of life	AR (POMGNT2; Entrez #84892)	Generalized muscle weakness
MD-dystroglycanopathy type A9 (MDDGA9) (OMIM #616538)	Congenital-death in the 1st year of life	AR (DAG1; Entrez #1605)	Generalized muscle weakness
MD-dystroglycanopathy type A10 (MDDGA10) (OMIM #615041)	Congenital-death in the 1st year of life	AR (RXYLT1; Entrez #10329)	Generalized muscle weakness
MD-dystroglycanopathy type A11 (MDDGA11) (OMIM #615181)	Congenital-death in the 1st year of life	AR (B3GALNT2; Entrez #148789)	Generalized muscle weakness
MD-dystroglycanopathy type A12 (MDDGA12) (OMIM #615249)	Congenital-death in the 1st year of life	AR (POMK; Entrez #841897)	Generalized muscle weakness
MD-dystroglycanopathy type A13 (MDDGA13) (OMIM #615287)	Congenital-death in the 1st year of life	AR (B3GALNT1; Entrez #8706)	Generalized muscle weakness
MD-dystroglycanopathy type A14 (MDDGA14) (OMIM #615350)	Congenital-death in the 1st year of life	AR (GMPBB; Entrez #29925)	Generalized muscle weakness
Ullrich CMD type 1 (UCMD1) (OMIM #254090)	Congenital	AD/AR (COL6A1; Entrez #1291; COL6A2; Entrez #1292; COL6A3; Entrez #1293)	Generalized muscle weakness
Ullrich CMD type 2 (UCMD2) (OMIM #616470)	Congenital	AR (COL12A1; Entrez #1303)	Generalized muscle weakness
CMD megaconial type (MDCMC) (OMIM #602541)	Congenital	AR (CHKB; Entrez #1120)	Generalized muscle weakness
Rigid spine muscular dystrophy 1 (RSMD1) (OMIM #602771)	Congenital	AR (SELENO1; Entrez #57190)	Proximal limb and facial muscles
CMD due to ITGA7 (OMIM #513204)	Congenital	AR (ITGA7; Entrez #3679)	Proximal muscles
Emery-Dreifuss muscular dystrophy (EDMD)			
EDMD1 (OMIM #310300)	Adulthood	XR (EMD; Entrez #2010)	Calf muscles and upper extremities
EDMD2 (OMIM #181350)	Adulthood	AD (LMNA; Entrez #4000)	Scapulohumerous muscles
EDMD3 (OMIM #616516)	Adulthood	AR (LMNA; Entrez #4000)	Proximal muscles
EDMD4 (OMIM #612998)	Adulthood	AD (SYNE1; Entrez #23345)	Proximal muscles
EDMD5 (OMIM #612999)	Adulthood	AD (SYNE2; Entrez #23324)	Upper limb muscles
EDMD6 (OMIM #3000696)	Adulthood	XR (FHL1; Entrez #2273)	Proximal muscles
EDMD7 (OMIM #614302)	Adulthood	AD (TMEM43; Entrez #79188)	Proximal muscles

(Continued)

Table 1. (Continued)

Disease name	Age of onset	Pattern of inheritance (gene affected)	Muscle affected
Facioscapulohumeral muscular dystrophy (FSHD)			
FSHD1 (OMIM #158900)	Adulthood	AD (DUX4; Entrez #100288687)	Facial muscles and upper extremities
FSHD2 (OMIM #158901)	Adulthood	AD (SMCHD1; Entrez #23347)	Facial muscles and upper extremities
Limb-girdle muscular dystrophies (LGMD)			
LGMD1A (OMIM #159000)	Adulthood	AD (MYOT; Entrez #9499)	Proximal muscles
LGMD1C (OMIM #607780)	Childhood and adulthood	AD (CAV3; Entrez #859)	Proximal muscles
LGMD1D (OMIM #603511)	Adulthood	AD (DNAJB6; Entrez #10049)	Proximal muscles
LGMD1E (OMIM #602067)	Adulthood	AD (DES; Entrez #1674)	Proximal muscles
LGMD1F (OMIM #608423)	Young adulthood and adulthood	AD (TNPO3; Entrez #23534)	Proximal muscles
LGMD1G (OMIM #609115)	Adulthood	AD (HNRNPDL; Entrez #9987)	Proximal muscles
LGMD1H (OMIM #613530)	Adulthood	AD (unknown)	Proximal muscles
LGMD1I (OMIM #618129)	Young adulthood and adulthood	AD (CAPN3; Entrez #825)	Proximal muscles
LGMD2A (OMIM #253600)	Childhood	AR (CAPN3; Entrez #825)	Proximal muscles
LGMD2B (OMIM #253601)	Young adulthood	AR (DYSF; Entrez #8291)	Proximal muscles
LGMD2C (OMIM #253700)	Childhood	AR (SGCG; Entrez #6445)	Proximal muscles
LGMD2D (OMIM #608099)	Childhood	AR (SGCA; Entrez #6442)	Proximal muscles
LGMD2E (OMIM #604286)	Young adulthood	AR (SGCB; Entrez #6443)	Proximal muscles
LGMD2F (OMIM #604287)	Childhood	AR (SGCD; Entrez #6444)	Proximal muscles
LGMD2G (OMIM #601954)	Childhood	AR (TCAP; Entrez #8557)	Proximal muscles
LGMD2H (OMIM #254110)	Childhood	AR (TRIM32; Entrez #22954)	Proximal muscles
LGMD2I (OMIM #607155)	Childhood and adulthood	AR (FKRP; Entrez #79147)	Proximal muscles
LGMD2J (OMIM #608807)	Adulthood	AR (TTN; Entrez #7273)	Proximal muscles
LGMD2K (OMIM #608808)	Childhood	AR (POMT1; Entrez #10585)	Proximal muscles
LGMD2L (OMIM #611307)	Childhood and adulthood	AR (ANOS; Entrez #203859)	Proximal muscles
LGMD2M (OMIM #611588)	Childhood	AR (FKTN; Entrez #2218)	Proximal muscles
LGMD2N (OMIM #613158)	Childhood	AR (POMT2; Entrez #29954)	Proximal muscles
LGMD2O (OMIM #613157)	Childhood	AR (POMGNT1; Entrez #1605)	Proximal muscles
LGMD2P (OMIM #613818)	Childhood	AR (DAG1; Entrez #55624)	Proximal muscles
LGMD2Q (OMIM #613723)	Early childhood	AR (PLEC1; Entrez #5339)	Proximal muscles
Oculopharyngeal muscular dystrophy (OPMD) OMIM(#164300)	Late-onset	AD (PABPN1; Entrez #8106)	Ocular and pharyngeal muscles. Proximal and distal muscles.
Distal muscular myopathies (MPD1)			
MPD1 (OMIM #160500)	Congenital to adulthood	AD (MYH7; Entrez #4625)	Distal muscles
MPD2 (OMIM #606070)	Adulthood	AD (MATR3; Entrez #9782)	Distal muscles with vocal cords weakness
MPD3 (OMIM #610099)	Adulthood	AD (Unknown)	Distal muscles
MPD4 (OMIM #614965)	Adulthood	AD (FLNC; Entrez #2318)	Distal muscles
MPD5 (OMIM #617030)	Young adulthood	AR (ADSS1; Entrez #122622)	Lower limb muscles
MPD6 (OMIM #618655)	Adulthood	AD (ACTN2; Entrez #88)	Lower limb muscles

OMIM = online mendelian inheritance in man; AD = autosomal dominant; AR = autosomal recessive; XR = X-linked recessive; Entrez = entrez molecular sequence database.

rare diseases, the overall prevalence of combined muscular dystrophies was 16.14 per 100,000,⁶ and therefore, they have a great impact on society.

Palliative treatments are available for these diseases, although there is no cure for any muscular dystrophy to date. Remarkably, in the last decade, some drugs for specific muscular disorders have been developed, including small molecules and antisense oligonucleotides.^{7–11} However, these treatments must demonstrate efficacy and safety in the clinical phases before being widely used in patients. The development of a new drug takes years, even decades, from preclinical studies to reach the market and it is a very costly process.¹² Drug development implies three main stages: discovery, preclinical studies, and clinical trials. During the preclinical stage, extensive studies with *in vitro* and animal models provide preliminary information on the efficacy, toxicity, pharmacokinetics, and safety of a drug candidate. However, the probability of success of a molecule after entering the clinical phases is only 10%.¹³ This low success rate is mostly due to the high toxicity or low efficacy of the drug in humans. This suggests that current preclinical models should be improved to reduce costs and accelerate drug development time. Furthermore, the heterogeneity of muscular dystrophy manifestations anticipates that each patient would respond to treatments differently. Therefore, there is also a clinical need for personalized therapies to target these diseases effectively. Human bioengineered *in vitro* tissues are emerging as new tools for preclinical research.^{14,15} Specifically, bioengineered *in vitro* skeletal muscles would provide more efficient and predictive models to improve drug development for muscular dystrophies. Here, we discuss the recent advances in skeletal muscle tissue engineering, focusing on new human *in vitro* models for muscle analyses and their application in the study of muscular dystrophies. This review was designed with two main purposes: to bring the clinician community closer to the bioengineering technologies for skeletal muscle and to show a general overview of the complexity of muscular dystrophies to researchers working on skeletal muscles tissue engineering.

Skeletal muscle structure and myogenesis regulation

Skeletal muscle is the largest tissue in the body, accounting for almost 40% of body mass.¹⁶ Skeletal muscle architecture is characterized by a very particular and well-described arrangement of muscle fibers, also called myofibers. Groups of myofibers form the fascicles, and bundles of fascicles make up the whole muscle tissue (Figure 1). Myofibers are formed by the fusion of myoblasts to produce multinucleated myotubes, which mature further in myofibers.¹⁷ The dimensions of a single myofiber are approximately 100 μm in diameter and 1 cm in length, and

its nuclei are located along the periphery of the whole fiber. The mature skeletal myofiber contains a highly organized cytoskeleton made up of aligned myofibrils, which are repeating consecutive sections of the functional unit of skeletal muscle, the sarcomere.¹⁸ Sarcomere complex structure is composed of two main alternating sets of protein filaments: thin filaments (α -actin and associated proteins) and thick filaments (myosin and associated proteins), which run parallel to the muscle fiber axis. At a molecular level, the sarcomeric contraction consists of the movement of the myosin heads on actin filaments. Thus, the formation of correctly aligned myofibrils is fundamental for muscle function. So, to engineer skeletal muscle *in vitro*, its complex anatomy structure must be mimicked using biomaterial scaffolds and specific biofabrication techniques.

Muscle development and regeneration are regulated by a hierarchy of myogenic regulatory factor (MRF) family of transcription factors¹⁹ (Figure 2). Stem cells in the muscle are called satellite stem cells (SSCs) and are produced by activation of precursor cells expressing PAX3 and PAX7.^{20,21} The expression of MYF5 and MYOD1 in SSCs induces the myogenic program to produce myoblasts. Myogenesis process continues with the activation of MYOG and MEF2 and the downregulation of MYF5 and MYOD1. Activation of a second wave of MRFs (MYOG and MRF4) induces terminal differentiation of myoblasts into myotubes. Mature myotubes additionally express muscle-specific genes such as the contractile proteins of the muscle as myosin heavy chain (MHC), actin, titin, among others, and a reduction in expression of MYOG.²²

The skeletal muscle extracellular matrix

As mentioned above, the formation of aligned myofibers is an essential factor for skeletal muscle tissue engineering. Nonetheless, it is important to consider that *in vivo*, these fibers are embedded within a 3D scaffold, the skeletal muscle extracellular matrix (ECM), mainly composed of collagens, non-collagenous glycoproteins, proteoglycans, and elastin.²³ Besides being a scaffold for cell-matrix interactions, the skeletal muscle ECM plays a crucial role in skeletal muscle function. For instance, it allows a uniform distribution and transmission of force within muscle and from muscle to tendon. Furthermore, the ECM interactions are critical to maintaining the mechanical homeostasis within the muscle.¹⁸

The skeletal muscle ECM is traditionally classified into three organized layers: endomysium, perimysium, and epimysium (Figure 1). The endomysium (also called basement membrane) surrounds individual myofibers. The perimysium is a thickened ECM that encapsulates the fascicles, and the epimysium is a dense layer that

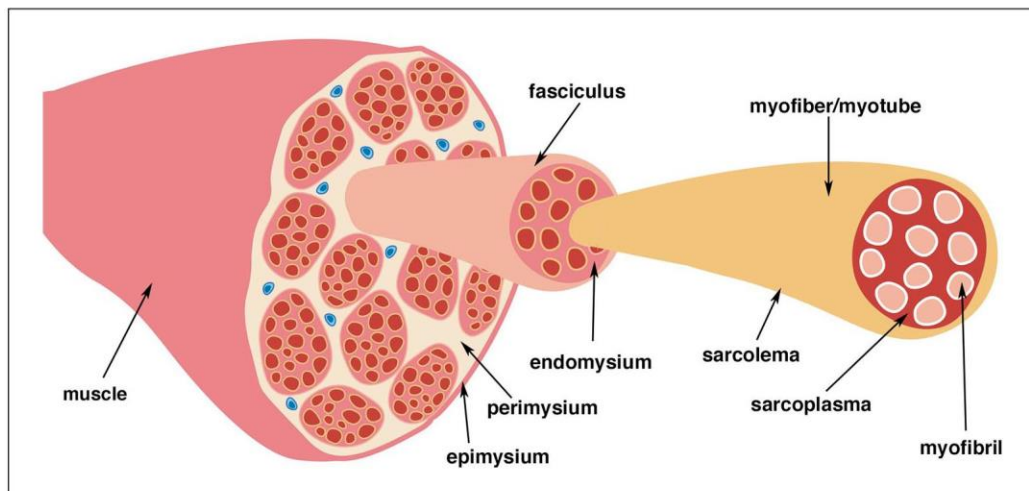


Figure 1. Structure of muscle anatomy. Epimysium covers each muscle. Muscle fibers are grouped forming bundles (fascicles). Each fasciculus is surrounded by perimysium while endomysium surrounds the myofibers. Each individual myofiber or myotube have a membrane (sarcolemma) and is composed of hundreds of myofibrils. Myofibrils are the functional contractile unit of the muscle and are surrounded by sarcoplasm.

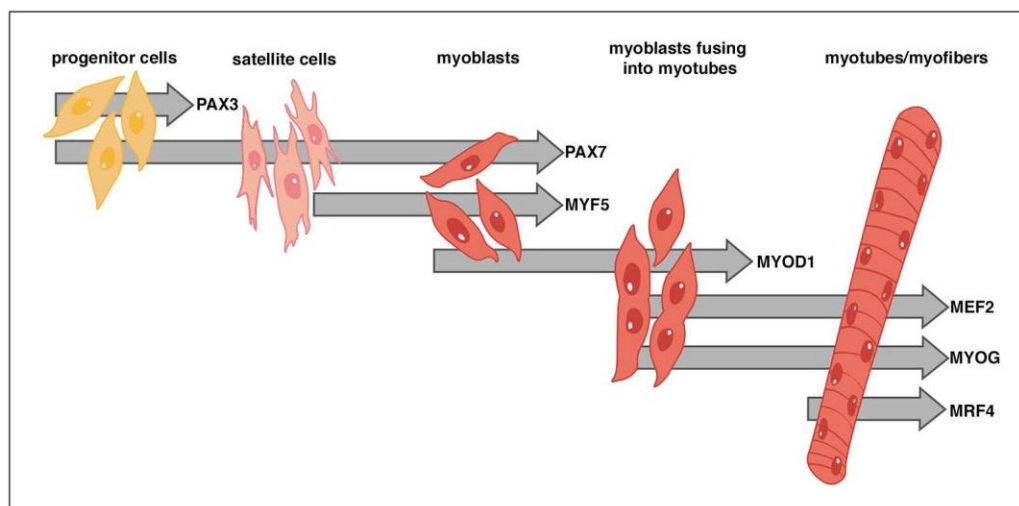


Figure 2. Regulation of myogenic differentiation by a hierarchy of transcription factors. Satellite cells expressing PAX7 derive from the PAX3/PAX7 expressing progenitor cells. Following activation of MYF5 expression in satellite myogenic cells, the myogenic program starts, and MYOD1 expression is activated. Activation of MYOG and MEF2, with downregulation of MYF5 and later MYOD1, marks the start of terminal differentiation into myofibers. Activation of MRF4 happens several days after the induction of differentiation, following a reduction in MYOG expression.

surrounds the whole muscle. However, as the knowledge about the ECM roles and complexity increases, it has been argued that a less simplistic ECM organization should be established.^{18,23,24}

Among the skeletal muscle ECM proteins, collagens are the most abundant, glycoproteins are involved in tissue organization and cell-matrix interactions, and proteoglycans are involved in signaling and tissue regeneration.¹⁸ The basement membrane consists mainly of collagen type IV and laminins, whereas collagen type I is found mostly in the peri- and epimysium. Together all types of collagens provide

structural support and allow tissue mechanotransduction.²⁵ Briefly, fibrillar collagen type I provides tensile strength and rigidity, while collagen type III fibers form a loose mesh that gives elasticity to the inner layers of the intramuscular connective tissue. Moreover, collagen type IV integrates laminins and other proteins into a stable structure. In less abundance, collagen type VI is present in all ECM layers.²³ Interestingly, collagen type VI mutations cause disorders involving both muscle and connective tissue, such as congenital muscular dystrophies as Ullrich CMD type 1 (UCMD1) and Bethlem Myopathy type 1 (BTHLM1) (see Table 1).²⁶

Engineering topographical cues for skeletal muscle 2D culture

Skeletal muscle represents a complex and challenging tissue for *in vitro* generation through tissue engineering. Given the importance of the aligned structure of myofibers for their correct functionality, the main fabrication strategies are focused on providing geometric cues (Table 2). The most recent published approaches to culture myofibers on aligned structures can be classified into three main types: micropatterning, electrospinning, and bioprinting.

Micropatterning

The simplest models for generating skeletal muscle *in vitro* are based on the 2D culture of myoblasts seeded on micro-molded substrates. RNAseq analyses of C2C12 murine myotubes on micropatterned gelatin hydrogels showed that cells display an increased ability to form aligned sarcomeres and increased contractile protein expression, demonstrating the effect of topographic cues in the maturation of muscle cells.²⁷ Another technique to generate 2D micropatterned scaffolds is microcontact printing. For example, Vajanthri and collaborators used the microchanneled flowed plasma process to generate different cell adhesive micropattern coated glass with 3-amino-Propyltriethoxysilane (APTES) and Octadecyltrichlorosilane (OTS).²⁸ Aligned myotubes grew onto stamped micropatterned regions. Micropatterned substrates also emerged as great potential substrates to align and differentiate myoblasts.²⁹ In this study, the authors generated a new platform by crumpling graphene uniaxially (Figure 3(a)). Micropattern dimensions were modulated by applying compressing strain. Culture of C2C12 mouse myoblast on this uniaxially crumpled graphene promoted the alignment and elongation at a single-cell level and enhanced differentiation and maturation of myotubes. Other graphene-based approaches used femtosecond laser ablation to generate a patterned substrate in polyacrylamide hydrogels.³⁰ Studying different pattern distances, the authors concluded that 50 μm of spacing produced the better alignment and maturation of myotubes. Myogenic differentiation could also be improved by applying electrical stimulation to these micropatterned cultures. An alternative approximation used poly(ethylene glycol) (PEG)-based microgrooved hydrogels to provide topographical and electrical stimuli to cells.³¹ To enhance hydrogel electrical properties and cell attachment, poly(3,4-ethylenedioxythiophene) (PEDOT) and tripeptide Arg-Gly-Asp (RGD) were combined with the PEG-hydrogel.

Electrospinning

One of the most common techniques for 2D cell guidance and tissue engineering is electrospinning.³² Electrospinning technique has been successfully used to generate mature

myotubes over microfibrils fibrin bundles.³³ Mechanical strains were applied to enhance the myogenic differentiation of the immature myoblasts. In this study, several strain cycles were tested, and delayed strain onset improved or maintained myogenic outcomes. Electrospinning technique has also been used to co-culture C2C12 murine myoblasts and human umbilical vein endothelial cells (HUVEC).³⁴ To guide the cells and promote their fusion, the authors used Polyvinyl alcohol (PVA)-leached polycaprolactone (PCL) and collagen struts as mechanical supporters with topographical cues. HUVECs-laden alginate bioink was uniaxially electrospun on these supporters. C2C12 myoblasts seeded on this vascularized scaffold formed mature myofibers with striated myosin heavy chain (MHC) protein patterns. Recently, poly(vinylidene fluoride) (PVDF) was used as an electroactive biomaterial to enhance the myoblasts fusion and myogenic maturation due to its piezoelectric properties.³⁵ A piezoelectric material becomes electrically polarized upon a mechanical stimulation.³⁶ This propriety can be used to give an electrical signal to the cells. In this work, C2C12 cells were seeded on an electrospun aligned matrix of PVDF. Charged surfaces improved the fusion of muscle cells into differentiated myotubes.

Bioprinting

Similar to electrospinning, bioprinting and other 3D-based approaches have been widely used to generate highly aligned fibers.^{37–42} E-field printing, a combination of e-field and 3D printing, was used to engineer PCL highly hierarchical scaffolds.³⁷ The growth of C2C12 myotubes on top of these scaffolds enhanced cell alignment and increased myogenic markers. Another technique to promote myotubes alignment is culturing them on bioprinted gelatin methacryloyl (GelMA) over a thermoresponsive poly(N-isopropylacrylamide) (PNIPAm) coated substrate.³⁸ After seeding cells, the temperature was lowered to detach cells from PNIPAm surfaces. With this approximation, directed collective cell migration was regulated (Figure 3(b)). Similarly, microfluidic spun GelMA fibers with have a well-defined surface morphology have been generated by extrusion through a microgrooved mold (Figure 3(c)).^{39,40} Topographical cues on micropatterned GelMA fibers promoted alignment of C2C12 myoblasts and myotube formation. The combination of topographical cues with agrin treatment further enhanced myotube maturation and functionality, as shown by improved contractility under electrical stimulation.⁴⁰ Extrusion of collagen fibers has also been used as geometrical cues to fabricate endothelialized and aligned skeletal muscle.^{41,42} Co-culture murine myoblasts with endothelial cells on nano-fibrillar collagen scaffold strips promotes the formation of highly organized myofibers and microvasculature (Figure 3(d)). Remarkably, the implantation of these scaffolds in injured mice muscle favored vascular regeneration as a promising

Table 2. Novel bioengineering approaches to fabricate skeletal muscle models.

Biomaterial	Cellular type	Biofabrication technique	Highlights	Reference
Alginate—PEO bioink with PLC	C2C12 myoblasts and HUVEC endothelial cells	3D printing and electrospinning	Biophysical and biochemical cues facilitate myoblast alignment	Yeo and Kim ³⁴
Alginate—pluronic PF127	C2C12 myoblasts	3D bioprinting	High-throughput fabrication of small muscle bundles	Mozetic et al. ⁵²
Collagen	C2C12 myoblasts and Human microvascular endothelial cells	Extrusion technique	Implantation of endothelialized skeletal muscle tissue enhances microvascularization	Nakayama et al. ⁴¹
Collagen	C2C12 myoblasts	Micromolding	Development of a 3D myogenesis approach with a vessel embedded system	Wan et al. ⁵⁸
Collagen with gold nanowires	C2C12 myoblasts	3D bioprinting	New bioink with gold nanowires as cell aligners that improve the cell orientation when applying an electrical field	Kim et al. ⁴⁹
Collagen—Matrigel®	Primary myoblasts from mdx mouse model	3D casting	Automated drug screening BAM-based platform	Vandenburgh et al. ³⁸
Collagen—Matrigel®	Primary human myoblasts	3D casting	High throughput micro-muscle platform.	Mills et al. ⁷⁶
dECM	C2C12 myoblasts	Thermal gelation	New biomaterial that enhances muscle regeneration when transplanted	Lee et al. ⁶⁵
dECM	Primary human myoblasts and HUVEC endothelial cells	3D bioprinting	Enhanced muscle regeneration after implantation of prevascularized muscle bundles in a rodent model	Choi et al. ⁸³
dECM—MA	C2C12 myoblasts	3D bioprinting	Development of a biochemical and topographical cued biomaterial scaffold	Kim et al. ³⁷
Fibrin	Human primary muscle progenitor cells (hMPCs)	3D bioprinting	Functional recovery after implantation of multilayered bundles in a rodent model	Kim et al. ⁸¹
Fibrin	Primary human myoblasts	3D casting	Intramuscular drug delivery in vitro model	Gholobova et al. ⁸²
Fibrin	iPSCs from DMD, LGMD other CDM patients	3D casting	Mature myotube recapitulates pathogenic hallmarks	Maffioletti et al. ⁹²
Fibrin	C2C12 myoblasts	Electrospinning	Study of different mechanical strains to improve myogenic outcomes	Somers et al. ³³
Fibrin	C2C12 myoblasts	Micromolding	Fabrication of a high-throughput multiassay platform for the generation of engineered contractile muscle bundles	Christensen et al. ⁵⁹
Fibrin—Gelatin	C2C12 myoblasts	3D bioprinting	Study of force modulation and adaptability of 3D printed muscles	Mestre et al. ⁴⁹
Fibrin—Geltrex®	Primary human myoblasts and human stem cells-derived motoneurons	Hydrogel molding of bundles attached to Velcro® anchors	Myobundles with neuromuscular junctions in long-lasting cultures	Bakooshli et al. ⁸⁰
Fibrin—Matrigel®	Primary human myoblasts	Hydrogel molding of bundles within nylon frame	First functional engineered skeletal muscle	Madden et al. ⁷⁷
Fibrin—Matrigel®	Human induced pluripotent stem cells	Hydrogel molding of bundles within nylon frame	First functional engineered human skeletal muscle from induced pluripotent stem cells	Rao et al. ⁷⁸
Fibrin—Matrigel®	Primary human myoblasts	Hydrogel molding of bundles within nylon frame	Engineered myobundles with the highest specific forces reported to date	Khodabakus et al. ⁷⁹
Gelatin	C2C12 myoblasts	Micropatterning	Enhancing of the expression sarcomeric genes	Denes et al. ²⁷
Gelatin—CMC	C2C12 myoblasts	Cryogelation	New volumetric and conductive anisotropic scaffold that allows microscale constructs	Velasco-Mallorqui et al. ⁶¹
GelMA	C2C12 myoblasts	Microfluidic extrusion device	Patterned surface fibers enhance myogenic differentiation	Shi et al. ³⁹ and Ebrahimi et al. ⁴⁰
GelMA	C2C12 myoblasts	3D casting	Characterization of geometrical confinement and mechanical stiffness of scaffolds	Costantini et al. ⁵⁵
GelMA—Alginate	C2C12 myoblasts	3D bioprinting	New biomaterial with oxygen-generating source	Seyedmahmoud et al. ⁴⁴

(Continued)

Table 2. (Continued)

Biomaterial	Cellular type	Biofabrication technique	Highlights	Reference
GelMA and collagen methacrylate	C2C12 myoblasts, human adipose stem cells and human primary muscle progenitor cells (hMPCs)	3D bioprinting	Functional GelMA-based bioink for highly aligned scaffolding	Kim and Kim ⁴⁸
GelMA on poly(N-isopropylacrylamide) (PNIPAm)	C2C12 myoblasts	Printing	New method to study the regulation of cell migration	Du et al. ³⁸
GelMA, CMCMA—GelMA, AlgMA—GelMA and PEGDA—GelMA	C2C12 myoblasts	3D Bioprinting	Characterization of different GelMA composite biomaterials for skeletal muscle tissue engineering	García-Lizarribar et al. ⁵⁰
GelMA—Alginate	C2C12 myoblasts	3D Bioprinting	A new method to induce macroscale cell alignment with multi-layered scaffolds	Lee and Yeong ⁶⁵
GelMA—CMCMA	C2C12 myoblasts	Micromolding	Integration of skeletal muscle tissue with microfluidic sensing platform	Ortega et al. ⁵⁶
Graphene	C2C12 myoblasts	Micropatterning	New graphene 2D platform that enhances cell alignment and differentiation	Kim et al. ⁴⁹
Graphene oxide—polyacrylamide	C2C12 myoblasts	Micropatterning	Development of a conductive multifunctional biomaterial that enhances myogenic maturation by applying electrical pulse stimulation	Park et al. ³⁰
Laminin, fibrin, or Matrigel® OTS and APTES	Primary myoblasts from DMD patient C2C12 myoblasts	2D micropatterning Micropatterning	Myotubes with DMD pathological hallmarks New method of micropatterning to obtain aligned muscle cultures	Serena et al. ⁹¹ Vajanthri et al. ²⁸
Oxidized alginate—Gelatin	C2C12 myoblasts	3D Bioprinting	Easy method to align cells by combining bioprinting with appropriate shear stress	Djstler et al. ⁴⁷
PEG—Fibrin	C2C12 myoblasts	3D bioprinting	Novel approach to generate skeletal muscle using a self-made 3D bioprinting	Costantini et al. ⁵¹
Poly lactic-co-glycolic acid (PLGA)	C2C12 myoblasts	E-jet 3D printing	3D printed platform with 50 µm fibrillar gap enhances cell adhesion and proliferation	Chen et al. ⁵³
Poly(ethylene glycol) (PEG)—poly(3,4-ethylenedioxythiophene) (PEDOT)	C2C12 myoblasts	Micropatterning	Fabrication of a conductive microgrooved hydrogel for myogenic differentiation	Gong et al. ³¹
Poly(lactic-co-glycolic acid) (PLGA)	C2C12 myoblasts	Microfluidic droplet emulsion	Generation of a porous spheres microcarriers for cell delivery	Kankala et al. ^{4,62}
Poly(vinylidene fluoride) (PVDF)	C2C12 myoblasts	Electrospinning	Piezoelectric scaffold enhances in vitro muscle regeneration	Ribeiro et al. ³⁵
Polycaprolactone (PCL)	C2C12 myoblasts	E-field assisted 3D printing	New technique to generate highly aligned skeletal muscle tissue	Kim et al. ³⁷

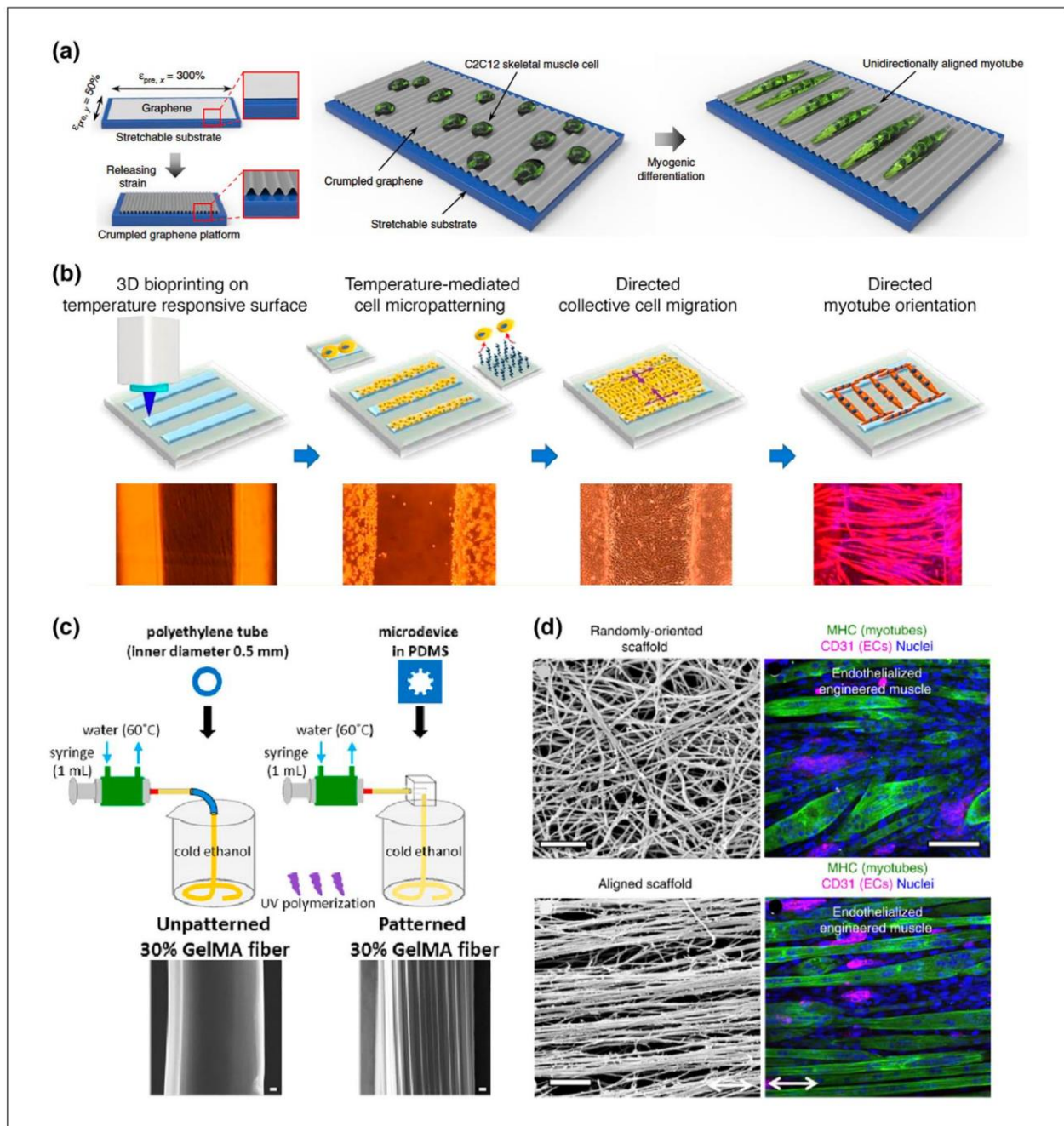


Figure 3. Engineering topographical cues for the 2D culture of skeletal muscle. (a) Fabrication of an anisotropically crumpled graphene platform by releasing the elastomeric substrate on which a graphene film was attached. C2C12 cells were cultured on top of these substrates to differentiate and align C2C12 cells on crumpled graphene. Adapted from Kim et al.²⁹. (b) Gelatin methacryloyl (GelMA) hydrogel micropatterns were 3D printed on a thermo-responsive polymer (poly(N-isopropylacrylamide), PNIPAm). Temperature control was used to promote directed collective C2C12 cell migration on the GelMA patterns to induce myotube formation and orientation. Adapted with permission from Du et al.³⁸. Copyright 2019 American Chemical Society. (c) Schematic representation of the fabrication process of unpatterned and micropatterned GelMA fibers. Field emission-scanning electron microscope images showing surface structures of the GelMA fibers. Scale bars: 20 μm . Adapted with permission from Ebrahimi et al.⁴⁰. (d) Characterization of endothelialized engineered murine muscle. Scanning electron microscopy images of randomly oriented or aligned scaffold nanofibers. Confocal microscopy images showing myosin heavy chain (MHC, green) and CD31 (magenta) staining in differentiated myotubes in randomly oriented or aligned scaffolds. Adapted from Nakayama et al.⁴¹. The images in panel (c) are not published under the terms of the CC-BY license of this article. For permission to reuse, please see Ebrahimi et al.⁴⁰.

treatment of volumetric muscle loss.⁴¹ In summary, the results obtained by micropatterning, electrospinning, and bioprinting approaches confirm that the geometrical cues are fundamental for engineering mature myotubes *in vitro*.

3D Engineering for skeletal muscle culture

Bioengineering approaches in 2D models have been useful to study biomaterials and the importance of the topological cues for *in vitro* culture of skeletal muscle tissue. However, these techniques do not resemble the environment of the native skeletal muscle. For this reason, three-dimensional scaffolds have become the gold standard to generate skeletal muscle tissue. In order to mimic the extracellular environment and the native cellular morphology, the main bioengineering strategy is focused on the 3D encapsulation of muscular cell precursors in biocompatible materials. In the last years, 3D bioprinting,^{43–54} hydrogel molding,^{55–59} and microporous scaffolds^{60–62} have been implemented to fabricate skeletal muscle tissues.

3D Bioprinting

Several biomaterials can be used as bioinks to print encapsulated myoblasts in various 3D structures to obtain aligned myotubes. Among these, GelMA and other methacrylated polymers are the most used biomaterials in bioprinting due to its photocrosslinkable properties. 3D bioprinting was used to fabricate tissue constructs using GelMA with alginate and C2C12 cells.⁴⁴ Interestingly, the metabolic activity of myotubes was improved by adding calcium peroxide, an oxygen-generating particle, to the bioink. Oxidized alginate has also been used in combination with gelatin as a bioink. The cells orientate with the proper nozzle size and extrusion pressure due to the shear stress during the bioprinting process.⁴⁷ The cells grow in the direction of printing, migrate to the hydrogel surface over time, and differentiate into aligned myotubes. 3D printed GelMA-alginate hydrogels with Pluronic F-127 as a sacrificial layer were used to induce a macroscale level of controlled cell alignment with angle variation. The variation in the grid pattern angles was designed to mimic the fibril orientation of native tissues, where angles of cell alignment vary across the different layers. In a similar approach, GelMA and collagen methacrylate were bioprinted and UV crosslinked to generate different 3D structures and obtain mature aligned myotubes.⁴⁸ To better control the cell alignment, cell aligners could be added to the bioinks. One way to achieve this was by printing collagen with gold nanowires and applying a field into this extruded biomaterial. These gold nanowires were aligned following the desired directionality by applying an electric field. The use of gold nanowires enhanced myoblast alignment inside the hydrogel by contact guidance.⁴⁹ Moreover, the addition of gold

nanowires improves the electrical properties of the scaffolds. These works used bioinks based on natural polymers as gelatin or collagen due to their biocompatibility. However, these materials are degradable by mammalian cells, causing a loss of the hydrogel structure, limiting long-term cell cultures. To overcome this, materials that are non-degradable by mammalian cells have been combined with these natural polymers to improve the mechanical properties of the scaffolds. C2C12 cells were encapsulated in different combinations of GelMA-based composite bioinks.⁵⁰ A structure of hydrogel filaments was bioprinted with these bioinks (Figure 4(a)). The combination of GelMA with methacrylated carboxymethylcellulose (CMCMA) resulted in the most suitable properties for skeletal muscle tissue engineering. Remarkably, the GelMA-CMCMA composite biomaterial has been used for the long-term culture of C2C12 myotubes. The 3D structure of the hydrogel remained in time for 3 weeks, enhancing myotube maturation.⁵⁷ Alternative combinations of natural and synthetic biomaterials are suitable for bioprinting skeletal muscle cells. Aligned myoblast-laden hydrogels of PEG-fibrinogen have been produced using microfluidic-enhanced 3D bioprinting.⁵¹ Moreover, Pluronic/alginate blends have been investigated as a model system for culture of C2C12 murine myoblast.⁵² Fabricated constructs exhibited high cell viability, as well as a significantly improved expression of myogenic markers. To mimic the extracellular matrix, poly lactic-co-glycolic acid (PLGA) multilayered scaffolds were made with E-jet 3D printing.⁵³ By comparing different fibrillar gaps in the scaffolds, the authors concluded that 50 μm gaps enhance cell adhesion and proliferation. In all the previous works, the bioprinting design was based on lines or meshes to guide the alignment of myotubes. Alternatively, hydrogels can be printed to compact around post structures and generate skeletal muscle tissue.^{45,46,54} These kinds of platforms allow the force measurement of skeletal muscle after electrical stimulation. Skeletal muscle tissue contractions cause the bending of the pillar. This displacement is used as a proportional measurement of the muscle bundle forces.

Micromolding

To generate aligned scaffolds, an alternative technique to bioprinting is hydrogel micromolding. Molds of polydimethylsiloxane (PDMS), a biocompatible transparent polymer, are the most used to transfer aligned micropatterns to the 3D hydrogels.^{63,64} Optimal stiffness of hydrogels for skeletal muscle bioengineering was determined by changing GelMA concentration and UV crosslinking time. Using molds with channels of different widths, the authors investigated the effect of geometrical confinement and hydrogel stiffness for C2C12 myotube culture.⁵⁵ The best results were obtained with the thinnest 0.5 mm channels and a low stiffness between 1 to 3 kPa. Murine skeletal muscle tissue

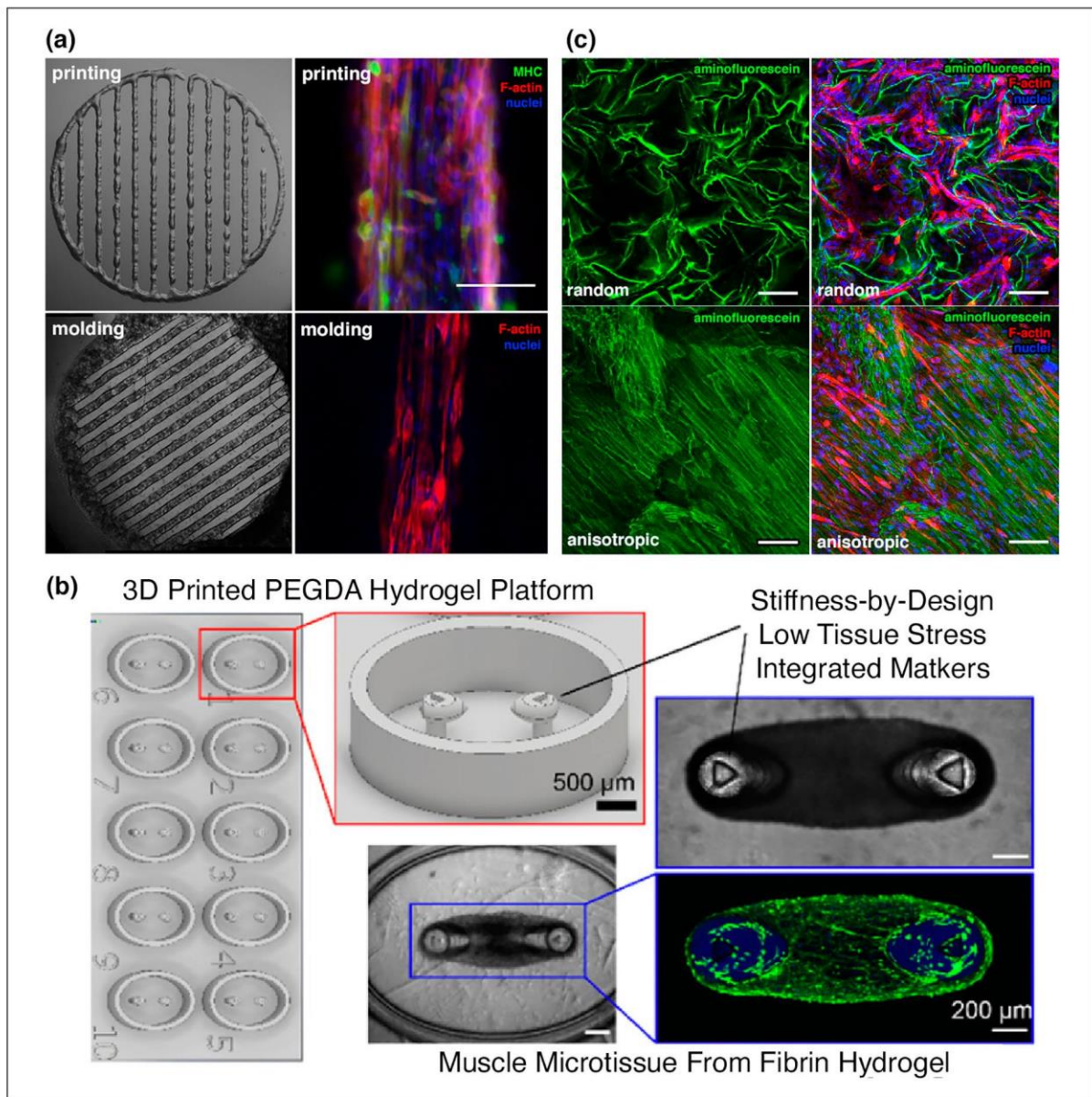


Figure 4. Engineering strategies for the 3D culture of skeletal muscle tissue. (a) C2C12 myotubes formation in biprinted or molded composite hydrogels. Top view images of the composite hydrogels after fabrication. Confocal microscopy showing F-actin in red, MHC in green, and nuclei in blue. Scale bar: 200 μm. Adapted with permission from Garcia-Lizarribar et al.⁵⁰ and authors unpublished results. (b) Multi-assay 3D printed poly(ethylene glycol) diacrylate (PEGDA) hydrogel platforms for casting fibrin hydrogel muscle bundles. Adapted with permission from Christensen et al.⁵⁹. Copyright 2020 American Chemical Society. (c) Confocal microscopy images showing aminofluorescein-marked cryogels in green, cells marked with phalloidin in red and cell nuclei counterstained in blue with DAPI. Scale bars: 100 μm. Adapted from Velasco-Mallorqui et al.⁶¹. The images in panel (a) are not published under the terms of the CC-BY license of this article. For permission to reuse, please see Garcia-Lizarribar et al.⁵⁰.

has also been generated by micromolding of GelMA-CMCMA hydrogels.^{56,57} Here, C2C12 cells were encapsulated by photomold patterning of the hydrogel using a microgrooved PDMS stamp (Figure 4(a)). Interestingly, these tissues were implemented in cytokine sensing platforms to analyze responses to biological and electrical stimuli. Micromolding and micromilling techniques were combined with posts to develop a new organ-on-a-chip set

up with a vessel embedded system.⁵⁸ To vascularize the engineered muscle bundle, C2C12 and HUVEC were cocultured by using collagen and a sacrificial layer and supported by pillars. To mass-produce structures with posts or cantilevers, Christensen et al. described a stereolithographic method to 3D print poly(ethylene glycol) diacrylate (PEGDA) hydrogels with high precision and high accuracy (Figure 4(b)).⁵⁹ These PEGDA platforms with

anchored cantilevers were used to cast fibrin hydrogel muscle bundles around these pillars.

Extracellular matrix derived materials obtained by decellularization (dECM) have emerged as novel natural hydrogels to engineer muscle tissue.^{65,66} These dECM-derived hydrogels contain growth factors, cytokines, proteoglycans, and structural adhesive proteins, which represent tissue-specific biochemical cues.⁶⁷ Murine skeletal muscle generated with dECM scaffolds present more mature myotubes than with collagen scaffolds.⁶⁵ Moreover, a significantly greater number of myofibers were observed when compared to collagen scaffolds after implantation of both engineered skeletal tissues in a rabbit tibialis anterior (TA) muscle defect model. Going a step further, methacrylation of dECM allows bioprinting and photocrosslinking of the hydrogels, providing topological cues for skeletal muscle engineering.⁶⁶

Microporous scaffolds

An alternative fabrication method that allows the generation of millimeter range scaffolds is cryogelation.⁶⁰ Cryogels are microporous scaffolds with a pore range from a few micrometers up to hundreds of micrometers.⁶⁸ After freezing the polymer solution, ice crystals are formed. Once the cryogel is thawed, the ice crystals leave behind empty pores. The pore morphology can be modulated by applying different freezing directionalities.^{69,70} Highly aligned morphology is a necessary geometrical cue for skeletal muscle maturation. For this reason, anisotropic gelatin-cellulose cryogels were generated to engineer volumetric skeletal muscle using C2C12 myoblasts.⁶¹ Anisotropic cryogels improve cell alignment, myotube fusion, and myogenic maturation (Figure 4(c)). Moreover, the addition of carbon nanotubes (CNTs) to the cryogel improves the electrical properties of the scaffolds, which enhances early myogenic maturation steps when electric pulse stimulation is applied. Interestingly, these gelatin-cellulose cryogels are easy to handle without affecting their shape. Therefore, this technique has strong possibilities for tissue engineering and organ-on-a-chip technologies.

Microporous scaffolds can also be used for skeletal muscle cell delivery by generating highly open porous microspheres (HOMPs).⁶² These microspheres were fabricated of biocompatible PLGA by microfluidic droplet emulsion. These HOMPs with interconnected pores facilitated a high cell adhesion rate, continuous proliferation, and augmented myogenic differentiation of C2C12 after transplantation in mouse muscle.

Computational modeling

Despite the promising potential of all these approaches to generate 3D muscle tissues *in vitro*, there are still many technical limitations. To complement the lack of chemical

or mechanical information of many experimental models, computational modeling has gained a relevant role. Using computational methodologies as agent-based model (ABM) for individual cell modeling, or finite element method (FEM) for cellular population density, it is possible to study the cell behavior inside scaffolds and between cells. As a clear example of this combination between technical and computational methods, Torri et al.⁷¹ used the data from the previous work from Smith et al.⁷² to analyze the muscle cell behavior *in silico*. They applied both modeling approaches with successful results achieving a good resemblance between their approximations *in silico* and the *in vitro* studies. These analyses point to the potential of computational modeling to predict uncertain variables and complement *in vitro* experiments.

Functional human skeletal muscle tissue models

In the last decade, skeletal muscle bioengineering techniques have been developed using mainly murine myoblasts as a cell model. These studies shed light on important features for skeletal muscle tissue engineering, such as topological cues, biomaterials, and biochemical factors. The next step in skeletal muscle bioengineering is incorporating human cells to obtain more relevant models for muscular dystrophies. Human skeletal muscle tissue models have been developed from primary and immortalized human myoblasts and human induced pluripotent stem cells (hiPSCs) [reviewed in⁷³]. It has recently been shown that human amniotic mesenchymal stem cells (hAMCs) can undergo myogenic differentiation. Moreover, hAMCs express key growth factors that promote endothelial cell proliferation and angiogenesis, representing a great advantage as a cell source for skeletal muscle tissue engineering.⁷⁴

In general, human myogenic precursor cells are encapsulated in hydrogel scaffolds that aim to mimic the 3D environment of native muscle tissues. The most common hydrogels are those of natural origin, especially collagen,^{75,76} fibrin,^{77–82} and dECM.⁸³ The main fabrication strategies have been hydrogel molding^{75–80} or 3D printing^{81–83} (Table 2). In this way, cell alignment is achieved through passive tension, allowing long-term cell culture, and enhancing muscle maturation and function. The first 3D skeletal muscle tissues reported consisted of myoblasts encapsulation in a collagen I matrix that contracts around pillars.^{84,85} The contraction of the matrix promotes cell alignment in the direction of the anchoring points, producing long multinucleated myofibers.⁷⁵ Collagen I is one of the main components of the skeletal muscle extracellular matrix.²³ However, it has been observed that myogenic maturation and contractile force of the tissue can be compromised by the relatively high stiffness of the collagen hydrogel, especially for large macroscopic constructs.^{25,86} For this reason, in the last years, efforts have been directed

to incorporate materials with better mechanical properties. Fibrin composite hydrogels have resulted in the most promising materials to generate functional skeletal muscle constructs due to their ability to be remodeled by cells and induce ECM synthesis.⁸⁷

Functional human skeletal muscle tissues or bioartificial muscles (BAMs) were developed for the first time in the Bursac lab using primary human myoblasts. By molding fibrin-Matrigel® hydrogels within PDMS molds inside a nylon frame, the authors created muscle 3D bundles⁷⁷ (Figure 5(a)). In this platform, active force measurements were performed in response to electrical and biological stimulation. In 2018, following the same biofabrication approach, the authors reported the generation of skeletal muscle tissues derived from direct reprogramming of hiP-SCs.⁷⁸ Overexpression of PAX7 was induced to generate satellite cell-like cells. Remarkably, human muscle 3D bundles were kept in culture for up to 4 weeks, being the longest culture time reported to the date. Of note, muscle constructs presented a correct membrane localization of dystrophin and generated active twitch and tetanic contractions. Interestingly, after 4 weeks of culture, these tissues retained a pool of PAX7+ cells together with MYOG+ myotubes, mimicking the satellite-cells presence in native muscle. Although these models present different myotube maturation levels, it has been shown that electrical stimulation training enhances myofiber hypertrophy and metabolic flux.⁷⁹ Electrical stimulation training during 1 week of human myoblasts-derived muscle 3D bundles promoted an increase of myotube diameter by 40%. Using this electrical stimulation protocol, the authors measured the highest specific forces reported to date for an engineered human muscle (19.3 mN/mm²). A more complex human skeletal muscle model was achieved by coculturing primary human myoblasts with human stem cells-derived motoneurons in a fibrin-based hydrogel.⁸⁰ Briefly, Fibrin-Geltrex® hydrogels were fabricated by molding with Velcro® anchors that acted as artificial tendons to apply uniaxial tension. The resulting bioengineered human skeletal muscle tissues were able to form neuromuscular junctions (NMJs) in a long-lasting culture for up to 3 weeks (Figure 5(b)). NMJs play a key role in several muscular dystrophies,⁸⁸ which could be modeled following this innovative approximation.

3D bioprinting has also been applied to fabricate human skeletal muscle bundles.^{81,83} Cell-laden fibrin bioink was bioprinted using gelatin as a sacrificial material to generate organized multilayered muscle bundles supported by a PCL pillar structure.⁸¹ Myofibers in these bioartificial muscles were densely packed and highly aligned. The generated constructs were studied *in vivo*, where they achieved 82% of functional recovery in a rodent model of tibialis anterior muscle defect at 8 weeks of post-implantation. Good integration with host vascular and neural networks was observed. Alternatively, dECM have been used as a

bioink for 3D printing of human skeletal muscle bundles.⁸³ Primary human myoblasts were printed with dECM from porcine muscular tissues in granule-based reservoirs. Moreover, coaxial printing with endothelial cells, using porcine blood vessel-derived dECM bioink, has allowed the prevascularization of these muscle bundles (Figure 5(c)). Implantation of these prevascularized muscle bundles in an injured muscle rodent model resulted in the high viability of the cells without generating hypoxia and enhanced *de novo* muscle formation.

Bioartificial muscles have been recently tested as drug screening platforms. Human myoblasts encapsulated in fibrin hydrogels were introduced in a device with a stereotactic setup that allows controllable injection at BAMs.⁸² While most of the biological stimulation assays in 2D and 3D *in vitro* models are performed by adding a compound to the culture media, this setup allows modeling intramuscular drug delivery *in vitro*. Using spectrophotometry and luminescence, the release of the injected compounds and their metabolites were measured over time. Although these models are useful for intramuscular drug injection studies, their relatively large size limits their potential as a drug screening platform. BAMs fabrication requires large numbers of cells, which can be costly and difficult to obtain. Current microfabrication technologies have allowed the miniaturization of these tissues to obtain high-throughput systems.^{46, 76, 89, 90} For example, a 96-well micro-muscle platform using primary human myoblasts.⁷⁶ Cells were encapsulated in a collagen-Matrigel® composite matrix around micropillars. The authors affirmed that with this approach, they could reduce the size, reagents, and cost by a factor of ≈ 25 compared to the state-of-the-art skeletal muscle bioengineering approaches mentioned above.^{77,78} However, the reported specific forces and protein expression levels obtained with this miniaturized system are representative of immature muscle in a fetal-like state. Hence, intensive efforts in training and maturation of the micro-BAMs are needed to develop a successful high-throughput screening platform.

Modeling muscular dystrophies using tissue engineering

The intrinsic heterogeneity of muscular dystrophies means that the future of effective treatments for patients lies in personalized medicine. To date, mutations that cause specific muscular dystrophies have been described in more than 50 genes (Table 1). As a consequence of this genetic heterogeneity, specific muscle types are affected with a variable degree of progression in the dystrophic syndromes. Moreover, in some muscular dystrophies, disease progression and severity depend on individual patients. Therefore, developing *in vitro* bioengineered tissues in the laboratory from patient-derived cells is necessary to study personalized therapies. To date, much effort has been put

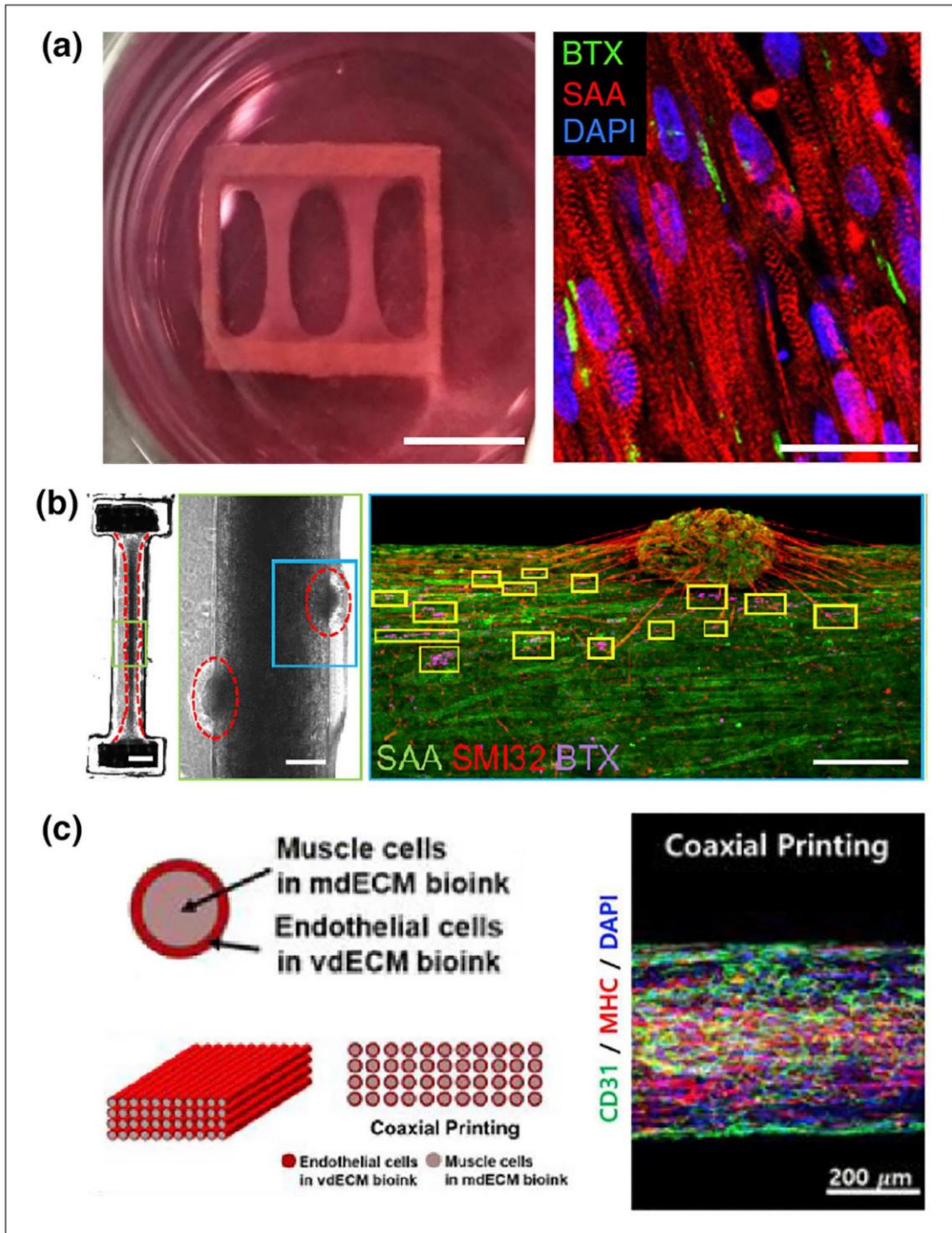


Figure 5. Human 3D engineered skeletal muscles. (a) Structure of hiPSC-derived muscle bundles anchored within a nylon frame. Scale bar: 5 mm. Representative longitudinal section of 2-week differentiated bundles showing aligned, cross-striated myotubes SAA=sarcomeric alpha-actinin, BTX= α -bungarotoxin labeling acetylcholine receptors (AChR) and DAPI counterstain myotube nuclei. Scale bar=25 μ m. Adapted from Rao et al.⁷⁸. (b) Stitched phase contrast image of a representative 3D skeletal muscle-motor neuron (MN) co-culture. Neuromuscular tissue is outlined with a red dashed line in the left panel. The region outlined in the green box is magnified in the image to the immediate right. Red dashed lines in the right panel outline motoneuron clusters. Scale bars: 2 mm (left panel) and 200 μ m (right panel). Adapted from Bakooshi et al.⁸⁰. (c) Schematic representation of coaxial printing. Immunofluorescent image of a 3D printed muscle construct CD31=cluster of differentiation 31 labeling endothelial cells, MHC=myosin heavy chain, and DAPI=stained nuclei. The images were taken from the center of the construct. Adapted with permission from Choi et al.⁸³. The images in panel (c) are not published under the terms of the CC-BY license of this article. For permission to reuse, please see Choi et al.⁸³.

into developing better scaffolds or studying new biofabrication methods to develop skeletal muscle tissues *in vitro*. However, few works have introduced patient-derived cells, going a step further to create these personalized platforms. One of the first approximations was to culture myoblasts from Duchenne muscular dystrophy (DMD) patients on micropatterned polyacrylamide hydrogels functionalized with either laminin, fibronectin, or Matrigel®.⁹¹ In this work, the authors functionalized the surface in parallel lines by micro-contact printing of these adhesion proteins. After 7 days of culture onto these hydrogels, the cells formed mature aligned myotubes with sarcomeric organization. Remarkably, myotubes cultured onto hydrogel with Matrigel® showed the highest level of expression of the muscle maturation markers as myosin heavy chain II and α -actinin. Moreover, DMD myotubes showed particular pathological hallmarks, such as the decreased expression of dystrophin, while the formation of sarcomeres remained unchanged. Although mature aligned myotubes could be obtained by culturing patient cells onto functionalized micropatterned polyacrylamide hydrogels, these 2D models do not represent the complexity of skeletal muscle tissues. In a recent study, human induced pluripotent stem cells (hiPSCs) were used to generate 3D engineered skeletal muscle tissues.⁹² The authors cultivated human hiPSCs derived from Duchenne (DMD), limb-girdle, and other congenital muscular dystrophy patients encapsulated in fibrin hydrogels (Figure 6(a)). To mechanically stimulate myogenic differentiation, the hydrogels were cultured under tension. The resulting tissues showed mature myotube markers and recapitulated the pathogenic hallmarks of these muscular dystrophies. The authors investigate whether the 3D nature of the engineered skeletal muscle tissues would facilitate the detection of pathological hallmarks that are less evident in standard 2D cultures. To examine this, they generated artificial muscles from patient-derived hiPSC with muscular dystrophies caused by mutations in the LMNA gene. These diseases are also called laminopathies, and abnormalities in nuclear morphology are a key histological feature. LMNA mutant hiPSCs from patients with skeletal muscle laminopathies were used to create engineered skeletal muscle tissues, referred to by their mutation (i.e. LMNA L35P or LMNA R249W). Remarkably, 3D nuclear reconstruction of the engineered muscles highlighted features that were less prominent in traditional monolayer cultures. All mutant LMNA 3D engineered muscles showed a significant proportion of cells with nuclear aberrations (Figure 6(b)). These results demonstrate that these bioengineered skeletal muscle tissues from patient-derived cells are great tools to study the pathogenic pathways of muscular diseases and assay potential drugs. Nevertheless, the use of these platforms to test potential treatments for muscular dystrophies has not been reported yet. In 2009, Vandenburg and colleagues developed an automated drug screening platform

using contractile muscle tissue engineered from dystrophic myoblasts.⁹⁰ Primary myoblasts from the DMD mouse model (mdx mice) were encapsulated in a collagen-Matrigel® matrix and cast around two PDMS micro-pillars to engineer miniature bioartificial muscle (mBAMs).⁴⁶ These dystrophic mBAMs were electrically stimulated, and the force generation was measured. Then 31 drugs with potential anti-DMD effects were screened by measuring changes in force generation. Eleven drugs increased the dystrophic mBAMs tetanic force, similar to the response of DMD patients to many identical compounds. These results demonstrate the potential of this platform as a preclinical model. However, the use of mouse-derived cells is an important limitation of this approach since the heterogeneity of muscular dystrophy patients is not considered. Therefore, the integration of engineered skeletal muscle tissue from patient-derived cells in these automated drug screening platforms will bring powerful preclinical tools for these diseases.

Conclusions and perspectives

The latest advances in skeletal muscle tissue engineering have demonstrated the relevance of geometrical cues for the fabrication of *in vitro* muscle models. Aligned structures guide myotubes fusion and enhance the maturation of the myofibers.^{37,39–42} Structured scaffolds can be obtained by bioprinting or molding biomaterials. Of note, the biomaterials for muscle engineering must provide mechanical support and allow nutrient diffusion through the scaffolds. Several studies conclude that electrical stimulation and mechanical tension favor the maturation of the tissues.^{35,61,79} Current studies to develop human functional bioartificial muscle use fibrin-based hydrogels. Fibrin composite matrices have tunable mechanical properties, can be remodeled by cells, and allow long-term cultures.⁷⁸ The biomaterials developed to date successfully provide geometrical and mechanical cues for engineered skeletal muscle. In the native muscle, the ECM not only acts as a scaffold but is essential for cell signaling. Accordingly, the future biomaterials for skeletal muscle tissue engineering should combine physical and biochemical properties that better mimic the complexity of native ECM. Extensive works have developed new fabrication techniques and biomaterials compositions to obtain functional skeletal muscle tissues. Nevertheless, high maturation levels of myofibers have not yet been reached. Thus, the bioartificial tissues have not accurately modeled functional adult muscles. Several approaches have recently attempted to improve the maturation of the *in vitro* muscles, for example, implementing electrical stimulation training protocols and co-cultures.^{79,80,83} Furthermore, incorporating endothelial cells to vascularize the tissues or innervation of the tissue with motoneurons are emerging strategies to obtain more complex skeletal muscle models. Innervation of

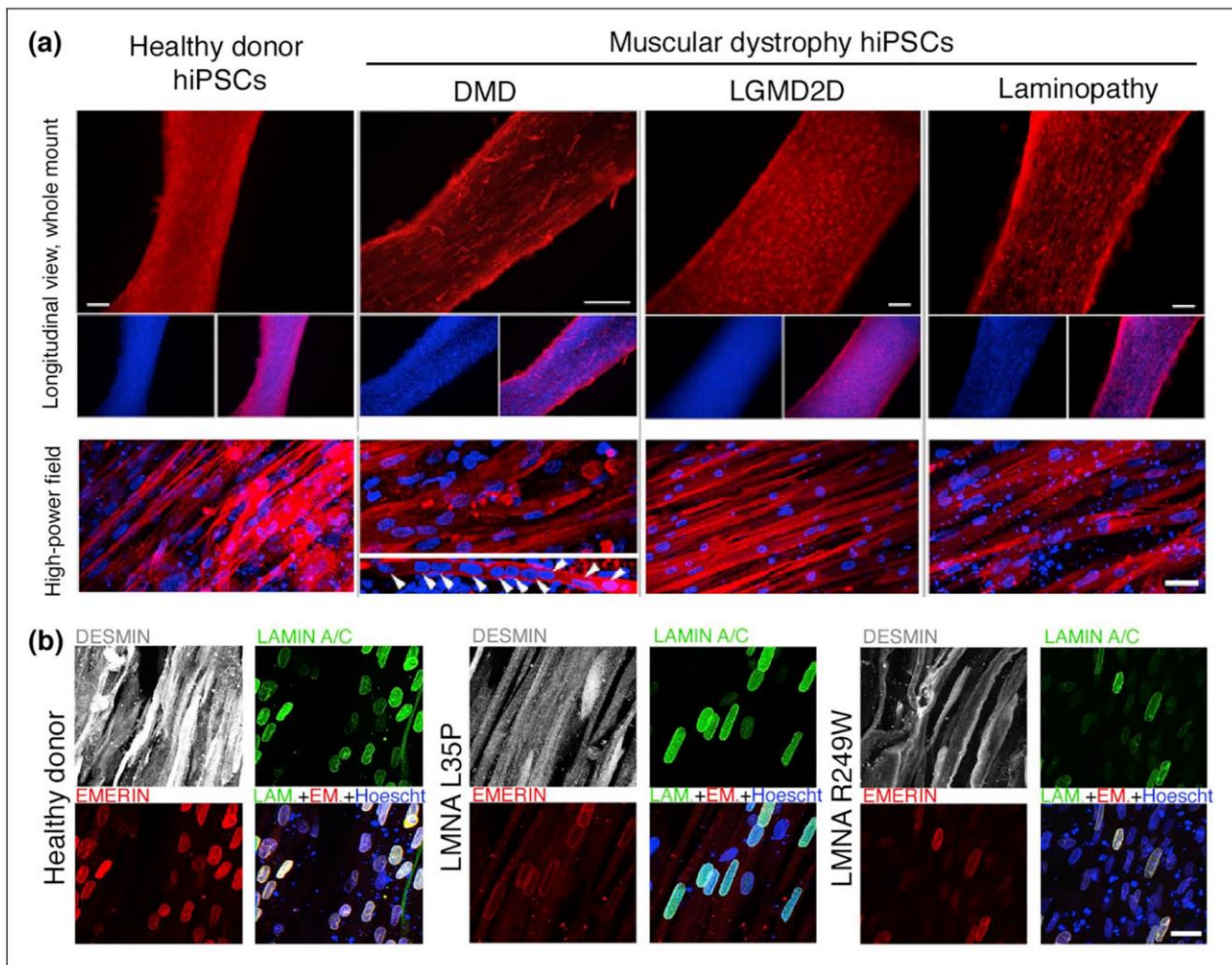


Figure 6. Modeling muscular dystrophies using tissue engineering. (a) 3D artificial skeletal muscle constructs derived from healthy and dystrophic hPSCs. Immunofluorescence for myosin heavy chain (MyHC) on muscle constructs derived from hESCs and dystrophic hiPSCs (DMD, LGMD2D, and skeletal muscle LMNA) differentiated in 3D for 10 days. Nuclei are counterstained with Hoechst. Arrowheads: multinucleated myotubes. Scale bars: top 250 μm , bottom 25 μm . (b) Confocal (z stacks merge) immunofluorescence for DESMIN (myotubes), LAMIN A/C, and EMERIN (nuclear lamina) on hiPSC-derived (healthy and LMNA mutant) artificial muscles. Hoechst: nuclei. Scale bars: 15 μm . Adapted from Maffioletti et al.⁹²

muscle tissues with motoneurons is key for tissue maturation. Unfortunately, the protocols to obtain and co-culture motoneurons are complicated and not very well established. Hence, intensive research on co-culture techniques is one of the main future challenges. On the other hand, angiogenesis is still an important issue in tissue engineering. To date, full vascularization of engineered skeletal muscle tissue has not been achieved. Similar to motoneurons, it is essential to optimize protocols for co-culture. Besides, to mimic vascularized tissues, a specialized research field is focused on generating *in vitro* angiogenesis. The future perspective will be the confluence of both research areas to recreate the extensive network of blood capillaries in skeletal muscle.

Drug screening platforms exploiting new bioengineered skeletal muscle tissue models are promising tools to find treatments for muscular dystrophies. Interestingly, the

integration of patient-derived cells to fabricate these bioartificial muscles could fill the gap in preclinical studies accelerating drug development. Moreover, patient-derived bioartificial muscles would allow testing personalized treatments *in vitro*, which are crucial due to the intrinsic heterogeneity of muscular dystrophy pathologies. Going a step further, these patient-derived bioartificial skeletal muscles can be integrated into microfluidic devices (organ-on-a-chip) with biosensors.^{56,93,94} These microfluidic chips permit the precise control of drug administration. In addition, muscle metabolism and disease-specific markers could be analyzed in real-time. Classically, the outcomes of these drug experiments are measured at time series or end-points. The challenge in this technological field is to integrate new sensing platforms that obtain data during the assays in a non-destructive manner. Altogether, the studies reviewed in this article show that tissue engineering

technologies to develop these personalized drug screening platforms have a bright future perspective. Therefore, new efforts must point toward integrating patient-derived cells, biofabrication techniques, stimulation systems, and biosensors in personalized organ-on-a-chip preclinical platforms for muscular dystrophies.

Author contributions

JMF-C, XF-G, FV-M, and JR-A conceived this review. JMF-C coordinated the literature search and review design. JMF-C, XF-G, FV-M performed the literature search and wrote the paper. JMF-C generated the figures. JMF-C, XF-G, FV-M revised the manuscript and participated in the discussion with the input of JR-A.

Declaration of conflicting interests

The author(s) declared no potential conflicts of interest with respect to the research, authorship, and/or publication of this article.

Funding

The author(s) disclosed receipt of the following financial support for the research, authorship, and/or publication of this article: The authors acknowledge financial support from the European Research Council program under grants ERC-StG-DAMOC (714317), the Spanish Ministry of Economy and Competitiveness, through the “Severo Ochoa” Program for Centres of Excellence in R&D (SEV-2016-2019) and “Retos de investigación: proyectos I+D+i” (TEC2017-83716-C2-2-R), the CERCA Programme/Generalitat de Catalunya (2014-SGR-1460) and Fundació Bancaria “la Caixa”-Obra Social “la Caixa” (project IBEC-La Caixa Healthy Ageing) to JR-A. JMF-C was awarded with a postdoctoral fellowship (APOSTD/2017/088) from the Generalitat Valenciana, and XF-G was supported by a predoctoral fellowship (BES-2016-076681) from the Ministerio de Economía y Competitividad.

ORCID iDs

Juan M. Fernández-Costa  <https://orcid.org/0000-0002-1854-6082>
 Xiomara Fernández-Garibay  <https://orcid.org/0000-0002-0697-985X>
 Ferran Velasco-Mallorquí  <https://orcid.org/0000-0002-5681-800X>
 Javier Ramón-Azcón  <https://orcid.org/0000-0002-3636-8013>

References

- Mercuri E, Bönnemann CG and Muntoni F. Muscular dystrophies. *Lancet* 2019; 394: 2025–2038.
- Benarroch L, Bonne G, Rivier F, et al. The 2020 version of the gene table of neuromuscular disorders (nuclear genome). *Neuromuscul Disord* 2019; 29: 980–1018.
- Carter JC, Sheehan DW, Prochoroff A, et al. Muscular dystrophies. *Clin Chest Med* 2018; 39: 377–389.
- Vydra DG and Rayi A. *Myotonic dystrophy*. Treasure Island: StatPearls Publishing, 2020.
- Yiu EM and Kornberg AJ. Duchenne muscular dystrophy. *J Paediatr Child Health* 2015; 51: 759–764.
- Mah JK, Korngut L, Fiest KM, et al. A systematic review and meta-analysis on the epidemiology of the muscular dystrophies. *Can J Neurol Sci/J Can des Sci Neurol* 2016; 43: 163–177.
- Verhaart IEC and Aartsma-Rus A. Therapeutic developments for Duchenne muscular dystrophy. *Nat Rev Neurol* 2019; 15: 373–386.
- Datta N and Ghosh PS. Update on muscular dystrophies with focus on novel treatments and biomarkers. *Curr Neurol Neurosci Rep* 2020; 20: 14.
- López Castel A, Overby SJ and Artero R. MicroRNA-based therapeutic perspectives in myotonic dystrophy. *Int J Mol Sci* 2019; 20: 5600.
- Reddy K, Jenquin JR, Cleary JD, et al. Mitigating RNA toxicity in myotonic dystrophy using small molecules. *Int J Mol Sci* 2019; 20: 4017.
- Overby SJ, Cerro-Herreros E, Llamusi B, et al. RNA-mediated therapies in myotonic dystrophy. *Drug Discov Today* 2018; 23: 2013–2022.
- Wouters OJ, McKee M and Luyten J. Estimated research and development investment needed to bring a new medicine to market, 2009–2018. *JAMA* 2020; 323: 844–853.
- Dowden H and Munro J. Trends in clinical success rates and therapeutic focus. *Nat Rev Drug Discov* 2019; 18: 495–496.
- Kankala RK, Wang S-B and Chen A-Z. Microengineered organ-on-a-chip platforms towards personalized medicine. *Curr Pharm Des* 2019; 24: 5354–5366.
- Martinez E, St-Pierre J-P and Variola F. Advanced bioengineering technologies for preclinical research. *Adv Phys X* 2019; 4: 1622451.
- Frontera WR and Ochala J. Skeletal muscle: a brief review of structure and function. *Calcif Tissue Int* 2015; 96: 183–195.
- Chal J and Pourquie O. Making muscle: skeletal myogenesis in vivo and in vitro. *Development* 2017; 144: 2104–2122.
- Mukund K and Subramaniam S. Skeletal muscle: a review of molecular structure and function, in health and disease. *Wiley Interdiscip Rev Syst Biol Med* 2020; 12: e1462.
- Zammit PS. Function of the myogenic regulatory factors Myf5, MyoD, myogenin and MRF4 in skeletal muscle, satellite cells and regenerative myogenesis. *Semin Cell Dev Biol* 2017; 72: 19–32.
- Yin H, Price F and Rudnicki MA. Satellite cells and the muscle stem cell niche. *Physiol Rev* 2013; 93: 23–67.
- Buckingham M. Skeletal muscle progenitor cells and the role of Pax genes. *C R Biol* 2007; 330: 530–533.
- Sanger JW, Chowrashi P, Shaner NC, et al. Myofibrillogenesis in skeletal muscle cells. *Clin Orthop Relat Res* 2002; 403: S153–S162.
- Csapo R, Gumpfenberger M and Wessner B. Skeletal muscle extracellular matrix – what do we know about its composition, regulation, and physiological roles? A narrative review. *Front Physiol* 2020; 11: 1–15.
- Gillies AR and Lieber RL. Structure and function of the skeletal muscle extracellular matrix. *Muscle Nerve* 2011; 44: 318–331.
- Hinds S, Bian W, Dennis RG, et al. The role of extracellular matrix composition in structure and function of bioengineered skeletal muscle. *Biomaterials* 2011; 32: 3575–3583.
- Bushby KMD, Collins J and Hicks D. Collagen type VI myopathies. In: Halper J (ed.) *Progress in heritable soft*

- connective tissue diseases*. Dordrecht, Netherlands: Springer, pp.185–199.
27. Denes LT, Riley LA, Mijares JR, et al. Culturing C2C12 myotubes on micromolded gelatin hydrogels accelerates myotube maturation. *Skelet Muscle* 2019; 9: 17.
 28. Vajanthri KY, Sidu RK and Mahto SK. Micropatterning and alignment of skeletal muscle myoblasts using microflowed plasma process. *Irbm* 2020; 41: 48–57.
 29. Kim J, Leem J, Kim HN, et al. Uniaxially crumpled graphene as a platform for guided myotube formation. *Microsyst Nanoeng* 2019; 5: 53.
 30. Park J, Choi JH, Kim S, et al. Micropatterned conductive hydrogels as multifunctional muscle-mimicking biomaterials: Graphene-incorporated hydrogels directly patterned with femtosecond laser ablation. *Acta Biomater* 2019; 97: 141–153.
 31. Gong HY, Park J, Kim W, et al. A novel conductive and micropatterned PEG-based hydrogel enabling the topographical and electrical stimulation of myoblasts. *ACS Appl Mater Interfaces* 2019; 11: 47695–47706.
 32. Xue J, Wu T, Dai Y, et al. Electrospinning and electrospun nanofibers: methods, materials, and applications. *Chem Rev* 2019; 119: 5298–5415.
 33. Somers SM, Zhang NY, Morrisette-McAlmon JBF, et al. Myoblast maturity on aligned microfiber bundles at the onset of strain application impacts myogenic outcomes. *Acta Biomater* 2019; 94: 232–242.
 34. Yeo M and Kim GH. Micro/nano-hierarchical scaffold fabricated using a cell electrospinning/3D printing process for co-culturing myoblasts and HUVECs to induce myoblast alignment and differentiation. *Acta Biomater* 2020; 107: 102–114.
 35. Ribeiro S, Gomes AC, Etxebarria I, et al. Electroactive biomaterial surface engineering effects on muscle cells differentiation. *Mater Sci Eng C* 2018; 92: 868–874.
 36. Ribeiro C, Sencadas V, Correia DM, et al. Piezoelectric polymers as biomaterials for tissue engineering applications. *Colloids Surf B Biointerfaces* 2015; 136: 46–55.
 37. Kim J, Kim W and Kim G. Scaffold with micro/nanoscale topographical cues fabricated using E-field-assisted 3D printing combined with plasma-etching for enhancing myoblast alignment and differentiation. *Appl Surf Sci* 2020; 509: 145404.
 38. Du W, Hong S, Scapin G, et al. Directed collective cell migration using three-dimensional bioprinted micropatterns on thermoresponsive surfaces for myotube formation. *ACS Biomater Sci Eng* 2019; 5: 3935–3943.
 39. Shi X, Ostrovidov S, Zhao Y, et al. Microfluidic spinning of cell-responsive grooved microfibers. *Adv Funct Mater* 2015; 25: 2250–2259.
 40. Ebrahimi M, Ostrovidov S, Salehi S, et al. Enhanced skeletal muscle formation on microfluidic spun gelatin methacryloyl (GelMA) fibres using surface patterning and agrin treatment. *J Tissue Eng Regen Med* 2018; 12: 2151–2163.
 41. Nakayama KH, Quarta M, Paine P, et al. Treatment of volumetric muscle loss in mice using nanofibrillar scaffolds enhances vascular organization and integration. *Commun Biol* 2019; 2: 170.
 42. Lai ES, Huang NF, Cooke JP, et al. Aligned nanofibrillar collagen regulates endothelial organization and migration. *Regen Med* 2012; 7: 649–661.
 43. Ostrovidov S, Salehi S, Costantini M, et al. 3D Bioprinting in skeletal muscle tissue engineering. *Small* 2019; 15: 1–14.
 44. Seyedmahmoud R, Çelebi-Saltik B, Barros N, et al. Three-dimensional bioprinting of functional skeletal muscle tissue using gelatinmethacryloyl-alginate bioinks. *Micromachines* 2019; 10: 679.
 45. Mestre R, Patiño T, Barceló X, et al. Force modulation and adaptability of 3D-bioprinted biological actuators based on skeletal muscle tissue. *Adv Mater Technol* 2019; 4: 1800631.
 46. Vandenburg H, Shansky J, Benesch-Lee F, et al. Drug-screening platform based on the contractility of tissue-engineered muscle. *Muscle Nerve* 2008; 37: 438–447.
 47. Distler T, Solisito AA, Schneiderei D, et al. 3D printed oxidized alginate-gelatin bioink provides guidance for C2C12 muscle precursor cell orientation and differentiation via shear stress during bioprinting. *Biofabrication* 2020; 12: 045005.
 48. Kim WJ and Kim GH. 3D bioprinting of functional cell-laden bioinks and its application for cell-alignment and maturation. *Appl Mater Today* 2020; 19: 100588.
 49. Kim WJ, Jang CH and Kim GH. A Myoblast-laden collagen bioink with fully aligned Au nanowires for muscle-tissue regeneration. *Nano Lett* 2019; 19: 8612–8620.
 50. García-Lizarribar A, Fernández-Garibay X, Velasco-Mallorquí F, et al. Composite biomaterials as long-lasting scaffolds for 3D bioprinting of highly aligned muscle tissue. *Macromol Biosci* 2018; 18: 1800167.
 51. Costantini M, Testa S, Mozetic P, et al. Microfluidic-enhanced 3D bioprinting of aligned myoblast-laden hydrogels leads to functionally organized myofibers in vitro and in vivo. *Biomaterials* 2017; 131: 98–110.
 52. Mozetic P, Giannitelli SM, Gori M, et al. Engineering muscle cell alignment through 3D bioprinting. *J Biomed Mater Res—Pt A* 2017; 105: 2582–2588.
 53. Chen H, Zhong J, Wang J, et al. Enhanced growth and differentiation of myoblast cells grown on E-jet 3D printed platforms. *Int J Nanomedicine* 2019; 14: 937–950.
 54. Kalman B, Monge C, Bigot A, et al. Engineering human 3D micromuscles with co-culture of fibroblasts and myoblasts. *Comput Methods Biomech Biomed Eng* 2015; 5842: 1–2.
 55. Costantini M, Testa S, Fornetti E, et al. Engineering muscle networks in 3D gelatin methacryloyl hydrogels: influence of mechanical stiffness and geometrical confinement. *Front Bioeng Biotechnol* 2017; 5: 1–8.
 56. Ortega MA, Fernández-Garibay X, Castaño AG, et al. Muscle-on-a-chip with an on-site multiplexed biosensing system for: in situ monitoring of secreted IL-6 and TNF- α . *Lab Chip* 2019; 19: 2568–2580.
 57. Hernández-Albors A, Castaño AG, Fernández-Garibay X, et al. Microphysiological sensing platform for an in-situ detection of tissue-secreted cytokines. *Biosens Bioelectron X* 2019; 2: 100025.
 58. Wan L, Flegle J, Ozdoganlar B, et al. Toward vasculature in skeletal muscle-on-a-chip through thermo-responsive sacrificial templates. *Micromachines* 2020; 11: 907.
 59. Christensen RK, Von Halling Laier C, Kiziltay A, et al. 3D printed hydrogel multiassay platforms for robust generation of engineered contractile tissues. *Biomacromolecules* 2020; 21: 356–365.

60. Singh D, Nayak V and Kumar A. Proliferation of myoblast skeletal cells on three-dimensional supermacroporous cryogels. *Int J Biol Sci* 2010; 6: 371–381.
61. Velasco-Mallorqui F, Fernández-Costa JM, Neves L, et al. New volumetric CNT-doped gelatin–cellulose scaffolds for skeletal muscle tissue engineering. *Nanoscale Adv* 2020; 2: 2885–2896.
62. Kankala RK, Zhao J, Liu CG, et al. Highly porous micro-carriers for minimally invasive in situ skeletal muscle cell delivery. *Small* 2019; 15: 1–15.
63. Bettadapur A, Suh GC, Geisse NA, et al. Prolonged culture of aligned skeletal myotubes on micromolded gelatin hydrogels. *Sci Rep* 2016; 6: 1–14.
64. Tanaka N, Ota H, Fukumori K, et al. Micro-patterned cell-sheets fabricated with stamping-force-controlled micro-contact printing. *Biomaterials* 2014; 35: 9802–9810.
65. Lee H, Ju YM, Kim I, et al. A novel decellularized skeletal muscle-derived ECM scaffolding system for in situ muscle regeneration. *Methods* 2020; 171: 77–85.
66. Kim W, Lee H, Lee J, et al. Efficient myotube formation in 3D bioprinted tissue construct by biochemical and topographical cues. *Biomaterials* 2020; 230: 119632.
67. Badylak SF, Freytes DO and Gilbert TW. Extracellular matrix as a biological scaffold material: structure and function. *Acta Biomater* 2009; 5: 1–13.
68. Bédier A, Braschler T, Peric O, et al. A compressible scaffold for minimally invasive delivery of large intact neuronal networks. *Adv Healthc Mater* 2015; 4: 301–312.
69. Wu X, Liu Y, Li X, et al. Preparation of aligned porous gelatin scaffolds by unidirectional freeze-drying method. *Acta Biomater* 2010; 6: 1167–1177.
70. Wu J, Zhao Q, Sun J, et al. Preparation of poly(ethylene glycol) aligned porous cryogels using a unidirectional freezing technique. *Soft Matter* 2012; 8: 3620.
71. Torii R, Vellio R-I, Hodgson D, et al. Modelling multi-scale cell–tissue interaction of tissue-engineered muscle constructs. *J Tissue Eng* 2018; 9: 204173141878714.
72. Smith AST, Passey S, Greensmith L, et al. Characterization and optimization of a simple, repeatable system for the long term in vitro culture of aligned myotubes in 3D. *J Cell Biochem* 2012; 113: 1044–1053.
73. Wang J, Khodabukus A, Rao L, et al. Engineered skeletal muscles for disease modeling and drug discovery. *Biomaterials* 2019; 221: 119416.
74. Zhang D, Yan K, Zhou J, et al. Myogenic differentiation of human amniotic mesenchymal cells and its tissue repair capacity on volumetric muscle loss. *J Tissue Eng* 2019; 10: 204173141988710.
75. Powell CA, Smiley BL, Mills J, et al. Mechanical stimulation improves tissue-engineered human skeletal muscle. *Am J Physiol Cell Physiol* 2002; 283: 1557–1565.
76. Mills RJ, Parker BL, Monnot P, et al. Development of a human skeletal micro muscle platform with pacing capabilities. *Biomaterials* 2019; 198: 217–227.
77. Madden L, Juhas M, Kraus WE, et al. Bioengineered human myobundles mimic clinical responses of skeletal muscle to drugs. *Elife* 2015; 2015: 1–14.
78. Rao L, Qian Y, Khodabukus A, et al. Engineering human pluripotent stem cells into a functional skeletal muscle tissue. *Nat Commun* 2018; 9: 126.
79. Khodabukus A, Madden L, Prabhu NK, et al. Electrical stimulation increases hypertrophy and metabolic flux in tissue-engineered human skeletal muscle. *Biomaterials* 2019; 198: 259–269.
80. Bakooshli MA, Lippmann ES, Mulcahy B, et al. A 3D culture model of innervated human skeletal muscle enables studies of the adult neuromuscular junction. *Elife* 2019; 8: 1–29.
81. Kim JH, Seol YJ, Ko IK, et al. 3D bioprinted human skeletal muscle constructs for muscle function restoration. *Sci Rep* 2018; 8: 1–15.
82. Gholobova D, Gerard M, Decroix L, et al. Human tissue-engineered skeletal muscle: a novel 3D in vitro model for drug disposition and toxicity after intramuscular injection. *Sci Rep* 2018; 8: 1–14.
83. Choi Y-J, Jun Y-J, Kim DY, et al. A 3D cell printed muscle construct with tissue-derived bioink for the treatment of volumetric muscle loss. *Biomaterials* 2019; 206: 160–169.
84. Okano T and Matsuda T. Tissue engineered skeletal muscle: preparation of highly dense, highly oriented hybrid muscular tissues. *Cell Transplant* 1998; 7: 71–82.
85. Vandenburg HH, Karlisch P and Farr L. Maintenance of highly contractile tissue-cultured avian skeletal myotubes in collagen gel. *Vitr Cell Dev Biol* 1988; 24: 166–174.
86. Khodabukus A and Baar K. Factors that affect tissue-engineered skeletal muscle function and physiology. *Cells Tissues Organs* 2016; 202: 159–168.
87. Chiron S, Tomczak C, Duperray A, et al. Complex interactions between human myoblasts and the surrounding 3D fibrin-based matrix. *PLoS One* 2012; 7: 2–9.
88. Rudolf R, Khan MM, Labeit S, et al. Degeneration of neuromuscular junction in age and dystrophy. *Front Aging Neurosci* 2014; 6: 99.
89. Ramade A, Legant WR, Picart C, et al. Microfabrication of a platform to measure and manipulate the mechanics of engineered microtissues. In: *Methods in cell biology*. London: Elsevier Inc., pp.191–211.
90. Vandenburg H, Shansky J, Benesch-Lee F, et al. Automated drug screening with contractile muscle tissue engineered from dystrophic myoblasts. *FASEB J* 2009; 23: 3325–3334.
91. Serena E, Zatti S, Reghelin E, et al. Soft substrates drive optimal differentiation of human healthy and dystrophic myotubes. *Integr Biol (Camb)* 2010; 2: 193–201.
92. Maffioletti SM, Sarcar S, Henderson ABH, et al. Three-dimensional human iPSC-derived artificial skeletal muscles model muscular dystrophies and enable multilineage tissue engineering. *Cell Rep* 2018; 23: 899–908.
93. Agrawal G, Aung A and Varghese S. Skeletal muscle-on-a-chip: an in vitro model to evaluate tissue formation and injury. *Lab Chip* 2017; 17: 3447–3461.
94. Osaki T, Uzel SGM and Kamm RD. On-chip 3D neuromuscular model for drug screening and precision medicine in neuromuscular disease. *Nat Protoc* 2020; 15: 421–449.

